A sedimentological and geochemical study of stromatolitic carbonate rocks of the Mesoarchaean Pongola Supergroup, South Africa, and inferred environmental conditions

Dissertation zur Erlangung des Doktorgrades
an der Fakultät für Geowissenschaften
der Ludwig-Maximilians-Universität München

Vorgelegt von
Mehrnaz Siahi
Shahrood, Iran

München im Februar 2017

Erstgutachter: Prof. Dr. Ernst Hegner

Zweitgutachter: Prof. Dr. Axel Hofmann

Tag der mündlichen Prüfung: 1. Februar 2017

Tag des Antrags auf Zulassung: 10. November 2016

Abstract

Chemical sediments, such as carbonate rocks, iron formations and cherts, record physico-chemical conditions of the hydrosphere, atmosphere, and biosphere at the time of their formation. In order to reconstruct the depositional environment, chemical composition of ancient seawater, and atmosphere-biosphere evolution, sedimentological, mineralogical, isotope and trace-element geochemical studies of the c. 3-billion-years-old microbial carbonates of the Pongola Supergroup were undertaken. Sedimentary carbonates are extremely rare in the Palaeo- to Mesoarchaean Eras as compared to Neoarchaean and younger rock records. A brief review of the occurrences and characteristics of Archaean carbonate rocks revealed that they display specific characteristics in terms of thickness, mineralogy, texture and diversity in microbial structures, which are unique in each Era.

Stromatolitic carbonate rocks of the Chobeni Formation of the Nsuze Group, Pongola Supergroup, were studied in the White Mfolozi River valley of KwaZulu-Natal in South Africa. The 3.0-2.9 Ga old Pongola Supergroup was deposited on continental crust of the southeastern Kaapvaal Craton and is one of the oldest well-preserved successions of epicratonic volcanic and sedimentary rocks. Four carbonate-bearing stratigraphic horizons ranging from 2 to 28 m in thickness were encountered in the siliciclastic-dominated Chobeni Formation, and three of them were studied in detail. Sedimentological and facies analyses of carbonate and associated siliciclastic rocks suggest deposition in a tide-dominated, shallow-marine environment. In total, fourteen facies were identified and grouped into three facies assemblages, which formed in subtidal, intertidal and supratidal sub-environments under the influence of cyclic variations of Mesoarchaean sea level. Various types of microbialites were observed in rocks of different sedimentary sub-environments. Field observations, petrographic studies and mineralogical analyses revealed that microorganisms were responsible for microbialite formation by inducing carbonate precipitation via metabolic processes, *in- situ* carbonate precipitation and, to a lesser extent, by trapping and binding of sediments.

Well-preserved ooids with a variety of fabrics (concentric, radial, radial-concentric and micritic) and preserving carbonaceous matter were discovered that merited detailed petrographic and mineralogical-geochemical analyses. NanoSIMS ion mapping and Raman spectroscopic imaging confirmed the biogenicity of carbonaceous matter, and along with scanning electron microscopy, the distribution of mineral and elemental phases within ooids was determined. Based on major and trace-element data obtained by electron microprobe and

LA-ICP-MS, the absence/ presence of carbonaceous matter, the level of fabric preservation in ooids with different fabrics, and the similarity of Chobeni ooids with their modern counterparts, a combination of both biogenic and non-biogenic processes (environmental conditions) are suggested responsible for ooid formation.

For better constraining the degree of alteration of the rocks and investigating their suitability as a geochemical proxy for the chemical characteristics of the depositional environment and Mesoarchaean seawater, carbon (C), oxygen (O) and Strontium (Sr) isotopic analyses were undertaken on selected carbonate samples. These data were compared and interpreted together with their major and trace-element geochemical compositions. The Sr, Fe and Mn contents of the carbonate samples from the different sections of the main, middle and upper carbonate are variable. The main section carbonate is characterized by relatively low FeO and MnO concentrations, higher SrO content, and higher C and O isotopic values as compared to those of the upper and middle sections, which indicates a less pronounced diagenetic and metamorphic overprint. The lower $\delta^{18}O$ values in the upper and middle carbonate sections are probably a result of meteoric diagenesis, alteration by hydrothermal/ metamorphic fluids and isotopic exchange with clastic material. The highest $\delta^{13}C$ value of these carbonates (2.4 $‰_{PDB}$) is interpreted to represent the value closest to that of coeval seawater. $^{87}Sr/^{86}Sr$ ratios correlate positively with the concentration of siliciclastic detritus. The least radiogenic $^{87}Sr/^{86}Sr$ ratio of ca. 0.708 is higher than the ratio proposed for a depleted mantle-buffered Archaean ocean. The elevated ratio in the sample may be due to overprinting by fluids with highly radiogenic Sr from intercalated shales during diagenetic/ metamorphic processes, yet, it could well be a primary signal recording radiogenic continental Sr derived from riverine input into the shallow epicontinental Pongola Sea.

Shale-normalized rare earth element and yttrium (REE+Y) distribution patterns and positive shale-normalised La, Gd and Y anomalies are similar to Archaean marine chemical precipitates. Relatively subdued marine signals along with a convex upward pattern of the middle REE may be a result of organic matter complexation, and fractionation during estuarine mixing, suggesting that the Pongola carbonates were deposited in a restricted marine setting with riverine input and variable exchange to the open-ocean as also indicated by their Sr isotope composition. The presence of a slightly negative Ce anomaly and $Th/U > 2$ in some samples may indicate mildly oxygenated conditions in line with the likely presence of photosynthetic microorganisms responsible for microbialite formation.

Zusammenfassung

Chemische Sedimentgesteine (z.B. Karbonate, Eisensteine, Cherts) können als Anzeiger der physikalisch-chemischen Bedingungen der Hydrosphäre, Atmosphäre und Biosphäre zum Zeitpunkt der Ablagerung interpretiert werden. Sedimentologische, mineralogische, sowie geochemische Untersuchungen wurden an 3 Milliarden Jahre alten mikrobiellen Karbonaten durchgeführt, um Ablagerungsmilieu und chemische Eigenschaften des Meerwassers zu rekonstruieren. Sedimentäre Karbonate paläo- und mesoarchaischen Alters sind im Vergleich zu jüngeren Abfolgen äusserst selten. Ausserdem zeigen archaische Karbonate durch die Erdgeschichte hindurch Unterschiede in ihrer Mächtigkeit, Mineralogie, Textur und Diversifizierung mikrobieller Strukturen.

Stromatolithische Karbonate der Chobeni Formation (Nsuze Gruppe, Pongola Supergruppe) wurden im Tal des White Mfolozi Flusses in KwaZulu-Natal (Südafrika) untersucht. Die 3.0-2.9 Milliarden Jahre alte Pongola Supergruppe wurde auf kontinentaler Kruste des südöstlichen Kaapvaal Kratons abgelagert und ist eine der ältesten intrakontinentalen Vulkanit-/ Sedimentabfolgen. Drei karbonatführende Horizonte der Chobeni Formation mit einer Mächtigkeit von 2 bis 28 Metern wurden detailliert untersucht. Eine sedimentologische Faziesanalyse der Karbonate und damit assoziierten siliziklastischen Gesteinen zeigt ein flachmarines Gezeitenmilieu an. Insgesamt wurden 14 Faziestypen unterschieden und in drei Faziesassoziationen gruppiert, welche unter dem Einfluss von Meeresspiegelschwankungen in sub-, inter-, und supratidalen Milieus abgelagert wurden. Verschiedene Mikrobialithtypen unterschiedlicher Ablagerungsräume wurden angetroffen. Deren Ursprung ist auf mikrobielle Prozesse zurückzuführen, welche Karbonatausfällungen sowie Anbindung detritischer Substanz verursachten.

Guterhaltene Ooide unterschiedlicher Texturen und mit organischer Substanzführung wurden beobachtet und im Detail untersucht. Element- und Mineralkartierungen mit Hilfe von Elektronenmikroskop, NanoSIMS und Raman Spektroskop erlaubten eine Charakterisierung von Mineraleinschlüssen und zeigten eine wahrscheinlich biogene Herkunft der organischen Substanz an. Eine Kombination von biogenen und abiogenen, milieubedingten Prozessen kann die Herkunft der Ooide erklären.

Eine Analyse der C, O, und Sr Isotopenverhältnisse in Kombination mit Haupt- und Spurenelementanalysen (z.B. Sr, Fe und Mn) ermöglichte eine Abschätzung des Alterationsgrades der Gesteine. Sekundäre Überprägung durch meteorische Diagenese,

Alteration durch hydrothermale/metamorphe Fluide, und Alteration durch Wechselwirkung mit klastischem Detritus ist im Hauptkarbonathorizont am geringsten. Der höchste $\delta^{13}C$ Wert (2.4 $‰_{PDB}$) von Karbonaten aus diesem Bereich spiegelt am ehesten die isotopische Zusammensetzung des Meerwassers zum Ablagerungszeitraum wider. Sr Isotopenverhältnisse korrelieren positiv mit der Konzentration siliziklastischen Detritus. Das am wenigsten radiogene $^{87}Sr/^{86}Sr$ Verhältnis (0.708) ist im Vergleich zum angenommenen Wert des archaischen Meerwasssers relativ hoch und weist sowohl auf eine diagenetische/metamorphe Überprägung, als auch auf einen hohen Anteil kontinentalen und radiogenen Sr-Eintrages in das flachmarine epikontinentale Pongola Meer hin.

Pelit-normierte seltene Erdelementmuster sind marinen chemischen Sedimentgesteinen aus dem Archaikum sehr ähnlich. Ein marines Signal ist jedoch nur schwach ausgeprägt, da positive La, Gd und Y Anomalien relativ klein sind. Dies mag an Komplexbildung der seltenen Erden mit organischer Substanz und deren Fraktionierung bei Mischung mit ästuarinen Wassermassen liegen. Ein eingeschränkt marines Milieu mit einem bedeutenden Eintrag von Frischwasser ist somit wahrscheinlich. Das Vorhandensein einer schwach ausgeprägten negativen Ce Anomalie und $Th/U > 2$ in manchen Proben deutet auf schwach oxidierende Bedingungen. Diese Beobachtungen unterstützen die Interpretation, daβ photosynthetische Mikroorganismen die Mikrobialithbildung in der Pongola Supergruppe verursacht haben.

Acknowledgements

I am deeply grateful to many people for their long-lasting support and encouragement, which were invaluable for the successful completion of this thesis. Here, I would like to express my sincere gratitude to my supervisor Prof. Ernst Hegner, and my co-supervisors, Prof. Axel Hofmann and Dr. Sharad Master for their support through hours of fruitful discussion, their intellectual guidance and patience. I am grateful to Prof. Axel Hofmann for his guidance in the field and Prof. Ernst Hegner for support in the radiogenic isotope laboratory and his mentorship.

Thanks to Dr. Christoph Mayer and Dr. Markus Oehlerich (Ludwig-Maximilians-University, Munich) for assisting with stable isotope measurements. Special thanks to Dr. Axel Gerdes (Goethe-University Frankfurt), Dr. Christian Reinke and Mrs Eve Kroukamp (University of Johannesburg), Prof. Allan Wilson and Mr. Marlin Patchappa (University of the Witwatersrand), Dr. Carsten Müller and Mr. Johann Lugmeier (Technical University Munich) for assisting with a variety of a analytical instrumentation including LA-ICP-MS, XRF, XRD, SEM, microprobe, and Nano-SIMS. I am also grateful to Prof. Roger Gibson, School of Geosciences, University of the Witwatersrand, for providing office space during research in South Africa.

I would like to take this opportunity to thank the organization who provided scientific and financial support to make this work possible. I am grateful to the National Research Foundation of South Africa (NRF) for supporting field work of my doctoral research in South Africa, and the German Academic Exchange Service (DAAD) for financial support during stays in Germany.

I also extend my sincere thanks to colleagues and friends in the Geology Departments of Ludwig-Maximilians-University and the University of the Witwatersrand, who helped me to confront all the difficulties of life during my study and who gave me advice on my research work.

Table of Contents

Chapter 1: Introduction

Carbonate rocks in Palaeo- to Mesoarchaean successions are not as widespread as in Neoarchaean strata. Different factors were responsible for the rise of carbonate precipitation in Neoarchaean as compared to earlier times. A higher rate of continental crustal growth and stabilization of the first cratons in the Neoarchaean followed by a decline of atmospheric CO_2 and CH_4 due to increased subaerial weathering, which led to a decline of surface temperature, provided suitable environments for the appearance of photosynthetic microorganisms. The rise of atmospheric oxygen played a major role in changing oceanic chemistry and removal of inhibitors of carbonate precipitation (Lowe and Tice, 2004).

Mesoarchaean stromatolitic carbonate precipitates are some of the oldest marine carbonates known. They are found in the Pongola Supergroup of South Africa, Kaapvaal Craton, and several greenstone belts of the Superior Province, Canadian Shield. Stromatolitic carbonates are defined as laminated structures of biological origin. They formed due to the interaction of microbes and sediment at the interface of the atmosphere and hydrosphere. They have the potential to record important information on the early Earth ocean chemistry, atmospheric conditions and the habitat of early life, as chemical and biochemical precipitates may encode isotopic and chemical properties of surrounding environment at the time of their formation.

The focus of this study is a detailed sedimentological and geochemical analysis of Mesoarchaean carbonate smples from the Pongola Supergroup in order to reconstruct the depositional environment, delineate mechanisms of carbonate precipitation and the chemical composition of seawater. This study provides insights into the geochemical evolution of the ocean and atmosphere and the habitat of early life in the Mesoarchaean.

The 3.0-2.9 Ga old (Hegner et al., 1994; Mukasa et al., 2013) Pongola Supergroup of South Africa was deposited on the southeastern Kaapvaal Craton and is one of the oldest well-preserved successions of epicratonic volcanic and sedimentary rocks (Fig. 1). This succession unconformably rests on a granite-greenstone basement. It crops out in inliers surrounded by younger sedimentary cover of Karoo rocks in an area approximately 100 km wide and 275 km long in the Mpumalanga and KwaZulu-Natal provinces of South Africa and in Swaziland. The Pongola Supergroup is comprised of two stratigraphic units, a lower mainly volcanic Nsuze Group and an overlying mainly sedimentary Mozaan Group (e.g. Matthews, 1967; Weilers, 1990; Dixon, 2004).

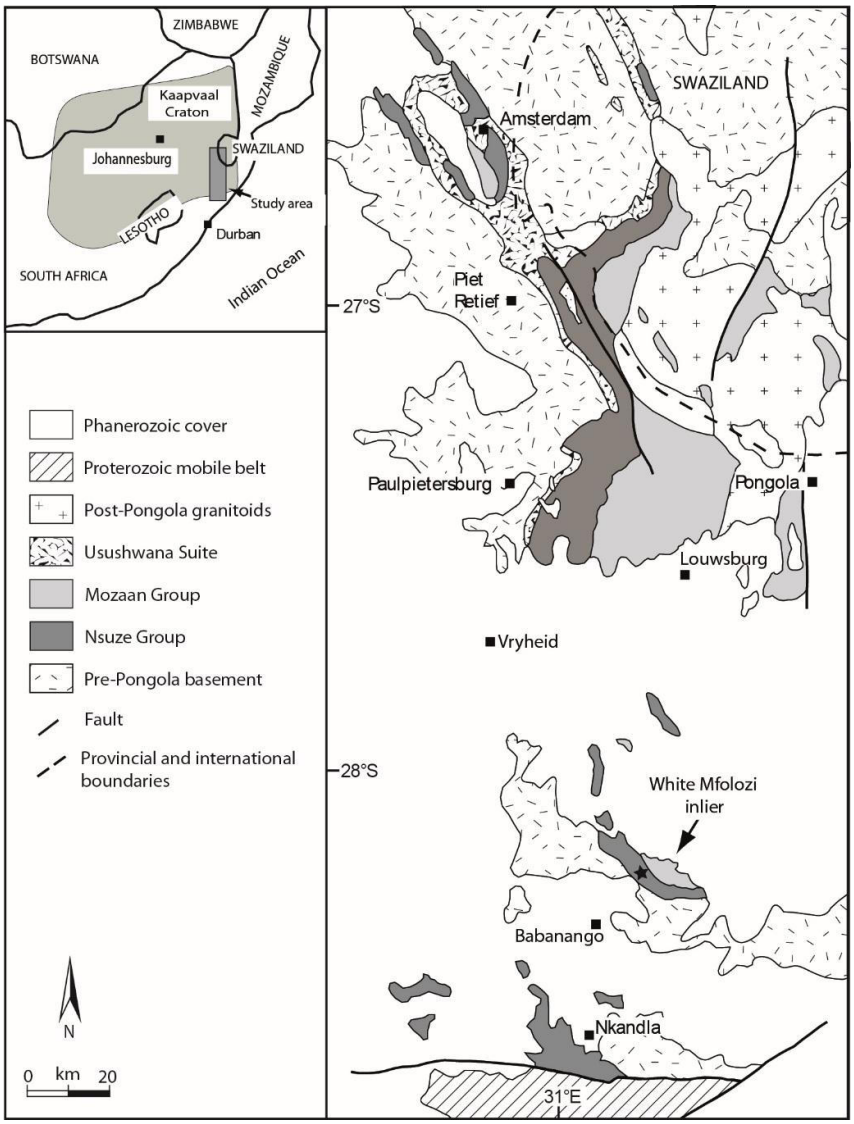

Fig. 1. Geological sketch map of the distribution of the Pongola Supergroup in South Africa and Swaziland and location of the study area in the White Mfolozi inlier (modified after Gold, 2006). Asterisk shows locality of the study area (White Mfolozi inlier).

Sedimentary carbonates are rare in the Pongola basin. Several horizons of dolomite with well-developed stromatolites occur in the Chobeni Formation of the Nsuze Group in the White Mfolozi inlier. Detailed sedimentological and microfacies analyses are a prerequisite to delineate depositional environments of carbonate rocks. Based on sedimentary structures and diverse stromatolite morphologies, these dolomites have been interpreted to have formed in a shallow, tide-dominated marine setting (Beukes and Lowe, 1989; this study).

The analysis of C, O, S and Sr isotopes in association with trace-elements and rare earth element (REE) + yttrium (Y) distributions in carbonate samples provide information on the fluxes into the ocean (continental input vs. oceanic hydrothermal input) and reveal palaeoenvironmental conditions, diagenetic processes, water depth and oxygenation, changes in continental weathering, tectonic process, terrestrial evolution, palaeogeography and depositional models (e.g. Veizer et al., 1990; Kamber and Webb, 2001; Allwood et al., 2010). As a result, detailed geochemical investigations of Archaean stromatolitic carbonates are helpful for deciphering isotopic and chemical signatures and processes in early Earth oceans.

1.1 Previous studies

No detailed stratigraphic and geochemical work on the Nsuze carbonate rocks in the White Mfolozi inlier have been undertaken to date, except for limited stratigraphic studies of one carbonate section (Beukes and Lowe, 1989) and geochemical studies using a limited suite of samples (Veizer et al., 1990; Bolhar et al., 2015).

Matthews (1967) was first to map Pongola strata within the White Mfolozi inlier. He recognized compositionally distinct lower and upper stratigraphical units and correlated them with the Nsuze and Mozaan Groups of the Pongola Supergroup. Mason and Von Brunn (1977) and Von Brunn and Mason (1977) examined parts of the quartzite-dolomite zone of the Nsuze Group in the White Mfolozi River valley. They suggested that the presence of sedimentary structures including lenticular, flaser and wavy bedding, herringbone cross- lamination and ripple bedforms indicate that the siliciclastic and carbonate sediments were deposited in a tide-dominated depositional environment of an epeiric sea that gave rise to several coarsening- and fining-upward sequences. They noted the presence of stromatolites and classified them according to their morphologies to the space-linked hemispheroids (LLH-S), close-linked hemispheroids (LLH-C) and vertically stacked hemispheroids (SH) types. They considered a significant role of volcanic activity for the provision of inorganic nutrients that made the environment favourable for microbial growth.

Beukes and Lowe (1989) re-examined part of the stromatolitic dolomite succession and suggested that stromatolites were formed in a range of shallow, tidal settings. The depositional environments were regarded as having controlled the diverse morphologies of stromatolites. The stromatolites were suggested to have formed as a result of activities of filamentous,

oxygen-producing, photoautotrophic cyanobacteria. Since the sedimentological study of Beukes and Lowe (1989), no recent work has been undertaken on these unique carbonate rocks.

A restricted number of carbonate samples of the Nsuze Group were analysed for C, O, and Sr isotopes. Several studies of these carbonate rocks revealed that their $\delta^{13}C$ signature is similar to that of Phanerozoic carbonates and that they provide the primary isotopic composition of their oceanic bicarbonate precursors (Perry and Tan, 1972; Schidlowski et al., 1983). Furthermore, Veizer (1983) proposed that the high $^{87}Sr/^{86}Sr$ ratios are indicative of a non-marine depositional environment. Veizer et al (1990) re-examined these carbonate rocks and suggested that their isotopic and chemical signatures were overprinted by low-grade metamorphism, which led to an increase in their $^{87}Sr/^{86}Sr$ ratios, while recrystallization at elevated temperatures mostly did not affect their $\delta^{13}C$ values. There is a general agreement that the light $\delta^{18}O$ values of ca. -20 ‰ PDB in the carbonate rocks resulted from pervasive meteoric diagenesis and metamorphic overprint (Perry and Tan, 1972; Schidlowski et al., 1983; Veizer et al., 1990). The original carbonate minerals of the Pongola carbonate rocks was suggested to have been aragonite based on the presence of elevated Sr contents of ~ 220 + 120/- 80 ppm in dolostones (Veizer et al., 1990). Precambrian carbonate rocks with predominant dolomite mineralogy have higher Fe and Mn contents compared to their Phanerozoic counterparts at a similar degree of preservation. This finding may be related to post-depositional alteration, and major volcanic input enriched in these elements into the coeval seawater. It has been suggested that chemical precipitates such as carbonates with higher amounts of Fe and Mn and little radiogenic Sr indicate intense interaction between anoxic seawater and mantle-derived rocks (e.g. Veizer et al., 1989; Veizer et al., 1990).

A major and trace-element study of a limited number of carbonate rock samples of the Nsuze Group by Bolhar et al. (2015) revealed that their deposition probably took place in an anoxic shallow-water epicontinental basin with variable exchange with the open-ocean and dominant fluvial and minor high-temperature hydrothermal input. A Pb isotopic analysis indicated a widespread, tectono-thermal or fluid percolation event at around 2.4 Ga. Modelling of Pb isotopic data and reported Sr and Nd isotopic data (Veizer et al., 1990; Eglington et al., 2003; Alexander et al., 2008) showed that the radiogenic Pb isotopic compositions were derived from evolved continental material with elevated U/Pb ratios.

1.2 Aims and objectives

This study has the following main objectives:

(1) Sedimentological and microfacies analyses of carbonate rocks of the Nsuze Group from different sections in the White Mfolozi inlier to reconstruct their depositional environments and to shed light on Mesoarchaean surface processes influencing the habitat of early life.

(2) Macro- and microscopic study of the diverse suite of microbialites to determine the influence of environmental conditions and biological controls on microbialite formation and morphology.

(3) Investigation of the mineralogy, isotope and rare earth element geochemistry of carbonate rocks of the Nsuze Group to evaluate the complex diagenetic/ metamorphic history and to identify the most primary carbonate material. The geochemical composition of the most pristine carbonate rocks will assist to delineate their possible precipitation mechanisms, physico-chemical conditions of the seawater, and hydrothermal vs. riverine input into the basin. This will expand our understanding of Archaean ocean chemistry.

1.3 Analytical methodology

The various analytical methods are briefly summarized below. Analytical protocols are discussed in more detail in the different chapters of this thesis.

a) Field work: Field studies included detailed, layer-by-layer stratigraphic measurements of several different carbonate sections. Sampling of key lithologies was undertaken by carefully avoiding destruction of rock faces.

b) Microscopy and microstructure analyses: The carbonate texture and microstructure of samples were inspected with binocular and polarizing petrographic microscopes. Microfacies analyses included the inspection of structures and textures of sample components in polished slabs and thin sections on the centimetre to micron scale, using transmitted and reflected light.

c) Scanning Electron Microscopy (SEM) and X-ray Diffraction (XRD) analyses for determination of mineral assemblage: The mineralogical composition of the carbonate rock samples was determined with a Tescan SEM equipped with an Oxford INCA Energy-Dispersive Spectrometer (EDS) that provided qualitative element compositions and element

distribution maps of the samples. XRD analysis of bulk samples was performed with a Panalytical X-PertPro series X-ray diffractometer at the University of Johannesburg.

Laser-Raman Micro-Spectroscopy and Nano Secondary Ion Mass Spectrometry (NanoSIMS) for mineral and elemental identification and spatial distribution: The distribution of carbonaceous matter and associated minerals in selected samples was identified by Raman Spectroscopy. Raman analyses were carried out with a WITec alpha 300R Raman spectroscope configured with a frequency-doubled Nd-YAG laser (wavelength 532 nm) at the University of Johannesburg. Elemental maps at the nanometre scale were acquired with a Cameca NanoSIMS 50L at the Technical University of Munich on drilled samples from selected thin sections following Raman analysis.

Electron Probe Micro-Analyzer (EPMA) and X-Ray Fluorescence Spectrometry (XRF) for major elements analysis: Quantitative determination of major element compositions of carbonate components was carried out by means of a Cameca SX-100 EPMA on selected thin sections and XRF on bulk sample powders using a PANalytical MagiX PRO wavelength-dispersive XRF spectrometer at the University of Johannesburg.

Inductively-Coupled Plasma Mass Spectrometry (ICP-MS) and Laser-Ablation (LA) ICP-MS analyses of trace and rare earth elements: Trace-elements were determined at the School of Geosciences, University of the Witwatersrand, using a Perkin Elmer Sciex ELAN DRC-e calibrated with primary standard solutions and validated with certified rock reference materials. LA-ICP-MS was used for *in-situ* trace-element measurements in selected thin sections at the University of Frankfurt, Germany.

Carbon, Oxygen and Strontium isotopic analyses: The isotopic compositions of these elements were determined at the Isotope Laboratory of the Dept. of Earth and Environmental Sciences at Ludwig-Maximilians-University. The stable isotopes were measurend on microfacies-specific carbonate samples using an isotope ratio mass spectrometer. Sr isotopic compositions were determined on selected samples using a thermal ionisation mass spectrometer.

1.4 Outline of thesis and scientific contributions of co-authors

This thesis consists of six chapters. The first chapter "Introduction" provides general information regarding the geology of the study area, previous work, goals of this research and methodologies that were used for approaching those goals.

In the second chapter "A review of Archaean shallow-water carbonate rocks" the occurrence, age, mineralogy/ geochemistry, stratigraphic relationships, and palaeontology of Archaean carbonate rocks are reviewed. The chapter aims to understand if differences existed in carbonate deposition through Archaean times, and to shed light on causative factors, including tectonic development, change in seawater composition and atmospheric/ biological evolution.

Chapter three "Sedimentology and facies analysis of Mesoarchaean stromatolitic carbonate rocks of the Pongola Supergroup, South Africa" provides a detailed sedimentological and facies analysis of three stratigraphic sections in the White Mfolozi inlier. A detailed study of microbialites with a variety of morphologies and sizes along with sedimentary structures was used as a tool for deciphering sub-environments. In total fifteen facies were subdivided into three facies assemblages. Various types of microbialites were found in different sedimentary sub-environments and range from laminated (stratiform, domal and conical/ columnar stromatolites; oncoids) to structureless lenticular-domal types. Variations in morphologies, macro-fabric, and size of microbialites suggest the presence of distinct assemblages of microorganisms responding to different physico-chemical and environmental conditions. Chapter three was published in Precambrian Research, 2016, 278, 244-264, doi: 10.1016/j.precamres.2016.03.004. It was authored by Mehrnaz Siahi, Axel Hofmann, Ernst Hegner and Sharad Master. MS carried out several field trips, acquired, analysed, and interpreted the data, and wrote the manuscript. She conducted work on the scanning electron microscope and X-ray diffractometer. AH supervised this research, contributed to the field-work, data interpretations and helped with the writing of the manuscript. AH also conducted Raman spectroscopy analysis. EH and SM supervised this research and made critical comments and edited the manuscript.

In chapter four "Carbonate ooids of the Mesoarchaean Pongola Supergroup, South Africa", a detailed petrographic and mineralogical-geochemical analysis was undertaken on well-preserved ooids, using a combination of polarizing petrographic microscope, scanning electron microscope imaging, LA-ICP-MS and microprobe analyses. Ooids are almost the only carbonate component within the three sections that show the presence of carbonaceous matter.

The biogenicity and distribution of carbonaceous matter and minerals within ooids was determined by a combination of NanoSIMS ion mapping and Raman imaging. Results argue for a biological origin of the Mesoarchaean ooids. This chapter is aimed to be submitted as a manuscript to an international journal. Authors include Mehrnaz Siahi, Axel Hofmann, Ernst Hegner, Sharad Master, Carten Müller and Axel Gerdes. MS developed the idea presented in this chapter. She conducted the work on the scanning electron microscope (SEM) and electron microprobe elemental mapping. She processed and interpreted the data and wrote the manuscript. AH supervised this research and contributed to the interpretations and writing of the manuscript. He also conducted Raman spectroscopy analysis. EH and SM supervised this research and provided critical comments. CM facilitated the NanoSIMS work, gave advice on the interpretation of the data and contributed to the analytical techniques section. AG operated the LA-ICP-MS and acquired and processed raw data jointly with AH and MS.

Geochemical analyses, such as stable and radiogenic isotope analyses along with the major and trace-element determinations, were undertaken on these carbonate rocks, and the results are presented in chapter five entitled "Trace-element and stable (C, O) and radiogenic (Sr) isotope geochemistry of stromatolitic carbonate rocks of the Mesoarchaean Pongola Supergroup: implications for seawater composition". The low $\delta^{18}O$ values along with elevated iron and manganese content of these carbonates indicate that their primary chemical composition was altered during syn/ post-depositional diagenetic alteration. Shale-normalized rare earth element and yttrium distribution patterns and Sr isotope ratios suggest deposition in restricted seawater with riverine input and variable exchange to the open-ocean. Chapter five is aimed to be submitted as a manuscript to an international journal. Authors include Mehrnaz Siahi, Axel Hofmann, Ernst Hegner, Sharad Master, Allan Wilson and Christoph Mayr. MS conducted most of analyses, processed and interpreted the data, and wrote the chapter. AH and EH supervised this research and contributed to the interpretations and writing of the chapter. EH acquired data jointly with MS. SM made critical comments and edited the chapter. AW conducted the work on inductively coupled plasma-mass spectrometry (ICP-MS). CM conducted the work on isotope ratio mass spectrometer (IR-MS) jointly with MS. He contributed to the analytical procedures section and edited the chapter.

Chapter six summarizes the findings and provides an outlook for future studies.

1.5 References

Alexander, B.W., Bau, M., Andersson, P., and Dulski, P. (2008). Continentally-derived solutes in shallow Archean seawater: Rare earth element and Nd isotope evidence in iron formation from the 2.9 Ga Pongola Supergroup, South Africa. Geochim. Cosmochim. Acta, 72, 378-394.

Allwood, A.C., Kamber, B.S., Walter, M.R., Burch, I.W., and Kanik, I. (2010). Trace elements record depositional history of an Early Archean stromatolitic carbonate platform. Chem. Geol., 270, 148-163.

Beukes, N.J., and Lowe, D.R. (1989). Environmental control on diverse stromatolite morphologies in the 3000 Ma Pongola Supergroup, South Africa. Sedimentology, 36, 383-397.

Bolhar, R., Hofmann, A., Siahi, M., Feng, Y., and Delvigne, C. (2015). A trace element and Pb isotopic investigation into the provenance and deposition of stromatolitic carbonates, iron stones and associated shales of the ~ 3.0 Ga Pongola Supergroup, Kaapvaal Craton. Geochim. Cosmochim. Acta, 158, 57-78.

Dixon, J.G.P. (2004). Archaean geology of the Buffalo River gorge, PhD thesis, University of KwaZulu-Natal, Durban, 263 p.

Eglington, B.M., Talma, A.S., Marais, S., Matthews, P.E., and Dixon, J.G.P. (2003). Isotopic composition of Pongola Supergroup limestones from the Buffalo River gorge, South Africa: constraints on their regional depositional setting. S. Afr. J. Geol., 106, 1-10.

Gold, D.J.C. (2006). The Pongola Supergroup. In: The geology of South Africa. Johnston, M.R., Anhaeusser, C.R., and Thomas, R.J. (Eds.), Geol. Soc. S. Afr. / Council for Geoscience S. Afr., 135-147.

Hegner, E., Kröner, A., and Hunt, P. (1994). A precise U-Pb zircon age for the Archaean Pongola Supergroup volcanics in Swaziland. J. Afr. Earth. Sci., 18 (4), 339-341.

Kamber, B.S., and Webb, G.E. (2001). The geochemistry of late Archaean microbial carbonate: Implications for ocean chemistry and continental erosion history. Geochim. Cosmochim. Acta, 65, 2509-2525.

Lowe, D.R., and Tice, M.M. (2004). Geologic evidence for Archean atmospheric and climatic evolution: Fluctuating levels of CO_2, CH_4, and O_2 with an overriding tectonic control. Geol. Soc. Am., 32 (6), 493-496.

Mason, T.R., and Von Brunn, V. (1977). 3-Gyr-old stromatolites from South Africa. Nature, 266, 47-49.

Matthews, P.E. (1967). The pre-Karoo formations of the White Umfolozi inlier, northern Natal. Trans. Geol. Soc. S. Afr., 70, 39-63.

Mukasa, S.B., Wilson, A.H., and Young, K.R. (2013). Geochronological constraints on the magmatic and tectonic development of the Pongola Supergroup (Central Region), South. Africa. Precambrian Res., 224, 268-286.

Perry, E.C., and Tan, F.C. (1972). Significance of oxygen and carbon isotope variations in early Precambrian cherts and carbonate rocks of Southern Africa. Geol. Soc. Am. Bull., 83, 647-664.

Schidlowski, M., Hayes, J.M., and Kaplan, I.R. (1983). Isotopic inferences of ancient biochemistries: Carbon, sulfur, hydrogen and nitrogen. In: Earth's earliest biosphere: Its origin and evolution. Schopf, J.W. (Ed.). Princeton University Press. 149-186.

Veizer, J. (1983). Geologic evolution of the Archean-Early Proterozoic Earth. In: Earth's earliest biosphere: Its origin and evolution. Schopf, J.W., (Ed.), Princeton University. Press, 240-259.

Veizer, J., Hoefs, J., Lowe, D.R., and Thurston, P.C. (1989). Geochemistry of Precambrian carbonates: II. Archean greenstone belts and Archean sea water. Geochim. Cosmochim. Acta, 53, 859-871.

Veizer, J., Clayton, R.N., Hinton, R.W., Von Brunn, V., Mason, T.R., Buck, S.G., and Hoefs, J. (1990). Geochemistry of Precambrian carbonates: 3-shelf seas and non-marine environments of the Archean. Geochim. Cosmochim. Acta, 54, 2717-2729.

Von Brunn, V., and Mason, T.R. (1977). Siliciclastic-carbonate tidal deposits from the 3000 m.y. Pongola Supergroup, South Africa. Sediment. Geol., 18, 245-255.

Weilers, B.F. (1990). A review of the Pongola Supergroup and its setting on the Kaapvaal Craton. Economic Geology Research Unit, University of the Witwatersrand, Information Circular No. 228, 69 p.

Chapter 2: A review of Archaean shallow-water carbonate rocks

2.1 Introduction

Carbonate rocks form at the interface of the atmosphere, biosphere, hydrosphere and lithosphere, i.e. in shallow-water, near-coastal environments influenced by microbial processes. They provide, therefore, important constraints on the development and evolution of carbonate sequences through time, climatic conditions and linked global tectonic processes, seawater composition, and biological evolution. In this chapter, a brief review of the occurrence, mineralogy/ geochemistry, stratigraphic relationships, and palaeontology of Archaean shallow-water carbonate rocks is presented. Deep-water carbonate rocks associated with banded iron formation will not be discussed here. The time scale for the Precambrian rock record follows that of the International Union of Geological Sciences Chronostratigraphic Chart. Distribution and characteristics of Archaean carbonate rocks are presented in Figure 1 and Table 1.

2.2 The missing Hadean rock record (~ 4.5-4.0 Ga)

No Hadean rocks are preserved and there is barely a rock record prior to the Mesoarchaean Era. Our knowledge about the nature of the Earth's very early surface conditions, such as hydrospheric/ atmospheric composition, and early history of life is based on indirect evidence, from the study of meteorites, observation of the modern Earth, experiments, and model calculations (Garrels and Mackenzie, 1971; Veizer, 1988; Mackenzie and Morse, 1992, Morse and Mackenzie, 1998).

Vestiges of the early Earth occur in the form of detrital zircons > 4 Ga old, which have been found within ~ 3 Ga old metamorphosed sediments of the Yilgarn Craton, Western Australia (Froude et al., 1983; Compston and Pidgeon, 1986), and which represent the oldest minerals found on Earth. The heavy $\delta^{18}O$ values of these zircons have been interpreted to indicate the existence of a hydrosphere, the most significant ingredient for the origin of life, and the presence of voluminous supracrustal rocks by 4.3 Gyr ago (Mojzsis et al., 2001; Wilde et al., 2001; Cavosie et al., 2005).

Morse and Mackenzie (1998) calculated approximate values of important seawater parameters during the Hadean Eon based on a linear temperature change from 100 $^{\circ}$C to 70 $^{\circ}$C and log PCO_2 change from 1 to -1.5. They suggested that the ocean of the early Earth, in comparison to the modern oceans, was a NaCl-dominated aqueous solution (Knauth, 1998, 2005) with a

higher amount of dissolved inorganic carbon (DIC) and alkalinity, and acidic pH (~ 5.8 ± 0.2), which changed to an almost neutral pH of ~ 6.8 by the late Hadean. By this time, DIC and alkalinity were more similar to present day values. Purported high surface temperature and acidic rainfall at that time were probably the most significant factors for an elevated flux of bicarbonate, calcium and magnesium to the oceans (Walker et al., 1981; Berner et al., 1983). Carbonate precipitation and accumulation from seawater supersaturated with respect to calcite was one of the characteristic features of the Hadean and early Archaean oceans (Morse and Mackenzie, 1998), but a faster rate of recycling of carbonate rocks into the mantle or destruction during the late heavy bombardment may have resulted in their non-preservation. The chemical composition of the Hadean oceans may have changed between 4.3 and 3.8 Ga, as a result of a dramatic decrease in the concentration of atmospheric CO_2 and temperature (Morse and Mackenzie, 1998). The seawater composition and temperature of this time made the young Earth a habitable place for bacteria and cyanobacteria (Brock, 1973).

2.3 Eoarchaean carbonate rocks (4.0-3.6 Ga)

The sparse rock record of the Eoarchaean indicate a small volume of continental crust that survived reworking by plate tectonics, weathering, and erosional processes over billions of years (Nutman, 2006). Eoarchaean rocks occur in gneiss complexes of several cratons scattered around the world, including the Itsaq Gneiss Complex of southwest Greenland, the Napier Complex in Antarctica, the Uivak Gneisses of Labrador, the Narryer Gneiss Complex of Western Australia, the Nuvvuagittuq greenstone belt of the northeastern Superior Province, the Acasta Gneiss in the westernmost part of the Slave Province, gneisses in the Anshan area of northeastern China and the Ancient Gneiss Complex in northwestern Swaziland (Compston and Kröner, 1988; Schiotte et al., 1989; Nutman et al., 1991, 1996a, 2007; Kinny and Nutman, 1996; Bowring and Williams, 1999; Harley and Kelly, 2007; Iizuka et al., 2007; Liu et al., 2007; O'Neil et al., 2007). Good exposure and relatively low strain and metamorphic overprint makes the Itsaq Gneiss Complex, situated in the Nuuk district of southwest Greenland, the best site for the study of rare Eoarchaean rocks. The Isua belt within the Itsaq Gneiss Complex is one of the most significant sites where supracrustal rocks are preserved (Nutman et al., 1996a, 2014). Metamorphosed carbonates of debated affinity are found in the Isua supracrustal sequence.

Table 1. Distribution and mineralogical/ depositional characteristics of Archaean carbonate rocks

Area	Age (Ga)	Dolomite	Ankerite	Calcite	Thickness	Depositional environment	Specific features
Isua greenstone belt	~ 3.8-3.7	x	-	-	?	Shallow-marine environment? Metasomatic?	Carbonates present as dolomitic marbles and calcsilicates; graphite globules as the oldest traces of terrestrial life (Rosing, 1999; Ohtomo et al., 2014); conical and domical stromatolites
Onverwacht Group	~ 3.55-3.26	x	x	x	Up to 14 m	Hypersaline marine coastal setting	Nahcolite pseudomorphs (Lowe and Fisher Worrell, 1999)
Dresser Formation	~ 3.49	x	x	-	8 m	Within volcanic caldera dominated by hydrothermal processes (Van Kranendonk, et al., 2008)	Couplets of centimetre-thick ankerite and chert layers; chert-barite units; stratiform, columnar, domal, and conical stromatolites (Van Kranendonk, 2003, 2006)
Strelley Pool Chert	3.42-3.35	x	-	-	30 m	Partially restricted shallow marine environment	Stratiform, conical and columnar stromatolites; gypsum pseudomorphs
Nondweni Group	~ 3.4	-	-	-	5-8 m	Evaporitic shallow-water environment	Silicified domal stromatolites; gypsum pseudomorphs (Wilson and Versfeld, 1994)
Fig Tree Group	~ 3.26-3.23	x	-	x	10 m	Fan delta platform/ shallow water	Stratiform, domal and pseudocolumnar stromatolites (Byerly et al., 1986)
Nsuze Group	3.0-2.9	x	Rare	-	Up to 50 m	Tide-dominated shallow marine environment	Stratiform, columnar, domal, digitate and conical stromatolites; structureless microbialites
Wallace Lake greenstone belt	3.0-2.9	x	-	-	50 m	Shallow-marine environment	Stratiform and domal stromatolites
Red Lake greenstone belt	~ 2.9	x	-	-	?	Hypersaline shallow-marine environment	Dolomitic marble-chert beds; stratiform, bulbous mounds, pseudocolumnar and columnar stromatolites (Hofmann et al., 1985); gypsum pseudomorphs (Thurston and Chivers, 1990)

Area	Age (Ga)	Dolomite	Ankerite	Calcite	Thickness	Depositional environment	Specific features
Uchi-Confederation lakes greenstone belt	~ 2.9-2.7	-	-	-	Up to 90 m	Shallow-marine environment	Non-stromatolitic and stromatolitic marble; stratiform, domal and columnar stromatolites (Hofmann et al., 1985); gypsum pseudomorphs (Thurston and Chivers., 1990)
Lumby Lake greenstone belt/ Pinecone assemblage	~ 2.8	-	x	x	Up to 80 m	Shallow-marine environment	Marble consists of interlayered of decimetre-scale calcite and chert beds (Fralick et al., 2008; Buse et al., 2009); Stratiform stromatolites (Jackson, 1985)
Steep Rock Group/ Mosher Carbonate	~2.8-2.7	x	x	x	500 m	Shallow-marine environment with short-lived hypersaline conditions	Stratiform, columnar, domal, and conical stromatolites; giant stromatolitic mounds; aragonite fans; herringbone calcite; gypsum moulds
Yellowknife Supergroup	~ 2.7	x	-	-	40 m	Reefs fringed volcanos	Stratiform, pseudocolumnar and domal stromatolites; aragonite fans (Henderson, 1975)
Fortescue Group/ Tumbiana Formation	~ 2.7	Rare	-	x	Up to 50 m	Lacustrine/shallow-marine environment?	Domal and columnar stromatolites (Lipple, 1975; Thorne and Trendall, 2001; Sakurai et al., 2005); cyanobacterial microfossils (Schopf and Walter, 1983); rare halite pseudomorphs (Buick, 1992)
Ventersdorp Supergroup	2.7	x	-	x	-	Lacustrine environment	Stratiform and domal stromatolites; giant ooids
Chitradurga Group	~ 2.7	x	-	x	Up to several hundred metres	Shallow-marine environment	Stratiform, pseudocolumnar, columnar and cup-shaped, bowl to saucer like stromatolites (Srinivasan et al., 1989; Sharma and Shukla, 2004)
Sandur schist belt	~ 2.7	-	x	x	Up to a few metres	Shallow-marine environment	Columnar stromatolites
Manjeri Formation	~ 2.7	x	-	x	50 m	Shallow-marine environment	Stromatolitic carbonates

Area	Age (Ga)	Dolomite	Ankerite	Calcite	Thickness	Depositional environment	Specific features
Cheshire Formation	~ 2.6	Rare	-	x	Up to 350 m	Open marine environment? Restricted shallow-marine environment?	Stratiform, columnar and domal stromatolites; calcite pseudomorphs after aragonite or gypsum (Martin et al., 1980; Abell et al., 1985; Sumner and Grotzinger, 2000)
Hamersley Group/ Carawine Dolomite	~ 2.6	x	Rare	-	> 500 m	Shallow-marine environment	Stratiform, domal and columnar stromatolites; giant stromatolitic mounds; aragonite fans; herringbone calcite; pseudomorphs of gypsum; halite casts; zebraic dolomite cement
Schmidtsdrif Subgroup	~ 2.6	x	-	x	> 200 m	Shallow-marine environment	Stratiform stromatolites; giant ooids up to 4 mm (Wright and Altermann, 2000)
Hamersley Group/ Wittenoom Formation	~ 2.56	x	-	x	> 400 m	Off-platform deposits in deeper-marine water	Large stromatolitic mounds and laminites with roll-up structures
Campbellrand Subgroup	~ 2.5	x	-	x	Up to 2500 m	Shallow-marine environment	Stratiform, columnar, domal, digitate**,** club-shaped and conical stromatolites and giant elongated stromatolitic domes; laminoid fenestrated dolomites (Altermann and Wotherspoon, 1995; Altermann and Siegfried, 1997); aragonite fans; herringbone calcite layers; fibrous calcite encrustations; halite casts (Sumner and Grotzinger, 2000, 2004)
Malmani Subgroup	~ 2.5	x	-	Rare	Up to 1700 m	Shallow-marine environment	Giant elongated stromatolitic domes; aragonite fans; herringbone calcite layers; fibrous calcite encrustations; halite casts

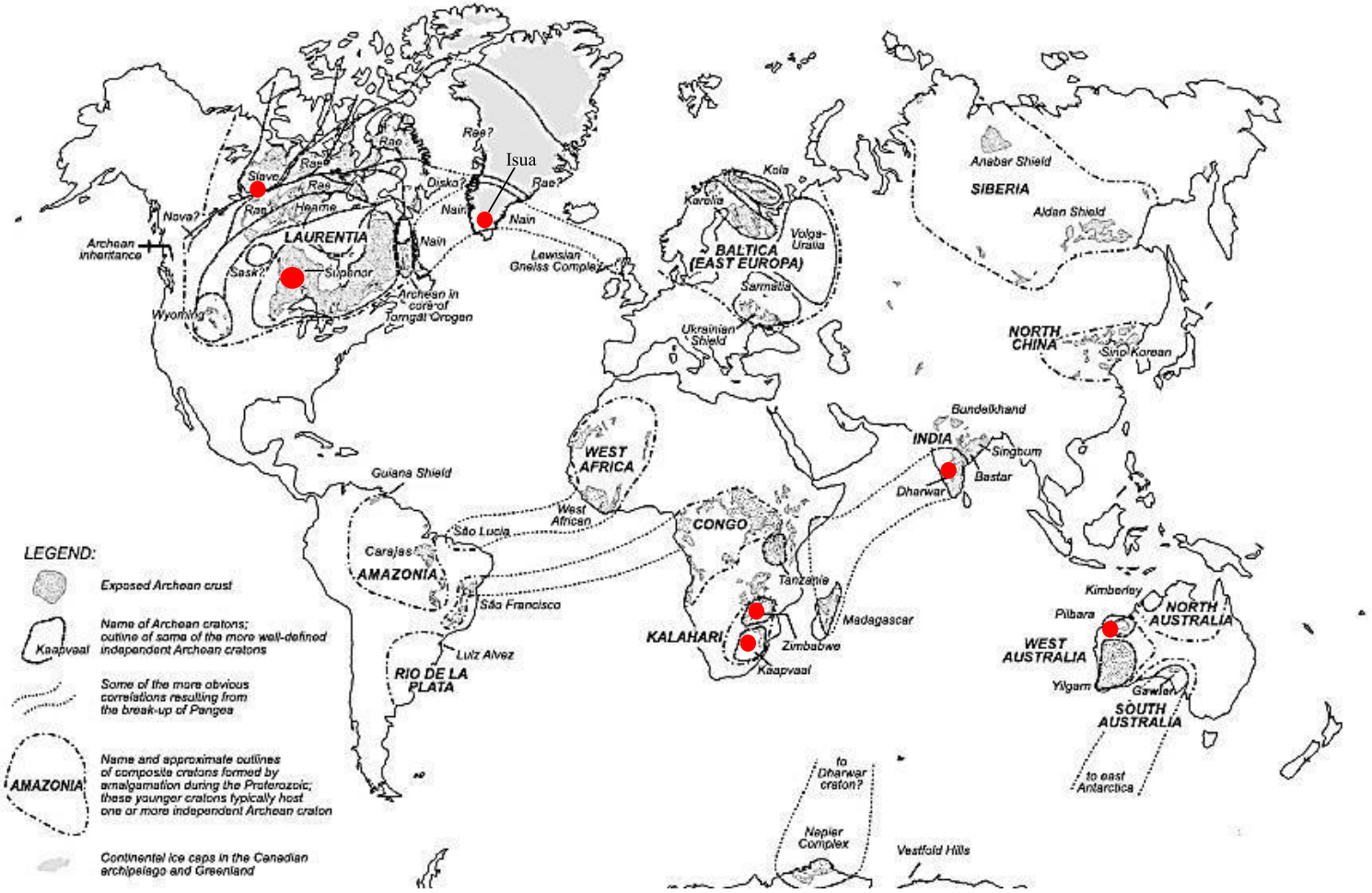

Fig. 1. Global distribution of exposed Archaean carbonate rocks shown by red dots (modified after Bleeker, 2003).

2.3.1 Isua supracrustal belt

The ~ 3.8-3.7 Ga Isua supracrustal sequence of southwest Greenland comprises the oldest known metavolcanic and metasedimentary rocks on Earth and provides evidence for the presence of ocean and landmasses in the early Archaean (Mojzsis and Harrison, 2000; Myers and Crowley, 2000; Nutman et al., 2009; Nisbet and Fowler, 2013). The major components of the Isua greenstone belt consist of deformed and metamorphosed basaltic pillow lava and pillow lava breccia with smaller amounts of layered mafic-ultramafic intrusive sheets, ultramafic rocks and a minor component of clastic and chemical sedimentary rocks, including metamorphosed chert and banded iron formation (BIF), calc-silicate rocks, dolomitic marbles and dolomite (Komiya et al., 1999; Fedo, 2000; Myers and Crowley, 2000; Nutman et al., 2016). Dimroth (1982) suggested that the marbles represent shallow subtidal sedimentary deposits. However, carbonate has been recognized as a major replacement mineral in many lithologies in the Isua belt (Rose et al., 1996; Fedo, 2000). Composition and field relations indicated to these authors that the Isua metacarbonate rocks are largely metasomatic in origin and formed by carbonation and desilicification of various country rocks by metamorphic fluids at deep crustal levels (Rose at al., 1996; Rosing et al., 1996). Several stromatolitic dolomite beds up to several cm in thickness were recently described from a newly exposed outcrop from the Isua Supracrustal belt and were attributed to have formed in a shallow-marine environment (Nutman et al., 2016). Seawater-like REE + Y signatures of the metacarbonate rocks are in agreement with this interpretation (Nutman et al., 2016).

2.4 Palaeoarchaean carbonate rocks (3.6-3.2 Ga)

The Palaeoarchaean supracrustal rock record mainly consists of altered, metamorphosed and deformed volcano-sedimentary rocks in greenstone belts, including the ~ 3.5-3.2 Ga Barberton greenstone belt of the Kaapvaal Craton, South Africa (Kröner et al., 1991, 1996; Lowe and Byerly, 2007) and ~ 3.5-2.8 Ga greenstone belts of the Pilbara Craton, Western Australia (Van Kranendonk et al., 2002, 2007; Hickman, 2012). They are dominated by komatiitic, tholeiitic, felsic volcanic and volcaniclastic rocks associated with siliciclastic, predominantly deep-water sediments and thin horizons of BIF, chert and rare carbonates (Lowe and Byerly, 2007; Hickman, 2012). Palaeoarchaean carbonate units are present in the Warrawoona Group of the Pilbara Supergroup, Western Australia, the Onverwacht and Fig Tree groups of the Swaziland Supergroup and the Nondweni Group, South Africa. They are variably silicified and mostly

form thin layers, less than a few metres in thickness, intercalated with volcanic and volcaniclastic rocks. Palaeoarchaean carbonate precipitates have been interpreted as sedimentary, diagenetic and hydrothermal in origin (Veizer et al., 1989; Nakamura and Kato, 2004; Rouchon et al., 2009, Allwood et al., 2010).

2.4.1 Warrawoona Group

The ~ 3.5-3.4 Ga Warrawoona Group of the East Pilbara granite-greenstone terrane, Western Australia, is composed mainly of mafic volcanic rocks interlayered with lesser felsic volcanic rocks, bedded chert, sandstone, carbonate and pyroclastic deposits (Van Kranendonk et al., 2002, 2006, 2007). The ~ 3.49 Ga Dresser Formation (Thorpe et al., 1992) consists of pillow basalt and interbedded chert and barite units, and forms the lowest unit of the Warrawoona Group. The chert-barite unit is composed predominantly of bedded chert, units of coarsely crystalline barite and, locally, metres-thick layers of conglomerate, sandstone, and dolomite (up to 8 m) with stromatolites with diverse morphologies (Buick and Dunlop, 1990; Van Kranendonk, 2006).

Stratigraphically higher up in the Warrawoona Group, other chert units are present, including the Marble Bar Chert Member of the Duffer Formation, up to 100 m thick (Van Kranendonk et al., 2004), the Apex chert and, close to the top, the 3.42-3.35 Ga Strelley Pool Chert at the base of the Kelly Group (Lowe, 1980; Van Kranendonk, 2006). The latter is a 30-1000 m thick cherty sedimentary unit with well-preserved stromatolites that consists of three units (Lowe, 1983). 1) A basal quartzite with conglomerate and locally volcaniclastic rocks that were deposited in a fluvial to shallow marine environment. 2) A middle unit, up to 30 m in thickness, composed of variably silicified carbonates with stratiform and conical to columnar stromatolites, radiating crystals (aragonite or gypsum precursor) replaced by dolomite and gypsum pseudomorphs interpreted to have been deposited in a partially restricted hypersaline basin. 3) An upper unit of conglomerates and sandstones, which were deposited in a subaerial to tide-dominated shallow-marine environment (Lowe, 1980, 1983; Buick and Dunlop, 1990; Hofmann et al., 1999; Van Kranendonk et al., 2003; Van Kranendonk, 2006). The presence of predominantly low energy depositional conditions, paucity of terrigenous detrital particles and appearance of evaporite crystal pseudomorphs suggest large hypersaline lake or partially restricted peritidal marine environments. Allwood et al. (2007), in a careful study of

stromatolite morphology, suggested that halophilic and possibly phototrophic microorganisms were involved in forming the stromatolitic build-ups.

2.4.2 Onverwacht and Fig Tree groups

The Swaziland Supergroup of the Barberton greenstone belt is divided into the lower, predominantly volcanic Onverwacht Group, the middle volcaniclastic and terrigenous clastic Fig Tree Group, and upper quartzose terrigenous Moodies Group (Viljoen and Viljoen, 1969a, b; Lowe and Byerly, 1999). The ~ 3.55-3.26 Ga Onverwacht Group (Kröner et al., 1996) predominantly consists of mafic and ultramafic volcanic rocks, subordinate felsic tuff and lavas, and diverse interbedded silicified sedimentary rocks. Chert units have been reported from different levels of the stratigraphy and were interpreted as replacements of fine-grained carbonates or other orthochemical sediments (Viljoen and Viljoen, 1969a, b; Lowe and Knauth, 1977; Lowe and Byerly, 1999).

The ~ 3.26-3.23 Ga Fig Tree Group (Kröner et al., 1991; Byerly et al., 1996) consists of interlayered terrigenous, volcanic and volcaniclastic units (Lowe and Byerly, 1999, 2007). The basal Mapepe Formation consists mainly of terrigenous clastic units, felsic pyroclastic rocks and minor jasper, banded ferruginous chert (deep-water precipitate), barite, carbonate and silicified carbonate, which consist of limestone, dolomite and calcareous chert with minor quartz particles deposited in a fan delta platform (Lowe and Knauth, 1977; Lowe and Byerly, 1999, 2007; Lowe and Nocita, 1999). Byerly et al. (1986) described commonly low-relief, nearly stratiform, laterally-linked domes and rare pseudocolumns and crinkly stratiform stromatolites in thin chert layers within the Fig Tree Group.

2.4.3 Nondweni Group

The Nondweni Group of the ~ 3.4 Ga Nondweni greenstone belt (Xie et al., 2012), situated near the southern margin of the Kaapvaal Craton, South Africa, and predominantly consists of volcanic rocks. The uppermost stratigraphic unit (Witkop Formation) is composed of basalt and komatiitic basalt intercalated with less than 5 % of sedimentary rocks, including chert layers and clastic sedimentary rocks (Wilson and Versfeld, 1994). A silicified carbonate horizon (5 to 8m thick) with domal stromatolites occurs at one locality and is overlain by barite

and layered accretionary lapilli tuffs. The presence of stromatolites, coarse clastic sediments and gypsum has been used as arguments for a shallow-water, evaporitic environment (Wilson and Versfeld, 1994).

2.5 Mesoarchaean carbonate rocks (3.2-2.8 Ga)

Mesoarchaean carbonates are found in the 3.0-2.9 Ga Pongola Supergroup and several other greenstone belts of the Superior Province, Canadian Shield.

2.5.1 Nsuze Group

The 3.0-2.9 Ga Pongola Supergroup (Hegner et al., 1984, 1994; Mukasa et al., 2013) of South Africa was deposited on the stable continental crust of the Kaapvaal Craton, is one of the oldest well-preserved succession of epicratonic volcanic and sedimentary rocks (Gold, 2006). The carbonate rocks from the Nsuze Group of the Pongola Supergroup are exposed in several inliers within the White Mfolozi River valley and the Buffalo River gorge (Beukes and Lowe, 1989; Dixon, 2004). The carbonates of the White Mfolozi inlier are the focus of this study. In the White Mfolozi inlier, several horizons of carbonate rocks up to 30 m in thickness with locally well-preserved stromatolites have been reported from the Chobeni Formation. The dolomites and intercalated siliciclastic rocks were deposited within a tide-dominated shallow-marine environment (Beukes and Lowe, 1989; this study). In the Buffalo River gorge 20 m and 50 m thick stromatolitic carbonate layers, mainly dolomite, overlie amygdaloidal metalava and were deposited in an intertidal sedimentary environment (Dixon, 2004).

2.5.2 Wallace Lake greenstone belt

The 3.0-2.9 Ga volcano-sedimentary Wallace Lake assemblage is located at the southern margin of the North Caribou terrane in the western Superior Province, Canada (Turek and Weber, 1991; Davis, 1994; Sasseville et al., 2006). The basal Conley Formation consists predominantly of clastic sedimentary rocks with some intercalations of chemical sedimentary rocks, including a 50 m thick unit of dolomite. The latter include stratiform and domal

stromatolites that precipitated in a shallow-marine environment (Sasseville et al., 2006; Fralick et al., 2008).

2.5.3 Uchi-Confederation lakes greenstone belt

The ~ 2.9-2.7 Ga Uchi-Confederation lakes greenstone belt (Nunes and Thurston, 1980) is a predominantly metavolcanic sequence with minor metasedimentary rocks within volcanic-granitic Uchi Subprovince of the Superior Province of the Canadian Shield (Ayres et al., 1971; Nunes and Thurston, 1980). The ~ 2.96 Ga metavolcanic rocks of Balmer assemblage (Nunes and Thurston, 1980), 5300 m in thickness, mainly consists of pillowed and massive basalts and felsic volcanic rocks, which is conformably covered by 90 m of non-stromatolitic marble in the northwest and by sulphide-facies iron formation and chert in the south. The ~ 2.8 Ga Woman assemblage (Wallace et al., 1986) mainly consists of mafic to felsic volcanic rocks (Nunes and Thurston, 1980; Thurston and Fryer, 1983), which are locally capped by 60 m thick shallow water stromatolitic marble (Hofmann et al., 1985; Van Staal., 1998).

2.5.4 Red Lake greenstone belt

The Red Lake greenstone belt in the Uchi Subprovince of the Superior Province is subdivided into the ~ 2.9 Ga older basaltic komatiites with minor felsic metavolcanics and metasediments in the east and overlying calc-alkaline sequences in the northern and southern parts of the belt (Pirie, 1981). In the west, the Ball sequence predominantly consists of tholeiitic rocks and felsic calc-alkalic flows and pyroclastic rocks with horizons of ~ 2.9 Ga chemical sediments such as dolomitic marble-chert beds with stromatolite, and magnetite iron formation, which are under and overlain by felsic volcanic rocks (Corfu and Wallace, 1986; Stott and Corfu, 1991). Stromatolitic dolomites formed in intertidal to shallow-deep subtidal environments (Hofmann et al., 1985).

2.6 Neoarchaean carbonate rocks (2.8-2.5 Ga)

In contrast to the paucity of sedimentary carbonates from the Palaeo-Mesoarchaean, Neoarchaean carbonate rocks ~ 2.8-2.5 Ga old are more abundant in the geological record. The

development of large cratonic masses in the Mesoarchaean, including the Kaapvaal and Pilbara cratons, and the stabilization of cratons in the Late Archaean, including the Zimbabwe, Yilgarn, Slave, and Superior cratons/ provinces (e.g. Condie, 1995; Rey et al., 2003) provided stable land surfaces that were episodically flooded by shallow seas. The generation of major volumes of continental crust in the Neoarchaean at about 2.75 to 2.65 Ga and subsequent weathering of continental crust (Condie, 1995; Rey et al., 2003; Lowe and Tice, 2007), led to supersaturation of deep subtidal seawater with respect to calcite, which was deposited directly on the seafloor as *in-situ* precipitates (Sumner, 1997). Carbonate deposition following weathering of continental crust led to a reduction of atmospheric CO_2 and oxygenation of the atmosphere in the Palaeoproterozoic (Karhu and Holland, 1996; Farquhar et al., 2000). It was suggested that the presence of oxygen-producing cyanobacteria led to the oxidative iron removal from seawater and resulted in limestone precipitation over Fe-carbonate precipitation (Riding et al., 2014; Fralick and Riding, 2015). These conditions favoured the flourishing of life and the accumulation of major carbonate units (Grotzinger, 1989; Lowe, 1992; Lowe and Tice, 2007). The Neoarchaean carbonates formed in a variety of depositional environments, including continental platform and foredeep basins (Grotzinger, 1989). Sedimentary carbonates from the Neoarchaean are known from the Yellowknife Supergroup and the Steep Rock Group of Canada, the Fortescue and Hamersley groups of Western Australia, the Ventersdorp and Transvaal supergroups of South Africa, the Ngezi Group of Zimbabwe, and from a variety of greenstone belts from the Dharwar Craton of India.

2.6.1 Steep Rock Group

The Steep Rock Group and its equivalent, the northern tectono-stratigraphic assemblage of the Lumby Lake greenstone belt, Superior Province, Canada rests unconformably on a ~ 3.0 Gaa tonalitic gneiss basement (Tomlinson et al., 2003, 2004). The 2.8-2.78 Ga Steep Rock Group contains one of the world's thickest Archaean carbonate platform successions (Fralick and Riding, 2015). The Mosher Carbonate up to 500 m in thickness, consists of stromatolitic carbonates (ankerite, dolomite and calcite) with minor quartz and pyrite. Stromatolites show diverse morphologies, include tabular, domal, columnar and conical morphologies, and large stromatolite mounds with relics of aragonite fans and botryoids, herringbone calcite and gypsum moulds (Wilks and Nisbet, 1988; Kusky and Hudleston, 1999). Carbonate layers grade laterally into chert due to replacement of carbonate by chert (Walter, 1983; Wilks and Nisbet,

1985, 1988). The carbonates were interpreted to represent shallow marine precipitates that formed under short-lived anaerobic and hypersaline conditions based on the presence of gypsum moulds and herringbone calcite (Kusky and Hudleston, 1999; Fralick and Riding, 2015). The presence of abiotic carbonate precipitates, such as giant aragonite fans and botryoids, suggests that the chemistry of Neoarchaean seawater may have favoured abiotic carbonate deposition (Grotzinger and Kasting, 1993).

2.6.2 Yellowknife Supergroup

The ~ 2.7 Ga Yellowknife Supergroup (van Breemen et al., 1992), Slave Province, and its stratigraphic equivalents consists of immature greywacke-mudstone turbidites, mafic to felsic volcanics, and minor amounts of conglomerate and carbonate (Henderson, 1975). A discontinuous stromatolitic dolomite unit up to 40 m in thickness is locally present. The dolomite unit occurs in black carbonaceous mudstone that grades upward into felsic volcanic tuffs, sandstones and conglomerates of the overlying felsic volcanic sequence (Henderson, 1975). Carbonates may have formed as short-lived reefs that fringed subsiding volcanoes (Henderson, 1975; Grotzinger, 1986, 1989; Lambert, 1998).

2.6.3 Fortescue Group

The 2.7-2.6 Ga Fortescue Group, Mount Bruce Supergroup, Pilbara Craton, up to 6500 m in thickness, consists of flood basalts intercalated with volcaniclastic and siliciclastic rocks with carbonates (Thorne and Trendall, 2001; Blake et al., 2004; Van Kranendonk et al., 2006). It is subdivided into six formations, three of which consist of tholeiitic flood basalts with subordinate felsic rocks, intercalated with three sedimentary formations. The ~ 2.7 Ga Tumbiana Formation (Blake et al., 2004), which ranges from a few metres to 320 m in thickness, consists of limestone, rare dolostone, siliciclastic rocks, tuff, and basalt (Buick, 1992) and is underlain and overlain by amygdaloidal basalts (Thorne and Trendall, 2001; Awramik and Buchheim, 2009). In the northeast Pilbara sub-basin the Tumbiana Formation has been subdivided into two members. 1) The lower Mingah Member consists of predominantly volcaniclastic sandstone, minor mudstone, stromatolitic limestone (up to several centimetres in thickness), and basalt (Lipple, 1975; Buick, 1992; Thorne and Trendall, 2001). 2) The upper Meentheena Member (30 to 50 m thick) consists of stromatolitic limestone

(75 % calcite and 25 % dolomite) and siliciclastic rocks. The depositional setting of the carbonates is controversial, and both a shallow-marine environment (Sakurai et al., 2005) and a lacustrine environment (Buick, 1992; Bolhar and Van Kranendonk, 2007; Awramik and Buchheim, 2009) have been proposed.

2.6.4 Hamersley Group

The Hamersley Group of Western Australia consists of volcaniclastic-chemical sedimentary deposits (Trendall, 1983) and contains two extensive well-preserved carbonate occurrences, the Carawine Dolomite and the Paraburdoo Member of the Wittenoom Formation (Simonson et al., 1993). The ~ 2.6 Ga Carawine Dolomite (Rasmussen et al., 2005), which is restricted to the eastern part of the Hamersley Basin, conformably rests on the Lewin Shale and the Marra Mamba Iron Formation and unconformably is overlain by the Pinjian Chert Breccia (Hickman, 1978; Hickman et al., 1983). The Carawine Dolomite in the Oakover River area reaches to > 500 m in thickness in places (Simonson and Hassler, 1997). This carbonate succession almost entirely consists of dolomite with stromatolites and in places is intercalated with argillite and chert. These carbonates were formed directly on or close beneath the seafloor as inorganic crystalline precipitate, such as prismatic and acicular crystals, zebraic dolomite cement, stubby, vertically oriented crystals and hollow-faced cubes, probably via evaporative concentration in restricted areas (Simonson et al., 1993). The precursor for the prismatic and acicular crystals and zebraic dolomite was proposed to have been aragonite and calcite, respectively (Sumner et al., 1991; Simonson et al., 1993).

The ~ 2.56 Ga Wittenoom Formation (Rasmussen et al., 2005) is subdivided into the three members. 1) The West Angelas Shale Member, up to 100 m in thickness, consists of carbonate, argillite and minor banded iron formation (Simonson et al., 1992; Blockley et al., 1993). 2) The Paraburdoo Member, up to 400 m thick locally, consists of thinly laminated lutites (entirely dolomite) with roll-up structures and minor argillite. 3) The Bee Gorge Member, up to 225 m thick, predominantly consists of argillite but also contains dolomite, limestone, chert, iron formation and volcaniclastic strata. The carbonate rocks of the Wittenoom Formation and some parts of the Carawine Dolomite with large stromatolitic domes and laminites with roll-up structures have been interpreted as off-platform deposits in relatively deep water (Simonson et al., 1992, 1993).

2.6.5 Ventersdorp Supergroup

The 2.7 Ga Ventersdorp Supergroup represents a volcano-sedimentary sequence on the Kaapvaal Craton (Armstrong et al., 1991). It is subdivided into different groups that predominantly consist of subaerially extruded mafic volcanic rocks, terrigenous and chemical sedimentary rocks and a mixture of both. Sedimentary rocks from the Platberg Group comprise shales, sandstones, conglomerates, stratiform to small-scale domal stromatolites made of dolomite and cherty laminae and giant ooids inferred to have been deposited in a lacustrine setting (Van der Westhuizen et al., 1991, 2006).

Correlative to the Platberg Group is the Sodium Group along the SW extremity of the craton. The upper unit of the Sodium Group, the Omdraaivlei Formation, consists of mafic to intermediate lava flows, pillow lavas intercalated with arkose, tuff and stromatolitic cherty limestone. Nine silicified carbonate units, 10-90 cm thick, are intercalated with tuffaceous shale and show various stromatolite morphologies (Grobler et al., 1989; Altermann and Lenhardt, 2012).

2.6.6 Transvaal Supergroup

The ~ 2.6-2.0 Ga Transvaal Supergroup of the Kaapvaal Craton (Walraven et al., 1990; Cornell et al., 1996; Altermann and Nelson, 1998) unconformably overlies the 2.7 Ga Ventersdorp Supergroup and older granitic and greenstone basement (Armstrong et al., 1991; Sumner and Bowring, 1996). The Schmidtsdrif Subgroup 10-275 m in thickness is the lowermost unit of the Ghaap Group, Transvaal Supergroup. It is composed of > 200 m thick subtidal to tidal-flat deposits, including siliciclastics, wavy laminated, stromatolitic and oolitic dolomites, calc- and dolarenites, shale, calcareous shale and quartzite (Beukes, 1983, 1987; Altermann and Wotherspoon, 1995; Altermann and Siegfried, 1997).

The ~ 2.5 Ga overlying Campbellrand Subgroup of the Ghaap Group (Barton et al., 1994; Sumner and Bowring, 1996) consists of eight continuous carbonate formations up to 2500 m in thickness, and its correlative, the Malmani Subgroup up to 1700 m thick represent peritidal carbonate deposits of the Transvaal Supergroup (Beukes, 1987). The stromatolitic carbonate rocks are intercalated with lava, chert and shale layers, cm-thin tuff beds and minor clastic rocks (Altermann and Wotherspoon, 1995; Altermann and Siegfried, 1997).

Beukes (1987) subdivided the Campbellrand Subgroup into two main facies domains: i) the Ghaap Plateau facies, and ii) the Prieska facies. The Prieska facies consists of < 600 m of pyritic carbonaceous non-stromatolitic carbonates (mostly limestone and minor dolomite) and shale, minor interbeds of dolomite breccia, chert, iron formation and mafic tuff deposited in a deeper part of the basin, and is overlain and underlain by carbonaceous shale. Dolomite is the main component and probably has a limestone precursor (Beukes, 1977, 1987). It was suggested by Beukes (1987) that limestones of the Campbellrand Sequence consist of calcite after an aragonite precursor based on the presence of acicular calcite pseudomorphs of aragonite.

Dolomites that are replaced in places by chert are the predominant lithology of the Malmani Subgroup with minor limestone and clastic sediments. They were precipitated in a tide-dominated, shallow-marine environment. Aragonite and high-magnesium calcite have been considered as dolomite precursor (Truswell and Eriksson, 1975; Eriksson, 1977). Herringbone calcite cements are present in supratidal to tidal flat facies as millimetre- to decimetre-thick coatings on elongated giant stromatolites, breccia blocks and other depositional surfaces. Pseudomorphed aragonite fans, herringbone calcite layers and fibrous calcite encrustations are present in all depositional environments of the Campbellrand-Malmani carbonate platform except the deepest slope and basin. Cubic pseudomorphs after halite, filled with chert or dolomite cement, are present in some micrite layers associated with the most restricted depositional environments. The abundance of decimetre-thick calcite crusts and aragonite fans in shallow depositional environments implies the absence of sediment influx, low sedimentation rates and very high carbonate precipitation rates (Sumner and Grotzinger, 2000, 2004).

2.6.7 Belingwe greenstone belt

The Belingwe greenstone belt, situated in the southeastern part of the Zimbabwe Craton, predominantly consists of mafic lavas and sedimentary rocks (Martin et al., 1993). The uppermost unit of the Belingwe greenstone belt, Ngezi Group, comprises four formations. The ~ 2.7 Ga basal sedimentary Manjeri Formation (Bolhar et al., 2002), 50-100 m in thickness, typically consists of fluvial and shallow-water deposits such as conglomerate, sandstone, shale, ironstone and locally stromatolitic carbonates in the lower part, and immature, alluvial fans to fan delta deposits in the upper part, indicating deepening conditions (Bickle et al., 1975; Nisbet et al., 1993; Hunter et al., 1998). A 50 m thick limestone is restricted to the southeast of the

greenstone belt and probably formed in intertidal conditions (Bickle et al., 1975; Martin et al., 1980, 1993).

The Manjeri Formation is succeeded by komatiites and komatiitic basalts of the Reliance Formation and basaltic lavas of the Zeederbergs Formation (Nisbet et al., 1977; Martin et al., 1980), followed by sedimentary rocks of the ~ 2.6 Gyr old Cheshire Formation (Bolhar et al., 2002). In the western part of the Cheshire Formation, carbonates occur as shallowing-upward cycles of limestone interbedded with fine-grained terrigenous sedimentary rocks up to 350 m in thickness with minor dolomite (Martin et al., 1980; Abell et al., 1985; Hofmann et al., 2001, 2004). Stromatolitic carbonates with a variety of morphologies formed in a very shallow-marine environment to protected lagoon (Martin et al., 1980, 1993; Abell et al., 1985). Hofmann et al. (2001) suggested that these carbonates were deposited in a shallow, wave and storm dominated open marine environment.

2.6.8 Dharwar Craton

The ~ 2.9-2.6 Ga volcanic and sedimentary rocks of the Dharwar Supergroup (Russell et al., 1996) were deposited on the 3.3-2.9 Ga old Peninsular Gneiss of the western part of the Dharwar Craton of southwestern India (Beckinsale et al., 1980, 1982; Chadwick et al., 1997). Supracrustal rocks of the greenstone (schist) belts have been divided into two groups based on sedimentary facies, the Bababudan and Chitradurga groups (Swami Nath and Ramakrishnan, 1981).

The lower part of the ~ 2.7 Ga Chitradugra Group (Peucat et al., 1995; Nutman et al., 1996b; Trendall et al., 1997) consists mainly of siliciclastic rocks, representing alluvial or shallow-marine fan deposits, that grade into layers and lenses of shallow-marine calcitic/dolomitic limestone ranging from a few metres to rarely a few hundred metres thick. Carbonate rocks are overlain by mafic and felsic volcanic rocks that are locally interbedded with greywacke, banded ferruginous chert and limestone (Chadwick et al., 1985, 1988, 1992). In several areas of the Chitradurga Group columnar and pseudocolumnar stromatolites occur in a cherty dolomite (Srinivasan et al., 1989).

In the eastern part of the Dharwar Craton, the ~ 2.7 Ga Sandur Schist Belt (Nutman et al., 1996b) rests on ~ 3.0 Ga gneisses (Taylor et al., 1984) and predominantly consists of mafic-ultramafic rocks, followed by siliciclastic rocks and some layers of stromatolitic dolomitic

limestone, turbiditic and volcanic rocks (Baral, 1986; Manikyamba and Naqvi, 1997, 1998). The depositional environment of the carbonates and arenites was suggested as shallow marine (Chadwick et al., 1988, 1991, 1997).

2.7 Characteristics of Archaean carbonate rocks

Carbonate rocks of Eoarchaean to Mesoarchaean age are scarce, as indicated in this review of Archaean carbonate occurrences. A secular change from the Eoarchaean to the Neoarchaean with respect to thickness, chemical composition, texture/ structure and mechanism of precipitation is evident. In general, carbonate rocks are minor components in the predominantly mafic/ ultramafic sequences, and occur along with siliciclastic rocks, cherts and banded iron-formation. Carbonates were deposited mostly in a shallow-marine to evaporitic shallow-water settings, although deeper-water carbonates, mainly as siderite, are present as a part of many BIFs (e.g. Klein, 2005). The chemical and mineralogical characteristics of carbonate rocks and changes of their depositional environments through the Archaean has been summarized in the following.

Thickness: The thickness of preserved carbonate rocks has increased with time. Thickness changes from several metres in the Palaeoarchaean, up to 90 m in the Mesoarchaean and over 500 m in the Neoarchaean. Neoarchaean carbonate sequences with a thickness less than a hundred metres were mostly deposited in environments interpreted as fringing reefs of volcanoes and lacustrine settings.

Mineralogy and chemical composition: Palaeoarchaean carbonates are mainly made of dolomite and ankerite, whereas Mesoarchaean carbonate rocks are predominantly dolomite and to a lesser extent ankerite. Limestones are common in some Neoarchaean successions. It was suggested that higher Fe and Mn contents of Archaean carbonate rocks compared with their Phanerozoic counterparts are not due to post-depositional alteration phenomena, but reflect the composition of the Archean seawater (Veizer, 1989; Veizer et al., 1990).

Depositional setting: The environment of deposition of Eo- to Palaeoarchaean carbonate rocks is enigmatic, and both sedimentary and hydrothermal/ metasomatic processes have been proposed. Sedimentary, diagenetic and hydrothermal carbonates are known and most of them were deposited in hypersaline, restricted, shallow-marine environments. Mesoarchaean carbonate rocks were deposited within shallow-marine, in part hypersaline settings.

Neoarchaean carbonate rocks were deposited in shallow-marine to lacustrine settings and in rare cases in restricted shallow-marine settings and reef-fringed volcanoes. Prominent carbonate platforms make their first appearance in the Neoarchaean.

Stromatolite morphology: The oldest putative stromatolites are recorded from the ~ 3.8-3.7 Ga Isua supracrustal sequence of southwest Greenland. Stromatolites with diverse morphologies, including stratiform, domal, columnar, pseudocolumnar and conical shapes, are already present in Palaeoarchaean successions. Mesoarchaean stromatolites are morphologically as diverse as those of the Palaeoarchaean, but also include digitate stromatolites and tabular to domal structureless microbialites reported here from the Nsuze Group for the first time (chapter 3). Neoarchaean stromatolites display additional morphologies, such as giant elongated domes, club-shaped/ bowl- to saucer-like forms and giant ooids.

Texture and structure: Textural features that differentiate Neoarchaean carbonate successions from their more ancient counterparts is the presence of *in-situ* carbonate precipitates on the seafloor, such as aragonite fans, herringbone calcite, zebraic dolomite cements, and fibrous calcite encrustations.

The paucity of carbonate rocks earlier than the Neoarchaean, different carbonate compositions through the Archaean and the presence of distinctive features that differ from the Palaeoarchaean to Neoarchaean will be described below. The aim is to shed light on the factors behind the drastic changes in carbonate rocks through the Archaean.

2.8 Environmental factors responsible for differences of carbonate rocks through the Archaean

The mineralogical assemblage and texture of carbonate rocks are controlled by the chemical, biological, and physical conditions of their depositional settings (e.g. Sumner and Grotzinger, 1996a). Several dominant factors influenced patterns of sedimentation and the production of carbonate through the Archaean. Existence of stable depositional basement, extended periods of tectonic quiescence that led to reduction of siliciclastic influx, the presence and evolution of life (e.g. Grotzinger, 1989), and the removal of inhibitors (e.g. Fe^{2+}, Mn^{2+}, SO_4^{2-}, Mg^{2+}) to carbonate precipitation (e.g. Meyer, 1984) were responsible for the drastic change of carbonate

characteristics and their depositional environments through the Archaean (e.g. Sumner and Grotzinger, 1996a).

The rarity of carbonate rocks of Palaeo-Mesoarchaean age may be explained by the absence of extensive stable continents and high siliciclastic input, as a result of active tectonism, rather than the chemical composition of ambient seawater and biological influence (Grotzinger, 1989; Lowe and Tice, 2007). Veizer et al. (1990) interpreted depleted mantle-like $^{87}Sr/^{86}Sr$ ratios, Fe^{2+} and Mn^{2+} enrichment, and $\delta^{18}O$ depletion of Archaean carbonate rocks, in contrast to their Phanerozoic counterparts, as evidence for stronger interaction of the Archaean oceans with mantle-derived rocks rather than continental crust and intense continental flux until the Palaeoproterozoic. It was the stabilization of many cratons, confined to the Archaean/ Proterozoic transition, that strongly influenced the long-term evolution of the first carbonate platforms, by creating spatially extensive, stable continental masses on which carbonates formed (Grotzinger, 1989).

Veizer et al. (1989) reported that seawater Sr isotopic composition may have commenced, its trend towards ^{87}Sr enrichment as early as 2.5 Ga ago, which was concomitant with continental growth and a decline in the intensity of hydrothermal circulation of seawater through oceanic crust. Grotzinger (1989) concluded that carbonate platforms with almost similar features of Phanerozoic platforms were well developed by the Neoarchaean. The enhanced growth of the continental crust in the late Archaean at ~ 2.7 Ga was associated with significant eustatic sea-level rise, peak of stromatolitic growth, rise of atmospheric oxygen and significant changes in ocean composition (Condie, 2004; Ohtomo, 2004).

Continental growth and input of continental detritus into the ocean on the one hand and a decreasing temperature of the mantle with less interaction of mantle-derive material with the ocean on the other hand, has been supported by several studies. For instance, the elevated non-mantle-like $^{87}Sr/^{86}Sr$ ratios of carbonate samples of the 2.7 Ga Ventersdorp Supergroup suggest their drainage basin incorporated not only volcanic rocks but also rocks of crustal affinities (Veizer et al., 1990). Kamber and Webb (2001) reported that a positive Eu- anomaly of carbonate samples of the Campbellrand platform were due to a clear shift from hydrothermally dominated rare earth element flux ratio in the Archaean to continental erosion- dominated one in the Phanerozoic.

The onset of major growth of the continental crust around 3.2-2.9 Ga and stabilization of cratons in the Neoarchaean (e.g. Condie, 1995; Rey et al., 2003), was followed by an increase

in subaerial weathering and resulting declining atmospheric CO_2 and CH_4 concentrations. The declining level of greenhouse gases led to a decreasing surface temperature, and formation of favourable environmental conditions for the flourishing of oxygenic photosynthetic microbes at 3.0-2.7 Ga (Sumner and Grotzinger, 1996a; Lowe and Tice, 2007). These microorganisms played a major role in the evolution of Earth´s atmosphere from an initial anoxic state to well-oxygenated conditions. The timing of evolution of oxygenic photosynthesis has been a matter of debate for a long time. The initial rise to significant levels of atmospheric O_2 during the Great Oxidation Event (GOE, Holland, 2006), a transition that took place between 2.5 to 2.3 Ga ago (Kopp et al., 2005; Kirschvink and Kopp, 2008), postdated the evolution of oxygen-producing bacteria by many millions, if not billions of years. The currently oldest evidence for the onset of oxygenic photosynthesis comes from evidence for elevated oxygen levels inferred from Cr and Mo isotopic studies of palaeosols and banded-iron formations of the Pongola Supergroup in the White Mfolozi inlier, South Africa (Crowe et al., 2013; Planavsky et al., 2014). The data support O_2 accumulation in the atmosphere long before the GOE. Several studies have suggested that O_2 might have been produced by cyanobacteria in isolated shallow-water environments (Kasting, 1992; Fralick and Riding, 2015; Riding et al., 2014), giving rise to accumulation of O_2 in oases even under an anoxic atmosphere (Pavlov and Kasting, 2002; Olson et al., 2013).

It has been suggested that dissolved Fe^{2+}, Mn^{2+} and to a lesser extent, Mg^{2+}, SO_4^{2-} and PO_4^{3-} inhibit calcite precipitation (Busenberg and Plummer, 1985; Meyer, 1984; Burton and Walter, 1990; Dromgoole and Walter, 1990a, 1990b). The presence of high concentrations of Fe^{2+} in reducing Palaeo-Mesoarchaean seawater (Holland, 2003), is a viable option for the absence of thick carbonate succession in these periods of time due to maintenance of the carbonate supersaturation of seawater by reducing crystallization rates and crystal nuclei formation (e.g. Sumner and Grotzinger, 1996a). Under reducing conditions, such as those present in the Palaeo-Mesoarchaean atmosphere and hydrosphere, Fe and Mn occur as highly soluble divalent cations (Holland, 1984), that can enter the structure of marine carbonates. This may explain the elevated concentrations of these elements in Palaeo-Mesoarchaean carbonates compared to those of Neoarchaean, Proterozoic and Phanerozoic carbonate rocks, which indicate precipitation from alkaline seawater saturated with respect to Fe and Mn (Veizer et al., 1989; Veizer et al., 1990).

The rise of O_2 concentrations was one of the important events that led to removal of Fe^{2+} from seawater and resulted in carbonate precipitation and formation of thick carbonate sequences by

the end of the Archaean (Sumner and Grotzinger, 1996a). Riding et al. (2014) studied the REE distribution in limestone and iron-rich sediments of the Steep Rock Group in Canada and argued for cyanobacteria to have played a major role in limestone precipitation due to not only increasing seawater pH and lowering of CO_2 concentrations, but also by removal of Fe^{2+} as inhibitor of calcite precipitation. Therefore, a high content of atmospheric O_2 led to major chemical changes in ocean and atmospheric compositions, which had a major influence on the chemical compositon of carbonate materials and their textures. The geochemical evidence for Neoarchaean seawater suggests that it has been supersaturated with respect to dissolved calcite and aragonite, which is indicated by the growth of *in-situ* calcite and aragonite on the sea floor (Sumner and Grotzinger, 2000; Sumner, 2002). The abundance of large-scale aragonite fan pseudomorphs and calcite crusts suggest a lower sedimentation rate and higher crystal growth-rate and rapid carbonate precipitation in the Neoarchaean in comparison with the Proterozoic and Phanerozoic (Grotzinger, 1989; Sumner and Grotzinger, 2000, 2004). The inhibitors of calcite precipitation such as Fe^{2+} and Mn^{2+} could have affected the texture of carbonate precipitates by limiting micrite precipitation and promoting growth of carbonate crystals on the sea floor that resulted in the precipitation of herringbone-textured calcite (Sumner and Grotzinger, 1996b; Lowe and Tice, 2007). It has been suggested that Neoarchaean carbonates formed abiotically as *in-situ* sea-floor precipitates from massive whitings (Grotzinger, 1994; Grotzinger and Knoll, 1995).

2.9 References

Abell, P.I., McClory, J., Martin, A., and Nisbet, E.G. (1985). Archaean stromatolites from the Ngesi Group, Belingwe greenstone belt, Zimbabwe: preservation and stable isotopes-preliminary results. Precambrian Res., 27, 357-383.

Allwood, A.C., Walter, M.R., Burch, I.W., and Kamber, B.S. (2007). 3.43 billion year old stromatolite reef from the Pilbara Craton of Western Australia: Ecosystem-scale insights to early life on Earth. Precambrian Res., 158, 198-227.

Allwood, A.C., Kamber, B.S., Walter, M.R., Burch, I.W., and Kanik, I. (2010). Trace elements record depositional history of an Early Archean stromatolitic carbonate platform. Chem. Geol., 270, 148-163.

Altermann, W., and Lenhardt, N. (2012). The volcano-sedimentary succession of the Archean Sodium Group, Ventersdorp Supergroup, South Africa: Volcanology, sedimentology and geochemistry. Precambrian Res., 214-215, 60-81.

Altermann, W., and Nelson, D.R. (1998). Sedimentation rates, basin analysis and regional correlations of three Neoarchaean and Palaeoproterozoic sub-basins of the Kaapvaal craton as inferred from precise U-Pb zircon ages from volcanoclastic sediments. Sediment. Geol., 120, 225-256.

Altermann, W., and Siegfried, H.P. (1997). Sedimentology and facies development of an Archean shelf-carbonate platform transition in the Kaapvaal Craton, as deduced from a deep borehole at Kathu, South Africa. J. Afr. Earth Sci., 24, 391-410.

Altermann, W., and Wotherspoon, J.McD. (1995). The carbonates of the Transvaal and Griqualand West Sequences of the Kaapvaal craton, with special reference to the Lime Acres limestone deposit. Mineral. Deposite, 30, 124-134.

Armstrong, R.A., Compston, W., Retief, E.A., Williams, I.S., and Welke, H.J. (1991). Zircon ion microprobe studies bearing on the age and evolution of the Witwatersrand triad. Precambrian Res., 53, 243-266.

Awramik, S.M., and Buchheim, H.P. (2009). A giant, Late Archean lake system: The Meentheena Member (Tumbiana Formation; Fortescue Group), Western Australia. 174, 215-240.

Ayres, L.D., Lumbers, S.B., Milne, V.G., and Robenson, D.W. (1971). Explanatory text, legend, diagrams, title, scale for Ontario geological map. Ontario Department of Mines and Northern Affairs, Map 2196.

Baral, M.C. (1986). Archaean stromatolites from Dodguni belt of Karnataka craton, India. J. Geol. Soc. India, 28, 328-333.

Barton, E.S., Altermann, W., Williams, I.S., and Smith, C.B. (1994). U-Pb zircon age for a tuff in the Campbell Group, Griqualand West Sequence, South Africa: Implications for Early Proterozoic rock accumulation rates. Geology, 22 (4), 343-346.

Beckinsale, R.D., Drury, S.A., and Holt, R.W. (1980). 3360-Myr old gneisses from the South Indian Craton. Nature (London), 283, 469-470.

Beckinsale, R.D., Reeves-Smith, G., Gale, N.H., Holt, R.W., and Thompson, B. (1982). Rb-Sr and Pb-Pb whole rock isochron ages and REE data for Archaean gneisses and granites, Karnataka state, South India (abstr.). Indo-U.S. Workshop on Precambrians of South India. Nat. Geophys. Res. Inst., Hyderabad, India, 35-36.

Berner, R.A., Lasaga, A.C., and Garrels, R.M. (1983). The carbonate-silicate geochemical cycle and its effect on atmospheric carbon dioxide over the past 100 million years. Am. J. Sci., 283, 641-683.

Beukes, N.J. (1977). Transition from siliciclastic to carbonate sedimentation near the base of the Tranvaal Supergroup, Northern Cape Province, South Africa. Sediment. Geol., 18, 201-221.

Beukes, N.J. (1983). Paleoenvironmental setting of iron formations in the depositional basin of the Transvaal Supergroup, South Africa. In: Iron Formation: facts and problems. Developments in Precambrian geology, 6. Trendall, A.F. and Morris, R.C. (Eds.), Elsevier, Amsterdam, 131-210.

Beukes, N.J. (1987). Facies relations, depositional environments and diagenesis in a major early Proterozoic stromatolitic carbonate platform to basinal sequence, Campbellrand Subgroup, Transvaal Supergroup, Southern Africa. Sediment. Geol., 54, 1-46.

Beukes, N.J., and Lowe, D.R. (1989). Environmental control on diverse stromatolite morphologies in the 3000 Ma Pongola Supergroup, South Africa. Sedimentology, 36, 383-397.

Bickle, M.J., Martin, A., and Nisbet, E.G. (1975). Basaltic and peridotitic komatiites, stromatolites and a basal unconformity in the Belingwe greenstone belt, Rhodesia. Earth Planet. Sci. Lett., 27, 155-162.

Blake, T.S., Buick, R., Brown, S.J.A., and Barley, M.E. (2004). Geochronology of a Late Archaean flood basalt province in the Pilbara Craton, Australia: constraints on basin evolution, volcanic and sedimentary accumulation and continental drift rates. Precambrian Res., 133, 143-173.

Bleeker, W. (2003). The late Archean record: a puzzle in ca. 35 pieces. Lithos, 71, 99-134.

Blockley, J.G., Tehnas, I.J., Mandyczewsky, A., and Morris, R.C. (1993). Proposed stratigraphic subdivisions of the Marra Mamba Iron Formation and the lower Wittenoom Dolomite, Hamersley Group, Western Australia. Geol. Surv. West. Aust. Report 34, 47-63.

Bolhar, R., and Van Kranendonk, M.J. (2007). A non-marine depositional setting for the northern Fortescue Group, Pilbara Craton, inferred from trace element geochemistry of stromatolitic carbonates. Precambrian Res., 155 (3), 229-250.

Bolhar, R., Hofmann, A., Woodhead, V., Hergt, J., and Dirks, P. (2002). Pb- and Nd-isotope systematics of stromatolitic limestones from the 2.7 Ga Ngezi Group of the Belingwe greenstone belt: constraints on timing of deposition and provenance. Precambrian Res., 114, 277-294.

Bowring, S., and Williams, I.S. (1999). Priscoan (4.00-4.03 Ga) orthogneisses from northwestern Canada. Contrib. Mineral. Petrol., 134, 3-16.

Brock, T.D. (1973). Lower pH limit for the existence of blue-green algae: Evolutionary and ecological implications. Science, 179, 480-483.

Buick, R. (1992). The antiquity of oxygenic photosynthesis-evidence from stromatolites in sulfate-deficient Archean lakes. Science, 255, 74-77.

Buick, R., and Dunlop, J.S.R. (1990). Evaporitic sediments of Early Archaean age from the Warrawoona Group, North Pole, Western Australia. Sedimentology, 37, 247-277.

Burton, E.A., and Walter, M. (1990). The role of pH in phosphate inhibition of calcite and aragonite precipitation rates in seawater. Geochim. Cosmochim. Acta, 54, 797-808.

Buse, S., Lewis, D., and Magnus, S. (2009). Field investigations in the Lumby Lake greenstone belt, northwestern Ontario: new insights into the geology, structure and economic potential; in summary of field work and other activities 2009, Ontario Geol. Surv., open file report 6240, 15/1-15/15.

Busenberg, E. and Plummer, L.N. (1985). Kinetic and thermodynamic factors controlling the distribution of SO_4^{2-} and Na^+ in calcites and aragonites. Geochim. Cosmochim. Acta, 49, 713-725.

Byerly, G.R., Lowe, D.R., and Walsh, M.M. (1986). Stromatolites from the 3,300-3,500 Myr Swaziland Supergroup, Barberton Mountain Land, South Africa. Nature, 319, 489-491.

Byerly, G.R., Lowe, D.R., Todt, W., and Walsh, M.M. (1996). Prolonged magmatism and time constraints for sediment deposition in the early Archean Barberton greenstone belt: Evidence from the Upper Onverwacht and Fig Tree groups. Precambrian Res., 78, 125-138.

Cavosie, A.J., Valley, J.W., and Wilde, E.I.M.F. (2005). Magmatic $\delta^{18}O$ in 4400-3900 Ma detrital zircons: A record of the alteration and recycling of crust in the Early Archean. Earth Planet. Sci. Lett., 235, 663-681.

Chadwick, B., Ramakrishnan, M., and Viswanatha, M.N., (1985). Bababudan-A Late Archaean intracratonic volcano-sedimentary basin, Karnataka, South India. J. Geol. Soc. India, 26, 769-821.

Chadwick, B., Vasudev, V.N. and Jayaram, S. (1988). Stratigraphy and structure of Late Archaean, Dharwar volcanic and sedimentary rocks and their basement in a part of the Shimoga Basin east of Bhadravathi, Karnataka. J. Geol. Soc. India, 32, 1-19.

Chadwick, B., Vasudev, V.N., and Hedge, G.V. (1997). The Dharwar craton, southern India, and its Late Archaean plate tectonic setting: current interpretations and controversies. Proc. Indian Acad. Sci. Earth Planet Sci., 106, 249-258.

Chadwick, B., Vasudev, V.N., Krishna Rao, B., and Hegde, G.V. (1991). The stratigraphy and structure of the Dharwar Supergroup adjacent to the Honnali Dome: Implications for Late Archaean basin development and regional structure in the Western part of Karnataka. J. Geol. Soc. India, 38, 457-484.

Compston, W., and Kröner, A. (1988). Multiple zircon growth within early Archean Tonalitic gneiss from the Ancient Gneiss Complex, Swaziland. Earth Planet. Sci. Lett., 87, 13-28.

Compston, W., and Pidgeon, R.T. (1986). Jack Hills, evidence of more very old detrital zircons in Western Australia. Nature, 321, 766-769.

Condie, K.C. (1995). Episodic ages of greenstones: a key to mantle dynamics? Geophys. Res. Lett., 22, 2215-2218.

Condie, K.C. (2004). Precambrian superplume events. In: The Precambrian earth: tempos and events. Eriksson, P.G., Altermann, W., Nelson, D.R., Mueller, W.U. and Catuneanu, O., (Eds.), Amsterdam, Elsevier, 163-73.

Corfu, F., and Wallace, H. (1986). U-Pb zircon ages for magmatism in the Red Lake greenstone belt, northwestern Ontario. Can. J. Earth Sci., 23, 27-42.

Cornell, D.H., Schutte, S.S., and Eglington, B.L. (1996). The Ongeluk basaltic andesite formation in Griqualand West, South Africa: submarine alteration in a 2222Ma Proterozoic sea. Precambrian Res., 79, 101-123.

Crowe, S., Dossing, L.N., Beukes, N.J., Bau, M., Kruger, S.J., Frei, R., and Candfield, D.E. (2013). Atmospheric oxygenation three billion years ago. Nature, 501, 535-538.

Davis, D.W. (1994). Report on the geochronology of rocks from the Rice Lake Belt, Manitoba, Toronto, Ontario, Canada, Royal Ontario Museum Report, 11p.

Dimroth, E. (1982). The oldest rocks on Earth: stratigraphy and sedimentology of the 3.8 billion years old Isua supracrustal sequence. In: Sedimentary geology of the highly metamorphosed Precambrian complexes. Sidorenko, A.V., (Ed.), Nauka, Moscow, 16-27.

Dixon, J.G.P. (2004). Archaean geology of the Buffalo River gorge, PhD thesis, University of KwaZulu-Natal, 263p.

Dromgoole, E.L., and Walter, L.M. (1990a). Iron and manganese incorporation into calcite: Effects of growth kinetics, temperature and solution chemistry. Chem. Geol., 81, 311-336.

Dromgoole, E.L., and Walter, L.M. (1990b). Inhibition of calcite growth rates by Mn^{2+} in $CaCl_2$ solutions at 10.25 and 50°C: Geochim. Cosmochim. Acta, 54, 2991-3000.

Eriksson, K.A. (1977). Tidal flat and subtidal sedimentation in the 2250 MY Malmani dolomite, Transvaal, South Africa. Sed. Geol., 18, 223-244.

Farquhar, J., Bao, H., and Thiemens, M. (2000). Atmospheric influence of earth's earliest sulfur cycle. Science, 289, 756-758.

Fedo, C.M. (2000). Setting and origin for problematic rocks from the > 3.7 Ga Isua Greenstone Belt, southern West Greenland: Earth's oldest coarse clastic sediments. Precambrian Res., 101, 69-78.

Fralick, P., and Riding, R. (2015). Steep Rock Lake: Sedimentology and geochemistry of an Archean carbonate platform. Earth Sci. Rev., 151, 132-175.

Fralick, P., Hollings, P., and King, D. (2008). Stratigraphy, geochemistry, and depositional environments of Mesoarchean sedimentary units in western Superior Province: implication for generation of early crust. In: When did plate tectonics begin on planet Earth? Geol. Soc. Am., Spec. Papers 440, 77-96.

Froude, D.O., Ireland, T.R., Kinny, P.D., Williams, I.S., Compston, W., Williams, I.R., and Myers, J.S. (1983). Ion microprobe identification of 4100-4200 Myr old terrestrial zircons. Nature, 304, 616-618.

Garrels, R.M., and Mackenzie, F.T. (1971). Evolution of sedimentary rocks. W.W. Norton and Company. New York, 397p.

Gold, D.J.C. (2006). The Pongola Supergroup. In: The geology of South Africa. Johnston, M.R., Anhaeusser, C.R. and Thomas, R.J. (Eds.), Geol. Soc. S. Afr. / C.G.S. Afr., 135-147.

Grobler, N.J., Van der Westhuizen, W.A., and Tordiffe, E.A.W. (1989). The Sodium Group, South Africa reference section for late Archaean-early Proterozoic cratonic cover sequences. Aust. J. Earth Sci., 36, 41-64.

Grotzinger, J.P. (1986). Cyclicity and paleoenvironmental dynamics, Rocknest platform, northwest Canada: Geol. Soc. Am. Bull., 97, 1208-1231.

Grotzinger, J.P. (1989). Facies and evolution of Precambrian carbonate depositional systems: Emergence of the modern platform archetype. In: Controls on carbonate platform and basin development. Grevello, P.D., Wilson, J.L., Sarg, J.F. and Read, J.F. (Eds.), Soc. Econ. Paleontol. Mineral. Spec. Publ. No. 44, Tulsa, UK, 79-106.

Grotzinger, J.P. (1994). Trends in Precambrian carbonate sediments and their implication for understanding evolution. In: Early life on Earth. Bengtson, S. (Editor), New York: Columbia Univ. Press, 245-58.

Grotzinger, J.P., and Kasting, J.F. (1993). New constraints on Precambrian ocean composition. J. Geol., 101, 235-243.

Grotzinger, J.P., and Knoll, A.H. (1995). Anomalous carbonate precipitates: is the Precambrian the key to the Permian? Palaios, 10, 578-596.

Harley, S.M., and Kelly, N.M. (2007). Ancient Antarctica: The Archaean of the East Antarctic Shield. In: Earth's oldest rocks. Van Kranendonk, M.J., Smithies, R.H. and Bennett, V.C. (Eds.), Elsevier, 149-186.

Hegner, E., Kröner, A., and Hofmann, A.W. (1984). Age and isotopic geochemistry of the Archaean Pongola and Ushushwana suites in Swaziland, Southern Africa: A case for crustal contamination of mantle-derived magmas. Earth Planet. Sci. Lett., 70, 267-279.

Hegner, E., Kröner, A., and Hunt, P. (1994). A precise U-Pb zircon age for the Archean Pongola Supergroup volcanics in Swaziland. J. Afr. Earth. Sci., 18 (4), 339-341.

Henderson, J.B. (1975). Archean stromatolites in the northern Slave Province. Northwest Territories, Canada. Can. J. Earth Sci., 12, 1619-1630.

Hickman, A.H. (1978). Nullagine, Western Australia. West. Aust. Geol. Surv., 1:250 000 Geol. Ser., Explanatory Notes.

Hickman, A.H. (2012). Review of the Pilbara Craton and Fortescue Basin, Western Australia: crustal evolution providing environments for early life. Island Arc, 21, 1-31.

Hickman, A.H., Chin, R. J., and Gibson, D.L. (1983). Yarrie, Western Australia: West. Aust. Geol. Surv., 1:250 000 Geol. Ser., Explanatory Notes.

Hofmann, A., Dirks, P., and Jelsma, H. (2001). Late Archaean foreland basin deposits, Belingwe greenstone belt, Zimbabwe: Sediment. Geol., 141-142, 131-168.

Hofmann, A., Dirks, P., and Jelsma, H. (2004). Shallowing-upward carbonate cycles in the Belingwe greenstone belt, Zimbabwe: A record of Archean sea-level oscillations. J. Sediment. Res., 74 (1), 64-81.

Hofmann, H.J., Thurston, P.C., and Wallace, H. (1985). Archean stromatolites from Uchi greenstone belt, northwestern Ontario. In: Evolution of Archean supracrustal sequences. Ayres, L.D., Thurston, P.C., Card, K.D. and Weber, W. (Eds.), Geol. Assoc. Can. Spec. Paper, 28, 125-132.

Hofmann, H.J., Grey, K., Hickman, A.H., and Thorpe, R. (1999). Origin of 3.45 Ga coniform stromatolites in Warrawoona Group, Western Australia. Geol. Soc. Am. Bull., 111, 1256-1262.

Holland, H.D. (1984). The chemical evolution of the atmosphere and oceans. Princeton, New Jersey, Princeton University Press, 582p.

Holland, H.D. (2003). The geologic history of seawater. In: Treatise on geochemistry. Holland, H.D. and Turekian, K.K., (Editors), 6, 538-625.

Holland, H.D. (2006). The oxygenation of the atmosphere and oceans. Phil. Trans. R. Soc. B361, 903-915.

Hunter, M.A., Bickle, M.J., Nisbet, E.G., Martin, A., and Chapman, H.J. (1998). Continental extensional setting for the Archean Belingwe greenstone belt, Zimbabwe. Geology, 26, 883-886.

Iizuka, T., Komiya, T., Uenoa, Y., Katayama, I., Uehara, Y., Maruyama, S., Hirata, T., Johnson, S.P., and Dunkley, D.J. (2007). Geology and zircon geochronology of the Acasta Gneiss Complex, northwestern Canada: New constraints on its tectonothermal history. Precambrian Res., 153, 179-208.

Jackson, M.C. (1985). Geology of the Lumby Lake area, western part, districts of Kenora and Rainy River; Ontario Geol. Surv., open file report 5534, 178p.

Kamber, B.S., and Webb, G.E. (2001). The geochemistry of late Archaean microbial carbonate: Implications for ocean chemistry and continental erosion history. Geochim. Cosmochim. Acta, 65, 15, 2509-2525.

Karhu, J.A., and Holland, D.D. (1996). Carbon isotopes and the rise of atmospheric oxygen. Geology, 24, 867-870.

Kasting, J.F. (1992). Models relating to Proterozoic atmospheric and oceanic chemistry. In: Schopf, J.W., Klein, C. (Eds.), the Proterozoic Biosphere, a multi-disciplinary study. Cambridge University Press, Cambridge, UK, 1185-1187.

Kinny, P.D., and Nutman, A.P. (1996). Zirconology of the Meeberrie gneiss, Yilgarn Craton, Western Australia: an early Archaean migmatite. Precambrian Res., 78, 165-178.

Kirschvink, J.L., and Kopp, R.E. (2008). Paleoproterozic icehouses and the evolution of oxygen mediating enzymes: The case for a late origin of photosystem-II. Phil. Trans. R. Soc. Lond. B. Biol. Sci., 363 (1504), 2755-2765.

Klein, C. (2005). Some Precambrian banded iron-formations (BIFs) from around the world: Their age, geologic setting, mineralogy, metamorphism, geochemistry, and origin. Am. Mineral., 90, 1473-1499.

Knauth, L.P. (1998). Salinity history of the Earth's early ocean. Nature, 395, 554-555.

Knauth, L.P. (2005). Temperature and salinity history of the Precambrian ocean: implications for the course of microbial evolution. Palaeogeogr. Palaeoclimatol. Palaeoecol., 219, 53-69.

Komiya, T., Maruyama, S., Masuda, T., Nohda, S., Hayashi, M., and Okamoto, K. (1999). Plate tectonics at 3.8-3.7 Ga: Field evidence from the Isua accretionary complex, southern West Greenland. J. Geol., 107, 515-554.

Kopp, R.E., Kirschvink, J.L., Hilburn, I.A., and Nash, C.Z. (2005). The Paleoproterozoic snowball Earth: A climate disaster triggered by the evolution of oxygenic photosynthesis. Proc. Natl. Acad. Sci. U.S.A., 102, 11131-11136.

Kröner, A., Byerly, C.R., and Lowe, D.R. (1991). Chronology of early Archaean granite-greenstone evolution in the Barberton Mountain Land, South Africa, based on precise dating by single zircon evaporation. Earth Planet. Sci. Lett., 103, 41-54.

Kröner, A., Hegner, E., Wendt, J.I. and Byerly, G.R. (1996). The oldest part of the Barberton granitoid-greenstone terrain, South Africa: evidence for crust formation between 3.5 and 3.7 Ga. Precambrian Res., 78, 105-124.

Kusky, T.M., and Hudleston, P.J. (1999). Growth and demise of an Archaean carbonate platform, Steep Rock Lake, Ontarioo, Canada. Can. J. Earth. Sci., 36, 565-584.

Lambert, M.B. (1998). Stromatolites of the late Archean Back River stratovolcano, Slave structural province, Northwest Territories, Canada. Can. J. Earth Sci., 35, 290-301.

Lipple, L.S. (1975). Definitions of new and revised stratigraphic units of the eastern Pilbara region. West. Aust. Geol. Surv., Annu. Report 1971, 58-63.

Liu, D., Wan, Y., Wu, J.S., Wilde, S.A., Zhou, H.Y., Dong, C.Y., and Yin, X.Y. (2007). Eoarchean rocks and zircons in the North China Craton. In: Earth's oldest rocks. Van Kranendonk, M.J., Smithies, R.H. and Bennett, V.C. (Eds.), Elsevier, 251-274.

Lowe, D.R. (1980). Stromatolites 3.400 Myr old from the Archean of Western Australia. Nature, 284, 441-443.

Lowe, D.R. (1983). Restricted shallow-water sedimentation of early Archean stromatolitic and evaporitic strata of the Strelley Pool Chert, Pilbara Block, Western Australia: Precambrian Res., 19, 239-283.

Lowe, D.R. (1992). Major events in the geological development of the Precambrian earth. In: The Proterozoic biosphere. Schopf, J.W., Klein, C. (Eds.), Cambridge University Press, Cambridge, 67-76.

Lowe, D.R., and Byerly, G.R. (1999). Stratigraphy of the west-central part of the Barberton greenstone belt, South Africa. In: Geological evolution of the Barberton greenstone belt, South Africa. Lowe, D.R. and Byerly, G.R. (Eds.), Geol. Soc. Am., Spec. Papers, 1-36.

Lowe, D.R., and Byerly, G.R. (2007). An overview of the geology of the Barberton greenstone belt and vicinity: implications for early crustal development: Dev. Precambrian Geol., 15, 481-526.

Lowe, D.R., and Fisher Worrell, G. (1999). Sedimentology, mineralogy, and implications of silicified evaporites in the Kromberg Formation, Barberton Greenstone Belt, South Africa. In: Geological evolution of the Barberton Greenstone Belt, South Africa. Lowe, D.R. and Byerly, G.R. (Eds.), Geol. Soc. Am., Spec. Papers, 167-188.

Lowe, D.R., and Knauth, L.P. (1977). Sedimentology of the Onverwacht Group (3.4 billion years), Transvaal, South Africa, and its bearing on the characteristics and evolution of the early Earth: J. Geol., 85, 699-723.

Lowe, D.R., and Nocita, B.W. (1999). Foreland basin sedimentation in the Mapepe Formation, southern-facies Fig Tree Group. Geol. Soc. Am., Spec. papers, 329, 233-258.

Lowe, D.R., and Tice, M.M. (2007). Tectonic controls on atmospheric, climatic, and biological evolution 3.5-2.4 Ga. Precambrian Res., 158, 177-197.

Mackenzie, F.T., and Morse, J.W. (1992). Sedimentary carbonates through Phanerozoic time. Geochim. Cosmochim. Acta, 56, 3281-3296.

Manikyamba, C., and Naqvi, S.M. (1997). Mineralogy and geochemistry of Archaean greenstone belt-hosted Mn formations and deposits of the Dharwar Craton: redox potential of proto-oceans. In: Manganese mineralization: Geochemistry and mineralogy of terrestrial and marine deposits. Geol. Soc. Spec. Publ., 119, 91-103.

Manikyamba, C., and Naqvi, S.M. (1998). Types and processes of Greenstone Belt formation. In: The Indian Precambrian. Paliwal, B.S. (Editor), Scientific Publishers (India), Jodhpur, 18-32.

Martin, A., Nisbet, E.G., and Bickle, M.J. (1980). Archean stromatolites of the Belingwe greenstone belt, Zimbabwe (Rhodesia). Precambrian Res., 13, 337-362.

Martin, A., Nisbet, E.G., and Orpen, J.L. (1993). Rock units and stratigraphy of the Belingwe greenstone belt: The complexity of the tectonic setting. In: The geology of the Belingwe greenstone belt Zimababwe. A study of the evolution of Archaean continental crusts. Bickle, M.J. and Nisbet, E.G. (Eds.), Geol. Soc. Zim. Spec. Publ., 2, 13-38.

Meyer, H.J. (1984). The influence of impurities on the growth rate of calcite. J. Cryst. Growth, 66, 639-646.

Mojzsis, S.J., and Harrison, T.M. (2000). Vestiges of a beginning: Clues to the emergent biosphere recorded in the oldest known sedimentary rocks. GSA Today, 10, 1-6.

Mojzsis, S.J., Harrison, T.M., and Pidgeon, R.T. (2001). Oxygen isotope evidence from ancient zircons for liquid water at the Earth's surface 4,300 Myr ago. Nature, 409, 178-181.

Morse, J.W., and Mackenzie, F.T. (1998). Hadean ocean carbonate geochemistry. Aquat. Geochim., 4, 301-319.

Mukasa, S.B., Wilson, A.H., and Young, K.R. (2013). Geochronological constraints on the magmatic and tectonic development of the Pongola Supergroup (Central Region), South. Africa. Precambrian Res., 224, 268-286.

Myers, J.S., and Crowley, J.L. (2000). Vestiges of life in the oldest Greenland rocks? A review of early Archean geology in the Godthabsfjord region, and reappraisal of field evidence for the 3,850 Ma life on Akilia. Precambrian Res., 103, 101-124.

Nakamura, K., and Kato, Y. (2004). Carbonatization of oceanic crust by the seafloor hydrothermal activity and its significance as a CO_2 sink in the Early Archean. Geochim. Cosmochim. Acta, 68 (22), 4595-4618.

Nisbet, E.G., and Fowler, M. (2013). The early history of life. In: Treatise on geochemistry. Holland, H.D. and Turekian, K.K. (Eds.), 2nd edition. Oxford: Elsevier, 10, 1-35.

Nisbet, E.G., Bickle, M.J., and Martin, A. (1977). The mafic and ultramafic lavas of the Belingwe greenstone belt. S. Rhodesia. J. Petrol., 18, 521-566.

Nisbet, E.G., Martin, A., and Bickle, M.J. (1993). The Ngezi Group: Komatiites, basalts and stromatolites on continental crust. In: The geology of the Belingwe greenstone belt Zimababwe. A study of the evolution of Archaean continental crusts. Bickle, M.J. and Nisbet, E.G. (Eds.), Geol. Soc. Zim. Spec. Publ., 2, 121-165.

Nunes, P.D., and Thurston, P.C. (1980). Two hundred and twenty million years of Archean evolution: a zircon U-Pb age stratigraphic study of the Uchi-Confederation Lakes greenstone belt, Northwestern Ontario. Can. J. Earth Sci., 17 (6), 710-721.

Nutman, A.P. (2006). Antiquity of the oceans and continents. Elements, 2, 223-227.

Nutman, A.P., Bennet, V.C., and Friend, C.R.L. (2014). The emergence of the Eoarchaean proto-arc: evolution of a c. 3700 Ma convergent plate boundary at Isua, southern West Greenland. Geol. Soc. Spec. Publ., 389, 113-133.

Nutman, A.P., Friend, C.R.L., and Paxton, S. (2009). Detrital zircon sedimentary provenance ages for the Eoarchaean Isua supracrustal belt southern West Greenland: Juxtaposition of ca. 3700 Ma juvenile arc assemblages against an older complex with 3920-3800 Ma components: Precambrian Res., 172, 212-233.

Nutman, A.P., Chadwick, B., Krishna Rao, B., and Vasudev, V.N. (1996b). SHRIMP U/Pb zircon ages of acid volcanic rocks in the Chitradurga and Sandur groups and granites adjacent to the Sandur schist belt, Karnataka. J. Geol. Soc. India, 47,153-164.

Nutman, A.P., Friend, C.R.L., Horie, K., and Hidaka, H. (2007). The Itsaq Gneiss Complex of southern West Greenland and the construction of Eoarchaean crust at convergent plate boundaries. In: Earth's oldest rocks. Van Kranendonk, M.J., Smithies, R.H. and Bennett, V.C. (Eds.), Elsevier, 187-218.

Nutman, A.P., Kinny, P.D., Compston, W., and Williams, I.S. (1991). Shrimp U-Pb zircon geochronology of the Narryer Gneiss Complex, Western Australia: Precambrian Res., 52, 275-300.

Nutman, A.P., Bennet, V.C., Friend, C.R.L., Van Kranendonk, M.J., and Chivas, A.R. (2016). Rapid emergence of life shown by discovery of 3,700-million-year-old microbial structures. Nature, 537, 535-538.

Nutman, A.P., McGregor, V.R., Friend, C.R.L., Bennett, V.C., and Kinny, P.D. (1996a). The Itsaq Gneiss Complex of southern West Greenland; the world's most extensive record of early crustal evolution (3900-3600 Ma). Precambrian Res., 78, 1-39.

Ohtomo, H. (2004). The Archaean atmosphere, hydrosphere and biosphere. In: The Precambrian earth: tempos and events. Eriksson, P.G., Altermann, W., Nelson, D.R., Mueller, W.U. and Catuneanu, O. (Eds.), Amsterdam, Elsevier, 361-88.

Ohtomo, Y., Kakegawa, T., Ishida, A., Nagase, T., and Rosing, M.T. (2014). Evidence for biogenic graphite in early Archaean Isua metasedimentary rocks. Nature, 7, 25-28.

Olson, S.L., Kump, L.R., and Kasting, J.F. (2013). Quantifying the areal extent and dissolved oxygen concentrations of Archean oxygen oases. Chem. Geol., 362, 35-43.

O'Neil, J., Maurice, C., Stevenson, R.K., Larocque, J., Cloquet, C., David, J., and Francis, D. (2007). The geology of the 3.8 Ga Nuvvuagittuq (Porpoise Cove) greenstone belt, northeastern Superior Province, Canada. In: Earth's oldest rocks. Van Kranendonk, M.J., Smithies, R.H. and Bennett, V.C. (Eds.), Elsevier, 219-250.

Pavlov, A.E., and Kasting, J.F. (2002). Mass-independent fractionation of sulfur isotopes in Archean sediments: strong evidence for an anoxic Archean atmosphere. Astrobiology, 2, 27-41.

Peucat, J.J., Bouhallier, H., Fanning, C.M., and Jayananda, M. (1995). Age of the Holenarsipur greenstone belt, relationships with the surrounding gneisses (Karnataka, South India). J. Geol., 103, 701-710.

Pirie, J. (1981). Regional geological setting of gold deposits in the Red Lake area, northwestern Ontario. In: Genesis of Archean, volcanic-hosted gold deposits, symposium held at the University of Waterloo, March 7, 1980. Ontario Geol. Surv., Miscellaneous Paper 97, 7 1-93.

Planavsky, N., Asael, D., Hofmann, A., Reinhard, Ch.T., Lalonde, S.V., Knudsen, A., Wang, X., Ossa Ossa, F., Pecoits, E., Smith, A.J.B., Beukes, N.J., Bekker, A., Johnson, T.M., Konhauser, K.O., Lyons, T.W., and Rouxel, O.J. (2014). Evidence for oxygenic photosynthesis half a billion years before the Great Oxidation Event. Nature, 7, 283-286.

Rasmussen, B, Blake, T.S., and Fletcher, I.R. (2005). U-Pb zircon age constraints on the Hamersley spherule beds: Evidence for a single 2.63 Ga Jeerinah-Carawine impact ejecta layer. Geology, 33, 725-728.

Rey, P.F., Philippot, P., and Th´ebaud, N. (2003). Contribution of mantle plumes, crustal thickening and greenstone blanketing to the 2.75-2.65 Ga global crisis. Precambrian Res., 127, 43-60.

Riding, R., Fralick, P., and Liang, L. (2014). Identification of an Archean marine oxygen oasis. Precambrian Res., 251, 232-237.

Rose, N.M., Rosing, M.T., and Bridgwater, D. (1996). The origin of metacarbonate rocks in the Archaean Isua supracrustal belt, West Greenland. Am. J. Sci., 296, 1004-1044.

Rosing, M.T. (1999). ^{13}C-depleted carbon microparticles in > 3700 Ma sea-floor sedimentary rocks from West Greenland. Science, 283, 674-676.

Rosing, M.T., Rose, N.M., Bridgwater, D., and Thomsen, H.S. (1996). Earliest part of Earth's stratigraphic record: a reappraisal of the> 3.7Ga Isua (Greenland) supracrustal sequence. Geology, 24, 43-46.

Rouchon, V., Orberger, B., Hofmann, A., and Pinti, D.L. (2009). Diagenetic Fe-carbonates in Paleoarchean felsic sedimentary rocks (Hooggenoeg Formation, Barberton greenstone belt, South Africa): implications for CO_2 sequestration and the chemical budget of seawater. Precambrian Res., 172, 255-278.

Russell, J., Chadwick, B., Krishna Rao, B., and Vasudev, V.N. (1996). Whole-rock Pb/Pb isotopic ages of Late Archaean limestones, Karnataka, India. Precambrian Res., 78 261-272.

Sakurai, R., Ito, M., Ueno, Y., Kitajima, K., and Maruyama, S. (2005). Facies architecture and sequence-stratigraphic features of the Tumbiana Formation in the Pilbara Craton, northwestern Australia: Implications for depositional environments of oxygenic stromatolites during the Late Archean. Precambrian Res., 138 (3-4), 255-273.

Sasseville, C., Tomlinson, K.Y., Hynes, A., and McNicoll, V. (2006). Stratigraphy, structure, and geochronology of the 3.0-2.7 Ga Wallace Lake greenstone belt, western Superior Province, southeast Manitoba, Canada. Can. J. Earth Sci., 43, 929-945.

Schiotte, L., Compston, W., and Bridgwater, D. (1989). Ion probe U-Th-Pb zircon dating of polymetamorphic orthogneisses from northern Labrador, Canada. Can. J. Earth Sci., 26, 1533-1556.

Schopf, J.W., and Walter, M.R. (1983). Archean microfossils: New evidence of ancient microbes. In: Earth's earliest biosphere. Schopf, J.W. (Ed.), Princeton University Press, Princeton, 214-239.

Sharma, M., and Shukla, M. (2004). A new Archaean stromatolite from the Chitradurga Group, Dharwar Craton, India and its significance. Palaeobotanist, 53, 5-16.

Simonson, B.M. (1992). Geological evidence for a strewn field of impact spherules in the early Precambrian Hamersley Basin of Western Australia. Geol. Soc. Am. Bull., 104, 829-839.

Simonson, B.M., and Hassler, S.W. (1997). Revised correlations in the Early Precambrian Hamersley Basin based on a horizon of resedimented impact spherules. Aust. J. Earth Sci., 44, 37-48.

Simonson, B.M., Schubel, K.A., and Hassler, S.W. (1993). Carbonate sedimentology of the early Precambrian Hamersley Group of Western Australia. Precambrian Res., 60, 287-335.

Srinivasan, R., Shukla, M., Naqvi, S.M., Yadav, V.K., Venkatachala, B.S., Uday Raj, B., and Subba Rao, D.V. (1989). Archaean stromatolites from the Chitradurga Schist Belt, Dharwar Craton, South India. Precambrian Res., 43, 239-250.

Stott, G.M., and Corfu, F. (1991). Uchi Subprovince. In: The geology of Ontario; Ontario Geol. Surv. Spec., Volume 4, Part 1, 145-238.

Sumner, D.Y. (1997). Carbonate precipitation and oxygen stratification in late Archean seawater as deduced from facies and stratigraphy of the Gamohaan and Frisco Formations, Transvaal Supergroup, South Africa. Am. J. Sci., 297, 455-487.

Sumner, D.Y. (2002). Decimetre-thick encrustations of calcite and aragonite on sea-floor and implications for Neoarchaean and Neoproterozoic ocean chemistry. In: Precambrian sedimentary environments: A modern approach to ancient depositional systems, special publication number 33 of the international association of sedimentologists. Altermann, W. and Corcoran, P.L., (Eds.), Blackwell Science, 107-120.

Sumner, D.Y., and Bowring, S.A. (1996). U–Pb geochronologic constrains on deposition of the Campbellrand Subgroup, Transvaal Supergroup, South Africa. Precambrian Res., 79 (1/2), 25-36.

Sumner, D.Y., and Grotzinger, J.P. (1996a). Were kinetics of Archean calcium carbonate precipitation related to oxygen concentration? Geology, 24, 119-122.

Sumner, D.Y., and Grotzinger, J.P. (1996b). Herringbone calcite: petrography and environmental significance. J. Sediment. Res., 66, 419-429.

Sumner, D.Y., and Grotzinger, J.P. (2000). Late Archean aragonite precipitation: petrography, facies associations, and environmental significance. In: Carbonate sedimentation and diagenesis in the evolving Precambrian world. Grotzinger, J.P. and James, N.P. (Eds.), SEPM Spec. Publ., 33, 107-120.

Sumner, D.W., and Grotzinger, J.P. (2004). Implication for Neoarchaean ocean chemistry from primary carbonate mineralogy of the Campbellrand-Malmani Platform, South Africa. Sedimentology, 51, 1273-1299.

Sumner, D.Y., Beukes, N.J., and Grotzinger, J.P. (1991). Massive marine cementation of the Archean Campbellrand-Malmani carbonate platform, South Africa. Geol. Assoc. Can. Program with Abstracts, 16: A120.

Swami Nath, J., and Ramakrishnan, M. (1981). Early Precambrian supracrustals of southern Karnataka. Geol. Surv. India, Mem. 112, 350p.

Taylor, P.N., Moorbath, S., Chadwick, B., Ramakrishnan, M., and Viswanatha, M.N. (1984). Petrology, chemistry and isotopic ages of Peninsular Gneiss, Dharwar acid volcanic rocks and the Chitradurga granite with special reference to the late Archaean evolution of the Karnataka Craton, Southern India. Precambrian Res., 23, 349-375.

Thorne, A.M., and Trendall, A.F. (2001). Geology of the Fortescue Group, Pilbara Craton, Western Australia. West. Aust. Geol. Surv. Bull., 249p.

Thorpe, R.I., Hickman, A.H., Davis, D.W., Mortensen, J.K., and Trendall, A.F. (1992). Constraints to models for Archaean lead evolution from precise U-Pb geochronology from the Marble Barregion, Pilbara Craton, Western Australia. In: The Archaean: terrains, processes and metallogeny. Glover, J.E. and Ho, S. (Eds.), Geology Department and University Extension, The University of Western Australia, Publication, 22, 395-408.

Thurston, P.C., and Chivers, K.M. (1990). Secular variation in greenstone sequence development emphasizing Superior Province, Canada. Precambrian Res., 46, 21-58.

Thurston, P.C., and Fryer, B.J. (1983). The geochemistry of repetitive volcanism from basalt trough rhyolite in the Uchi-Confederation greenstone belt, Canada. Contrib. Mineral. Petrol., 83, 204-226.

Tomlinson, K.Y., Davis, D.W., Stone, D., and Hart, T.R. (2003). U-Pb age and Nd isotopic evidence for Archean terrane development and crustal recycling in the south-central Wabigoon Subprovince, Canada. Contrib. Mineral. Petrol., 144, 684-702.

Tomlinson, K.Y., Stott, G.M., Percival, J.A., and Stone, D. (2004). Basement terrane correlation and crustal recycling in the western Superior Province: Nd isotopic character of granitoid and felsic volcanic rocks in the Wabigoon Subprovince, N. Ontario, Canada; Precambrian Res., 132, 245-274.

Trendall, A.F. (1983). The Hamersley Basin. In: Iron-formations: facts and problems. Trendall, A.F. and Morris, R.C. (Eds.), Elsevier, Amsterdam, 69-129.

Trendall, A.F., Laeter, de J.R., Nelson, D.R., and Mukhopadhyay, D. (1997). A precise zircon U-Pb age for the base of the BIF of the Mulaingiri Formation (Bababudan Group, Dharwar Supergroup) of the Karnataka craton. J. Geol. Soc. India, 50, 161-170.

Truswell, J.F., and Eriksson, K.A. (1975). A palaeoenvironmental interpretation of the early Proterozoic Malmani dolomite from Zwartkops, South Africa. Precambrian Res., 2, 277-303.

Turek, A., and Weber, W. (1991). New U–Pb ages for the Rice Lake area; evidence for 3 Ga crust. Manitoba Energy and Mines, Mineral Division, report of activities 1991. 53-55.

Van Breemen, O., Davis, W.J., and King, J.E. (1992). Temporal distribution of granitoid plutonic rocks in the Archean Slave province, northwest Canadian Shield. Can. J. Earth Sci., 29, 2186-2199.

Van der Westhuizen, W.A., De Bruiyn, H., and Meintjes, P.G. (1991). The Ventersdorp Supergroup: An overview. J. Afr. Earth Sci., 13, 83-105.

Van der Westhuizen, W.A., De Bruiyn, H., and Meintjes, P.G. (2006). The Ventersdorp Supergroup. In: The geology of South Africa. Johnson, M.R., Anhaeusser, C.R. and Thomas, R.J. (Eds.), Geol. Soc. S. Afr. /Council for Geoscience, Johannesburg/Pretoria, 187-208.

Van Kranendonk, M.J. (2006). Volcanic degassing, hydrothermal circulation and the flourishing of early life on Earth: A review of the evidence from c. 3490-3240 Ma rocks of the Pilbara Supergroup, Pilbara Craton, Western Australia. Earth Sci. Rev., 74, 197-240.

Van Kranendonk, M.J., Webb, G.E., and Kamber, B.S. (2003). Geological and trace element evidence for a marine sedimentary environment of deposition and biogenicity of 3.45 Ga stromatolitic carbonates in the Pilbara Craton, and support for a reducing Archean ocean. Geobiology, 1 (2), 91-108.

Van Kranendonk, M.J., Smithies, R.H., Hickman, A.H., and Champion, D.C. (2007). Review: Secular tectonic evolution of Archaean continental crust: interplay between horizontal and vertical processes in the formation of the Pilbara Craton, Australia. Terra Nova 19, 1-38.

Van Kranendonk, M.J., Hickman, A.H., Smithies, R.H., Nelson, D.N., and Pike, G. (2002). Geology and tectonic evolution of the Archaean North Pilbara terrain, Pilbara Craton, Western Australia. Econ. Geol., 97, 695-732.

Van Kranendonk, M.J., Philippot, P., Lepot, K., Bodorkos, S., and Piranjo, F. (2008). Geological setting of Earth's oldest fossils in the ca. 3.5 Ga Dresser Formation, Pilbara Craton, Western Australia. Precambrian Res., 167, 93-124.

Van Kranendonk, M.J., Hickman, A.H., Smithies, R.H., Williams, I.R., Bagas, L., and Farrell, T.R. (2006). Revised lithostratigraphy of Archean supracrustal and intrusive rocks in the northern Pilbara Craton, Western Australia. West. Aust. Geol. Sur., Record 2006/15, 57p.

Van Kranendonk, M.J., Smithies, R.H., Hickman, A.H., Bagas, L., Williams, I.R., and Farrell, T.R. (2004). Event stratigraphy applied to 700 million years of Archaean crustal evolution, Pilbara Craton, Western Australia. West. Aust. Geol. Sur. Annu. Rev. 2003-2004, 49-61.

Van Staal, C.R. (1998). Some notes on the assemblage boundaries and internal structure of the Uchi-Confederation greenstone belt, northwestern Ontario; and current research 1998-C; Geol. Surv. Can., 107-114.

Veizer, J. (1988). The evolving exogenic cycle. In: Chemical cycles in the evolution of the Earth. Gregor, C.B., Garrela, R.M., Mackenzie, F.T., and Maynard, J.B., (Eds.), Wiley, New York, 175-220.

Veizer, J., Hoefs, J., Lowe, D.R., and Thurston, P.C. (1989). Geochemistry of Precambrian carbonates: II. Archean greenstone belts and Archean seawater. Geochim. Cosmochim. Acta, 53, 859-871.

Veizer, J., Clayton, R.N., Hinton, R.W., Von Brunn, V., Mason, T.R., Buck, S.G., and Hoefs, J. (1990). Geochemistry of Precambrian carbonates: 3-shelf seas and non-marine environments of the Archean. Geochim. Cosmochim. Acta, 54, 2717-2729.

Viljoen, M.J., and Viljoen, R.P. (1969a). An introduction to the geology of the Barberton granite-greenstone terrain. Geol. Soc. South Afr. Spec. Publ., 2, 9-28.

Viljoen, M.J., and Viljoen, R.P. (1969b). The geological and geochemical significance of the upper formations of the Onverwacht Group. Geol. Soc. South Afr. Spec. Publ., 2, 113-152.

Walker, J.C.G., Hays, P.B., and Kasting, J.F. (1981). A negative feedback mechanism for the long-term stabilization of Earth's surface temperature. J. Geophys. Res., 86, 9776-9782.

Wallace, H., Thurston, P.C., and Corfu, F. (1986). Development in stratigraphic correlation: Western Uchi Subprovince. In: Volcanology and mineral deposits. Wood, J. and Wallace, H. (Eds.), Ontario Geol. Surv., Miscellaneous Paper 129, 88-102.

Walraven, F., Armstrong, R.A., and Kruger, F.J. (1990). A chronostratigraphic framework for the north-central Kaapvaal Craton, the Bushveld Complex and the Vredeford structure, Tectonophysics, 171, 23-48.

Walter, M.R. (1983). Archean stromatolites: evidence of the Earth's earliest benthos. In: Earth's earliest biosphere. Schopf, J.W. (Ed.), Princeton University Pres, Princeton, 187-213.

Wilde, S.A., Valley, J.w., Peck, W.H., and Graham, C.M. (2001). Evidence from detrital zircons for the existence of continental crust and oceans on the Earth 4.4 Gyr ago. Nature, 409, 175-178.

Wilks, M.E., and Nisbet, E.G. (1985). Archaean stromatolites from the Steep Rock Group, northwestern Ontario, Canada. Can. J. Earth. Sci., 22, 792-799.

Wilks, M.E., and Nisbet, E.G. (1988). Stratigraphy of the Steep Rock Group, north-western Ontario, A major Archean unconformity and Archaean stromatolites. Can. J. Earth. Sci., 25, 370-391.

Wilson, A.H., and Versfeld, J.A. (1994). The early Archaean Nondweni greenstone belt, southern Kaapvaal Craton, South Africa; Part 2. Characteristics of the volcanic rocks and constraints on magma genesis. Precambrian Res., 67 (3-4), 277-320.

Wright, D.T., and Altermann, W. (2000). Microfacies development in Late Archaean stromatolites and oolites of the Ghaap Group of South Africa. In: Carbonate platform systems: components and interactions. Insalaco, E., Skelton, P.W. and Palmer, T.J. (Eds.), Geol. Soc. London, Spec. Publ., 178, 51-70.

Xie, H., Hofmann, A., Hegner, E., Wilson, A.H., Wan, Y., and Liu, D. (2012). Zircon SHRIMP dating confirms a Palaeoarchaean supracrustal terrain in the southeastern Kaapvaal Craton, Southern Africa. Gondwana Res., 21 (4), 818-828.

Chapter 3: Sedimentology and facies analysis of Mesoarchaean stromatolitic carbonate rocks of the Pongola Supergroup, South Africa

Sedimentology and facies analysis of Mesoarchaean stromatolitic carbonate rocks of the Pongola Supergroup, South Africa

M. Siahi [a, c], A. Hofmann [b], E. Hegner [a], S. Master [c]

[a] Department of Earth and Environmental Sciences, Ludwig-Maximilians-University, Munich, Germany

[b] Department of Geology, University of Johannesburg, Johannesburg, South Africa

[c] Economic Geology Research Institute, School of Geosciences, University of Witwatersrand, Johannesburg, South Africa

doi: 10.1016/j.precamres.2016.03.004

Abstract

The c. 3.0 Ga old Chobeni Formation (Nsuze Group, Pongola Supergroup) contains several carbonate successions interpreted to have been deposited in a tide-dominated, shallow-marine environment. Facies consist of mixed siliciclastic and carbonate rocks and include subtidal cross-bedded sandstone and oncolitic dolostone, intertidal wave-rippled oodolarenite, and supratidal wrinkly-laminated dolarenite–dololutite. Sedimentary facies are partially arranged in a shallowing-upward pattern reflecting cyclic variations of Mesoarchaean sea level. Microbialites occur in a variety of sedimentary sub-environments and include laminated as well as structureless, lenticular-domal types. Differences in microbialite morphology, macrofabric, and size suggest potentially distinct assemblages of microorganisms responding to different physicochemical and environmental conditions. Microbialite textures are consistent with *in-situ* carbonate precipitation and to a lesser extent by trapping and binding of sediment. Despite their great age, the Pongola carbonates are compositionally and texturally very similar to much younger carbonate successions preserved in the geological record.

3.1 Introduction

Archaean sedimentary carbonate rocks are most commonly found in the Neoarchaean Era. The Wittenoom Formation and Carawine Dolomite of the Hamersley Group, Australia (Simonson et al., 1993) and the Campbellrand-Malmani subgroups of the Transvaal Supergroup, South

Africa (Beukes, 1987; Sumner and Grotzinger, 2004) straddle the Archaean-Proterozoic boundary and represent the oldest large-scale carbonate platform deposits. These rocks are well known for their record of marine life (Beukes, 1987; Altermann and Schopf, 1995) and have provided important information on seawater composition (Sumner and Grotzinger, 2004). Similarly, carbonate rocks are widely developed in a number of greenstone belts, specifically in the Slave, Superior, Dharwar, and Zimbabwe cratons (Henderson, 1975; Srinivasan et al., 1989; Hofmann et al., 2004; Fralick and Riding, 2015). Carbonate rocks of inferred lacustrine setting have also been reported from intracontinental volcano-sedimentary basins of the Kaapvaal and Pilbara cratons (Ventersdorp and Fortescue Supergroups, respectively; Buck, 1980; Bolhar and Van Kranendonk, 2007; Altermann and Lenhardt, 2012). Prior to the Neoarchaean Era carbonate rocks are relatively rare. This is specifically the case for Mesoarchaean carbonate rocks, exposures of which can be found in the c. 3.0 Ga Nsuze Group of the Pongola Supergroup, South Africa (Mason and Von Brunn, 1977; Beukes and Lowe, 1989; Dixon, 2004). Palaeoarchaean carbonate rocks are commonly silicified and include those from the 3.49 Ga Dresser Formation, the 3.42-3.35 Ga Strelley Pool Formation of the Pilbara Supergroup, Western Australia (Lowe, 1980; Van Kranendonk, 2006), and the 3.41 Ga Witkop Formation, Nondweni Group, South Africa (Wilson and Versfeld, 1994; Xie et al., 2012). Palaeoarchaean carbonate rocks typically form units less than 20 m thick and are believed to have been deposited in low-energy, shallow-marine environments between episodes of volcanism (Grotzinger, 1989; Van Kranendonk et al., 2003; Allwood et al., 2006). Here we report on carbonate and associated siliciclastic facies from the Nsuze Group of the Pongola Supergroup in the White Mfolozi inlier of KwaZulu-Natal. Since the sedimentological study of Beukes and Lowe (1989) of a single outcrop, no detailed facies analysis has been undertaken on these rocks. This paper outlines and interprets the sedimentological characteristics and facies of three stratigraphically distinct sections in the White Mfolozi inlier with the goal to reconstruct depositional environments and to shed light on surface processes influencing the habitat of early life.

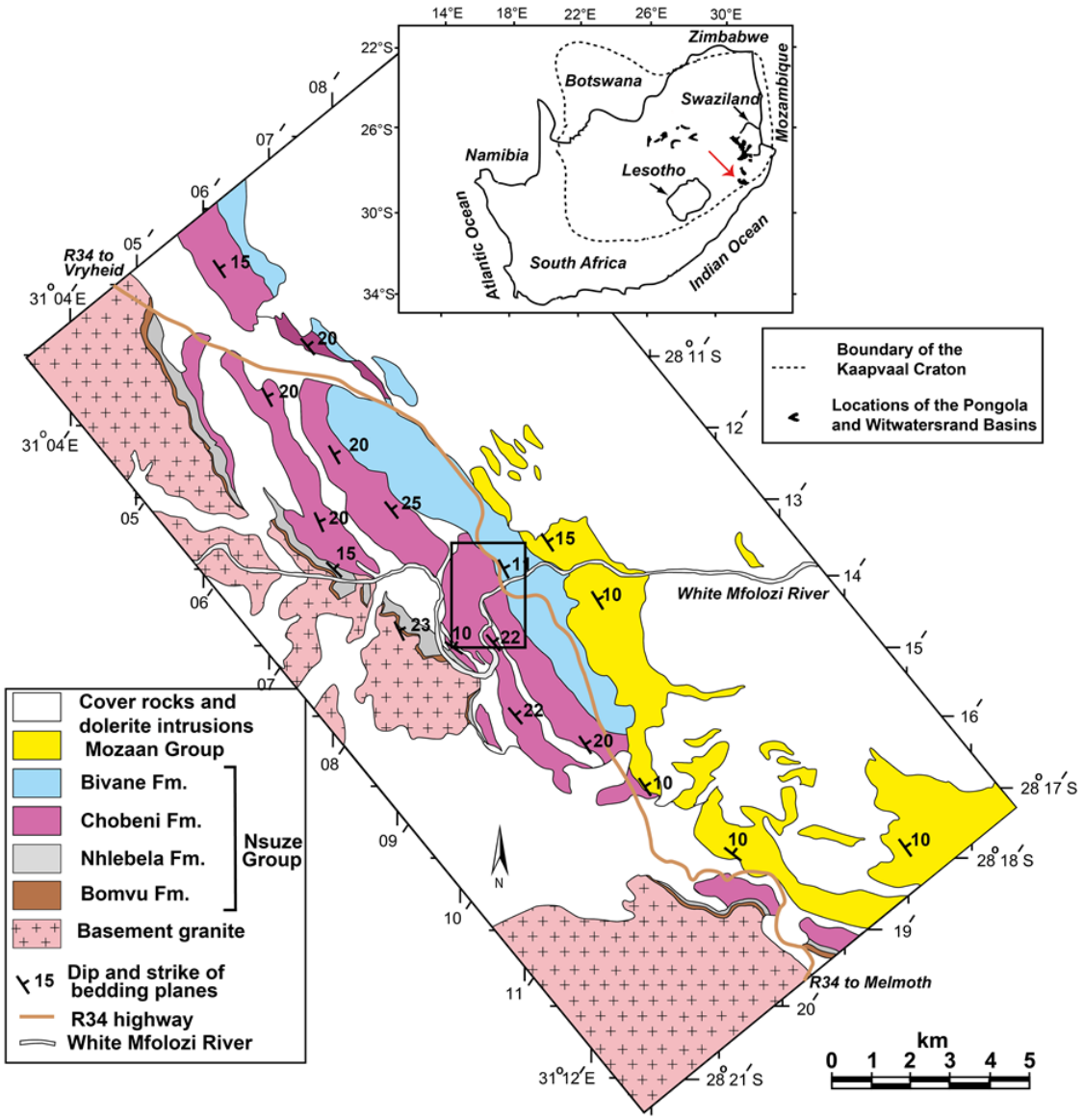

Fig. 1. Geological map of the White Mfolozi inlier (modified after Wilson et al., 2013). Rectangle shows outline of the study area (Fig. 3). Inset shows distribution of the Pongola and Witwatersrand supergroups in relation to the Kaapvaal Craton in South Africa; red arrow points to White Mfolozi inlier. (For interpretation of the references to color in this figure legend, the reader is referred to the web version of this article.)

3.2 Geological setting

The Mesoarchaean Pongola Supergroup was deposited on the south-eastern Kaapvaal Craton and is one of the oldest well-preserved successions of epicratonic volcanic and sedimentary rocks (Fig. 1).

It unconformably overlies granitoid-greenstone basement and crops out as inliers surrounded by younger Phanerozoic sedimentary rocks of the Karoo Supergroup. Following deposition between c. 3.0 and 2.9 Ga ago (Hegner et al., 1984, 1994; Mukasa et al., 2013), the Pongola Supergroup was intruded by mafic and ultramafic dykes and sheets of the c. 2.99-2.87 Ga Usushwana Complex, by granite plutons as young as 2.72 Ga, and by several distinct suites of dolerite dykes and sills (Schoene and Bowring, 2010; Olsson et al., 2010; Mukasa et al., 2013; Gumsley et al., 2015). The Pongola Supergroup is composed of two stratigraphic units: the mainly volcanic Nsuze Group and overlying strata of the mainly sedimentary Mozaan Group (Fig. 2). Deposition occurred in a shallow-marine basin in which sediments were supplied from the northwest (Von Brunn and Hobday, 1976; Beukes and Cairncross, 1991; Gold, 2006). The study area in the White Mfolozi inlier exposes the c. 1.4 km thick Nsuze Group and the c. 0.7 km thick Mozaan Group, the latter of which is overlain unconformably by Permian sedimentary rocks of the Karoo Supergroup (Matthews, 1967; Wilson and Grant, 2006; Hicks and Hofmann, 2012). The Nsuze Group comprises five formations in the White Mfolozi inlier (Fig. 2). The Bomvu Formation overlies granitoid basement along an irregular contact and consists of coarse-grained sandstones up to 10 m thick with local intercalations of pebble conglomerate. The Nhlebela Formation is up to 110 m thick, rests with a sharp contact on the basal sandstone or directly on granite and consists of basaltic to andesitic lava with pillow-structures near the base. The Thembeni Formation is c. 60 m thick and consists of shale with local intercalations of pebbly greywacke at the base. Shale grades into sandstones of the basal Chobeni Formation, which is c. 450 m thick and sharply overlain by up to 400 m of amygdaloidal basaltic lava of the Bivane Formation.

The Chobeni Formation is the focus of this study. Although dominantly siliciclastic, the Chobeni Formation contains several units of dolomite with locally well-developed stromatolites. Dolomite facies have been previously interpreted to have formed in a shallow, tide-dominated, marine setting (Mason and Von Brunn, 1977; Von Brunn and Mason, 1977; Beukes and Lowe, 1989). Four sedimentary units containing dolomite admixed with siliciclastic and volcaniclastic particles (cemented, and partly replaced, by dolomite) are referred to as the lower, main, middle, and upper carbonate sections (Figs. 2 and 3).

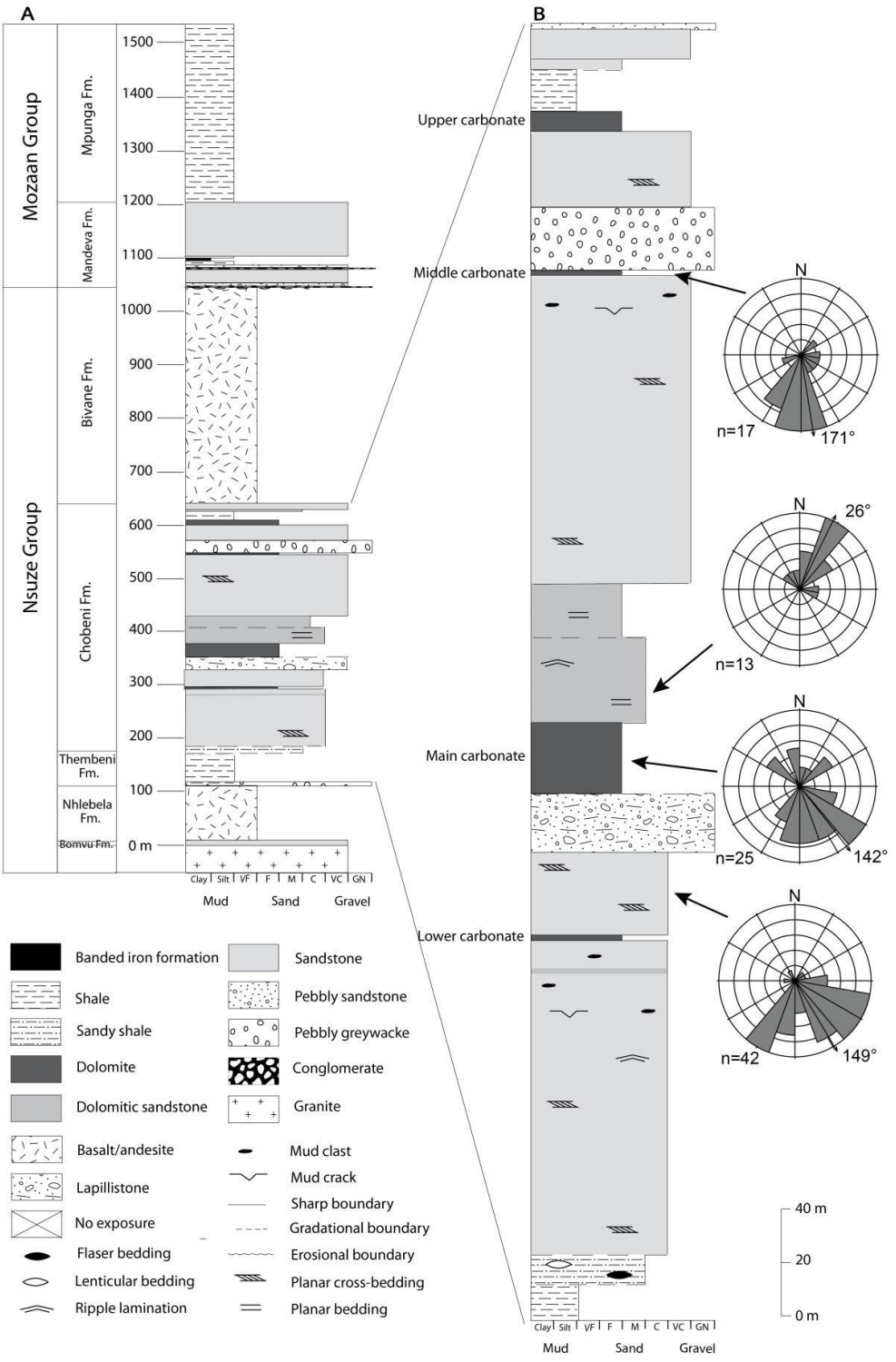

Fig. 2. Stratigraphic column of the Nsuze and Mozaan groups (column A) of the Pongola Supergroup in the White Mfolozi inlier. The Chobeni Formation, studied in detail, is shown in column B. Rose diagrams show results of palaeocurrent measurements of well-exposed, predominantly tabular cross-bedding from four stratigraphic intervals of the Chobeni Formation.

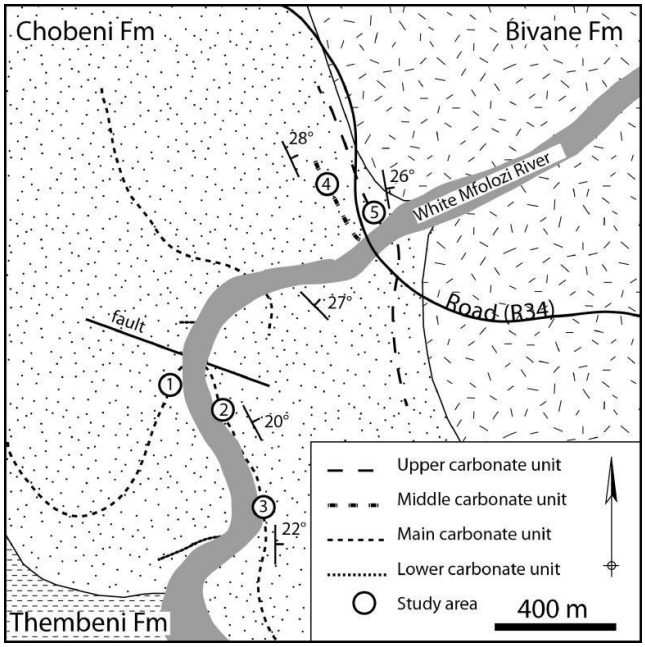

Fig. 3. Geological sketch map showing the localities of the five sections studied in the White Mfolozi inlier (see Fig. 1 for overview).

The Chobeni Formation commences with thinly bedded sandstone and shale with lenticular to flaser bedding suggestive of a tide-influenced environment (Fig. 4A). This is overlain by cross-bedded quartz-arenite that consists of tabular co-sets of cross-bedded coarse-grained sandstone. This assemblage probably formed in a subtidal environment. Higher in the section, thinly bedded sandstone-shale units that show wave ripples and mud-cracks are intercalated with cross-bedded sandstones, suggesting broadly intertidal conditions with periodic emergence. In this unit, mud-clasts (Fig. 4B) are common, indicating regular reworking of the mud-cracked tidal flats. Near the top of the sandstone succession there are two thin units of quartz sand-rich dolomite, showing cross-bedding, in addition to massive domains of micritic dolomite and oodolorudite. The more prominent upper horizon is referred to here as the lower carbonate section (Figs. 2 and 3) and was not studied in detail. Palaeocurrent measurements in this part of the section show a predominantly southeast- and likely offshore-directed sediment transport (Fig. 2). The sandstones are sharply overlain by a planar-bedded lapillistone (Fig. 2) containing accretionary lapilli that suggest an origin as a pyroclastic air fall deposit. The lapillistone is variably cemented or replaced by carbonate, especially near the top, and is gradationally overlain by the main carbonate section (Fig. 2). Small, non-laminated domal microbialites surrounded by lapillistone are present along the contact (Fig. 4C). The main carbonate section has a thickness of c. 28 m (Figs. 2 and 5) and is tectonically duplicated by faulting (Fig. 3).

Cross-bedding in sandstone facies within the main carbonate section shows bimodal, but predominantly southeast-directed, sediment transport (Fig. 2). The carbonate rocks are overlain by co-sets of thin to medium beds of planar-bedded, tabular cross-bedded, and locally wave ripple-laminated sandstone. The sandstone shows irregular carbonate-cemented or carbonate-replaced domains (Fig. 4D) and contains intercalations of irregularly bedded carbonate rocks. Cross-bedding in the sandstone reflects sediment transport to the northeast, suggesting either local basin reorganization or longshore currents. The dolomitic sandstone is overlain by a thick succession of medium to thick beds of planar- and cross-bedded, coarse-grained sandstone with minor mud clasts and thin intercalations of mud layers showing mud-cracks, interpreted as subtidal, and at times emerged, sand bars.

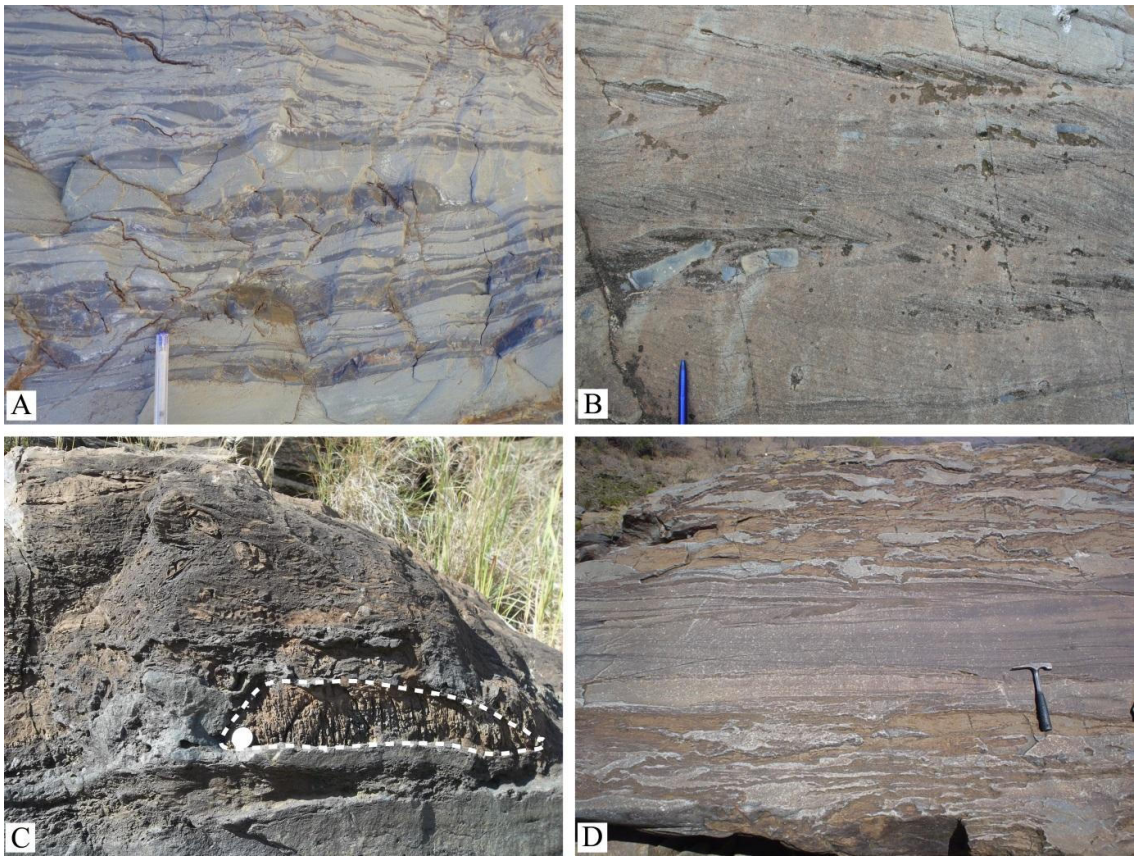

Fig. 4. Photographs of different stratigraphic units of the Chobeni Formation. (A) Alternating sandstone and shale with wavy-flaser bedding. (B) Cross-bedded sandstone with mudstone intraclasts (above pen). (C) Detail of gradational contact between lapillistone and carbonate. Non-laminated domal microbialites (outlined by dashed line) are surrounded by lapillistone. (D) Planar-bedded carbonate-cemented sandstone with irregular domains of primary and secondary dolomite.

The middle carbonate section rests with a sharp contact on cross-bedded sandstone with wave ripple marks on bedding planes. It is c. 2 m thick, shows evidence for sediment transport to the south-southeast, and is overlain along a sharp, planar contact by pebbly greywacke (Figs. 2 and 6). The pebbly greywacke is more than 20 m thick, shows crude planar stratification, consists of poorly sorted matrix-rich sandstone with pebbles and cobbles of chert and quartz, and is interpreted as a mass flow deposit. Dolomite clasts occur in its lower portion. The middle carbonate section is absent in places along strike, suggesting erosion during deposition of the pebbly greywacke.

The greywacke bed is overlain by cross-bedded sandstone and followed by the upper carbonate section, which is more than 9 m thick. Its upper contact is not exposed in the river section studied (Fig. 6). The upper carbonate is overlain by shale that coarsens upward into cross-bedded sandstones that form the top of the Chobeni Formation.

The rock assemblages in the White Mfolozi inlier have been subjected to greenschist facies metamorphism. Besides minor tilting, the cleavage in argillaceous dolomitic units indicates that this succession experienced open folding on a regional scale. Contact metamorphism occurs along the margin of some dolerite sills intrusive into the dolomite units, giving rise to talc-carbonate schists. Except for recrystallization of the carbonate rocks, their textures and sedimentary structures are very well-preserved.

3.3 Materials and methods of study

The main, middle and upper carbonate sections were studied in detail in the field. The main carbonate section was measured at three localities (Fig. 3, localities 1-3) in order to evaluate lateral facies changes. Sedimentary textures are best preserved in the main and middle sections, whereas the upper carbonate section is more extensively recrystallized. Sixty-five representative samples were collected from these sections for additional studies on facies variation. Forty five polished slabs and 110 polished thin sections were studied for carbonate texture and microstructure using binocular and petrographic microscopes. The terminology of carbonate textures follows that of Folk (1959, 1962). The mineralogical composition was determined by a combination of transmitted and reflected light microscopy, staining, scanning electron microscopy (SEM) and X-ray diffraction (XRD) analysis of bulk samples. Potassium ferricyanide and Alizarin red-S were used as staining agents to distinguish carbonate minerals

in a few selected thin sections (Friedman, 1959; Dickson, 1966). Raman spectroscopy was carried out on polished thin sections using an alpha300R (WITec) confocal laser Raman microscope configured with a frequency-doubled Nd-YAG laser (wavelength 532 nm) at the Department of Geology, University of Johannesburg. The system couples motorized sample positioning with a piezo-driven scan platform, allowing Raman mapping from micrometre- to centimetre-scale. The analyses were made using a 20 Nikon objective with a numerical aperture of 0.4 and with a maximum of 8 mW laser power to prevent thermal degradation. Carbon-coated thin sections were examined and analyzed with the aid of an Oxford INCA Energy-Dispersive Spectrometer (EDS) attached to a Tescan SEM. X-ray diffraction of selected samples was performed with a Panalytical X-PertPro series X-ray diffractometer, also at the University of Johannesburg.

3.4 Constituents and composition of the carbonate units

The composition of the carbonates differs with stratigraphic position. The dominant composition of carbonates of the middle carbonate section is ankerite, whereas the main and upper carbonate sections consist of dolomite. The good state of preservation of these carbonates indicates that they had a stable primary mineralogical composition, i.e. calcite rather than aragonite, or that they originally precipitated as dolomite. Dolomitization of high-Mg calcite generally provides better fabric retention than if low-Mg calcite is the precursor mineral (Sibley, 1982). However, since low-Mg calcite is present as a diagenetic phase, filling early diagenetic fenestrae and replacing dolomitic allochems marginally, we suggest that the primary composition of the carbonates was either high-Mg calcite subjected to very early diagenetic dolomitization, or, less likely, dolomite. No significant differences in composition were detected among micrite matrix, allochems, and microbialites. The carbonate rocks are rarely monomineralic, however, as they contain a variety of allochems, siliciclastic detritus, pyroclastic particles as well as secondary diagenetic and metamorphic phases.

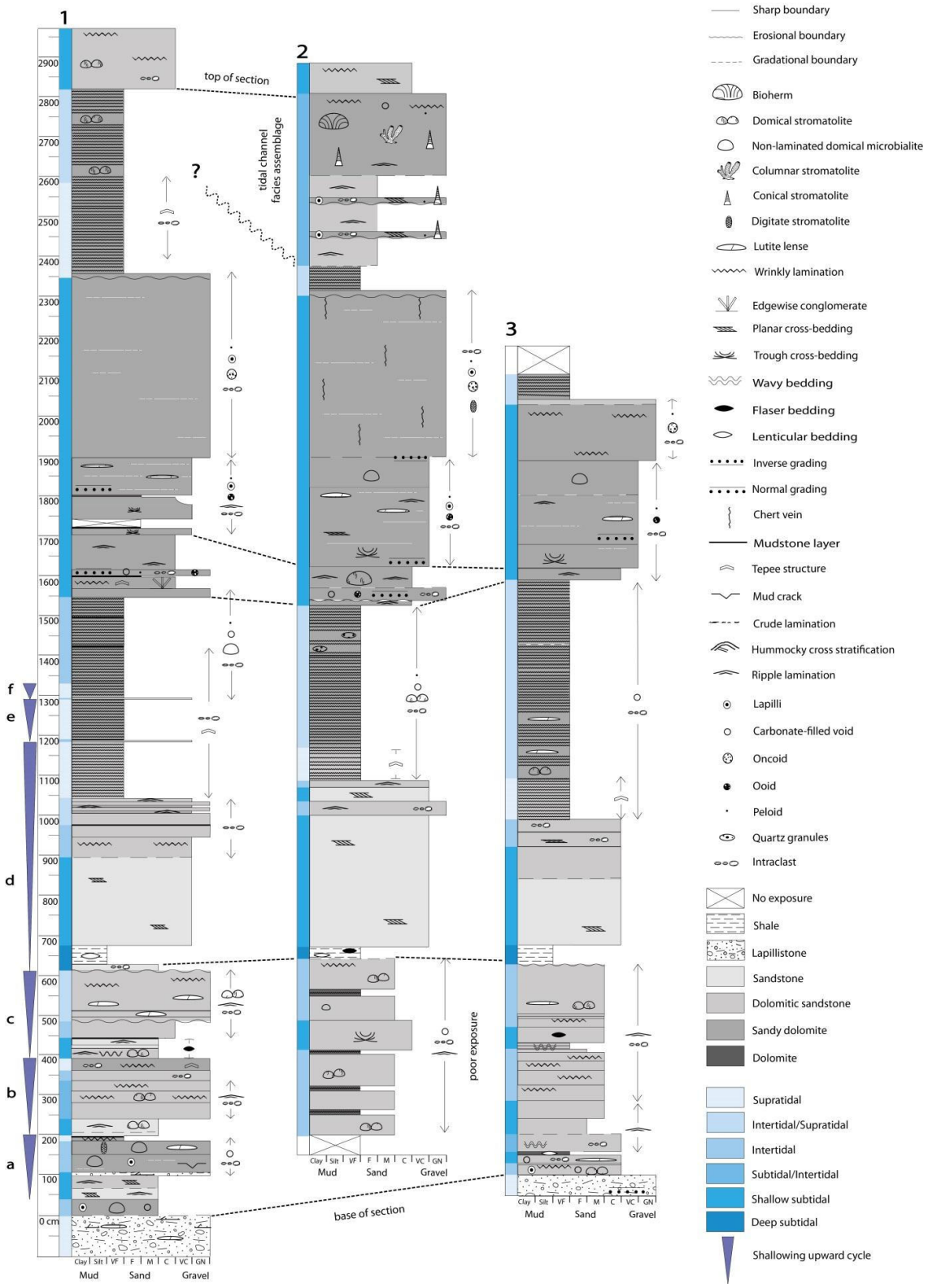

Fig. 5. Stratigraphic columns 1 to 3 of the main carbonate section of the Chobeni Formation. See Fig. 3 for locality.

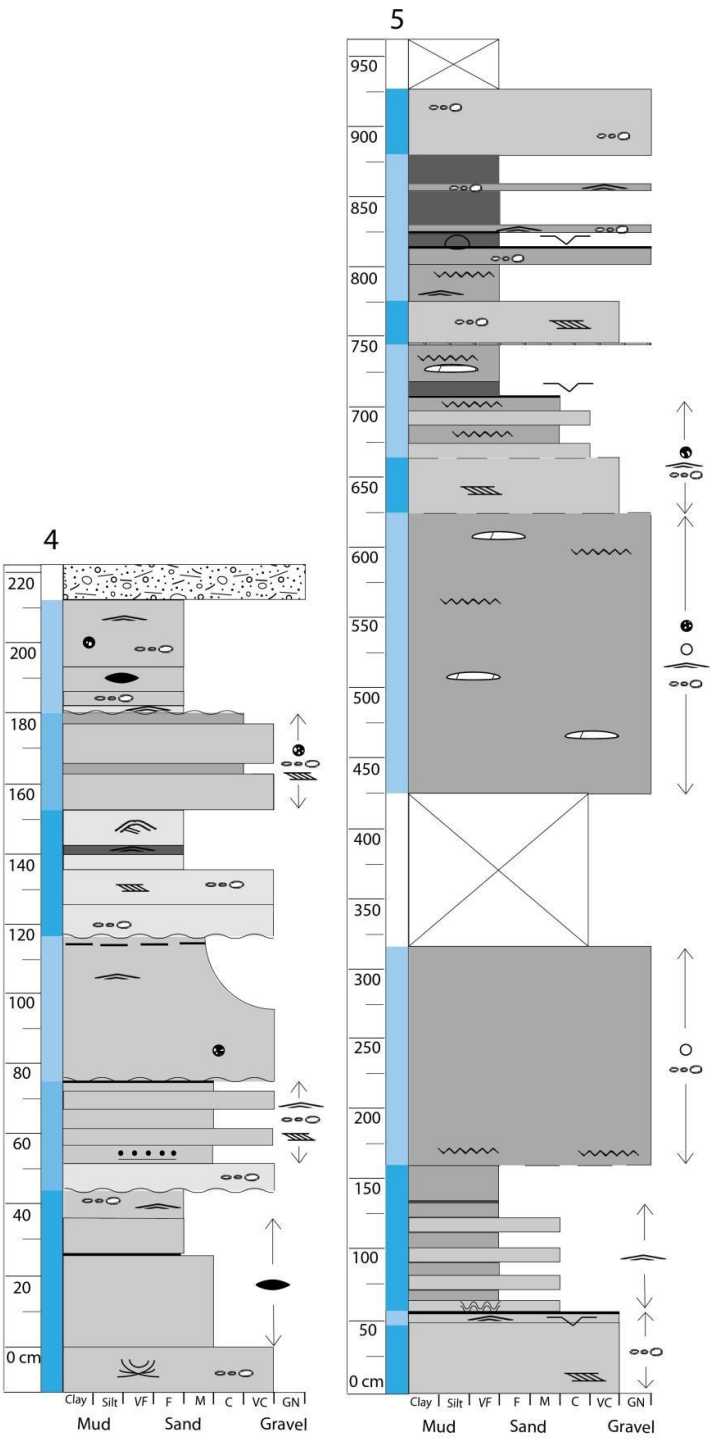

Fig. 6. Stratigraphic columns of the middle (4) and upper (5) carbonate sections of the Chobeni Formation. See Fig. 3 for locality and Fig. 5 for legend.

3.4.1 Allochems

A variety of allochems, including peloids, ooids, oncoids, and various intraclasts were identified in the carbonate facies. Peloids occur as partially silicified, structureless, sub-spherical micritic grains that range from 0.05 to 0.2 mm in diameter (Fig. 7A). When recrystallized, they are difficult to distinguish from the micrite matrix. Peloids are developed in several facies and are frequently associated with siliciclastic detritus and ooids. They are also common in microbialites and also constitute ripple bedforms.

Ooids occur as partially silicified, spherical to sub-spherical, single to compound grains 0.2-0.6 mm in diameter. The ooid nuclei consist of peloids, micritic and silicified rock fragments, and quartz grains. Their cortices are variable in thickness and show concentric, radial and radial-concentric laminae (Fig. 7B). In many cases, recrystallization results in partially to fully structureless, microcrystalline ooid types.

Oncoids occur as spherical to sub-spherical, discoidal and elongate forms of 2-10 mm in diameter, in which dominantly micritic nuclei are coated by micritic, microsparitic, and chert laminae. Their cortices are often thicker on the presumed upper side (Fig. 7C and D), and smaller oncoids show more regular laminae than larger ones. Compound oncoid grains are also present. Primary textures are commonly preserved, but affected by recrystallization and silicification to various degrees. There is no petrographic evidence for a trapped clastic component in the oncoids. Idiomorphic mica crystals 100-200 μm in length occur in some outer cortices, but they represent a secondary metamorphic phase. Nevertheless, they may point to the presence of a trapped, primary clay phase. Finally, intraclasts and aggregate grains (Fig. 7E) are tabular to ellipsoidal and mm to cm in length. They consist primarily of partially silicified micrite and sand fragments, as well as dolomicrite-cemented allochems.

Taken together, the variety of allochems suggests deposition in relatively high-energy, shallow-marine settings. The origin of the peloids is uncertain, but they likely represent either inorganic and organically-induced precipitation (Macintyre, 1985; Gerdes et al., 1994; Reitner and Neuweiler, 1995; Kazmierczak et al., 1996), or reworking of micrite sediment (Fahraeus et al., 1974). Ooids and oncoids form in a variety of sedimentary environments, ranging from freshwater lakes to marine settings, where they are formed by microbial processes (Dahanayake et al., 1985; Davaud and Girardclos, 2001; Flügel, 2004). Variations in the ooid cortices may reflect differences in the degree of agitation during formation (Loreau and Purser, 1973; Halley et al., 1983). Variation in oncoid cortex may also reflect differences in agitation, with uniform

laminae of smaller oncoids reflecting ease of movement. The presence of a variety of intraclasts and agglutinated grains further suggests the occurrence of high-energy events that resulted in erosion and reworking of early- cemented or microbially agglutinated substrate materials (Hardie and Ginsburg, 1977; Shinn, 1983).

3.4.2 Siliciclastic-volcaniclastic detritus

Siliciclastic detritus is composed of sub-angular to rounded, sand-sized quartz and subordinate microcline and plagioclase grains. Accessory detrital heavy minerals include rutile, monazite, pyrite, apatite, and zircon up to 200 μm. Scattered flakes of muscovite may also be of detrital origin. Clastic grains are found as disseminated particles in the micritic matrix of different facies or concentrated in detritus-rich laminae including those of laminated microbialites. Pyroclastic fragments include vesicular to non-vesicular lapilli that range from 0.2 to 20 mm in diameter and were observed in different facies (Fig. 7F). Lapilli frequently contain quartz sand particles entrained during lava/ sediment interaction at the source of the ejecta. Vesicles are filled with chert or dolomite. The lapilli are extensively replaced by dolomite, chert, and chlorite and contain micron-sized, secondary crystallites of titanium oxide and apatite.

3.4.3 Diagenetic and metamorphic phases and textures

Early diagenetic features include calcite-filled voids/ fenestrae and rare cm-sized pyrite nodules. Carbonate and chert partially replacing feldspar and other particles are probably also of early diagenetic origin. Stylolites formed during late diagenesis and contain high concentrations of accessory minerals (especially rutile), pyrite, and carbonaceous matter.

Metamorphic phases include quartz, sericite, muscovite, and chlorite. Quartz is present as fibrous crystals forming pressure fringes oriented parallel to bedding. Muscovite is concentrated in the margin and centre of micritized pyroclastic particles. Disseminated crystals of micron- to cm-sized euhedral pyrite, minor sphalerite and micron-sized apatite occur in specific facies and are likely metamorphic in origin.

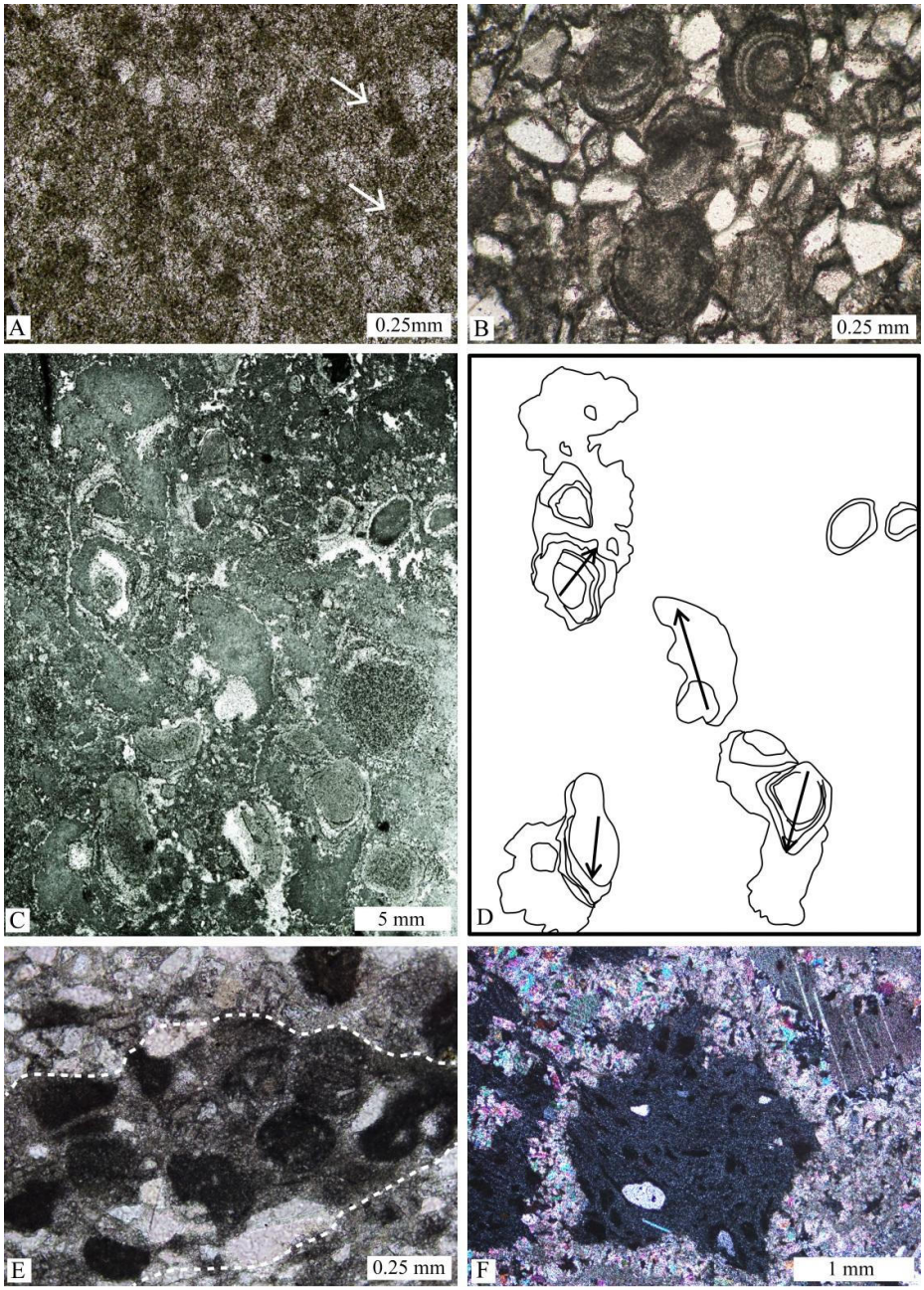

Fig. 7. Photomicrographs (A, B and E under plane-polarized light; F under crossed-polarized light) and thin section scan (C) showing different particles in the studied carbonate samples. (A) Peloids (arrows, dark spherical domains) and silicified particles (light spherical domains) in a partially recrystallized micritic matrix. (B) Concentric and micritic ooids surrounded by quartz sand. (C) Partially silicified oncoids; note thicker cortex on the one side of some oncoids reflecting the upper part of oncoid during cortex formation. (D) Sketch of C outlining some oncoids for better visualization; arrows show inferred growth directions of oncoids. (E) Composite grain of micritic ooids (dark subspherical particles) and siliciclastic particles (light grains) cemented by micrite and outlined by dashed line. (F) Pyroclastic fragments (dark) of chlorite with entrained quartz grains and surrounded by dolomitic cement.

3.4.4 Biogenic phases

Carbonaceous matter is rare, but locally present in ooids, peloids, intraclasts, and some microbialite laminae, where it is disseminated evenly or interwoven with authigenic dolomitic crystals. Recrystallization has, in some cases, led to the concentration of organic matter at crystal margins. Sub-micron sized apatite and pyrite crystals occur in close association with carbonaceous matter in coated grains. Their origin may be related to the activity and interaction of sulfate-reducing and sulfide-oxidizing bacteria (Donald and Southam, 1999; Crosby and Bailey, 2012).

3.5 Description of the characteristics of sedimentary facies

The carbonate-bearing sedimentary successions of the main, middle and upper carbonate sections have been subdivided into fourteen facies on the basis of field observations and sample petrography. These were grouped into three facies assemblages representing deposition in (1) supratidal to upper intertidal, (2) middle intertidal to subtidal and (3) tidal channel environments. In the following sections the characteristics of the facies and their assemblages will be described. Additional information is presented in Table 1. The term sandy refers to the presence of sand-sized siliciclastic particles, i.e. mainly quartz.

3.5.1 Supratidal to upper intertidal facies assemblage

Supratidal to upper intertidal depositional environments of the main and upper carbonate sections are dominated by stratiform stromatolite facies. Intraclast dolomitic sandstone and sandy intradolorudite facies are present as minor facies in these zones. The middle carbonate section lacks supratidal deposits.

Facies	Constituents	Bedding and sedimentary structures	Organo-sedimentary structures
Supratidal to upper intertidal facies assemblage			
Stratiform stromatolite	Dolomicritic/-microsparitic and detritus-rich laminae; intraclasts; partially silicified peloids; scattered detrital quartz particles	Wrinkly, continuous to discontinuous, partially silicified, sporadically disrupted laminae 0.1-4 mm in thickness; calcite-filled fenestrae up to 2 mm in diameter; mudcracks; tepees with up to 15 cm of vertical relief and a typical spacing of 50 cm	Stratiform stromatolites; isolated or laterally-linked, small-scale domal stromatolites with internal wrinkly lamination (up to 5 cm in diameter); massive microbialites
Intraclast dolomitic sandstone	Dolomite-cemented sandstone with rectangular, micritic and sandy intraclasts typically 1-3 cm but up to 20 cm in length	Disrupted thin bedding; calcite-filled fenestrae up to 1 cm in diameter	Stratiform and small-scale domal stromatolites (1-15 cm in width and 1-10 cm in height, synoptic relief up to 5 cm), massive microbialites
Sandy intradolorudite	Tabular micritic intraclasts up to 15 cm in length set in a matrix of fine to coarse sandy dolomite with scattered quartz particles; rare pyrite nodules	Massive; partially disrupted wrinkly laminae; calcite-filled fenestrae	Massive domal microbialites (c. 15 cm in width and height); stratiform stromatolites; single column digitate stromatolites (1 cm in width and up to 5 cm in height)
Middle-lower intertidal to subtidal facies assemblage			
Ripple-laminated dolomitic sandstone	Medium quartz sand; mud drapes	Wave-ripple lamination with mud drapes; flaser-wavy bedding	Domal stromatolites up to 20 cm in height and 10-15 cm in width
Planar cross-bedded sandstone	Well-sorted coarse to very coarse sand; local sandstone and micrite intraclasts concentrated along the foresets of cross-beds	Thin (< 12 cm) tabular beds with planar cross-bedding; wave-ripple laminated intervals; hummocky cross stratification in the middle carbonate section	Microbially-induced sedimentary structures
Wave-rippled dolarenite-dololutite	Quartz-rich fine-grained dolarenite and silicified dololutite pairs; partly silicified peloids	Wave-ripple lamination; mud drapes	Isolated polylobate domal microbialites up to 150 cm in width and 60 cm in height
Edgewise conglomerate	Randomly oriented, steeply inclined, or vertically stacked micrite intraclasts up to several cm in length	Massive	-
Sandy oolitic intradolorudite	Flat-lying to randomly oriented micrite intraclasts up to 4 cm length; fine-medium sand-sized quartz sand up to 10 vol.% in a recrystallized micrite to microsparite matrix; partially silicified micritic peloids, concentric and composite ooids	Massive; normal coarse tail grading; fenestrae	Sporadic wrinkly laminae; massive dololutite lenses
Sandy oodolarenite	Quartz-rich and quartz-free dolarenite pairs; partially silicified/micritized superficial ooids and peloids; intraclasts; lapilli	Tabular bedding; planar to trough cross-bedding; normal graded bedding; wave ripples occasionally	Silicified wrinkly lamina; massive dololutite lenses up to 10 cm in length

Oncolite	Micritic, marginally silicified symmetric, asymmetric to irregularly concentric oncoids (2-10 mm in diameter). Minor micrite intraclasts up to 3 cm in size; volcaniclastic and quartz sand particles; heterogeneous groundmass of micrite and dolomite/quartz cement	Massive to crude thin planar bedding; fold-like structure	Small-scale digitate-like stromatolites
Dolomitized lapillistone	Partially dolomitized vesicular to massive lapilli up to several millimetres; micritic intraclast up to 2 cm; medium to coarse sand-sized quartz grains, set in a dolomicrosparitic to dolosparitic cement	Massive; calcite-filled voids up to 3 mm	Massive domal microbialites up to several cm in size
Shale	Silt- to fine sand-sized quartz	Planar lamination; lenticular bedding	-
Tidal channel facies assemblage			
Cross-bedded sandy intradolorudite	Intraclasts, very coarse quartz sand, rare lapilli up to 3 mm in diameter in a dolomite and chert cement; pebble to cobble-sized, tabular rip-up clasts of rippled dolarenite facies and silicified stromatolitic clasts	Planar and trough cross-bedding; erosional base; rip-up clasts form imbricated lag deposits and are aligned and concentrated within foresets	Conical stromatolites typically silicified
Conical/columnar stromatolite	Alternation of dolomicritic-dolomicrosparitic laminae; laminae enriched in detrital particles and silicified laminae	Parabolic to steeply convex lamination	Single and composite conical and columnar stromatolites

Table 1. Description of facies

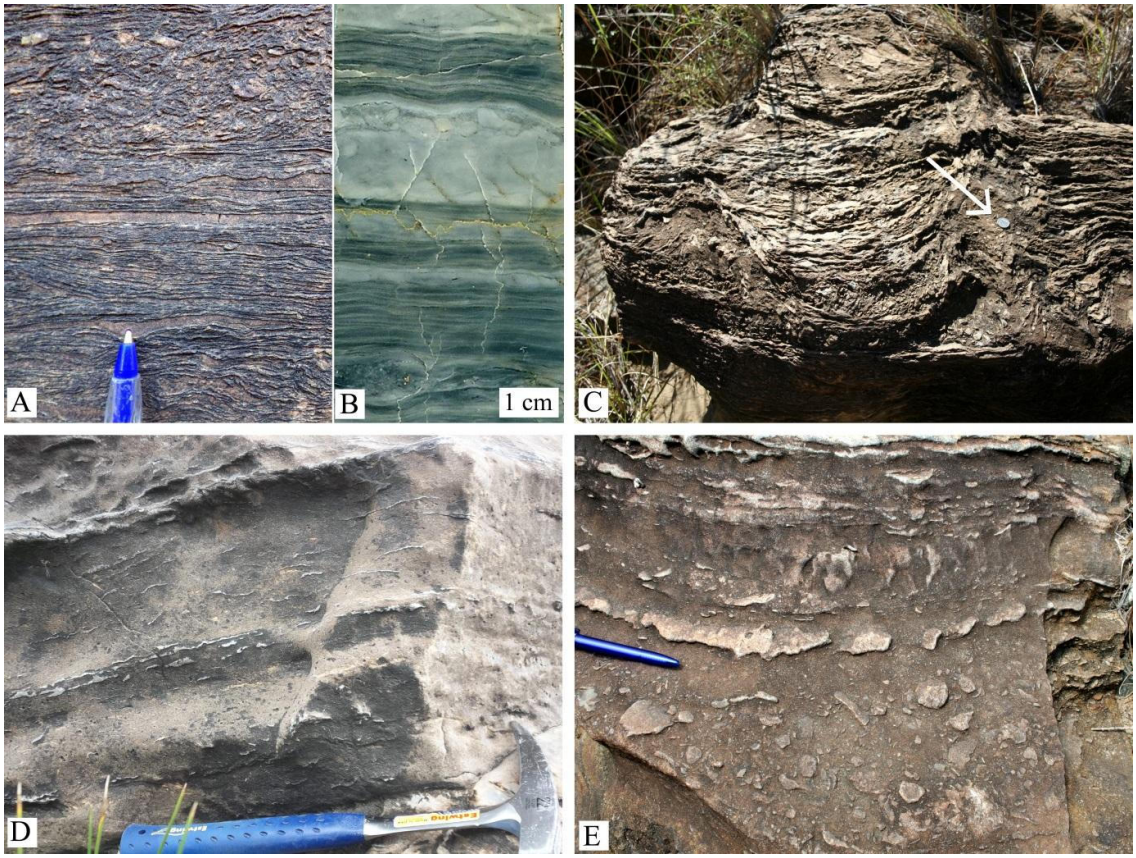

Fig. 8. Photographs showing features of the supratidal to upper intertidal facies assemblage. (A) Alternation of silicified stromatolitic (light bands) and dolomicritic laminae of the stratiform stromatolite facies. Note disrupted laminae and intraclasts at the top of photo. (B) Polished slab showing close-up image of stratiform stromatolite (laminated parts) and massive planar structureless microbialites. (C) Tepee structures in stratiform stromatolite facies; coin for scale (arrow). (D) Alternating intraclast dolomitic sandstone with ripple-laminated dolomitic sandstone. Note rip-up clasts of sandy rippled and wrinkled laminae. (E) Sandy intraclasts (positive relief) scattered in a micritic matrix of sandy dolomite.

3.5.1.1 Stratiform stromatolite facies

The stratiform stromatolite facies (Fig. 8A and B; Table 1) is particularly well-developed in the centre of the main carbonate section (Fig. 5, at c. 12 m). It occasionally hosts discontinuous beds, up to several centimetres thick, of intraclastic and peloidal dolorudite-dolarenite. Abundant evidence for sediment disruption, including abundant tepee structures (Fig. 8C), which are indicative of sediment convolution due to dewatering and/or gas escape, and small-scale domal stromatolites, suggest very shallow-water conditions and frequent subaerial

exposure and desiccation (Shinn, 1986; Beukes and Lowe, 1989; Pratt et al., 1992; Chakrabarti et al., 2014).

3.5.1.2 Intraclast dolomitic sandstone facies

This facies (Fig. 8D; Table 1) alternates with stratiform stromatolite and the wave ripple-laminated dolomitic sandstone facies. It is well-developed near the base of the main carbonate section (Fig. 5). The disruption and ripping up of micritic laminae and semi-cohesive, sandy laminae are indicative of periodic subaerial exposure. Reworking of disrupted sediment probably took place by storm surges inundating supratidal-intertidal environments (Hardie and Ginsburg, 1977; Shinn, 1983).

3.5.1.3 Sandy intradolorudite facies

Sandy intradolorudite (Fig. 8E; Table 1) is well-developed near the base of the main and near the top of the upper carbonate sections (Figs. 5 and 6). The considerable amount of micritic intraclasts indicates that this facies was subjected to occasional high energy events following desiccation on intertidal/ supratidal flats.

3.5.2 Middle-lower intertidal to subtidal facies assemblage

Nine facies were defined to have formed in mid-intertidal to deep subtidal environments. The abundance of the different facies varies between the different sections studied in the field and not all facies are present in all sections.

3.5.2.1 Ripple-laminated dolomitic sandstone facies

This facies (Table 1; Fig. 9A) is sporadically developed near the base of the main carbonate section (Fig. 5) where it is associated with intraclast dolomitic sandstone and stratiform stromatolite. Sedimentary structures are characteristic for lower intertidal to shallow subtidal environments and record tidal current and slack water phases.

3.5.2.2 Planar cross-bedded sandstone facies

This facies (Table 1; Fig. 9B) can be found in all sections, but it is very prominent in the lower half of the main carbonate section (Fig. 5, at c. 8 m) where it was subjected to palaeocurrent analysis (Fig. 2). It accumulated in a shallow subtidal environment and represents sheet-like deposits of sand that was moved during continuous wave activity. Rare hummocky cross stratification indicates storm-induced currents. Cross-bedded intraclast dolomitic sandstone is a sub-facies and mostly alternates with wave ripple laminated dolomitic sandstone. The latter shows a diverse assemblage of microbially-induced sedimentary structures (MISS, Noffke et al., 2001), including erosional pockets, microbial mat chips, sandy intraclasts, and gas escape holes that can be observed in plan view (Figs. 8E and 9C). Evidence for desiccation and rupturing of microbially-bound sand surfaces followed by reworking by currents and wind action indicates subaerial exposure at times.

3.5.2.3 Wave-rippled dolarenite-dololutite facies

This facies (Table 1; Fig. 9D) forms a distinct horizon in the main carbonate section (Fig. 5, at c. 16.5 m) that can be traced throughout the outcrop area. It is intercalated with sandy oolitic intradolorudite and sandy intradolorudite, but also occurs as part of the tidal channel facies assemblage. Wave ripple lamination indicates wave activity that, in association with mud drapes, point to periods of slack water in a tidal setting. The association with large domal stromatolite, the lack of evidence for exposure, and facies relationships indicate that this facies formed in a shallow subtidal setting.

3.5.2.4 Edgewise conglomerate facies

This facies (Table 1; Fig. 9E) was only observed at one locality (Fig. 5, at c. 16 m), where it formed a lenticular bed grading laterally into partially disrupted sandy dololutite. Edgewise conglomerates are characteristic deposits of high-magnitude storms in carbonate settings (Sepkoski, 1982; Mount and Kidder, 1993). The association of edgewise conglomerate with sandy dololutite indicate that this facies represents a storm deposit in a muddy subtidal setting.

Fig. 9. Photographs showing features of the middle-intertidal to subtidal-facies assemblage. (A) Wavy bedding (centre of photo) grades upward into flaser bedding (top of photo) of the ripple-laminated dolomitic sandstone facies. (B) Thinly planar cross-bedded sandstone facies; note dolomitized ripple-laminated intervals in the lower part. (C) Fossilized ‘‘gas holes” (arrows) on top of intertidal sandstone with wave-ripple bedforms. (D) Wave ripple cross-lamination of rippled dolarenite-dololutite facies. Note silicified ripple drapes (light color). (E) Edgewise intraclast conglomerate. (F) Alternation of normally graded beds of sandy oodolarenite and sandy intradolorudite. Lenses of lutite are indicated by arrows.

3.5.2.5 Sandy oolitic intradolorudite facies

Sandy oolitic intradolorudite (Table 1) is a rare facies that is locally intercalated with rippled dolarenite-dololutite facies (Fig. 5, at c. 16 m). The presence of concentric ooids is indicative of formation in the agitated lower intertidal zone or subtidal sand shoal (Simone, 1981; Halley et al., 1983; Chow and James, 1987; Dill, 1991). The association with coarse-tail grading suggests deposition of this facies by storm events onto intertidal flats subsequently affected by reworking and disruption.

3.5.2.6 Sandy oodolarenite facies

This facies alternates with the sandy intradolorudite facies (Table 1; Fig. 9F) and is well-developed below the prominent oncolite horizon in the main carbonate section (Fig. 5, at c. 18 m). Partially to completely silicified micritic ooids with indistinctive internal structures and superficial ooids are common (Fig. 10A). The association of ooids with current-induced sedimentary structures suggests that this facies formed in high-energy environments, likely in a lower intertidal to shallow subtidal environment that was agitated frequently. Normal graded bedding indicates rapid deposition and waning flow conditions during storm events.

3.5.2.7 Oncolite facies

The oncolite facies (Table 1; Fig. 10B) is particularly well-developed in the main carbonate section. Here it forms a massive to crudely planar-bedded horizon capped by an erosional contact (Fig. 5, at c. 23.5 m). Remnants of silicified small-scale digitate-like stromatolites are rarely preserved and may have resulted from asymmetrical growth of oncoids. The process of deposition of this facies is unclear due to the near-absence of sedimentary structures. In general, oncoids are regarded as an indicator of a low sedimentation rate (Flügel, 2004). The co-occurrence of different oncoid types (large irregular and small spherical oncoids) with rare clastic detritus and crude planar bedding indicate that the oncoids formed in a relatively high-energy subtidal zone episodically influenced by storms.

3.5.2.8 Dolomitized lapillistone facies

This facies (Table 1; Fig. 4C) forms the immediate substrate of the main carbonate section (Fig. 5), occupying the gradational interval between lapillistone below and carbonate above. It also occurs as a thin single bed (Fig. 10C) intercalated with dolomitic rippled sandstone facies near the base of the main carbonate section (Fig. 5, at c. 1 m). The lapillistone represents a volcanic airfall deposit. Intercalation of lapillistone with carbonate rocks indicates synsedimentary volcanism during the deposition of at least the lower part of the main carbonate section.

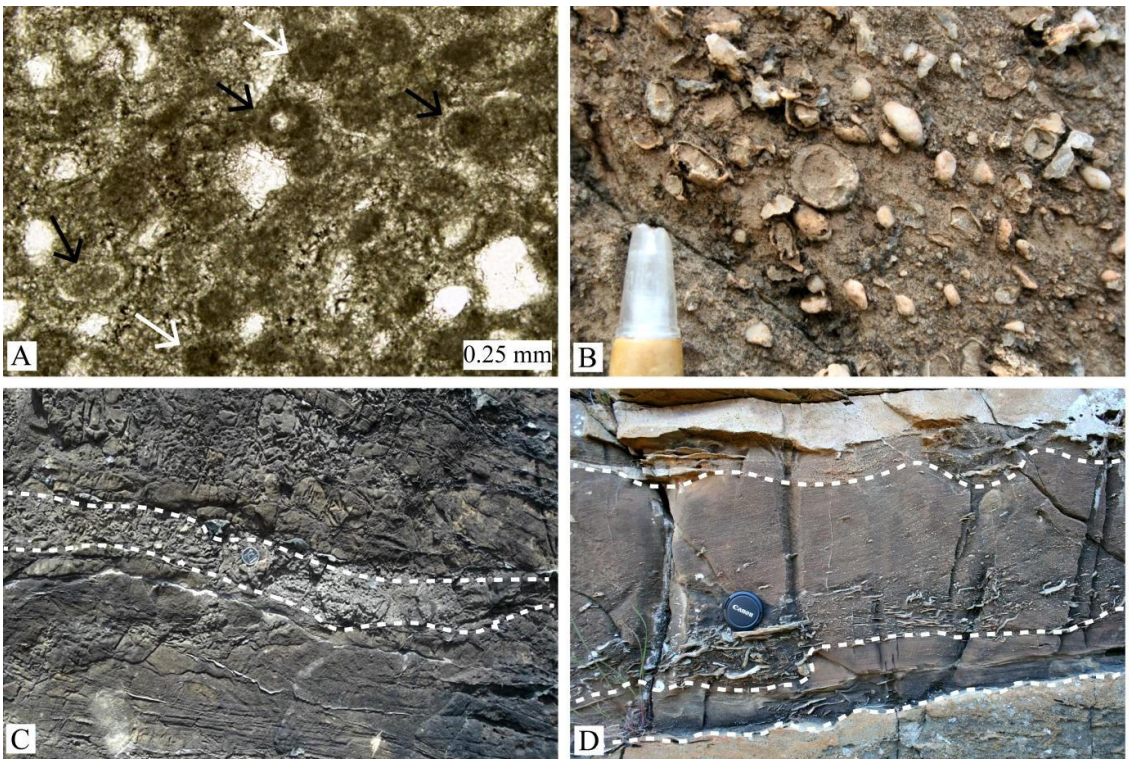

Fig. 10. Photographs showing features of the middle-intertidal to subtidal-facies assemblage. (A) Photomicrograph of micritic (white arrows) and superficial ooids (black arrows); some of the superficial ooids are partly silicified. (B) Silicified oncoids (light features) in a micritic matrix of the oncolite facies; pen tip for scale. (C) Thin bed of lapillistone (indicated by dashed-line) intercalated with dolomitic sandstone; coin for scale. (D) Three beds of the cross-bedded sandy intradolorudite facies of the tidal channel-facies assemblage showing basal lag and scour features; lense cap for scale; bedding planes indicated by dashed-lines.

3.5.2.9 Shale facies

Greenish-grey shale up to 45 cm in thickness is present in the lower part of the main carbonate section (Fig. 5). Some laminae consist of fine-grained sandstone and show lenticular bedding. This facies is interpreted to have been deposited in a subtidal environment below the fair-weather wave base. Lenticular bedding indicates the influence of storm waves at times.

3.5.3 Tidal channel facies assemblage

This assemblage occurs at the top of the main carbonate section (Fig. 5, Section 2). It is restricted to a lenticular unit of c. 5 m thickness and ≥ 50 m lateral extent, which is erosively incised into, but may also interfinger laterally with, stratiform stromatolite facies (Fig. 5). Conical/ columnar stromatolite and cross-bedded sandy intradolorudite facies are specific characteristics of this assemblage. The rippled dolarenite-dololutite facies, introduced earlier, is common to this association (Fig. 5, Section 2). The tidal channel facies assemblage and the diverse types of stromatolites associated with it was the focus of the study by Beukes and Lowe (1989), who argued for the formation of different stromatolite morphologies under different hydrodynamic regimes in the channel.

3.5.3.1 Cross-bedded sandy intradolorudite facies

This facies (Table 1; Fig. 10D) forms erosive, lenticular beds up to 50 cm thick and several metres in width and alternates with silicified rippled dolarenite-dololutite. Conical stromatolites are present in this facies and show growth from the base of the beds upwards. Bi-directional cross-bedding was reported by Beukes and Lowe (1989) from this facies. Bedding characteristics suggest deposition of this facies in a high-energy tidal channel within the lower intertidal to subtidal zone (Fenies and Faugères, 1998; Dalrymple, 2010). It is unclear whether rare lapilli were derived from synsedimentary volcanism or erosion of previously deposited volcaniclastic sediment.

3.5.3.2 Conical/ columnar stromatolite facies

This facies forms the uppermost horizon of the main carbonate section (Fig. 5, Section 2) and consists of morphologically different types of conical and columnar stromatolites that are partially silicified. The stromatolites alternate with, or are surrounded by, sandy dolarenite/ intradolorudite and wave-rippled dolarenite-dololutite. A detailed description of stromatolite morphologies was presented by Beukes and Lowe (1989). The close association of stromatolites with coarse clastic carbonate sediment in a high-energy, tidal channel sub-environment suggests that columnar and conical stromatolites formed and remained submerged in a subtidal marine environment similar to some of their modern-day counterparts (Dravis, 1983; Dill et al., 1986; Reid et al., 2003; Jahnert and Collins, 2012).

3.6 Microbialite types, their microfabrics and carbonate precipitation

Microbialites with a variety of morphologies were observed in different sub-environments, in accordance with previous work (Mason and von Brunn, 1977; Beukes and Lowe, 1989). Minor changes in the physical conditions of the environment can influence microbial assemblage and as a result change microbialite morphology (Burns et al., 2004; Andres and Reid, 2006; Jahnert and Collins, 2012). While there is a clear environmental control on the different carbonate facies, the origin of carbonate precipitation needs to be evaluated. Carbonates can precipitate abiotically from supersaturated waters (Fouke et al., 2000), induced by oxygen-producing photosynthetic bacteria or mediated by degradation of organic matter by heterotrophic bacteria (Canfield and Raiswell, 1991; Chafetz and Buczynski, 1992; Andres and Reid, 2006). The carbonates reported here are mostly confined to facies with microbialites, which indicates that microbial processes played a major role in carbonate precipitation.

3.6.1 Stromatolites

Supratidal environments are characterized by stratiform stromatolites that formed by lateral growth as a result of limited accommodation space. They consist of alternation of dolomicrite and dolomicrosparite laminae (Fig. 11A). This may indicate that *in- situ* precipitation of carbonate took place within microbial mats. This process has been recognized in Proterozoic stromatolites, considered comparable to some of their modern counterparts (Seong-Joo and

Golubic, 1999; Seong-Joo et al., 2000; Préat et al., 2011). In places, quartz-free dolomitic laminae alternate with dolomitic laminae agglutinated with remnants of carbonaceous matter and floating quartz particles (Fig. 11B-H). This relationship is probably indicative of trapping and binding of carbonate mud and clastic detritus by bacteria-derived exopolymeric substances (Awramik, 1984; Golubic, 1991; Gerdes et al., 1993; Dupraz et al., 2004, 2009; Dupraz and Visscher, 2005), similar to processes that formed the same facies described in the rock record and in modern supratidal to intertidal environments (Golubic, 1992; Visscher et al., 1998; Reid et al., 2000).

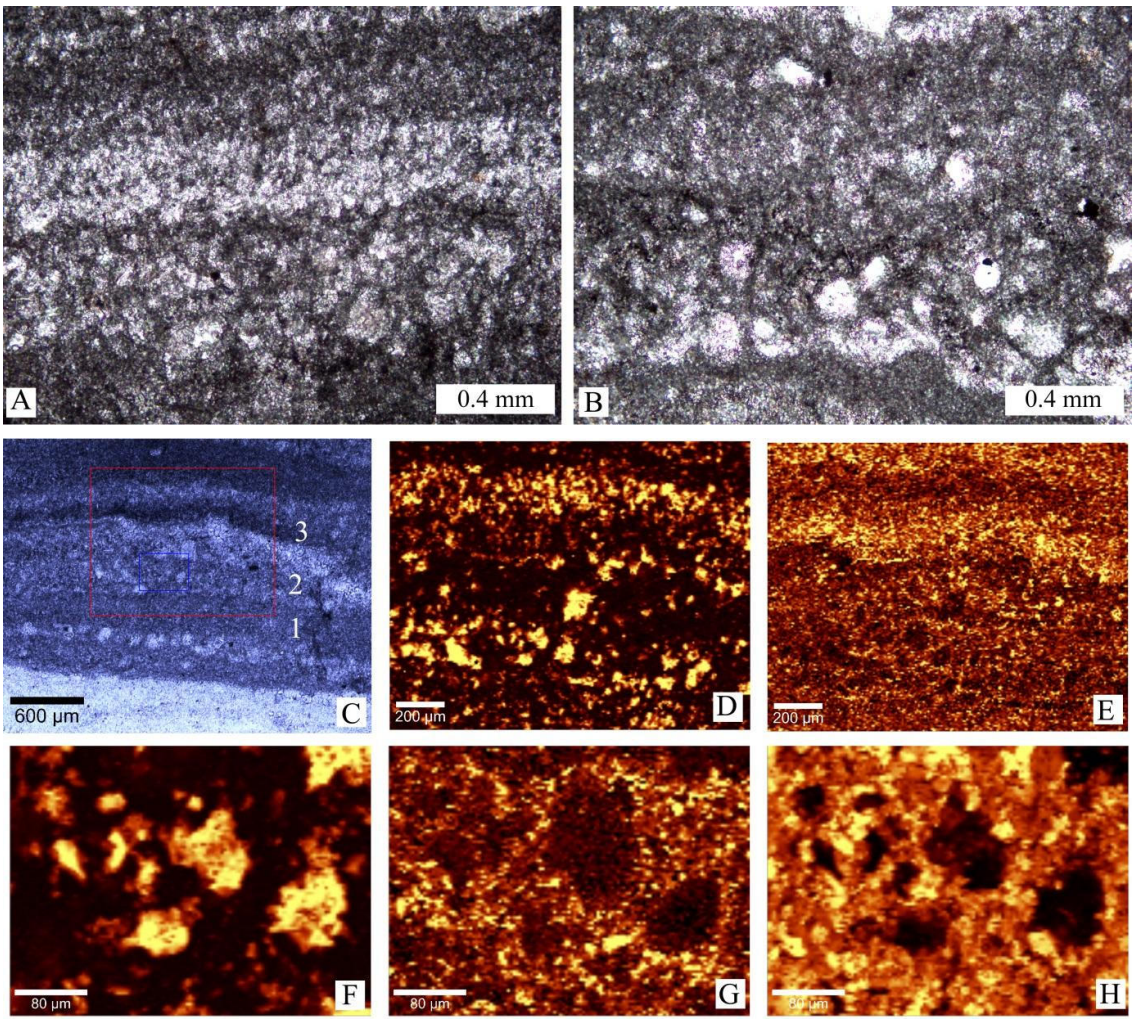

Fig. 11. Photomicrographs of stratiform stromatolite and results of Raman mapping of laminae of the stratiform stromatolite facies, showing relationship between dolomite, detrital quartz particles and carbonaceous matter. (A) Close-up image of the lower laminated part of stratiform stromatolite in image (8A), showing the alternation of dolomicrite and dolomicrosparite laminae, which are partially silicified. Dispersed dark material is carbonaceous

matter. (B) Stratiform stromatolite showing dolomitic laminae with varying abundances of sand-sized detritus. Particles float in a micritic matrix with remnants of carbonaceous matter. (C) Photomicrograph showing areas subjected to Raman mapping which comprise of alternation of dolomicrosparite laminae free of quartz particles (1), dolomicrosparite laminae with quartz particles agglutinated with carbonaceous matter (2) and carbonaceous matter-rich laminae (3). Boxes show mapped areas. (D and F) Raman maps of the distribution of the quartz band at ~ 467 cm^{-1}, (H) dolomite band at ~ 1100 cm^{-1} and (E and G) carbonaceous matter G band at ~ 1589 cm^{-1} in stromatolitic laminae. Brighter areas within Raman maps reflect higher intensities of mineral-specific spectra. Note carbonaceous matter surrounding detrital quartz (F and G), indicating trapping of quartz by microbial mat.

In supra- to intertidal environments, laterally linked, smallscale domal stromatolites are developed sporadically (Fig. 12A). Domes are eccentrically laminated, isolated to contiguous ovoids on bedding planes. Small-scale, digitate stromatolites can be observed locally (Fig. 12B). Restricted environmental conditions, subject to periodic wetting by strong currents, has previously been suggested for the development of ancient digitate stromatolites (Howe, 1966; Grey and Thorne, 1985).

Facies that formed in middle-lower intertidal to shallow subtidal environments contain domal stromatolites with their size correlating positively with inferred water depth (Table 1; Fig. 12C). Similar morphological types are known from modern marine intertidal mudflats, protected lagoons, and shallow subtidal environments (Logan et al., 1964; Monty, 1967; Jahnert and Collins, 2012). Domal stromatolites consist of alternations of silicified sandy dolomitic laminae and dololutite laminae. Carbonate precipitation and minor trapping and binding is indicated.

In the tidal channel facies assemblage, conical and columnar stromatolites are present as single and composite forms and display variations in size and shape (Fig. 13A). Isolated single conical stromatolites are predominantly erect, slender and unbranched with asymmetrical, smooth, parabolic to steeply convex laminae. The majority of the conical stromatolites have smooth walls. Laminae are sharply pointed or rounded at their tops. Low-relief cones are 1-5 cm in width and 3-10 cm in height. Laterally-linked contiguously to closely-spaced conical stromatolites of 20-60 cm in width and up to 130 cm in height and positioned 4-25 cm apart are developed sporadically (Fig. 13B). In conical stromatolites, a slight inclination from one set of laminae to the other set can be observed (Fig. 13C), although the number of lamina in each set could not be determined. The thickness of laminae changes across cones and becomes thicker at the crest (Fig. 13D). Columnar stromatolites vary in terms of size, shape of laminae,

and spacing from neighboring columns. Linkages between openly and closely spaced columns are common. Centimetre-sized branching columns, which are partly linked, form a compound mass of a colloform structure (Fig. 14A). Laminae are wrinkled, wavy and asymmetric and intersect uneven column margins at acute angles or are almost parallel thus forming thin-layered walls. Different types of laminae of columnar stromatolites were identified in polished slabs based on differences in color, composition and thickness (Fig. 14B). On the microscopic scale, they include dolomicritic to dolomicrosparitic laminae 0.2-0.8 mm in thickness, micritic laminae with detrital particles of quartz and micritic fragments up to 0.1 mmthick, and silicified laminae with remnants of dolomite 0.2 mm in thickness.

The space between the columns of conical and columnar stromatolites is filled by sandy dolarenite/ intradolorudite, while clastic particles within stromatolitic laminae consist of silt-sized grains. The linkage and extension of stromatolitic laminae into the surrounding dolarenite/dolorudite indicates concomitant stromatolite growth and coarse detrital sediment deposition (Fig. 13C).

Abundant accommodation space along with strong tidal and (storm) wave-induced currents provided a suitable environment for the growth of conical, as well as large-scale stromatolites in the tidal channel at the top of the main carbonate section. This finding highlights once more the role of physical processes in sculpturing morphology of stromatolites. The conical stromatolites described here formed in shallower environments than their younger, especially Proterozoic counterparts, which seem to have predominantly formed in relatively deep subtidal settings below or close to the fair-weather wave base (Grotzinger, 1989; Kah et al., 2006).

The conical shape and crestal thickening of conical stromatolites (Fig. 13D) together with variations in the inclination from one set of laminae to the other set (Fig. 13C) can be explained with the presence of phototrophic microorganisms (Walter et al., 1976; Walter, 1983; Beukes and Lowe, 1989). Petroff et al. (2010) suggested that centimetre-scale spacing between conical stromatolites reflects competition for nutrients and corresponds to rhythmically fluctuating metabolism related to the length of day in support of an origin of conical stromatolites by photosynthetic bacteria. Sim et al. (2012) suggested that conical stromatolites from the 2.7 Ga Tumbiana Formation (Flannery and Walter, 2012) argue for O_2-dependent behavior of microbes in shallow-water environments. Therefore, we assume immediateenvironmental conditions, such as availability and competition for nutrients, fluctuations in light intensities and microbial metabolic pathways, played an active role in shaping the conical morphology.

3.6.2 Oncoids

Microbialites in the form of coated grains are present as oncoids. Spherical oncoids with symmetric laminations are considered as products of continuous movement in high-energy conditions during growth from permanently submerged areas in lower intertidal and shallow subtidal environments (Logan et al., 1964; Leeder, 1975; Smith, 1986; Flügel, 2004). The larger, asymmetric oncoids with upright growth features (Fig. 7C and D) probably developed in static conditions below the wave base in which bacteria preferentially colonized the sides and top of nuclei, resulting in the asymmetric laminae in oncoids (Peryt, 1981; Ratcliffe, 1988). Variation in cortical thickness (thin cortex along the inferred undersides of oncoids in contrast to thicker laminae on opposite sides) is best explained by preferential growth along sides of a grain exposed to the sediment/ water interface of well-illuminated areas by phototrophic microorganisms. The absence of trapped detrital particles within oncoid's laminae suggests microbially induced carbonate precipitation, but may also point to the dearth of clastic material associated with the oncolite facies.

3.6.3 Structureless microbialites

Non-laminated, i.e. structureless microbialites occur as two types, (1) massive domes and (2) dololutite lenses. They are developed in various, most commonly inter- to supratidal facies (Figs. 5 and 6). Massive domal microbialites are typically c. 30 cm in width and 15 cm in height (Fig. 14C and D). Some domes contain different carbonate particles including peloids and coated grains admixed with siliciclastic detritus and embedded in micrite and microsparite (Fig. 14E). Others are made of dololutite fragments with floating coarse quartz grains separated by a quartz sand-rich matrix. Some domes show concave-upward walls and *in- situ* disruption of lamina remnants. Dololutite lenses are a few centimetres in height and a few decimetres in width (Fig. 9F). The lenses are typically massive or have a faint lamination. Irregular to wavy tops indicate lense formation by microbial processes. Irregular to sub-spherical fenestrae up to 1.5 cm in diameter are common. The lenses contain generally less quartz sand than their host rocks.

The presence of allochems within some massive microbialite domes may suggest trapping of particles within microbial colonies brought to the site by high-energy currents. In contrast, the large variety of particles may also suggest possible disruption of previously deposited sediment

during microbialite growth. *In-situ* disruption is compatible with the notion that some domes have been initiated as tepees that experienced modification by microbial carbonate precipitation and possible sedimentation within tepee centres. On the basis of variation in composition and morphology, non-laminated microbial structures may have formed as a result of different processes, including differences in microorganism assemblage, variation in the nature of sediment supply (Braga et al., 1995), desiccation and disruption, and a combination thereof. Non-laminated microbialites were reported to form by *in- situ* calcification of coccoid-dominated microbial communities (Awramik, 1984; Pratt, 1984; Chafetz and Buczynski, 1992).

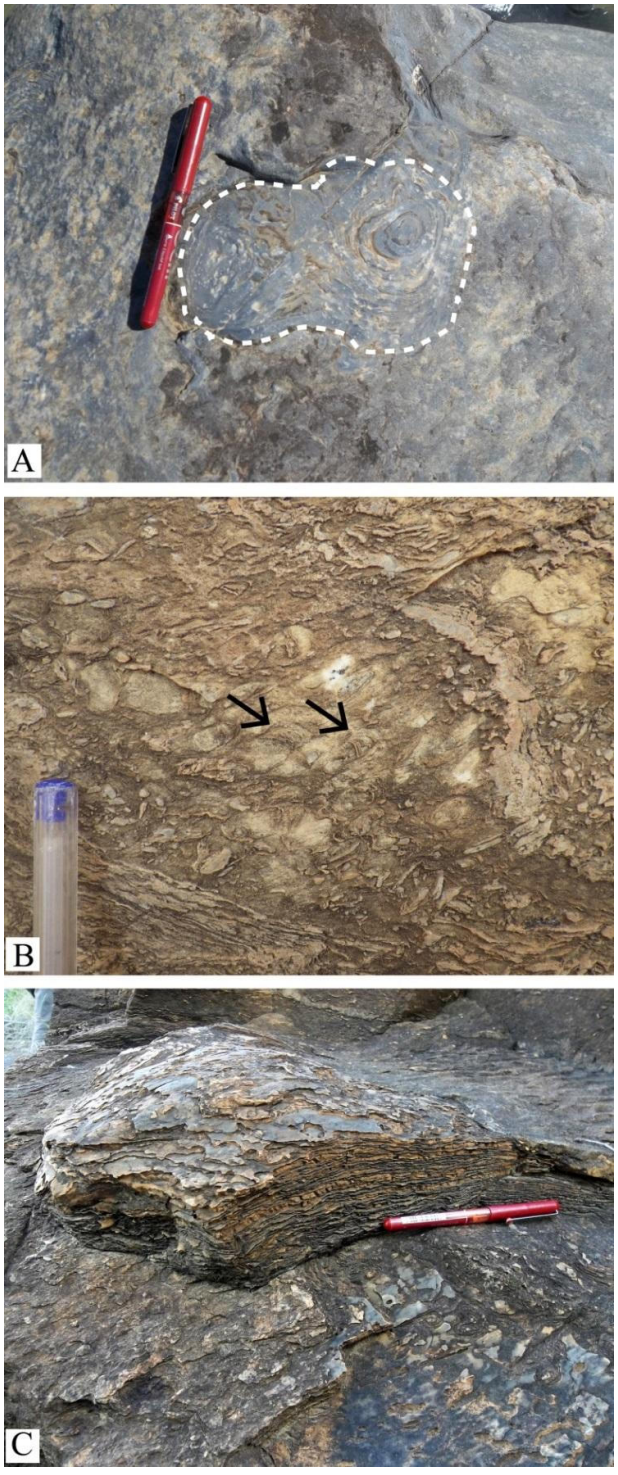

Fig. 12. Photographs showing different types of microbialites from supra- to shallow subtidal environments. (A) Plan view of laterally-linked domal stromatolites, outlined by dashed line, and surrounded by dolomitic sandstone of the intraclast dolomitic sandstone facies. (B) Digitate stromatolites (arrows) surrounded by intradolorudite. (C) Oblique view of partially silicified domal stromatolite in ripple-laminated dolomitic sandstone.

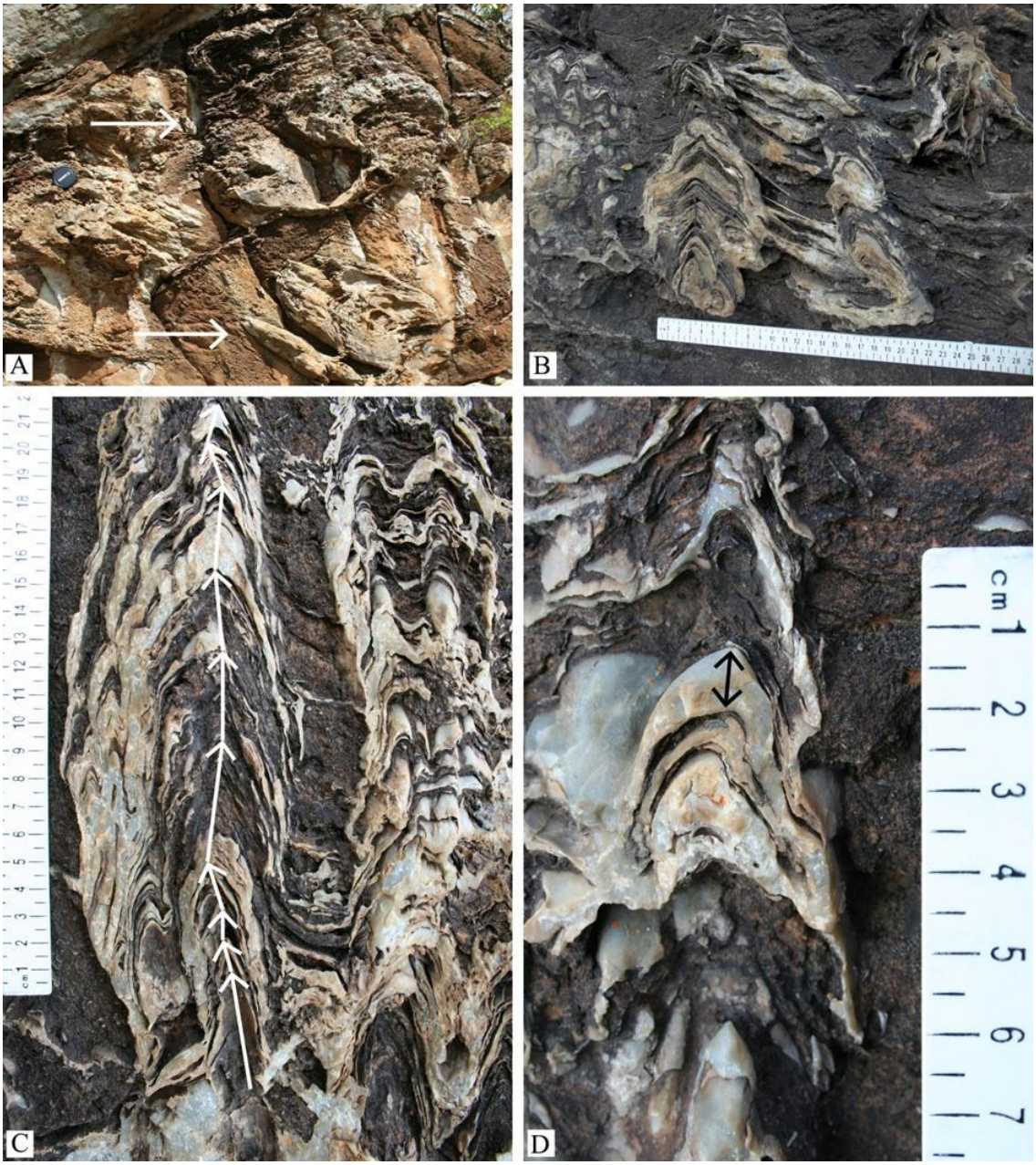

Fig. 13. Photographs showing different types of conical/columnar stromatolite facies; note the selective silicification of stromatolites in the light-colored domains. (A) Silicified composite conical stromatolite at the bottom and composite columnar stromatolites at the top of the image indicated by arrows. Note some rotation of the stromatolites into the plane of foliation. (B) Closely-spaced laterally-linked conical stromatolites. (C) Laterally linked conical stromatolite with centimetre-size silicified fragments within interspaces of cones; note inclination from one set of laminae to the other (arrows). (D) Crestal thickening (arrow) in a conical stromatolite.

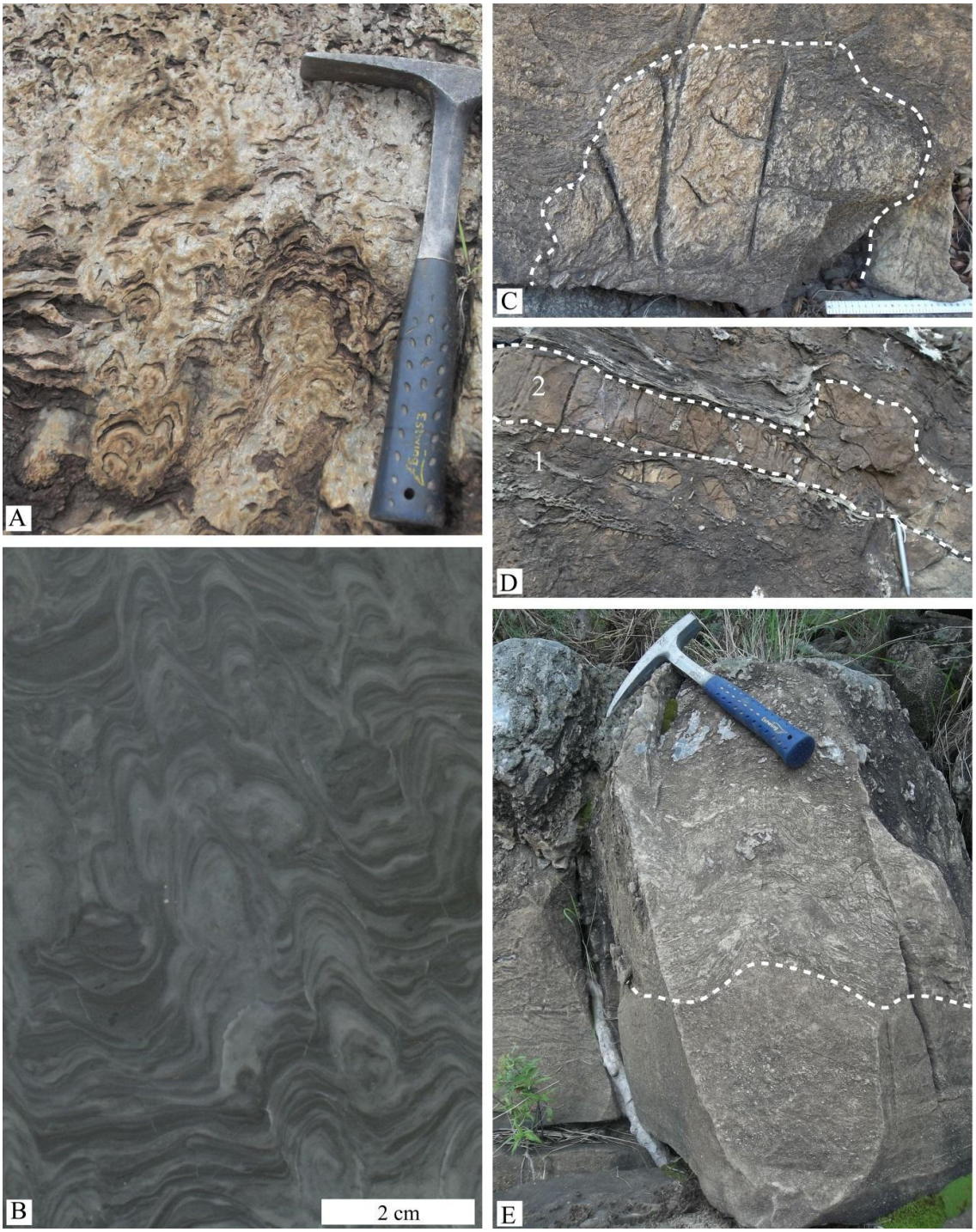

Fig. 14. Photographs showing different types of conical/ columnar stromatolite facies and structureless microbialites. (A) Columnar stromatolites form a composite mass with colloform structure. (B) Polished slab of columnar stromatolite showing alternating silicified laminae (light grey), dolomicritic and detrital-rich laminae (dark grey). (C) Structureless domal microbialite outlined by white dashed line in the lower part overlain by crudely laminated stromatolite; pen for scale. (D) Sandy intradolorudite facies (1) overlain by a bed of massive

micritic microbialite (2) forming a dome structure. (E) Structureless microbialites with a grain-dominated macrofabric below white dashed line.

3.7 Interpretation of depositional environments

The sedimentological features of the volcaniclastic-siliciclastic-carbonate succession of the Chobeni Formation support depositionin a tide-dominated shallow-marine environment (Mason and Von Brunn, 1977; Von Brunn and Mason, 1977; Beukes and Lowe, 1989; this study). The combination of symmetric and asymmetric ripple marks, abundant mud drapes, flaser, lenticular and wavy bedding, and evidence for bi-directional currents are consistent with tidal activity. The abundance of stratiform stromatolite facies with its characteristic assemblage of structures reflecting intermittent exposure and locally incised tidal channels reflects the presence of widespread intertidal flats at times. While lateral facies relationships could only be investigated for the main carbonate section, they nevertheless allow tracing of facies assemblages and even single beds over hundreds of metres (Figs. 3 and 5). The presence of coarse-grained clastic subtidal facies, ooids, evidence for storm deposits as well as the abundance of clastic detritus as part of the carbonate sections suggest deposition along a tide-influenced clastic-carbonate shoreline rather than a restricted lagoonal setting. A trace-element geochemical study of carbonates of the main and upper carbonate section supports deposition in a shallow-water epicontinental basin with restricted but variable exchange to the open-ocean (Bolhar et al., 2015).

3.7.1 Depositional environment of the main carbonate section

The lower part of the main carbonate section shows clearly defined sedimentary cycles that are best preserved in the western section (Fig. 5, Section 1). A total of 6 cycles were observed, ranging in thickness from 0.4 m to 5.7 m (Figs. 5 and 15). The facies are vertically arranged in a shallowing-upward succession that mostly commences with subtidal facies shallowing upward into intertidal and supratidal facies, the latter subjected to periods of subaerial exposure. Cycle boundaries are contacts along which there is an abrupt facies shift from intertidal-supratidal deposits to subtidal deposits. The contacts are sharp to erosional, and the immediately underlying strata show evidence of subaerial exposure.

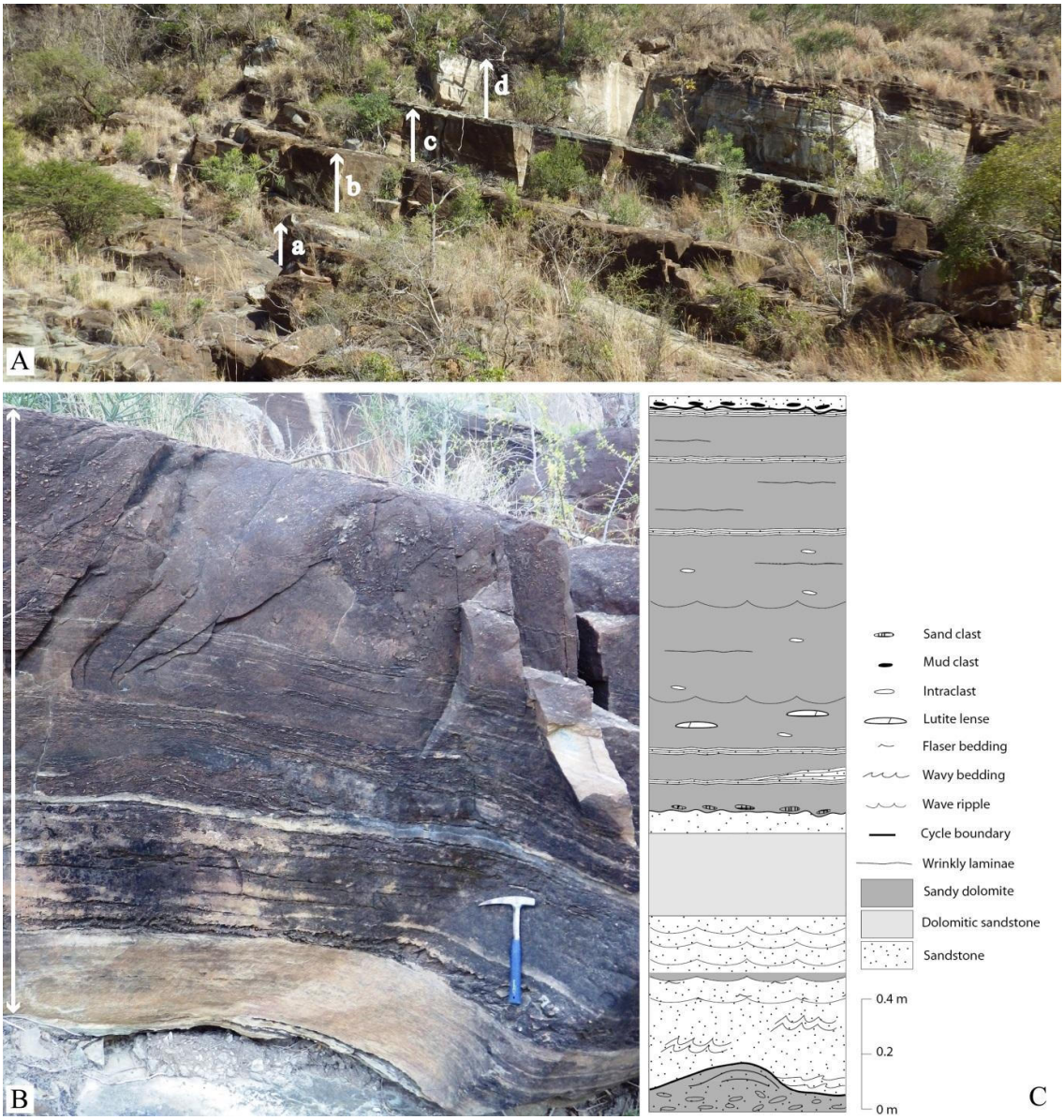

Fig. 15. Photographs showing four sedimentary cycles (a-d) of the lower part of the main carbonate section. See Fig. 5 for locality of cycles. (B) Close-up photograph of cycle c. Note decreasing amount of sand upwards as indicated by color change from light to dark. Arrow shows bottom and top of the cycle. (C) Stratigraphic column of shallowing-upward cycle c.

The cycles begin with a subtidal facies including shale, cross-bedded to flaser-wavy bedded sandstone, rippled dolarenite-dololutite and intradolorudite at the cycle base. Thin intradolorudite beds at the base of some cycles probably represent a transgressive facies. The

subtidal facies grade into those of the intertidal-supratidal assemblage such as sandy intradolorudite and stratiform stromatolite.

In one cycle (Fig. 5, cycle b), shale, the deepest sedimentary facies, is overlain by cross-bedded sandstone that grades upwards into intertidal rippled intraclast dolomitic sandstone. Several cycles start with cross-bedded to flaser-wavy bedded sandstone that is overlain by massive to wave-rippled, dolomitic sandstone and succeeded by stratiform stromatolite (Fig. 15B and C). The variation of cycle components may be related to non-deposition as a result of rapid transgression or removal due to subaerial exposure (Pratt and James, 1986).

In the field, cycles consisting of subtidal to inter-/ supratidal facies are conspicuous, as they are characterized by clastic-dominated facies at the base, and carbonate-dominated facies at the top (e.g. Fig. 15B and C). In the stratigraphic column (Fig. 5) they are commonly shown with a coarsening-upward pattern, due to the abundance of granule to pebble-sized carbonate allochems such as intraclasts in the carbonate-dominated facies.

Shallowing-upward sedimentary cycles are common components of ancient carbonate platforms (e.g. Pratt et al., 1992), and of tidal flat carbonates in particular (Hardie and Shinn, 1986). Shallowing-upward cycles are a result of relative sea-level changes, and the underlying reasons for their presence have been a topic of long-lasting debate. Various autocyclic and allocyclic models have been proposed to explain the origin of cyclicity (Hinnov, 2013).Despite variations in the form of carbonate production through time, cyclicity in carbonates is not uncommon in Precambrian carbonate successions. The hitherto oldest cyclic carbonates have been described from the late Archaean, c. 2650 Ma Cheshire Formation, Belingwe greenstone belt, Zimbabwe where the controlling mechanism for the cyclicity was ascribed to high-frequency eustatic sea-level changes (Martin et al., 1980; Hofmann et al., 2004).

The cyclic interval is succeeded by a prominent stratiform stromatolite unit containing conspicuous tepee structures (Fig. 8C). There is a hint of cyclic facies development in a sense that wrinkly laminated carbonates are rhythmically interlayered with thin beds of mudstone representing flooding of the supratidal flats. It is not clear if the flooding represents relative sea-level changes or simply large storm events.

The stratiform stromatolite facies is succeeded by rippled dolarenite-dololutite, sandy oolitic intradolorudite, and sandy oodolarenite, suggesting marine transgression to an overall subtidal setting (Fig. 5, at c. 16 m). The presence of edgewise conglomerate together with sandy oolitic

intradolorudite in this interval is indicative of episodic high-magnitude storm events. Microbialites are relatively rare in these facies, except for isolated domes.

The oolitic arenite facies grades into the more coarse-grained oncolite facies (Fig. 5, at c. 19 m), which probably formed in a moderately high-energy, permanently submerged subtidal setting. The reason for abundant oncoid formation at this level is unclear to us, but may be related to lack of input of siliciclastic material. This may be related to the formation of a barrier separating the offshore source of siliciclastic sediment from the carbonate tidal flat. The top of the oncolitic horizon is defined by an erosional surface overlain by intradolorudite containing reworked material (such as oncoids) from the underlying bed. Veins of translucent chert oriented perpendicular to bedding locally occur in the oncolite horizon, but seem not to transect the erosive surface (Fig. 5, Section 2). We thus interpret the erosive contact to have formed as a result of falling sea-level, giving rise to subaerial exposure and localized dissolution of the oncolitic carbonate horizon along narrow fissures. Exposure was followed by sea-level rise and deposition of transgressive intradolorudite overlain by stratiform stromatolite facies. The fissures were later filled with chert, although the timing of the silica precipitation needs to be clarified.

The tidal channel facies assemblage is erosively incised into stratiform stromatolite facies, contrary to the view of Beukes and Lowe (1989). However, discontinuous exposure does not exclude possible lateral interfingering of the two facies as proposed by these authors. Morphologically diverse stromatolites formed in the tidal channel. According to Beukes and Lowe (1989), it had a depth of c. 1.5 m. Single conical stromatolites with high synoptic relief near the base and coalesced domal stromatolites at the top formed as a result of filling of the channel over time.

Transgression led to the establishment of fully subtidal environmental conditions dominated by coarse-grained siliciclastic sediments. Minor carbonate beds and lenses in sandstone above the main carbonate section (Fig. 4D) suggest a return to conditions favorable for carbonate deposition at times.

In the main carbonate section, siliciclastic sediment is present throughout, but concentrated in deeper-water facies, specifically at the base of shallowing-upward cycles in the lower part of the section. Volcaniclastic lapillistone forms the base of the main carbonate section and also occurs as a thin bed interlayered with carbonate near the base. Upsection, the abundance of ash/ lapilli diminishes, but it does not disappear completely. While volcanic activity was

ongoing during deposition of the lower part, it is not clear if this was the case for the upper part, which may contain only reworked volcaniclastic particles. Hence, the question if the influence of volcanism provided a favorable local geochemical environment for biogenic processes and carbonate precipitation remains unresolved.

3.7.2 Depositional environment of the middle carbonate section

The middle carbonate section (Fig. 6) is dominated by poorly sorted sandstone. Carbonate is present as thin layers of dololutite, allochems, and matrix and/or cement in sandstone facies. Common facies include (1) wavy-flaser bedded intraclast sandstone indicative of bimodal currents, (2) mud-cracked mud or lutite layers suggesting periodic subaerial emergence in a tidal flat setting, and (3) cross-bedded, hummocky cross-bedded or normally graded intraclast sandstone with erosive bases suggesting regularly occurring storm events. All of these facies indicate formation in a shallow subtidal to intertidal, predominantly high-energy environment. Palaeocurrent analysis (Fig. 2) indicates unimodal, offshore-directed sediment transport. In contrast to the main carbonate section, upper intertidal and supratidal facies are rare. The only direct evidence for microbial activity in this section includes carbonaceous matter-bearing ooids, peloids and ooid-bearing aggregates. Indirect evidence for microbial activity may be found in the poor sorting of some fine-grained dolomitic sandstone layers containing scattered and very coarse sand grains that may reflect wind- or water-transported material possibly trapped by microbial mats.

3.7.3 Depositional environment of the upper carbonate section

The upper carbonate section overlies a succession of predominantly cross-bedded and very coarse-grained subtidal sandstones (Fig. 2). It commences with cross-bedded intraclast dolomitic sandstone grading into rippled intraclast dolomitic sandstone with cracked mud drapes suggesting shallowing from a subtital to an intertidal environment (Fig. 6). Wavy bedded sandy dolomite and dolomitic sandstone facies follow and they indicate fluctuation in wave energy in a shallow subtidal environment.

A relatively massive, incompletely exposed unit of oolitic sandy intradolorudite facies forms the middle part of the section (Fig. 6). It shows layers of stratiform stromatolite, dololutite

lenses, wave-ripple lamination and evidence for disruption. These features in combination with large intraclasts suggest deposition in a predominantly intertidal to supratidal setting.

Indistinct asymmetric cyclic stacking of facies is observed in the upper part of the succession (Fig. 6) where shallow subtidal facies are overlain by intertidal and supratidal carbonates that show frequent evidence for subaerial exposure. Typically, facies include (from base to top) cross-bedded intraclast dolomitic sandstone, rippled dolomitic sandstone or sandy oodolorudite and stratiform stromatolite with intercalations of intradolorudite that formed as a result of extensive sediment disruption. Lenses, continuous layers and domes of massive dololutite representing massive microbialites are present in supratidal facies of this part of the section. Wedge-shaped to irregular sand-filled fissures probably representing filled desiccation cracks are also common in this interval. Such cracks are frequently observed on the top of massive microbialite beds (Fig. 14D).

Siliciclastic material is present throughout the upper carbonate section, but is typically more concentrated in deeper water facies. Diagenetic pyrite nodules occur sporadically and have only been observed in this section. In contrast to the main carbonate section, microbialites are less diverse and include predominantly non-laminated microbialites and indistinct stratiform stromatolites. The absence of well-developed stromatolitic carbonates indicates unfavorable conditions for the flourishing of microbial communities that are responsible for the formation of laminated microbialites. This may be due to relatively high input of siliciclastic detritus.

3.8 Conclusions

1. Carbonate rocks of the c. 3.0 billion-years-old Nsuze Group in the White Mfolozi inlier are composed predominantly of dolomite and subordinate ankerite. Coarse-grained clastic subtidal facies, evidence for storm deposits, and the abundance of clastic detritus, as part of the carbonate sections, suggest deposition in a tide-influenced siliciclastic-carbonate shallow-marine environment.

2. Fluctuations of relative sea-level gave rise to cyclic stacking of lithofacies. There is insufficient preservation of sedimentary cycles to make any firm judgement on their origin. The cycles do however indicate that even as far back as 3 billion years ago, shallow-marine carbonates were subjected to cyclic variation in facies stacking much in the same way as in modern carbonate environments.

3. The carbonate rocks contain abundant microbially-induced sedimentary structures, stromatolites, massive microbialites, ooids, and oncoids. The morphology of the microbialites varies systematically with the depositional environment. In general, digitate, stratiform, and small-scale domal stromatolites are limited to supratidal and upper-intertidal settings. Larger domes, conical/columnar stromatolites and oncoids were formed in higher-energy, lower intertidal and shallow subtidal settings. The variations in macrofabric, morphology, and size among various microbialites suggest that microbial communities were responding to differences in physical factors that operated in the shallow-marine environment during sea-level changes.

4. The upward growth of oncoids together with crestal thickening, inclination from one set of laminae to the other, and the coniform shape of conical stromatolites is consistent with a phototrophic behavior of microorganisms. Whether these microbes were oxygenic photosynthetic microorganisms remains to be resolved.

3.9 Acknowledgements

Field work was supported by funds from the National Research Foundation of South Africa to AH. We thank Lisborn Mangwane and Baldwin Tshivhiahuvhi for preparing the thin sections and polished slabs. MS is grateful to Roger Gibson, School of Geosciences, University of the Witwatersrand, for providing office space during research in South Africa. Two anonymous referees are acknowledged for their constructive criticism. We thank Linda Kah for her substantial editorial input.

3.10 References

Allwood, A.C., Walter, M.R., Kamber, B.S., Marshall, C.P., Burch, I.W., 2006. Stromatolite reef from the Early Archaean era of Australia. Nature 441, 714-718.

Altermann, W., Lenhardt, N., 2012. The volcano-sedimentary succession of the Archaean Sodium Group, Ventersdorp Supergroup, South Africa: Volcanology, sedimentology and geochemistry. Precambrian Res. 214-215, 60-81.

Altermann, W., Schopf, J.W., 1995. Microfossils from the Neoarchaean Campbell Group, Griqualand West Sequence of the Transvaal Supergroup, and their paleoenvironmental and evolutionary implications. Precambrian Res. 75, 65-90.

Andres, M.S., Reid, P.R., 2006. Growth morphologies of modern marine stromatolites: a case study from Highborne Cay, Bahamas. Sediment. Geol. 185, 319-328.

Awramik, S.M., 1984. Ancient stromatolites and microbial mats. In: Cohen, Y., Castenholz, R.W., Halvorson, H.O. (Eds.), Microbial Mats: Stromatolites, pp. 1-22, New York, Liss.

Beukes, N.J., 1987. Facies relations, depositional environments and diagenesis in a major early Proterozoic stromatolitic carbonate platform to basinal sequence, Campbellrand Subgroup, Transvaal Supergroup, South Africa. Sediment. Geol. 54, 1-46.

Beukes, N.J., Cairncross, B., 1991. A lithologic-sedimentological reference profile for the Late Archaean Mozaan Group, Pongola-Sequence: application to sequence stratigraphy and correlation with the Witwatersrand Supergroup. South Afr. J. Geol. 94, 44-69.

Beukes, N.J., Lowe, D.R., 1989. Environmental control on diverse stromatolite morphologies in the 3000 Ma Pongola Supergroup, South Africa. Sedimentology 36, 383-397.

Bolhar, R., Van Kranendonk, M.J., 2007. A non-marine depositional setting for the northern Fortescue Group, Pilbara Craton, inferred from trace element geochemistry of stromatolitic carbonates. Precambrian Res. 155 (3), 229-250.

Bolhar, R., Hofmann, A., Siahi, M., Feng, Y., Delvigne, C., 2015. A trace element and Pb isotopic investigation into the provenance and deposition of stromatolitic carbonates, iron stones and associated shales of the ~3.0 Ga Pongola Supergroup, Kaapvaal Craton. Geochim. Cosmochim. Acta 158, 57-78.

Braga, J.C., Martin, J.M., Riding, R., 1995. Controls on microbial dome fabric development along a carbonate-siliciclastic shelf-basin transect, Miocene, SE Spain. Palaios 10, 347-361.

Buck, S.G., 1980. Stromatolite and ooid deposits within the fluvial and lacustrine sediments of the Precambrian Ventersdorp Supergroup of South Africa. Precambrian Res. 12, 311-330.

Burns, B.P., Goh, F., Allen, M., Neilan, B.A., 2004. Microbial diversity of extant stromatolites in the hypersaline marine environment of Shark Bay, Australia. Environ. Microbiol. 6, 1096-1101.

Canfield, D.E., Raiswell, R., 1991. Carbonate precipitation and dissolution: its relevance to fossil preservation. In: Alison, P.A., Briggs, D.E. (Eds.), Taphonomy: Releasing the data locked in the fossil record. Plenum Press, New York, pp. 411-453.

Chafetz, H.S., Buczynski, C., 1992. Bacterially induced lithification of microbial mats. Palaios 7, 277-293.

Chakrabarti, G., Shome, D., Kumar, S., Stephens 111, G.M., Kah, L.C., 2014. Carbonate platform development in a Paleoproterozoic extensional basin, Vempalle Formation, Cuddapah Basin, India. J. Asian Earth Sci. 91, 263-279.

Chow, N., James, N., 1987. Facies-specific, calcite and bimineralic ooids from Middle and Upper Cambrian platform carbonates, Western Newfoundland, Canada. J. Sediment. Petrol. 57 (5), 907-921.

Crosby, C.H., Bailey, J.V., 2012. The role of microbes in the formation of modern and ancient phosphatic mineral deposits. Front. Microbiol. 3, 3-9.

Dahanayake, K., Gerdes, G., Krumbein, W.E., 1985. Stromatolites, oncolites and oolites biogenically formed in situ. Naturwissenschaften 72, 513-518.

Dalrymple, R.W., 2010. Tidal depositional systems. In: James, N.P., Dalrymple, R.W. (Eds.), Facies Models 4. Geological Association of Canada, St. John's, Newfoundland, pp. 201-231, 6.

Davaud, E., Girardclos, S., 2001. Recent freshwater ooids and oncoids from western Lake Geneva (Switzerland): indications of a common organically mediated origin. J. Sediment. Res. 71 (3), 423-429.

Dickson, J.A.D., 1966. Carbonate identification and genesis as revealed by staining. J. Sediment. Petrol. 361 (2), 491-505.

Dill, R.F., 1991. Subtidal stromatolites, ooids and lime encrusted muds at the Great Bahama bank margin. In: Osborne, R.H. (Ed.), From Shoreline to Abyss. Contributions in Marine Geology in Honour of Farncis Parker Shephard, 46. SEPM Special Publication, pp. 147-171.

Dill, R.F., Shinn, E.A., Jones, A.T., Kelly, K., Steinen, R.P., 1986. Giant subtidal stromatolites forming in normal salinity water. Nature 324, 55-58.

Dixon, J.G.P., 2004. Archaean geology of the Buffalo River gorge (PhD thesis). University of KwaZulu-Natal, Durban, 263 p.

Donald, R., Southam, G., 1999. Low temperature anaerobic bacterial diagenesis of ferrous monosulfide to pyrite. Geochim. Cosmochim. Acta 63, 2019-2023.

Dravis, J.J., 1983. Hardened subtidal stromatolites, Bahamas. Science 219, 385-386.

Dupraz, C., Visscher, P.T., 2005. Microbial lithification in marine stromatolites and hypersaline mats. Trends Microbiol. 13, 429-438.

Dupraz, C., Visscher, P.T., Baumgartner, L.K., Reid, R.P., 2004. Microbe-mineral interactions: early carbonate precipitation in a hypersaline lake (Eleuthera Island, Bahamas). Sedimentology 51, 745-765.

Dupraz, C., Reid, R.P., Braissant, O., Decho, A.W., Sean Norman, R.S., Visscher, P.T., 2009. Processes of carbonate precipitation in modern microbial mats. Earth Sci. Rev. 96, 141-162.

Fahraeus, L.E., Slatt, R.M., Nowlan, G.S., 1974. Origin of carbonate pseudopellets. J. Sediment. Petrol. 44, 27-29.

Fenies, H., Faugères, J.C., 1998. Facies and geometry of tidal channel-fill deposits (Arcachon Lagoon, SW France). Mar. Geol. 150, 131-148.

Flannery, D.T., Walter, M.R., 2012. Archean tufted microbial mats and the Great Oxidation Event: New insights into an ancient problem. Aust. J. Earth Sci. 59, 1-11.

Flügel, E., 2004. Microfacies of carbonate rocks: Analysis, interpretation and application. Springer-Verlag, Germany, p. 976.

Folk, R.L., 1959. Practical petrographic classification of limestones. Am. Assoc. Pet. Geol. Bull. 43, 1-38.

Folk, R.L., 1962. Spectral subdivision of limestone types. In: Ham, W.E. (Ed.), Classification of Carbonate Rocks-A Symposium, vol. 1. American Association of Petroleum Geologists Memoir, pp. 62-84.

Fouke, B.W., Farmer, J.D., Des Marais, D.J., Pratt, L., Sturchio, N.C., Burns, P.C., Discipulo, M.K., 2000. Depositional facies and aqueous-solid geochemistry of travertine-depositing hot springs (Angel Terrace, Mammoth Hot Springs, Yellowstone National Park, USA). J. Sediment. Res. 70 (3), 565-585.

Fralick, P., Riding, R., 2015. Steep Rock Lake: Sedimentology and geochemistry of an Archean carbonate platform. Earth Sci. Rev. 151, 132-175.

Friedman, G.M., 1959. Identification of carbonate minerals by staining methods. J. Sediment. Petrol. 29, 87-97.

Gerdes, G., Claes, M., Dunajtschik-Piewak, K., Riege, H., Krumbein, W.E., Reineck, H. E., 1993. Contribution of microbial mats to sedimentary surface structures. Facies 29, 61-74.

Gerdes, G., Dunajtschik-Piewak, K., Riege, H., Taher, A.G., Krumbein, W.E., Reineck, H.E., 1994. Structural diversity of biogenic carbonate particles in microbial mats. Sedimentology 41, 1273-1294.

Gold, D.J.C., 2006. The Pongola Supergroup. In: Johnston, M.R., Anhaeusser, C.R., Thomas, R.J. (Eds.), The Geology of South Africa. Geological Society of South Africa/Council for Geoscience South Africa, pp. 135-147.

Golubic, S., 1991. Modern stromatolites-a review. In: Riding, R. (Ed.), Calcareous Algae and Stromatolites. Springer-Verlag, Heidelberg, pp. 541-561.

Golubic, S., 1992. Stromatolites of Shark Bay. In: Margulis, L., Olendzenski, L. (Eds.), Environmental Evolution: Effects of the Origin and Evolution of Life on Planet Earth. Cambridge University Press, Cambridge, pp. 131-147.

Grey, K., Thorne, A.M., 1985. Stratigraphic significance of stromatolites in shallowing sequences of the early Proterozoic Duck Creek dolomite, Western Australia. Precambrian Res. 29, 183-206.

Grotzinger, J.P., 1989. Facies and evolution of Precambrian carbonate depositional systems: emergence of the modern platform archetype. In: Crevello, P.D., Wilson, J.L., Sans, J.F., Read, J.F. (Eds.), Controls on carbonate platform and basin development, 44. SEPM Special Publication, Tulsa, pp. 79-106.

Gumsley, A.P., Olsson, J.R., Söderlund, U., De Kock, M.O., Hofmann, A., Klausen, M.B., 2015. Precise U-Pb baddeleyite age dating of the Usushwana Complex, southern Africa – implications for the Mesoarchaean magmatic and sedimentological evolution of the Pongola Supergroup, Kaapvaal Craton. Precambrian Res. 267, 174-185.

Halley, R.B., Harris, P.M., Hine, A.C., 1983. Bank margin environment. In: Scholle, P. A., Bebout, D.G., Moore, C.H. (Eds.), Carbonate depositional environments, vol. 33. American Association of Petroleum Geologists Memoir, pp. 463-506.

Hardie, L.A., Ginsburg, R.M., 1977. Layering: The origin and environmental significance of lamination and thin bedding. In: Hardie, L.A. (Ed.), Sedimentation on the modern carbonate tidal flats of Northwest Andros Island, Bahamas. Johns Hopkins University Press, Baltimore, pp. 50-123.

Hardie, L.A., Shinn, E.A., 1986. Carbonate depositional environments, modem and ancient. Part 3. Tidal flats. Colorado School Mines Q. 81, 1-74.

Hegner, E., Kröner, A., Hofmann, A.W., 1984. Age and isotopic geochemistry of the Archaean Pongola and Ushushwana suites in Swaziland, Southern Africa: A case for crustal contamination of mantle-derived magmas. Earth Planet. Sci. Lett. 70, 267-279.

Hegner, E., Kröner, A., Hunt, P., 1994. A precise U-Pb zircon age for the Archaean Pongola Supergroup volcanics in Swaziland. J. Afr. Earth Sci. 18 (4), 339-341.

Henderson, J.B., 1975. Archean stromatolites in the northern Slave province, Northwest Territories, Canada. Can. J. Earth Sci. 12, 1619-1630.

Hicks, N., Hofmann, A., 2012. Stratigraphy, geochemistry and provenance of the auriferous-uraniferous, fluvial to shallow-marine Sinqeni Formation, Mozaan Group, northern KwaZulu-Natal, South Africa. South Afr. J. Geol. 115 (3), 327-344.

Hinnov, L.A., 2013. Cyclostratigraphy and its revolutionizing applications in the earth and planetary sciences. Geol. Soc. Am. Bull. 125 (11-12), 1703-1734.

Hofmann, A., Dirks, P.H.G.M., Jelsma, H.A., 2004. Shallowing-upward carbonate cycles in the Belingwe Greenstone Belt, Zimbabwe: a record of Archaean sealevel oscillations. J. Sediment. Res. 74 (1), 64-81.

Howe, W.B., 1966. Digitate algal stromatolite structures from the Cambrian and Ordovician of Missouri. J. Paleontol. 40, 64-77.

Jahnert, R.J., Collins, L.B., 2012. Characteristics, distribution and morphogenesis of subtidal microbial systems in Shark Bay, Australia. Mar. Geol. 303-306, 115-136.

Kah, L.C., Bartley, J.K., Frank, T.D., Lyons, T., 2006. Reconstructing sea level change from the internal architecture of stromatolite reefs: an example from the Mesoproterozoic Sulky Formation, Dismal Lakes Group, arctic Canada. Can. J. Earth Sci. 43, 653-669.

Kazmierczak, J., Coleman, M.L., Gruszczynski, M., Kempe, S., 1996. Cyanobacterial key to the genesis of micritic and peloidal limestones in ancient seas. Acta Palaeont. Pol. 41, 319-338.

Leeder, M., 1975. Lower Border Group (Tournaisian) stromatolites from the Northumberland basin. Scot. J. Geol. 11, 207-226.

Logan, B.W., Rezak, R., Ginsburg, R.N., 1964. Classification and environmental significance of algal stromatolites. J. Geol. 72, 68-83.

Loreau, J.P., Purser, B.H., 1973. Distribution and ultrastructure of Holocene ooids in the Persian Gulf. In: Purser, B.H. (Ed.), The Persian Gulf. Springer, Berlin, pp. 279-328.

Lowe, D.R., 1980. Stromatolites 3400-Myr old from the Archaean of Western Australia. Nature 284, 441-443.

Macintyre, I.G., 1985. Submarine cements-the peloidal question. In: Schneidermann, N., Harris, P.M. (Eds.), Carbonate Cements, 36. SEPM Special Publication, Tulsa, USA, pp. 109-116.

Martin, A., Nisbet, E.G., Bickle, M.J., 1980. Archaean stromatolites of the Belingwe Greenstone Belt, Zimbabwe (Rhodesia). Precambrian Res. 13, 337-362.

Mason, T.R., Von Brunn, V., 1977. 3-Gyr-old stromatolites from South Africa. Nature 266, 47-49.

Matthews, P.E., 1967. The pre-Karoo formations of the White Umfolozi inlier, northern Natal. Trans. Geol. Soc. South Afr. 70, 39-63.

Monty, C.L.V., 1967. Distribution and structure of recent stromatolitic algal mats, eastern Andros Island, Bahamas. Ann. Soc. Geol. Belgique 90, 55-100.

Mount, J.F., Kidder, D., 1993. Combined flow origin of edgewise intraclast conglomerates: Sellick Hill Formation (Lower Cambrian), South Australia. Sedimentology 40, 315-329.

Mukasa, S.B., Wilson, A.H., Young, K.R., 2013. Geochronological constraints on the magmatic and tectonic development of the Pongola Supergroup (Central Region), South Africa. Precambrian Res. 224, 268-286.

Noffke, N., Gerdes, G., Klenke, Th., Krumbein, W.E., 2001. Microbially induced sedimentary structures-a new category within the classification of primary sedimentary structures. J. Sediment. Res. 71, 649-656.

Olsson, J.R., Söderlund, U., Klausen, M.B., Ernst, R.E., 2010. U-Pb baddeleyite ages linking major Archean dyke swarms to volcanic-rift forming events in the Kaapvaal Craton (South Africa), and a precise age for the Bushveld Complex. Precambrian Res. 183, 490-500.

Peryt, T.M., 1981. Phanerozoic oncoids – an overview. Facies 4, 197-214.

Petroff, A.P., Sim, M.S., Maslov, A., Krupenin, M., Rothman, D.H., Bosak, T., 2010. Biophysical basis for the geometry of conical stromatolites. Proc. Acad. Nat. Sci. 107, 9956-9961.

Pratt, B.R., 1984. Epophyton and Renalcis-diagenetic microfossils from calcification of coccoid blue-green algae. J. Sediment. Petrol. 54, 948-971.

Pratt, B.R., James, N.P., 1986. The St George group (Lower Ordovician) of western Newfoundland: tidal flat island model for carbonate sedimentation in shallow epeiric seas. Sedimentology 33, 313-343.

Pratt, B.R., James, N.P., Cowan, C.A., 1992. Peritidal carbonates. In: Walker, R.G., James, N.P. (Eds.), Facies Models: Response to Sea Level Change. Geological Association Canada, pp. 303-322.

Préat, A.L., Delpomdor, F., Kolo, K., Gillan, D.C., Prian, J.P., 2011. Stromatolites and cyanobacterial mats in peritidal evaporative environments in the Neoproterozoic of Bas-Congo (Democratic Republic of Congo) and South Gabon. In: Tewari, V.C., Seckbach, J. (Eds.), Stromatolites: Interaction of microbes with sediments, cellular origin, life in extreme habitats and astrobiology, 18. Springer, pp. 43-63.

Ratcliffe, K.T., 1988. Oncoids as environmental indicators in the Much Wenlock Limestone Formation of the English Midlands. J. Geol. Soc. London 145, 117-124.

Reid, R.P., Visscher, P.T., Decho, A.W., Stolz, J.F., Bebout, B.M., Dupraz, C., Macintyre, I.G., Paerl, H.W., Pinckney, J.L., Prufert-Bebout, L., Steppe, T.F., DesMarais, D.J.,2000. The role of microbes in accretion, lamination and early lithification of modem marine stromatolites. Nature 406, 989-992.

Reid, R.P., James, N.P., Macintyre, I.G., Dupraz, C.P., Burne, R.V., 2003. Shark Bay stromatolites: microfabrics and reinterpretation of origins. Facies 49, 45-53.

Reitner, J., Neuweiler, F., 1995. Mud mounds: A polygenetic spectrum of fine-grained carbonate buildups. Facies 32, 1-70.

Schoene, B., Bowring, S.A., 2010. Rates and mechanisms of Mesoarchaean magmatic arc construction, eatern Kaapvaal craton, Swaziland. Geol. Soc. Am. Bull. 122, 408-429.

Seong-Joo, L., Golubic, S., 1999. Microfossil populations in the context of synsedimentary micrite deposition and acicular carbonate precipitation: Mesoproterozoic Gaoyuzhuang Formation, China. Precambrian Res. 96, 183-208.

Seong-Joo, L., Browne, K.M., Golubic, S., 2000. On stromatolite lamination. In: Riding, R.E., Awramik, S.M. (Eds.), Microbial sediments. Springer-Verlag, Heidelberg, pp. 16-24.

Sepkoski, J.J., 1982. Flat-pebble conglomerates, storm deposits, and the Cambrian bottom fauna. In: Einsele, G., Seilacher, A. (Eds.), Cyclic and event stratification. Springer-Verlag, New York, pp. 371-385.

Shinn, E.A., 1983. Tidal flat environment. In: Scholle, P.A., Bebout, D.G., Moore, C.H. (Eds.), Carbonate depositional environments, vol. 33. American Association of Petroleum Geologists Memoir, pp. 171-210.

Shinn, E.A., 1986. Modern carbonate tidal flats: their diagnostic features. In: Hardie, L.A., Shinn, E.A. (Eds.), Carbonate depositional environments; Part 3: Tidal Flats, vol. 81. Colorado School of Mines Quarterly, pp. 7-35.

Sibley, D.F., 1982. The origin of common dolomite fabrics: clues from the Pliocene. J.Sediment. Res. 52 (4), 1087-1100.

Sim, M., Liang, B., Petroff, A.P., Evans, A., Klepac-Ceraj, V., Flannery, D.T., Walter, M.R., Bosak, T., 2012. Oxygen-dependent morphogenesis of modern clumped photosynthetic mats and implications for the Archean stromatolite record. Geosciences 2, 235-259.

Simone, L., 1981. Ooids: A review. Earth Sci. Rev. 16, 319-355.

Simonson, B.M., Schubel, K.A., Hassler, S.W., 1993. Carbonate sedimentology of the early Precambrian Hamersley Group of Western Australia. Precambrian Res. 60, 28-335.

Smith, D.B., 1986. The Trow Point Bed-a deposit of Upper Permian marine oncoids, peloids and columnar stromatolites in the Zechstein of NE England. Geol. Soc. Lond. Spec. Publ. 22, 113-125.

Srinivasan, R., Shukla, M., Naqvi, S.M., Yadav, V.K., Venkatachala, B.S., Raj, B.U., Rao, D.V.S., 1989. Archaean stromatolites from the Chitradurga schist belt, Dharwar Craton, South India. Precambrian Res. 43, 239-250.

Sumner, D.W., Grotzinger, J.P., 2004. Implication for Neoarchaean ocean chemistry from primary carbonate mineralogy of the Campbellrand-Malmani Platform, South Africa. Sedimentology 51, 1273-1299.

Van Kranendonk, M.J., 2006. Volcanic degassing, hydrothermal circulation and the flourishing of early life on Earth: A review of the evidence from c. 3490-3240 Ma rocks of the Pilbara Supergroup, Pilbara Craton, Western Australia. Earth Sci. Rev. 74, 197-240.

Van Kranendonk, M.J., Webb, G.E., Kamber, B.S., 2003. Geological and trace element evidence for a marine sedimentary environment of deposition and biogenicity of 3.45 Ga stromatolitic carbonates in the Pilbara Craton, and support for a reducing Archaean ocean. Geobiology 1 (2), 91-108.

Visscher, P.T., Reid, R.P., Bebout, B.M., Hoeft, S.E., Macintyre, I.G., Thompson Jr., J., 1998. Formation of lithified micritic laminae in modem marine stromatolites (Bahamas): the role of sulfur cycling. Am. Mineral. 83, 1482-1491.

Von Brunn, V., Hobday, D.K., 1976. Early Precambrian tidal sedimentation in the Pongola Supergroup of South Africa. J. Sediment. Res. 46, 670-679.

Von Brunn, V., Mason, T.R., 1977. Siliciclastic-carbonate tidal deposits from the 3000 m.y. Pongola Supergroup, South Africa. Sediment. Geol. 18, 245-255.

Walter, M.R., 1983. Archaean stuomatolites: Evidence of the earth's earliest benthos. In: Schopf, W. (Ed.), Earth's earliest biosphere: Its origin and evolution. Princeton University Press, Princeton, NJ, pp. 187-213.

Walter, M.R., Bauld, J., Brock, T.D., 1976. Microbiology and morphogenesis of columnar stromatolites (Conophyton, Vacerilla) from hot springs in Yellowstone National Park. In: Walter, M.R. (Ed.), Stromatolites: developments in sedimentology 20. Elsevier, Amsterdam, pp. 273-310.

Wilson, A.H., Grant, C.E., 2006. Physical volcanology and compositions of the basaltic lavas in the Archean Nsuze Group, White Mfolozi inlier, South Africa. In: Reimold, W.U., Gibson, R.L. (Eds.), Processes on the early Earth, vol. 405. Geological Society of American Special Papers, pp. 225-289.

Wilson, A.H., Versfeld, J.A., 1994. The early Archaean Nondweni greenstone belt, southern Kaapvaal Craton, South Africa; Part 2. Characteristics of the volcanic rocks and constraints on magma genesis. Precambrian Res. 67 (3-4), 277-320.

Wilson, A.H., Groenewald, B., Palmer, C., 2013. Volcanic and volcaniclastic rocks of the Mesoarchaean Pongola Supergroup in South Africa and Swaziland: distribution, physical characteristics, stratigraphy and correlations. South Afr. J. Geol. 116 (1), 119-168.

Xie, H., Hofmann, A., Hegner, E., Wilson, A.H., Wan, Y., Liu, D., 2012. Zircon SHRIMP dating confirms a Palaeoarchaean supracrustal terrain in the southeastern Kaapvaal Craton, Southern Africa. Gondwana Res. 21 (4), 818-828.

Chapter 4: Carbonate ooids of the Mesoarchaean Pongola Supergroup, South Africa

Carbonate ooids of the Mesoarchaean Pongola Supergroup, South Africa

Abstract

Ooids from the Mesoarchaean Chobeni Formation, Pongola Supergroup, KwaZulu-Natal, South Africa are the oldest known well-preserved microbial spheres. They are mostly made up of dolomite and to a lesser extent of ankerite, and show concentric, radial-concentric, micritic, and radial fabrics. It is likely that ooids with different fabrics had different primary compositions and were formed by different processes as has been shown for their modern- day counterparts. Radial ooids are interpreted to have originated from Mg-calcite and probably formed by microbial activity in a low-energy regime, while concentric ooids had an aragonite precursor and formed biotically under perturbed environmental conditions. Radial-concentric ooids probably formed in two different stages. Micritic ooids formed via the recrystallization of concentric ooids, which had an unstable primary mineralogy (e.g. aragonite). Carbonaceous matter was identified in ooids and other carbonate components, such as intraclasts and peloids, by Raman spectroscopy. The close association of carbonaceous matter within ooid cortices with metabolically important elements such as N, S and P, as identified by NanoSIMS analysis, allows us to propose a biologically induced origin of the ooids. By analogy with modern examples, a variety of microbial communities probably played a role in carbonate precipitation and ooid formation. Shale-normalized rare earth element distribution patterns of ooid-bearing carbonate rocks show positive La_{SN}, Gd_{SN} and Y_{SN} anomalies, superchondritic Y/Ho ratios, and depleted light rare earth elements (LREEs) relative to the heavy rare earth elements (HREEs), which resemble those of modern seawater. These anomalies are less pronounced as expected for an open marine setting, which is interpreted as evidence for deposition in restricted shallow-seawater environments. The oolitic, stromatolitic, and oncoid facies show enrichment in the middle REEs (MREEs), which is interpreted as microbial fractionation in coastal seas and estuaries. The presence of negative La and Ce anomalies and depletion of HREEs relative to LREEs in silicified/ recrystallized carbonate components such as intraclasts, ooids, oncoids and carbonate-filled fractures reflect redistribution of rare earth elements during meteoric/ burial diagenesis.

4.1 Introduction

Ooids are sand-sized, spherical to ellipsoidal coated grains < 2 mm in diameter. They are composed of a nucleus surrounded by one or more concentric laminae (cortex) and most commonly consist of carbonate minerals. Nuclei may include lithoclasts, peloids and siliciclastic detritus. The cortices of carbonate ooids have a variety of fabrics, which include radial, concentric, radial-concentric and micritic fabrics (Flügel, 2004). A tangential arrangement of aragonite crystals gives rise to concentric ooid types. A radial arrangement of high-Mg calcite (HMC) and, more rarely, aragonite forms radial-fibrous ooids (Bathurst, 1971; Milliman and Barretto, 1975; Simone, 1981; Tucker and Wright, 1990).

The mechanism of ooid formation has been a debated subject for a long time, and a number of formation mechanisms have been suggested, including (1) a purely inorganic physico-chemical mechanism, by which carbonate ooids precipitate from agitated shallow seawater supersaturated with calcium bicarbonate (Bathurst, 1971; Kahle, 1974; Sandberg, 1975; Simone, 1981; Rankey and Reeder, 2009; Duguid et al., 2010), and (2) a biologically mediated mechanism, by which carbonate ooids were synthesized in the presence of humic acids (Dahanayake et al., 1985; Reitner et al., 1997; Davaud and Girardclos, 2001; Brehm et al., 2006; Plée et al., 2006).

Calcareous ooids are known from the Late Archaean to modern day. They are abundant throughout the Phanerozoic carbonate rock record and in some modern, low- to high-energy, sedimentary environments (Opdyke and Wilkinson, 1990; Simonson and Jarvis, 1993; Plée et al., 2008; Pacton et al., 2012). Modern environments include warm areas of very shallow-marine as well as saline and freshwater- lacustrine environments (Davies and Martin, 1976; Halley, 1977; Harris, 1983; Davaud and Girardclos, 2001).

Ooids are of great importance in the study of surface processes through time. They are used as indicators of palaeo-environmental conditions (water depth, salinity, temperature, and water energy), palaeoclimate and palaeoceanography, seawater composition (specifically the Mg/Ca ratio), and atmospheric pCO_2 (Sandberg, 1983; Wilkinson et al., 1985; Opdyke and Wilkinson, 1990, 1993; Kiessling et al., 2002). We have recently identified c. 3 Ga old ooids from a stromatolitic carbonate succession of the Pongola Supergroup in South Africa (Siahi et al., 2016). The aim of the current study is to provide a detailed documentation and interpretation of ooid textures and their mineral assemblages, using a combination of *in-situ* analytical

instruments. Ultimately, we aim to address which factors may have played a role in the formation of the ooids and their various cortical fabrics in the Mesoarchaean.

4.2 Geological setting and samples

The 3.0-2.9 Gyr old (Hunter, 1974; Hegner et al., 1994; Mukasa et al., 2013) Pongola Supergroup, was deposited on continental crust of the south-eastern Kaapvaal Craton in South Africa and is one of the oldest well-preserved successions of epicratonic volcanic and sedimentary rocks on Earth. In the study area of the White Mfolozi inlier in the province of northern KwaZulu-Natal the Pongola Supergroup consists of the c. 1.4 km thick volcano-sedimentary succession of the Nsuze Group, which is unconformably overlain by the mainly siliciclastic Mozaan Group. It comprises five formations in the White Mfolozi inlier of which the Chobeni Formation is the only unit that contains several horizons of dolomite with well-developed stromatolites (Matthews, 1967; Hicks and Hofmann, 2012; Siahi et al., 2016). Carbonate samples containing different types of coated grains were collected from three different sections of the Chobeni Formation, which are referred to as the main, middle and upper carbonate section. Facies containing ooids are confined to cross-bedded dolomitic sandstone and sandy oodolarenite (Figs. 1A-C). To a lesser extent they are present within structureless microbialite facies (Fig. 1D). A detailed description of these facies is presented in Siahi et al. (2016). Ooids are admixed with sand-sized siliciclastic detritus, micritic intraclasts and microbial mat chips up to several millimetres in length, partially silicified peloids 0.05 mm to 0.2 mm in diameter, and sand-sized subspherical micritic particles.

4.3 Analytical techniques

Polished thin sections were studied for ooid fabrics, degree of preservation, and mineral assemblage under transmitted light microscopy. Carbon-coated thin sections were examined and analysed with the aid of a Tescan Scanning Electron Microscope (SEM) at the University of Johannesburg operated at 20 kV. Qualitative analysis of elemental concentrations and element distribution maps were obtained using an Oxford INCA Energy-Dispersive Spectrometer (EDS) attached to the Tescan SEM.

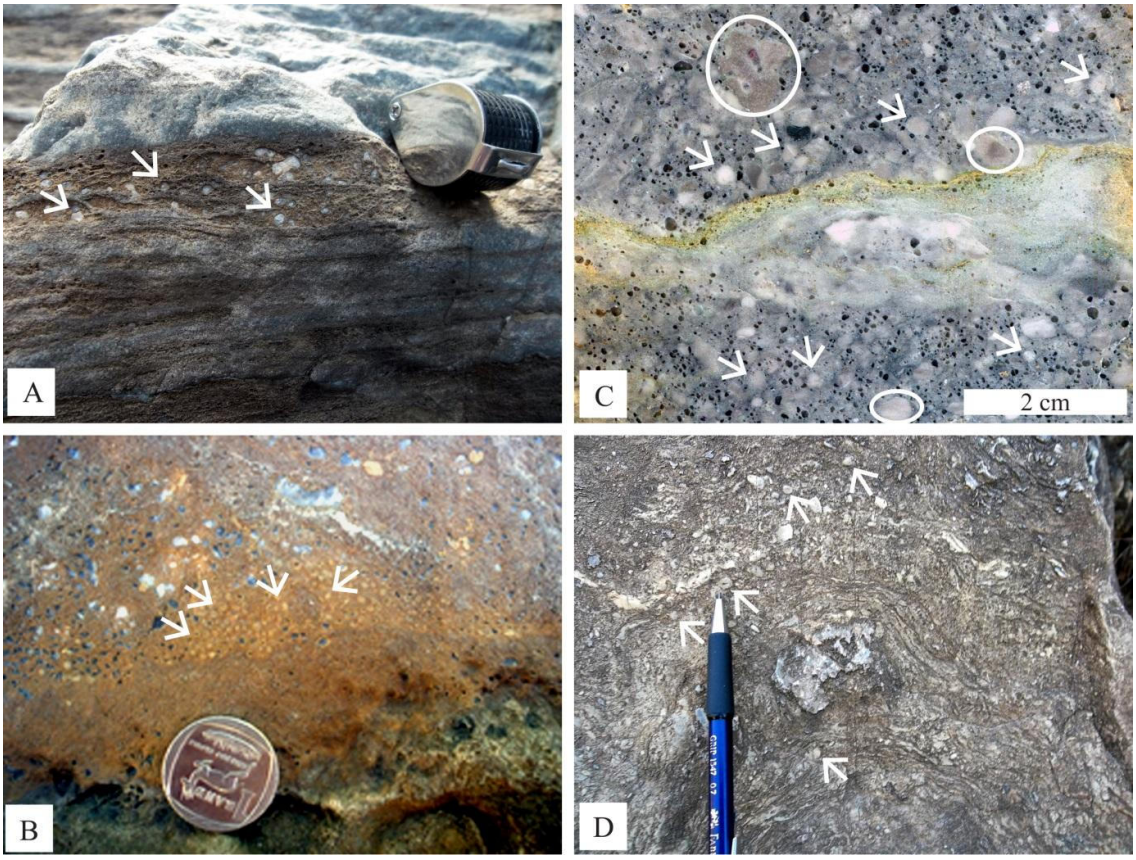

Fig. 1. Photographs showing different oolitic facies. (A) Calcite-replaced ooids (arrows) in cross-bedded dolomitic sandstone. (B) Partly calcified ooids (arrows) in sandy oodolarenite. Coin is 2 cm in diameter. (C) Polished slab showing ooids (arrows) and micritic intraclasts (grey particles, circles) and quartz grains (black grains) in sandy oodolarenite facies. (D) Grain-dominated structureless microbialite with scattered ooids.

The distribution of carbonaceous matter and minerals in the ooids was identified by Raman spectroscopy. Raman analyses of selected samples were carried out using a WITec alpha 300R configured with a frequency-doubled Nd-YAG laser (wavelength 532 nm). Most of the analyses were made using a 20× Nikon objective with a numerical aperture of 0.4 and with a maximum of 10 mW laser power to prevent thermal degradation. The system couples motorized sample positioning with a piezo-driven scan platform, allowing Raman mapping from micrometre- to centimetre-scale. Raman analyses focused on carbonaceous matter found in different particles. All the analyses were made by Raman mapping, whereby the parameters of acquisition were the same for each point and several thousands of spectra were acquired per image.

The major element concentrations of the carbonate components were determined with a Cameca SX-100 electron-probe microanalyzer (EPMA) at the University of Johannesburg. The operating conditions were a 15 kV beam voltage, 6 nA beam current, and 20 µm width of defocused beam. The analyzed elements comprise Ca, Mg, Fe, Mn, Sr, Si, Zn and Al. Results are presented in Table 1.

In-situ trace-element analyses on ooids and other carbonate components from different sections were carried out by laser ablation-inductively coupled plasma-mass spectrometry (LA-ICP-MS) at the Goethe University, Frankfurt, using a Thermo-Scientific Element 2 sector field ICP-MS coupled to a Resolution M-50 (Resonetics) 193 nm ArF excimer laser (CompexPro 102, Coherent) system. Analyses were performed on 50 µm thick polished sections in a S-155 Laurin 2 volume cell. Spots were ablated for ~ 28 s after a 32 s background measurement and a delay time of 15 s. The laser was used at a pulse frequency of 5 Hz and an energy pulse of ~ 2-2.5 J cm^{-2}, with spot sizes of 50 µm or 90 µm, resulting in a typical sample penetration depth of ~ 25 µm. The NIST SRM612 soda lime glass was used as external standard. Accuracy and external reproducibility of the analyses was verified by repeated analyses of reference materials JCP-1 (marine coral; pressed pellet) and GSC-1G (synthetic basalt glass). The detection limit was defined as three times the background signal. Calcium was used as internal standard. The raw data were processed off-line using the Glitter software. Results are presented in Table A1 (Appendix).

Elemental maps were acquired with a Cameca NanoSIMS 50L at the Technical University of Munich, Munich, "Lehrstuhl für Bodenkunde NanoSIMS laboratory". Sample selection considered the presence of carbonaceous matter and the quality of preservation of the ooids identified with Raman spectroscopy and microscopic investigation. Discs 8 mm in diameter were drilled from thin sections for NanoSIMS analysis. Reflected-light microscopic images of the drilled discs were taken for later orientation using the CCD camera of the NanoSIMS. The samples were cleaned ultrasonically several times and coated with ~ 5 nm film of Au/Pd. SEM and Raman mapping were performed on the discs to support interpretation of the NanoSIMS data. To remove surface contaminations and the gold/ paladium-coating, the primary ion beam of Cs^+ was sputtered across a ca. 50 × 50 µm area prior to analysis. Sample areas of 40 × 40 µm were analyzed using a focused primary beam of Cs^+ and a beam current of ~ 2.7 pA. The secondary ions ($^{12}C^-$, $^{12}C^{14}N^-$, $^{32}S^-$, $^{16}O^-$, $^{24}Mg^{16}O_2$ and $^{31}P^{16}O_2$) were detected simultaneously in image mode using electron-multipliers with an electronic dead time fixed at 44 ns. The ion images were acquired using a dwell time of 30 ms/pixel with image resolution of 256 × 256

pixels. The measurements were performed at high-mass resolution to avoid potential interference by other ions or molecules with similar masses as the ions of interest. For compensation of positive charging from the primary beam and minimize specimen charging effects, an electron flood gun was used for charge compensation. Before all measurements the instrument was regularly checked using a Si-engraved reference sample.

4.4 Results

4.4.1 Petrographic characteristics of ooids

The ooids have a spherical or ovoid shape, ranging from 0.1 to 2 mm in diameter (commonly 0.2-0.4 mm in diameter) and occur as single and composite grains (Figs. 1 and 2). In spite of the fact that the ooids having undergone considerable alteration to structureless micritic types, some exhibit well-preserved concentric, radial fibrous and radial-concentric fabrics. In addition, superficial and radial sparry ooids are present. Nuclei in some of the ooids consist of micritic fragments and peloids and, to a lesser extent, of quartz particles. No preferential fabric types occur relative to the size of ooids so that it can be concluded that the size of ooids apparently did not control its fabric. Dark brown to black carbonaceous matter (CM) occurs in almost all types of ooids, peloids, and intraclasts.

Characterisation of concentric ooids: The cortex of concentric ooids is composed of laminae of densely-packed dolomicrite and/or dolomicrosparite (Fig. 2A). They are variable in thickness and in the number of individual laminae. Carbonaceous matter is homogeneously distributed in concentric laminae (Fig. 2A). Sometimes the inner cortex consists of two to five concentric siliceous laminae with remnants of dolomicrite, which alternate with dolomicritic laminae, while the outer cortex consists of massive dolomite (Fig. 2B). Carbonaceous matter is heterogeneously distributed in the inner cortex and less abundant in the outer part (Fig. 2B).

Characterisation of radial ooids: Radial fibrous ooids are characterized by a spherulitic arrangement of acicular dolomite crystals (Fig. 2C). The distribution of carbonaceous matter is more homogeneous in radial ooids compared to concentric ooids (Fig. 2C). Radial sparry ooids are composed of several radiating spar crystals with micrite inclusions, and they differ distinctly from radial fibrous ooids with well-preserved acicular crystals (Fig. 2D).

Characterisation of radial-concentric ooids: Radial-concentric ooids show alternation of laminae with radial and concentric fabrics with heterogeneous distribution of carbonaceous matter (Fig. 2E). There is a strong correlation between lamina thickness and crystal orientation; laminae that exhibit a concentric-radial fabric are up to two times thicker than concentric-only laminae (Fig. 2E).

Characterisation of micritic ooids: Concentric and radial ooids have partially to completely lost their primary fabric giving rise to micritic ooids. The different types occur in the same sample with variable state of preservation (Fig. 2F).

Characterisation of superficial ooids: Superficial ooids have larger nuclei compared to the other ooid types. The cortex of such ooids consists of one lamina of micrite or sparite several tens of microns in thickness with carbonaceous matter concentrated along the outer rim (Fig. 2G). This type of ooid is present in domal microbialites and to a lesser extent in sandy oodolarenite facies. Composite ooids consist of ooids with different internal fabrics and other sand-sized grains, such as quartz and peloids, cemented together by micrite and/or sparite (Fig. 2H).

Characterisation of recrystallized ooids: Blocky calcite and dolomite crystals cut across sparry radial and concentric laminae of ooids in cases (Fig. 2H). Where ooids were subjected to secondary alteration processes such as micritization, calcitization, and silicification, their primary textures are partially obliterated, in which case cortices may be difficult to distinguish from nuclei (Figs. 2H and 3). Small ooids are commonly micritic or occur as oomolds with blocky calcite (now dolomite) infills (Fig. 3B). Replacement of internal structures of the ooids with dolomite crystals or pseudosparitic mosaics give rise to ooid “ghosts” that are distinguishable from the surrounding sparite by their micritic rims (Fig. 3).

4.4.2 Mineral composition of ooids

The mineral composition of ooids and their surronding matrix as derived from microprobe analyses is very similar in each section, but different between the sections. Dolomite to ferroan dolomite is the dominant phase in the main and upper carbonate sections, whereas ankerite is dominant in the middle carbonate section (Fig. 4). Some ooids and occasionally also the surrounding matrix in the main and middle carbonate sections were replaced by calcite.

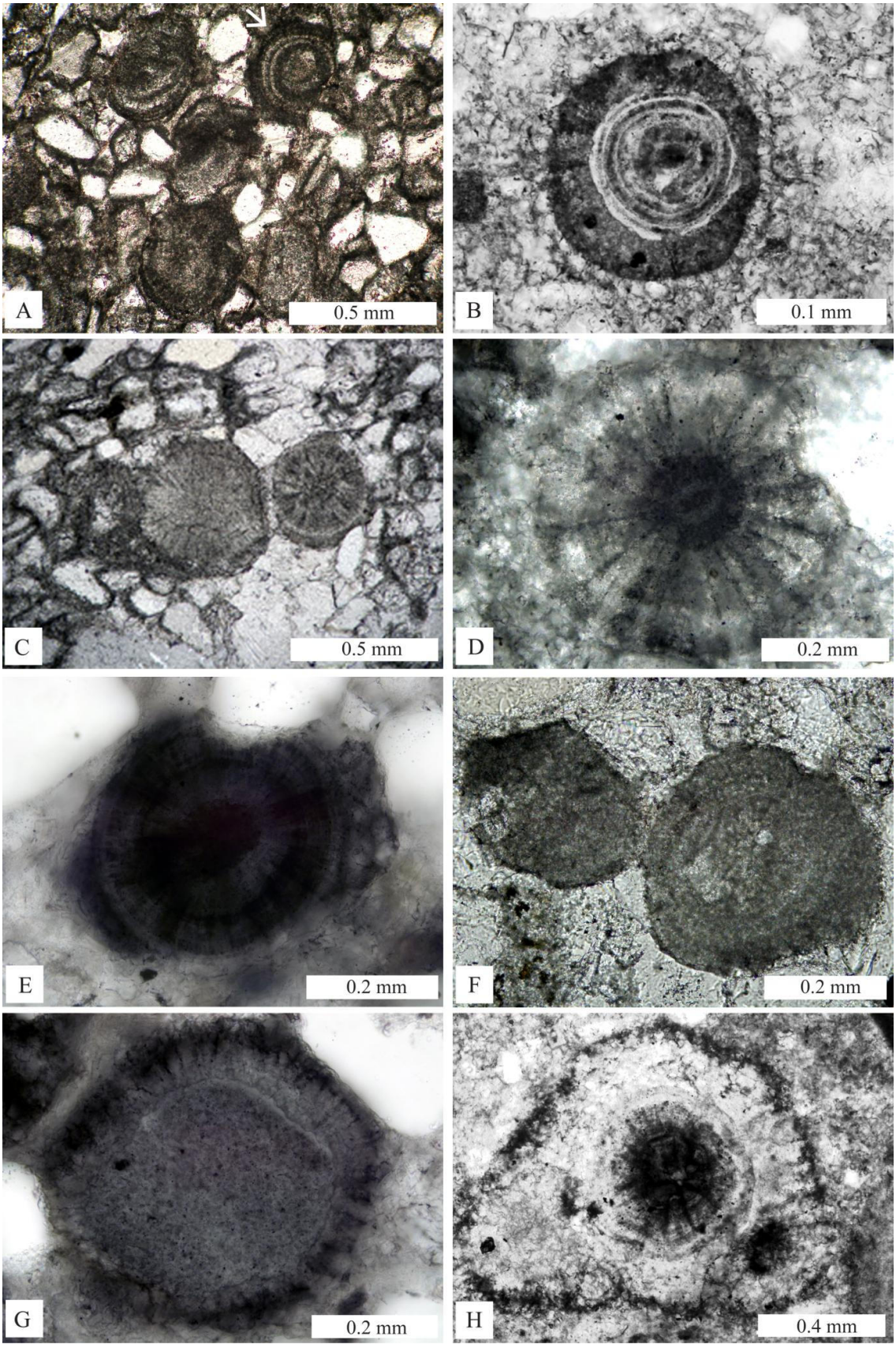
A
0.5 mm
B
0.1 mm
C
0.5 mm
D
0.2 mm
E
0.2 mm
F
0.2 mm
G
0.2 mm
H
0.4 mm

Fig. 2. Photomicrographs of ooids with various textures under plane-polarised light. (A) Oolitic sandstone with partially micritic concentric ooids (centre of image), and well-preserved concentric ooid (arrow at the top right of the image). The latter is composed of a concentric arrangement of densely-packed dolomicrite laminae. (B) Concentric ooid of alternating CM-bearing dolomitic (dark bands) and thin siliceous laminae (light bands). (C) Radial fibrous ooids made of a spherulitic arrangement of dolomitic needles. (D) A radial sparry ooid made of radiating spar crystals. (E) A radial-concentric ooid with dark carbonaceous matter distributed in thicker radial laminae. Concentric laminae are present as one to two laminea at the outer cortex. (F) A micritic ooid (left) and ooid with relict concentric fabric (right), showing partial to complete obliteration of primary fabrics by micritization. (G) A superficial ooid with a relatively large micritic nucleus. The outer rim is made of radiating sparitic crystals with carbonaceous matter (dark margin) concentrated along crystal boundaries. (H) Composite ooid of partially recrystallized radial-concentric ooid (centre) and smaller micritic and completely recrystallized ooids on either sides, and cemented by recrystallized dolomite.

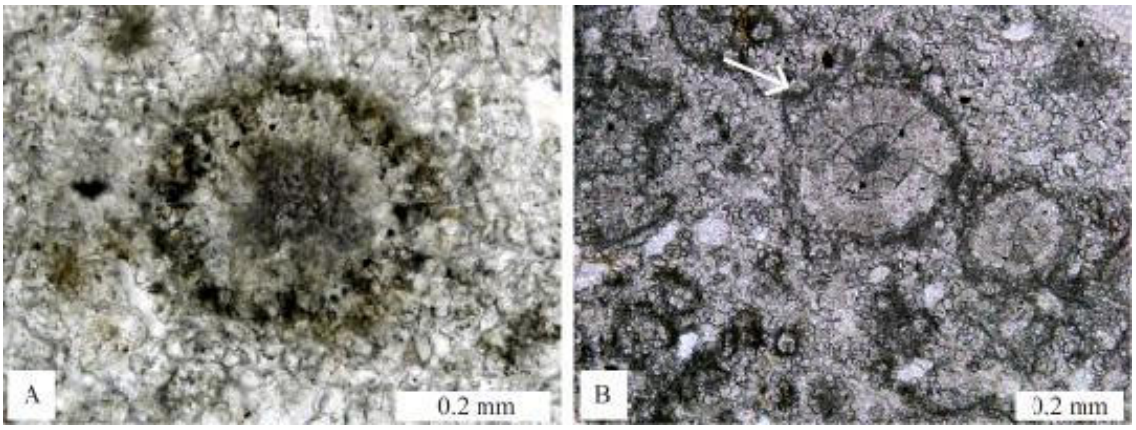

Fig. 3. Photomicrographs of recrystallized ooids under plane-polarised light. (A) Completely recrystallized ooid, in which organic matter is concentrated along the margin. (B) Radial-concentric ooids replaced by radial spars and characterized by dark micritic rim (arrow).

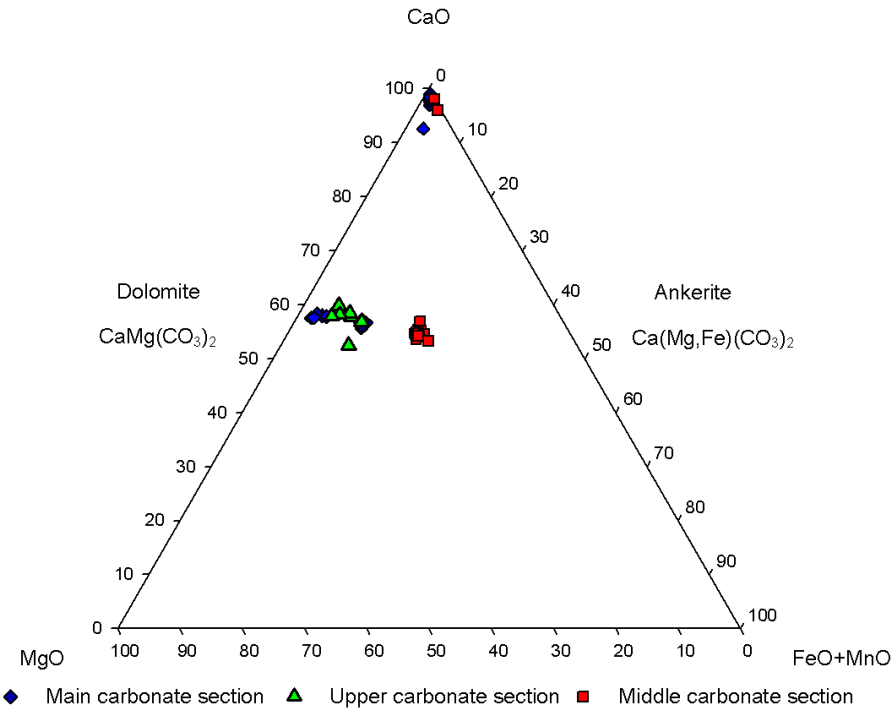

Fig. 4. Ternary diagram of major element oxides in ooid samples from the main, upper, and middle carbonate sections of the Chobeni Formation, White Mfolozi inlier. Note that some ooids of the main and middle carbonate sections were replaced by calcite, as they plot in the CaO corner. The ooid samples from the middle carbonate section are more enriched in Fe and Mn relative to those from the main and upper carbonate sections, suggestive of alteration from dolomite to ankerite.

Ooids contain different amounts of Sr, Fe and Mn (Table 1). The average FeO and MnO contents of ooids in the main carbonate section are 6.2 ± 4 wt. % and 0.7 ± 0.3 wt. %, respectively. In the upper carbonate section, the average amount of FeO and MnO are 6.5 ± 1.6 wt. % and 0.9 ± 0.1 wt. %, respectively. In the middle carbonate section, ooids contain the highest average content of FeO (18.5 ± 0.7 wt. %) and MnO (2.2 ± 0.2 wt. %) indicative of ankerite. In contrast, the average SrO content is highest in the main carbonate section (0.1 ± 0.04 wt. %) and lower in the upper and middle sections (~ 0.05 ± 0.03 wt. %). Both SiO_2 and Al_2O_3 contents with averages of 3.5 ± 4.6 wt. % and 1.1 ± 1.5 wt. % in the main section, 1.7 ± 1.5 wt. % and 0.9 ± 1.4 wt. % in the upper section and 1.2 ± 0.82 wt. % and 0.43 ± 0.34 wt. % in the middle section indicate the presence of non-carbonate minerals. With the exception of some outliers of high SiO_2, there is a pronounced positive correlation between SiO_2 and Al_2O_3

contents, indicating that high contents of SiO_2 are mainly due to the presence of Al-bearing silicate minerals rather than silicification.

Raman analyses identified the dark brown to black material in ooids, intraclasts and peloids, or parts thereof, as carbonaceous matter. The carbonaceous matter occurs in silicified nuclei of superficial ooids, dolomitic laminae of ooid's cortex irrespective of their fabric and microbial mat chips (Figs. 5K-L, 6B-D, 7A-C and 8B-C). During recrystallization the finely disseminated organic matter in ooids was not incorporated into authigenic carbonate crystals but became concentrated along the margins of newly formed crystals, which can be seen under the microscope and in Raman maps of recrystallized ooids (Figs. 3 and 5L). Micron-sized minerals of K-bearing phyllosilicates, pyrite, and apatite were detected by SEM and titanite, anatase and rutile by Raman analyses. These minerals are disseminated throughout the cortices (Figs. 5-7). Apatite is not a common mineral in ooids.

NanoSIMS elemental mapping was undertaken to investigate *in-situ* the organic matter-rich domains of the ooid's cortex. It revealed ellipsoidal to sub-spherical domains 2.5 to 6 μm in size, which have the following characteristics: (1) Intimate association of C, N, and S (Figs. 9B-D and 9F-H); these domains are interpreted as organic matter. (2) Presence of S but lack of C and N, which is indicative of the presence of pyrite (Figs. 9D and H). (3) Enrichment of P but lack of any correlation with other elements, except for C (Fig. 9E). (4) Lack of N and P, but enrichment in C, and, in cases, C plus moderately elevated S concentrations, which probably indicate another type of organic material than the one characterised by C, N and S. In general, domains enriched in N are present predominantly in the dolomitic laminae of ooids.

Chemical analysis of selected spots of carbonate grains (ooids and intraclasts), stromatolitic laminae, calcite-filled voids and matrix of carbonate rocks from different sections has been undertaken by LA-ICP-MS. Iron and Mn contents are generally positively correlated with each other, except for calcite in voids that is enriched in Mn but lacks concomitant Fe enrichment. There is no correlation between Fe and Mn with Ti, except when considering some Ti-rich samples in the upper carbonate section, where Fe has strong positive correlation with Ti ($R2= 0.68$), suggesting silicate minerals as a host for some Fe rather than dolomite. Trace metals analysed, such as Cr and V on the one hand, and Zr on the other hand, typically have concentrations below 20 ppm and 10 ppm, respectively, but may show higher concentrations in samples with elevated Ti contents.

Table 1. Selected EPMA analyses of various ooid types, the carbonate particles and matrix from the main, upper, and middle carbonate sections (concentration in wt. %) of Chobeni Formation, White Mfolozi inlier.

Section	Sample	CaO	MgO	SrO	SiO_2	Al_2O_3	FeO	MnO	ZnO	CO_2	Total
Main Carbonate	Micritic particle	29.78	20.81	0.07	0.04	0.03	1.07	0.11	b.d.	48.07	99.98
		29.88	20.81	0.09	0.09	b.d.	1.08	0.16	b.d.	47.86	99.97
	Matrix	30.29	20.88	0.05	0.03	0.01	1.30	0.14	0.02	47.27	99.99
		30.19	19.58	0.04	0.87	0.54	2.20	0.26	b.d.	46.30	99.98
	Partially calcified radial ooids	53.62	0.57	0.10	0.15	0.02	0.55	0.19	0.02	44.79	100.00
		55.12	0.25	0.08	0.06	0.02	0.31	0.14	b.d.	43.97	99.95
		55.22	0.16	0.06	0.05	0.01	0.26	0.15	0.05	44.03	99.99
		29.74	17.28	0.07	0.66	0.18	5.23	0.55	0.02	46.24	99.97
		29.96	17.19	0.08	0.52	0.23	5.23	0.57	0.06	46.16	100.00
		27.26	15.38	0.05	10.17	0.05	4.85	0.50	0.06	41.68	100.00
	Concentric ooids	29.50	17.08	0.06	0.85	0.36	5.21	0.61	0.01	46.31	99.99
		28.20	16.52	0.04	3.18	2.10	5.05	0.53	0.01	44.35	99.98
		27.30	16.19	0.04	5.02	1.45	5.02	0.55	0.03	44.39	99.99
	Matrix	30.05	17.56	0.02	1.42	0.80	5.24	0.70	0.01	44.18	99.98
		31.40	18.05	0.01	0.30	0.02	5.31	0.55	0.03	44.31	99.98
Upper Carbonate	Radial ooids	31.04	17.36	0.04	0.45	0.14	3.70	0.58	0.06	46.61	99.98
		30.11	17.50	0.04	1.52	0.44	4.01	0.50	b.d.	45.81	99.93
		30.85	17.65	b.d.	0.29	0.09	3.84	0.43	b.d.	46.82	99.97
	Matrix	30.23	17.17	0.04	0.36	0.22	5.11	0.61	b.d.	46.23	99.97
Middle Carbonate	Radial ooids	29.95	13.02	0.02	0.80	0.36	10.15	1.42	0.06	44.19	99.97
		30.47	13.12	0.05	0.68	0.20	10.04	1.29	0.04	44.1	99.99
		29.79	13.52	0.05	0.58	0.22	9.89	1.20	0.03	44.72	100.00
	Matrix	28.19	11.37	0.01	5.12	3.67	8.79	1.16	0.05	41.57	99.93
		29.31	13.84	0.03	0.12	0.02	10.43	1.22	b.d.	45.01	99.98

* element concentrations in wt. %; b.d. = below detection

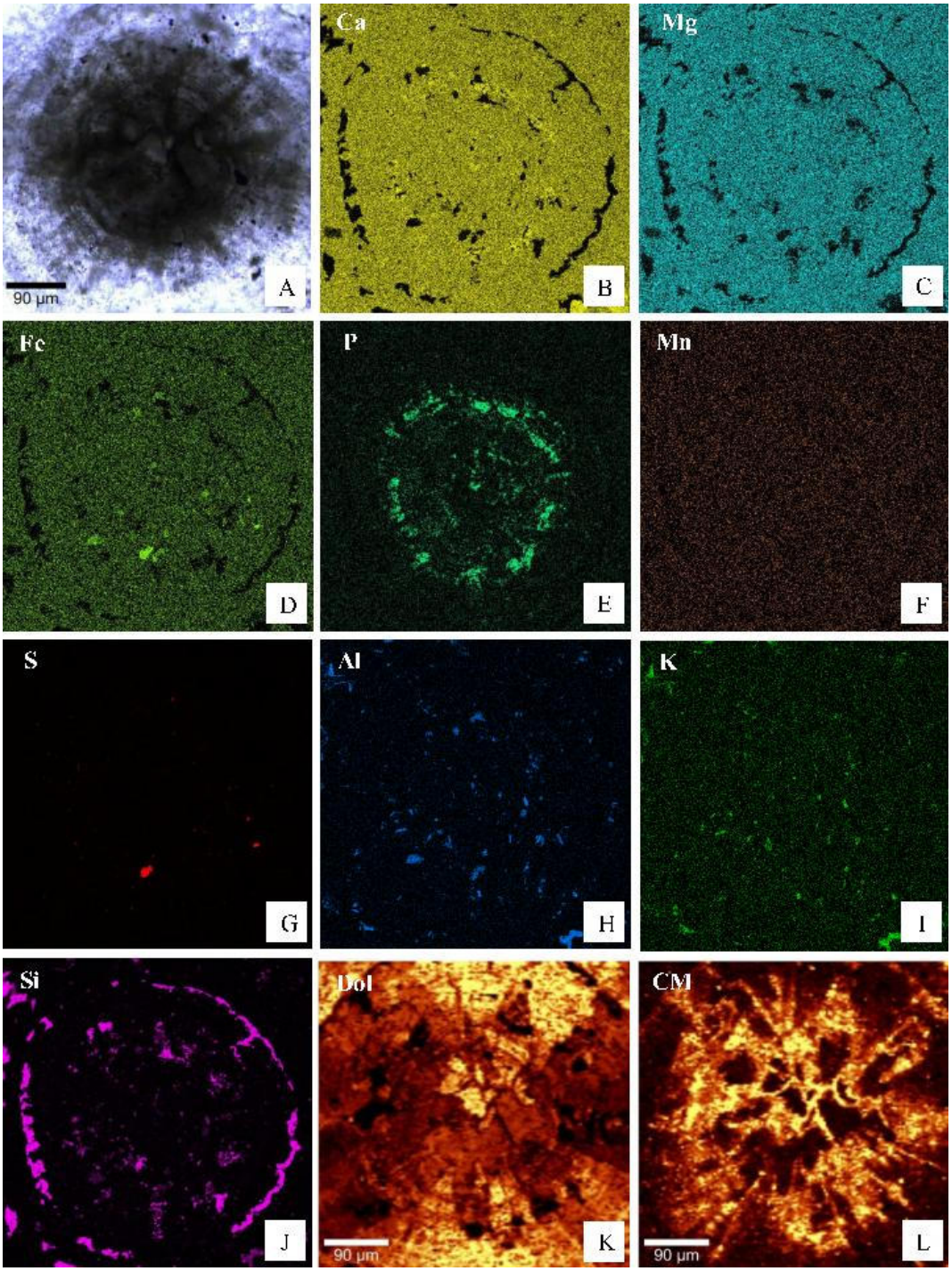

Fig. 5. SEM-EDS and Raman maps of a partially recrystallized radial-concentric ooid, showing distribution of minerals, elements, and carbonaceous matter. (A) Photomicrograph of an ooid showing radial-concentric texture. (B-J) Distribution of calcium (Ca), magnesium (Mg), iron (Fe), phosphorus (P), manganese (Mn), sulfur (S), aluminium (Al), potassium (K) and silica (Si). (K and L) Raman maps of the distribution of dolomite (Dol) major band at ~ 1100 cm^{-1} and carbonaceous matter (CM) G band at ~ 1589 cm^{-1} in ooid, respectively. Brighter areas within Raman maps reflect higher intensities of mineral-specific spectra.

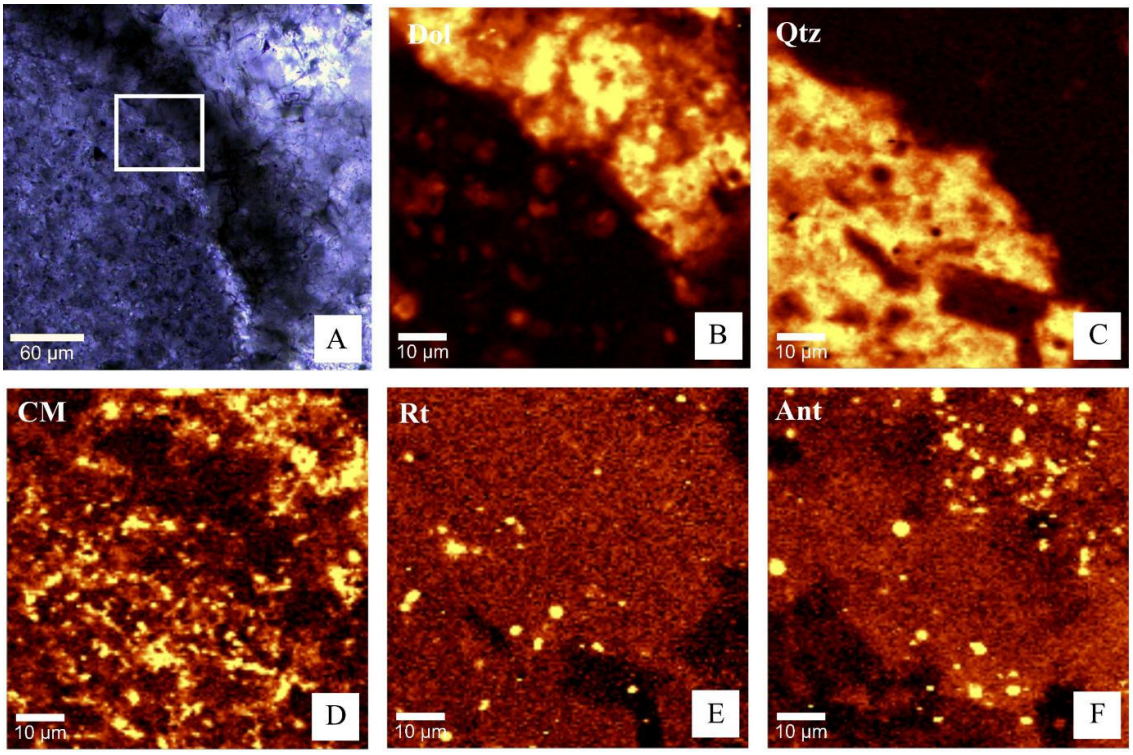

Fig. 6. Raman maps of part of a superficial ooid, showing distribution of minerals and carbonaceous matter in the ooid cortex and the outer part of the nucleus. (A) A photomicrograph of a superficial ooid; box shows area of Raman analysis. (B-F) Distribution of dolomite (Dol) major band at ~ 1100 cm^{-1}, quartz (Qtz) major band at ~ 470 cm^{-1}, carbonaceous matter (CM) G band at ~ 1589 cm^{-1}, the E_g rutile (Rt) mode (average peak position of ~ 440 cm^{-1}), and the E_g anatase (Ant) mode (average peak position of ~ 148 cm^{-1}), respectively. Brighter areas within Raman maps reflect higher intensities of mineral-specific spectra.

Higher concentrations of these elements are commonly found in stromatolitic laminae, micritic matrix and silicified particles, suggesting a higher amount of a detrital component in this material. Calcite-filled voids, in contrast, are trace metal poor.

Sr contents are variable in the main carbonate section in which analyzed carbonate components, calcite-filled voids and dolomite-filled fractures have average of 356 ± 71 ppm, 479 ± 195 ppm and 80 ± 38 ppm, respectively (Table A1, Appendix). The average Sr contents in the upper carbonate section of carbonate components and calcite-filled fractures are 251± 83 and 376 ± 43 ppm, respectively. There are minor differences in the Sr concentrations in ooids of different fabrics. Concentric ooids have the highest Sr contents of up to 350 ppm in comparison with radial ooids with 96 to 135 ppm.

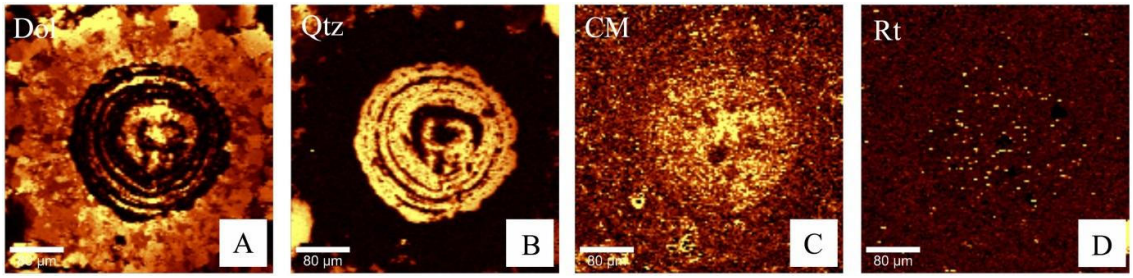

Fig. 7. Raman maps of a concentric ooid (Fig. 2A), showing distribution of minerals and carbonaceous matter. (A-D) Distribution of dolomite (Dol) major band at ~ 1100 cm^{-1}, quartz (Qtz) major band at ~ 470 cm^{-1}, carbonaceous matter (CM) G band at ~ 1589 cm^{-1}, the E_g rutile (Rt) mode (average peak position of ~ 440 cm^{-1}), respectively. Brighter areas within Raman maps reflect higher intensities of mineral-specific spectra.

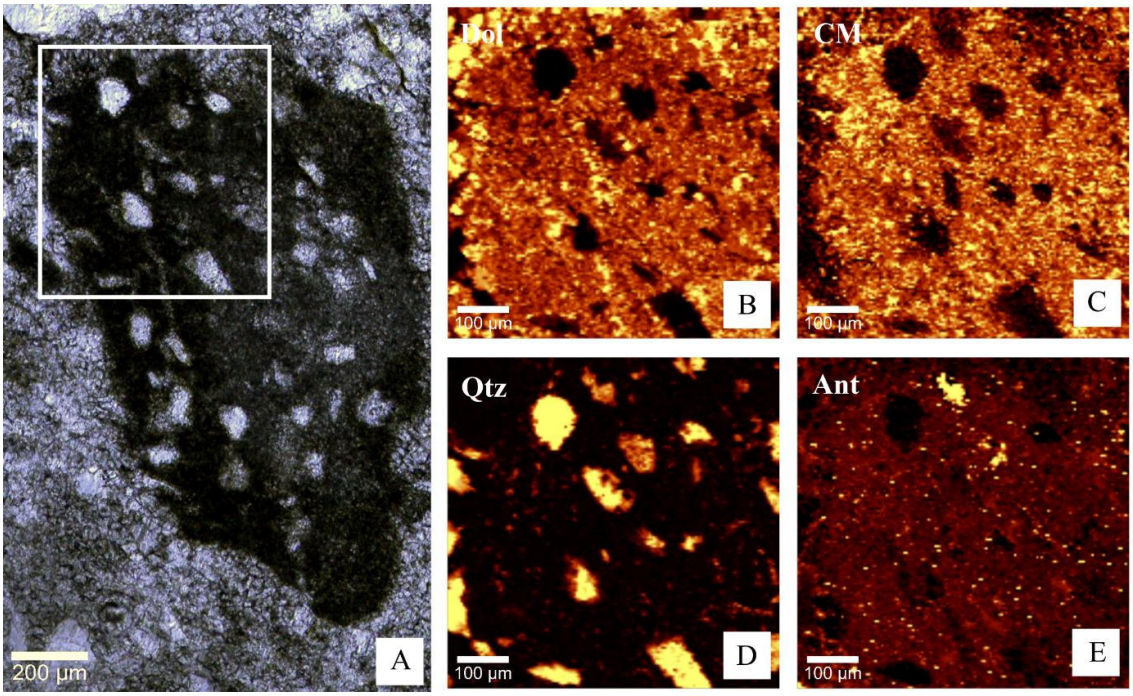

Fig. 8. Raman images of a microbial mat chips, showing distribution of minerals and carbonaceous matter. (A) A photomicrograph of a microbial mat chips; box shows area map of Raman analysis. (B-E) Distribution of dolomite (Dol) major band at ~ 1100 cm^{-1}, carbonaceous matter (CM) G band at ~ 1589 cm^{-1}, quartz (Qtz) major band at ~ 470 cm^{-1} and the E_g anatase (Ant) mode (average peak position of ~ 148 cm^{-1}), respectively. Brighter areas within Raman maps reflect higher intensities of mineral-specific spectra.

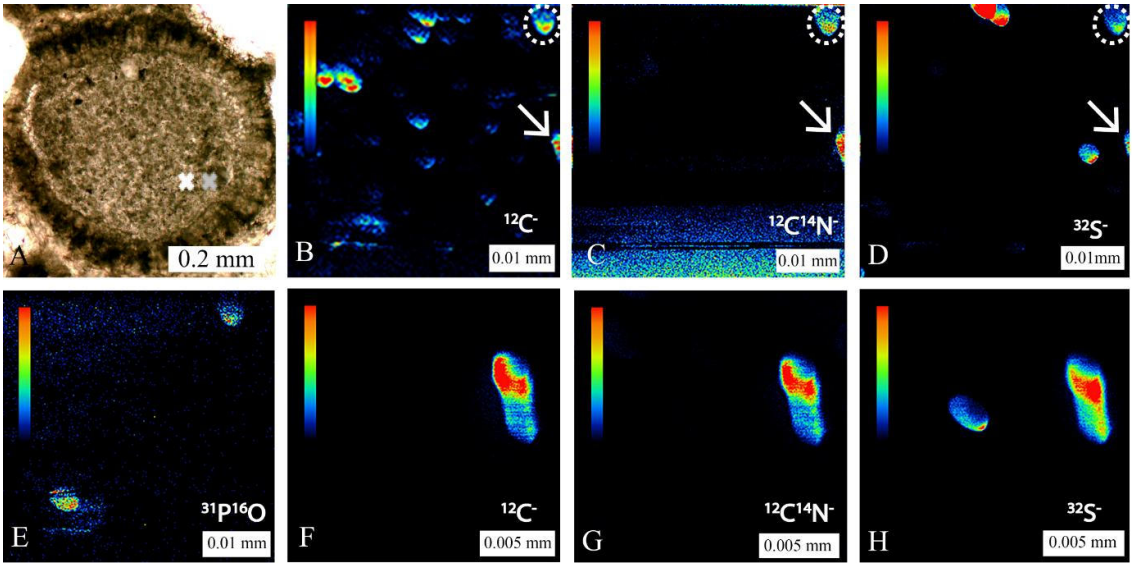

Fig. 9. Results of NanoSIMS element maps of parts of a superficial ooid. (A) Photomicrograph of the superficial ooid in transmitted light. White and grey crosses show location of mapped area. (B-E) Carbon, N, S and P maps (white cross in Fig. A shows location of mapped area) showing element concentrations in micron-scale ellipsoidal/ sub-spherical domains, which are shown by circles and arrows. Note the presence of S-rich domains in Fig. D that are not correlated with the other elements such as C, N and P. In Fig. E it can be seen that the P signal overlaps with that of C in Fig. B, but not with N and S in Figs. C and D, respectively. (F-H) Carbon, N, and S maps showing correlation among the elements in micron-scale domains (grey cross in Fig. A shows location of mapped area).

The shale-normalized (suffix SN; Post-Archaean average Australian Shale, PAAS; McLennan, 1989); rare earth element (REE) data of carbonate components (sample ratios listed in Table A1, Appendix) show enrichment in the middle REEs (MREEs), expressed as $(Pr/Tb)_{SN} < 1$ and $(Tb/Yb)_{SN} > 1$. MREE enrichment is present in ooids and stromatolitic laminae (Fig. 10A), and occasionally present in intraclasts and oncoids of the main carbonate section (not shown). In the main carbonate section, except stromatolitic laminae, which show depletion of LREEs relative to HREEs, the rest of carbonate components show $(Pr/Yb)_{SN}$ higher and lower than unity, specifically dolomite-filled fractures show LREEs > HREEs (Figs. 10A and B). In the upper carbonate section, the MREE enrichment is present in calcite-filled fractures and occasionally in different allochems and matrix. (Figs. 10C and D). Almost all components of the upper carbonate section show a light REE (LREE) depletion relative to the heavy REEs (HREEs), calculated as $(Pr/Yb)_{SN} < 1$), except in some of the calcite-filled fracture samples, (Figs. 10C and D). Ce anomaly calculated with Pr and Nd concentrations as $[(Pr/Pr^*)_{SN} =$

$Pr_{SN}/(0.5Ce_{SN} + 0.5Nd_{SN})$] to avoid interference of anomalous abundances of La (Bau and Dulski, 1996), is absent in the main and upper carbonate sections (Fig. 11).

Most of the allochems, matrix and calcite-filled voids (fenestrae), show a positive La_{SN} anomaly as can be inferred from the combination of $(Ce/Ce^*)_{SN} < 1$ calculated as [$(Ce/Ce^*)_{SN} = Ce_{SN}/(0.5La_{SN} + 0.5Pr_{SN})$], and $(Pr/Pr^*)_{SN} \leq 1$ as suggested by Bau and Dulski (1996), (Fig. 11). A negative La_{SN} anomaly is present in some silicified and recrystallized allochems and matrix, and calcite-filled fractures (Figs. 10D and 11). A positive Gd_{SN} anomaly expressed as [$(Gd/Gd^*)_{SN} = Gd_{SN}/(0.33Sm_{SN} + 0.67Tb_{SN})$] after Bau and Dulski (1996) has a value up to 1.5. Eu_{SN} displays a positive anomaly calculated as [$(Eu/Eu^*)_{SN} = Eu_{SN}/(0.66Sm_{SN} + 0.33Tb_{SN})$] after Bau and Dulski, (1996). In many samples, Y is elevated relative to Ho (Fig. 10). The average Y/Ho ratio for ooids and intraclasts is 30 ± 1 and for calcite and dolomite-filled fractures and voids is 36 ± 3, which is higher than the Y/Ho ratio for chondrite (~ 26-28) in most cases. The calcite-filled fractures and voids show strong positive correlation with Yb/Tb and weak negative correlation wit Fe. The concentration levels of ΣREE of carbonate components from different facies and sections vary significantly, while whitin specific facies they show very similar concentration levels, except in case of the presence of secondary filled carbonate voids/ fractures and highly silicified components. The ΣREE of the ooids, oncoids and stromatolitic laminae are 57.1 ± 110, 4.3 ± 0.3 and 20 ± 4, respectively. In the main and upper carbonate sections, ΣREE concentrations of the dolomite/ calcite-filled fractures are 71 ± 18 and 1145 ± 61, respectively.

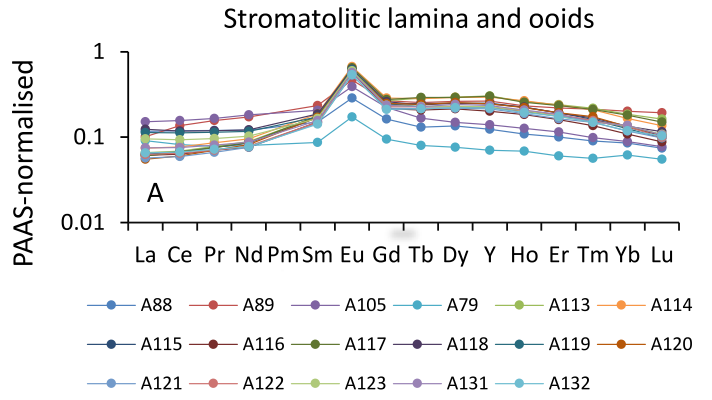
Stromatolitic lamina and ooids
PAAS-normalised
1
0.1
0.01
A
La Ce Pr Nd Pm Sm Eu Gd Tb Dy Y Ho Er Tm Yb Lu
A88 A89 A105 A79 A113 A114
A115 A116 A117 A118 A119 A120
A121 A122 A123 A131 A132

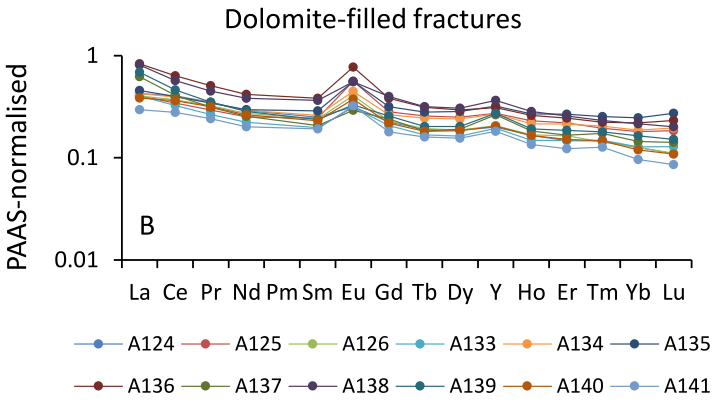
Dolomite-filled fractures
PAAS-normalised
1
0.1
0.01
B
La Ce Pr Nd Pm Sm Eu Gd Tb Dy Y Ho Er Tm Yb Lu
A124 A125 A126 A133 A134 A135
A136 A137 A138 A139 A140 A141

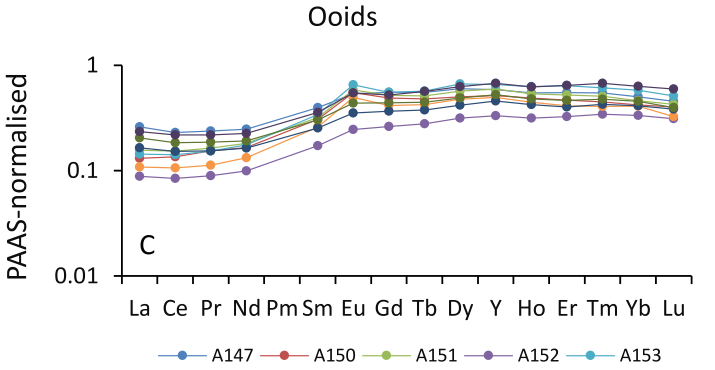
Ooids
PAAS-normalised
1
0.1
0.01
C
La Ce Pr Nd Pm Sm Eu Gd Tb Dy Y Ho Er Tm Yb Lu
A147 A150 A151 A152 A153

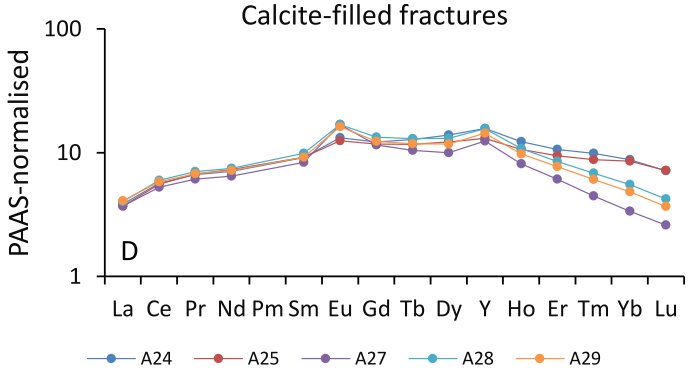
Calcite-filled fractures
PAAS-normalised
100
10
1
D
La Ce Pr Nd Pm Sm Eu Gd Tb Dy Y Ho Er Tm Yb Lu
A24 A25 A27 A28 A29

Fig. 10. PAAS-normalized REE + Y plots of ooids, stromatolite, and calcite-filled fractures from the main (A and B) and upper (C and D) carbonate sections. REE distribution patterns of ooids/ stromatolites (A and C). REE distribution patterns of dolomite/ calcite-filled fractures (B and D).

4.5 Discussion

The ooids from the Chobeni Formation show a variety of fabrics that are remarkably well preserved for c. 3-billion-years-old coated grains in a greenschist facies host rock. Several prerequisites for the formation of ooids have been suggested: (1) the presence of nuclei; (2) $CaCO_3$ precipitation in the presence of humic acids (e.g. Davies et al., 1978); (3) turbulent hydrodynamic conditions (e.g. Davies et al., 1978; Deelman, 1978); (4) waters supersaturated with respect to carbonate. The latter is regarded the most critical factor limiting the global distribution of oolitic sands (e.g. Rankey and Reeder, 2009). Elevated pH and high alkalinity play important roles in carbonate supersaturation state, which under appropriate hydrodynamic conditions lead to the formation of ooids (e.g. Lee et al., 2006). In some semi-restricted areas like Shark Bay and the Persian Gulf elevated salinities increase carbonate saturation state and favour formation of ooids (e.g. Rankey and Reeder, 2009). Furthermore, the physico-chemical conditions predicate primary cortical fabrics of ooids (Loreau and Purser, 1973; Fabricius, 1977; Halley, 1977; Medwedeff and Wilkinson, 1983; Plée et al., 2008).

4.5.1 Diagenetic processes and primary chemical composition of ooids

The ooids under investigation are made of dolomite and ankerite in more altered stratigraphic sections. Diagenetic and metamorphic processes affected the primary chemical composition and fabric of the Chobeni carbonate rocks. Dolomitization has been a pervasive process, whereas calcification and silicification operated more selectively. Early dolomitization of high-Mg calcite is generally fabric-retentive in contrast to dolomitization of aragonite, which is fabric destructive (Tucker, 1983). Ooids from the main carbonate section mostly retained their primary fabrics. Early silicification of ooids, early mimetic dolomite replacement of pre-existing aragonite (Zempolich and Baker, 1993) and stable primary mineralogy may also result in the preservation of primary textures and fabrics of these ooids

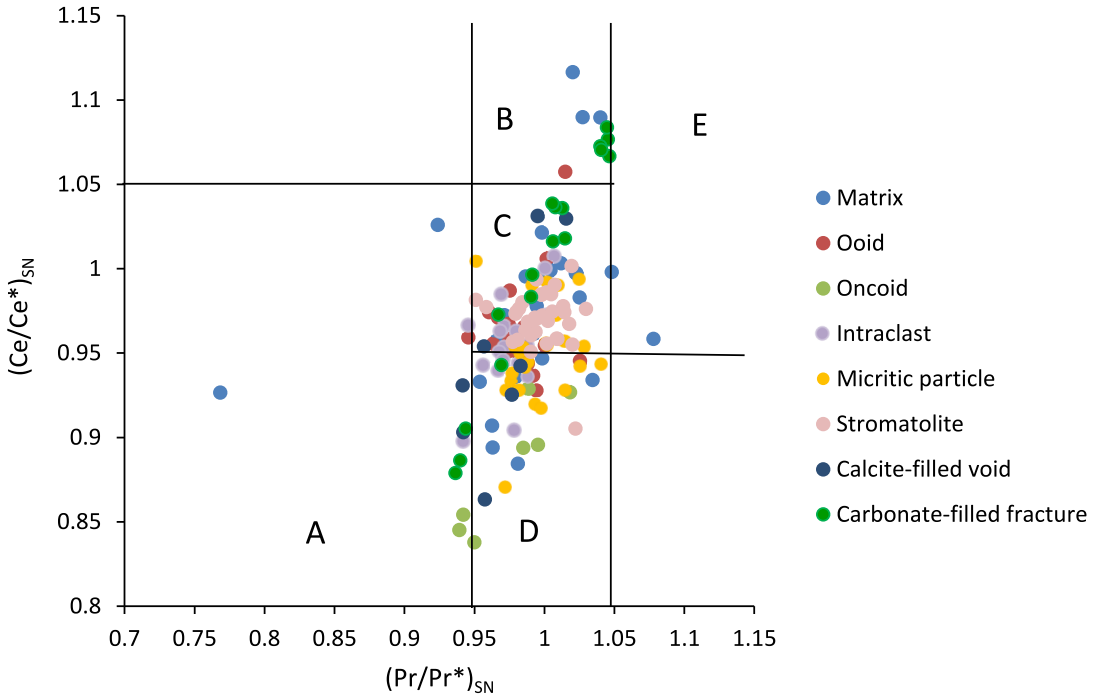

Fig. 11. Plot of $(Ce/Ce^*)_{SN}$ vs. $(Pr/Pr^*)_{SN}$ (Bau and Dulski, 1996) in selected samples of stromatolitic carbonate rock samples of the Chobeni Formation. Field A: positive CeSN anomaly, positive La_{SN} anomaly; Field B: negative La_{SN} anomaly, no Ce_{SN} anomaly; Field C: neither Ce_{SN} nor La_{SN} anomaly; field D: positive La_{SN} anomaly, no Ce_{SN} anomaly; Field E: negative Ce_{SN} anomaly, positive La anomly.

During dolomitization, aragonite (c. 9000 ppm Sr) and high magnesium calcite (c. 1500 ppm Sr) precursors will form dolomite with Sr contents of c. 550 ppm and c. 250 ppm, respectively (Warren, 2000). It is not possible to identify the primary composition of the Chobeni ooids based on their Sr content alone, which is not significantly different among ooids with different fabrics, and which is quite variable even within one type of ooid, probably due to the diagenetic and metamorphic overprint. Radial ooids have the lowest amounts of Sr and better fabric retention amongst the ooid types, which probably indicates that Mg-calcite was the primary mineral of this type of ooid. Regarding concentric ooids with lower Sr contents and lesser fabric retention compared to radial ooids, aragonite could be a suitable option as a precursor. No analyses of Sr concentration of different laminae in radial-concentric ooids are available, but based on the different Sr contents of radial and concentric ooids, we assume that radial-concentric ooids probably formed as bimineralic ooids. The micritic ooids show a relatively high Sr content, which probably indicates aragonite as the precursor mineral, in line with poor fabric retention.

Calcite is present as a replacement of some ooids and matrix as well as void infills. The calcite-filled voids have the highest Sr content as compared to the surrounding carbonate components. In the vadose zone, dissolution of components with aragonite mineralogy typically results in a rise of Sr concentrations of the pore waters, which may then result in the precipitation of high Sr carbonate cements (Pingitore, 1976; Singh, 1987). Therefore, the coexistence of high-Sr calcite in voids and surrounding dolomite components may relate to the alteration of aragonite precursor sediment during meteoric diagenesis, followed by precipitation of high Sr cements. Complete calcification of some ooids also indicates the presence of unstable primary minerals, such as aragonite, that led to moldic porosity formation as a result of dissolution in the under-saturated zone of the meteoric-phreatic environment (Longman, 1980; Moore and Druckman, 1981; Heckel, 1983). Later on, pore space was filled by blocky/ sparry cement, which obscured the original fabric.

Silicification also affected the ooids, especially the rims of radial ooids and individual laminae in the cortex of some of the concentric and radial-concentric ooids. Silicification may take place by different mechanisms including inorganic physico-chemical and biologically-induced silica precipitation (e.g. Knoll, 1985; Phoenix et al., 2000). It is not clear if bacteria were involved in silicification, but silicification of other components, such as matrix and mudclasts, which are free of carbonaceous matter indicate that to a large extent inorganic silicification during diagenesis was responsible.

4.5.2 REY distribution patterns of ooids and inferred seawater signal

Oxygenated modern seawater displays HREEs enrichment relative to the LREEs, a negative Ce_{SN} anomaly, positive La_{SN} and Gd_{SN} anomalies and a pronounced Y_{SN} anomaly (Elderfield, 1988; Alibo and Nozaki, 1999; Kamber et al., 2014). The shale-normalized REE distribution patterns of allochems, matrix, stromatolitic laminae and calcite/ dolomite-filled voids and fractures of the Chobeni Formation show positive Gd_{SN} and Y_{SN} anomalies (Table A1, Appendix). The majority of analysed carbonate particles show a positive La_{SN} anomaly and enrichment of HREEs relative to LREEs. The presence of negative La_{SN} anomaly and depletion of HREEs relative to LREEs was found in calcite/ dolomite-filled fractures and recrystallized matrix. The enrichment of LREEs relative to HREEs and absence of anomalous La were observed in some Archaean stromatolitic carbonates from Zimbabwe and Phanerozoic (Late Devonian) reefal carbonates of the Canning Basin in Western Australia (Kamber et al., 2004;

Nothdurft et al., 2004). The LREEs enrichment of Archaean biochemical precipitates could be due to their deposition in a restricted basin dominated by terrestrial waters (e.g. Johannesson et al., 2006) and/or caused by the mixing with non-carbonate phases such as clay or secondary iron oxyhydroxides commonly enriched in LREEs (e.g. Takahashi et al., 2005; Tostevin et al., 2016). The presence of only a small La anomaly or its complete absence, which has been reported from banded iron formation of the Isua Greenstone Belt, the Strelley Pool Chert and Holocene microbialites were interpreted as a result of deposition in a restricted environment influenced by terrestrial waters (e.g. Johannesson et al., 2006). Groundwater may be enriched in LREEs, for example due to interaction with bedrock granite (Munemoto et al., 2015). It is possible that the REE patterns of fracture carbonates record interaction of the meteoric waters with granitic detritus that is found in the siliciclastic component of the carbonate rocks. The near-chondritic Y/Ho ratio (< 40) of carbonate samples, which reflects deposition in a shallow marine setting with high terrestrial and freshwater input (Webb and Kamber, 2000; Johannesson et al., 2006; Zhao et al., 2009), is another clue, which reflects precipitation of oolitic carbonates whithin restricted shallow marine environments with high continental influx. In terms of seawater signatures, calcite-filled voids show apparently more primary signatures (relatively high Y/Ho), possibly because calcite precipitated as low-Mg calcite that was stable and was not further subjected to diagenesis. In contrast, other carbonate samples, especially those with high Fe concentrations (and thus higher degree of diagenetic overprint), were more strongly subjected to diagenesis, which likely lowered the Y/Ho ratio.

The Mesoarchaean carbonate rocks, just like all other Archaean chemical sedimentary rocks, show a strong positive Eu_{SN} anomaly, indicative of elevated flux of high-temperature (> 250 ºC) hydrothermal fluids into seawater (e.g. Michard and Albarède, 1986; Kamber et al., 2014), which in combination with the lack of a true Ce_{SN} anomaly, is suggestive of reducing conditions.

MREEs enrichment relative to HREEs and LREEs in carbonates with possible biotic origin such as stromatolitic, oolitic and oncoid facies, could be due to bacterial fractionation of MREEs in rivers, coastal seas and estuaries as it was suggested by other studies (Elderfield et al., 1990; Sholkovitz, 1995). The different factor might be responsible of the MREEs enrichment of secondary abiotic fracture filling calcite. Johannesson and Zhou (1999) suggested that dissolution of MREEs enriched minerals and/or amorphous phases are responsible for MREEs enriched signatures of the lake waters. The REE+Y patterns of these carbonate rocks apart from secondary carbonate precipitates and severely altered carbonate components suggests that the carbonate rocks (in particular oolitic facies) have been formed in

a restricted marine environment and that the processes, which control REEs distribution in modern seawater were operating by that time.

4.5.3 Role of bacteria in ooid formation

The possible role of bacteria in ooid formation has been the subject of many studies for a long time. Bacterial communities may form or colonize an ooid nucleus. Bacteria may then trigger, or act as nucleation sites for, calcite precipitation giving rise to ooid formation in shallow water environments (Malone and Towe, 1970; Krumbein, 1979; Chafetz, 1986; Gerdes et al., 1994; Kazmierczak et al., 1996). In contrast, Duguid et al. (2010) suggested that microbes do not play a role in ooid formation, but they rather alter the chemistry and texture of ooids after their formation. Investigation of freshwater ooids from Lake Geneva confirmed that photosynthetic bacteria enhance carbonate precipitation and control the formation of ooid cortices, while sulfate-reducing bacteria and methanogens play a negligible role (Plée et al., 2008, 2010; Pacton et al., 2012). Summons et al. (2013) examined lipid biomarkers in modern and Holocene ooids and measured their carbon and hydrogen isotopic values, which revealed that photoautotrophs, heterotrophs, and sulfate-reducing bacteria contribute to ooid formation.

The presence of carbonaceous matter in ooid cortices probably indicates that bacteria were directly and/or indirectly involved in ooid formation. Carbonaceous matter is not only confined to ooids, but also present in peloids, some intraclasts and microbial mat chips, which indicate widespread microbial colonization (Fig. 7). Superficial ooids are found within structureless microbialites along with other particles, such as quartz grains, peloids and intraclasts, which probably indicate that they were trapped within microbialites along with other detrital materials, a process not uncommon in modern microbialites (Decho et al., 2005; Dupraz and Visscher, 2005).

Raman and SEM analysis identified a heterogeneous distribution of apatite, pyrite, rutile and muscovite in the ooids (Figs. 5-6). Muscovite likely originated as trapped clay minerals that were transformed to muscovite during greenschist facies metamorphism. Nevertheless, the question arises if the others are all trapped particles or if some could be by-products of metabolism of specific types of microbial communities. In addition, how is the carbonaceous matter, which is distributed throughout the ooid cortex, related to various mineral phases? NanoSIMS elemental mapping showed the local association of metabolically important elements (N, S and P) with C within ooid cortices (Fig. 8). This association can be regarded as

evidence for the biogenic origin of the carbonaceous matter (Schlesinger, 1997; Oehler et al., 2006, 2009; Wacey et al., 2010a; Crosby and Bailey, 2012) even in the absence of microfossils. Nitrogen is an important element in microbially derived organic matter such as amino and nucleic acids and is less abundant in rock-forming, mainly K-rich minerals. The close association of N with carbonaceous matter in sedimentary rocks is evidence of biological fixation processes (Oehler et al., 2006, 2009). Furthermore, a correlation between N-rich domains with S and P (Fig. 8) may suggest incorporation of these elements into the organic compounds. The S could be representative of S-based metabolic pathways, such as sulfate-reduction or sulfur disproportionation (Wakeham et al., 1995; Lemelle et al., 2008; Wacey et al., 2010b, 2011; Kilburn and Wacey, 2011).

Micron-sized domains enriched in S or P that are apprently not correlated with C and N likely represent pyrite and apatite, respectively, as have been identified by SEM and Raman mapping (Fig. 4).These minerals could be metabolites of specific microbial communities with different metabolic pathways and/or preferably adsorbed or formed by bacteria's cell walls. Sulfides can form during degradation of organic matter by sulfate-reducing bacteria (SRB) in anoxic conditions (Berner et al., 1985; Donald and Southam, 1999). Microbial communities, such as cyanobacteria and fungal mats, were found to be associated with phosphate production (Soudry and Champetier, 1983; Soudry, 1987). Microbes may not only be involved in mineralization via their metabolism, but they can also influence mineral precipitation by providing nucleation sites for direct apatite precipitation on cyanobacterial mat structures (Southgate, 1980), and by lowering the activation energy required for apatite precipitation (Ferris, 1989). It would thus be necessary to undertake more complementary analyses to better define the microbial communities and the metabolic pathways employed by Mesoarchaean bacteria.

Nevertheless, the role of bacteria's extracellular polymeric substance (EPS) in trapping and binding of detrital particles is undeniable. Impurities, such as pyrite, clay minerals as trapped detrital particles, and organic matter as the remains of bacteria, have been reported in the cortex of ooids from the Great Salt Lake (Halley, 1977), the Sokoman Iron Formation (Dimroth and Chauvel, 1973) and the Gunflint Iron Formation (Markun and Randazzo, 1980).

4.5.4 Environmental/ depositional conditions controlling ooid formation and their fabrics

The similarity between Chobeni ooids and their modern counterparts with respect to variety in fabrics, presence of carbonaceous matter and mineral assemblage may allow to better understand mechanism of ooid formation and their depositional environment in the Mesoarchaean.

Concentric ooids: Concentric ooids with tangentially oriented aragonite crystals form under turbulent conditions in seawater supersaturated with respect to aragonite (e.g. Tucker and Wright, 1990). Ooids from the Bahama Bank consist of two different types of laminae in their cortex: 1) lamella contain tangentially oriented aragonite crystals free of organic matter that form as a chemical precipitate under agitated environmental conditions, and 2) lamella composed of un-oriented cryptocrystalline aragonite crystals associated with organic matter that form as a result of interstitial recrystallization and precipitation associated with organic matter incorporated in the grain (Newell et al, 1960). These observations are in agreement with experiments by Davies et al. (1978), in which ooids with tangentially oriented crystals were synthesized under agitated conditions abiotically from a supersaturated solution. For further growth, a new substrate is required, which may be provided by the development of organic matter around the grains in the quiet stage. Primary carbonate mineralogy also plays a role in the development of ooids with different fabrics. Medwedeff and Wilkinson (1983) noted that aragonite predominantly forms a concentric fabric in modern marine ooids. Based on these studies, both microbially influenced/ induced and abiotic, physico-chemical mechanisms may be involved in the formation of concentric ooids.

The carbonaceous matter in the concentric laminae of Chobeni ooids (Fig. 6) may point to a role of bacteria in their formation. The presence of concentric ooids within high-energy facies supports the formation of the Chobeni ooids under turbulent conditions. It is not possible to evaluate to what extent hydrodynamic conditions were responsible in their formation. With respect to siliceous laminae in concentric ooids, remains of dolomite crystals indicate they were probably derived from silicification of primary carbonate (Figs. 6A and B). The presence of carbonaceous matter in the inner cortex of concentric ooids indicates possible role of bacteria in their formation. The structureless outer cortex, which is free of carbonaceous matter may have formed by chemical precipitation under turbulent conditions abiotically.

Radial ooids: Radial fabric predominates in Mg-calcite ooids (e.g. Tucker and Wright, 1990) and to a lesser extent in some hypersaline lacustrine aragonite ooids (e.g. Halley, 1977) and

rarely in marine aragonite ooids (Loreau and Purser, 1973; Davies and Martin, 1976). They are commonly associated with weakly agitated, protected marine environments (Heller et al., 1980; Beukes, 1983). The presence of organic material under supersaturated quiet environmental condition is a critical parameter in radial ooid formation (Suess and Futterer, 1972; Davies et al., 1978). The radial ooids display similar characteristics with those of ancient and modern day examples, in terms of fabric preservation and distribution of carbonaceous matter, which probably indicates they were formed under similar conditions with more stable mineralogy (Mg-calcite) compared to concentric ooids.

Concentric-radial ooids: The radial and concentric laminae of this ooid type display the same features as entirely radial and entirely concentric ooids (Figs. 2C and F and 4K-L). The presence of two different fabrics in radial-concentric ooids could be a result of bimineralic cortices (i.e. aragonite in radial fabric and Mg-calcite in concentric fabric). Aragonite and Mg-calcite can co-occur in alternating laminae within one and the same ooid (Land et al., 1979; Major et al., 1988; Chatalov, 2005), as observed from both the Precambrian (Tucker, 1984) and the Phanerozoic record. Thermodynamic factors and saturation state of seawater, which are most probably controlled by subtle temperature and/or salinity changes, have been most influential in the precipitation of aragonite and calcite (Chatalov, 2005). The concentration and presence of specific organic acids in the environment at the time of precipitation may have also played a role, as the presence of certain organic acids may cause Mg-calcite to crystallize from solutions, while in their absence aragonite will crystallize (Kitano and Kanamori, 1966; Land et al., 1979). Two other mechanisms for their formation have been suggested: 1) Laminae with a radial fabric reflect a microbial growth pattern and concentric laminae develop when subjected to currents and waves (Swett, 1965). 2) Radial and concentric laminae reflect variable hydrodynamic conditions (Heller et al., 1980).

Superficial ooids: The presence of a thin cortex in this type of ooid is probably related to the large size of nuclei (Fig. 2E), which hinder grain mobility and slow down ooid growth (Harris, 1979). This may have provided favorable conditions for microbial colonization, as indicated by a radial fabric enriched in organic matter (Fig. 5).

Micritic ooids: These ooids share similar features with the other ooid types, and fabric relics (Fig. 2D) indicate they were not structureless (dense micrite) originally. Micritization of ooids and loss of a primary internal fabric may have resulted from dissolution of primary carbonate phases (e.g. aragonite) during burial and precipitation of micritic/ microsparitic calcite

(Richter, 1983; Richter and Besenecker, 1983; Tucker, 1984; Wilkinson et al., 1984). Microboring activity by endolithic microorganisms, such as heterotrophic coccoidal bacteria, may have also resulted in micritization (Harris et al., 1979; Campbell, 1982; Gaffey, 1983; Popp and Wilkinson, 1983). The presence of transitional fabrics (mostly concentric and rarely radial to massive micritic fabrics) indicate that micritic ooids formed by alteration of primary fabrics of other ooid types, most likely concentric ooids with unstable mineralogy, during diagenesis. There is no evidence for the presence of microborers and if they were involved in fabric destruction of the ooids.

4.6 Conclusions

1. The occurrence of oolitic facies in the Mesoarchaean Chobeni Formation is confined to high-energy intertidal to shallow-subtidal depositional settings and, to a lesser extent, to microbialite facies where they became trapped in microbial mats. Four different fabrics in cortices (concentric, radial, radial-concentric and micritic fabrics) were recognized.

2. The ooids are composed of dolomite and ankerite. By analogy to ooids from modern marine environments, it is possible that concentric ooids commonly featuring higher Sr contents were initially made of aragonite and radial ooids, which have less Sr and a better level of preservation, had a Mg-calcite precursor. The similarity between radial and concentric ooids with their modern day counterparts indicates they probably formed by a related mechanism, possibly by bacteria under quiet and turbulent environmental conditions, respectively. The presence of specific environmental conditions (agitated vs. low energy conditions, seawater chemistry), which dictate survival and activity of specific microbial communities are the key factors to the mineralogy, fabrics and ooid formation.

3. NanoSIMS elemental mapping of ooid cortices showed a spatial correlation of biologically relevant elements (N, S and P) with C, underlining the biogenicity of the carbonaceous matter confined inside the ooids.

4. Accessory apatite, pyrite, anatase, rutile, and muscovite occur in the cortices of ooids. They were probably incorporated by their trapping and binding by microbial communities during ooid formation, while pyrite may also be a product of microbial sulfate reduction.

5. REE patterns of most allochems characterize them as marine deposits, although the patterns

are subdued, either due to a restricted setting with much freshwater input, or alteration. Calcite-to dolomite-filled fractures show different REE patterns, which likely reflect precipitation from meteoric groundwater, which may have interacted with siliciclastic components present in the carbonates.

4.7 Acknowledgements

We thank Dr. Christian Reinke (University of Johannesburg) for assisting with microprobe analysis and Mr. Johann Lugmeier (Technical University Munich) for operating the NanoSIMS.

4.8 References

Alibo, D.S., and Nozaki, Y. (1999). Rare earth elements in seawater: Particle association, shale-normalization, and Ce oxidation. Geochim. Cosmochim. Acta, 63, 3/4, 363-372.

Bathurst, R.G.C. (1971). Carbonate sediments and their diagenesis. Developments in sedimentology, 12. Elsevier, Amsterdam, 658 p.

Bau, M., and Dulski, P. (1996). Distribution of yttrium and rare-earth elements in the Penge and Kuruman iron-formations, Transvaal Supergroup, South Africa. Precambrian Res., 79, 37-55.

Berner, R.A., De Leeuw, J.W., Spiro, B., Murchison, D.G., and Eglinton, G. (1985). Sulphate reduction, organic matter decomposition and pyrite formation [and discussion]. Philos. Trans. R. Soc. London Ser. A., Mathematical and Physical Sciences, 315 (1531), 25-38.

Beukes, N.J. (1983). Ooids and oolites of the proterophytic Boomplaas Formation, Transvaal Supergroup, Griqualand West, South Africa. In: Coated Grains. Peryt, T.M. (Ed.), 199-214.

Brehm, U., Krumbein, W.E., and Palinska, K.A. (2006). Biomicrospheres generate ooids in the laboratory. Geomicrobiol. J., 23, 500-545.

Campbell, S.E. (1982). Precambrian endoliths discovered. Nature. 299, 429-431.

Chafetz, H.S. (1986). Marine peloids: a product of bacterially induced precipitation of calcite. J. Sediment. Petrol., 56, 812-817.

Chatalov, A. (2005). Monomineralic carbonate ooid types in the Triassic sediments from Northwestern Bulgaria. Gologica Balcanica, 35 (1-2), 63-91.

Crosby, C.H., and Bailey, J.V. (2012). The role of microbes in the formation of modern and ancient phosphatic mineral deposits. Front. Microbiol., 3, 1-7.

Dahanayake, K., Gerdes, G., and Krumbein, W.E. (1985). Stromatolites, oncolites and oolites biogenically formed in situ. Naturwissenschaften, 72, 513-518.

Davaud, E., and Girardclos, S. (2001). Recent freshwater ooids and oncoids from western Lake Geneva (Switzerland): indications of a common organically mediated origin. J. Sediment. Res., 71 (3), 423-429.

Davies, P.J., and Martin, K. (1976). Radial aragonite ooids, Lizard Island, Great Barrier Reef. Geology, 4, 120-122.

Davies, P.J., Bubela, B., and Ferguson, J. (1978). The formation of ooids. Sedimentology, 25, 703-730.

Decho, A.W., Visscher, P.T., and Reid, R.P. (2005). Production and cycling natural microbial exopolymers (EPS) within a marine stromatolite. Palaeogeogr. Palaeoclimatol. Palaeoecol., 219, 71-86.

Deelman, J.C. (1978). Experimental ooids and grapestones: Carbonate aggregates and their origin. J. Sediment. Petrol., 48, 503-512.

Dimroth, E., and Chauvel, J.J. (1973). Petrography of the Sokoman Iron Formation in part of the Labrador Central Trough, Quebec, Canada. Geol. Soc. Am. Bull., 84, 111-134.

Donald, R., and Southam, G. (1999). Low temperature anaerobic bacterial diagenesis of ferrous monosulfide to pyrite. Geochim. Cosmochim. Acta, 63, 2019-2023.

Duguid, S.M.A., Kyser, T.K., James, N.P., and Rankey, E.C. (2010). Microbes and ooids. J. Sediment. Res., 80, 236-251.

Dupraz, C., and Visscher, P.T. (2005). Microbial lithification in marine stromatolites and hypersaline mats. Trends Microbiol., 13, 429-438.

Elderfield, H. (1988). The oceanic chemistry of the rare-earth elements. Phil. Trans. R. Soc. Lond. A 325, 105-126.

Elderfield, H., Upstill-Goddard, R., and Sholkovitz, E.R. (1990). The rare earth elements in rivers, estuaries, and coastal seas and their significance to the composition of ocean waters Geochim. Cosmochim. Acta, 54, 971-991.

Fabricius, F.H. (1977). Origin of marine ooids and grapestones. In: Contributions to sedimentology. Füchtbauer, H., Lisitzyn, A.P., Milliman, J.D., and Seibold, E. (Eds.), 7, 1-113.

Ferris, F.G. (1989). Metallic ion interactions with the outer membrane of gram-negative bacteria. In: Metal ions and bacteria. Beveridge, T.J., and Doyle, R.J. (Eds.), NewYork: Wiley, 295-323.

Flügel, E. (2004). Microfacies of carbonate rocks: analysis, interpretation and application. Springer-Verlag, Germany. 976 p.

Gaffey, S.J. (1983). Formation and infilling of pits in marine ooid surfaces. J. Sediment. Petrol., 53, 193-208.

Gerdes, G., Dunajtschik-Piewak, K., Riege, H., Taher, A.G., Krumbein, W.E., and Reineck, H.E. (1994). Structural diversity of biogenic carbonate particles in microbial mats. Sedimentology, 41, 1273-1294.

Halley, R. (1977). Ooid fabric and fracture in the Great Salt Lake and the geologic record. J. Sediment. Petrol., 47 (3), 1099-1120.

Harris, P.M. (1979). Facies anatomy and diagenesis of a Bahamian ooid shoal: Sedimenta VII. The Comparative Sedimentology Laboratory, University of Miami, Miami, FL, 163 p.

Harris, P.M. (1983). The Joulters ooids shoal, Great Bahama Bank. In: Coated grains. Peryt, T. (Ed.), Springer-Verlag, 132-141.

Harris, P.M., Halley, R.B., and Lukas, K.J. (1979). Endolith microborings and their preservation in Holocene-Pleistocene (Bahama-Florida) ooids. Geology, 7, 216-220.

Heckel, P.H. (1983). Diagenetic model for carbonate rocks in mid continent Pennsylvanian eustatic cyclothems. J. Sediment. Petrol., 53, 733-759.

Hegner, E., Kröner, A., and Hunt, P. (1994). A precise U-Pb zircon age for the Archean Pongola Supergroup volcanics in Swaziland. J. Afr. Earth. Sci., 18 (4), 3 39-341.

Heller, P.L, Komar, P.D., and Pevear, D.R. (1980). Transport processes in ooid genesis. J. Sediment. Petrol., 50 (3), 943-952.

Hicks, N., and Hofmann, A. (2012). Stratigraphy, geochemistry and provenance of the auriferous–uraniferous, fluvial to shallow-marine Sinqeni Formation, Mozaan Group, northern KwaZulu-Natal, South Africa. South Afr. J. Geol. 115 (3), 327-344.

Hunter, D.R. (1974). Crustal development in the Kaapvaal Craton, 11. The Proterozoic. Precambrian Res., 1, 295-326.

Johannesson, K.H., Hawkins Jr, D.L. and Cortés, A. (2006). Do Archean chemical sediments record ancient seawater rare earth element patterns? Geochem. Cosmochem.Acta, 70, 871-890.

Kahle, C.F. (1974). Ooids from Great Salt Lake, Utah, as an analogue for the genesis and diagenesis of ooids in marine limestones. J. Sediment. Petrol., 44, 30-39.

Kamber, B.S., Bolhar, R. and Webb, G.E. (2004). Geochemistry of late Archaean stromatolites from Zimbabwe: evidence for microbial life in restricted epicontinental seas. Precambrian Res., 132, 379-399.

Kamber, B.S., Webb, G.E., and Gallagher, M. (2014). The rare earth element signal in Archaean microbial carbonate: information on ocean redox and biogenicity. J. Geol. Soc. London, 171, 745-763.

Kazmierczak, J., Coleman, M.L., Gruszczynski, M., and Kempe, S. (1996). Cyanobacterial key to the genesis of micritic and peloidal limestones in ancient seas. Acta Palaeontol. Pol., 41, 319-338.

Kiessling, W., Flügel, E., and Golonka, J. (2002). Phanerozoic reef patterns. SEPM Spec. Publ., 72, 775 p.

Kilburn, M.R., and Wacey, D. (2011). Elemental and isotopic analysis by NanoSIMS: insights for the study of stromatolites and early life on Earth. In: Stromatolites: Interaction of microbes with sediments. cellular origin, life in extreme habitats and astrobiology 18. Seckbach, J., andTewari, V. (Eds.), Springer, 463-493.

Kitano, Y., and Kanamori, N. (1966). Synthesis of magnesian calcite at low temperatures and pressures: Geochem. J., 1, 1-10.

Knoll, A.H. (1985). Exceptional preservation of photosynthetic organisms in silicified carbonates and silicified peats. Phil. Trans. R. Soc. Lond. B 311, 111-122.

Krumbein, W.E. (1979). Calcification by bacteria and algae. In: Biogeochemical cycling of mineral forming elements: studies in environmental science. Trudinger, P.A., and Swaine, D.J. (Eds.), New York, Elsevier, 47-68.

Land, L.S., Behrens, E.W., and Frishman, S.A. (1979). The ooids of Baffin Bay, Texas. J. Sediment. Petrol., 49 (4), 1269-1278.

Lee, K., Tong, L.T., Millero, F.J., Sabine, C.L., Dickson, A.G., Goyet, C., Park, G.-H., Wanninkhof, R., Feely, R.A., and Key, R.M. (2006). Global relationships of total alkalinity with salinity and temperature in surface waters of the world's oceans: Geophys. Res. Lett., 33, L19605.

Lemelle, L., Labrot, P., Salome, M., Simionovici, A., Viso, M., and Westall, F. (2008). In situ imaging of organic sulfur in 700-800 My-old Neoproterozoic microfossils using X-ray spectromicroscopy at the SK-edge. Org. Geochem., 39, 188-202.

Longman, M.W. (1980). Carbonate diagenetic textures from near surface diagenetic environments. Am. Assoc. Pet. Geol. Bull., 64, 461-487.

Loreau, J.P., and Purser, B.H. (1973). Distribution and ultrastructure of Holocene ooids in the Persian Gulf. In: The Persian Gulf. Purser, B.H. (Ed.), Springer, Berline, Heidelberg, Newyork, 279-328.

Malone, P.G., and Towe, K.M. (1970). Microbial carbonate and phosphate precipitates from sea water cultures. Marine Geol., 9, 301-309.

Major, R.P., Halley, R.B., and Lukas, K.J. (1988). Cathodoluminescent bimineralic ooids from the Pleistocene of the Florida continental shelf. Sedimentology, 35, 843-855.

Markun, C.D., and Randazzo, A.F. (1980). Sedimentary structures in the Gunflint Iron Formation, Schreiber Beach, Ontario, Precambrian Res., 12, 287-310.

Matthews, P.E., (1967). The pre-Karoo formations of the White Umfolozi inlier, northern Natal. Trans. Geol. Soc. South Afr. 70, 39-63.

McLennan, S.B. (1989). Rare earth elements in sedimentary rocks. Influence of provenance and sedimentary processes. In: Geochemistry and mineralogy of the Rare Earth elements. Lipin, B.R., and McKay, G.A. (Eds.), Mineral. Soc. Am., Washington, 169-200.

Medwedeff, D.A., and Wilkinson, B.H. (1983). Cortical fabrics in calcite and aragonite ooids. In: Coated grains. Peryt, T. (Ed.). Springer-Verlag, 109-115.

Michard, A., and Albarède, F. (1986). The REE content of some hydrothermal fluids. Chem. Geol., 55, 51-60.

Milliman, J.D., and Barretto, H.T. (1975). Relict magnesian calcite oolite and subsidence of the Amazon shelf. Sedimentology, 22, 137-145.

Moore, C.H., and Druckman, Y. (1981). Burial diagenesis and porosity evolution, Upper Jurassic Smackover Formation, Arkansas and Louisiana. Am. Assoc. Pet. Geol. Bull., 65, 597-628.

Mukasa, S.B., Wilson, A.H., and Young, K.R. (2013). Geochronological constraints on the magmatic and tectonic development of the Pongola Supergroup (Central Region), South Africa. Precambrian Res., 224, 268-286.

Newell, N.D, Purdy, E.G., and Imbrie, J. (1960). Bahamian oolitic sand. J. Geol., 68 (5), 481-497.

Oehler, D.Z., Robert, F., Mostefaoui, S., Meibom, A., Selo, M., and McKay, D.S. (2006). Chemical mapping of Proterozoic organic matter at sub-micron spatial resolution. Astrobiology, 6, 838-850.

Oehler, D.Z., Robert, F., Walter, M.R., Sugitani, K., Allwood, A., Meibom, A., Mostefaoui, S., Selo, M.R., Thomen, A., and Gibson, E.K. (2009). NanoSIMS: insights to biogenicity and syngeneity of Archaean carbonaceous structures. Precambrian Res., 173, 70-78.

Opdyke, B.N., and Wilkinson, B.H. (1990). Paleolatitude distribution of Phanerozoic marine ooids and cements: Palaeogeogr. Palaeoclimatol. Palaeoecol., 7-8, 135-148.

Opdyke, B.N., and Wilkinson, R.H. (1993). Carbonate mineral saturation state and cratonic limestone accumulation. Am. J. Sci., 293, 217-234.

Pacton, M., Ariztegui, D., Wacey, D., Kilburn, M.R., RollionBard, C., Farah, R., and Vasconcelos, C. (2012). Going nano: a new step toward understanding the processes governing freshwater ooid formation. Geology, 40, 547-550.

Phoenix, V.R., Adams, D.G., and Konhauser, K.O. (2000). Cyanobacterial viability during hydrothermal biomineralisation. Chem. Geol., 169, 329-338.

Plée, K., Pacton, M., and Ariztegui, D. (2010). Discriminating the role of photosynthetic and heterotrophic microbes triggering low-Mg calcite precipitation in fresh water biofilms (Lake Geneva, Switzerland). Geomicrobiol. J., 27, 391-399.

Plée, K., Ariztegui, D., Martini, R., and Davaud, E. (2008). Unravelling the microbial role in ooid formation-results of an in situ experiment in modern freshwater Lake Geneva in Switzerland. Geobiology, 6, 341-350.

Plée, K., Ariztegui, D., Sahan, E., Martini, R., and Davaud, E. (2006). Microbes caught in the act: disentangling the role of biofilms in the formation of low-Mg calcite ooids in a freshwater lake. EOS Transactions AGU 87 (52), Fall Meeting Supplement, Abstract GC21A-1316.

Pingitore, N. (1976). Vadose and phereatic diagenesis: processes, products and their recognition in corals. J. Sediment.Petrol., 46 (4). 985-1006.

Popp, B.N., and Wilkinson, B.H. (1983). Holocene lacustrine ooids from Pyramid lake, Nevada. In: Coated grains. Peryt, T. (Ed.), Springer-Verlag, 142-153.

Rankey, E.C., and Reeder, S.L. (2009). Holocene ooids of Aitutaki Atoll, Cook Islands, South Pacific. Geology, 37, 971-974.

Reitner, S., Arp, G., Thiel, V., Gautret, P., Galling, U., and Michealsis, W. (1997). Organic matter in Great Salt Lake ooids (Utah, USA) first approach to a formation via organic matrices. Facies, 36, 210-219.

Richter, D.K. (1983). Calcareous ooids: a synopsis. In: Coated grains. Peryt, T. (Ed.), Springer-Verlag.71-99.

Richter, D.K., and Besenecker, H. (1983). Subrecent thermal ooids with tangentially oriented high-Sr aragonite (Tekke Ilica/Turkey). In: Coated grains. Peryt, T. (Ed.), Springer-Verlag. 154-162.

Sandberg, P.A. (1975). New interpretations of Great Salt Lake ooids and of ancient non-skeletal carbonate mineralogy. Sedimentology, 22, 497-537.

Sandberg, P.A. (1983). An oscillating trend in Phanerozoic non-skeletal carbonate mineralogy. Nature, 305, 19-22.

Schlesinger, W.H. (1997). Biogeochemistry: An analysis of global change. Elsevier, New York, 588 p.

Sholkovitz, E.R. (1995). The aquatic chemistry of the rare earth elements in rivers and estuaries. Aquat. Geochem., 1, 1-34.

Siahi, M., Hofmann, A., Hegner, H., and Master, S. (2016). Sedimentology and facies analysis of Mesoarchaean stromatolitic carbonate rocks of the Pongola Supergroup, South Africa. Precambrian Res., 278, 244-264.

Simone, L. (1981). Ooids: a review. Earth. Sci. Rev., 16, 319-355.

Simonson, B.M., and Jarvis, D.G. (1993). Microfabrics of oolites and pisolites in the Early Precambrian Carawine Dolomite of Western Australia. In: Carbonate microfabrics. Rezak, R., and Lavoie, D.L. (Eds.), Springer-Verlag. 227-237.

Singh, U. (1987). Ooids and cements from the Late Precambrian of the Flinders Ranges, South Austrailia. J. Sediment. Petrol., 57 (1), 117-127.

Soudry, D. (1987). Ultra-fine structures and genesis of the Campanian Negev high-grade phosphorites (southern Israel). Sedimentology, 34, 641-660.

Soudry, D., and Champetier, Y. (1983). Microbial processes in the Negev phosphorites (southern Israel). Sedimentology, 330, 311-423.

Southgate, P. (1980). Cambrian stromatolitic phosphorites from the Georgina Basin, Australia. Nature, 285, 395-397.

Suess, E., and Futterer, D. (1972). Aragonitic ooids: experimental precipitation from sea water in the presence of humic acid. Sedimentology, 19, 129-139.

Summons, R.E., Bird, L.R., Gillespie, A.L., Pruss, S.B., Roberts, M., and Sessions, A.L. (2013). Lipid biomarkers in ooids from different locations and ages: evidence for a common bacterial flora. Geobiology, 11 (5), 397-497.

Swett, K. (1965). Dolomitization, silicification and calcitization patterns in Cambro-Ordovician oolites from Nothwest Scotland. J. Sediment. Petrol., 35 (4), 928-938.

Takahashi, Y., Châtellier, X., Hattori, K.H., Kato, K. and Fortin, D. (2005). Adsorption of rare earth elements onto bacterial cell walls and its implication for REE sorption onto natural microbial mats.Chem. Geol., 219, 53-67.

Tostevin, R., Shields, G.A., Tarbuck, G.M., He, T., Clarkson, M.O. and Wood, R.A. (2016). Effective use of cerium anomalies as a redox proxy in carbonate-dominated marine settings. Chem. Geol., 438, 146-162.

Tucker, M.E. (1983). Diagenesis, geochemistry, and origin of a Precambrian dolomite: the Beck Spring Dolomite of eastern California. J. Sediment. Petrol., 53, 1097-1119.

Tucker, M.E. (1984). Calcitic, aragonitic and mixed calcitic-aragonitic ooids from the mid-Proterozoic Belt Supergroup, Montana. Sedimentology, 31, 627-644.

Tucker, M.E., and Wright, V.P. (1990). Carbonate sedimentology. Blackwell Science. London, England. 492 p.

Wacey, D., Gleeson, D., and Kilburn, M.R. (2010a). Microbialite taphonomy and biogenicity: new insights from NanoSIMS. Geobiology, 8, 403-416.

Wacey, D., McLoughlin, N., Whitehouse, M.J., and Kilburn, M.R. (2010b). Two co-existing sulfur metabolisms in a ca. 3400 Ma sandstone. Geology, 38, 1115-1118.

Wacey, D., Kilburn, M.R., Saunders, M., Cliff, J., and Brasier, M.D. (2011). Microfossils of sulfur metabolizing cells in ~ 3.4 billion year old rocks of Western Australia. Nature Geoscience, 4, 698-702.

Wakeham, S.G., Sinninghe Damste´, J.S., Kohnen, M.E.L., and deLeeuw, J.W. (1995). Organic sulphur compounds formed during early diagenesis in Black Sea sediments. Geochim. Cosmochim. Acta, 59, 521-533.

Warren, J. (2000). Dolomite: occurrence, evolution and economically important associations. Earth Sci. Rev., 52, 1-81.

Webb, G.E. and Kamber, B.S. (2000). Rare earth elements in Holocene reefal microbialites: A new shallow seawater proxy. Geochim. Cosmochim. Acta, 64, 1557-1565.

Wilkinson, B.H., Buczinski, C., and Owen, R.M. (1984). Chemical control of carbonate phases: implications from Upper Pennsylvanian calcite-aragonite ooids of Southeastern Kansas. J. Sediment. Petrol., 54, 932-947.

Wilkinson, B.H., Owen, R.M. and Carroll, A.R. (1985). Submarine hydrothermal weathering, global eustasy and carbonate polymorphism in Phanerozoic marine oolites. J. Sediment. Petrol., 55, 171-183.

Zempolich, W.G., and Baker, P.A. (1993). Experimental and natural mimetic dolomitization of aragonite ooids. J. Sediment. Petrol., 63 (4), 596-606.

Chapter 5: Trace-element and stable (C, O) and radiogenic (Sr) isotope geochemistry of stromatolitic carbonate rocks of the Mesoarchaean Pongola Supergroup: implications for seawater composition

Trace-element and stable (C, O) and radiogenic (Sr) isotope geochemistry of stromatolitic carbonate rocks of the Mesoarchaean Pongola Supergroup: implications for seawater composition

Abstract

The Mesoarchaean Pongola Supergroup hosts one of the oldest well-preserved stromatolitic carbonate successions. Major and trace-element geochemistry along with C, O, and Sr isotopic analyses of three stratigraphic sections of stromatolitic carbonate rocks were undertaken in order to infer the depositional environment, and to unravel the chemical characteristics of contemporaneous seawater. The carbonate rocks consist mainly of dolomite and, to a lesser extent, of ankerite. Their variable Sr concentrations of ~ 95 to 450 ppm are interpreted as resulting from early to late dolomitization of metastable carbonates (aragonite and/or high magnesium calcite), facies control and calcitization during meteoric diagenesis. $\delta^{18}O$ values range from ca. -19.6 to -12.0 ‰ VPDB and reflect water-rock interaction and recrystallization during diagenesis and metamorphism. A relatively high $\delta^{13}C$ value of 2.5 ‰ VPDB was measured in carbonate samples least affected by alteration, and we suggest that it approximates the composition of dissolved inorganic carbon in coeval seawater. The samples display variable Sr isotope ratios, of 0.777 to as low as 0.708. They are considerably higher than those expected in Archaean open-ocean water masses buffered by hydrothermal interaction with the mantle. We interpret the highly radiogenic Sr isotopic ratios in some carbonate samples to reflect isotopic exchange with radiogenic Sr from siliciclastic/ volcaniclastic components in the samples and fluids from clay-rich layers intercalated with the carbonates. The least radiogenic Sr isotope ratio may approximate the mixed isotopic composition of seawater in the epicontinental basin and of riverine freshwater draining the Kaapvaal Craton. The dolomitic carbonate samples show shale-normalized rare earth element and yttrium (REEs + Y) distribution patterns that resemble those of modern ocean water with positive La_{SN}, Gd_{SN} and Y_{SN} anomalies, superchondritic Y/Ho ratios, a small negative Ce anomaly and depleted light rare earth elements (LREEs) relative to the heavy rare earth elements (HREEs). These anomalies are not as pronounced as expected for an open marine setting, which together with the Sr isotope results support a more restricted setting with riverine input and fluctuations in marine ingressions. A convex-upward shale-normalized REE + Y pattern due to enrichment of middle REEs is probably a result of several factors, including organic matter complexation,

and element fractionation during estuarine mixing. The small negative Ce anomalies and Th/U > 2 may suggest limited amounts of free oxygen in shallow waters due to local microbial activity, which ultimately led to carbonate precipitation.

5.1 Introduction

Mineralogical, isotopic and trace-element data of sedimentary carbonate rock samples can be used to constrain the chemical and isotope composition of the ambient seawater (Veizer et al., 1989a; Kamber et al., 2014). In order to infer ancient seawater compositions, evaluation of the primary chemical and isotopic signatures of sedimentary carbonate rocks is of significance. Post-depositional diagenetic and metamorphic processes are likey to modify the mineralogical composition, concentrations of mobile trace-elements, in particular large-ion lithophile elements (LILE), and the primary isotopic compositions of fluid-mobile elements in carbonate samples (e.g. Veizer et al., 1990; Webb et al., 2009). It has also been shown that fluid-immobile elements, such as the rare-earth elements (REEs), and high-field strength elements (HFSE) remain largely unaffected by diagenesis (e.g. Webb et al., 2009) and are thus helpful for reconstructing ancient environmental conditions. The identification of the primary mineralogy of ancient Archaean carbonate rocks is not straightforward. There are many unknowns, such as the physico-chemical conditions of the early Earth's shallow seawater, which have controlled the chemical composition of the primary carbonates, and the degree of recrystallization and diagenetic/ metamorphic processes, which modified the composition of carbonate sediments after deposition. The aim of this study is to present new stable and radiogenic isotope as well as major and trace-element data of a stratigraphically resolved set of samples from different carbonate-bearing units of the Mesoarchaean Pongola Supergroup to determine their origin and subsequent alteration history. The data augment small sets of similar data previously published by different workers (e.g. Perry and Tan, 1972; Schidlowski et al., 1983; Veizer et al., 1990; Eglington et al., 2003; Bolhar et al., 2015). Our comprehensive data sets will be investigated for the preservation of primary geochemical characteristics and interpreted in the context of the chemical composition of seawater in which the microbial carbonate rocks formed.

5.2 Geological setting

The 3.0-2.9 Ga old (Hegner et al., 1994; Mukasa et al., 2013) Pongola Supergroup was deposited on continental crust of the south-eastern Kaapvaal Craton. The Pongola Supergroup is comprised of the lower, volcano-sedimentary Nsuze Group and the overlying, mainly sedimentary Mozaan Group (Gold, 2006; Wilson et al., 2013). In the study area of the White Mfolozi inlier, the c. 1.4 km thick Nsuze Group rests nonconformably on granitoid basement and is unconformably overlain by the Mozaan Group. The Nsuze Group is mainly composed of quartz-rich sandstones, two mafic volcanic and associated pyroclastic units, shale, mass-flow deposits and several dolomite horizons (Matthews, 1967; Siahi et al., 2016). Several stratigraphic intervals of mixed carbonate-siliciclastic facies occur in the Chobeni Formation of the Nsuze Group, in which three stratigraphic sections were measured and samples have been collected (Fig. 1). The main carbonate section is c. 28 m in thickness, rests on air-fall lapillistone and is overlain by cross-bedded sandstone, which contains minor carbonate beds (Fig. 2). Two sections separated c. 200 m apart were sampled. Higher up in the stratigraphy section, samples were collected from two other sections, called middle and upper carbonate sections (Fig. 3). The middle carbonate section, c. 2 m in thickness, rests with a sharp contact on cross-bedded sandstone and is erosively overlain by pebbly greywacke of mass flow origin. The greywacke is overlain by cross-bedded sandstone and followed by the upper carbonate section, c. 9 m in thickness, which is overlain by shale. Based on sedimentary structures and stromatolite morphologies, the carbonate rocks were interpreted to have been deposited in a shallow, tide-dominated, marine setting (Beukes and Lowe, 1989; Siahi et al., 2016). The dominant composition of carbonate differs stratigraphically. Dolomite is most common and ferroan dolomite (ankerite) occurs in the middle carbonate section. Calcite was observed in fenestrae and secondary voids (Siahi et al., 2016). The reader is referred to Siahi et al. (2016) for more information on stratigraphic columns and sedimentological interpretation.

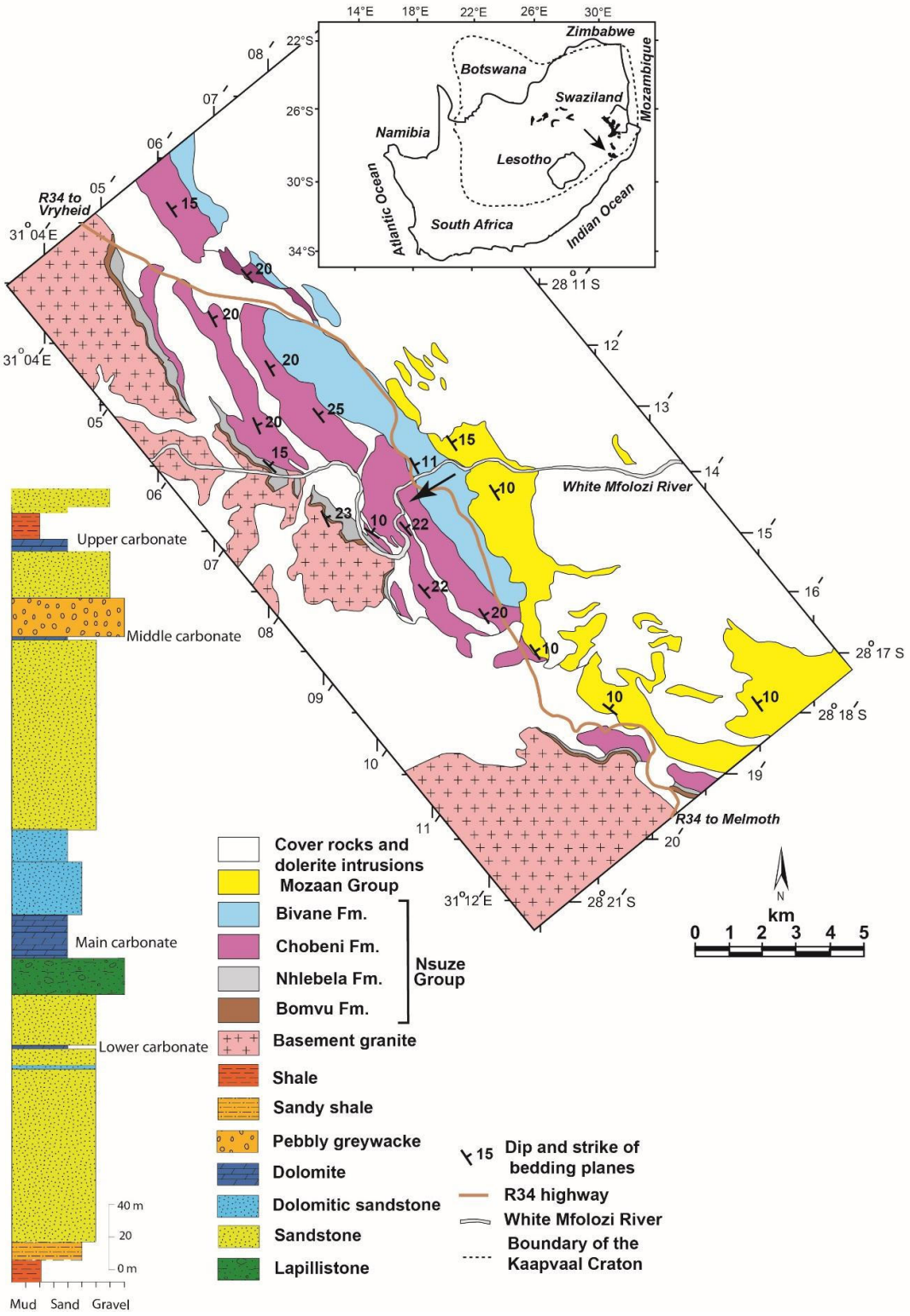

Fig. 1. Geological map of the White Mfolozi inlier (modified after Wilson et al., 2013) and stratigraphic column of the Chobeni Formation of the Mesoarchaean Nsuze Group, Pongola Supergroup. Inset shows distribution of the Pongola and Witwatersrand supergroups in relation to the Kaapvaal Craton in southern Africa. The arrow points to the study area.

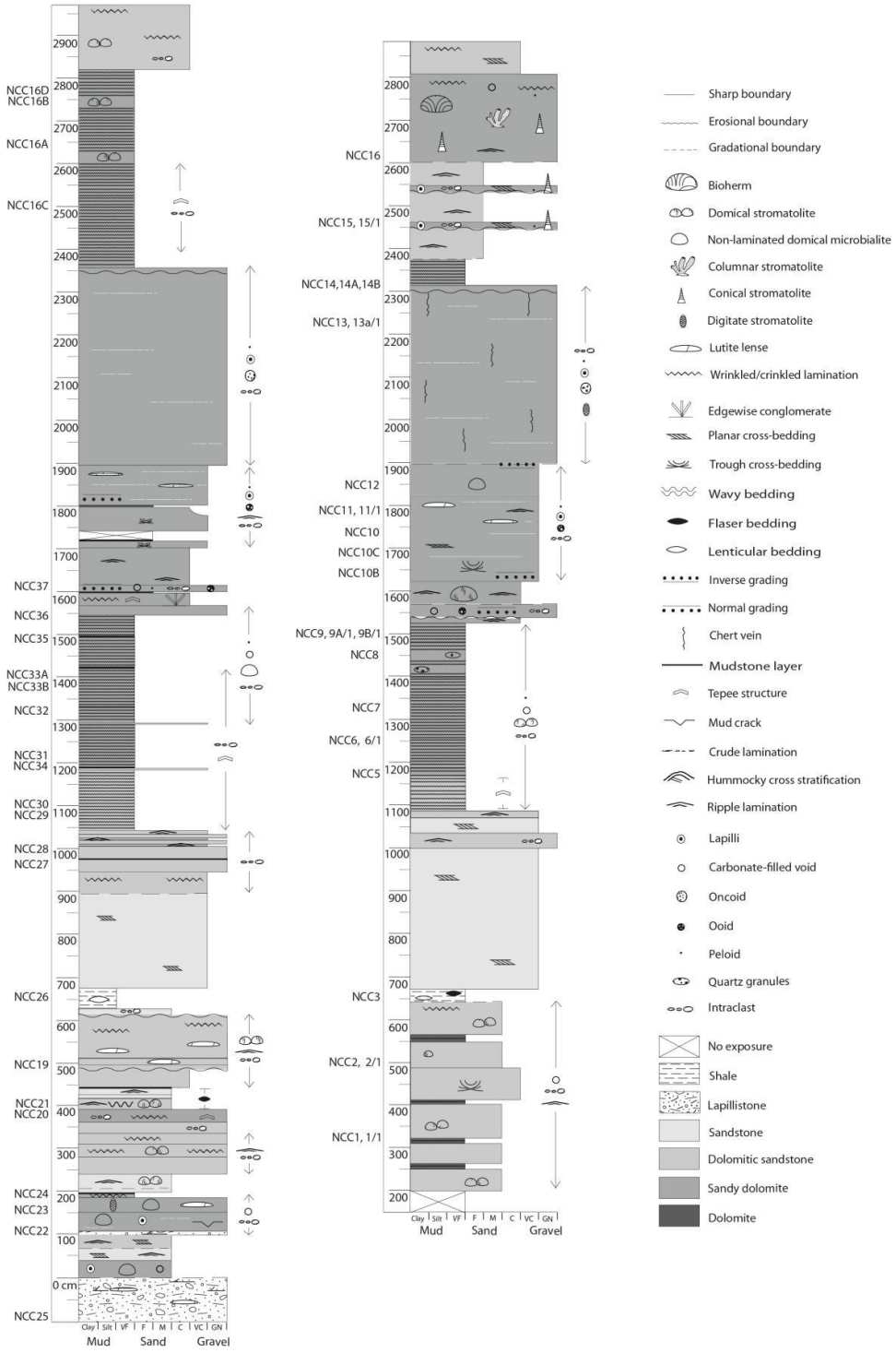

Fig. 2. Stratigraphic columns of the main carbonate section of the Chobeni Formation, White Mfolozi inlier measured c. 200 m apart (modified after Siahi et al., 2016). Note sample numbers to the left side of the thickness column. Samples NCC17A-B of oodolarenite interbedded with sandstone were obtained c. 40 m above the base of the section.

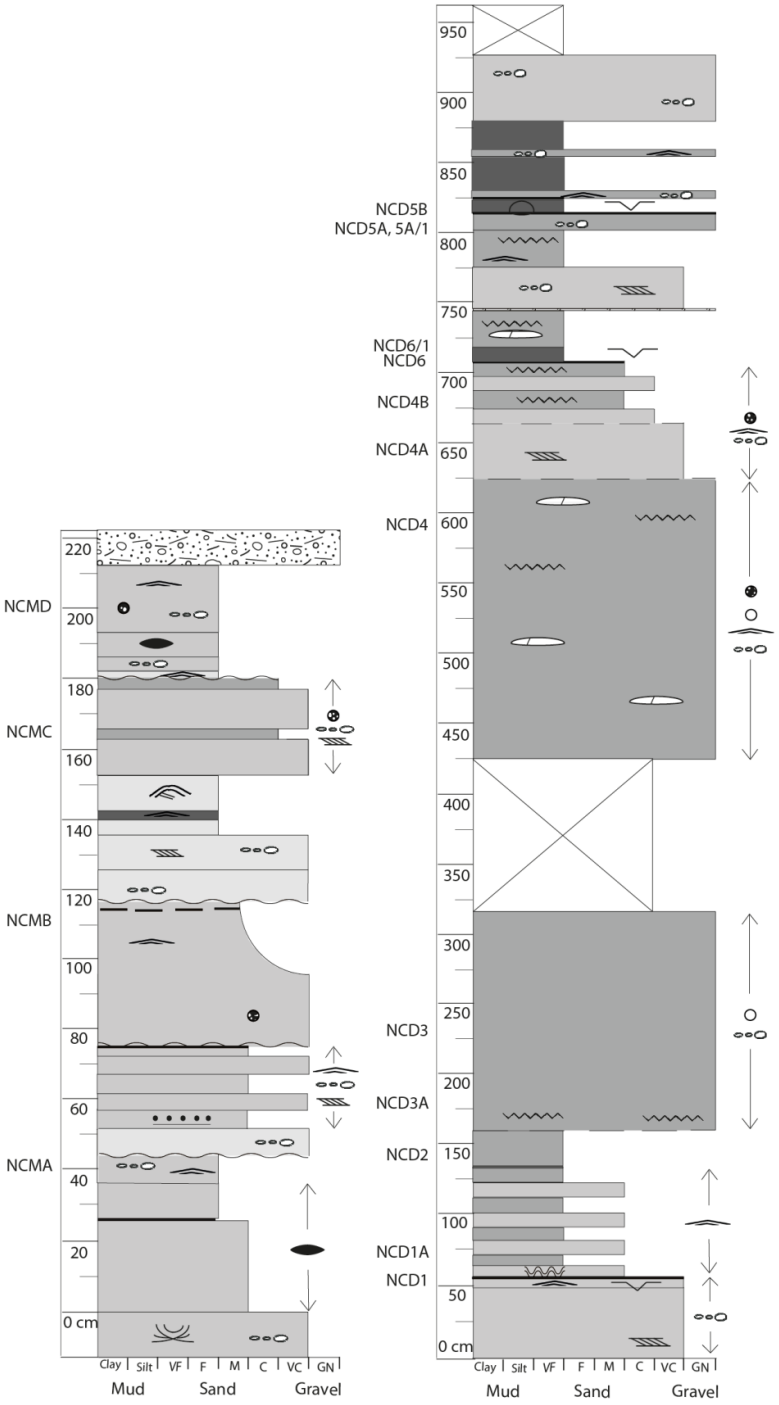

Fig. 3. Stratigraphic columns of the middle (left) and upper (right) carbonate sections of the Chobeni Formation, White Mfolozi inlier (modified after Siahi et al., 2016). See Fig. 2 for legend. Note sample numbers to the left side of the thickness column.

5.3 Analytical procedures

The mineralogical assemblage and major and trace-element concentrations of carbonate and associated carbonate-bearing sandstone, sandstone, and shale samples were determined by x-ray fluorescence spectrometry (XRF), inductively coupled plasma-mass spectrometry (ICP-MS), and microprobe (Table A2, Appendix). Carbon, O, and Sr isotope analyses were undertaken on whole-rock sample powders and micro-drilled cores. Results are presented in Tables 1 and 2.

Following a detailed microfacies study (Siahi et al., 2016), the best-preserved carbonate samples were selected from representative facies of all three stratigraphic sections. Samples affected by surface weathering and those containing secondary carbonate-filled voids, high amounts of siliciclastic detritus and microfaults/ veins were avoided. Fifty samples were crushed in a carbon-steel mill and pulverized in an agate mill. Their major element concentrations was analysed with a PANalytical MagiX PRO wavelength-dispersive XRF spectrometer at the University of Johannesburg. The analyses were performed on glass tablets made with a lithium borate flux (with $Li_2B_4O_7$ and $LiBO_2$ in equal amounts by mass and 0.5 mass % LiBr releasing agent), $LiNO_3$ as an oxidant and the dried sample powder at 115 ºC. The working curves were established certified international reference materials and mixtures of pure oxides, using the fundamental parameters model in PANalytical's SuperQ software. Analyses of a number of samples from the GeoPT proficiency-testing scheme met the "applied geochemistry" standard for Na_2O and loss on ignition (LOI) and the "pure geochemistry" standard for the remaining analytes (Thompson et al., 2015). Interpretation of correlation coefficients between element pairs followed the definition of Ratner (2009).

Ca, Mg, Fe, Mn, Sr, Si, Ba, Zn, and Al concentrations of carbonate components of selected carbonate samples were analysed from carbon-coated polished thin sections by means of a Cameca SX-100 electron-probe microanalyzer (EPMA) at the University of Johannesburg. The operating conditions were a 15 kV beam voltage, 6 nA beam current and 20 µm width of defocused beam. The data are listed in Table A3 (Appendix).

Table 1. $\delta^{13}C$ and $\delta^{18}O$ values for carbonate samples of the main, middle and upper sections of the Chobeni Formation, White Mfolozi inlier.

Section	Sample number	$\delta^{13}C$ (‰VPDB)	$\delta^{18}O$ (‰VPDB)	Section	Sample number	$\delta^{13}C$ (‰VPDB)	$\delta^{18}O$ (‰VPDB)	Section	Sample number	$\delta^{13}C$ (‰VPDB)	$\delta^{18}O$ (‰VPDB)
Main carbonate	**NCC1/1**	1.5	-15.3	Main carbonate	**NCC14A**	2.2	-13.1	Main carbonate	**NCC16B-71**	1.6	-15.8
	NCC2/1	1.7	-14.3		**NCC14B**	2.1	-14.0		**NCC16B-72**	1.7	-15.0
	NCC6/1	1.9	-15.0		**NCC15**	1.9	-16.4		**PO5-2**	1.8	-16.1
	NCC 8	2.1	-14.0		**NCC15-1**	1.8	-15.9		**PO5-3**	2.0	-12.3
	NCC9A/1	2.3	-12.0		**NCC16**	2.0	-16.4		**PO5-4**	2.2	-12.6
	NCC9B/1	2.2	-13.4		**NCC17A**	0.6	-19.4		**PO5-5**	2.2	-12.7
	NCC9-33	2.5	-13.0		**NCC17A/1**	0.4	-19.5				
	NCC9-34	2.3	-14.0		**NCC17B/1**	0.1	-19.6	Upper carbonate			
	NCC9-35	2.1	-13.5		**075A10A/1**	1.7	-16.0		**NCD1**	1.4	-16.3
	NCC9-38	0.2	-15.2		**075A10B/1**	2.1	-15.0		**NCD2**	1.4	-15.9
	NCC9-39	2.4	-13.7		**NCC22**	1.8	-15.5		**NCD3**	1.6	-13.9
	NCC9-40	0.1	-14.6		**NCC23**	1.7	-13.6		**NCD-32**	1.8	-13.0
	NCC9-41	2.4	-12.5		**NCC24**	1.5	-14.7		**NCD3-64**	-0.41	-16.6
	NCC9-42	2.3	-13.0		**NCC20**	1.8	-15.2		**NCD3-70**	1.4	-14.5
	NCC9-65	2.2	-12.5		**NCC21**	1.7	-15.6		**NCD4**	1.5	-17.1
	NCC9-73	2.4	-12.9		**NCC19**	1.7	-15.9		**NCD4-18**	1.4	-16.8
	NCC10C	2.3	-13.2		**NCC27**	1.8	-16.0		**NCD4-20**	2.0	-12.4
	NCC11/1	2.2	-13.1		**NCC29**	1.8	-16.1		**NCD4-22**	1.5	-16.0
	NCC11-26	2.5	-12.2		**NCC32**	1.9	-15.8		**NCD4-23**	1.9	-14.7
	NCC11-27	2.1	-13.8		**NCC33A-12**	2.1	-15.3		**NCD4-24**	1.4	-17.4
	NCC11-29	2.4	-12.9		**NCC33A-13**	2.1	-16.9		**NCD4-69**	1.6	-16.3
	NCC11-63	2.3	-13.9		**NCC33A-14**	2.1	-17.3		**NCD4-76**	1.4	-17.5
	NCC12A	1.5	-15.3		**NCC37**	2.2	-15.5		**NCD4A**	1.2	-17.5
	NCC13	2.4	-14.1		**NCC37-59**	2.2	-16.3		**NCD6/1**	1.4	-17.9
	NCC13a/1	2.4	-14.0		**NCC37-60**	1.1	-16.1		**NCD5B**	1.5	-16.2
	Ncc13b/1	2.4	-14.2		**NCC37-61**	-2.4	-14.5		**PO5-8**	1.1	-15.9
	NCC13-1	2.5	-15.4		**NCC37-62**	0.6	-16.4		**PO5-9**	1.4	-15.4
	NCC13-2	2.5	-14.2		**NCC37-74**	2.0	-15.9				
	NCC13-3	2.4	-15.		**NCC16B**	1.5	-16.3	Middle carbonate			
	NCC13-4	2.5	-16.0		**NCC16B-45**	1.2	-16.9		**NCMA**	0.20	-19.0
	NCC13-6	2.5	-15.2		**NCC16B-46**	1.2	-16.7		**NCMB**	0.40	-17.4
	NCC13-7	2.5	-14.7		**NCC16B-47**	1.2	-17.0		**NCMC**	0.30	-18.3
	NCC13-8	2.50	-14.4		**NCC16B-50**	1.1	-17.0		**NCMD**	0.10	-18.2
	NCC13-10	2.5	-14.2		**NCC16B-52**	1.3	-16.6				
	NCC13-66	2.4	-14.1		**NCC16B-53**	1.2	-16.7				
	NCC13-67	2.3	-14.2		**NCC16B-54**	2.3	-14.0				
	NCC13-75	2.4	-13.9		**NCC16B-55**	1.7	-15.5				

Table 2. $^{87}Sr/^{86}Sr$ isotopic ratios and Rb and Sr concentrations for acid-leached carbonate samples from the main, middle and upper carbonate sections of the Chobeni Formation, White Mfolozi inlier. The $^{87}Sr/^{86}Sr$ isotopic ratio of the NIST reference material measured along with the samples is also shown.

Section	Sample number	Rb (ppm)	Sr (ppm)	$^{87}Sr/^{86}Sr \pm 2$ SE
Main carbonate	NCC2/1			0.716485 ± 14
	NCC6/1			0.714489 ± 11
	NCC 8	0.82	340	0.712581 ± 11
	NCC9A/1	0.09	95.5	0.708032 ± 14
	NCC10C	0.04	110	0.709221 ± 11
	NCC11/1			0.709366 ± 13
	NCC13	0.009	89.9	0.714020 ± 12
	NCC13b			0.715607 ± 10
	NCC14A			0.713893 ± 11
	NCC14B			0.715284 ± 11
	NCC15-1	0.17	31.7	0.726667 ± 12
	NCC16			0.723020 ± 14
	NCC17A/1	2.72	371	0.742290 ± 12
	NCC17B/1			0.752643 ± 11
	075A10B/1			0.721405 ± 8
	NCC23	0.001	137	0.709727 ± 11
	NCC32			0.714220 ± 14
	NCC37			0.713564 ± 14
	PO5-4	0.81	270	0.710625 ± 15
	PO6-2			0.729671 ± 10
Upper carbonate	NCD2	0.50	70.5	0.759004 ± 16
	NCD3	0.001	85.6	0.734859 ± 10
	NCD5B	1.80	460	0.734160 ± 9
	PO5-8	0.53	142	0.739438 ± 11
Middle carbonate	NCMA	0.11	50.6	0.771946 ± 12
	NCMC	0.25	55.9	0.777379 ± 12
	NIST			0.710231 ± 5

The trace-element analyses of the carbonate samples were done on acid-leached sample powders. Two leaching procedures were applied to evaluate effects of possible digested siliciclastic detritus on trace-element concentrations and distribution patterns: i) c. 100 mg of sample powder were leached with ultrapure hydrochloric acid in three consecutive steps using different normality and volume (0.3 ml of 0.4 N, 0.5 ml of 2.5 N and 0.2 ml of 6.1 N HCl) until no further reaction was noticed; ii) ca. 100 mg of sample powder were leached with 1 ml of ultrapure 1N acetic acid. Leaching was undertaken while agitating the sample. Insoluble residue from both preparations was separated by centrifuging. Leaching with HCl for trace-element analysis was only done for one sample, as it liberated higher amounts of trace-elements associated with the silicate fraction as compared to acetic acid leaching. For non-carbonate samples as well as a selected suite of carbonate samples, 50 mg of rock powder was dissolved in a mixture of 3:2 HF and HNO_3 in a high pressure Teflon vessel in a CEM Mars Express Microwave digester with 40 minute digestion times and evaporated to dryness in Teflon beakers before being taken up in 5 % HNO_3 for analysis.

The trace-element concentrations were determined at the School of Geosciences, University of the Witwatersrand, using a Perkin Elmer Sciex ELAN DRC-e ICP-MS against primary standard solutions and validated against certified standard rock materials. Solutions were made up to 50 ml for analysis. Internal standards (10 ppb Rh, In, Re and Bi) and calibration solutions were prepared from certified single and multi-element standard solutions. The instrument was tuned to avoid interference by oxides and doubly charged species so that Ba^{2+}/Ba and CeO/Ce were < 0.03. Quality of data was monitored using the international standards BCR-1, BHVO-1 and BIR-1.

Dolomite and calcite samples for C and O stable isotope analysis were drilled from homogenous areas of polished slabs by means of a micro-drill. Micro-samples were drilled from different components of different facies. They were selected from stromatolitic facies (at c. 14, 15 and 27.4 m from the base), sandy oolitic intradolorudite, sandy oodolarenite and oncolite facies (at c. 16.1, 17.8, 22.3 m, respectively from the base) of the main carbonate section. Selected samples from the upper carbonate section are those from stromatolitic facies (at c. 2.3 m from the base) and sandy oolitic intradolorudite facies (at c. 5.7 m from the base), (Siahi et al., 2016). Micro-drilled cores were viewed under a binocular microscope and unwanted parts were removed by sand-paper.

Fifty-three core and 44 whole-rock sample powders were used for C and O isotope measurements using a Gasbench II linked to an isotope ratio mass spectrometer (DeltaPlus, ThermoFinnigan MAT, Bremen, Germany) at Ludwig- Maximilians- University of Munich. Carbonate isotope ratios are reported as δ-values [$\delta = (R_{sample}/R_{standard} - 1) \cdot 1000$] with R being the ratio of the heavy to the light isotope and δ given in per mil deviations from the international standard Vienna-Pee-Dee Belemnite (VPDB). International standards (NBS-18, NBS-19) and a lab standard (’Pfeil’) consisting of pure Solnhofen limestone were used for calibration. Each run contained varying amounts of the lab standard to account for eventual linearity corrections and adequate amounts of the respective sample powders (0.3 to 5.0 mg) depending on the carbonate content of the sample. After the septum vials had been automatically flushed with helium, drops of 103 % phosphoric acid were added to the samples manually with a syringe until the whole mixture was completely soaked (at least 6 drops). Isotope measurements were carried out after a reaction time of at least 12 hours at a constant temperature of 72 °C of phosphoric acid with rock powder. The analytical precision for the carbonates based on routine analysis of the internal reference standard ’Pfeil’ was ± 0.07 ‰ and ± 0.12 ‰ for $\delta^{13}C$ and $\delta^{18}O$, respectively. Further analytical details are given in Oehlerich et al. (2013). No correction

was applied for the difference in the $\delta^{18}O$ isotopic fractionation factor associated with phosphoric acid liberation of CO_2 from various co-existing carbonates, specifically in the case of calcite-dolomite mineral pairs (Sharma and Clayton, 1965).

The least altered carbonate samples assumed to be represented by those with the highest $\delta^{13}C$ and $\delta^{18}O$ values (Fairchild et al., 1990; Kaufman and Knoll, 1995) from representative facies were selected for Sr isotope analyses. Two different leaching procedures were performed on c. 100 mg of carbonate samples: i) a HCl-leaching procedure identical to that for trace- element analysis; ii) sequential steps leaching of the sample powder with ultraclean acetic acid (HAC) with different concentrations and volumes (5 %, 25 %, and 50 %) after the bulk had been pre-leached with 0.4 N HCl, to remove any acid-soluble Sr in diagenetic calcite and cements. The leaching procedure was continued on the residue with 1N HCl. The Sr in the leachate was chromatographically separated and measured on a W filament using a Spectromat upgraded MAT 261 thermal ionization mass spectrometer at Ludwig- Maximilians- University of Munich. A single analysis of the $^{87}Sr/^{86}Sr$ isotope ratio of the NIST 987 reference material during the sample analyis yielded 0.710231 ± 5 (2SE).

5.4 Results

5.4.1 Major elements

The XRF and microprobe analyses of carbonate samples show that ankerite is the dominant carbonate mineral in the middle carbonate section, while the main and upper carbonate sections mainly consist of dolomite with minor low-magnesium calcite (Fig. 4). Correlation among major elements of the samples in scatter diagrams indicates two compositionally distinct rock-forming components a non-carbonate clastic phase of silicates and a carbonate phase. A strong positive correlation exists among the non-carbonate components, which include SiO_2, Al_2O_3, K_2O, and TiO_2 in all of the three carbonate successions, whereas their correlation with the carbonate constituents, which include CaO, MgO, and, to a large extent, Fe_2O_3 and MnO, are either statistically not significant or negative (diagram is not shown).

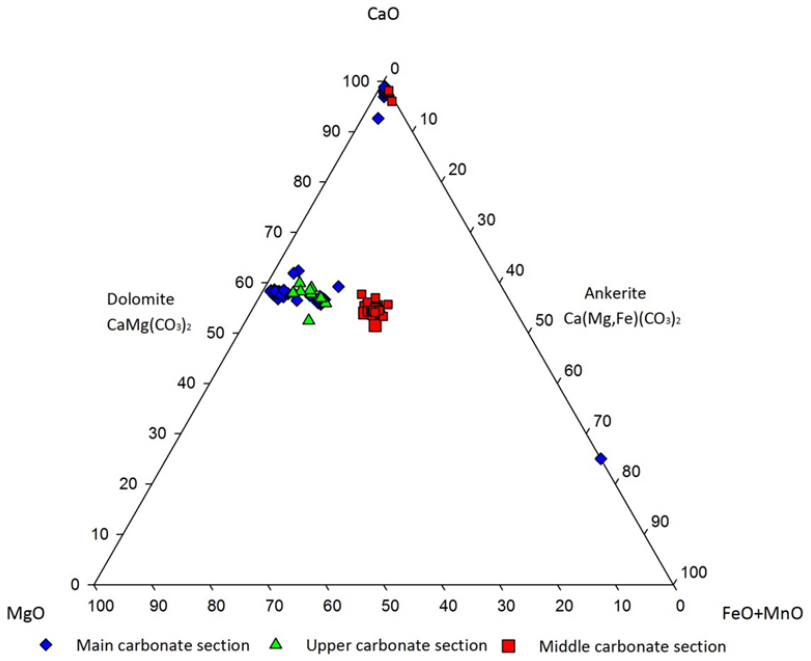

Fig. 4. Ternary diagram of major element compositions of different carbonate components (e.g. matrix, ooids, peloids, intraclasts) from the three sections as determined by EPMA. Note that some samples comprise calcite, which is plotted close to the CaO apex with up to 10 % FeO + MnO and interpreted as calcite replacement. The main and upper carbonate sections, have a lower amount of Fe and Mn, while samples from the middle carbonate section show consistently higher Fe and Mn, which indicate changing composition from dolomite to ankerite.

The average SiO_2 contents of carbonate and carbonate-bearing sandstone samples in the main, middle, and upper carbonate sections are 37 ± 18, 42 ± 12, and 29 ± 15 wt. %, respectively. Petrographic studies (Siahi et al., 2016) and microprobe analysis revealed that SiO_2 is hosted by detrital grains and secondary silica phases. SiO_2 concentrations have a positive correlation with Al_2O_3 concentrations in the middle section (R^2 = 0.94) and upper section (R^2 = 0.70), which is indicative of the dominance of Al-bearing silicates over chert and quartz, while they have weak positive correlation in the main section indicative of dominance of chert and quartz over Al-bearing silicates (Fig. 5). The average Al_2O_3 and K_2O contents of carbonate and carbonate-bearing sandstone samples from the main, middle and upper carbonate sections are 2.3 ± 1.7 and 0.78 ± 0.7 wt. %, 6.7 ± 3.4 and 2.5 ± 1.4 wt. %, and 4.5 ± 3.7 and 1.9 ± 1.4 wt. %, respectively. There is a strong positive correlation between K_2O and Al_2O_3 concentrations (R^2 = 0.98) of samples from the upper carbonate section, in the middle carbonate section (R^2 = 0.99), and in the main carbonate section (R^2 = 0.98), suggesting the presence of detrital K-

feldspar and detrital/ metamorphic K-bearing phyllosilicates (Fig. 6). A similar pattern applies to TiO_2 concentrations (diagram is not shown). The positive correlation of K_2O and TiO_2 concentrations with Al_2O_3 concentrations suggest their association with siliciclastic/ volcaniclastic detritus and secondary minerals, such as sericite and rutile. CaO and MgO concentrations show a strong positive correlation ($R^2 = 0.98$) indicative of the presence of dolomite (not shown). Fe_2O_3 and MnO concentrations correlate positively with CaO and MgO concentrations (not shown), suggesting substitution of these elements for Ca and Mg in the carbonate minerals. Except for the samples from middle carbonate section, Fe_2O_3 and MnO concentrations display moderate to weak positive correlation with CaO and MgO concentrations and weak positive correlation with SiO_2, Al_2O_3 and/or TiO_2 concentrations. This is indicative of an association of Fe_2O_3 and MnO with the carbonate phase, siliciclastic-volcaniclastic detrital material and their metamorphic products, such as chlorite. Strong and moderate positive correlations between Fe_2O_3 concentrations and LOI of samples from the middle ($R^2 = 0.99$) and upper ($R^2 = 0.40$) carbonate sections, respectively, and a weak positive correlation of samples from the main carbonate section ($R^2 = 0.20$) is related to the presence of compositionally homogeneous carbonate phase in the former and more variable carbonate phases in the latter (Fig. 7). The concentration of S (reported as SO_3 in Table A2, Appendix) is mostly below detection limit, suggesting low concentrations of sulphides, except for most samples from the upper carbonate section in which S was detected.

The major-element concentrations of the carbonate components as determined by EPMA are variable in the main, middle and upper carbonate sections and are reported in Table A3 (Appendix). Microprobe analysis of a variety of dolomitic components show that FeO concentrations in samples from the main carbonate section ranges from ca. 0.3 to 5.4 wt. % and MnO concentrations from below detection to 0.7 wt. % (Table A3, Appendix), suggesting the presence of minor amounts of these elements in the dolomite. In the upper carbonate section, the amount of FeO and MnO varies from 0.3 to 5.7 wt. % and from 0.4 to 0.8 wt. %, respectively, indicative of ferroan dolomite. In the middle section, carbonate contains the highest amounts of FeO (0.4-12.03 wt. %) and MnO (0.5-1.7 wt. %) concentrations, and is thus best referred to as ankerite (Table 4).

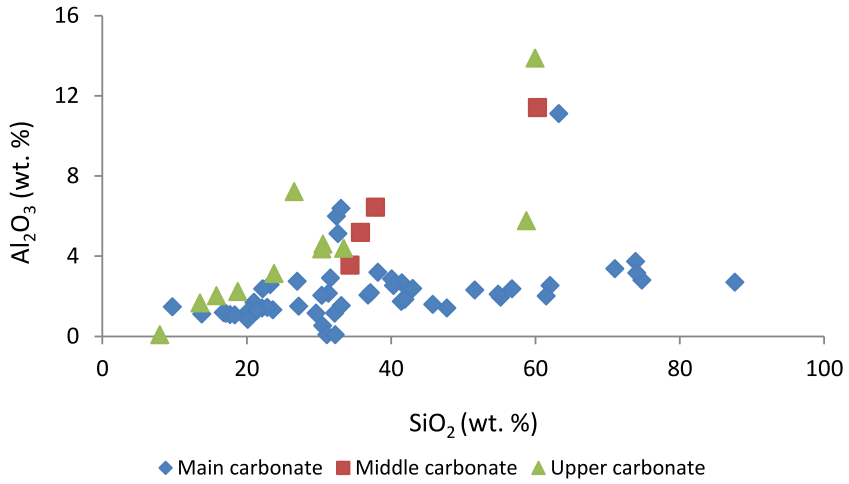

Fig. 5. SiO_2 vs. Al_2O_3 concentrations in carbonate samples from the main, middle and upper carbonate sections. Diagram shows a positive correlation between SiO_2 and Al_2O_3 in the middle and upper carbonate sections. Note that slopes of the correlation are steeper for the middle and upper carbonate sections that reflect a somewhat different mineralogy.

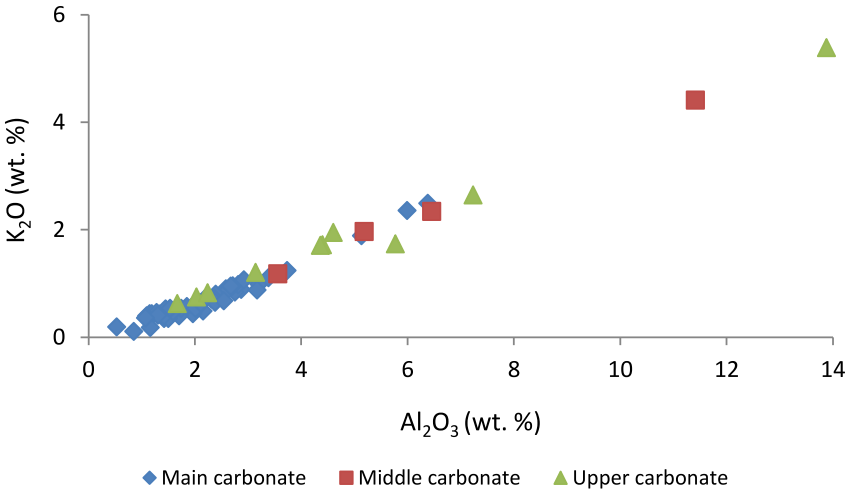

Fig. 6. K_2O vs. Al_2O_3 concentrations in carbonate samples from the main, middle and upper carbonate sections. Diagram shows a strong positive correlation between K_2O vs. Al_2O_3 in the three sections. It also shows higher concentrations of Al- and K-bearing silicates in the middle and upper carbonate sections.

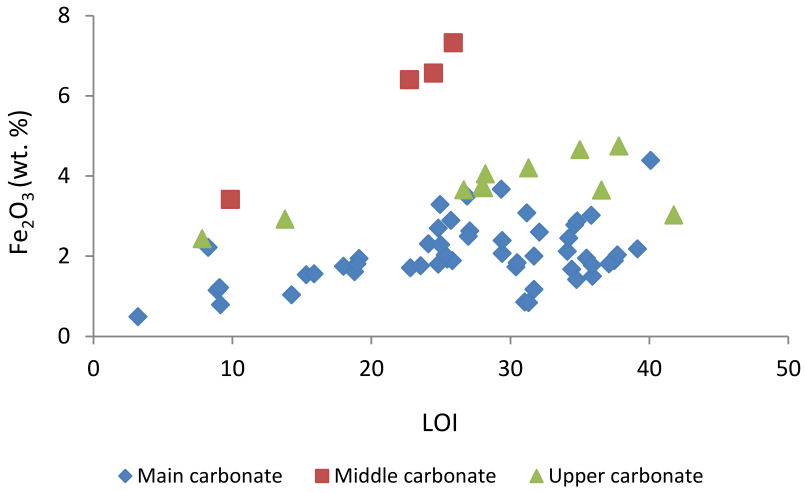

Fig. 7. Fe_2O_3 concentrations vs. LOI in carbonate samples from the main, middle and upper carbonate sections. The diagram shows positive correlation between Fe_2O_3 and LOI in the three sections. There are differences in the Fe content in the different sections.

5.4.2 Trace-elements

The concentrations of the trace-elements in carbonate samples are listed in Table A2. A comparison of the data obtained from the different leaching procedures of sample powders shows that concentrations of most of the alkali and transition metals as well as high field strength elements are higher in samples analysed following whole-rock digestion (HF-HNO_3 acid mixture) in comparison to those subjected to acetic acid leaching targeting carbonate components only. This finding indicates that these trace-elements are mostly hosted in siliciclastic detritus rather in carbonate minerals and leaching samples with weaker acetic acid preferentially targeted carbonate minerals and left siliciclastic materials intact. In the main carbonate section, almost all of the chalcophile, siderophile and lithophile elements are hosted in the non-carbonate phase, and show moderate to strong positive correlation with non-carbonate components (e.g. Al_2O_3) and weak to moderate positive correlation with Fe_2O_3 and MnO. Fe_2O_3 and MnO are in association with clay minerals due to the presence of moderate to strong positive correlation between Fe_2O_3 and MnO with Al_2O_3. In the upper and middle carbonate sections, chalcophile, siderophile and most of the lithophile (REEs, alkali metals and alkali earth metals) elements are hosted in carbonate phase (e.g. CaO) and show weak to moderate positive correlation with its components (diagram is not shown). The presence of

chalcophile elements hosted in carbonate phase may suggest that sulphides are associated with the carbonate phase.

Trace-element concentrations of digested whole-rock samples mostly show negative correlations with elements hosted in carbonate phase and positive correlation with elements hosted in the non-carbonate phase compared to leached samples that show commonly positive correlation with elements hosted in carbonate phase and negative correlation with non-carbonate-hosted elements. Some of trace-elements are present in both carbonate and non-carbonate phases.

The concentrations of Sr and its mineral host were studied in some detail to reconstruct primary composition of carbonate rocks. The Th/U ratio was used to inspect redox processes with regards to presence or absence of atmospheric O_2. ICP-MS analysis revealed that the Sr concentration is variable in dolomites leached by acetic acid and ranges from ca. 32 ppm in the main carbonate section up to 460 ppm in the upper carbonate section. The average concentration of Sr in the main, middle and upper carbonate sections are 206 ± 136 ppm (n = 13), 53 ± 19 ppm (n = 4), and 156 ± 170 ppm (n=5), respectively. In the main carbonate section, two groups of samples were identified with regard to Sr contents. Samples with high Sr content (Sr > 100 ppm) of this section are mostly from those facies, which were prone to secondary calcitization (e.g. intraclast dolomitic sandstone, sandy oodolarenite and stratiform stromatolite; refer to chapter 4 for more information on secondary calcitization). In the upper and middle carbonate sections, Sr does not show any correlation with trace-elements hosted in carbonate and non-carbonate phases likely due to the small number of samples. There is a strong positive correlation (R^2 = 0.75) between Sr and Ba in the main carbonate section representative of their substitution in Ca position (Fig. 8). The Th/U ratio in the majority of samples of three different sections is higher than 2 and ranges from 0.9 to 8, in which it has an average of 4.3 ± 1.8, 4.2 ± 2 and 3.5 ± 2.3 in the main, middle and upper carbonate sections, respectively. The Th/U ratio is close to the Th/U average in chondrite (4.1 ± 0.1) (Rocholl and Jochum, 1993; Collerson and Kamber, 1999).

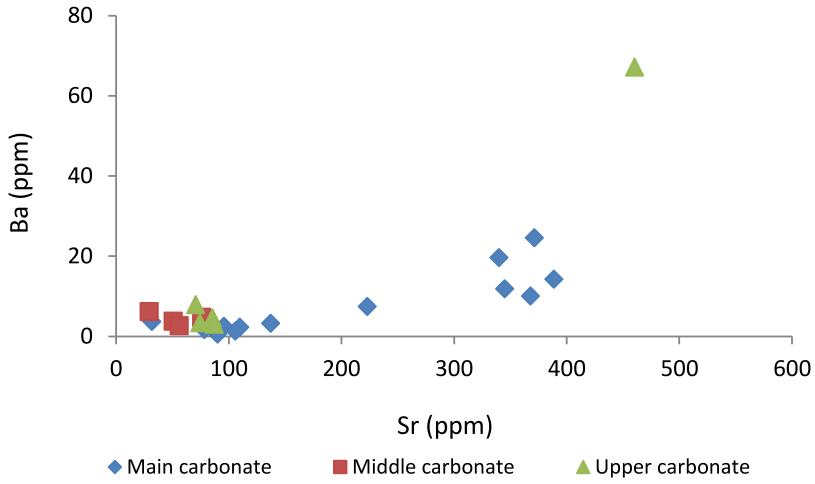

Fig. 8. Ba vs. Sr concentrations in carbonate samples from the main, middle and upper carbonate sections. The diagram shows a positive correlation between Sr and Ba in the main carbonate section and no trends in the middle and upper carbonate sections.

5.4.3 Rare earth elements

The REE + Y data of stromatolitic carbonate samples are listed in Table A2 and shown in shale-normalised diagrams (Fig. 9). Normalized REE + Y data presented in this chapter refer either to shale-normalized (suffix SN, Post-Archaean average Australian Shale, PAAS, after McLennan, 1989) or to chondrite-normalized (suffix CN, CI chondrite after Boynton, 1984) values. It can be seen that samples prepared with different leaching methods show similar REE patterns yet at different concentration levels (Fig. 10). The bulk-digested sample powders have higher ΣREE concentration, slightly flatter patterns and less pronounced anomalies (Fig. 10). Carbonate leached samples that show lower Zr, Th and Ti contents have higher Y/Ho ratios that are representative of less contaminated samples (Kamber et al., 2014). To evaluate the effects of clastic minerals on the REE + Y characteristics in leached samples, Zr was plotted vs. Y/Ho ratio (Fig. 11). It can be seen that Y/Ho ratios in the samples behaves invariant with Zr concentrations in samples from the main and upper carbonate sections. This observation indicates that there is no or negligible influence of clastic materials on the REE patterns for weak acid-leaching of the samples.

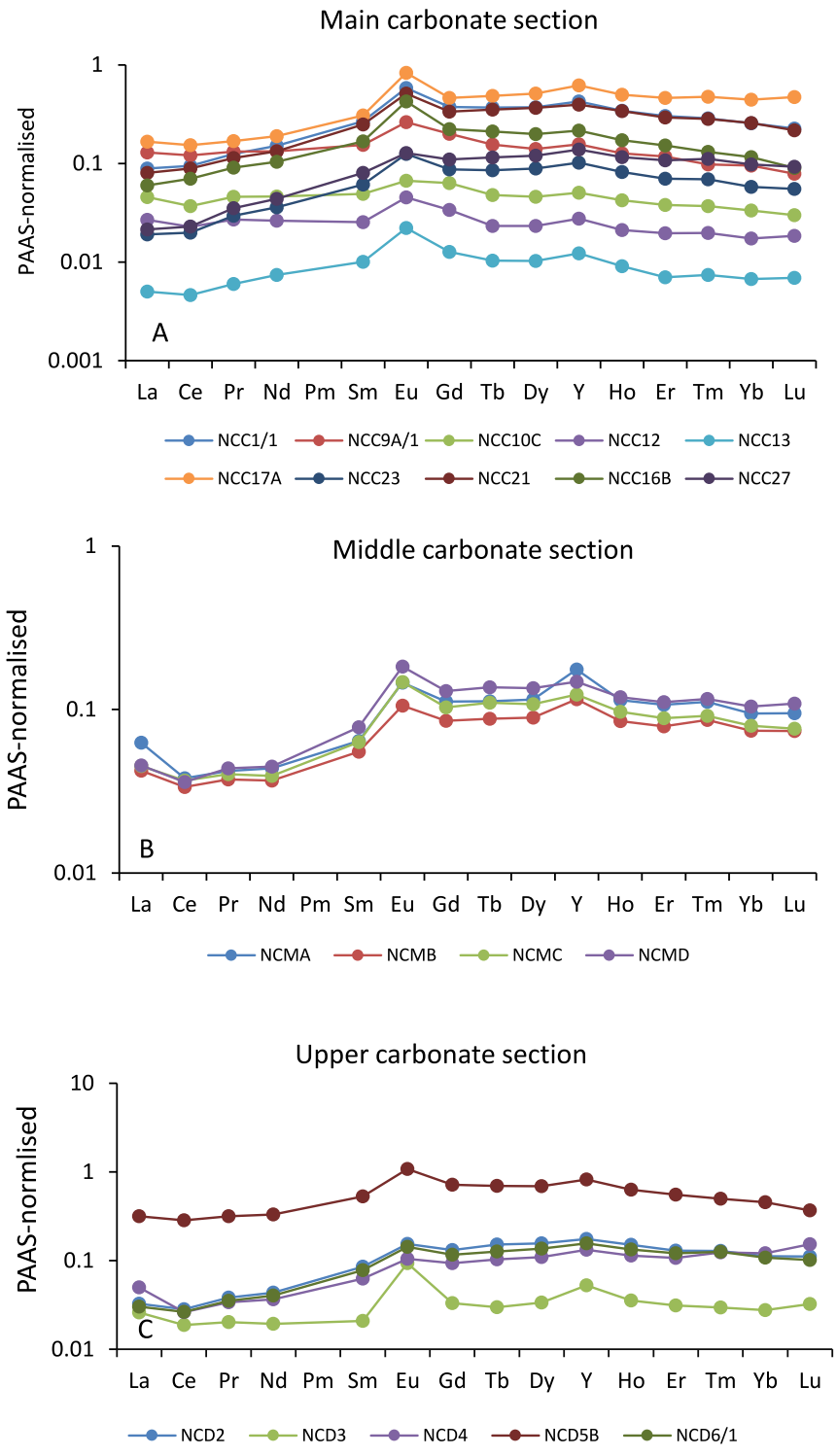

Fig. 9. PAAS-normalized REE + Y data. (A) Carbonate samples from the main carbonate section. (B and C) Carbonate samples from the middle and upper carbonate sections, respectively.

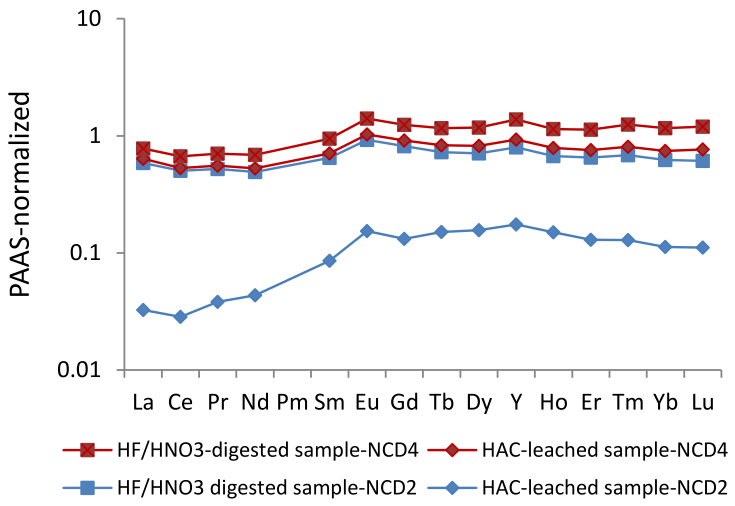

Fig. 10. PAAS-normalized REE+Y data of acid- leached (residues) and whole-rock carbonate sample pairs from the upper carbonate section.

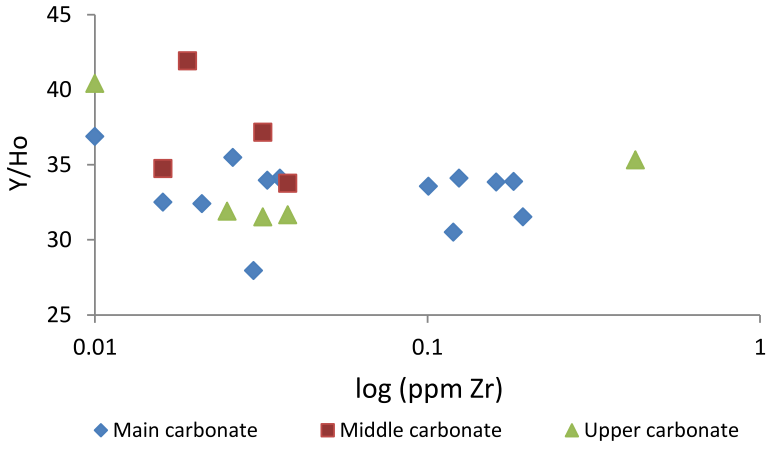

Fig. 11. Zr (log) content vs. Y/Ho ratio from three carbonate sections showing (A) no influence of Zr content on Y/Ho ratio in leached samples.

The concentration levels of REE in the acid-leached samples vary significantly and range from ca. 1 to 64 ppm. The average of the ΣREE in the main, middle and upper carbonate sections is 14.7 ± 11.8, 8.8 ± 0.9 and 18.4 ± 25.4, respectively. The highest REE concentration (~ 64 ppm) was found in a sample of structureless microbialite (sample NCD5B from upper carbonate section). The ΣREE of microbialites is three times higher than those of microbialite samples in the Devonian Caning Basin (~ 20 ppm) reported by Nothdurft et al. (2004). The majority of carbonate rock samples (leached samples) of the Nsuze Group from the three different stratigraphic sections are characterised by enrichment in the middle REEs (MREEs; $(Pr/Tb)_{SN} < 1$ and $(Tb/Yb)_{SN} > 1$))), and depleted light REEs (LREEs) relative to the heavy REEs (HREEs) calculated as [$(Pr/Yb)_{SN} < 1$], except some samples from the main carbonate sections, which show enrichment of LREEs relative to HREEs (Fig. 9). Ce_{SN} anomalies as expressed as [$(Pr/Pr^*)_{SN} = Pr_{SN}/(0.5Ce_{SN} + 0.5Nd_{SN})$] to avoid the influence of anomalous abundances of La (Bau and Dulski, 1996) are either slightly negative $(Pr/Pr^*)_{SN} > 1.05$ up to 1.12 in several samples or absent (Fig.12). A positive La_{SN} anomaly exists for most samples based on the combination of $(Ce/Ce^*)_{SN} < 1$ calculated as [$(Ce/Ce^*)_{SN} = Ce_{SN}/(0.5La_{SN} + 0.5Pr_{SN})$], and $(Pr/Pr^*)_{SN} \leq 1$ suggested by Bau and Dulski, (1996). A positive Gd_{SN} anomaly calculated as [$(Gd/Gd^*)_{SN} = Gd_{SN}/(0.33Sm_{SN} + 0.67Tb_{SN})$] > 1 after Bau and Dulski, (1996) is present in almost all samples (except for NCC15, dololutite-dolarenite facies) and has a value of up to 1.41. Eu_{SN} displays a positive anomaly (e.g. 1.37-2.27 for the main section, 1.60-1.88 for the middle section and 1.40-3.93 for the upper section) calculated as [$(Eu/Eu^*)_{SN} = Eu_{SN}/(0.67Sm_{SN} + 0.33Tb_{SN})$] > 1 after Bau and Dulski, (1996) except for NCC15 sample. Y is elevated relative to Ho in these carbonate rocks, as the average of Y/Ho ratio is 33.4 ± 2.2 for the main section, 36.9 ± 3.6 for the middle section and 34.2 ± 3.7 for the upper carbonate section, which is higher than Y/Ho ratio for chondrite (~ 26-28) but lower than Y/Ho ratio > 44 of Modern seawater (Nozaki et al., 1997; Bolhar et al., 2004). Y/Ho ratio, Gd_{SN} and Eu_{SN} anomalies display positive correlation with elements hosted in carbonate phase (e.g. CaO) from three carbonate sections. The highest Y/Ho ratio is correlated with the highest La_{SN} anomaly.

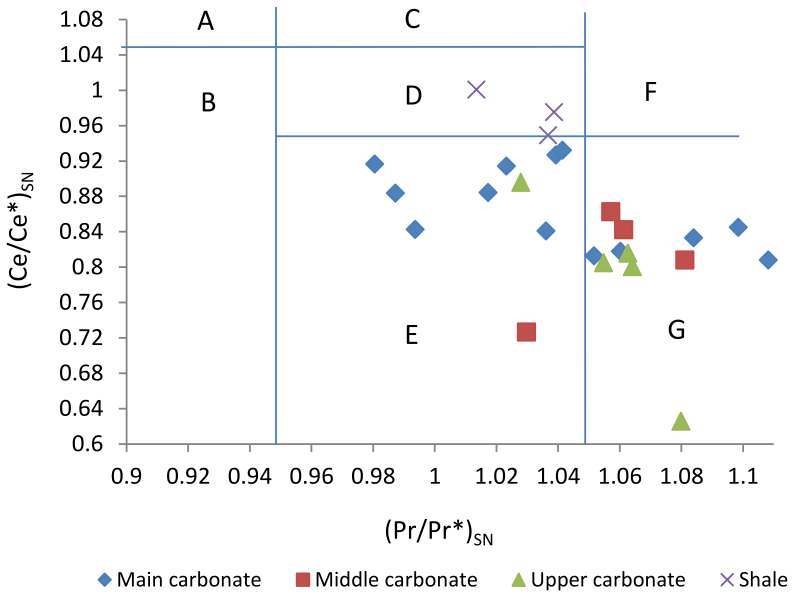

Fig. 12. $(Ce/Ce^*)_{SN}$ vs. $(Pr/Pr^*)_{SN}$ in carbonate rocks of the Chobeni Formation (calculations according to Bau and Dulski, 1996). Field A: positive Ce_{SN} anomaly; field C: negative La_{SN} anomaly, no Ce_{SN} anomaly; field D: neither Ce_{SN} nor La_{SN} anomaly; field E: positive La_{SN} anomaly, no Ce_{SN} anomaly; field G: negative Ce_{SN} anomaly. Note that carbonate samples from three sections fall mainly into fields E and G. Shale samples in the field D do not have Ce_{SN} and La_{SN} anomalies.

5.4.4 Carbon and oxygen isotopes

The $\delta^{13}C$ and $\delta^{18}O$ values of the Chobeni carbonate samples are listed in Table 1 and shown in Fig. 13. The data overlap the range of data for carbonate samples from the study area previously reported by Perry and Tan (1972), Schidlowski et al. (1983), and Veizer et al. (1990). The $\delta^{18}O_{VPDB}$ values from the main, middle and upper carbonate sections range from -19.6 to -11.97 ‰, -19 to -17.4 ‰ and -17.9 to -13.9 ‰, respectively. The $\delta^{13}C_{VPDB}$ values of carbonate samples from the main, middle and upper sections range from 0.12 to 2.40 ‰, 0.10 to 0.40 ‰ and 1.20 to 1.58 ‰, respectively. The highest $\delta^{13}C_{VPDB}$ and $\delta^{18}O_{VPDB}$ values are around +2.4 ‰ and -12 ‰, respectively, and these values were measured in samples from the main carbonate section. The positive correlation between $\delta^{18}O$ and $\delta^{13}C$ of the dataset as a whole suggests that diagenesis/ metamorphism has lowered the δ values.

When plotting the $\delta^{13}C$ and $\delta^{18}O$ values vs. stratigraphic height in the main carbonate section, the bulk samples in the middle of the section (at c. 15 m from the base) show the highest $\delta^{13}C$ and $\delta^{18}O$ values of ca. +2.5 ‰ and -12 ‰, respectively (Fig. 14). The $\delta^{13}C$ and $\delta^{18}O$ values of

micro-drilled samples from polished slabs (Fig. 15) show considerable isotopic heterogeneity on a small scale of the samples (Fig. 14). The average values are generally close to the whole rock value of the same or adjacent sample. The most negative $\delta^{13}C$ and $\delta^{18}O$ values were measured in calcite-filled voids with average $\delta^{13}C$ and $\delta^{18}O$ values of -15.5 ± 0.98 ‰ and -0.4 ± 1.2 ‰ VPDB, respectively.

In the main and upper carbonate sections, $\delta^{18}O$ values display strong positive correlation with $\delta^{13}C$ (Fig. 13). The $\delta^{13}C$ and $\delta^{18}O$ values display weak positive correlation with carbonate phase (CaO, MgO) in the main and upper carbonate sections. In the main carbonate section, $\delta^{13}C$ and $\delta^{18}O$ values display moderate negative correlation with Al_2O_3 (Fig. 16). In the main carbonate section, $\delta^{13}C$ and $\delta^{18}O$ values show moderate to strong positive correlation with Gd and Pr anomalies. The $\delta^{13}C$ and $\delta^{18}O$ of carbonate samples from the upper section display moderate to strong positive correlation with Y/Ho, Eu and Gd anomalies.

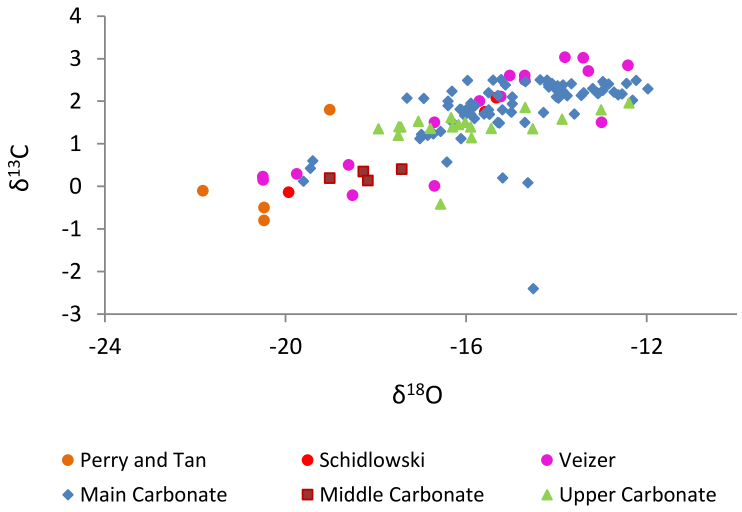

Fig. 13. The $\delta^{13}C$ vs. $\delta^{18}O$ values for the Mesoarchaean stromatolitc carbonate samples from main, middle and upper carbonate sections of the Chobeni Formation. Data of Perry and Tan (1972), Schidlowski et al. (1983) and Veizer et al. (1990) are plotted for comparison.

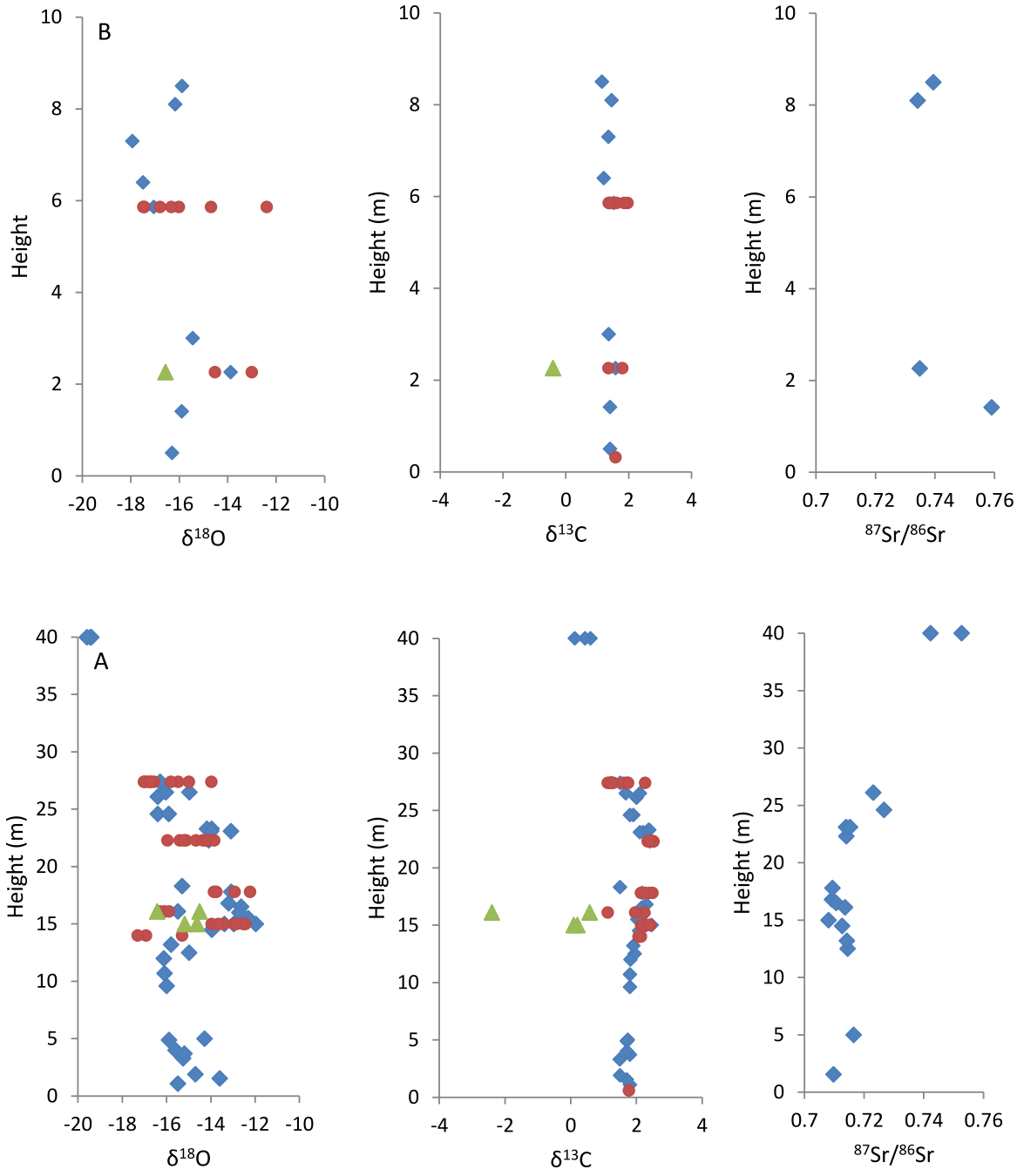

Fig. 14. The $\delta^{13}C$, $\delta^{18}O$ and $^{87}Sr/^{86}Sr$ values vs. height (m) from two main (A) and upper (B) carbonate sections of Chobeni Formation. Results from the two measured sections of the main carbonate section (Fig. 2) have been combined. Note samples in the middle of main carbonate section display more positive $\delta^{13}C$ and $\delta^{18}O$ values. Blue diamonds are bulk samples, red spots are micro-drilled dolomite samples from polished slabs and green triangles are micro-drilled calcite.

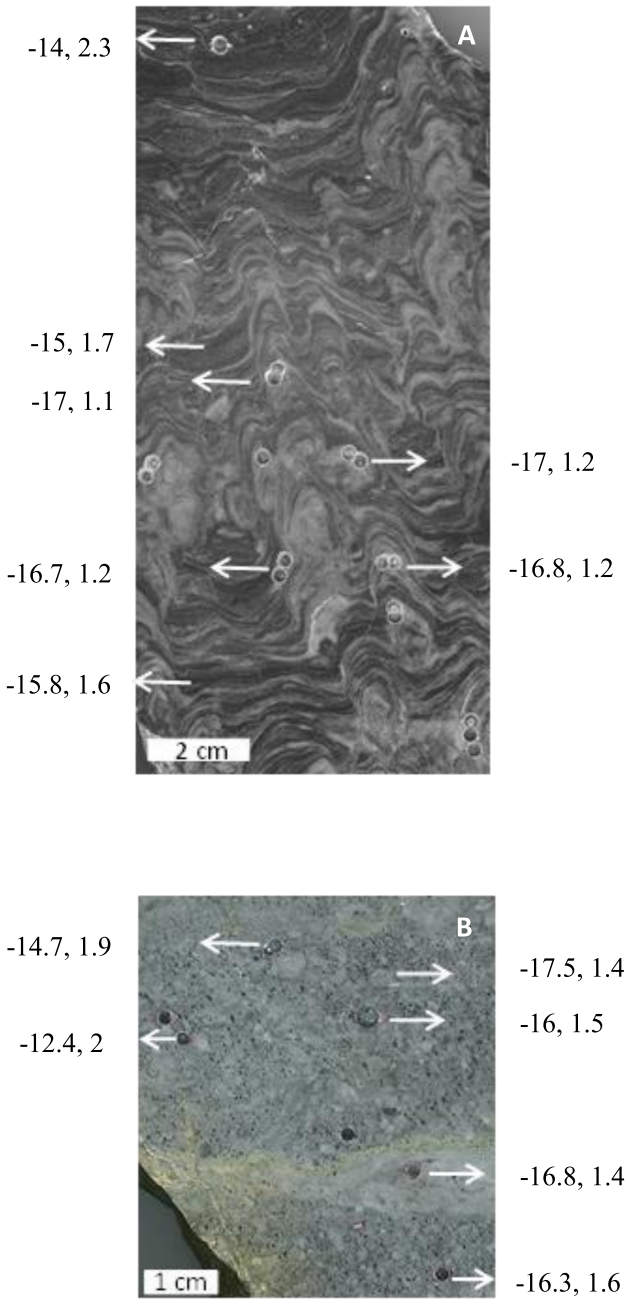

Fig. 15. Photographs of polished slabs showing $\delta^{18}O$ (left) and $\delta^{13}C$ (right) values for micro-drilled samples of different laminae of conical-columnar stromatolite, main carbonate section, sample NCC16B (A), and sandy oolitic intradolorudite, upper carbonate section, sample NCD4 (B). In (A) the dark laminae consist of dolomite with minor carbonaceous matter whereas light laminae show silicification.

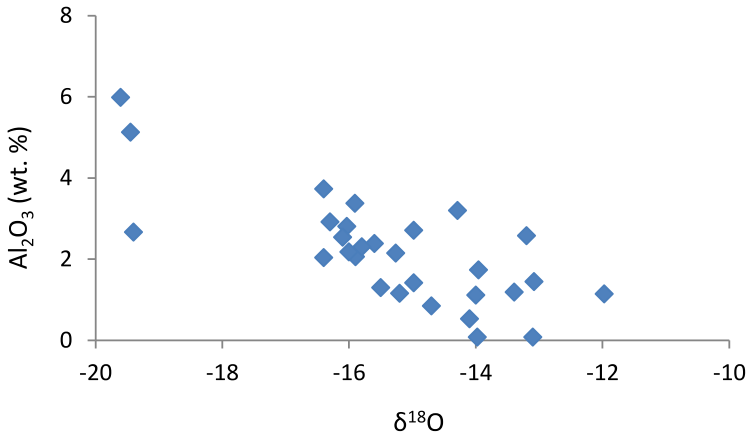

Fig. 16. Al_2O_3 concentrations vs. $\delta^{18}O$ values in carbonate samples from the main carbonate section. The diagram shows a moderate negative correlation ($R^2 = 0.6$) between Al_2O_3 concentrations and $\delta^{18}O$.

5.4.5 Strontium isotope compositions

The $^{87}Sr/^{86}Sr$ ratios of stromatolitic carbonate bulk samples of the main carbonate section range from 0.708 to 0.753 (n = 16), those of the middle carbonate section range from 0.772 to 0.777 (n = 2), and those of the upper carbonate section range from 0.734 to 0.759 (n = 3). The least radiogenic $^{87}Sr/^{86}Sr$ ratio of 0.70803 was obtained from a sample of a stratiform stromatolite facies of the main carbonate section. This sample shows the highest $\delta^{13}C$ and $\delta^{18}O$ values of all samples (Fig. 14A). In the main and upper carbonate sections, strontium isotope displays negative correlation with $\delta^{13}C$ and $\delta^{18}O$ values (Figs. 17A and B), and a positive correlation with Al_2O_3 representing Al-bearing silicates such as clay, which can explain the radiogenic Sr in samples showing high Al_2O_3 (Fig. 17C). In the main and upper carbonate sections, $^{87}Sr/^{86}Sr$ ratios display a positive correlation with both K_2O and Al_2O_3 (Fig. 17C, 18) consistent with a secondary Sr component derived from Rb (K)-rich Al-bearing silicates.

5.5 Discussion

Physico-chemical conditions of the hydrosphere may be recorded in the chemical and isotopic composition of chemical precipitates such as carbonate rocks at the time of deposition (Faure, 1982; Veizer, 1983b; Kamber et al., 2014). In order to obtain original chemical and isotopic composition of carbonates in equilibrium with the coeval seawater, it is essential to assess and eliminate post-depositional modification. The original unstable mineral assemblage of

carbonate sediments, such as aragonite and high Mg-calcite, transform into the more stable low-Mg calcite via dissolution-reprecipitation processes during meteoric and/or burial diagenesis (Veizer, 1992; Hoefs, 1997), and metamorphic alteration (e.g. Dipple and Ferry, 1992), which overprint the primary chemical and isotopic composition. We will discuss the possible primary composition of these carbonates and effects of diagenesis and metamorphism on their primary signatures.

5.5.1 Major and trace-elements

In order to evaluate the degree of alteration, the study of the preservation of primary textures along with major and trace-element covariance patterns is useful. Increasing levels of diagenetic alteration during meteoric and burial diagenesis may be accompanied by the loss of Sr, Mg, Ba, U and gain of Mn and Fe (Brand and Veizer, 1980; Veizer, 1983a, b; Moore, 1985; Prezbendowski, 1985; Webb et al., 2009). Indeed, the samples that have been altered the most, i.e. those of the middle carbonate section, appear to have gained appreciable amounts of Fe and Mn, resulting in their conversion to ferroan dolomite. However, dolomite is the dominant sedimentary carbonate mineral of Archaean carbonates in general, and Chobeni Formation carbonates in particular, which contain an order of magnitude higher Mn and Fe concentrations compared to their Phanerozoic counterparts with a comparable degree of preservation (Veizer et al., 1989a; Veizer et al., 1990). These differences are not necessarily a result of post-depositional alteration phenomena only. The higher amounts of Fe and Mn in Archaean carbonate rocks are generally ascribed to high concentration of Mn^{2+} and Fe^{2+} in the mainly anoxic Archaean oceans, which became incorporated into the carbonate structure (Bekker et al., 2014).

Veizer et al. (1990) suggested that aragonite was the primary mineral of the Pongola carbonate rocks based on relatively high average Sr contents (~ 220 + 120/- 80 ppm). This value is close to the average Sr content obtained from the main carbonate section, while the other more altered sections show lower Sr values. However, it is important to note that samples with the highest amount of Sr from the main carbonate section are those, which were prone to secondary calcitization. High Sr contents were observed in calcite-filled voids and samples with calcitized components (refer to Chapter 4 for more information on secondary calcitization).

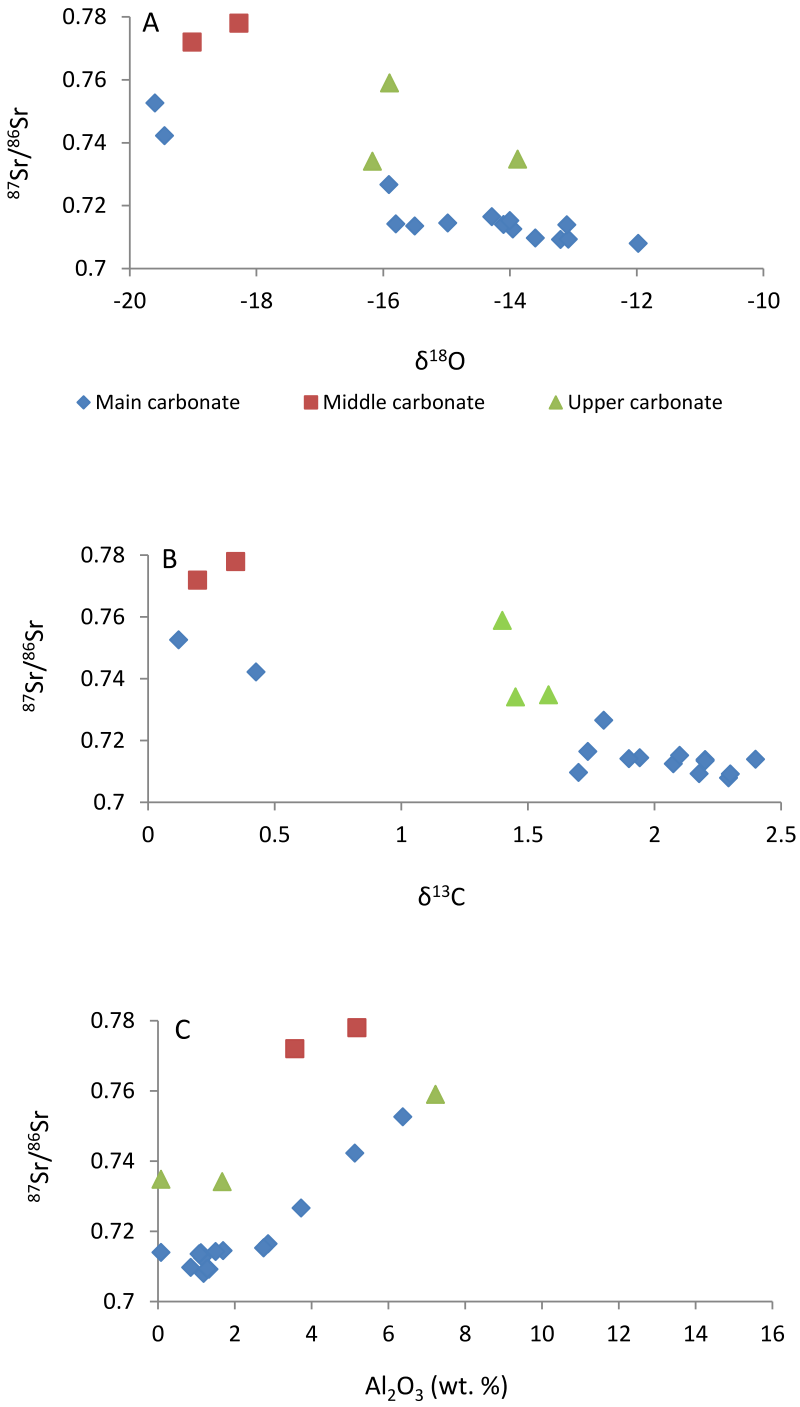

Fig. 17. $^{87}Sr/^{86}Sr$ ratios vs. (A) $\delta^{18}O$, (B) $\delta^{13}C$ values and (C) Al_2O_3 concentrations from the main, middle, and upper carbonate sections. The $^{87}Sr/^{86}Sr$ ratios show negative correlation with $\delta^{13}C$ and $\delta^{18}O$ values and a positive correlation with Al_2O_3 concentrations from the main and upper carbonate sections.

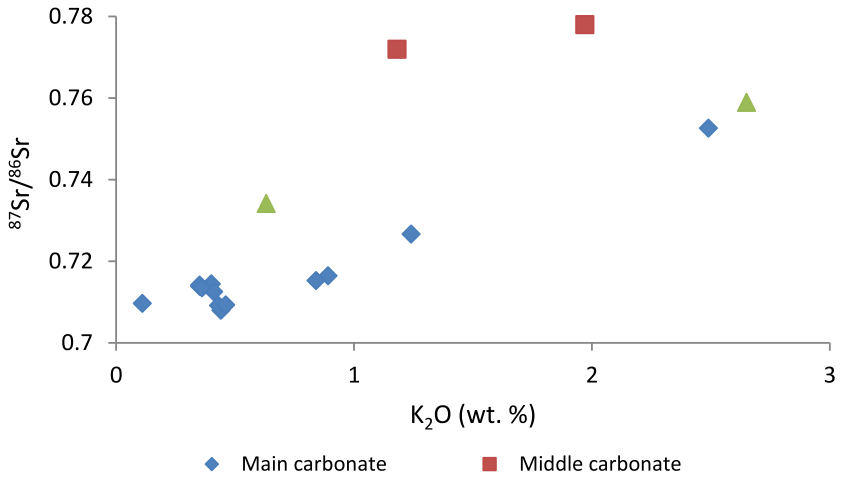

Fig. 18. $^{87}Sr/^{86}Sr$ ratios vs. K_2O concentrations in carbonate samples from the main, middle, and upper carbonate sections. The diagram shows positive correlation between $^{87}Sr/^{86}Sr$ ratios and K_2O concentrations from the main and upper carbonate sections.

Diagenesis plays an important role in Sr redistribution. Different carbonate minerals react differently during diagenesis. The recrystallization of aragonite leads to the loss of primary fabric and Sr due to complete dissolution or neomorphic transformation to calcite with lower Sr contents (e.g. Maliva, 1998). Recrystallization thus results in an increase in the concentration of Sr in pore waters, from which high Sr cements may precipitate (Pingitore, 1976; Singh, 1987), explaining the elevated Sr concentrations of secondary calcite in some samples. However, the variable Sr content within the main carbonate section could also be a result of coexistence of both calcite and aragonite as primary mineral phases. Sr and Ba can substitute for Ca in the aragonite lattice (Tucker and Wright, 1990), which may explain the positive correlation between these two elements (Fig. 8).

In addition to recrystallization and neomorphism, the carbonates were subjected to dolomitization. The timing of dolomitization is the most important factor in determining the dolomite Sr content. Early dolomitization of metastable marine carbonates (aragonite and/or HMC) will result in Sr-rich dolomite (> 100 ppm), whereas later dolomitization of marine carbonates, which may have undergone stabilization to diagenetic LMC, leads to the formation of Sr-poor (< 100 ppm) coarsely crystalline dolomites with significant amounts of Fe and Mn (Veizer et al., 1978; Tucker and Wright, 1990). In addition, a higher degree of recrystallization leads to a coarser crystal size and a decrease in Sr concentration (Dunham and Olson, 1980;

M'Rabat, 1981). Therefore, mimetic replacement of pre-existing metastable carbonates into non-stoichiometric, Ca-rich and poorly ordered dolomite during early diagenesis is another viable option for the formation of carbonate rocks from the main section with higher amount of Sr and better level of preservation, compared to the less-preserved carbonate rocks from the upper and middle sections with coarser crystal size, lower Sr contents and higher Fe and Mn contents of probably metastable carbonates, which experienced later dolomitization during burial diagenesis (Dawans and Swart, 1988; Sibley, 1991; Gregg et al., 1992). The high amount of FeO and MnO in the upper, middle and some samples of main carbonate sections are probably introduced to pore fluids during burial diagenesis. This statement does not reject the presence of reducing conditions in the time of carbonate precipitation and the presence of high amounts of dissolved Fe^{+2} and Mn^{+2} in seawater.

U is a redox-sensitive metal that can be used as a proxy to track reducing conditions. Uranium can be removed from solution onto particle surfaces from seawater as insoluble U^{4+} under reducing conditions, and can be preserved in the sediment, whereas under oxidizing conditions, it is converted to the soluble uranyl (U^{6+}) ion, which is removed in solution (Morford and Emerson, 1999; Algeo and Maynard, 2004; Brennecka et al., 2011). On the other hand, Th has only one redox state (Th^{4+}) and its concentration in sediments is not controlled by redox processes. Therefore, the Th/U ratio can be used as a proxy for ocean redox chemistry. In anoxic sediments, the Th/U ratio is below 2, while ratios above 2 may indicate oxic conditions (Myers and Wignall, 1987; Wignall and Twitchett, 1996). The Th/U ratio is > 2 for the majority of samples of all sections (except in sandy intradolorudite facies), which could indicate the presence of some oxygen at the time of carbonate precipitation.

5.5.2 Oxygen and carbon isotopes

The oxygen isotope composition of carbonates has been used to reconstruct the isotopic composition of seawater and/or the temperature at the time of their precipitation (e.g. Vasconcelos et al., 2005). It is also a sensitive indicator of the degree of diagenesis, as the least altered samples in a sedimentary succession show the highest $\delta^{13}C$ and $\delta^{18}O$ values (Brand and Veizer, 1980; Kaufman and Knoll, 1995).

Carbonates of the three sections probably underwent different degrees of diagenetic overprint, because of differences in stratigraphic position, host rocks and thus diagenetic fluid

chemistries, resulting in different levels of chemical and textural alteration. Meteoric diagenesis almost always lowers both $\delta^{13}C$ and $\delta^{18}O$ values of marine carbonate (Killingley, 1983; Kaufman and Knoll, 1995; Fairchild and Kennedy, 2007). The recrystallization at the elevated temperatures during deep burial diagenesis causes progressively lower $\delta^{18}O$ values compared to the earlier meteoric alteration but not at the same rate with $\delta^{13}C$ (Anderson and Arthur, 1983; Choquette and James, 1987; Reinhold, 1998; Fu et al., 2006; Mabrouk et al., 2006). The $\delta^{13}C$ values of carbonate rocks that undergo burial diagenesis usually remain constant (Zenger, 1983; Tucker and Wright, 1990; Gao and Land, 1991). The reason is that a major component of diagenetic fluids is oxygen, whereas carbon is a trace component (Brand and Veizer, 1981; Veizer et al., 1989a; Marshall, 1992; Sharp, 2007).

In general, carbonate rocks of the main section have the highest $\delta^{18}O$ and $\delta^{13}C$ values (Fig. 13), which is in line with better fabric preservation compared to those of the middle and upper sections with the lowest values (Siahi et al., 2016). In the main section, the highest $\delta^{13}C$ and $\delta^{18}O$ values were obtained from samples in the central part (Fig. 14). This may be explained by these samples having lower silicate components compared to their surrounding samples (Fig.16), as a high intensity of silicate-water exchange at low temperature could have resulted in depletion of the ocean in $\delta^{18}O$ (Perry et al., 1978; Veizer et al., 1982). The higher values of $\delta^{13}C$ and $\delta^{18}O$ of the main and upper carbonate sections, which have positive correlation with elements hosted in carbonate phase, compared to stable isotopes from middle section, which display positive correlation with elements hosted in non-carbonate phase probably indicates that primary isotopic values are better preserved in more pure carbonates. Apart from interaction with siliciclastic materials, late dolomitization of diagenetic stable carbonate during burial diagenesis led to a decrease of primary isotopic signatures of the middle and to a lesser extent upper carbonate rocks in comparison to the main carbonate rocks, which experienced early dolomitization with minor impact of siliciclastic materials on its isotopic signatures.

A considerable spread in the $\delta^{18}O$ and to a lesser extent in the $\delta^{13}C$ values between whole rock samples and micro-drilled sub-samples is present (Fig. 14). The average of $\delta^{18}O$ and $\delta^{13}C$ values of sub-samples (-16.1 ± 1 ‰, 1.5 ± 0.4 ‰) is close to those of whole rock samples (-16.3 ‰, 1.5 ‰) in the stromatolitic facies of the main carbonate section (Fig. 15A). There are differences between $\delta^{18}O$ and $\delta^{13}C$ values among drilled samples. For instance, the presence of different isotopic values between dark and light laminae (Fig. 15A), which are probably a result of differences in their primary composition and absence/ presence of siliciclastic materials. For instance, lower $\delta^{18}O$ and $\delta^{13}C$ values are present from lighter bands in conical stromatolite,

which are silicified, compared to the darker bands, which are mostly dolomite and contain carbonaceous matter (Fig. 15A). The preferentially silicification of one set of laminae over the other could be a result of differences in their chemical composition and/or mechanism of their formation (biotical vs. abiotical). The O and C isotopic differences between average of sub-samples (-15.9 ± 1.8 ‰, 1.6 ± 0.24 ‰) and whole rock sample (-17.06 ‰, 1.5 ‰) of sandy oolitic intradolorudite facies (Fig. 15B) of upper carbonate section are due to the presence of particles from different sites with possible primary isotopic variation and variable degree of alteration, which probably brought to the site by high-energy currents. There are apparent differences in average of $\delta^{18}O$ and $\delta^{13}C$ values between sub-samples and whole-rock samples, in case of calcite-filled voids, which display the $\delta^{18}O$ and $\delta^{13}C$ values least enriched in the heavy isotopes. The depletion of ^{13}C and especially ^{18}O isotopes probably occurred during post-depositional interaction with meteoric water.

Taken together, the light $\delta^{18}O$ values of the Pongola carbonate rocks may be attributed largely, to alteration of metastable carbonates and exchange with siliciclastic and volcaniclastic components during meteoric/ burial diagenesis and greenschist facies metamorphism. The $\delta^{13}C$ values of the Pongola carbonate rocks probably are largely inherited from sedimentary carbonate precursor, which reflects the $\delta^{13}C$ value of dissolved inorganic carbon (DIC) of seawater. The best estimates of $\delta^{13}C$ and $\delta^{18}O$ values for the "least altered samples" of the Pongola carbonate rocks are +0.9 ± 2.1 and -6 ± 1 ‰ PDB, respectively (Veizer et al., 1990), which display better preserved $\delta^{18}O$ and $\delta^{13}C$ values compared to the least altered Pongola $\delta^{13}C$ and $\delta^{18}O$ values (+2.5 and -11.97 ‰ PDB, respectively) in this study. Therefore, $\delta^{18}O$ and $\delta^{13}C$ of the Pongola samples are not representative of Archaean seawater due to the post-depositional alteration.

5.5.3 Strontium isotope compositions

The Sr isotopic composition of modern seawater is controlled by several factors including 1) river influx of radiogenic Sr derived from the weathering of continental crust; 2) mantle influx (Sr derived from interaction of hydrothermal fluids with basaltic oceanic crust); and 3) flux of Sr derived from diagenetic recrystallization of old carbonate sediments into groundwater and its flow to the ocean (Veizer and Compston, 1976; Lawrence et al., 1979; Wadleigh et al., 1985). In the Archaean there was a different situation as compared to younger times, such as paucity of Sr flux from diagenesis of older carbonate rocks, relatively young rocks with low

radiogenic Sr, intense volcanic activity and the small Sr flux from the weathering of continental silicates, which resulted in less radiogenic Sr input into the ocean (e.g. Godderis and Veizer, 2000). The average Sr isotopic composition of present seawater is 0.7092 (McArthur, 1994), which is controlled by river flux with Sr isotopic composition of 0.711 and mantle flux with $^{87}Sr/^{86}Sr$ ratio of 0.703, respectively (Veizer, 1984; Goldstein and Jacobsen, 1987; Palmer and Edmond, 1989). It was suggested that prior to ~ 2.8 ± 0.2 Ga ago, the Sr composition of Archaean seawater was mantle-like, which is reflected in near-mantle Sr isotopic ratio of carbonate rocks with negative $\delta^{18}O$ value and high Mn and Fe contents (Veizer et al. 1989b, 1990; Godderis and Veizer, 2000). The least radiogenic Sr isotopic ratio of ~0.70305 in Pongola carbonates was measured on a sample from the Buffalo River gorge inlier by Eglington et al. (2003). It is similar to that in the depleted mantle and implies formation from a mantle-buffered open- seawater. The least radiogenic Sr isotopic ratio of Pongola carbonate samples from the White Mfolozi inlier is ~ 0.712 and has been reported by Veizer et al. (1982). The radiogenic Sr isotopic ratio of carbonate rocks in the White Mfolozi inlier thus could be due to carbonate deposition within an intracratonic, non-marine environment (Veizer et al., 1982), or be a result of sample alteration during low- grade metamorphism (Veizer et al., 1990). The least radiogenic $^{87}Sr/^{86}Sr$ ratio from the main carbonate section is about 0.708, from a sample with heaviest $\delta^{18}O$ and $\delta^{13}C$ values thus indicating low degrees of alteration (Figs. 17A-B). It is commonly assumed that the least radiogenic Sr isotope ratio obtained from a carbonate succession represents the most reasonable estimate of its coeval seawater isotopic composition (e.g. Mirota and Veizer, 1994). However, our "best" $^{87}Sr/^{86}Sr$ ratio (~ 0.708) is higher than that expected for Archaean seawater, if it indeed was characterized by a mantle-like isotopic signature. Problems with this interpretation have been highlighted previously (Gibbs et al, 1986; Lawrence et al., 1979) due to aspects of differences in provenance and alteration. The primary isotopic signature of the carbonate rocks has been overprinted during burial diagenesis and metamorphism as a result of exchange with siliciclastic materials. Even samples with the best level of preservation have been altered, thus the primary value must have less than 0.708. The most radiogenic Sr isotopic composition (~ 0.777) was found in a sample with the highest component of clastic material ($Al_2O_3 \approx 11.4$ wt. %), (Fig. 17C), supporting isotopic exchange with a non-carbonate clastic component during deep burial diagenesis (Wadleigh et al., 1985; Veizer et al., 1990). The positive correlation between $^{87}Sr/^{86}Sr$ ratio and relative potassium content (Fig. 18) could have been a result of potassium-rich minerals presence, which may contain sufficient rubidium to cause measurable enrichment in radiogenic ^{87}Sr (Peterman and Hedge, 1971; Faure and Powell, 1972).

The relatively high Sr isotopic ratios of the Pongola samples may have been caused by different factors. The extraction of Sr for isotopic measurements involved acid leaching of the carbonate samples, which may have resulted in contamination by partial digestion of clay minerals, particularly when bulk rocks were digested, although acetic acid was applied in order to minimize contamination by siliciclastic materials.

The Sr isotopic composition of the Pongola carbonate rocks may not necessarily need to reflect Archaean seawater composition, as they were deposited in a shallow-water epicontinental basin with restricted exchange to the ocean and dominated fluvial input as discussed by Bolhar et al. (2015). Nd isotope data of iron formation stratigraphically above the carbonate rocks investigated here are also consistent with a continental rather than an open ocean source for solutes of the Pongola epicontinental sea (Alexander et al., 2008).

5.5.4 Rare earth elements

Chemical sediments record the trace-element geochemical signatures of the coeval fluids they have been in equilibrium with during their precipitation (e.g. Kamber et al., 2014). The absolute and relative concentrations of REEs in ocean waters reflect different input such as river flux and aeolian transport (Elderfield, 1988; Goldstein and Jacobsen, 1988a, b), hydrothermal alteration of oceanic crust (e.g. Michard and Albarede, 1986), and input from sediments as a result of diagenesis (e.g. Elderfield, 1988; Derry and Jacobsen, 1990). The study of REEs of chemical precipitates such as carbonate rocks is a useful tool to address different aspects relating to the reconstruction of the depositional environment, such as freshwater vs. marine settings (e.g. Bolhar and Van Kranendonk, 2007), the scale of hydrothermal input (e.g. Derry and Jacobsen, 1990; Allwood et al., 2010), and redox conditions (De Baar et al., 1988; Elderfield, 1988; Kato et al., 2002). It may also allow to distinguish between primary precipitates vs. secondary replacement products by determining the level of alteration and contribution of different sources such as continental, marine and hydrothermal fluxes (e.g. Kamber et al., 2014; Bolhar et al., 2015). The primary distribution pattern of REEs in many carbonates has survived irrespective of their age, provenance, post-depositional processes, and metamorphic grade (e.g. Bau and Möller, 1993; Webb et al., 2009).

The detrital and authigenic components (e.g. clastic and volcanic detritus, oxides and sulphides) disturb the primary signal as these may be enriched in REE + Y more than two

orders of magnitude compared to seawater precipitates (Bau, 1993; Bolhar et al., 2015). Nevertheless, the similarity of REE patterns between leached and complete digested samples argue against an overwhelming influence of detrital materials on REE patterns (Fig. 10). The microbialites of the Chobeni Formation show high REE concentrations similar to the Late Devonian and Holocene reefal microbialites (Webb and Kamber, 2000; Nothdurft et al., 2004), which propbably indicate that Chobeni microbialites may have concentrated REEs in the $CaCO_3$ lattice more efficiently and/or it could be due to the trapped siliciclastic materials within microbialites.

Almost all samples have superchondritic Y/Ho ratio with highest value of 42. It was suggested that samples with the highest Y/Ho ratio have a composition closest to seawater (e.g. Allwood et al., 2010). Yttrium has similar chemical characteristics to Ho (e.g. Bau and Dulski, 1995; Bau, 1996), but displays different complexation properties in aqueous solutions, in which Ho is scavenged on particulate matter two times faster than Y, resulting in super-chondritic Y/Ho ratio expressed as a prominent positive Y anomaly in shale-normalized REE + Y distribution pattern in seawater (Bau et al., 1995; Bau and Dulski, 1996, 1999; Nozaki et al., 1997).

A positive La_{SN} anomaly is another indicator of marine REE signatures (e.g. Bau and Dulski, 1996) and is present in the Pongola carbonate rocks indicating preservation of marine REE signatures (Fig. 12). The positive La_{SN} anomaly is a result of higher stability of La in seawater and its longer oceanic residence time among those of its light and middle REEs neighbours (Alibo and Nozaki, 1999). The samples with the highest Y/Ho ratio, which is correlated with the highest La_{SN} anomaly have the closest signature to that of Archaean open seawater, while those with less pronounced and/or absent Y/Ho ratio and La_{SN} anomaly are suggested to be contaminated with clastic and volcaniclastic detrital or represent deposition during estuarine mixing with open seawater (Allwood et al., 2010). A positive Gd_{SN} anomaly is another common feature of seawater (e.g. Bau et al., 1997; Alibo and Nozaki, 1999). De Baar et al. (1985a) suggested that the positive Gd_{SN} anomaly is related to the high stability of Gd in seawater relative to neighbouring REE(III)s during scavenging.

Archaean chemical sediments, such as detritus-free iron formations, display $Eu_{SN} > 1$ due to more intense hydrothermal activity, fluids of which are enriched in Eu under high-temperature (> 250 ºC) conditions (De Baar et al., 1985b; Derry and Jacobsen, 1988, 1990; Elderfield, 1988; Bau and Dulski, 1996). The $Eu_{SN} > 1$ (positive Eu_{SN} anomaly) from three different sections

indicates elevated high temperature (> 250ºC) hydrothermal flux into seawater, which is characteristic for all Archaean chemical precipitates.

The enrichment of HREEs relative to the LREEs in the open ocean is due to the HREEs forming stronger complexes with dissolved ligands such as [CO_3^{2-}] (e.g. Cantrell and Byrne, 1987) and organic compounds (e.g. Stanley and Byrne, 1990) in solution compared to the LREEs, which results in preferentially release of HREEs into solution during weathering of source rocks and the preferential uptake and removal of LREEs onto particle surfaces from solution relative to HREEs (Elderfield, 1988; Byrne and Kim, 1990; Elderfield et al., 1990; Bau and Möller, 1992, 1993; Koeppenkastrop and De Carlo, 1992; De Carlo and Green, 2002). Bau and Möller (1993) suggested that HREEs enrichment was more pronounced in seawater during the early Precambrian than present day due to the higher availability of active ligands like [CO_3^{2-}] in Early Precambrian coastal and river waters and/or redox cycling of the REEs at an ocean-wide chemocline separating anoxic bottom water masses from slightly oxygenated surface waters. The enrichment of LREEs relative to HREEs are reported from of the Archaean stromatolitic carbonates from Zimbabwe, which reflects deposition in a restricted basin dominated by continental sources (Kamber et al., 2004). Therefore, enrichment of LREEs compared to HREEs in several samples from the main carbonate section is probably a result of their deposition in near-shore seawater under control of terrestrial water.

MREEs are enriched relative to HREEs and LREEs in the Pongola carbonate rocks. Organic-based colloidal fractionation in rivers, coastal seas and estuaries may be responsible for MREE enrichment in such waters (Elderfield et al., 1990; Sholkovitz, 1995). The presence of microbial communities, evidenced by as stromatolitic carbonates, may have contributed to the development of MREE enrichment by providing organic complexation as it was suggested in other studies (Alexander et al., 2008; Bolhar et al., 2015). The other reason for the convex REE pattern could be due to colloidal fraction carried by rivers and fractionation during estuarine mixing (Elderfield et al., 1990; Alexander et al., 2008; Bolhar et al., 2015). This would be consistent with the inferred depositional setting of the Pongola carbonate rocks in an epicontinental shallow marine environment with riverine influx (e.g. Bolhar et al., 2015; Siahi et al., 2016).

The Mesoarchaean Pongola carbonate rocks show characteristics typical of Archaean seawater, including the depletion of LREE vs. HREE (Pr/Yb < 1), a superchondritic Y/Ho ratio (> 30), positive Eu_{SN}, La_{SN}, Y_{SN} and Gd_{SN} anomalies (Derry and Jacobsen, 1990; Kamber and Webb,

2001; Bolhar et al., 2004; Kamber et al., 2004; Allwood et al., 2010). A Ce anomaly is absent except for a slight negative anomaly in some samples. Ce displays anomalous pattern in response to oceanic redox condition, unlike the other REEs, which remain trivalent in seawater. In the presence of oxygen, the preferential oxidation of Ce(III) to the less soluble Ce(IV)-oxide phase leads to the adsorption onto particles and its removal from seawater, which causes depletion of Ce relative to other REEs and, as a result, produces a negative Ce anomaly (De Baar et al., 1985b, 1988; Elderfield, 1988; Kamber and Webb, 2001; Kato et al., 2002). Therefore, Ce anomalies in chemical deposits from marine environments reflect redox processes (e.g. Kato et al., 2002).

The average of $(Pr/Pr^*)_{SN}$ is slightly higher than unity in most of our samples (Table A3, Appendix), which indicates the presence of negative Ce anomaly, influence of secondary processes on REE patterns or analytical uncertainty. Samples with $(Pr/Pr^*)_{SN}$ higher than unity have the most positive $\delta^{18}O$ values, which is indicative of the most pristine signatures (Fig. 19). The presence of a small negative Ce anomaly in samples from three sections indicates their possible deposition in an oxidizing environment relative to the Ce^{3+}/Ce^{4+} redox couple. The lack of a Ce anomaly in some of the samples indicates that Ce(III) oxidation was not pervasive in the shallow-marine environment, possibly due to variable and generally low amounts of free O_2. This result shows that the shallow-marine settings was not completely devoid of O_2, and possibly free O_2 was produced by microbes via oxygenic photosynthesis locally. The Ce concentration in very shallow seawater is highly variable and a Ce anomaly might not be sufficient evidence to infer the redox state of seawater (Webb and Kamber, 2000; Kamber and Webb, 2001). However, Riding et al. (2014) reported a negative Ce anomaly from limestones of the ~ 2.8 Ga Steep Rock Group, indicative of development of an oxygen oasis in a nutrient-rich isolated shallow-marine environment. The previous study of the Pongola carbonate rocks by Bolhar et al. (2015) did not detect a Ce anomaly in their sample set, which they argued was consistent with Pongola carbonates having precipitated from reducing seawater.

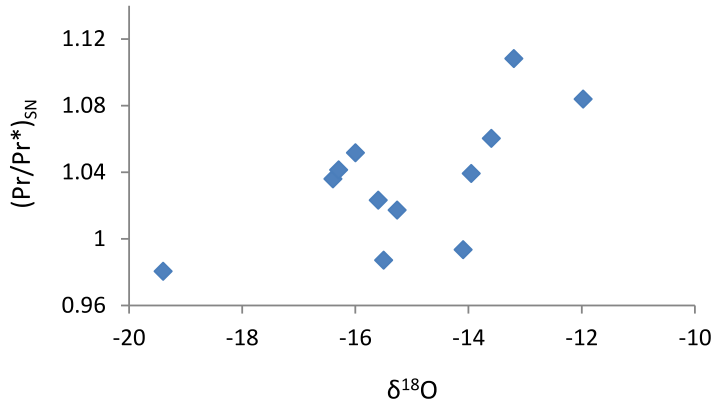

Fig. 19. $(Pr/Pr^*)_{SN}$ anomaly vs. $\delta^{18}O$ values from the main carbonate section. The diagram shows moderate positive correlation between $(Pr/Pr^*)_{SN}$ anomaly and $\delta^{18}O$ values.

In summary, the shale-normalized REE distribution patterns of the Mesoarchaean carbonate rocks display several features common to oxygenated modern open seawater including HREE enrichment relative to LREE, negative Ce_{SN} anomaly, positive La_{SN} anomaly, moderate positive Gd_{SN} anomaly and pronounced Y_{SN} anomaly (De Baar et al., 1983, 1988; Elderfield, 1988; German and Elderfield, 1989; Bau et al., 1997; Alibo and Nozaki, 1999; Kamber et al., 2014) with important differences including MREE enrichment, a strong positive Eu_{SN} anomaly and lack of a pronounced negative Ce_{SN} anomaly. The specific differences can be attributed to low oxygen level and high hydrothermal fluid input into the oceans, and the epicontinental setting of the Pongola Basin.

5.6 Conclusions

1. A comprehensive geochemical study of stromatolitic carbonates of the Mesoarchaean Pongola Supergroup was undertaken for the first time. Three stratigraphic sections were investigated in the White Mfolozi inlier in South Africa.

2. The dominant mineralogy of the Pongola carbonate rocks is dolomite, with minor ankerite. The least altered samples are those with the highest $\delta^{18}O$ and $\delta^{13}C$ values, and least FeO and MnO contents.

3. Elevated Sr contents (Sr > 100 ppm) in most of the samples from the main carbonate section with a higher level of preservation, as deduced by fabric retention and isotopic composition, may be the result of a combination of factors, which include early dolomitization of metastable carbonates (aragonite and high magnesium calcite), facies control and secondary calcite replacement. The low Sr content of the middle and upper carbonate sections is a result of late dolomitization of low Sr carbonate such as diagenetic low magnesium calcite.

4. The variable $\delta^{18}O$ values within different sections indicate different levels of diagenetic evolution. Highly negative $\delta^{18}O$ values are a result of water-rock interaction during burial and, to a lesser extent, meteoric diagenesis. The alteration of volcaniclastic and siliciclastic detrital components, and metamorphic fluids, contributed to lowering of the $\delta^{18}O$ values. The highest $\delta^{13}C$ value is 2.5 ‰ PDB and thus the closest value to that of coeval seawater. Samples with highest $\delta^{13}C$ values do not correspond with samples with highest Sr content, which indicate they had a more stable original mineralogy. i.e. calcite rather than aragonite.

5. Samples with the least radiogenic $^{87}Sr/^{86}Sr$ ratio (0.708) are the best proxy for the Sr isotopic signature of seawater, which is lower than the value reported previously for these rocks by Veizer et al. (1982), but still much higher than assumed mantle-like signatures of seawater. The most radiogenic $^{87}Sr/^{86}Sr$ ratio (0.777) was obtained from a sample with the highest amount of clastic component, which indicate contribution of radiogenic Sr from the clastic detritus in carbonates. This may indicate that continental input had a significant role in the Mesoarchaean seawater isotopic composition. We do not generalize this for all Mesoarchaean depositional basins, as Pongola carbonates were deposited within a restricted shallow marine environment with much fluvial input, and thus cannot be used as a proxy for the isotopic and chemical composition of the Mesoarchaean ocean.

6. The shale-normalized rare earth element and yttrium (REE+Y) distribution patterns of carbonate rocks are characterized by enrichment of HREEs relative to LREEs, positive La_{SN}, Gd_{SN} and Y_{SN} anomalies, superchondritic Y/Ho ratios and slightly negative Ce anomaly. They are similar, but not as pronounced as those of modern open marine settings, which could be a result of their precipitation in a restricted depositional setting. The relative enrichment of MREEs could be a result of organic matter complexation and fractionation during estuarine mixing. The negative Ce anomaly and Th/U ratio higher than 2 are evidence of free oxygen produced by microbial activity on the early Earth. The presence of a positive Eu anomaly

indicates the contribution of high-temperature hydrothermal fluids into Mesoarchaean seawater.

5.7 Acknowledgements

We thank Dr. Christian Reinke and Mrs. Eve Kroukamp (University of Johannesburg), Dr. Markus Oehlerich (Ludwig-Maximilians-University, Munich) and Mr. Marlin Patchappa (Witwatersrand University) for assisting with XRF, microprobe, IR-MS, and ICP-MS analysis respectively.

5.8 References

Alexander, B.W., Bau, M., Andersson, P., and Dulski, P. (2008). Continentally-derived solutes in shallow Archean seawater: Rare earth element and Nd isotope evidence in iron formation from the 2.9 Ga Pongola Supergroup, South Africa. Geochim. Cosmochim. Acta, 72, 378-394.

Algeo, Th.J., and Maynard, J.B. (2004). Trace-element behavior and redox facies in core shales of Upper Pennsylvanian Kansas-type cyclothems. Chem. Geol., 206, 289-318.

Allwood, A.C., Kamber, B.S., Walter, M.R., Burch, I.W., and Kanik, I. (2010). Trace elements record depositional history of an Early Archean stromatolitic carbonate platform. Chem. Geol., 270, 148-163.

Alibo, D.S., and Nozaki, Y. (1999). Rare earth elements in seawater: Particle association, shale-normalization, and Ce oxidation. Geochim. Cosmochim. Acta, 63, 3/4, 363-372.

Anderson, T.F., and Arthur, M.A. (1983). Stable isotopes of oxygen and carbon and their application to sedimentologic and paleoenvironmental problems. In: Stable isotopes in sedimentary geology. Arthur, M.A., Anderson, T.F., Kaplan, I.R., Veizer, J., and Land, L.S., (Eds.), SEPM Short Course No. 10, 1/1-1/151.

Bau, M. (1993). Effects of syn- and post-depositional processes on the rare-earth element distribution in Precambrian iron-formations. Eur. J. Mineral., 5, 257-267.

Bau, M. (1996). Controls on the fractionation of isovalent trace elements in magmatic and aqueous systems: evidence from Y/Ho, Zr/Hf, and lanthanide tetrad effect. Contrib. Mineral. Petrol., 123, 323-333.

Bau, M., and Dulski, P. (1995). Comparative study of yttrium and rare-earth element behaviors in fluorine-rich hydrothermal fluids. Contrib. Mineral. Petrol., 119, 213-223.

Bau, M., and Dulski, P. (1996). Distribution of yttrium and rare-earth elements in the Penge and Kuruman iron-formations, Transvaal Supergroup, South Africa. Precambrian Res., 79, 37-55.

Bau, M., and Dulski, P. (1999). Comparing yttrium and rare earths in hydrothermal fluids from the Mid-Atlantic Ridge: implications for Y and REE behaviour during near-vent mixing and for the Y/Ho ratio of Proterozoic seawater. Chem. Geol., 155, 77-90.

Bau, M., and Möller, P. (1992). Rare earth element fractionation in metamorphogenic hydrothermal calcite, magnesite, and siderite. Mineral. Petrol., 45, 23 1-246.

Bau, M., and Möller, P. (1993). Rare earth element systematics of the chemically precipitated component in Early Precambrian iron formations and the evolution of the terrestrial atmosphere-hydrosphere-lithosphere system. Geochim. Cosmochim. Acta, 57, 2239-2249.

Bau, M., Dulski, P., and Möller, P. (1995). Yttrium and holmium in South Pacific seawater: vertical distribution and possible fractionation mechanisms. Chem. Erde, 55, 1-15.

Bau, M., Möller, P., and Dulski, P. (1997). Yttrium and lanthanides in eastern Mediterranean seawater and their fractionation during redox-cycling. Mar. Chem., 56, 123-131.

Bekker, A., Planavsky, N.J., Krapež, B., Rasmussen, B., Hofmann, A., and Slack, J.F. (2014). Iron formations: their origins and implications for ancient seawater chemistry. In: Treatise of geochemistry, sediments, diagenesis and sedimentary rocks. Mackenzie, F.T. (Ed.), Amsterdam, Elsevier, 9, 561-628.

Beukes, N.J., and Lowe, D.R. (1989). Environmental control on diverse stromatolite morphologies in the 3000 Ma Pongola Supergroup, South Africa. Sedimentology, 36, 383-397.

Bolhar, R., and Van Kranendonk, M.J. (2007). A non-marine depositional setting for the northern Fortescue Group, Pilbara Craton, inferred from trace element geochemistry of stromatolitic carbonates. Precambrian Res., 155, 229-250.

Bolhar, R., Kamber, B.S., Moorbath, S., Fedo, C.M., and Whitehouse, M.J. (2004). The characterization of early Archaean chemical sediments by trace element signatures. Earth Planet. Sci. Lett., 222, 43-60.

Bolhar, R., Hofmann, A., Siahi, M., Feng, Y., and Delvigne, C. (2015). A trace element and Pb isotopic investigation into the provenance and deposition of stromatolitic carbonates, ironstones and associated shales of the ~ 3.0 Ga Pongola Supergroup, Kaapvaal Craton. Geochim. Cosmochim. Acta, 158 57-78.

Boynton, W.V. (1984). Geochemistry of the rare earth elements: meteorite studies. In: Geochemistry of the rare earth elements. Henderson, P. (Ed.), Elsevier, Oxford, 63-114.

Brand, U., and Veizer, J. (1980). Chemical diagenesis of a multicomponent system-1: Trace elements: J. Sediment. Petrol., 50, 1219-1236.

Brand, U., and Veizer, J. (1981). Chemical diagenesis of a multicomponent system-2: Stable isotopes: J. Sediment. Petrol., 51, 987-998.

Brennecka, G.A., Herrmanna, A.D., Algeoc, Th.J., and Anbara, A.D. (2011). Rapid expansion of oceanic anoxia immediately before the end-Permian mass extinction. PNAS, 108 (43), 17631-17634.

Byrne, R.H., and Kim, K-H. (1990). Rare earth element scavenging in seawater. Geochim. Cosmochim. Acta, 54, 2645-2656.

Cantrell, K.J., and Byrne, R.H. (1987). Rare earth element complexation by carbonate and oxalate ions. Geochim. Cosmochim. Acta, 51, 597-605.

Choquette, P.W., and James, N.P. (1987). Diagenesis in limestones, 3. The deep burial environment. Geoscience Canada, 14, 3-35.

Collerson, K.D., and Kamber, B.S. (1999). Evolution of the continents and the atmosphere inferred from Th-U-Nb systematics of the depleted mantle. Science, 283, 1519-1521.

Dawans, J.M., and Swart, P.K. (1988). Textural and geochemical alterations in Late Cenozoic Bahamian dolostones. Sedimentology, 35, 385-403.

De Baar, H.J.W., Bacon, M.P., and Brewer, P.G. (1983). Rare earth distributions with positive Ce anomaly in the Western North Atlantic Ocean. Nature, 301, 324-327.

De Baar, H.J.W., Brewer, P.G., and Bacon, M.P. (1985a). Anomalies in rare earth distributions in seawater: Gd and Tb. Geochim. Cosmochim. Acta, 49, 1961-1969.

De Baar, H.J.W., Bacon, M.P., and Brewer, P.G. (1985b). Rare earth elements in the Pacific and Atlantic Oceans. Geochim. Cosmochim. Acta, 49, 1943-1985.

De Baar, H.J.W., German, C.R., Elderfield, H., and Van Gaans, P. (1988). Rare earth element distributions in anoxic waters of the Cariaco Trench. Geochim. Casmochim. Acta, 52, 1203-I219.

De Carlo, E.H., and Green, W.J. (2002). Rare earth elements in the water column of Lake Vanda, McMurdo Dry Valleys, Antarctica. Geochim. Cosmochim. Acta, 66 (8), 1323-1333.

Derry, L.A., and Jacobsen, S.B. (1988). The Nd and Sr isotopic evolution of Proterozoic seawater. Geophys. Res. Lett., 15, 397-400.

Derry, L.A., and Jacobsen, S.B. (1990). The chemical evolution of Precambrian seawater: Evidence from rare earth elements in banded iron formations. Geochim. Cosmochim. Acta, 54, 2965-2977.

Dipple, G.M., and Ferry, J.M. (1992). Fluid flow and stable isotopic alteration in rocks at elevated temperatures with applications to metamorphism. Geochim. Cosmochim. Acta, 56 (9), 3539-3550.

Dunham, J.B., and Olson, E.R. (1980). Shallow subsurface dolomitization of subtidally deposited carbonate sediments in the Hanson Creek Formation (Ordovician-Silurian) of central Nevada. In: Concepts and models of dolomitization. Zenger, D.H., Dunham, J.B., and Ethington, R.L. (Eds.), SEPM Spec. Publ. No. 28, 139-161.

Eglington, B.M., Talma, A.S., Marais, S., Matthews, P.E., and Dixon, J.G.P. (2003). Isotopic composition of Pongola Supergroup limestones from the Buffalo River gorge, South Africa: constraints on their regional depositional setting. S. Afr. J. Geol., 106, 1-10.

Elderfield, H. (1988). The oceanic chemistry of the rare-earth elements. Phil. Trans. R. Soc. Lond. A 325, 105-126.

Elderfield, H., Upstill-Goddard, R., and Sholkovitz, E.R. (1990). The rare earth elements in rivers, estuaries, and coastal seas and their significance to the composition of ocean waters Geochim. Cosmochim. Acta, 54, 971-991.

Fairchild, I.J., and Kennedy, M.J. (2007). Neoproterozoic glaciation in the Earth system. J. Geol. Soc., 164, 895-921.

Fairchild, I.J., Marshall, J.D., and Bertrand-Sarfati, J. (1990). Stratigraphic shifts in carbon isotopes from Proterozoic stromatolitic carbonates (Mauritania): influences of primary mineralogy and diagenesis. Am. J. Sci., 290-A, 46-79.

Faure, G. (1982). The marine-strontium geochronometer. In: Numerical dating in stratigraphy. Odin, G.S. (Ed.), John Wiley and Sons. 73-79.

Faure, G., and Powell, J.L. (1972). Strontium isotope geology, Springer-Verlag, 188 p.

Fu, Q., Qing, H., and Bergman, K.M. (2006). Early dolomitization and recrystallization of carbonate in an evaporite basin: the Middle Devonian Ratner laminite in southern Saskatchewan, Canada. J. Geol. Soc., 163, 937-948.

Gao, G., and Land, L.S. (1991). Early Ordovician Cool Creek dolomite, Middle Arbuckle Group, Slick Hills, SW Oklahoma, U.S.A., Origin and modification. J. Sediment. Petrol., 61, 2, 161-173.

German, C.R., and Elderfield, H. (1989). Rare earth elements in Saanich Inlet, British Columbia, a seasonally anoxic basin. Geochim. Cosmochim. Acta, 53, 2561-2571.

Gibbs, A.L., Montgomery, C.W., O'day, P.A., and Erslev, E.A. (1986). The Archean-Proterozoic transition: Evidence from the geochemistry of metasedimentary rocks of Guyana and Montana. Geochim. Cosmochim. Acta, 50, 2125-2141.

Godderis, Y., and Veizer, J. (2000). Tectonic control of chemical and isotopic composition of ancient oceans: The impact of continental growth. Am. J. Sci., 300, 434-461.

Gold, D.J.C. (2006). The Pongola Supergroup. In: The Geology of South Africa. Johnston, M.R., Anhaeusser, C.R., and Thomas, R.J. (Eds.), Geol. Soc. S. Afr. / C.G.S. Afr., 135-147.

Goldstein, S.J., and Jacobsen, S.B. (1987). The Nd and Sr isotope systematics of river water dissolve material: Implications for the source of Nd and Sr in seawater. Chem. Geol., 66, 245-272.

Goldstein, S.J., and Jacobsen, S.B. (1988a). Nd and Sr isotopic systematics of river water suspended material: Implications for crustal evolution. Earth Planet. Sci. Lett., 87, 249-265.

Goldstein, S.J., and Jacobsen, S.B. (1988b). REE in the Great Whale River Estuary, NW Quebec. Earth Planet. Sci. Lett., 88, 241-252.

Gregg, J.M., Howard, S.A., and Mazzullo, S.J. (1992). Early diagenetic recrystallization of Holocene (< 3000 years old) peritidal dolomites, Ambergris Cay, Belize. Sedimentology, 39, 143-160.

Hegner, E., Kröner, A., and Hunt, P. (1994). A precise U-Pb zircon age for the Archean Pongola Supergroup volcanics in Swaziland. J. Afr. Earth. Sci., 18 (4), 339-341.

Hoefs, J. (1997). Stable isotope geochemistry. Berlin, Heidelberg, New York, London, Paris, Tokyo, Hong Kong: Springer-Verlag. 4th ed. xi + 200 p.

Kamber, B.S., and Webb, G.E. (2001). The geochemistry of late Archaean microbial carbonate: Implications for ocean chemistry and continental erosion history. Geochim. Cosmochim. Acta, 65, 2509-2525.

Kamber, B.S., Bolhar, R., and Webb, G.E. (2004). Geochemistry of late Archaean stromatolites from Zimbabwe: evidence for microbial life in restricted epicontinental seas. Precambrian Res., 132, 379-399.

Kamber, B.S., Webb, G.E., and Gallagher, M. (2014). The rare earth element signal in Archaean microbial carbonate: information on ocean redox and biogenicity. J. Geol. Soc. London, 171, 745-763.

Kato, Y., Kano, T., and Kunugiza, K. (2002). Negative Ce Anomaly in the Indian Banded Iron Formations: Evidence for the emergence of oxygenated deep-sea at 2.9~2.7 Ga. Resource Geol., 52, 101-110.

Kaufman, A.J., and Knoll, A.H. (1995). Neoproterozoic variations in the C-isotopic composition of seawater: stratigraphic and biogeochemical implications. Precambrian Res., 73, 22-49.

Killingley, J.S. (1983). Effects of diagenetic recrystallization on $^{18}O/^{16}O$ values of deep-sea sediments. Nature, 301, 594-597.

Koeppenkastrop, D., and De Carlo, E.H. (1992) Sorption of rare-earth elements from seawater onto synthetic mineral particles: An experimental approach. Chem. Geol., 95, 251-263.

Lawrence, J.R., Drever, J.L., Anderson, T.F., and Brueckner, H.K. (1979). Importance of alteration of volcanic material in the sediments of deep sea drilling site 323: chemistry, $^{18}O/^{16}O$ and $^{87}Sr/^{86}Sr$. Geochim. Cosmochim. Acta, 43, 573-588.

Mabrouk, A., Belayouni, H., Jarvis, I., and Moody, R.T.J. (2006). Strontium, $\delta^{18}O$ and $\delta^{13}C$ as palaeo-indicators of unconformities: Case of the Aleg and Abiod formations (Upper Cretaceous) in the Miskar Field, southeastern Tunisia. Geochem. J., 40, 405-424.

Maliva, R.G. (1998). Skeletal aragonite neomorphism-quantitative modelling of a two-water diagenetic system. Sediment. Geol., 121, 179-190.

Marshall, J.D. (1992). Climatic and oceanographic isotopic signals from the carbonate rock record and their preservation. Geol. Mag., 129 (2), 143-160.

Matthews, P.E. (1967). The pre-Karoo formations of the White Umfolozi inlier, northern Natal. Trans. Geol. Soc. S. Afr., 70, 39-63.

McArthur, J.M. (1994). Recent trends in strontium isotope stratigraphy. Terra Nova, 6, 331-358.

McLennan, S.B. (1989). Rare earth elements in sedimentary rocks. Influence of provenance and sedimentary processes. In: Geochemistry and mineralogy of the Rare Earth elements. Lipin, B.R., and McKay, G.A. (Eds.), Mineral. Soc. Am., Washington, 169-200.

Michard, A., and Albarede, F. (1986). The REE content of some hydrothermal fluids. Chem. Geol., 55, 51-60.

Mirota, M.D., and Veizer, J. (1994). Geochemistry of Precambrian carbonates: IV, Aphebian Albanel formations, Quebec, Canada. Geochim. Cosmochim. Acta, 58, 1735-1745.

Moore, C.H. (1985). Upper Jurassic subsurface cements: a case history. In: Carbonate cements. Harris, P.M., and Schneidermann, N. (Eds.), SEPM Spec. Publ. No., 36, 291-308.

Morford, J.L., and Emerson, S. (1999). The geochemistry of redox sensitive trace metals in sediments. Geochim. Cosmochim. Acta, 63, 1735-1750.

M'Rabat, A. (1981). Differentiation of environments of dolomite formation, Lower Cretaceous of Central Tunisia. Sedimentology, 1981, 28, 331-352.

Mukasa, S.B., Wilson, A.H., and Young, K.R. (2013). Geochronological constraints on the magmatic and tectonic development of the Pongola Supergroup (Central Region), South. Africa. Precambrian Res., 224, 268-286.

Munemoto, T., Ohmori, K. and Iwatsuki, T. (2015). Rare earth elements (REE) in deep groundwater from granite and fracture-filling calcite in the Tono area, central Japan: Prediction of REE fractionation in paleo- to present-day groundwater. Chem. Geol., 417, 58-67.

Myers, K. J., and Wignall, P. B. (1987). Understanding Jurassic organic-rich mudrocks- new concepts using gamma ray spectrometry and palaeoecology: examples from the Kimmeridge Clay of Dorset and the Jet Rock of Yorkshire. In: Marine clastic environments: concepts and case studies. Legget, J.K., and Zuffa, G.G. (Eds.), Graham and Trotman, London, 175-192.

Nothdurft, L.D., Webb, G.E., and Kamber, B.S. (2004). Rare earth element geochemistry of Late Devonian reefal carbonates, Canning basin, Western Australia: confirmation of a seawater REE proxy in ancient limestones. Geochim. Cosmochim. Acta, 68, 263-283.

Nozaki, Y., Zhang, J., and Amakawa, H. (1997). The fractionation between Y and Ho in the marine environment. Earth Planet. Sci. Lett., 148, 329-340.

Oehlerich, M., Baumer, M., Lücke, A., and Mayr, C. (2013). Effects of organic matter on carbonate stable isotope ratios ($\delta^{13}C$, $\delta^{18}O$ values)-implications for analyses of bulk sediments. Rapid Commun Mass Spectrom., 27 (6), 707-712.

Palmer, M.R., and Edmond, J.M. (1989). Strontium isotope budget of the modern ocean. Earth Planet. Sci. Lett., 92, 11-26.

Perry, E.C., and Tan, F.C. (1972). Significance of oxygen and carbon isotope variations in early Precambrian cherts and carbonate rocks of southern Africa. Geol. Soc. Am. Bull., 83, 647-664.

Perry, C., Ahmad, S. N., and Swulius, T. M. (1978). The oxygen isotopic composition of 3800 m. y. old metamorphosed chert from Isukasia, West Greenland. J. Geol., 86, 223-239.

Peterman, Z.E., and Hedge, C.E. (1971). Related strontium isotopic and chemical variations in oceanic basalt. Geol. Soc. Amr. Bull., 82, 493-500.

Pingitore, N.E. (1976). Vadose and phreatic diagenesis: processes, products and their recognition in corals. J. Sediment. Petrol., 46, 985-1006.

Prezbendowski, D.R. (1985). Burial cementation- is it important? A case study, Stuart City Trend, south-central Texas. In: Carbonate cements. Harris, P.M., and Schneidermann, N. (Eds.), SEPM Spec. Publ. No., 36, 241-264.

Ratner, B. (2009). The correlation coefficient: Its values range between +1/-1, or do they? Journal of targeting, measurement and analysis for marketing, 17 (2), 139-142.

Reinhold, C. (1998). Multiple episodes of dolomitization and dolomite recrystallization during shallow burial in Upper Jurassic shelf carbonates: eastern Swabian Alb, southern Germany. Sediment. Geol., 121, 71-95.

Riding, R., Fralick, Ph., and Liang, L. (2014). Identification of an Archean marine oxygen oasis. Precambrian Res., 251, 232-237.

Rocholl, A., and Jochum, K.P. (1993). Th, U and other trace elements in carbonaceous chondrites: Implications for the terrestrial and solar-system Th/U ratios. Earth Planet. Sci. Lett., 117, 265-278.

Schidlowski, M., Hayes, J.M., and Kaplan, I.R. (1983). Isotopic inferences of ancient biochemistries: Carbon, sulfur, hydrogen and nitrogen. In: Earth's earliest biosphere: Its origin and evolution. Schopf, J.W. (Ed.), Princeton University Press. 149-186.

Sharma, T., and Clayton, R.N. (1965). Measurement of O^{18}/O^{16} ratios of total oxygen of carbonates. Geochim. Cosmochim. Acta, 29, 1347-1353.

Sharp, Z. (2007). Principles of stable isotope geochemistry. Pearson/ Prentice Hall. 344 p.

Sholkovitz, E.R. (1995). The aquatic chemistry of the rare earth elements in rivers and estuaries. Aquat. Geochem., 1, 1-34.

Siahi, M., Hofmann, A., Hegner, H., and Master, S. (2016). Sedimentology and facies analysis of Mesoarchaean stromatolitic carbonate rocks of the Pongola Supergroup, South Africa. Precambrian Res., 278, 244-264.

Sibley, D.F. (1991). Secular changes in the amount and texture of dolomite. Geology, 15, 151-154.

Singh, U. (1987). Ooids and cements from the Late Precambrian of the Flinders Ranges, South Austrailia. J. Sediment. Petrol., 57 (1), 117-127.

Stanley, J.K., and Byrne, R.H. (1990). The influence of solution chemistry on REE uptake by Ulva lactuca L. in seawater. Geochim. Cosmochim. Acta, 54, 1587-1595.

Thompson, M., Webb, P.C., and Potts, P.J. (2015). The GeoPT proficiency testing scheme for laboratories routinely analysing silicate rocks: A review of the operating protocol and proposals for its modification. Geostandards and Geoanalytical Res., 39 (4), 433-442.

Tucker, M.E., and Wright, V.P. (1990). Carbonate sedimentology. Blackwell Science. London, England. 492 p.

Vasconcelos, C., McKenzie, J.A., Warthmann, R., and Bernasconi, S.M. (2005). Calibration of the $\delta^{18}O$ paleothermometer for dolomite precipitated in microbial cultures and natural environments. Geology, 33 (4), 317-320.

Veizer, J. (1983a). Chemical diagenesis of carbonates: Theory and application of trace element technique. In: Stable isotopes in sedimentary geology. Arthur, M.A., Anderson, T.F., Kaplan, I.R., Veizer, J., and Land, L.S., (Eds.), SEPM Short Course No. 10, 3/1-3/100.

Veizer, J. (1983b). Trace elements and isotopes in sedimentary carbonates. Rev. Mineral., 11, 265-300.

Veizer, J. (1984). The evolving earth: water tales. Precambrian Res., 25, 5-12.

Veizer, J. (1992). Depositional and diagenetic history of limestones: stable and radiogenic isotopes. In: Isotopic signatures and sedimentary records. Clauer, N., and Chaudhuri, S. (Eds.), Springer Berlin Heidelberg, lecture notes in earth sciences, 43, 13-48.

Veizer, J., and Compston, W. (1976). $^{87}Sr/^{86}Sr$ in Precambrian carbonates as an index of crustal evolution. Geochim. Cosmochim. Acta, 40, 905-914.

Veizer, J., Compston, W., Hoefs, J., and Nielsen, H. (1982). Mantle buffering of the early oceans. Naturwissenschaften, 69, 173-180.

Veizer, J., Hoefs, J., Lowe, D.R., and Thurston, P.C. (1989a). Geochemistry of Precambrian carbonates: II. Archean greenstone belts and Archean sea water. Geochim. Cosmochim. Acta, 53, 859-871.

Veizer, J., Hoefs, J., Ridler, R.H., Jensen, L.S., and Lowe, D.R. (1989b). Geochemistry of Precambrian carbonates: I. Archean hydrothermal systems. Geochim. Cosmochim. Acta, 53, 845-857.

Veizer, J. Lemieljx, J., Jones, B., Gibling, R.M., and Savelle, J. (1978). Paleosalinity and dolomitization of a Lower Paleozoic carbonate sequence, Somerset and Prince of Wales Islands, Arctic Canada. Canadian J. Earth Sci., 15, 1448-1461.

Veizer, J., Clayton, R.N., Hinton, R.W., Von Brunn, V., Mason, T.R., Buck, S.G., and Hoefs, J. (1990). Geochemistry of Precambrian carbonates: 3-shelf seas and non-marine environments of the Archean. Geochim. Cosmochim. Acta, 54, 2717-2729.

Wadleigh, M.R., Veizer, J., and Brooks, C. (1985). Strontium and its isotopes in Canadian rivers: Fluxes and global implications. Geochim. Cosmochim. Acta, 49, 1727-1736.

Webb, G.E., and Kamber, B.S. (2000). Rare earth elements in Holocene reefal microbialites: A new shallow seawater proxy. Geochim. Cosmochim. Acta, 64, 1557-1565.

Webb, G.E., Nothdurft, L.D., Kamber, B.S., Kloprogge, J.T., and Zhao, J.X. (2009). Rare earth element geochemistry of scleractinian coral skeleton during meteoric diagenesis: A sequence through neomorphism of aragonite to calcite. Sedimentology, 56, 1433-1463.

Wilson, A.H., Groenewald, B., and Grant, C.E. (2013). Volcanic and volcaniclastic rocks of the Mesoarchaean Pongola Supergroup in South Africa and Swaziland: distribution, physical characteristics, stratigraphy and correlations. S. Afr. J. Geol., 116, 119-168.

Wignall, P.B., and Twitchett, R.J. (1996). Oceanic Anoxia and the End Permian Mass Extinction. Science, 272, 1155-1158.

Zenger, D.H. (1983). Burial dolomitization in the Lost Burro Formation (Devonian), east-central California, and the significance of late diagenetic dolomitization. Geology, 11, 519-522.

Zhao, Y.Y., Zheng, Y.F. and Chen, F. (2009). Trace element and strontium isotope constraints on sedimentary environment of Ediacaran carbonates in southern Anhui, South China. Chem. Geol., 265, 345-362.

Chapter 6: Conclusions and outlook

Detailed sedimentological and microfacies analyses have been undertaken on three carbonate-siliciclastic successions (main, middle and upper sections) of the Nsuze Group in the White Mfolozi inlier. Dolomite and, to a lesser extent, ankerite now form these carbonates. The presence of sedimentary structures representative of tidal activity (i.e. symmetric and asymmetric ripple marks, flaser-lenticular and wavy bedding, evidence for bi-directional currents) along with traceable facies assemblages for over hundreds of metres, presence of storm deposits and abundance of clastic detritus as part of these carbonate successions indicate deposition of three sections along a tide-dominated clastic-carbonate shoreline. In total, fourteen sedimentary facies were identified based on sedimentary structures as well as diverse stromatolite morphology and size. Facies were partially arranged in shallowing-upward cycles reflecting cyclic variations of Mesoarchaean sea level. These facies were grouped into three facies assemblages representative of their depositional sub-environments of supratidal to upper intertidal, middle intertidal to subtidal and tidal channel.

Microbialites occur as laminated types (stromatolite) with variable morphology and non-laminated (structureless microbialite) types with domal to lenticular morphology. Microbialites with specific morphology, macrofabric and size were identified within different sub-environments subjected to distinct physico-chemical conditions, suggestive of adaptation and response of microorganisms to environmental conditions. For instance, stratiform, digitate and small-scale domal stromatolites were formed in the supratidal and upper-intertidal settings characterized by high subaerial index, while large-scale domal microbialites, ooids and oncoids were limited to high-energy environments such as middle intertidal to shallow subtidal settings. Large conical/ columnar stromatolites are only present within a tidal channel setting with high energy and enough accommodation space suitable for their growth. Microbially induced sedimentary structures, such as microbial mat chips, fossilized gas holes and sandy intraclasts, are present on bedding planes of sandstone and sandy dolomite facies, respectively, suggesting wide colonization of sedimentary surfaces by microbial mats.

Several lines of evidence point to the presence of microorganisms with phototrophic characteristics including a coniform shape of some stromatolites, inclination of one set of laminae to the other, crestal thickening of conical stromatolites and upward growth of oncoids. No microfossils were observed probably due to post-depositional diagenetic processes except for remains of carbonaceous matter along the margin of some stromatolites and in peloids and ooids. Meteoric diagenesis gave rise to secondary calcification of selected facies. Silicification

preferentially affected stromatolites. Further detailed study is required to unravel the source of silica and the reasons behind selective silicification of stromatolites.

Ooids and peloids are the only carbonate components with carbonaceous matter and were selected for further detailed *in-situ* analyses. Ooids with a variety of fabrics (radial, concentric, radial-concentric and micritic) are present in high-energy facies and to a lesser extent in microbialites. The mechanism of their formation is a matter of debate, and two mechanisms have been suggested, a purely physico-chemical and a biologically mediated process. The combination of *in-situ* Raman spectroscopic imaging and NanoSIMS ion mapping confirmed the biogenecity of carbonaceous matter distributed in ooids. *In-situ* trace-element analyses by means of LA-ICP-MS displays slight differences in Sr content of ooids with different fabrics. Radial ooids with better fabric retention, homogeneous distribution of carbonaceous matter and lower Sr content had a more stable chemical composition, possible Mg-calcite, and microbes played a direct role in their formation. Concentric ooids with poor fabric preservation, homogeneous distribution of carbonaceous matter along with higher Sr content had an unstable precursor, possibly aragonite, and both factors, environmental conditions (preferentially turbulent condition) and microbial activity were responsible for their formation. Micritic ooids show partial to entirely micritic fabrics and some of them display transitional fabric, from concentric to micritic, which is indicative of recrystallization of ooids with an unstable primary mineralogy during diagenesis. Large nuclei of superficial ooids were probably an obstacle for their regular movement giving rise to single lamina cortices. This type of ooid was found within structureless domal microbialites, and may have been transported to the site by high energy currents and trapped in microbial surfaces. The type of microbial community responsible for ooid formation remains unknown.

The Sr content of the carbonates is not only a result of the precursor minerals, but also secondary calcitization during meteoric diagenesis, time of dolomitization and facies type. Therefore, samples with higher Sr contents are not necessary the least altered ones. The combination of several tools was used to evaluate the preservation of primary geochemical signatures. Samples with the highest $\delta^{18}O$ and $\delta^{13}C$ values, and lowest FeO and MnO contents are the least altered. Low $\delta^{18}O$ values are a result of burial and to a lesser extent meteoric diagenesis. Samples with very negative $\delta^{18}O$ values are from the middle and upper carbonate sections, which have higher amounts of siliciclastic/ volcaniclastic detritus, contributing to the lowering of the $\delta^{18}O$ value during their alteration. During diagenesis carbon isotopes did not

change much from their original value, and the highest carbon isotope value of about 2.5 ‰ VPDB is probably close to that of coeval seawater.

The least radiogenic Sr isotope ratio (~0.708) was derived from a sample in the main carbonate section also showing the highest carbon and oxygen isotope values. This value is not representative of the Sr isotopic ratio of the mantle-buffered Archaean ocean due to a strong diagenetic/ metamorphic overprint of these carbonates and/or mixing with radiogenic Sr derived from fluvial input into the shallow epicontinental sea.

Shale-normalized rare earth element and yttrium (REE + Y) distribution patterns of carbonate rocks are similar to seawater chemical precipitates. They have HREEs > LREEs, positive La_{SN}, Gd_{SN} and Y_{SN} anomalies, but not as pronounced as those in modern open marine settings. These similarities along with enrichment of middle REEs, may be a result of organic matter complexation and fractionation during estuarine mixing, suggesting that the Pongola basin was laterally restricted with fluvial input and variable exchange with the open-ocean water. The presence of a slightly negative Ce_{SN} anomaly along with Th/U > 2 in some samples may reflect presence of minor free oxygen possibly produced by photosynthetic microorganisms locally in restricted shallow seawater, but it does not mean that hydrosphere and atmosphere were oxygenated entirely.

Appendix

- Table A1
- Table A2
- Table A3

- Bolhar, R., Hofmann, A., Siahi, M., Feng, Y., and Delvigne, C. (2015). A trace element and Pb isotopic investigation into the provenance and deposition of stromatolitic carbonates, ironstones and associated shales of the ~ 3.0 Ga Pongola Supergroup, Kaapvaal Craton. Geochim. Cosmochim. Acta, 158, 57-78.

- Siahi, M., Hofmann, A., Hegner, H., and Master, S. (2016). Sedimentology and facies analysis of Mesoarchaean stromatolitic carbonate rocks of the Pongola Supergroup, South Africa. Precambrian Res., 278, 244-264.

- Siahi, M., Hofmann, A., Hegner, E., and Master, S. (2014). Diverse microbialite morphologies in the 3 Ga Nsuze Group, Pongola Supergroup, South Africa. 18th Biennial Conference of the Palaeontological Society of Southern Africa, Abstract Volume, p. 44-45.

- Siahi, M., Hofmann, A., Hegner, E., Master, S., and Mayr, C. (2014). Stromatolitic carbonates of the Pongola Supergroup, South Africa: a unique record of surface conditions 3 billion years ago. 21th General Meeting of IMA, Johannesburg, South Africa, Abstract Volume, p. 407.

- Siahi, M., Master, S., and Hofmann, A. (2016). Mesoarchaean oxidative shallow marine environment in the Pongola Supergroup, South Africa. Goldschmidt Conference 2016, Yokohama, Japan, A2856.

- Siahi, M., Master, S., Hegner, E. and Hofmann, A. (2016). Unravelling of Mesoarchaean environmental conditions in the Pongola Supergroup, South Africa. 35th IGC, Capetown, South Africa. Paper number, 4843.

- Wilson, A.H., Hofmann, A. and Siahi, M. (2016). The Mid-Archaean Pongola Supergroup: volcanism, sedimentation and early life development on Earth's oldest stable continental margin. 35th IGC, Capetown, South Africa. Paper number, 866.

- Curriculum Vitae

Table A1. Trace element data (in ppm) for carbonate particles, matrix and secondary void/ fracture fills from samples of the main and upper carbonate sections. Element concentrations in ppm; b.d. = below detection; SN = shale-normalised; Ce* = $(0.5La + 0.5Pr)_{SN}$; Gd* = $(0.33Sm + 0.67Tb)_{SN}$; Pr* = $(0.5Ce + 0.5Nd)_{SN}$; Eu* = $(0.67Sm + 0.33Tb)_{SN}$.

Sample no. & section	**NCC9, main carbonate section**										
Spot	A74	A75	A76	A91	A92	A94	A95	A96	A102	A99	A110
Component	Dolomitic matrix	as A74	as A74	Microsparitic matrix	Microsparitic matrix	Microsparitic matrix	Dolomitic matrix	as A95	Dolomitic matrix	Silicified matrix	Dolomitic matrix
Mg	105000	106000	106000	109000	106000	107000	111000	111000	113000	112000	116000
Si	19000	19700	12200	399000	7900	200000	190000	380000	12000	71000	28000
Ti	10.7	12.6	9.92	12.7	10.2	10.5	12.6	9.51	9.57	12.1	10.0
V	9.15	15.6	4.09	12.7	6.79	10.9	28.4	4.49	5.87	26.0	8.08
Cr	9.92	19.3	6.18	19.6	9.83	13.1	29.5	7.64	6.89	34.5	9.84
Mn	3300	3000	2800	3700	3700	3600	3200	3500	3100	3000	2900
Fe	32200	31200	29000	45900	43700	44000	38700	45400	38100	39300	41600
Sr	412	409	421	341	344	352	391	336	377	396	387
Y	3.60	2.90	2.44	7.70	8.30	11.3	3.00	9.20	2.30	4.30	2.70
Zr	3.70	2.18	1.00	2.50	12.4	11.7	4.10	1.20	1.00	2.80	1.30
Ba	58.0	109	201	64.0	45.0	59.0	190	11.0	30.4	164	49.0
La	3.48	3.94	4.07	4.02	3.86	4.67	4.38	4.12	4.69	3.94	3.88
Ce	7.73	7.93	7.99	12.3	12.2	15.6	8.81	13.8	8.63	9.16	7.79
Pr	0.912	0.894	0.872	1.56	1.60	2.09	0.951	1.78	0.907	1.08	0.858
Nd	3.68	3.41	3.33	6.56	6.60	8.99	3.65	7.54	3.34	4.40	3.26
Sm	0.769	0.682	0.603	1.43	1.50	2.03	0.722	1.61	0.582	0.910	0.590
Eu	0.283	0.231	0.253	0.457	0.467	0.622	0.276	0.534	0.235	0.332	0.244
Gd	0.766	0.624	0.525	1.35	1.42	2.09	0.621	1.69	0.525	0.877	0.570
Tb	0.109	0.089	0.075	0.218	0.225	0.293	0.087	0.236	0.071	0.126	0.083
Dy	0.632	0.491	0.424	1.28	1.38	1.82	0.500	1.52	0.417	0.748	0.450
Ho	0.124	0.094	0.082	0.244	0.265	0.356	0.101	0.288	0.075	0.137	0.088
Er	0.300	0.242	0.225	0.651	0.707	0.946	0.255	0.768	0.191	0.378	0.251
Tm	0.041	0.032	0.025	0.099	0.106	0.134	0.034	0.113	0.030	0.047	0.031
Yb	0.255	0.203	0.166	0.568	0.674	0.885	0.210	0.724	0.159	0.328	0.179
Lu	0.036	0.027	0.023	0.082	0.097	0.127	0.032	0.099	0.024	0.047	0.023
Pb	8.43	1.86	2.98	1.91	1.07	1.48	1.55	0.468	0.810	0.710	1.00
U	0.083	0.061	0.033	0.055	0.234	0.252	0.108	0.058	0.043	0.080	0.043
Y/Ho	28.7	30.4	29.6	31.4	31.2	31.6	29.8	31.8	31.2	31.0	30.2
$(Pr/Yb)_{SN}$	1.14	1.41	1.68	0.877	0.758	0.754	1.45	0.785	1.82	1.05	1.53
$(Pr/Tb)_{SN}$	0.734	0.880	1.03	0.627	0.623	0.625	0.961	0.661	1.12	0.752	0.907
$(Tb/Yb)_{SN}$	1.56	1.60	1.64	1.40	1.22	1.21	1.50	1.19	1.63	1.40	1.69
$(Ce/Ce^*)_{SN}$	0.999	0.975	0.978	1.10	1.09	1.09	0.995	1.12	0.962	1.02	0.985
$(Gd/Gd^*)_{SN}$	1.17	1.14	1.12	1.06	1.07	1.20	1.13	1.21	1.17	1.15	1.14
$(Pr/Pr^*)_{SN}$	1.00	1.01	0.994	1.01	1.04	1.03	0.987	1.02	0.993	0.998	1.00
$(Eu/Eu^*)_{SN}$	1.90	1.80	2.26	1.61	1.58	1.57	2.08	1.69	2.19	1.90	2.14

Sample no. & section	NCC9, main carbonate section										
Spots	A111	A88	A89	A105	A79	A81	A82	A90	A98	A103	A104
Component	as A110	Concentric ooid	Silicified particle	Micritic ooid	Peloid	Calcite-filled fenestrae	as A81	Calcite-filled void	Calcite-filled void	Calcite-filled void	Calcite-filled void
Mg	115000	105000	106000	108000	105000	1700	1800	2000	1800	1900	1600
Si	24000	5400	440000	92000	507	178	185	170	170	186	197
Ti	13.9	9.45	13.3	12.8	9.81	17.5	17.7	17.3	17.2	17.2	17.1
V	10.7	5.09	24.3	14.6	27.3	0.509	0.460	0.580	0.199	0.956	0.232
Cr	12.4	4.93	44.0	12.6	11.3	1.17	1.20	1.30	1.25	1.62	1.34
Mn	3000	4300	4000	4400	3200	2000	2000	3000	2500	2100	1700
Fe	42000	46000	45000	56000	39000	3600	3600	3000	3800	5600	5900
Sr	383	350	345	331	323	474	633	825	557	468	385
Y	3.48	3.34	7.14	3.77	1.90	2.74	3.98	4.50	4.02	3.36	3.64
Zr	1.23	1.14	22.9	6.43	0.211	<0.006	<0.006	0.018	<0.006	0.011	<0.006
Ba	63.7	10.1	168	53.0	6.62	1.69	1.91	3.71	4.70	2.53	1.99
La	4.72	4.46	3.86	5.80	3.47	0.989	2.64	6.50	3.42	6.89	2.83
Ce	9.69	9.49	10.8	12.5	6.54	3.00	6.81	10.9	5.82	9.29	4.34
Pr	1.07	1.06	1.38	1.46	0.692	0.417	0.857	1.10	0.563	0.795	0.412
Nd	4.13	4.10	5.83	6.19	2.71	1.94	3.58	4.02	2.04	2.42	1.51
Sm	0.800	0.833	1.30	1.14	0.483	0.479	0.730	0.672	0.398	0.379	0.313
Eu	0.285	0.310	0.504	0.422	0.186	1.03	0.988	0.262	0.146	0.138	0.126
Gd	0.793	0.762	1.24	1.04	0.442	0.584	0.819	0.689	0.461	0.402	0.349
Tb	0.105	0.101	0.196	0.129	0.062	0.073	0.100	0.094	0.074	0.059	0.064
Dy	0.631	0.633	1.23	0.700	0.357	0.383	0.591	0.643	0.522	0.454	0.451
Ho	0.113	0.108	0.230	0.126	0.068	0.065	0.102	0.118	0.109	0.098	0.106
Er	0.321	0.285	0.625	0.328	0.172	0.148	0.255	0.347	0.356	0.314	0.338
Tm	0.043	0.037	0.087	0.040	0.023	0.016	0.030	0.054	0.055	0.048	0.047
Yb	0.251	0.240	0.566	0.251	0.174	0.070	0.154	0.344	0.361	0.334	0.331
Lu	0.035	0.032	0.084	0.033	0.024	0.008	0.017	0.045	0.046	0.049	0.047
Pb	1.27	0.740	2.64	2.26	1.98	1.58	2.81	9.74	4.92	2.10	1.71
U	0.071	0.032	0.520	0.212	0.032	0.004	0.004	0.031	0.004	0.014	0.001
Y/Ho	30.9	30.9	31.0	29.9	27.9	42.0	39.2	38.1	36.8	34.2	34.2
$(Pr/Yb)_{SN}$	1.36	1.41	0.779	1.86	1.27	1.92	1.78	1.02	0.498	0.760	0.398
$(Pr/Tb)_{SN}$	0.891	0.918	0.617	0.992	0.982	0.501	0.751	1.03	0.665	1.18	0.567
$(Tb/Yb)_{SN}$	1.53	1.54	1.26	1.87	1.29	3.83	2.37	0.991	0.749	0.647	0.701
$(Ce/Ce^*)_{SN}$	0.995	1.01	1.06	0.987	0.971	1.03	1.03	0.925	0.954	0.863	0.903
$(Gd/Gd^*)_{SN}$	1.23	1.19	1.08	1.25	1.15	1.37	1.35	1.22	1.13	1.17	1.02
$(Pr/Pr^*)_{SN}$	0.995	1.00	1.01	0.975	0.967	0.995	1.02	0.977	0.957	0.957	0.942
$(Eu/Eu^*)_{SN}$	1.88	2.02	1.96	2.05	2.06	10.87	7.07	2.02	1.71	1.82	1.81

Sample no. & section	NCC9, main carbonate section						NCC11, main carbonate section				
Spots	A106	A107	A97	A101	A77	A78	A112	B78	B79	B80	B82
Component	Calcite-filled void	as A106	Dolomitic intraclast	Dolomitic intraclast	Microsparitic intraclast	as A77	Dolomitic intraclast	Microsparitic matrix	as B78	as B78	Microsparitic matrix
Mg	2800	2700	112000	117000	102000	106000	117000	99000	99000	10000	99000
Si	162	178	5600	2800	22000	6800	29000	5100	1500	3800	4600
Ti	17.0	17.0	9.63	11.5	11.6	9.97	9.43	113	109	112	114
V	0.058	0.090	4.55	4.95	19.7	6.41	3.50	4.57	4.48	5.20	6.36
Cr	1.15	1.12	5.75	4.46	15.8	6.22	4.39	18.9	16.1	24.4	20.3
Mn	6200	6200	3100	2400	4400	3000	2600	1800	1800	1800	1800
Fe	7100	7000	36000	29000	46000	31000	37000	24000	24000	24000	25000
Sr	256	237	381	412	337	377	402	322	314	310	312
Y	4.03	3.94	3.63	2.26	3.50	2.32	2.35	2.36	2.08	2.26	2.27
Zr	0.018	0.096	1.00	1.02	14.1	1.78	2.61	2.09	0.350	0.105	0.136
Ba	3.28	2.72	19.3	21.1	42.1	22.6	15.2	23.1	15.6	33.2	39.6
La	2.05	2.16	3.65	4.50	3.57	3.79	3.43	2.97	2.92	3.06	3.22
Ce	3.78	3.71	8.18	8.03	7.74	7.25	6.71	6.17	6.10	6.43	6.55
Pr	0.416	0.385	0.958	0.826	0.892	0.778	0.719	0.706	0.682	0.723	0.772
Nd	1.64	1.56	3.82	3.00	3.55	2.88	2.84	2.66	2.524	2.69	2.71
Sm	0.368	0.374	0.774	0.546	0.716	0.547	0.542	0.475	0.451	0.503	0.505
Eu	0.151	0.146	0.281	0.192	0.255	0.199	0.202	0.166	0.156	0.169	0.164
Gd	0.466	0.451	0.762	0.495	0.711	0.505	0.483	0.448	0.430	0.471	0.452
Tb	0.077	0.079	0.105	0.066	0.097	0.075	0.068	0.067	0.059	0.065	0.066
Dy	0.506	0.522	0.650	0.398	0.592	0.389	0.420	0.417	0.361	0.424	0.415
Ho	0.106	0.111	0.119	0.073	0.122	0.078	0.077	0.079	0.072	0.078	0.074
Er	0.313	0.303	0.302	0.199	0.331	0.221	0.218	0.211	0.192	0.197	0.197
Tm	0.046	0.040	0.045	0.024	0.049	0.028	0.027	0.031	0.026	0.028	0.029
Yb	0.284	0.272	0.267	0.157	0.285	0.166	0.163	0.192	0.161	0.179	0.182
Lu	0.035	0.032	0.036	0.021	0.044	0.024	0.025	0.028	0.025	0.026	0.026
Pb	2.77	3.47	1.03	0.630	1.54	2.48	2.84	4.38	2.41	2.57	2.37
U	0.001	0.002	0.034	0.071	0.390	0.065	0.058	0.113	0.045	0.035	0.040
Y/Ho	37.9	35.5	30.4	31.0	28.7	29.9	30.6	29.7	28.8	29.0	30.6
$(Pr/Yb)_{SN}$	0.468	0.452	1.15	1.68	1.00	1.50	1.41	1.18	1.36	1.29	1.35
$(Pr/Tb)_{SN}$	0.473	0.425	0.799	1.10	0.803	0.910	0.923	0.928	1.01	0.980	1.03
$(Tb/Yb)_{SN}$	0.989	1.06	1.43	1.52	1.25	1.64	1.53	1.27	1.336	1.32	1.32
$(Ce/Ce^*)_{SN}$	0.942	0.931	1.01	0.955	1.00	0.972	0.985	0.983	0.997	0.997	0.958
$(Gd/Gd^*)_{SN}$	1.13	1.06	1.19	1.19	1.20	1.11	1.13	1.118	1.19	1.18	1.12
$(Pr/Pr^*)_{SN}$	0.983	0.941	1.01	0.988	1.00	1.00	0.969	1.025	1.02	1.02	1.08
$(Eu/Eu^*)_{SN}$	1.82	1.73	1.90	1.91	1.86	1.90	2.00	1.81	1.83	1.79	1.73

Sample no. & section	NCC11, main carbonate section										
Spots	B85	B71	B72	B73	B74	B76	B77	B83	B84	B89	B75
Component	Microsparitic matrix	Dolomitic particle	as B71	as B71	as B71	as B71	as B71	as B71	as B71	as B71	Silicified particle
Mg	99000	101000	100000	98000	100000	98000	100000	100000	101000	99000	101000
Si	4900	5800	11000	4400	6500	9100	3300	5300	18800	3500	1426000
Ti	111	112	122	114	116	117	117	113	112	114	293
V	4.47	4.99	9.34	4.15	6.53	8.78	4.21	4.73	4.88	5.49	56.5
Cr	15.6	14.9	36.1	14.4	21.8	28.8	16.2	20.7	17.0	24.6	166
Mn	1900	1500	1900	2000	1900	1900	1800	1700	1700	2000	1900
Fe	26000	18000	24000	24000	23000	24000	23000	23000	23000	28000	26000
Sr	318	416	351	462	343	328	417	405	379	387	340
Y	3.27	2.63	2.61	2.55	2.53	2.40	2.29	2.15	2.65	3.35	4.01
Zr	0.167	0.469	0.139	3.72	0.337	0.186	4.05	2.85	4.15	18.0	24.9
Ba	26.6	45.2	88.2	39.9	57.4	74.2	26.3	39.7	32.9	31.2	553
La	2.70	4.93	4.45	6.09	4.24	3.82	4.38	4.29	4.24	4.63	3.75
Ce	6.31	8.85	8.36	9.93	8.01	7.45	7.82	7.51	7.81	8.35	7.29
Pr	0.779	0.919	0.909	0.988	0.883	0.817	0.814	0.778	0.833	0.873	0.850
Nd	3.02	3.44	3.32	3.41	3.18	3.05	3.03	2.86	3.06	3.25	3.26
Sm	0.595	0.600	0.590	0.580	0.570	0.562	0.530	0.481	0.583	0.647	0.653
Eu	0.178	0.196	0.212	0.204	0.188	0.177	0.196	0.174	0.183	0.237	0.250
Gd	0.582	0.501	0.541	0.521	0.514	0.482	0.515	0.443	0.498	0.600	0.711
Tb	0.092	0.074	0.079	0.070	0.074	0.067	0.067	0.060	0.073	0.093	0.093
Dy	0.582	0.473	0.481	0.437	0.443	0.438	0.396	0.394	0.489	0.554	0.657
Ho	0.110	0.087	0.088	0.085	0.085	0.078	0.075	0.075	0.087	0.116	0.128
Er	0.294	0.227	0.232	0.236	0.220	0.214	0.210	0.209	0.255	0.327	0.386
Tm	0.042	0.033	0.033	0.031	0.029	0.029	0.028	0.026	0.033	0.047	0.061
Yb	0.269	0.193	0.196	0.194	0.179	0.172	0.187	0.182	0.228	0.347	0.429
Lu	0.039	0.028	0.028	0.029	0.029	0.024	0.026	0.026	0.030	0.049	0.062
Pb	1.78	2.17	3.29	3.17	3.68	3.88	4.02	2.27	2.69	5.23	4.97
U	0.037	0.044	0.042	0.212	0.057	0.039	0.318	0.164	0.208	0.900	0.562
Y/Ho	29.8	30.3	29.7	29.9	29.7	30.7	30.5	28.5	30.3	29.0	31.4
$(Pr/Yb)_{SN}$	0.925	1.52	1.48	1.63	1.57	1.52	1.39	1.37	1.17	0.803	0.633
$(Pr/Tb)_{SN}$	0.741	1.10	1.02	1.23	1.05	1.07	1.07	1.15	0.996	0.821	0.800
$(Tb/Yb)_{SN}$	1.25	1.39	1.46	1.32	1.50	1.42	1.30	1.19	1.17	0.979	0.791
$(Ce/Ce^*)_{SN}$	0.998	0.954	0.957	0.920	0.954	0.972	0.950	0.942	0.956	0.953	0.942
$(Gd/Gd^*)_{SN}$	1.08	1.08	1.13	1.17	1.13	1.13	1.24	1.19	1.09	1.08	1.28
$(Pr/Pr^*)_{SN}$	1.05	0.979	1.01	0.993	1.03	1.01	0.983	0.986	1.00	0.985	1.03
$(Eu/Eu^*)_{SN}$	1.50	1.77	1.89	1.91	1.75	1.72	1.98	1.96	1.68	1.88	1.97

Sample no. & section	NCC11, main carbonate section				NCC13, main carbonate section						
Spots	B87	B90	B86	B88	A52	A53	A54	A55	A69	A73	A43
Component	as B75	as B75	Micritic/microsparitic particle	as B86	Dolomitic matrix	as A52	as A52	Dolomitic matrix	Dolomitic matrix	Dolomitic matrix	Oncoid,dololutite
Mg	98000	100000	100000	101000	101000	101000	102000	101000	106000	106000	98000
Si	420000	375000	5700	42000	30000	13500	23900	134000	41000	4600	254000
Ti	118	161	113	112	9.88	9.83	10.1	9.79	9.88	9.68	9.85
V	10.4	27.1	4.71	3.65	1.43	0.804	0.858	1.11	2.40	0.809	1.62
Cr	36.7	124	16.0	13.0	2.47	1.76	1.78	2.72	3.67	1.86	3.11
Mn	1700	1900	1700	1700	2000	1900	1800	2000	2300	1700	2200
Fe	25000	27000	24000	25000	14000	13000	13000	15000	19000	15000	14000
Sr	339	341	509	399	336	358	360	315	320	341	361
Y	2.49	3.25	2.33	2.67	1.38	0.644	0.658	1.03	2.05	0.808	1.47
Zr	2.36	1.36	2.49	4.53	0.254	0.52	0.061	1.00	0.58	1.55	2.91
Ba	109	256	59.2	26.1	2.16	2.61	2.55	1.36	4.15	2.01	1.31
La	3.73	3.44	3.75	6.79	0.637	0.703	0.634	0.504	0.538	0.739	0.681
Ce	7.21	7.52	6.93	11.0	1.39	1.23	1.17	1.13	1.56	1.30	1.49
Pr	0.785	0.884	0.744	1.05	0.184	0.143	0.138	0.155	0.213	0.155	0.198
Nd	2.96	3.42	2.75	3.62	0.888	0.614	0.608	1.07	1.11	0.66	0.904
Sm	0.526	0.677	0.491	0.554	0.243	0.144	0.153	0.183	0.319	0.168	0.260
Eu	0.203	0.198	0.167	0.188	0.099	0.085	0.087	0.106	0.108	0.082	0.119
Gd	0.495	0.603	0.447	0.519	0.236	0.144	0.138	0.174	0.345	0.161	0.244
Tb	0.068	0.091	0.064	0.075	0.036	0.019	0.019	0.028	0.053	0.024	0.036
Dy	0.446	0.582	0.412	0.454	0.211	0.109	0.112	0.143	0.309	0.117	0.245
Ho	0.081	0.107	0.082	0.088	0.046	0.018	0.021	0.034	0.056	0.024	0.039
Er	0.234	0.292	0.227	0.248	0.107	0.048	0.052	0.079	0.157	0.068	0.104
Tm	0.034	0.044	0.031	0.035	0.013	0.006	0.007	0.012	0.019	0.008	0.017
Yb	0.169	0.248	0.194	0.235	0.080	0.030	0.032	0.066	0.130	0.043	0.075
Lu	0.033	0.035	0.027	0.032	0.012	0.005	0.005	0.009	0.018	0.008	0.012
Pb	4.96	3.27	3.30	2.86	1.06	1.12	1.14	0.840	0.652	1.02	0.880
U	0.125	0.068	0.180	0.276	0.040	0.065	0.041	0.053	0.038	0.105	0.377
Y/Ho	30.6	30.5	28.4	30.4	30.0	36.6	31.8	30.4	36.7	34.4	37.7
$(Pr/Yb)_{SN}$	1.48	1.14	1.22	1.43	0.735	1.54	1.37	0.746	0.523	1.15	0.845
$(Pr/Tb)_{SN}$	1.01	0.853	1.03	1.23	0.444	0.651	0.629	0.492	0.353	0.564	0.485
$(Tb/Yb)_{SN}$	1.47	1.33	1.19	1.16	1.66	2.37	2.18	1.51	1.48	2.05	1.74
$(Ce/Ce^*)_{SN}$	0.971	0.994	0.954	0.928	0.933	0.894	0.907	0.927	1.03	0.885	0.929
$(Gd/Gd^*)_{SN}$	1.18	1.09	1.14	1.14	1.10	1.23	1.15	1.07	1.14	1.12	1.13
$(Pr/Pr^*)_{SN}$	0.999	1.02	1.00	0.973	0.954	0.963	0.962	0.768	0.924	0.981	0.989
$(Eu/Eu^*)_{SN}$	2.05	1.54	1.81	1.78	0.74	1.54	1.37	0.75	1.65	2.52	2.38

Sample no. & section	**NCC13, main carbonate section**										
Spots	A44	A46	A47	A63	A64	A70	A71	A56	A59	A68	B06
Component	as A43	Oncoid	as A46	Oncoid	as A63	Oncoid	as A70	Micritic ooid	Dolomitic intraclast	Dolomitic intraclast	Micritic stromatolitic laminae
Mg	98000	100000	98000	104000	104000	104000	106000	102000	103000	105000	92000
Si	804000	3700	3200	382	411	63000	56000	245000	2000	5000	147000
Ti	9.33	9.84	9.88	9.68	9.77	9.67	9.63	9.74	9.71	9.72	125
V	1.66	0.734	2.06	0.766	0.538	0.916	0.972	1.04	0.947	0.789	6.11
Cr	5.16	1.19	1.50	1.41	1.34	1.97	2.00	1.87	1.93	2.03	15.0
Mn	2400	1900	2900	1800	1300	2000	1900	2000	2000	1900	2990
Fe	17000	18000	23000	16000	12000	16000	16000	15000	15000	15000	30000
Sr	340	303	287	302	294	360	352	332	363	361	311
Y	1.18	0.548	0.777	0.580	0.611	0.915	1.02	0.765	0.805	0.711	6.45
Zr	0.057	0.185	1.38	0.14	0.221	0.023	0.030	0.063	0.044	0.550	5.47
Ba	1.85	9.68	7.01	5.04	5.27	1.33	1.39	3.22	3.16	2.09	21.2
La	0.679	0.992	1.29	1.14	1.18	0.856	0.885	1.02	0.827	0.635	2.50
Ce	1.51	1.43	1.84	1.68	1.72	1.59	1.63	1.66	1.48	1.18	6.50
Pr	0.205	0.145	0.189	0.174	0.251	0.196	0.200	0.187	0.174	0.143	0.884
Nd	0.902	0.577	0.744	0.703	0.706	0.835	0.865	0.770	0.789	0.619	4.01
Sm	0.235	0.124	0.142	0.138	0.141	0.205	0.205	0.170	0.178	0.165	1.15
Eu	0.108	0.074	0.111	0.099	0.095	0.110	0.106	0.107	0.106	0.088	0.625
Gd	0.259	0.113	0.152	0.134	0.138	0.187	0.219	0.174	0.155	0.147	1.26
Tb	0.036	0.014	0.021	0.015	0.017	0.023	0.026	0.025	0.025	0.021	0.193
Dy	0.210	0.083	0.115	0.094	0.104	0.154	0.163	0.135	0.130	0.121	1.20
Ho	0.040	0.017	0.024	0.017	0.018	0.025	0.034	0.022	0.025	0.021	0.216
Er	0.090	0.047	0.061	0.044	0.038	0.065	0.085	0.053	0.056	0.053	0.577
Tm	0.009	0.004	0.009	0.006	0.006	0.010	0.010	0.008	0.009	0.006	0.074
Yb	0.067	0.031	0.051	0.034	0.034	0.055	0.050	0.039	0.046	0.043	0.458
Lu	0.009	0.004	0.006	0.004	0.005	0.005	0.008	0.006	0.006	0.005	0.061
Pb	2.39	5.34	4.74	1.40	1.45	1.30	1.23	1.57	1.17	0.950	42.2
U	0.016	0.049	0.083	0.026	0.029	0.015	0.017	0.048	0.047	0.059	0.216
Y/Ho	29.6	33.2	32.5	34.5	34.3	37.3	30.4	34.5	31.7	33.7	29.8
$(Pr/Yb)_{SN}$	0.977	1.49	1.19	1.64	2.35	1.14	1.28	1.55	1.21	1.07	0.616
$(Pr/Tb)_{SN}$	0.503	0.920	0.808	1.04	1.29	0.754	0.664	0.645	0.617	0.603	0.402
$(Tb/Yb)_{SN}$	1.94	1.62	1.47	1.58	1.83	1.52	1.93	2.40	1.95	1.78	1.53
$(Ce/Ce^*)_{SN}$	0.927	0.845	0.838	0.854	0.729	0.896	0.894	0.870	0.898	0.904	0.986
$(Gd/Gd^*)_{SN}$	1.24	1.25	1.25	1.37	1.28	1.26	1.34	1.16	1.04	1.13	1.15
$(Pr/Pr^*)_{SN}$	1.02	0.939	0.950	0.942	1.34	0.995	0.985	0.972	0.942	0.979	1.00
$(Eu/Eu^*)_{SN}$	2.32	3.33	4.02	4.03	3.66	2.98	2.76	3.19	3.10	2.87	2.64

Sample no. & section	**NCC16B, main carbonate section**										
Spots	B12	B18	B22	B08	B11	B13	B14	B15	B16	B19	B20
Component	Micritic str. laminae	Micritic str. laminae	Micritic str. laminae	Microsparitic str. laminae	Microsparitic str. laminae	Microsparitic str. laminae	as B13	as B13	as B13	as B13	as B13
Mg	94000	94000	94000	92000	93000	93000	93000	93000	96000	93000	93000
Si	62000	161000	21000	30000	19000	13000	32000	22000	15000	146000	17000
Ti	168	122	118	116	147	159	146	118	118	114	121
V	26.1	7.51	7.29	5.26	15.0	6.82	21.2	7.41	6.97	3.00	7.07
Cr	44.0	17.4	17.1	8.32	31.5	16.3	57.2	13.9	12.8	7.64	18.1
Mn	3000	3000	2800	2800	3000	2600	3200	2900	2700	2900	3000
Fe	31000	32000	32000	30000	31000	29000	32000	29000	29000	33000	33000
Sr	332	311	292	287	293	307	290	286	296	316	297
Y	6.18	6.31	5.30	5.29	11.2	6.39	7.40	6.73	6.34	7.26	8.68
Zr	6.46	6.57	5.14	2.98	7.33	5.01	5.85	8.05	3.63	4.58	4.68
Ba	107	20.7	16.6	9.45	60.6	18.1	80.2	16.5	14.4	9.25	18.7
La	2.40	2.42	2.66	2.26	2.40	2.35	3.13	2.79	2.65	2.36	2.82
Ce	6.22	6.12	6.19	5.66	7.73	6.29	7.80	6.83	6.66	6.43	7.76
Pr	0.861	0.839	0.817	0.742	1.158	0.874	1.05	0.921	0.888	0.913	1.09
Nd	3.87	3.87	3.58	3.32	5.43	4.00	4.71	4.04	4.00	4.18	4.98
Sm	1.06	1.06	0.921	0.870	1.63	1.10	1.32	1.12	1.06	1.24	1.37
Eu	0.659	0.594	0.497	0.460	0.833	0.525	0.722	0.571	0.532	0.700	0.695
Gd	1.25	1.20	1.05	1.03	1.88	1.26	1.44	1.23	1.14	1.34	1.59
Tb	0.185	0.189	0.159	0.157	0.301	0.192	0.226	0.191	0.182	0.208	0.245
Dy	1.15	1.14	0.943	0.980	1.98	1.22	1.34	1.20	1.16	1.27	1.49
Ho	0.214	0.207	0.184	0.181	0.367	0.218	0.254	0.228	0.209	0.243	0.286
Er	0.527	0.532	0.463	0.463	0.950	0.548	0.655	0.594	0.570	0.609	0.748
Tm	0.065	0.071	0.060	0.062	0.132	0.077	0.090	0.082	0.076	0.079	0.102
Yb	0.441	0.442	0.388	0.406	0.833	0.458	0.518	0.526	0.472	0.495	0.603
Lu	0.055	0.060	0.051	0.057	0.116	0.063	0.076	0.071	0.064	0.066	0.087
Pb	18.6	17.8	17.2	31.5	17.4	10.3	67.7	16.4	15.8	18.0	17.2
U	0.210	0.215	0.181	0.153	0.203	0.196	0.249	0.271	0.168	0.191	0.179
Y/Ho	28.9	30.5	28.9	29.2	30.5	29.3	29.1	29.5	30.3	29.9	30.3
$(Pr/Yb)_{SN}$	0.624	0.606	0.672	0.584	0.444	0.609	0.649	0.559	0.601	0.589	0.576
$(Pr/Tb)_{SN}$	0.409	0.389	0.452	0.414	0.337	0.398	0.409	0.423	0.427	0.385	0.389
$(Tb/Yb)_{SN}$	1.53	1.56	1.49	1.41	1.32	1.53	1.59	1.32	1.41	1.53	1.48
$(Ce/Ce^*)_{SN}$	0.974	0.970	0.958	0.994	1.00	0.985	0.975	0.967	0.985	0.978	0.990
$(Gd/Gd^*)_{SN}$	1.20	1.13	1.18	1.17	1.13	1.16	1.13	1.14	1.11	1.13	1.16
$(Pr/Pr^*)_{SN}$	1.01	0.995	1.01	0.994	1.02	1.00	1.01	1.02	0.997	1.01	1.01
$(Eu/Eu^*)_{SN}$	2.98	2.66	2.60	2.50	2.40	2.29	2.65	2.46	2.43	2.75	2.40

Sample no. & section	NCC16B, main carbonate section								NCC17A, main carbonate section		
Spots	B21	B23	B25	B07	B09	B10	B17	B24	A113	A114	A115
Component	as B13	as B13	as B13	Silicified str.laminae	Partially Silic.micritic str.laminae	as B09	Partially Silic.micritic str.laminae	Partially Silic.micritic str.laminae	Dolomitic stromatolite	as A113	as A113
Mg	93000	95000	93000	93000	91000	91000	95000	93000	103000	102000	102000
Si	73000	51000	41000	619000	287000	25000	333000	604000	32000	15000	13000
Ti	115	189	254	235	122	132	478	162	11.5	10.9	10.3
V	4.22	22.0	14.6	34.3	3.84	6.42	56.5	23.3	5.00	2.95	2.66
Cr	10.2	47.5	48.4	192	12.3	13.9	126	71.0	16.1	17.7	7.35
Mn	3000	2700	3000	3000	2900	3000	3000	3000	6800	6800	7000
Fe	33000	31000	34000	34000	30000	31000	35000	35000	117000	118000	120000
Sr	324	303	314	280	317	304	317	301	347	352	345
Y	7.35	7.04	8.05	15.2	5.99	6.96	12.3	6.68	8.18	7.96	6.74
Zr	5.13	9.48	14.1	21.2	9.95	14.3	43.0	13.4	5.83	1.77	0.980
Ba	12.7	79.3	52.5	171	13.8	21.2	220	92.7	63.4	37.1	29.6
La	2.56	2.42	2.82	3.94	2.40	2.99	2.69	2.37	2.52	2.84	2.42
Ce	7.01	6.34	7.20	12.29	6.22	7.64	8.01	6.34	5.44	6.11	5.33
Pr	1.00	0.893	1.02	1.72	0.846	1.04	1.16	0.926	0.687	0.762	0.669
Nd	4.48	4.14	4.62	7.98	3.88	4.75	5.48	4.10	3.01	3.24	2.90
Sm	1.28	1.16	1.33	2.35	1.08	1.28	1.70	1.18	0.972	1.04	0.944
Eu	0.733	0.598	0.735	1.124	0.625	0.667	0.966	0.707	0.704	0.724	0.650
Gd	1.45	1.33	1.48	2.58	1.19	1.40	2.11	1.28	1.24	1.34	1.13
Tb	0.227	0.203	0.229	0.396	0.176	0.214	0.331	0.200	0.222	0.219	0.192
Dy	1.32	1.23	1.45	2.57	1.15	1.30	2.12	1.23	1.38	1.36	1.16
Ho	0.251	0.233	0.265	0.492	0.205	0.241	0.386	0.221	0.259	0.265	0.221
Er	0.596	0.629	0.671	1.35	0.514	0.639	1.08	0.535	0.682	0.674	0.551
Tm	0.081	0.081	0.082	0.177	0.076	0.086	0.151	0.084	0.088	0.085	0.065
Yb	0.459	0.512	0.585	1.15	0.406	0.517	1.07	0.460	0.525	0.468	0.369
Lu	0.065	0.071	0.079	0.160	0.057	0.073	0.134	0.069	0.071	0.059	0.045
Pb	26.7	18.2	15.7	136	34.9	31.9	17.0	20.3	19.1	20.8	20.3
U	0.196	0.311	0.462	1.94	0.346	0.403	1.62	0.430	0.942	0.477	0.338
Y/Ho	29.3	30.2	30.4	30.9	29.2	28.9	31.7	30.2	31.6	30.0	30.5
$(Pr/Yb)_{SN}$	0.696	0.557	0.557	0.477	0.665	0.645	0.347	0.643	0.418	0.520	0.579
$(Pr/Tb)_{SN}$	0.386	0.386	0.390	0.380	0.422	0.428	0.308	0.407	0.271	0.305	0.305
$(Tb/Yb)_{SN}$	1.80	1.44	1.43	1.26	1.58	1.51	1.13	1.58	1.54	1.70	1.90
$(Ce/Ce^*)_{SN}$	0.976	0.969	0.955	1.04	0.985	0.977	1.00	0.954	0.951	0.956	0.963
$(Gd/Gd^*)_{SN}$	1.14	1.17	1.15	1.15	1.18	1.15	1.17	1.14	1.07	1.14	1.09
$(Pr/Pr^*)_{SN}$	1.03	1.00	1.02	1.00	0.995	1.00	1.00	1.05	0.990	1.00	0.994
$(Eu/Eu^*)_{SN}$	2.72	2.47	2.66	2.32	2.84	2.53	2.61	2.91	3.10	3.10	3.10

Sample no. & section	NCC17A, main carbonate section										
Spots	A116	A117	A118	A119	A120	A121	A122	A123	A131	A132	A124
Component	as A113	as A113	as A113	as A113	as A113	as A113	as A113	as A113	Dolomitic stromatolite	as A131	Sparite-filled void
Mg	102000	103000	99000	102000	104000	104000	103000	99000	107000	108000	93000
Si	21000	11000	20000	21000	18000	12000	35000	18000	24000	34000	178
Ti	10.4	10.1	10.3	10.4	9.83	10.0	10.7	9.51	10.4	10.8	9.11
V	3.51	1.98	3.69	3.09	1.61	1.32	3.96	2.14	4.62	5.90	3.44
Cr	6.98	4.64	6.32	4.89	3.67	3.29	5.87	3.52	6.51	5.42	1.09
Mn	6000	6900	6000	6000	6700	6800	6000	5900	6000	6000	4900
Fe	118000	123000	112000	122000	127000	126000	126000	116000	138000	140000	57000
Sr	375	348	320	358	366	353	368	323	365	362	54.6
Y	5.44	8.11	6.60	6.02	6.64	5.81	6.10	6.15	6.32	5.95	5.41
Zr	0.790	5.42	0.500	0.820	1.11	1.46	1.61	0.325	0.394	0.227	<0.005
Ba	49.5	22.6	43.4	42.8	17.2	14.4	55.9	19.5	67.6	87.5	3.72
La	2.34	2.31	4.74	4.34	2.11	2.18	2.40	3.65	2.87	2.49	16.3
Ce	5.02	5.31	9.40	8.92	4.80	4.71	5.15	7.43	6.00	5.31	32.1
Pr	0.621	0.668	1.05	1.01	0.621	0.587	0.619	0.848	0.711	0.636	3.10
Nd	2.59	2.95	4.13	3.95	2.77	2.59	2.66	3.48	2.97	2.63	9.84
Sm	0.831	0.984	1.04	0.959	0.948	0.810	0.830	0.921	0.869	0.788	1.39
Eu	0.624	0.700	0.671	0.662	0.634	0.575	0.633	0.648	0.614	0.581	0.343
Gd	1.01	1.28	1.21	1.15	1.16	1.02	1.06	1.10	1.10	0.987	1.05
Tb	0.161	0.226	0.185	0.176	0.188	0.168	0.175	0.177	0.176	0.166	0.147
Dy	1.00	1.36	1.17	1.06	1.19	1.02	1.07	1.08	1.13	1.04	0.873
Ho	0.183	0.253	0.224	0.199	0.220	0.187	0.200	0.203	0.206	0.193	0.164
Er	0.457	0.666	0.548	0.498	0.552	0.470	0.523	0.501	0.529	0.499	0.421
Tm	0.055	0.085	0.068	0.065	0.071	0.061	0.063	0.061	0.061	0.060	0.059
Yb	0.306	0.511	0.377	0.355	0.376	0.332	0.374	0.385	0.389	0.335	0.355
Lu	0.038	0.065	0.050	0.042	0.046	0.043	0.043	0.047	0.046	0.045	0.048
Pb	21.3	19.0	40.6	13.2	8.33	14.1	12.9	21.9	21.8	5.20	2.07
U	0.284	2.41	0.297	0.227	0.185	0.412	0.346	0.387	0.202	0.164	0.010
Y/Ho	29.7	32.1	29.5	30.3	30.2	31.1	30.5	30.3	30.7	30.8	33.0
$(Pr/Yb)_{SN}$	0.648	0.417	0.891	0.906	0.527	0.565	0.529	0.703	0.584	0.606	2.79
$(Pr/Tb)_{SN}$	0.338	0.259	0.498	0.502	0.290	0.306	0.310	0.420	0.354	0.336	1.85
$(Tb/Yb)_{SN}$	1.92	1.61	1.79	1.81	1.82	1.84	1.70	1.68	1.65	1.81	1.51
$(Ce/Ce^*)_{SN}$	0.959	0.98	0.971	0.984	0.960	0.958	0.973	0.974	0.969	0.972	1.04
$(Gd/Gd^*)_{SN}$	1.15	1.08	1.17	1.18	1.14	1.13	1.13	1.13	1.16	1.11	1.07
$(Pr/Pr^*)_{SN}$	1.01	0.98	0.993	0.998	0.990	0.981	0.979	0.980	0.988	0.998	1.01
$(Eu/Eu^*)_{SN}$	3.45	3.04	3.07	3.24	3.04	3.17	3.38	3.24	3.19	3.27	1.39

Sample no. & section	NCC17A, main carbonate section										
Spots	A125	A126	A133	A134	A135	A136	A137	A138	A139	A140	A141
Component	as A124	as A124	Sparitic-filled void	as A133	as A133	as A133	as A133	as A133	as A133	Sparitic-filled void	as A140
Mg	97000	93000	95000	90000	84000	95000	90000	91000	93000	99000	101000
Si	197	175	641	177	899	173	174	170	191	181	177
Ti	9.03	9.10	9.00	9.00	9.00	8.99	8.91	8.85	8.96	8.86	8.80
V	2.42	3.95	0.692	1.06	0.957	0.324	0.163	0.379	0.127	1.02	1.09
Cr	1.38	1.35	1.08	0.97	1.01	1.02	1.08	1.03	1.05	1.13	1.05
Mn	4000	4000	2900	6600	6000	4000	3000	3000	3000	4000	3000
Fe	60000	46000	47000	78000	72000	70000	72000	60000	66000	59000	56000
Sr	144	86.9	63.7	78.1	127	153	36.6	61.4	44.7	70.6	66.1
Y	7.37	5.60	5.24	7.29	8.66	8.40	7.13	9.86	7.36	5.49	4.91
Zr	<0.005	<0.005	<0.005	0.007	0.011	<0.005	0.018	0.017	0.019	0.005	<0.004
Ba	3.64	9.14	4.70	4.34	4.17	2.68	4.16	6.39	4.52	5.28	5.32
La	15.4	15.4	15.4	16.2	17.4	31.9	23.7	31.0	26.4	14.7	11.3
Ce	27.3	29.4	25.9	31.3	31.8	50.5	32.6	45.5	36.7	28.9	22.2
Pr	2.60	2.85	2.34	3.07	3.04	4.50	2.75	3.98	3.09	2.79	2.13
Nd	8.52	9.23	7.55	9.90	10.0	14.2	8.66	13.0	9.62	8.94	6.80
Sm	1.36	1.33	1.10	1.44	1.60	2.12	1.15	2.02	1.31	1.28	1.06
Eu	0.607	0.440	0.338	0.482	0.602	0.836	0.316	0.598	0.356	0.406	0.349
Gd	1.31	1.06	0.966	1.23	1.47	1.78	1.12	1.86	1.20	1.02	0.838
Tb	0.199	0.150	0.130	0.189	0.217	0.242	0.142	0.245	0.157	0.141	0.124
Dy	1.17	0.872	0.765	1.12	1.33	1.38	0.890	1.43	0.950	0.862	0.727
Ho	0.228	0.166	0.147	0.214	0.266	0.258	0.181	0.281	0.190	0.164	0.134
Er	0.625	0.469	0.421	0.610	0.762	0.700	0.474	0.731	0.529	0.433	0.350
Tm	0.079	0.058	0.060	0.083	0.102	0.090	0.070	0.094	0.073	0.059	0.052
Yb	0.509	0.357	0.362	0.528	0.693	0.618	0.408	0.606	0.462	0.337	0.272
Lu	0.080	0.048	0.056	0.085	0.118	0.101	0.061	0.087	0.066	0.047	0.037
Pb	2.89	6.00	2.33	1.92	1.59	2.40	0.80	2.72	0.90	6.04	4.11
U	0.020	0.013	0.015	0.010	0.027	0.063	0.435	0.069	0.069	0.011	0.007
Y/Ho	32.3	33.7	35.6	34.1	32.6	32.6	39.4	35.1	38.7	33.5	36.6
$(Pr/Yb)_{SN}$	1.63	2.55	2.06	1.86	1.40	2.33	2.15	2.10	2.14	2.64	2.50
$(Pr/Tb)_{SN}$	1.15	1.67	1.58	1.42	1.23	1.63	1.70	1.42	1.73	1.73	1.51
$(Tb/Yb)_{SN}$	1.42	1.53	1.31	1.30	1.14	1.43	1.27	1.47	1.24	1.52	1.66
$(Ce/Ce^*)_{SN}$	0.983	1.02	0.973	1.02	0.996	0.943	0.879	0.905	0.886	1.04	1.04
$(Gd/Gd^*)_{SN}$	1.11	1.09	1.17	1.06	1.12	1.14	1.26	1.20	1.20	1.10	1.05
$(Pr/Pr^*)_{SN}$	0.991	1.01	0.967	1.01	0.991	0.969	0.936	0.944	0.940	1.01	1.01
$(Eu/Eu^*)_{SN}$	2.28	1.83	1.68	1.77	1.97	2.18	1.48	1.61	1.48	1.77	1.80

Sample no. & section	NCC17A, main carbonate section						NCC23, main carbonate section				
Spots	A127	A128	A129	B26	B27	B29	B30	B31	B32	B33	B34
Component	Spartie-filled fracture	as A127	as A127	Bladed cement	as B26	as B26	Sparitic particle	as B30	as B30	as B30	as B30
Mg	98000	89000	96000	101000	94000	95000	96000	98000	94000	95000	95000
Si	185	174	168	<26.7	7500	4100	510	3100	17000	213	149
Ti	9.03	9.07	9.00	107	107	107	117	126	127	112	117
V	0.702	0.969	1.02	1.40	3.74	1.83	2.38	2.74	2.51	2.05	1.56
Cr	1.13	1.10	1.15	2.88	6.95	3.17	12.6	14.5	14.1	10.7	10.6
Mn	2800	5000	5000	2500	4000	4000	1000	1000	2000	1000	1000
Fe	45000	52000	51000	25000	38000	38000	16000	14000	29000	20000	16000
Sr	27.9	104	73.8	713	497	430	306	519	423	266	304
Y	5.53	6.51	5.85	4.00	6.97	5.81	2.42	2.59	5.43	1.96	2.43
Zr	<0.005	<0.005	<0.005	0.298	0.229	0.468	1.76	2.96	4.87	1.23	1.24
Ba	2.07	8.09	6.77	8.43	7.78	6.36	13.5	22.7	15.9	11.5	11.4
La	21.8	10.7	12.8	1.28	2.28	5.45	1.617	1.60	2.00	1.36	1.34
Ce	33.2	21.8	25.3	3.21	5.76	10.9	3.17	3.16	4.78	2.64	2.79
Pr	2.86	2.20	2.48	0.428	0.776	1.23	0.384	0.381	0.662	0.317	0.346
Nd	8.97	7.49	8.22	1.97	3.45	4.80	1.56	1.65	2.85	1.36	1.50
Sm	1.18	1.26	1.22	0.521	0.972	0.922	0.419	0.412	0.784	0.336	0.385
Eu	0.270	0.542	0.442	0.227	0.428	0.339	0.150	0.177	0.355	0.134	0.154
Gd	0.956	1.25	1.06	0.635	1.16	0.970	0.432	0.459	0.877	0.389	0.449
Tb	0.124	0.180	0.154	0.099	0.179	0.142	0.064	0.067	0.144	0.054	0.064
Dy	0.723	1.01	0.910	0.660	1.13	0.930	0.392	0.426	0.911	0.340	0.404
Ho	0.146	0.199	0.168	0.123	0.221	0.182	0.080	0.078	0.169	0.062	0.077
Er	0.393	0.517	0.468	0.309	0.538	0.477	0.191	0.203	0.465	0.167	0.193
Tm	0.050	0.066	0.058	0.042	0.069	0.065	0.029	0.032	0.061	0.022	0.026
Yb	0.337	0.399	0.356	0.263	0.474	0.396	0.173	0.192	0.394	0.139	0.169
Lu	0.052	0.053	0.048	0.034	0.065	0.056	0.023	0.024	0.054	0.018	0.021
Pb	0.465	12.9	2.26	1.39	2.63	2.18	3.97	3.22	2.4	5.13	4.93
U	0.008	0.012	0.004	0.066	0.074	0.058	0.091	0.239	0.232	0.057	0.055
Y/Ho	37.9	32.7	34.8	32.4	31.5	31.9	30.1	33.1	32.1	31.7	31.6
$(Pr/Yb)_{SN}$	2.71	1.76	2.22	0.520	0.523	0.994	0.707	0.633	0.537	0.726	0.653
$(Pr/Tb)_{SN}$	2.02	1.07	1.41	0.377	0.379	0.759	0.528	0.499	0.402	0.513	0.475
$(Tb/Yb)_{SN}$	1.34	1.64	1.58	1.38	1.38	1.31	1.34	1.27	1.33	1.42	1.38
$(Ce/Ce^*)_{SN}$	0.932	1.03	1.03	0.983	0.981	0.969	0.928	0.933	0.943	0.928	0.945
$(Gd/Gd^*)_{SN}$	1.16	1.16	1.10	1.16	1.17	1.17	1.16	1.20	1.10	1.25	1.23
$(Pr/Pr^*)_{SN}$	0.951	1.01	1.00	0.986	1.01	1.00	1.01	0.976	1.04	0.980	0.988
$(Eu/Eu^*)_{SN}$	1.30	2.22	1.94	2.02	2.06	1.84	1.80	2.12	2.12	1.96	1.96

Sample no. & section	NCC23, main carbonate section					NCD4, upper carbonate section					
Spots	B35	B36	B37	B39	B40	A06	A41	A09	A10	A11	A30
Component	as B30	as B30	as B30	a B30	as B30	Dolomitic intraclast	as A06	Dolomitic intraclast	Dolomitic intraclast	as A10	Dolomitic intraclast
Mg	96000	103000	104000	92000	90000	91000	85000	87000	83000	87000	96000
Si	260	10000	1000	167	2000	5900	884	2400	6900	860	421
Ti	112	112	112	114	110	9.91	10.1	9.86	9.17	8.99	8.79
V	1.84	2.99	3.01	1.58	2.42	4.35	0.890	3.71	3.31	3.20	1.37
Cr	8.69	10.9	10.3	8.21	11.0	5.91	1.84	4.14	2.47	2.13	2.53
Mn	1000	927	1000	1000	1000	6000	6000	6000	7000	7000	5000
Fe	16000	13000	16000	20000	20000	32000	39000	37000	52000	52000	35000
Sr	301	574	662	280	272	178	162	248	359	393	202
Y	1.97	2.20	3.03	2.20	2.99	5.45	4.20	9.55	15.3	15.5	6.21
Zr	1.06	1.49	2.24	1.37	0.986	2.53	0.484	2.75	1.36	1.43	0.950
Ba	12.4	29.5	32.9	12.1	15.7	34.2	18.2	20.9	33.2	39.7	11.9
La	1.27	1.84	1.79	1.30	3.20	2.65	2.10	3.73	4.35	4.52	2.72
Ce	2.53	3.99	4.02	2.59	5.70	5.09	4.01	7.78	8.84	9.23	5.42
Pr	0.304	0.468	0.487	0.325	0.623	0.585	0.458	0.925	1.07	1.10	0.656
Nd	1.31	1.86	2.06	1.40	2.44	2.46	1.97	4.00	4.62	4.78	2.79
Sm	0.350	0.442	0.512	0.379	0.566	0.645	0.526	1.16	1.29	1.36	0.825
Eu	0.142	0.154	0.198	0.148	0.210	0.240	0.170	0.417	0.471	0.491	0.272
Gd	0.373	0.406	0.549	0.393	0.589	0.773	0.645	1.43	1.79	1.81	0.994
Tb	0.051	0.064	0.077	0.058	0.080	0.131	0.112	0.252	0.326	0.328	0.162
Dy	0.320	0.387	0.504	0.354	0.511	0.879	0.711	1.59	2.22	2.27	1.01
Ho	0.064	0.072	0.098	0.065	0.090	0.178	0.134	0.322	0.473	0.488	0.196
Er	0.151	0.195	0.245	0.170	0.241	0.475	0.371	0.862	1.44	1.44	0.552
Tm	0.019	0.024	0.034	0.021	0.031	0.067	0.049	0.120	0.220	0.208	0.073
Yb	0.124	0.159	0.229	0.142	0.211	0.445	0.318	0.830	1.49	1.40	0.469
Lu	0.016	0.022	0.029	0.018	0.030	0.058	0.042	0.117	0.222	0.195	0.057
Pb	4.41	2.44	3.68	4.05	5.27	6.66	10.6	2.33	1.60	1.48	5.95
U	0.062	0.672	0.422	0.070	0.075	0.432	0.135	0.355	0.160	0.141	0.098
Y/Ho	31.0	30.4	30.8	33.7	33.3	30.6	31.3	29.7	32.4	31.7	31.7
$(Pr/Yb)_{SN}$	0.784	0.941	0.679	0.733	0.943	0.420	0.460	0.356	0.230	0.251	0.447
$(Pr/Tb)_{SN}$	0.520	0.642	0.557	0.488	0.681	0.391	0.357	0.322	0.288	0.295	0.355
$(Tb/Yb)_{SN}$	1.51	1.47	1.22	1.50	1.38	1.07	1.29	1.11	0.797	0.854	1.26
$(Ce/Ce^*)_{SN}$	0.938	0.990	0.990	0.918	0.928	0.943	0.943	0.966	0.944	0.954	0.936
$(Gd/Gd^*)_{SN}$	1.23	1.07	1.22	1.15	1.23	1.09	1.08	1.07	1.07	1.06	1.13
$(Pr/Pr^*)_{SN}$	0.977	1.01	0.991	0.998	0.982	0.971	0.956	0.971	0.982	0.971	0.988
$(Eu/Eu^*)_{SN}$	2.07	1.79	1.96	1.96	1.91	1.68	1.42	1.58	1.49	1.51	1.51

Sample no. & section	**NCD4, upper carbonate section**										
Spots	A31	A32	A40	A07	A16	A12	A13	A14	A15	A17	A18
Component	A30, rim	as A30, rim	Dolomitic intraclast	Concentric ooid	Concentric ooid	Superficial ooid	Superficial ooid	Rim of superficial ooid	Superficial ooid	Dolomicritic laminae	as A17
Mg	96000	97000	83000	91000	88000	91000	90000	90000	93000	94000	92000
Si	14000	22000	532	13000	82000	198000	110000	9000	52000	9094	28113
Ti	11.0	9.53	10.1	9.97	9.44	11.0	9.36	10.1	11.9	11.0	11.6
V	10.7	4.63	1.09	9.19	5.28	13.7	6.35	7.81	18.2	8.20	11.8
Cr	8.26	4.86	1.46	4.34	3.99	10.5	3.32	7.13	14.0	7.85	12.5
Mn	7000	7000	6000	5000	7000	7600	7900	7900	7600	7000	6820
Fe	51000	49000	35000	34000	38000	45000	47000	50000	47000	45000	43000
Sr	221	296	261	182	212	249	173	212	238	246	289
Y	9.76	10.8	8.37	11.2	7.31	10.9	10.6	11.2	10.2	9.88	12.0
Zr	7.75	3.45	0.384	4.72	3.71	9.06	4.08	17.7	7.44	7.10	11.6
Ba	51.2	23.2	14.4	23.0	21.4	53.9	15.0	41.3	117	42.8	84.7
La	3.34	3.99	3.88	5.74	3.43	3.88	4.33	3.69	3.67	3.41	3.54
Ce	6.97	8.20	7.75	11.1	6.62	7.94	8.51	7.61	7.73	7.15	7.94
Pr	0.834	0.991	0.933	1.24	0.775	0.955	0.951	0.916	0.912	0.870	0.986
Nd	3.57	4.37	4.11	b.d.	3.18	4.13	3.87	3.79	4.00	3.79	4.33
Sm	1.01	1.24	1.14	1.26	0.850	1.16	1.04	1.04	1.12	1.10	1.24
Eu	0.401	0.743	0.349	0.390	0.295	0.435	0.354	0.415	0.446	0.409	0.483
Gd	1.34	1.61	1.34	1.56	0.989	1.43	1.32	1.41	1.39	1.36	1.63
Tb	0.228	0.279	0.219	0.273	0.176	0.266	0.235	0.252	0.251	0.245	0.291
Dy	1.60	1.80	1.34	1.83	1.15	1.74	1.60	1.72	1.65	1.60	1.98
Ho	0.323	0.361	0.279	0.394	0.244	0.365	0.354	0.368	0.339	0.331	0.410
Er	0.938	0.994	0.739	1.16	0.715	1.06	1.02	1.12	0.963	0.921	1.17
Tm	0.133	0.131	0.102	0.166	0.097	0.159	0.143	0.166	0.133	0.131	0.163
Yb	0.905	0.852	0.640	1.14	0.662	0.975	0.915	1.15	0.877	0.847	1.07
Lu	0.114	0.113	0.077	0.161	0.103	0.134	0.131	0.150	0.119	0.109	0.149
Pb	3.82	2.43	6.05	9.80	8.03	2.14	8.38	5.23	2.84	2.62	3.14
U	0.508	0.570	0.946	0.427	0.526	0.631	0.733	1.22	0.666	0.480	0.628
Y/Ho	30.2	29.8	30.0	28.4	30.0	29.9	30.0	30.4	30.0	29.8	29.4
$(Pr/Yb)_{SN}$	0.294	0.371	0.466	0.349	0.374	0.313	0.332	0.254	0.332	0.328	0.294
$(Pr/Tb)_{SN}$	0.321	0.311	0.373	0.398	0.386	0.315	0.355	0.32	0.318	0.311	0.297
$(Tb/Yb)_{SN}$	0.918	1.19	1.25	0.876	0.969	0.994	0.936	0.80	1.04	1.05	0.990
$(Ce/Ce^*)_{SN}$	0.963	0.951	0.940	0.961	0.937	0.951	0.967	0.95	0.974	0.957	0.976
$(Gd/Gd^*)_{SN}$	1.12	1.09	1.12	1.07	1.05	1.02	1.07	1.08	1.05	1.05	1.07
$(Pr/Pr^*)_{SN}$	0.979	0.968	0.967	2.01	0.992	0.976	0.974	1.00	0.960	0.977	0.982
$(Eu/Eu^*)_{SN}$	1.71	2.58	1.41	1.36	1.55	1.60	1.46	1.67	1.72	1.61	1.65

Sample no. & section	**NCD4, upper carbonate section**										
Spots	A19	A20	A21	A22	A24	A25	A27	A28	A29	A33	A34
Component	as A17	as A17	as A17	as A17	Calcite-filled fracture	as A24	Calcite-filled fracture	as A27	as A27	Dolomitic matrix	as A33
Mg	91000	91000	92000	93000	1300	1200	1300	1300	1300	95000	76000
Si	7300	8500	4300	15000	141	97.5	<26.2	<26.3	40.4	7500	12000
Ti	10.7	9.95	9.78	18.9	15.6	15.6	15.5	15.4	15.6	10.9	12.6
V	4.94	3.68	2.76	7.03	0.347	0.280	0.331	0.298	0.319	8.14	9.82
Cr	6.56	4.97	3.82	9.88	1.15	1.17	1.11	1.05	1.07	9.27	11.0
Mn	6800	6700	6800	6900	16000	15000	14000	15000	15000	6800	7900
Fe	42000	42000	44000	44000	5200	5000	5000	5100	5200	49000	56000
Sr	293	290	285	281	336	355	448	360	380	225	301
Y	12.2	10.8	10.9	11.1	424	353	335	422	387	9.11	11.6
Zr	33.2	6.55	11.7	14.0	0.016	0.012	0.022	0.015	0.017	10.9	8.76
Ba	31.3	19.9	13.8	42.3	6.25	6.08	3.41	3.68	4.92	38.6	61.1
La	3.90	4.18	2.90	3.15	147	142	141	153	156	3.92	4.81
Ce	8.51	8.63	6.47	6.98	450	443	418	476	463	7.79	9.71
Pr	1.04	0.993	0.792	0.879	58.7	59.4	53.8	62.1	59.8	0.919	1.14
Nd	4.38	4.28	3.64	3.87	239	247	219	254	244	3.75	4.90
Sm	1.24	1.18	1.10	1.15	50.7	51.1	46.3	54.9	51.1	1.04	1.30
Eu	0.490	0.466	0.435	0.450	14.2	13.5	18.2	18.3	17.6	0.388	0.506
Gd	1.64	1.50	1.36	1.48	57.0	54.6	54.0	62.1	57.6	1.29	1.67
Tb	0.289	0.262	0.266	0.262	9.90	9.06	8.07	10.0	9.12	0.212	0.280
Dy	1.93	1.76	1.77	1.81	64.8	57.0	46.9	61.0	54.8	1.47	1.82
Ho	0.412	0.361	0.368	0.393	12.2	10.6	8.03	10.7	9.70	0.306	0.388
Er	1.23	0.976	1.07	1.05	30.2	26.9	17.4	24.2	22.0	0.864	1.11
Tm	0.185	0.139	0.152	0.149	3.99	3.56	1.81	2.77	2.46	0.127	0.154
Yb	1.24	0.914	0.977	1.01	24.8	24.1	9.50	15.6	13.7	0.849	1.04
Lu	0.176	0.121	0.137	0.135	3.10	3.11	1.12	1.83	1.59	0.118	0.142
Pb	3.30	1.52	3.15	3.14	1.92	2.49	2.05	1.40	2.02	4.16	5.31
U	0.958	0.352	0.675	0.736	0.003	0.002	0.023	0.003	0.005	0.572	0.584
Y/Ho	29.7	29.8	29.7	28.3	34.9	33.5	41.7	39.3	39.9	29.8	30.0
$(Pr/Yb)_{SN}$	0.268	0.347	0.259	0.278	0.757	0.789	1.81	1.27	1.40	0.346	0.350
$(Pr/Tb)_{SN}$	0.316	0.332	0.261	0.294	0.519	0.575	0.584	0.542	0.575	0.380	0.356
$(Tb/Yb)_{SN}$	0.849	1.04	0.992	0.945	1.46	1.37	3.09	2.35	2.43	0.910	0.983
$(Ce/Ce^*)_{SN}$	0.971	0.977	0.982	0.964	1.08	1.07	1.07	1.08	1.07	0.947	0.958
$(Gd/Gd^*)_{SN}$	1.09	1.09	0.990	1.08	1.06	1.08	1.19	1.12	1.13	1.13	1.12
$(Pr/Pr^*)_{SN}$	1.00	0.958	0.951	0.986	1.05	1.05	1.04	1.04	1.04	0.998	0.966
$(Eu/Eu^*)_{SN}$	1.68	1.71	1.65	1.68	1.29	1.26	1.88	1.56	1.63	1.68	1.71

Sample no. & section	NCD4, upper carbonate section				NCD4A, upper carbonate section						
Spots	A36	A37	A38	A39	A147	A150	A151	A152	A153	A155	A156
Component	as A33	as A33	Dolomitic matrix	as A38	Micritic ooid	Micritc ooid	as A150.rim	Sparitic ooid	Micritic ooid	Micritic ooid	Radial ooid
Mg	82000	83000	83000	82000	111000	116000	113000	114000	110000	109000	109000
Si	3500	3600	11000	5100	6400	266000	48000	9800	22000	16000	9300
Ti	11.8	11.8	12.3	12.3	10.8	15.8	11.9	10.6	13.0	10.4	10.4
V	6.02	6.64	9.67	7.65	9.47	25.3	9.52	25.4	9.19	6.83	17.3
Cr	6.40	8.88	10.7	7.46	6.36	23.2	7.75	7.89	8.10	5.66	6.54
Mn	8000	6600	7800	8000	7600	7800	8400	4200	9700	8300	6400
Fe	60000	52000	61000	61000	117000	195000	183000	150000	213000	184000	239000
Sr	249	290	234	232	148	103	273	129	312	279	96.2
Y	10.7	b.d.	9.20	10.0	15.8	13.9	16.0	8.95	17.7	13.4	12.3
Zr	10.2	4.34	6.90	8.97	4.92	11.3	7.66	3.68	7.72	3.25	3.56
Ba	23.1	29.6	53.6	39.4	35.7	216	62.6	32.1	78.2	46.5	28.2
La	3.94	4.11	3.57	6.16	9.91	5.00	5.96	3.37	5.48	4.13	6.26
Ce	8.06	8.03	7.28	12.2	18.3	10.7	12.2	6.72	11.3	8.43	12.1
Pr	0.961	0.954	0.904	1.33	2.09	1.36	1.44	0.787	1.35	0.995	1.36
Nd	4.12	4.06	3.61	5.09	8.34	5.62	6.16	3.36	5.96	4.49	5.54
Sm	1.18	1.18	1.02	1.19	2.19	1.70	1.77	0.958	1.89	1.43	1.41
Eu	0.440	0.462	0.380	0.416	0.579	0.594	0.628	0.264	0.704	0.534	0.380
Gd	1.44	1.43	1.25	1.42	2.58	2.28	2.41	1.22	2.57	1.93	1.70
Tb	0.255	0.249	0.231	0.242	0.429	0.370	0.396	0.215	0.438	0.328	0.291
Dy	1.71	1.63	1.50	1.56	2.79	2.35	2.65	1.47	3.10	2.22	1.95
Ho	0.361	0.337	0.308	0.325	0.542	0.482	0.531	0.312	0.620	0.440	0.418
Er	1.03	0.900	0.856	0.956	1.56	1.33	1.48	0.928	1.82	1.17	1.14
Tm	0.149	0.127	0.122	0.133	0.221	0.182	0.205	0.139	0.247	0.165	0.172
Yb	0.992	0.837	0.812	0.895	1.41	1.18	1.30	0.940	1.63	1.15	1.16
Lu	0.132	0.104	0.105	0.119	0.197	0.174	0.184	0.134	0.221	0.141	0.166
Pb	5.19	25.3	6.07	7.40	14.6	5.22	7.99	12.3	5.28	3.18	18.9
U	0.632	0.602	0.421	0.552	0.726	0.915	0.932	0.339	0.585	0.645	0.490
Y/Ho	29.6	-	29.9	30.8	29.2	28.9	30.1	28.7	28.5	30.4	29.5
$(Pr/Yb)_{SN}$	0.309	0.364	0.356	0.474	0.473	0.368	0.354	0.267	0.265	0.276	0.374
$(Pr/Tb)_{SN}$	0.330	0.336	0.343	0.481	0.427	0.322	0.319	0.321	0.270	0.266	0.410
$(Tb/Yb)_{SN}$	0.937	1.08	1.04	0.985	1.11	1.14	1.11	0.833	0.979	1.04	0.914
$(Ce/Ce^*)_{SN}$	0.955	0.936	0.934	0.982	0.928	0.945	0.958	0.952	0.956	0.959	0.953
$(Gd/Gd^*)_{SN}$	1.06	1.07	1.03	1.09	1.10	1.16	1.15	1.07	1.12	1.12	1.09
$(Pr/Pr^*)_{SN}$	0.977	0.979	1.03	0.992	0.994	1.03	0.975	0.971	0.963	0.946	0.978
$(Eu/Eu^*)_{SN}$	1.63	1.73	1.60	1.57	1.21	1.53	1.53	1.19	1.58	1.60	1.21

Sample no. & section	NCD4A, upper carbonate section								
Spots	A158	A159	A162	A163	A160	A161	A165	A148	A166
Component	Concentric ooid	as A158.rim	Silicified particle	as A162	Dolomitic intraclast	as A160	Dolomitic intraclast	Micritic laminae	Matrix
Mg	115000	114000	1020000	505000	115000	116000	117000	110000	116000
Si	10000	93000	b.d.	b.d.	115000	98000	33000	35000	44000
Ti	11.1	13.8	2874	1293	16.6	14.6	13.2	13.2	11.1
V	10.4	13.0	3870	1629	21.5	19.6	13.2	18.7	11.4
Cr	5.53	8.21	8998	2849	23.0	21.5	16.2	17.7	11.9
Mn	6400	6900	8900	9300	7800	8200	7900	8200	8900
Fe	178000	192000	4300000	2190000	223000	233000	245000	187000	263000
Sr	144	217	583	362	245	275	303	258	251
Y	14.2	18.1	815	441	16.1	15.7	14.6	20.3	13.9
Zr	4.66	19.1	5800	3100	15.4	17.4	11.0	18.9	3.73
Ba	26.2	73.4	35190	16553	180	169	120	161	88.3
La	7.82	8.93	609	590	5.45	5.04	7.80	12.6	4.60
Ce	14.7	17.4	1154	1103	10.6	9.70	14.9	22.8	9.19
Pr	1.64	1.93	117	107	1.18	1.11	1.62	2.68	1.07
Nd	6.50	7.64	408	396	5.06	4.65	6.52	10.4	4.50
Sm	1.68	1.98	73.0	53.2	1.57	1.55	1.73	2.57	1.43
Eu	0.472	0.591	17.8	10.7	0.536	0.558	0.605	0.904	0.498
Gd	2.05	2.42	68.6	42.3	2.09	2.08	2.17	3.22	1.88
Tb	0.345	0.435	12.2	7.31	0.383	0.366	0.366	0.546	0.342
Dy	2.28	2.92	104	56.9	2.55	2.52	2.44	3.70	2.31
Ho	0.475	0.616	26.3	16.0	0.524	0.526	0.500	0.771	0.480
Er	1.32	1.83	106	60.1	1.53	1.51	1.39	2.30	1.33
Tm	0.193	0.272	18.4	10.5	0.227	0.213	0.196	0.319	0.192
Yb	1.28	1.78	146	83.3	1.51	1.47	1.27	2.05	1.21
Lu	0.171	0.257	22.6	12.6	0.206	0.210	0.176	0.294	0.172
Pb	9.45	6.30	4632	3245	2.52	1.55	2.21	2.97	3.28
U	0.611	1.43	328	182	0.900	0.990	0.712	1.10	0.377
Y/Ho	29.8	29.4	31.0	27.6	30.7	29.9	29.2	26.3	29.0
$(Pr/Yb)_{SN}$	0.409	0.346	0.256	0.411	0.250	0.241	0.407	0.418	0.282
$(Pr/Tb)_{SN}$	0.417	0.39	0.85	1.29	0.270	0.266	0.388	0.43	0.274
$(Tb/Yb)_{SN}$	0.982	0.89	0.30	0.32	0.924	0.907	1.05	0.97	1.03
$(Ce/Ce^*)_{SN}$	0.944	0.97	0.99	1.00	0.967	0.946	0.963	0.91	0.956
$(Gd/Gd^*)_{SN}$	1.10	1.05	0.99	0.96	1.06	1.09	1.11	1.10	1.06
$(Pr/Pr^*)_{SN}$	0.988	0.99	1.00	0.95	0.945	0.971	0.968	1.02	0.976
$(Eu/Eu^*)_{SN}$	1.26	1.30	1.19	1.05	1.42	1.52	1.55	1.55	1.46

Table A2. Major- (wt. %) and trace- (ppm) element data for carbonates and minor sandstone and shale samples from the main, middle and upper carbonate sections. HAC: acetic acid. Element concentrations in wt. % and ppm; b.d. = below detection; SN = shale-normalised; Ce* = $(0.5La + 0.5Pr)_{SN}$; Gd* = $(0.33Sm + 0.67Tb)_{SN}$; Pr* = $(0.5Ce + 0.5Nd)_{SN}$; Eu* = $(0.67Sm + 0.33Tb)_{SN}$.

Section	**Main carbonate section**									
Sample number	NCC9	NCC9A/1	NCC9B/1	NCC10B	NCC10C	NCC10C	NCC11	NCC11/1	NCC12	NCC12
Digestion method	HAC			HAC	HAC	HF/HNO_3			HAC	HF/HNO_3
Facies	Str.	Str.	Str.	S.int.dlr.	S.int.dlr.		S.oo.dla.		S.int.dlr.	
SiO2	17.11	16.78	17.69	23.26	23.64		22.86	20.30	30.53	
Al2O3	1.15	1.19	1.09	2.58	1.33		1.45	1.28	0.53	
Fe2O3	1.89	2.03	1.81	2.12	1.67		1.42	1.50	1.17	
MnO	0.21	0.23	0.21	0.24	0.20		0.19	0.18	0.15	
MgO	16.21	16.56	15.83	15.27	14.99		15.39	16.01	13.96	
CaO	24.60	24.35	25.07	22.68	22.42		22.59	23.40	20.57	
K2O	0.44	0.44	0.40	0.90	0.43		0.53	0.46	0.19	
TiO2	0.06	0.07	b.d.	0.09	0.05		0.05	b.d.	b.d.	
P2O5	b.d.	b.d.	b.d.	b.d.	b.d.		b.d.	b.d.	b.d.	
BaO	b.d.	b.d.	b.d.	b.d.	b.d.		b.d.	b.d.	b.d.	
SO3										
Total	99.14	99.35	99.20	101.22	99.15		99.24	99.03	98.79	
L.O.I	37.47	37.70	37.10	34.08	34.42		34.76	35.9	31.69	
Li		0.350			0.319	1.05				
P		5.33			1.83	79.8				
Sc		0.387			0.278	0.705				
Ti		0.688			0.584	587				
V		1.32			0.496	8.29				
Cr		2.47			2.21	23.8				
Co		1.28			1.35	4.84				
Ni		8.43			9.05	56.3				
Cu		0.208			0.492	10.3				
Zn		3.14			2.89	8.10				
Ga		0.079			0.083	1.01				
As		0.011			0.016	0.198				
Rb		0.094			0.042	9.90				
Sr		95.5			110	206				
Y		1.023			1.36	3.72				
Zr		0.036			0.021	15.6				
Nb		0.002			0.002	2.72				
Ba		2.51			2.27	32.8				
La		1.24			1.74	4.29				
Ce		2.15			2.95	7.44				
Pr		0.285			0.407	0.991				
Nd		1.10			1.57	3.82				
Sm		0.195			0.273	0.704				
Eu		0.065			0.072	0.199				
Gd		0.214			0.295	0.761				
Tb		0.027			0.037	0.103				
Dy		0.156			0.215	0.591				
Ho		0.030			0.042	0.114				
Er		0.080			0.108	0.317				
Tm		0.011			0.015	0.048				
Yb		0.070			0.094	0.300				
Lu		0.010			0.013	0.044				
Hf		0.002			0.002	0.373				
Ta		0.002			0.003	0.168				
W		0.001			0.001	0.147				
Pb		2.63			0.344	0.845				
Th		0.065			0.083	0.464				
U		0.013			0.013	0.136				
Y/Ho		34.1			32.4	32.6				
$(Pr/Yb)_{SN}$		1.30			1.38	1.05				
$(Pr/Tb)_{SN}$		0.925			0.964	0.843				
$(Tb/Yb)_{SN}$		1.40			1.43	1.25				
$(Ce/Ce^*)_{SN}$		0.833			0.808	0.833				
$(Gd/Gd^*)_{SN}$		1.31			1.31	1.25				
$(Pr/Pr^*)_{SN}$		1.08			1.11	1.09				
$(Eu/Eu^*)_{SN}$		1.72			1.37	1.44				

Section	Main carbonate section									
Sample number	NCC 13	NCC 13	NCC13a/1	NCC14A	NCC14B	NCC14	NCC 15	NCC 15	NCC15/1	NCC16
Digestion method	HAC	HF/HNO_3					HAC	HF/HNO_3		
Facies	Oncolite			Int.dlr.	S.int.dlr.	S.int.dlr.	Ss.	Ss.	Dlr.dlt.	S.int.dlr.
SiO2	31.10		32.27	13.77	26.99	30.42	71.00		73.87	62.05
Al2O3	0.08		0.08	1.12	2.75	2.04	3.38		3.73	2.54
Fe2O3	0.86		0.84	2.18	2.00	1.84	1.04		1.15	1.54
MnO	0.12		0.11	0.20	0.17	0.17	0.06		0.07	0.12
MgO	14.63		14.31	17.41	14.27	13.52	3.68		4.11	6.88
CaO	20.85		20.40	25.27	20.32	19.85	4.75		5.41	9.87
K2O	b.d.		b.d.	0.35	0.84	0.66	1.11		1.24	0.80
TiO2	b.d.		b.d.	b.d.	0.09	0.10	0.15		0.20	0.08
P2O5	b.d.		b.d.	b.d.	b.d.	b.d.	b.d.		b.d.	b.d.
BaO	b.d.		b.d.	b.d.	b.d.	b.d.	b.d.		b.d.	b.d.
SO3	b.d.		b.d.	b.d.	b.d.	b.d.	b.d.		b.d.	b.d.
Total	98.67		99.31	99.43	99.13	99.08	99.43		98.68	99.18
L.O.I	31.03		31.30	39.13	31.70	30.48	14.26		8.90	15.30
Li	0.167	1.27					0.172	9.16		
P	0.001	9.13					0.487	121		
Sc	0.001	b.d.					0.356	3.27		
Ti	0.219	17					0.719	889		
V	0.255	0.956					0.818	28.9		
Cr	1.19	3.24					0.642	62.5		
Co	0.525	3.02					0.884	8.42		
Ni	5.51	17.6					5.50	43.7		
Cu	0.081	0.357					9.92	27.8		
Zn	1.87	26.2					2.10	33.1		
Ga	0.042	0.136					0.053	4.64		
As	0.002	0.011					0.027	1.24		
Rb	0.009	1.37					0.168	46.5		
Sr	89.9	227					31.7	54.2		
Y	0.332	0.967					2.63	6.62		
Zr	0.010	1.53					0.030	48.2		
Nb	0.002	0.049					0.002	2.99		
Ba	0.571	3.16					3.75	148		
La	0.192	0.560					0.271	10.7		
Ce	0.370	0.993					0.719	19.1		
Pr	0.053	0.123					0.127	2.10		
Nd	0.252	0.568					0.635	6.99		
Sm	0.056	0.138					0.253	1.17		
Eu	0.024	0.057					0.059	0.263		
Gd	0.059	0.151					0.336	1.32		
Tb	0.008	0.022					0.070	0.176		
Dy	0.048	0.130					0.464	1.06		
Ho	0.009	0.025					0.094	0.218		
Er	0.020	0.062					0.230	0.636		
Tm	0.003	0.008					0.034	0.095		
Yb	0.019	0.041					0.190	0.658		
Lu	0.003	0.005					0.028	0.094		
Hf	0.001	0.027					0.003	1.22		
Ta	0.002	0.004					0.002	0.237		
W	0.001	0.001					0.001	0.212		
Pb	0.484	1.17					0.778	4.41		
Th	0.028	0.091					0.068	1.90		
U	0.008	0.066					0.014	0.730		
Y/Ho	36.9	38.7					27.9	30.3		
$(Pr/Yb)_{SN}$	0.891	0.958					0.213	1.02		
$(Pr/Tb)_{SN}$	0.581	0.490					0.159	1.05		
$(Tb/Yb)_{SN}$	1.53	1.95					1.34	0.975		
$(Ce/Ce^*)_{SN}$	0.891	0.873					0.841	0.930		
$(Gd/Gd^*)_{SN}$	1.23	1.19					0.953	1.27		
$(Pr/Pr^*)_{SN}$	0.994	0.953					1.036	1.06		
$(Eu/Eu^*)_{SN}$	2.18	2.05					0.905	1.96		

Section	Main carbonate section								
Sample number	075A10	075A10A/1	075A10-B/1	NCC 17A	NCC 17A	NCC17A/1	NCC17B	NCC17B/1	NCC 22
Digestion method				HAC	HF/HNO_3				HAC
Facies	Conical.str.		Dlt.	S.oo.dlr.			S.dla.		Dol.lap.
SiO2	74.75	87.63	41.50	32.64			32.46	33.05	12.71
Al2O3	2.81	2.71	2.67	5.13			5.99	6.38	2.59
Fe2O3	0.79	0.49	1.80	3.50			1.89	2.03	5.52
MnO	0.06	b.d.	0.15	0.31			0.21	0.22	0.39
MgO	4.01	1.59	10.95	10.28			4.91	5.32	16.49
CaO	5.62	1.95	16.10	18.34			25.40	24.16	24.69
K2O	0.98	0.96	0.95	1.89			2.36	2.49	0.19
TiO2	0.15	0.14	0.14	0.14			0.13	0.13	0.19
P2O5	b.d.	b.d.	b.d.	0.06			0.05	0.05	0.09
BaO	b.d.	b.d.	b.d.	b.d.			b.d.	b.d.	b.d.
SO3	b.d.	b.d.	b.d.	0.07			b.d.	b.d.	b.d.
Total	98.30	98.67	99.06	99.23			99.23	99.13	100.11
L.O.I	9.13	3.20	24.80	26.87			25.83	25.30	37.25
Li				1.30	3.44				1.29
P				3.72	240				0.883
Sc				0.704	0.799				0.934
Ti				2.87	b.d.				1.21
V				0.916	11.15				1.72
Cr				4.17	52.9				10.5
Co				8.78	10.8				2.22
Ni				29.2	23.51				14.5
Cu				143	34.6				5.29
Zn				89.7	51.12				3.98
Ga				0.390	4.32				0.131
As				0.193	1.50				0.005
Rb				2.72	43.8				0.153
Sr				371	158				115
Y				16.7	11.0				2.74
Zr				0.182	189				0.121
Nb				0.001	13.7				b.d.
Ba				24.6	129				6.15
La				6.37	9.50				0.946
Ce				12.2	17.6				1.88
Pr				1.49	1.91				0.254
Nd				6.44	6.66				1.17
Sm				1.71	1.50				0.328
Eu				0.899	0.607				0.125
Gd				2.16	1.66				0.391
Tb				0.376	0.257				0.062
Dy				2.40	1.53				0.401
Ho				0.494	0.319				0.078
Er				1.31	0.888				0.209
Tm				0.192	0.135				0.028
Yb				1.25	0.925				0.190
Lu				0.204	0.141				0.027
Hf				0.024	4.37				0.005
Ta				0.001	1.50				0.001
W				0.001	0.307				0.001
Pb				159	33.0				1.96
Th				2.71	4.37				0.097
U				1.18	1.23				0.051
Y/Ho				33.8	34.50				35.2
$(Pr/Yb)_{SN}$				0.379	0.662				0.428
$(Pr/Tb)_{SN}$				0.347	0.654				0.356
$(Tb/Yb)_{SN}$				1.09	1.01				1.20
$(Ce/Ce^*)_{SN}$				0.917	0.948				0.884
$(Gd/Gd^*)_{SN}$				1.08	1.15				1.14
$(Pr/Pr^*)_{SN}$				0.981	1.04				0.987
$(Eu/Eu^*)_{SN}$				2.27	1.96				1.74

Section	Main carbonate section									
Sample number	NCC 22	NCC 23	NCC 24	NCC 20	NCC 21	NCC 21	NCC19	NCC 27	NCC 28	NCC 29
Digestion method	HF/HNO_3	HAC			HAC	HF/HNO_3		HAC		HAC
Facies		S.int.dlr.	Str.	Str.	Dl.ss.		Int.dl.ss.	Int.dl.ss.	Int.dl.ss.	Str.
SiO2		20.13	29.63	43.00	36.79		37.13	41.91	56.78	54.86
Al2O3		0.85	1.16	2.39	2.06		2.18	1.85	2.37	2.11
Fe2O3		3.02	3.08	2.31	2.63		2.50	2.29	1.75	1.81
MnO		0.27	0.25	0.16	0.18		0.18	0.20	0.15	0.14
MgO		15.60	13.71	10.51	11.91		11.65	10.74	8.02	8.41
CaO		23.34	20.46	15.61	17.65		17.49	15.96	11.40	12.02
K2O		0.11	0.18	0.80	0.58		0.71	0.57	0.72	0.64
TiO2		b.d.	0.06	0.09	0.08		0.09	0.05	0.10	0.11
P2O5		0.10	0.08	b.d.	b.d.		b.d.	b.d.	b.d.	b.d.
BaO		b.d.	b.d.	b.d.	b.d.		b.d.	b.d.	b.d.	b.d.
SO3		b.d.	b.d.	b.d.	b.d.		b.d.	b.d.	b.d.	b.d.
Total		99.24	99.79	98.97	98.96		98.94	98.54	99.28	99.05
L.O.I		35.82	31.18	24.10	27.08		26.96	24.97	17.99	18.95
Li	4.14	0.632			0.825	3.09		0.230		0.845
P	432	6.13			b.d.	92.5		3.15		3.38
Sc	1.43	0.324			1.07	0.714		0.225		2.41
Ti	969	0.315			1.72	400		0.367		2.49
V	28.4	0.438			1.83	13.0		0.810		6.21
Cr	195	2.10			6.05	64.4		1.69		8.29
Co	15.7	1.59			12.7	10.3		1.87		8.87
Ni	123	8.53			42.9	63.7		8.02		50.9
Cu	24.8	0.175			9.50	5.21		0.859		31.6
Zn	49.3	3.55			8.95	41.1		3.61		10.0
Ga	3.58	0.099			0.223	2.13		0.095		0.319
As	0.104	0.013			0.091	0.67		0.033		0.039
Rb	5.55	0.001			0.734	24.3		0.034		0.595
Sr	280	137			345	250		78.4		368
Y	8.34	2.75			10.7	8.32		3.74		14.0
Zr	21.9	0.033			0.194	39.4		0.016		0.120
Nb	2.45	0.002			b.d.	1.56		0.001		b.d.
Ba	27.2	3.26			11.8	67.3		1.70		10.1
La	4.67	0.728			3.08	5.76		0.819		3.30
Ce	8.90	1.58			7.07	11.1		1.83		8.24
Pr	1.14	0.261			1.00	1.34		0.311		1.29
Nd	4.62	1.22			4.52	5.05		1.49		6.10
Sm	1.09	0.340			1.38	1.14		0.447		1.80
Eu	0.373	0.135			0.554	0.401		0.138		0.532
Gd	1.25	0.406			1.57	1.28		0.513		2.07
Tb	0.197	0.066			0.272	0.203		0.089		0.354
Dy	1.19	0.415			1.71	1.24		0.561		2.26
Ho	0.256	0.081			0.338	0.246		0.115		0.460
Er	0.735	0.200			0.837	0.698		0.306		1.20
Tm	0.113	0.028			0.115	0.098		0.045		0.160
Yb	0.741	0.163			0.726	0.662		0.276		1.03
Lu	0.105	0.024			0.094	0.091		0.040		0.138
Hf	0.521	0.003			0.016	0.916		0.004		0.019
Ta	0.174	0.002			0.001	0.121		0.001		0.001
W	0.293	0.001			0.001	0.118		0.001		0.001
Pb	4.94	2.75			6.14	4.68		1.12		7.96
Th	0.375	0.062			0.482	0.936		0.096		0.513
U	0.701	0.043			0.086	0.407		0.012		0.121
Y/Ho	32.6	33.9			31.5	33.8		32.5		30.5
$(Pr/Yb)_{SN}$	0.492	0.511			0.442	0.647		0.360		0.400
$(Pr/Tb)_{SN}$	0.508	0.347			0.323	0.579		0.306		0.318
$(Tb/Yb)_{SN}$	0.969	1.48			1.37	1.12		1.17		1.26
$(Ce/Ce^*)_{SN}$	0.889	0.818			0.915	0.921		0.813		0.893
$(Gd/Gd^*)_{SN}$	1.14	1.13			1.06	1.13		1.06		1.08
$(Pr/Pr^*)_{SN}$	1.04	1.06			1.02	1.05		1.05		1.03
$(Eu/Eu^*)_{SN}$	1.62	1.81			1.82	1.67		1.39		1.35

Section		**Main carbonate section**									
Sample number	NCC 29	NCC30	NCC31	NCC32	NCC33B	NCC33A	NCC35	NCC36	NCC37	NCC16C	NCC16A
Digestion method	HF/HNO_3										
Facies		Str.	Str.	Str.	Str.	Str.	Str.	Str.	S.oo.int.dlr.	Str.	Str.
SiO2		61.48	51.59	27.19	47.76	45.78	22.24	21.45	18.35	74.06	31.61
Al2O3		2.01	2.31	1.50	1.42	1.59	2.38	1.30	1.07	3.17	2.92
Fe2O3		1.56	1.61	2.60	1.71	1.76	2.45	1.95	1.78	1.22	2.07
MnO		0.13	0.14	0.26	0.17	0.18	0.24	0.22	0.20	0.07	0.16
MgO		7.35	7.96	14.18	10.23	10.45	15.22	15.34	15.76	4.61	12.61
CaO		10.07	11.30	20.63	14.60	15.07	21.70	23.00	25.32	5.51	19.12
K2O		0.54	0.71	0.35	0.40	0.48	0.65	0.41	0.36	0.88	1.07
TiO2		0.08	0.11	0.07	0.07	0.10	0.11	0.06	b.d.	0.14	0.13
P2O5		b.d.	b.d.	b.d.	b.d.	b.d.	b.d.	b.d.	b.d.	b.d.	b.d.
BaO		b.d.	b.d.	b.d.	b.d.	b.d.	b.d.	b.d.	b.d.	b.d.	b.d.
SO3		b.d.	b.d.	b.d.	b.d.	b.d.	b.d.	b.d.	b.d.	b.d.	b.d.
Total		99.08	94.51	98.87	99.16	98.95	99.19	99.20	98.71	98.73	99.10
L.O.I		15.86	18.78	32.09	22.80	23.54	34.20	35.47	35.87	9.07	29.41
Li	4.73										
P	93.6										
Sc	2.58										
Ti	570										
V	20.8										
Cr	62.2										
Co	5.67										
Ni	46.4										
Cu	24.7										
Zn	36.02										
Ga	2.33										
As	0.116										
Rb	25.6										
Sr	132										
Y	6.44										
Zr	28.2										
Nb	1.68										
Ba	90.4										
La	9.30										
Ce	15.9										
Pr	1.70										
Nd	5.65										
Sm	1.03										
Eu	0.29										
Gd	1.20										
Tb	0.167										
Dy	0.993										
Ho	0.200										
Er	0.581										
Tm	0.084										
Yb	0.562										
Lu	0.081										
Hf	0.706										
Ta	0.119										
W	0.150										
Pb	2.97										
Th	1.09										
U	0.382										
Y/Ho	32.2										
$(Pr/Yb)_{SN}$	0.968										
$(Pr/Tb)_{SN}$	0.894										
$(Tb/Yb)_{SN}$	1.08										
$(Ce/Ce^*)_{SN}$	0.918										
$(Gd/Gd^*)_{SN}$	1.25										
$(Pr/Pr^*)_{SN}$	1.05										
$(Eu/Eu^*)_{SN}$	1.36										

Section	Main carbonate section									
Sample number	NCC 16B	NCC 16B	NCC16D	NCC18	NCC12A	NCC3	NCC 10	NCC 25	NCC 26	NCC 34
Digestion method	HAC	HF/HNO_3				HF/HNO_3	HF/HNO_3	HF/HNO_3	HF/HNO_3	HF/HNO_3
Facies	Str.		Str.	Str.	Mbl.	Shale	Shale	Lap.	Shale	Shale
SiO2	33.13		40.34	63.26	21.46	68.86	52.41	71.72	55.41	56.98
Al2O3	1.53		2.54	11.12	1.28	9.09	26.28	11.42	23.45	21.63
Fe2O3	2.39		3.29	2.22	2.30	4.06	0.54	3.32	2.27	1.31
MnO	0.24		0.39	0.10	0.51	b.d.	b.d.	b.d.	b.d.	b.d.
MgO	12.44		10.61	4.69	15.00	5.20	3.05	3.50	4.05	4.31
CaO	19.39		16.25	4.87	22.96	3.64	0.66	1.19	0.23	0.66
K2O	0.54		0.68	4.21	0.41	1.77	9.19	3.73	8.01	7.32
TiO2	0.08		0.11	0.17	0.05	0.41	1.69	0.63	1.31	1.83
P2O5	b.d.		0.05	b.d.	b.d.	0.08	0.46	0.11	0.16	b.d.
BaO	b.d.		b.d.	b.d.	b.d.	b.d.	0.15	b.d.	0.15	0.12
SO3	b.d.		0.05	0.08	b.d.	0.19	b.d.	b.d.	b.d.	b.d.
Total	99.15	99.15	99.24	98.97	99.11	98.78	99.19	99.15	99.19	98.99
L.O.I	29.41	29.41	24.93	8.25	35.14	5.48	4.51	3.43	3.99	4.63
Li	0.517	1.46					61.8	29.0	27.3	39.8
P	5.85	76.0					1636	449	648	140
Sc	0.789	0.974					9.42	10.4	6.85	9.90
Ti	1.12	444					8848	3461	6564	b.d.
V	1.065	14.3					161	91.5	229	200
Cr	2.15	28.4					1366	797	634	1337
Co	4.50	5.52					3.52	32.2	13.5	7.33
Ni	22.3	27.6					190	263	114	121
Cu	10.3	8.24					41.8	134	30.2	16.9
Zn	9.17	33.5					43.8	58.9	48.1	64.5
Ga	0.189	1.79					25.9	14.7	20.1	23.5
As	0.053	0.223					4.03	4.10	0.436	0.458
Rb	0.551	24.0					185	92.6	50.6	110
Sr	223	202					15.9	26.7	2.69	8.29
Y	5.83	6.49					8.49	11.7	8.41	7.30
Zr	0.124	23.0					1172	144	379	681
Nb	b.d.	1.38					33.7	11.1	24.6	31.2
Ba	7.44	44.5					691	567	395	502
La	2.30	3.80					37.3	24.5	29.1	33.5
Ce	5.59	8.13					63.7	49.6	48.2	54.7
Pr	0.800	1.04					5.86	5.35	6.25	5.05
Nd	3.52	4.15					16.2	19.4	22.1	14.1
Sm	0.928	0.950					2.02	3.76	3.67	1.77
Eu	0.460	0.436					0.733	0.975	0.67	0.613
Gd	1.04	1.07					2.17	3.336	3.09	1.93
Tb	0.163	0.160					0.185	0.388	0.309	0.163
Dy	0.927	0.940					0.986	1.99	1.39	0.896
Ho	0.171	0.179					0.260	0.391	0.269	0.222
Er	0.434	0.492					1.11	1.20	0.921	0.924
Tm	0.053	0.067					0.224	0.182	0.142	0.174
Yb	0.328	0.456					1.87	1.22	1.011	1.35
Lu	0.039	0.059					0.329	0.185	0.153	0.225
Hf	0.010	0.552					29.1	3.59	9.74	17.2
Ta	0.001	0.102					2.97	0.882	4.01	2.40
W	0.001	0.111					4.59	0.922	2.49	3.42
Pb	89.0	43.1					28.8	2.97	3.78	5.13
Th	0.227	0.985					9.19	4.81	5.51	9.54
U	0.100	0.467					8.83	1.69	2.26	4.71
Y/Ho	34.1	36.3					32.7	30.0	31.2	32.9
$(Pr/Yb)_{SN}$	0.779	0.731					0.998	1.40	1.97	1.19
$(Pr/Tb)_{SN}$	0.430	0.572					2.77	1.21	1.77	2.71
$(Tb/Yb)_{SN}$	1.81	1.28					0.360	1.16	1.11	0.440
$(Ce/Ce^*)_{SN}$	0.932	0.938					0.976	1.00	0.823	0.949
$(Gd/Gd^*)_{SN}$	1.13	1.18					1.66	1.28	1.37	1.68
$(Pr/Pr^*)_{SN}$	1.04	1.05					1.04	1.01	1.12	1.04
$(Eu/Eu^*)_{SN}$	2.35	2.23					2.13	1.47	1.09	2.03

Section	**Middle carbonate section**							
Sample number	NCMA	NCMA	NCMB	NCMB	NCMC	NCMC	NCMD	NCMD
Digestion method	HAC	HF/HNO_3	HAC	HF/HNO_3	HAC	HF/HNO_3	HAC	HF/HNO_3
Facies	Int.ss.		Int.ss.		Ss.		Oo.dl.ss.	
SiO2	34.31		60.31		35.77		37.83	
Al2O3	3.56		11.41		5.18		6.45	
Fe2O3	7.32		3.42		6.57		6.40	
MnO	0.88		0.26		0.73		0.69	
MgO	8.33		3.48		8.02		7.09	
CaO	17.15		5.81		16.07		15.33	
K2O	1.18		4.41		1.97		2.34	
TiO2	0.14		0.22		0.14		0.13	
P2O5	b.d.		0.09		0.05		0.07	
BaO	b.d.		0.05		b.d.		b.d.	
SO3	b.d.		b.d.		0.06		b.d.	
Total	98.75		99.35		99.02		99.06	
L.O.I	25.88		9.84		24.46		22.73	
Li	0.448	5.73	0.364	14.9	0.389	7.91	0.38	10.2
P	8.30	166	6.503	393	8.58	243	7.80	300
Sc	0.465	3.57	0.646	3.71	0.536	2.91	0.555	3.91
Ti	0.343	799	0.691	1137	0.474	825	0.463	813
V	0.948	29.1	1.06	24.5	0.844	22.2	0.883	24.5
Cr	0.857	57.3	0.833	60.6	0.760	52.9	0.942	35.6
Co	1.47	9.01	0.695	5.74	1.24	8.40	1.88	13.0
Ni	4.71	25.4	3.09	14.8	4.66	23.7	6.08	29.6
Cu	4.08	180	0.407	30.7	0.978	25.2	1.68	38.0
Zn	9.62	81.6	3.88	70.7	5.41	58.1	18.8	115
Ga	0.280	5.55	0.174	11.9	0.250	6.60	0.273	8.84
As	0.017	0.293	0.006	0.55	0.019	0.824	0.025	1.64
Rb	0.113	49.7	0.963	135	0.253	84.2	0.561	99.0
Sr	50.6	128	29.2	44.2	55.9	115	75.8	148
Y	4.74	20.8	3.12	13.0	3.34	13.2	3.98	15.4
Zr	0.019	27.1	0.032	167	0.016	57.8	0.038	63.6
Nb	0.001	3.00	0.001	6.77	0.001	4.16	0.001	3.41
Ba	3.77	128	6.20	479	2.67	218	4.72	277
La	2.39	28.0	1.61	10.8	1.72	15.7	1.74	14.5
Ce	3.03	44.4	2.67	18.4	2.93	27.6	2.86	24.0
Pr	0.371	4.92	0.329	2.24	0.355	3.17	0.385	2.98
Nd	1.48	18.0	1.25	8.40	1.33	11.3	1.52	11.0
Sm	0.356	3.15	0.306	1.99	0.355	2.36	0.433	2.42
Eu	0.158	0.903	0.114	0.69	0.159	0.740	0.198	0.819
Gd	0.522	3.54	0.398	1.89	0.479	2.40	0.604	2.50
Tb	0.087	0.442	0.068	0.28	0.085	0.331	0.106	0.367
Dy	0.538	2.41	0.417	1.73	0.505	1.86	0.632	2.10
Ho	0.113	0.516	0.084	0.37	0.096	0.370	0.118	0.415
Er	0.305	1.49	0.225	1.11	0.252	1.05	0.316	1.15
Tm	0.045	0.226	0.035	0.18	0.037	0.16	0.047	0.174
Yb	0.266	1.60	0.209	1.23	0.224	1.07	0.294	1.16
Lu	0.041	0.216	0.032	0.20	0.033	0.158	0.047	0.185
Hf	0.004	0.723	0.004	4.12	0.001	1.57	0.004	1.59
Ta	0.001	0.202	0.002	0.69	0.001	0.310	0.001	0.303
W	0.001	0.287	0.004	0.38	0.005	0.232	0.005	0.237
Pb	1.921	6.803	2.14	15.6	2.33	12.0	3.70	14.1
Th	0.067	1.60	0.605	4.96	0.173	2.17	0.192	2.32
U	0.041	0.747	0.095	1.65	0.048	0.907	0.038	0.713
Y/Ho	41.9	40.2	37.2	35.7	34.8	35.7	33.8	37.0
$(Pr/Yb)_{SN}$	0.445	0.985	0.503	0.583	0.506	0.948	0.418	0.824
$(Pr/Tb)_{SN}$	0.374	0.977	0.424	0.708	0.366	0.839	0.318	0.712
$(Tb/Yb)_{SN}$	1.19	1.01	1.19	0.824	1.38	1.13	1.31	1.16
$(Ce/Ce^*)_{SN}$	0.940	0.954	0.886	0.893	0.894	0.904	0.846	0.861
$(Gd/Gd^*)_{SN}$	1.16	1.33	1.11	1.13	1.09	1.16	1.10	1.16
$(Pr/Pr^*)_{SN}$	1.03	1.02	1.06	1.06	1.06	1.05	1.08	1.08
$(Eu/Eu^*)_{SN}$	1.83	1.49	1.60	1.80	1.87	1.62	1.88	1.71

Section	Upper carbonate section								
Sample number	NCD1	NCD1A	NCD2	NCD2	NCD3A	NCD3	NCD3	NCD4	NCD4
Digestion method	-	-	HAC	HF/HNO_3	-	HAC	HF/HNO_3	HAC	HF/HNO_3
Facies	Dl.ss.	S.dlt.	Dl.ss.		Str.	S.int.dlr.		S.oo.int. dlr.	
SiO2	58.76	59.95	26.59		15.80	7.98		23.79	
Al2O3	5.77	13.88	7.23		2.03	0.08		3.14	
Fe2O3	2.92	2.44	3.71		3.65	3.03		4.20	
MnO	0.25	0.13	0.54		0.56	0.44		0.44	
MgO	6.13	4.18	11.19		14.51	16.42		12.04	
CaO	9.49	4.09	18.69		24.78	29.39		22.16	
K2O	1.74	5.39	2.65		0.75	b.d.		1.21	
TiO2	0.20	0.45	0.27		0.05	b.d.		0.12	
P2O5	0.07	0.11	b.d.		b.d.	b.d.		0.10	
BaO	b.d.	b.d.	b.d.		b.d.	b.d.		b.d.	
SO3	0.08	0.17	b.d.		0.37	b.d.		0.75	
Total	99.18	98.66	98.94		99.06	99.10		99.26	
L.O.I	13.77	7.82	28.07		36.56	41.76		31.31	
Li			0.308	17.8		1.57	1.37	0.256	1.77
P			7.53	349		5.36	43.8	8.34	446
Sc			0.906	8.82		0.001	0.056	0.303	1.82
Ti			0.757	1462		0.222	5.46	0.493	735
V			0.933	55.2		0.066	0.357	0.488	18.4
Cr			2.59	226		0.798	1.44	1.12	44.1
Co			1.08	7.64		0.599	3.70	0.610	8.22
Ni			8.76	51.0		6.54	22.0	5.97	25.2
Cu			2.98	20.2		0.114	11.3	0.432	20.5
Zn			20.3	77.8		9.89	256	66.9	71.1
Ga			0.193	9.03		0.134	0.459	0.134	2.77
As			0.008	0.141		0.009	0.101	0.029	1.89
Rb			0.491	108		0.001	1.23	0.243	23.5
Sr			70.5	170		85.6	185	74.3	166
Y			4.72	16.8		1.42	2.98	3.56	12.1
Zr			0.038	89.1		0.010	0.353	0.032	121
Nb			0.002	4.67		0.002	0.029	0.002	3.92
Ba			7.88	314		4.64	10.8	3.38	91.2
La			1.25	21.1		0.989	2.34	1.91	5.49
Ce			2.26	37.8		1.50	3.37	2.09	11.1
Pr			0.337	4.26		0.179	0.403	0.299	1.33
Nd			1.47	15.2		0.655	1.46	1.24	5.35
Sm			0.474	3.12		0.116	0.256	0.347	1.32
Eu			0.166	0.831		0.101	0.216	0.113	0.409
Gd			0.612	3.20		0.154	0.334	0.434	1.54
Tb			0.117	0.445		0.023	0.051	0.080	0.256
Dy			0.733	2.59		0.157	0.330	0.511	1.68
Ho			0.149	0.517		0.035	0.069	0.113	0.354
Er			0.369	1.49		0.089	0.182	0.304	1.05
Tm			0.052	0.225		0.012	0.025	0.050	0.177
Yb			0.316	1.44		0.078	0.141	0.341	1.18
Lu			0.048	0.225		0.014	0.020	0.066	0.187
Hf			0.006	2.24		0.001	0.009	0.004	2.62
Ta			0.002	0.374		0.001	b.d.	0.001	0.358
W			0.001	0.486		0.001	0.042	0.001	0.346
Pb			10.8	28.3		36.6	67.7	5.43	17.9
Th			0.169	2.96		0.01	0.012	0.218	1.29
U			0.027	0.949		0.01	0.026	0.050	0.631
Y/Ho			31.7	32.6		40.4	43.2	31.5	34.3
(Pr/Yb)SN			0.341	0.944		0.733	0.913	0.280	0.362
(Pr/Tb)SN			0.252	0.839		0.682	0.693	0.328	0.456
(Tb/Yb)SN			1.35	1.13		1.07	1.32	0.855	0.794
(Ce/Ce*)SN			0.801	0.917		0.816	0.793	0.626	0.948
(Gd/Gd*)SN			1.01	1.20		1.23	1.21	1.04	1.10
(Pr/Pr*)SN			1.06	1.04		1.06	1.07	1.08	1.01
(Eu/Eu*)SN			1.44	1.37		3.93	3.73	1.93	1.42

Section	**Upper carbonate section**							
Sample number	NCD4A	NCD4B	NCD6	NCD6	NCD6/1	NCD5A	NCD5B	NCD5B
Digestion method	-	-	HCl	HF/HNO_3	HAC	-	HAC	HF/HNO_3
Facies	Ss.	Str.	S.int.dlr.		Dlt.	S.int.dlr.	Mbl.	
SiO2	33.43	30.58	24.80		18.78	30.39	13.52	
Al2O3	4.40	4.60	3.85		2.24	4.36	1.67	
Fe2O3	3.66	3.76	4.24		4.66	4.05	4.75	
MnO	0.41	0.40	0.45		0.49	0.45	0.60	
MgO	10.15	10.55	11.77		13.67	11.05	14.85	
CaO	18.27	19.10	21.41		23.65	18.72	25.16	
K2O	1.72	1.95	1.47		0.83	1.71	0.63	
TiO2	0.12	b.d.	0.11		0.08	0.12	0.07	
P2O5	0.13	0.06	0.08		b.d.	0.09	b.d.	
BaO	b.d.	b.d.	b.d.		b.d.	b.d.	b.d.	
SO3	0.23	0.10	0.17		b.d.	0.19	b.d.	
Total	99.16	99.08	99.29		99.40	99.33	99.05	
L.O.I	26.64	27.98	30.94		35.00	28.20	37.80	
Li			0.427	2.32	0.192		7.28	0.929
P			95.8	350	5.29		2.03	113
Sc			1.13	1.81	0.324		1.91	1.28
Ti			4.68	672	0.418		2.69	370
V			1.08	15.1	0.303		3.37	11.9
Cr			1.28	31.2	1.04		7.10	21.1
Co			2.97	8.34	1.14		10.7	6.01
Ni			17.7	27.3	7.46		72.8	27.9
Cu			1.16	8.04	0.585		32.2	10.1
Zn			8.62	22.4	4.89		93.3	52.7
Ga			0.424	4.34	0.170		1.11	2.18
As			0.028	0.677	0.008		0.067	0.208
Rb			0.390	38.2	0.101		1.82	26.0
Sr			210	200	87.1		460	94.0
Y			8.21	12.4	4.21		22.1	6.04
Zr			1.03	79.7	0.025		0.422	15.2
Nb			0.008	4.05	0.001		b.d.	1.50
Ba			6.64	125	3.06		67.2	48.7
La			1.87	7.15	1.15		12.1	5.62
Ce			4.03	12.7	2.10		22.6	9.95
Pr			0.516	1.63	0.311		2.79	1.13
Nd			2.22	7.85	1.37		11.2	4.09
Sm			0.713	1.53	0.433		2.93	0.833
Eu			0.281	0.517	0.154		1.16	0.282
Gd			0.983	1.74	0.544		3.34	0.940
Tb			0.172	0.287	0.098		0.538	0.139
Dy			1.17	1.83	0.640		3.21	0.841
Ho			0.236	0.388	0.132		0.625	0.166
Er			0.633	1.10	0.344		1.58	0.458
Tm			0.088	0.176	0.051		0.201	0.063
Yb			0.556	1.13	0.304		1.28	0.414
Lu			0.075	0.173	0.044		0.159	0.059
Hf			0.036	1.72	0.005		0.035	0.361
Ta			0.008	0.381	0.002		0.001	0.111
W			0.020	0.261	0.001		0.001	0.111
Pb			3.15	9.44	1.80		24.8	6.85
Th			0.176	1.03	0.058		0.848	0.772
U			0.107	0.919	0.051		0.350	0.401
Y/Ho			34.8	32.1	31.9		35.3	36.4
$(Pr/Yb)_{SN}$			0.296	0.458	0.327		0.694	0.869
$(Pr/Tb)_{SN}$			0.263	0.497	0.278		0.455	0.711
$(Tb/Yb)_{SN}$			1.13	0.923	1.17		1.52	1.22
$(Ce/Ce^*)_{SN}$			0.942	0.857	0.805		0.896	0.910
$(Gd/Gd^*)_{SN}$			1.10	1.10	1.06		1.12	1.19
$(Pr/Pr^*)_{SN}$			1.00	0.942	1.05		1.03	1.04
$(Eu/Eu^*)_{SN}$			1.65	1.57	1.52		1.84	1.65

Dla: Dolarenite, Dl: Dolomite, Dlr: Dolorudite, Dlt: Dololutite, Int: Intraclast, Lap: Lapillistone, Mbl: Microbialite, Oo: Ooid, S: Sandy, Ss: Sandstone, Str: Stromatolite.

Table A3. EPMA analyses of selected elements (wt. % of oxide) of carbonate minerals from three different sections. Rec., recrystallized. Element concentrations in wt. %; b.d. = below detection.

Sample no.	Component	CaO	MgO	SrO	SiO_2	Al_2O_3	FeO	MnO	CO_2	Total
Main carbonate section										
NCC10	Matrix	30.29	20.88	0.05	0.03	0.01	1.30	0.14	47.27	100.00
		30.19	19.58	0.04	0.87	0.54	2.20	0.26	46.30	100.00
	Micritic particle 1	29.78	20.81	0.07	0.04	0.03	1.07	0.11	48.07	99.99
		29.88	20.81	0.09	0.09	b.d.	1.08	0.16	47.86	99.99
	Micritic particle 2	28.32	18.62	0.05	2.17	1.54	1.68	0.25	47.34	100.00
		29.90	19.95	0.07	0.14	0.06	1.31	0.17	48.37	99.98
NCC11	Rec. Particle1	29.23	20.49	0.12	0.06	b.d.	1.49	0.27	48.32	99.97
		30.29	20.15	0.18	0.04	0.03	1.56	0.17	47.57	99.99
	Rec. Particle 2	30.10	19.05	0.04	0.02	b.d.	2.45	0.63	47.66	100.00
		30.20	19.71	0.06	0.05	b.d.	1.88	0.13	47.95	99.98
	Rec. Particle 3	29.79	19.74	0.05	0.15	0.04	1.78	0.24	48.2	99.97
		29.45	19.39	0.06	0.80	0.48	1.64	0.21	47.88	99.97
	Matrix	29.43	19.78	0.06	0.04	0.01	1.66	0.16	48.83	100.00
		29.03	19.16	0.04	1.17	0.84	1.79	0.24	47.67	100.00
		29.92	20.21	0.03	0.14	0.06	1.71	0.26	47.66	100.00
NCC13	oncoid1	30.59	21.07	0.03	0.33	0.01	0.67	0.11	47.20	100.00
		30.53	21.01	0.05	0.17	b.d.	0.63	0.08	47.46	99.93
	oncoid2	30.36	20.64	0.05	0.06	0.01	1.00	0.22	47.59	99.98
		30.08	20.61	0.04	0.06	0.02	1.04	0.16	47.97	100.00
	Matrix	30.27	20.39	0.05	0.06	0.01	0.85	0.15	48.16	99.94
	Cement	29.74	20.02	0.06	0.11	0.05	1.22	0.15	48.63	99.98
	Intraclast/ oncoid	30.12	20.83	0.05	0.19	0.01	0.64	0.09	48.04	99.98
		29.84	20.30	0.04	1.87	b.d.	1.00	0.17	46.68	99.93
NCC14	Rec. Particle 1	30.13	19.59	0.03	0.03	b.d.	3.54	0.09	46.52	99.95
		29.61	20.00	0.05	0.04	b.d.	2.05	0.10	48.12	99.97
		29.90	20.47	0.05	0.05	0.01	1.33	0.03	48.11	100.00
	Micritic particle 2	30.24	20.53	0.08	0.07	0.01	1.04	0.09	47.88	99.95
		30.11	19.70	0.05	0.05	b.d.	1.87	0.18	48.01	99.98
	Micritic particle 4	29.19	19.66	0.07	1.44	1.08	1.64	0.22	46.69	99.99
	Matrix	21.50	13.93	0.03	29.08	b.d.	1.20	0.13	34.07	99.96
NCC17	Radial ooid 1	54.41	0.20	0.08	0.05	b.d.	0.69	0.22	44.31	100.00
		52.00	0.75	0.11	0.64	0.36	0.70	0.18	45.22	99.99
		53.62	0.57	0.10	0.15	0.02	0.55	0.19	44.79	100.00
		55.12	0.25	0.08	0.06	0.02	0.31	0.14	43.97	99.95
		55.22	0.16	0.06	0.05	0.01	0.26	0.15	44.03	100.00
		29.74	17.28	0.07	0.66	0.18	5.23	0.55	46.24	100.00
		29.96	17.19	0.08	0.52	0.23	5.23	0.57	46.16	100.00
		27.26	15.38	0.05	10.17	0.05	4.85	0.50	41.68	100.00
	Radial ooid 2	28.30	16.08	0.04	5.05	0.94	4.74	0.51	44.30	99.95
		29.36	17.08	0.06	0.94	0.56	5.19	0.54	46.22	99.96
		29.43	16.87	0.06	1.86	0.24	5.15	0.57	45.76	100.00
		29.43	16.89	0.05	2.08	0.24	5.19	0.51	45.55	99.95
	Radial ooid 3	29.30	16.84	0.06	2.47	0.45	5.15	0.54	45.10	99.93
		29.23	16.54	0.05	1.80	0.38	5.27	0.57	46.11	99.97
		28.33	16.28	0.07	3.20	1.03	5.16	0.63	45.25	99.99
		47.85	2.38	0.08	2.64	1.65	1.18	0.26	43.91	99.97
		28.88	16.74	0.04	1.90	0.88	5.15	0.48	45.88	99.95
	Radial ooid 4	53.51	0.45	0.09	0.02	b.d.	0.46	0.22	45.23	99.99
		54.90	0.33	0.08	0.03	b.d.	0.32	0.22	44.09	99.97
		29.42	17.12	0.08	1.03	0.66	5.35	0.47	45.77	99.94

Sample no.	component	CaO	MgO	SrO	SiO_2	Al_2O_3	FeO	MnO	CO_2	Total
NCC17	Concentric ooid 5	29.50	17.08	0.06	0.85	0.36	5.21	0.61	46.31	99.99
		28.20	16.52	0.04	3.18	2.10	5.05	0.53	44.35	100.00
		27.30	16.19	0.04	5.02	1.45	5.02	0.55	44.39	100.00
	Radial ooid 6	26.36	14.79	0.01	10.96	4.24	4.82	0.57	38.20	100.00
		30.68	17.43	0.09	1.20	0.38	5.32	0.62	44.24	99.96
		31.05	17.47	0.04	0.77	0.36	5.39	0.60	44.23	100.00
	Calcified particle 1	54.50	0.16	0.07	0.01	b.d.	0.32	0.11	44.78	99.98
		55.03	0.22	0.04	0.02	0.01	0.29	0.12	44.24	99.96
		55.35	0.19	0.03	0.03	0.01	0.26	0.19	43.94	100.00
		54.94	0.17	0.08	0.05	b.d.	0.29	0.15	44.28	99.99
		59.64	0.15	0.03	0.05	0.01	0.45	0.18	39.45	99.95
	Calcified particle 2	56.78	0.28	0.07	0.13	b.d.	0.40	0.19	42.12	99.98
		54.54	0.30	0.10	0.10	b.d.	0.44	0.16	44.34	99.98
		55.29	0.25	0.05	0.04	0.02	0.30	0.13	43.84	99.94
	Matrix	30.05	17.56	0.02	1.42	0.80	5.24	0.70	44.18	100.00
		31.40	18.05	0.01	0.30	0.02	5.31	0.55	44.31	99.99
NCC17a	Stromatolite	27.88	16.54	0.05	4.39	1.62	4.83	0.50	44.07	99.87
		2.61	1.24	0.07	81.07	0.52	0.49	0.07	13.82	99.93
		29.00	16.94	0.06	2.52	0.20	5.02	0.53	45.68	100.00
		29.24	16.80	0.05	1.91	0.03	5.03	0.53	46.37	99.96
		28.37	16.82	0.04	3.23	0.91	4.81	0.50	45.26	99.95
	Sparite filled void	32.53	17.49	0.01	0.05	b.d.	1.83	0.33	47.69	100.00
		0.02	b.d.	0.06	89.02	b.d.	0.06	b.d.	10.80	99.98
		32.33	18.05	0.02	0.03	0.01	1.64	0.23	47.67	99.98
	Matrix	29.36	17.17	0.05	0.73	0.29	4.84	0.48	46.99	99.92
		29.94	17.71	0.05	0.08	0.02	4.08	0.44	47.63	99.98
Upper carbonate section										
NCD4A	Sparite filled void	55.27	0.20	0.04	0.10	0.04	0.39	0.73	43.18	99.95
		54.30	0.15	0.02	0.05	0.03	0.30	0.75	44.36	99.98
	Micritic particle 1	30.52	17.32	0.05	0.19	0.10	4.96	0.61	46.17	100.00
	Micritic particle 2	29.82	17.11	0.07	0.12	0.04	5.65	0.79	46.32	99.98
	Rec. ooid 1	31.04	17.36	0.04	0.45	0.14	3.70	0.58	46.61	99.98
		30.11	17.50	0.04	1.52	0.44	4.01	0.50	45.81	99.94
		30.85	17.65	b.d.	0.29	0.09	3.84	0.43	46.82	99.98
	Rec. ooid 2	26.84	18.76	0.03	2.61	2.24	4.99	0.57	43.91	99.99
		31.15	17.98	0.03	0.45	0.16	2.45	0.47	47.30	100.00
	Rec. ooid 3	30.17	18.26	0.04	0.69	0.18	2.93	0.47	47.19	100.00
		30.24	19.15	0.02	0.50	0.17	2.37	0.46	47.04	100.00
	Rec. matrix	30.23	17.17	0.04	0.36	0.22	5.11	0.61	46.23	99.98
Middle carbonate section										
NCMA	Matrix	30.21	13.63	0.02	0.28	0.05	9.61	1.21	44.94	100.00
		30.53	13.12	0.03	0.19	0.05	10.04	1.65	44.32	99.96
		30.29	13.78	0.01	0.11	0.02	9.98	1.13	44.62	100.00
	Micritic particle, upper	28.24	12.85	0.02	5.39	0.24	9.72	1.45	42.03	100.00
		28.79	12.96	0.03	2.26	1.02	9.48	1.52	43.91	100.00
	Matrix, middle	30.07	13.29	0.02	0.13	0.04	10.77	1.20	44.44	99.95
		30.53	13.35	b.d.	0.06	b.d.	9.46	1.70	44.80	99.94
	Micritic particle, lower	29.64	13.64	0.03	0.95	0.27	9.99	1.30	44.12	99.95
		29.82	13.54	0.02	0.32	0.15	10.04	1.26	44.79	99.96
	Matrix, lower	29.50	12.99	0.03	1.06	0.36	10.39	1.46	44.16	100.00
		30.07	13.95	0.04	0.14	0.04	9.51	1.09	45.14	99.99

Sample no.	component	CaO	MgO	SrO	SiO_2	Al_2O_3	FeO	MnO	CO_2	Total
NCMB	Particle 1	30.00	13.41	0.02	0.64	0.20	10.23	1.51	43.95	99.98
		29.12	14.16	0.04	0.62	0.18	9.64	1.05	45.12	100.00
	Particle 2	13.64	6.81	b.d.	27.79	18.42	5.59	0.45	27.21	100.00
		29.80	13.75	0.03	0.25	0.06	9.74	1.31	45.01	99.95
	Particle 3	30.06	13.29	0.04	0.48	0.12	10.31	0.95	44.73	100.00
		29.88	13.00	0.03	0.70	0.11	9.90	1.23	45.11	99.98
NCMD	Radial ooid	29.95	13.02	0.02	0.80	0.36	10.15	1.42	44.19	100.00
		30.47	13.12	0.05	0.68	0.20	10.04	1.29	44.10	100.00
		29.79	13.52	0.05	0.58	0.22	9.89	1.20	44.72	99.99
	Ooid 1	30.18	12.95	0.02	1.05	0.30	10.38	1.27	43.81	100.00
	Radial ooid	29.37	13.42	0.02	1.63	0.66	10.02	1.11	43.76	99.99
		29.99	13.37	0.01	0.78	0.14	9.99	1.23	44.47	100.00
		29.94	13.36	0.04	0.15	0.03	10.39	1.11	44.97	100.00
	Micritic particle	29.68	13.13	0.11	0.02	0.02	10.95	1.55	44.52	100.00
		31.34	13.58	0.03	0.11	0.02	8.78	0.65	45.46	99.98
		30.72	13.52	0.06	0.37	0.07	9.31	1.18	44.76	100.00
	Matrix	28.19	11.37	0.01	5.12	3.67	8.79	1.16	41.57	100.00
		29.31	13.84	0.03	0.12	0.02	10.43	1.22	45.01	99.98
		55.90	0.03	0.03	0.08	0.02	0.39	0.66	42.76	99.88
		51.14	0.30	0.23	0.06	b.d.	0.89	0.91	46.42	99.95
	Rec. particle 1	30.70	13.36	0.02	0.03	0.01	11.03	0.61	44.24	100.00
		30.92	11.90	0.02	0.07	0.03	12.03	0.70	44.29	99.97
	Micritic particle 2	29.89	13.01	0.02	0.80	0.14	10.47	0.95	44.58	100.00
	Matrix	29.80	13.52	b.d.	0.10	0.03	10.43	1.22	44.85	99.95
		29.18	12.81	b.d.	0.06	0.01	11.18	1.56	45.07	99.96
	Rec. particle 3	29.73	13.41	0.01	0.04	b.d.	10.53	0.99	45.19	99.91
		29.62	13.54	b.d.	0.06	0.02	10.20	1.26	45.24	99.97
	Rec. particle 4	29.53	13.31	0.02	1.13	0.44	10.24	1.08	44.20	100.00
	Rec. radial ooid 4	29.78	12.84	0.02	0.13	0.06	10.93	1.10	45.10	99.97
	Rec. radial ooid 5	29.57	13.37	0.05	0.45	0.18	10.52	1.22	44.59	100.00

Available online at www.sciencedirect.com

ScienceDirect

Geochimica et Cosmochimica Acta 158 (2015) 57–78

Geochimica et Cosmochimica Acta

www.elsevier.com/locate/gca

A trace element and Pb isotopic investigation into the provenance and deposition of stromatolitic carbonates, ironstones and associated shales of the ~3.0 Ga Pongola Supergroup, Kaapvaal Craton

Robert Bolhar [a,c,*], Axel Hofmann [b], Mehrnaz Siahi [a,d], Yue-xing Feng [c], Camille Delvigne [e]

[a] School of Geosciences, University of the Witwatersrand, Wits 2050, South Africa
[b] Department of Geology, University of Johannesburg, Auckland Park 2006, South Africa
[c] School of Earth Sciences, University of Queensland, St Lucia, Qld 4072, Australia
[d] Department of Geo- and Environmental Sciences, LMU, 80333 München, Germany
[e] Department of Earth Sciences, Royal Museum of Central Africa, 3080 Tervuren, Belgium

Received 11 April 2014; accepted in revised form 19 February 2015; Available online 3 March 2015

Abstract

Major and trace element, and Pb isotopic data for chemical and clastic sedimentary rocks of the Mesoarchaean Pongola Supergroup are employed to infer aspects of the provenance and depositional environment, including ambient seawater composition. Stromatolitic carbonates of the Nsuze Group were formed in a tidal-flat setting, whereas ironstones of the Mozaan Group were deposited in an outer-shelf setting during marine transgression. Geochemical criteria, employed to test for crustal contamination and diagenetic/metamorphic overprinting, demonstrate that carbonates and ironstones preserved their primary chemical signature. In comparison to other documented Precambrian stromatolites, shale-normalised REE+Y patterns for Nsuze carbonates show pronounced enrichment in middle REE, but lack strong elemental anomalies (La, Gd, Y) that are diagnostic for derivation from open marine waters. In contrast, normalised REE+Y for ironstones exhibit distinct positive La, Gd and Y anomalies. Both rock types are devoid of normalised Ce anomalies and show only minor enrichment in Eu, suggesting deposition in anoxic environments (with respect to the Ce^{3+}/Ce^{4+} redox couple) accompanied by minor high-temperature hydrothermal input. Trace element geochemical data are most consistent with deposition of Nsuze carbonates in a shallow-water epicontinental basin with restricted but variable exchange to the open-ocean and dominant fluvial input, whereas ironstone precipitated in a deeper-water, epicontinental sea. Estuarine fractionation and organic complexation due to microbial activity is possibly indicated by MREE enrichment of the carbonates, also consistent with a restricted environment.

Shales belonging to the Mozaan Group are characterised by high concentrations of Al and K relative to Ca, Na and Sr, indicative of pronounced in-situ weathering, coupled with K-metasomatism. The provenance is mixed, comprising (ultra)-mafic and granitic source rocks.

Pb isotope regression for Nsuze carbonates documents a widespread, tectono-thermal or fluid percolation event at around 2.4 Ga. Two-stage modelling of Pb isotope data, in association with published Sr and Nd isotope data, requires a source for

* Corresponding author at: School of Geosciences, University of the Witwatersrand, Wits 2050, South Africa.

http://dx.doi.org/10.1016/j.gca.2015.02.026

Nzuse carbonates that was derived from evolved continental crust with an elevated U/Pb ratio (μ-value) and an approximate crustal residence time of ~100–600 Ma.

1. INTRODUCTION

Archaean chemical sedimentary rocks, including carbonates and banded iron formation, provide important information on the physico-chemical conditions on the Earth surface in general, and the hydrosphere in particular (e.g., Hofmann and Bolhar, 2007; Hofmann et al., 2014). Clastic sedimentary rocks, especially shales, on the other hand, hold clues to provenance and the influence of weathering processes, thus providing constraints on atmospheric conditions in the past (e.g., Wronkiewicz and Condie, 1987; Bolhar et al., 2005a). Since secondary processes, such as metamorphism, can strongly overprint primary geochemical signatures, only the best-preserved rocks should be relied on to unravel conditions in the distant past. For the Mesoarchaean time period (3.2–2.8 Ga), the best preserved supracrustal rocks can be found in South Africa, represented by the Pongola and Witwatersrand supergroups deposited on continental crust of the Kaapvaal Craton. Although metamorphism at greenschist-facies grade affected the Pongola Supergroup, textures, structures and composition of the volcano-sedimentary succession are generally well preserved (Beukes and Cairncross, 1991; Wilson et al., 2013). Several important studies on the Pongola Supergroup have recently emerged using trace element and isotope geochemistry to unravel aspects relating to seawater composition, continental weathering and oxygenation of the early atmosphere. For instances, relative fluxes of solutes from mid-oceanic ridge versus continental weathering were investigated by Alexander et al. (2008), based on REE and Nd isotopes of Mozaan ironstones. More recently, Delvigne et al. (2012) employed a combination of REE+Y data, Ge/Si ratios and Si isotopes to infer a common parental water reservoir of mixed freshwater and open ocean seawater for precipitation of both Fe- and Si-rich layers in Mozaan ironstones. Mo and Cr isotopic data obtained from Mozaan ironstones and a palaeo-weathering horizon within the Nsuze Formation were used to place the timing of oxygenic photosynthesis in the Kaapvaal Craton at around 2.95–3.0 Ga (Crowe et al., 2013; Planavsky et al., 2014), 450–700 myr before the Great Oxidation Event at 2.5–2.3 Ga (Bekker et al., 2004).

A geochemical study, comprising major and trace element, and Pb isotopic, data of marine sedimentary rocks, including stromatolitic carbonates and banded iron formation, as well as a suite of fine-grained clastic sedimentary rocks, from the Pongola Supergroup was conducted in the White Mfolozi Inlier in KwaZulu-Natal in order to better constrain the environment and tectonic setting in which sedimentation took place.

Specifically, REE and isotope geochemistry was used to (i) test if primary geochemical signatures were retained, (ii) to evaluate contributions from hydrothermal, marine and terrestrial sources, (iii) to provide geochronological constraints on the timing of deposition or thermal overprinting and (iv) to characterise source material that was available for weathering at the time of deposition.

2. REGIONAL GEOLOGY

The Archaean Pongola Supergroup is a volcano-sedimentary succession that was deposited ca. 3.0–2.9 Ga ago on continental crust of the south-eastern part of the Kaapvaal Craton (Fig. 1; Gold, 2006). It is lithologically and stratigraphically similar to the Witwatersrand Supergroup, which is well known for its rich gold mineralization. The Pongola and Witwatersrand supergroups are the oldest preserved successions of epicratonic volcanic and sedimentary rocks.

A twofold subdivision of the Pongola Supergroup has been established, namely the lower volcano-sedimentary Nsuze Group and the upper, largely sedimentary Mozaan Group (SACS, 1980; Weilers, 1990; Gold, 2006; Wilson et al., 2013). The succession has been regionally metamorphosed to lower greenschist facies, although higher metamorphic grades have been reported locally (Horvath et al., 2013; Hofmann et al., 2015). The Pongola Supergroup is exposed in a number of erosive inliers and structural remnants that extend for ca. 250 km from Amsterdam in the north to Nkandla in the south (Fig. 1) and that probably once formed part of a single sedimentary basin. The Nsuze Group rests nonconformably on granitoid rocks. Nsuze Group basement includes the Mpuluzi batholith in the Amsterdam area, which has been dated at 3107 ± 4 Ma (U–Pb single zircon; Kamo and Davis, 1994). Mukasa et al. (2013) reported two U–Pb zircon dates for Nsuze Group volcanic rocks: an andesitic flow near the base of the sequence yielded an age of 2980 ± 10 Ma, whilst a rhyolite flow further up in the stratigraphy yielded an age of 2968 ± 6 Ma. Hegner et al. (1994) reported a U–Pb single zircon date of 2985 ± 1 Ma for Nsuze Group lavas, whilst Nhleko (2003) reported a U–Pb SHRIMP zircon date of 2977 ± 5 Ma from a rhyolite flow. Lava flows are rare in the Mozaan Group. Mukasa et al. (2013) obtained a U–Pb zircon age of 2954 ± 9 Ma for an andesite lava flow within the upper part of the sedimentary succession. In contrast, a geochronological study of detrital zircons from the Mozaan Group (Nhleko, 2003) has identified zircons as young as 2902 ± 9 Ma in a sample from near the top of the sequence, suggesting that the date obtained by Mukasa et al. (2013) from the lava flow may reflect the age of a xenocrystic zircon. Emplacement of the Ususwana Complex at 2989.2 ± 0.8 Ma (U–Pb, baddeleyite, Olsson et al., 2012), much earlier than previously assumed (2873 ± 31 Ma, Sm–Nd: Hegner et al., 1984;

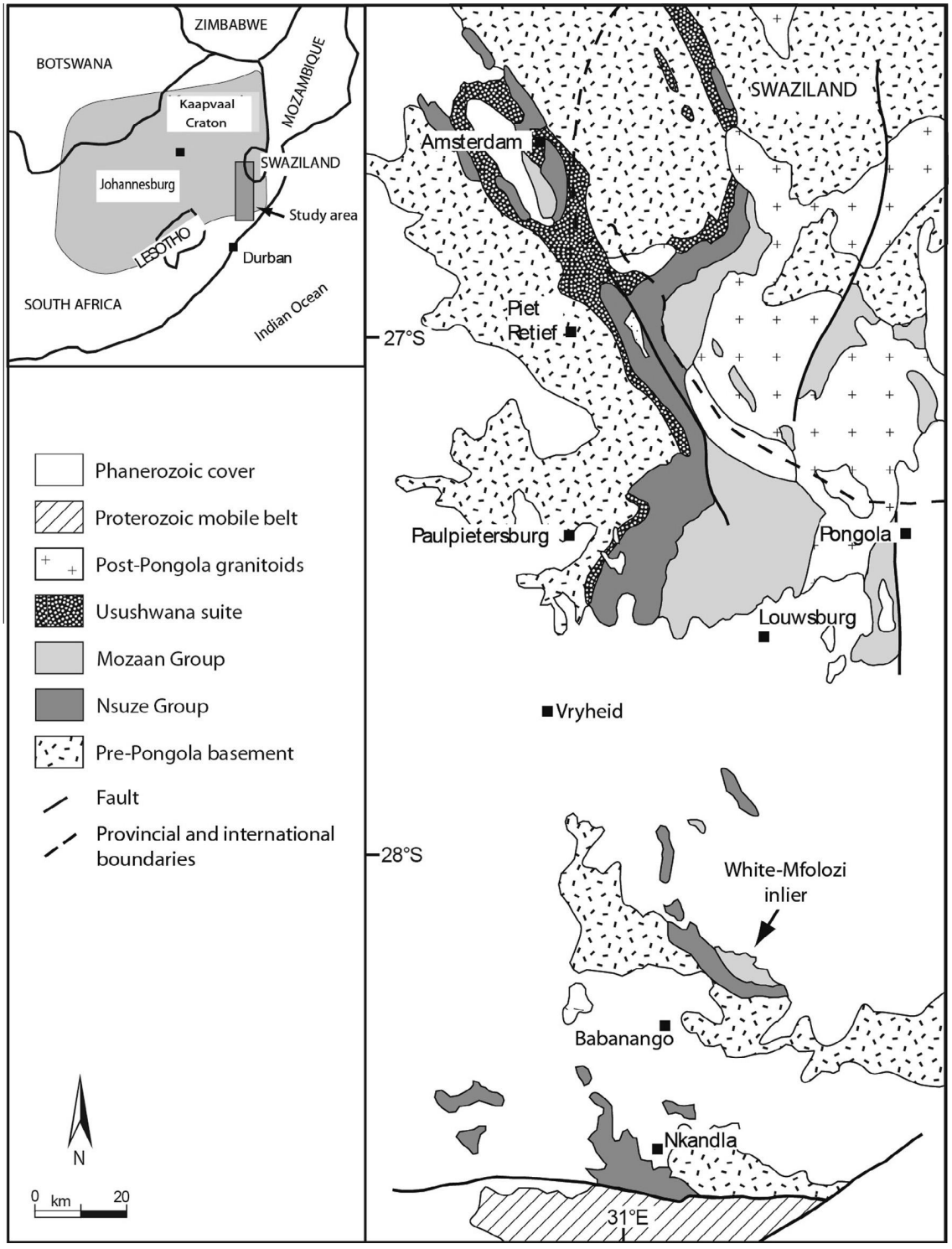

Fig. 1. Simplified geological map showing the distribution of the Nsuze and Mozaan groups of the Pongola Supergroup in the main Pongola basin, White Mfolozi inlier and Nkandla area (after Gold and von Veh, 1995).

2875 ± 40 Ma, Rb–Sr whole rock: Layer et al., 1988), suggests temporal association with an early phase of Nsuze Group volcanism. The Mozaan Group was intruded by a quartz porphyry sill at 2837 ± 5 Ma (U–Pb, zircon, Gutzmer et al., 1999), providing a minimum age of deposition of this unit, as well as by undeformed "post-Pongola granites", which typically fall in the age range between 2.8 and 2.7 Ga (Mukasa et al., 2013, and references

therein). Walraven and Pape (1994) reported a Pb–Pb age of 2860 ± 26 Ma for ferruginous shale from the Madola Member, the lateral equivalent of BIF from the Sinqeni Formation at the base of the Mozaan Group elsewhere. This age was regarded as the age of deposition of the BIF (Walraven and Pape, 1994), although the zircon evidence (Nhleko, 2003) indicates this age to be too young.

The Nsuze Group consists of packages of mafic to felsic volcanic and volcaniclastic rocks hundreds of metres thick that are intercalated with sandstone-dominated sedimentary packages of similar thickness. It attains a thickness of approximately 4600 m in the Main Pongola Basin (Fig. 1), whilst in the White Mfolozi Inlier it is only ~1100 m thick (Cole, 1994; Wilson et al., 2013). The reduced thickness in the latter area can be at least partly attributed to erosion prior to deposition of the Mozaan Group. The presence of thick lava flows intercalated with clastic sediments and lateral thickness variations has led most workers to suggest a continental rift environment for the Nsuze Group (Hegner et al., 1984; Burke et al., 1985; Crow et al., 1990; Matthews, 1990). Several authors also suggested a volcanic arc setting for the Nsuze Group (Tankard et al., 1982; Mukasa et al., 2013; Wilson et al., 2013).

The up to 4800 m thick Mozaan Group is made up predominantly of quartz-rich sandstones and shales. Minor lithologies include conglomerates that can be gold-bearing, jaspilitic banded iron formation (BIF), diamictites of possible glacial origin, and a single unit of amygdaloidal basaltic lavas. The mature and sheet-like character of the lithologies of the Mozaan Group suggests a passive margin or epicontinental setting (Beukes and Cairncross, 1991). Development of the Mozaan basin may be related to thermal subsidence that followed the Nsuze Group rifting event (Burke et al., 1985; Matthew, 1990).

2.1. Stratigraphy of the White Mfolozi Inlier

The Pongola Supergroup in this area contains both Nsuze and Mozaan strata. The latter rests with an angular unconformity of ca. 15° on the Nsuze Group. The succession was mapped by Matthews (1967). Further references can be found in Weilers (1990), Wilson and Grant (2006), Hicks and Hofmann (2012) and Wilson et al. (2013). Carbonate from the Nsuze Group and jaspilitic BIF and shale from the Mozaan Group were collected within this area and form the subject of this study.

2.1.1. Nsuze Group

The Nsuze Group in the White Mfolozi Inlier can be subdivided into five formations (stratigraphy after Matthews, 1967; Fig. 2). The Bomvu Formation is of variable thickness (0–20 m thick) but of considerable lateral extent. It nonconformably overlies basement granites and consists of cross-bedded arenites that have been interpreted as shallow, marginal marine, transgressive deposits (Matthews, 1967). The Nhlebela Formation overlies the Mantonga Formation along a sharp contact and consists of amygdaloidal lava flows of basaltic to andesitic composition that extruded under predominantly subaerial conditions (Wilson and Grant, 2006). The volcanic rocks are overlain by shales and interbedded sandstones of the Thembeni Formation, which, in turn, is overlain by the Chobeni Formation. This sequence comprises a sedimentary succession of quartz arenite, carbonate-cemented sandstone, shale, volcaniclastic rocks, and several horizons of dolomite. One dolomite horizon is some 25 m thick and locally contains well-developed stromatolites. The depositional environment of the Chobeni Formation is regarded as a tidal flat setting (Von Brunn and Mason, 1977; Mason and Von Brunn, 1977; Beukes and Lowe, 1989). The Chobeni Formation is overlain by the volcanic Bivane Formation, which is lithologically similar to the Nhlebela Formation, except for a larger proportion of pyroclastic material (Wilson and Grant, 2006). The Bivane Formation is the uppermost stratigraphic unit of the Nsuze Group in the White Mfolozi inlier, as it is overlain along an angular unconformity by strata of the Mozaan Group. A palaeosol horizon is well developed immediately below the unconformity (Nhleko, 2003; Delvigne, 2012; Crowe et al., 2013).

2.1.2. Mozaan Group

The base of the Mozaan Group is known as the Mandeva Formation, correlated with the Sinqeni Formation further to the north, which is characterised by two quartz arenite units separated by a unit of shale and BIF (Fig. 2; Hicks and Hofmann, 2012). The lower unit is characterised by cross-bedded quartz arenites that contain beds of chert/quartz pebble conglomerate, some of which contain sulphide and subeconomic gold and uranium mineralization (Saager et al., 1986; Hicks and Hofmann, 2012). Dix (1984) interpreted this lower unit as a fluvial braided stream deposit. The arenites are sharply overlain by a ca. 15 m thick succession of (from base to top) shale locally showing wave-ripple lamination, jaspilitic BIF and ferruginous green shale. Deposition took place in a shallow shelf setting following transgression, probably far away from terrigenous input (Beukes and Cairncross, 1991; Alexander et al., 2008). The shale/BIF unit is sharply overlain by quartz arenites that show well-preserved sedimentary structures indicative of a clastic tidal flat environment (Von Brunn and Hobday, 1976; Von Brunn and Mason, 1977; Dix, 1984; Noffke et al., 2008; Hicks and Hofmann, 2012). The Mandeva Formation is overlain by shales of the Mpunga Formation that form the uppermost exposed unit of the Mozaan Group in the White Mfolozi Inlier. The Mozaan BIF represents a Superior-type iron formation as it is interbedded with quartz arenites and shales, indicative of deposition on a continental shelf, during times of elevated sea levels (e.g., Gross, 1983; Bekker et al., 2010).

3. SAMPLING AND METHODS

A total of six carbonate samples of common lithofacies from separate carbonate outcrops (main section: PO5-2, PO5-3, PO5-4, PO5-5; upper section: PO5-8, PO5-9) of the Nsuze Group (Fig. 2) were investigated (Table 1). In addition, we examined eight samples of shale (Fig. 2; drill

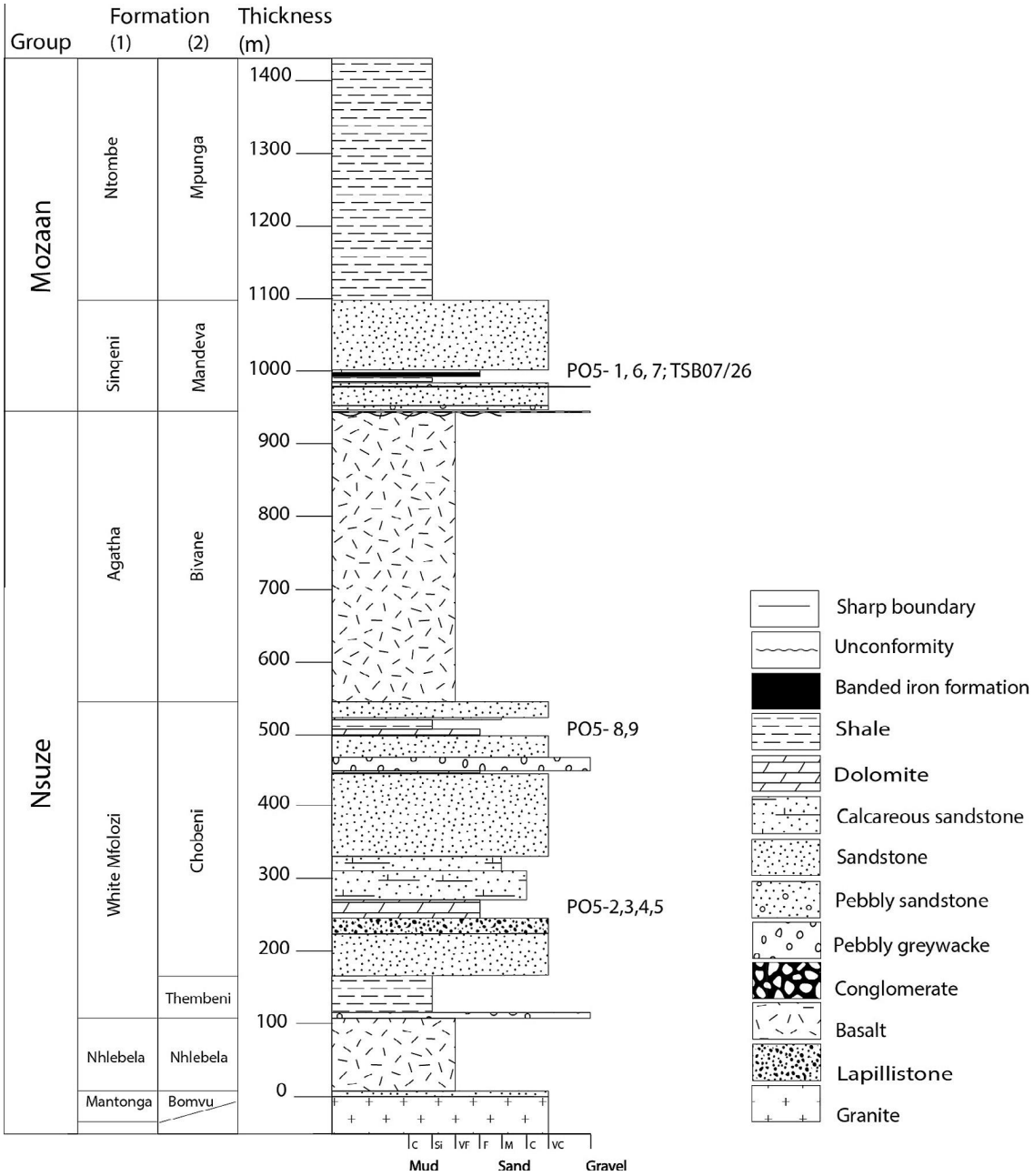

Fig. 2. Lithostratigraphic column of the Nsuze and Mozaan groups in the White Mfolozi inlier. Formation names are after Joubert and Johnson, 1998 (column 1) and Matthews, 1967 (column 2). Sample locations are indicated.

core TSB07-26, samples 163.9, 165.2, 168, 169.4, 170.6, 173, 174, 175; numbers indicate depth of core in metres) and banded iron formation (PO5-6, PO5-8, derived from outcrop). Carbonate samples represent homogeneous domains of a particular facies (see Table 1). Ironstone samples comprise of several 0.5–1 cm thick layers of hematite–magnetite and jaspilite. Samples typically weighing 50–100 g were crushed and chips (approximately 1–3 mm in size) were handpicked, ultrasonically cleaned in deionised water, and milled in agate.

Major element concentrations of all samples were determined by XRF spectrometry (Philips X'Unique XRFS) on glass tablets at the School of Geological Sciences, University of KwaZulu-Natal (UKZN), using the method described in Wilson (2003). Accuracy for major elements was checked against international standard NIM-G and found to be better than 1%.

Trace elements were determined by ICP-MS, using bulk sample material for ironstones, and selective acid digests for carbonates. Carbonate powders (~200 mg) were digested at room temperature in 2% HNO_3. The ironstone powders were digested on a hotplate in conc. HNO_3 and HF. After centrifuging, supernatants (carbonate) were split into two aliquots for trace element and Pb isotope analysis. One

Table 1
Petrographic characterisation of Nsuze Formation carbonates.

Sample	Facies	Constituents	Bedding/sedimentary structures	Non-carbonate content
PO5-2	Stratiform stromatolite (Fig. 3a and b)	Partially silicified dolomite and flattened allochems/particles (0.1–6 mm across) with pressure fringes of fibrous quartz	Discontinuous thin bedding, wrinkly lamination, tepee structure	Ch (30%), Qtz (5%), Ccp, Rt, Zrn, Ms (1%)
PO5-3	Intrapeldolorudite, (Fig. 3c and e)	Alternation of stratiform stromatolite with layers of intrapeldolorudite (intraclasts, peloids); spar-filled voids	Finely laminated, disrupted locally dolarenite–dolorudite, massive siliceous dolomite	Ch (10%), Qtz (5%), Ms (3%), Ap, Hem, Zrn, Chl, Rt, Py (1%)
PO5-4	Peldololutite/-arenite, (Fig. 3f)	Silicified dolomite, partially silicified micritic peloids up to 0.1 mm	Massive to faint ripple lamination	Ch (20%), Qtz, Chl, Ms, Py, Rt, Zrn (2%)
PO5-5	Wave-ripple laminated dololutite/-arenite, (Fig. 3d)	Dololutite-chert couplets, silicified peloids	Wave ripple lamination	Ch (20%), Qtz (10%), Chl, Ms (5%), Zrn, Rt, Py, Ccp (1%)
PO5-8	Crystalline dolostone	Recrystallized dolomite	Massive	Qtz (5%), Ch (5%), Ms, Rt, Py, Ccp, Hem (5%)
PO5-9	Dololutite/-arenite	Siliceous dololutite, irregular spar-filled voids	Massive, discontinuous wrinkly lamination	Qtz (15%), Ch (5%), Ccp, Py, Ms, Chl, Plg, Rt, Zrn (5%)

Ap: Apatite, Ccp: Chalcopyrite, Ch: Chert, Chl: Chlorite, Hem: Haematite, Mnz: Monazite, Ms: Muscovite, Pl: Plagioclase, Py: Pyrite, Qtz: Quartz, Rt: Rutile, Zrn: Zircon.

aliquot was diluted by factors ranging from ~1200 (carbonates) to ~100 (ironstones) in 2% HNO_3 and spiked with 6 ppb internal standard (Eggins et al., 1997). Oxide levels were monitored with elemental solution and appropriate corrections were employed. Instrumental drift was monitored with an interleaved solution and corrected for. Trace element concentrations were determined on a Thermo Xseries ICP-MS at the University of Queensland. Instrument operating conditions and analytical procedures were adopted from Eggins et al. (1997). One hotplate digestion of W-2 (US Geological Survey standard) was used for calibration. Preferred concentrations for W-2 are given in Table 2, along with basalt standard BHVO-1 and BIF standard IF-G. Standards and ironstone samples were digested by the same method. Analytical precision was typically within 5% for all elements measured, based on replicate analysis of the standards.

The aliquot for isotope analysis was evaporated, and Pb was separated using miniaturised HBr–HCl chromatography. Details of Pb separation and isotope analysis are reported elsewhere (Bolhar et al., 2007). Pb isotope ratios were corrected for instrumental mass fractionation of 1.2‰ per amu based on replicate measurements of the NIST NBS981 standard. In-run precision was <0.1% (1 sigma standard error). Five analyses of NBS981 standard ($^{206}Pb/^{204}Pb = 16.941$; $^{207}Pb/^{204}Pb = 15.494$; $^{208}Pb/^{204}Pb = 36.718$: Todt et al., 1996) produced $^{206}Pb/^{204}Pb = 16.905 \pm 0.011$, $^{207}Pb/^{204}Pb = 15.446 \pm 0.014$, $^{208}Pb/^{204}Pb = 36.567 \pm 0.044$. The software package ISOPLOT 3 (Ludwig, 2003) was utilised for age regression. Dates (calculated with a correlation coefficient of 0.9 and input errors of 0.1%) are quoted at the 95% confidence level.

For REE+Y analysis of shale samples, about 50 mg of powdered samples were dissolved by fusion with lithium metaborate (99.999% purity; American Element) at 1000 °C for 1 h in platinum crucibles with a 1:8 flux to sample ratio. The fusion beads were dissolved in 5% HNO_3. Solutions were analysed by HR-ICP-MS (Element 2) at RMCA (Belgium) in low-resolution mode with indium as internal standard (Robinson et al., 1999). Specific BaO interference on Eu and PrO and CeOH on Gd were corrected following Aries et al. (2000) calculations with Th (a 0.5 ppb Th spike was added to all samples) as the normalizing element. Typical accuracy is better than 5% for Y, Ba, La, Ce, Pr, Gd, Tb, Dy, Ho, Er, Yb and Lu, and within 10% for Nd, Eu and Sm as checked against geostandard IF-G and a 0.1 ppb artificial multi-element solution.

4. RESULTS

4.1. Petrography

Macroscopic and microscopic investigation of the sampled carbonates (Fig. 3, Table 1) revealed various amounts of allochems and carbonate-replaced extraclasts set in a recrystallized, micritic-microsparitic dolomitic matrix. Allochems include intraclasts, peloids, pseudo-ooids, granule-sized, (sub)spherical particles, and stromatoclasts in various sizes and amounts. Some of these particles represent altered volcaniclastic material. In addition, the carbonates contain various amounts of siliciclastic detritus of poorly sorted, subangular-subrounded, very fine to medium sand-sized quartz grains, minor plagioclase, and some accessory phases including zircon, rutile and monazite. Siliciclastic detritus is a common component in all samples. Secondary minerals include muscovite, chert, chlorite, pyrite, chalcopyrite, and apatite. X-ray diffraction analysis (X-PertPro, University of Johannesburg) indicated dolomite with minor calcite and ankerite as the carbonate phases. Samples do not show evidence for recent

Table 2
Major (wt%) and trace (ppm) element data for standards, stromatolitic carbonates, ironstones and shales from the Nsuze and Mozaan groups.

	BHVO-1	RSD (%)	IFG	RSD (%)	W-2	Stromatolitic carbonates									Iron stones		Shales						
						PO5-2	PO5-2	PO5-3	PO5-3	PO5-4	PO5-4	P05-5	PO5-8	PO5-9	PO5-6	PO5-7	TSB07/26-175	TSB07/26-174	TSB07/26-173	TSB07/26-170.6	TSB07 26-169.4	TSB07/26-168	TSB07/26-165.2	TSB07/26-163.9
Digestion method						2% HNO3	1 M acetic acid	2% HNO3	1 M acetic acid	2% HNO3	1 M acetic acid	2% HNO3	2% HNO3	2% HNO3										
SiO_2						50.48		28.78		40.14		39.49	21.66	23.24	64.54	82.13	54.77	63.34	53.27	57.99	54.45	24.23	37.49	47.87
Al_2O_3						2.66		2.28		1.80		2.02	3.54	3.32	0.11	0.00	33.23	25.30	28.98	30.22	27.11	2.96	9.96	14.61
Fe_2O_3						3.60		3.51		2.96		2.99	10.03	6.04	33.92	16.74	1.84	3.46	9.13	3.16	11.32	51.66	43.67	30.08
MnO						0.31		0.42		0.33		0.32	1.03	0.72	1.52	1.29	0.14	0.20	0.58	0.22	0.74	11.78	3.32	1.37
MgO						17.06		25.08		22.25		22.20	23.61	23.90	0.03	0.05	0.31	0.90	2.31	0.73	2.64	8.34	3.65	4.74
CaO						25.08		39.03		32.12		32.05	39.05	41.80	0.02	0.04	0.07	0.04	0.03	0.05	0.04	0.87	0.53	0.11
Na_2O						0.00		0.20		0.05		0.25	0.06	0.01	0.00	0.00	2.56	1.26	0.96	1.75	0.40	0.04	0.00	0.00
K_2O						0.65		0.71		0.56		0.57	0.86	1.06	0.05	0.03	5.86	4.39	3.53	5.25	2.63	0.00	1.03	0.54
TiO_2						0.14		0.10		0.08		0.11	0.13	0.06	0.00	0.00	1.20	0.97	1.06	0.87	0.82	0.11	0.38	0.57
P_2O_5						0.03		0.03		0.02		0.03	0.05	0.08	0.01	0.02	0.05	0.04	0.04	0.05	0.05	0.09	0.20	0.05
TOTAL						100.01		100.14		100.32		100.03	100.02	100.24	100.21	100.30	100.03	99.90	99.89	100.29	100.20	100.08	100.23	99.94
L.O.I.						29.47		37.79		34.68		34.30	37.68	38.89	0.65	1.61	5.37	4.87	5.81	4.99	5.60	27.70	15.85	8.95
Sc	31.87	1.7	0.28	3.2	36.07	1.97		1.42		1.17		2.01	1.19	1.15	0.09	0.03	7.08	2.11	10.44	0.86	11.65	1.47	5.85	14.98
V	310.5	1.4	1.77	0.7	261.6	5.79		3.96		3.34		9.51	2.85	6.03	2.81	0.594	220	140	145	111	111	6.96	54.81	111
Cr	295.2	2.4	17.65	1.2	92.79	10.55		4.77		6.99		22.80	2.51	308.1	3.36	1.52	481	382	377	291	286	38.37	164	309
Co	45.06	1.4	28.21	0.6	44.53	5.45		3.57		3.13		3.80	4.74	3.73	1.96	0.990	12.03	18.39	12.80	11.84	11.18	7.76	11.19	20.58
Ni	116.7	3.0	23.86	0.2	69.99	23.17		16.36		16.39		20.81	9.89	11.90	4.70	3.07	33.96	78.02	106	34.46	45.36	45.52	69.76	109
Cu	135.3	3.0	8.86	0.2	103.0							2.26		22.26			5.58	26.53	16.13	7.71	4.75	9.87	67.48	12.46
Rb	9.32	0.8	0.29	0.3	19.80	1.19		1.08		0.81		9.64	0.53	18.43	0.32	0.23	118	55.91	17.99	77.87	22.31	0.029	29.19	17.37
Sr	396	0.5	3.61	0.6	195	273		337		270		285	143	274	2.12	17.87	43.98	13.62	41.97	6.30	37.30	1.86	19.56	6.04
Y	24.61	0.8	9.14	0.5	20.11	6.63		4.13		3.03		4.22	7.15	4.14	0.82	0.80	22.54	20.36	23.19	21.14	21.16		16.82	14.16
Zr	170	1.4	0.56	1.4	87.87	0.08		0.07		0.05		5.57	0.025	0.346	0.269	0.150	224	267	227	163	148	23.48	60.43	104
Nb	18.48	1.0	0.10	0.4	7.28							0.069		0.26			21.07	18.77	20.62	19.58	16.99	0.501	3.95	7.77
Ba	132	0.8	2.02	0.3	170	22.79		20.13		9.56		32.66	49.90	45.03	6.77	2.61	364	279	230	340	172		203	52.28
La	15.43	0.7	2.71	0.5	10.52	2.61	1.21	4.86	3.64	2.98	2.11	3.94	3.59	4.00	1.03	0.330	56.68	34.69	50.38	42.49	37.93	3.13	16.13	20.40
Ce	38.24	0.7	3.90	0.3	23.22	6.45	3.15	9.65	6.85	6.78	4.65	8.50	6.88	7.95	1.72	0.562	112	70.04	100	89.10	75.56	6.48	32.01	40.26
Pr	5.46	0.7	0.430	0.4	3.03	0.900	0.449	1.16	0.765	0.831	0.552	1.07	0.832	0.927	0.171	0.068	12.39	7.93	11.29	10.43	8.66	0.778	3.67	4.59
Nd	24.72	0.6	1.73	0.9	12.91	3.89	2.01	4.55	2.99	3.14	2.10	4.17	3.45	3.47	0.598	0.278	43.37	28.29	40.44	39.65	31.14	3.37	13.83	17.14
Sm	6.13	0.9	0.399	0.6	3.27	1.06	0.564	0.930	0.570	0.636	0.416	0.905	0.970	0.691	0.117	0.062	8.19	5.56	7.68	8.39	6.17	0.981	3.13	3.61
Eu	2.07	0.9	0.362	0.4	1.09	0.378	0.203	0.299	0.176	0.175	0.113	0.225	0.371	0.391	0.042	0.026	2.30	1.42	1.83	1.94	1.39	0.295	0.959	1.03
Gd	6.29	0.8	0.667	1.2	3.71	1.16	0.642	0.857	0.564	0.621	0.400	0.878	1.24	0.701	0.127	0.083	6.20	4.51	5.58	6.11	5.07	1.11	3.09	3.21
Tb	0.946	0.9	0.112	0.8	0.615	0.185	0.104	0.129	0.084	0.091	0.059	0.135	0.204	0.111	0.019	0.011	0.899	0.709	0.896	0.891	0.792	0.168	0.490	0.479
Dy	5.30	0.9	0.791	1.7	3.81	1.07	0.630	0.714	0.497	0.503	0.333	0.796	1.17	0.674	0.106	0.067	4.57	3.94	4.63	4.43	4.32	0.982	2.97	2.81
Ho	1.01	0.9	0.207	0.5	0.803	0.219	0.128	0.138	0.100	0.102	0.066	0.160	0.234	0.144	0.022	0.016	0.995	0.873	1.020	0.938	0.917	0.191	0.668	0.634
Er	2.53	1.0	0.619	0.6	2.22	0.560	0.334	0.362	0.265	0.252	0.170	0.418	0.569	0.385	0.058	0.043	3.06	2.71	3.16	2.80	2.70	0.531	1.81	1.91
Tm	0.343	1.2	0.092	0.4	0.327	0.076	0.046	0.049	0.037	0.034	0.023	0.058	0.077	0.053	0.008	0.006						0.071		
Yb	2.01	1.0	0.580	1.4	2.06	0.445	0.274	0.285	0.225	0.212	0.133	0.346	0.445	0.331	0.045	0.032	3.09	2.74	3.11	2.58	2.55	0.476	1.51	1.95
Lu	0.278	1.3	0.090	2.3	0.301	0.059	0.037	0.041	0.032	0.028	0.018	0.051	0.060	0.050	0.006	0.005	0.480	0.438	0.487	0.404	0.401	0.070	0.226	0.304
Hf	4.35	1.4	0.018	0.6	2.36							0.147		0.014			6.17	7.25	6.24	4.55	4.11	0.57	1.51	2.72
Ta	1.16	1.2	0.171	0.2	0.454												1.70	1.55	1.69	1.61	1.46	0.025	0.326	0.628
Pb	2.01	3.7	2.52	1.5	7.53	28.38		2.28		1.49		1.17	49.71	352.2	0.821	1.65	20.75	12.28	13.42	12.07	41.90	7.23	4.89	3.91
Th	1.20	1.1	0.043	3.2	2.10	0.310		0.216		0.170		0.616	0.424	0.470	0.020	0.011	2.69	1.15	4.24	0.904	6.29	1.11	3.39	6.07
U	0.427	1.3	0.021	2.5	0.505	0.087		0.046		0.036		0.250	0.101	0.150	0.130	0.016	1.94	1.51	1.81	0.62	1.49	0.492	0.81	1.29
CIW																	88	92	95	91	97	64	91	99
CIA																	76	79	84	78	88	64	83	95

BHVO-1 data represent the average of 262 analyses from 71 digestions; IFG data represent the average of 3 analyses from 2 digestions. Ba, Y and REE data for shales from Delvigne (2012).
CIW = $[Al_2O_3/(Al_2O_3 + CaO + Na_2O)] \times 100$; CIA = $[Al_2O_3/(Al_2O_3 + CaO + Na_2O + K_2O)] \times 100$.

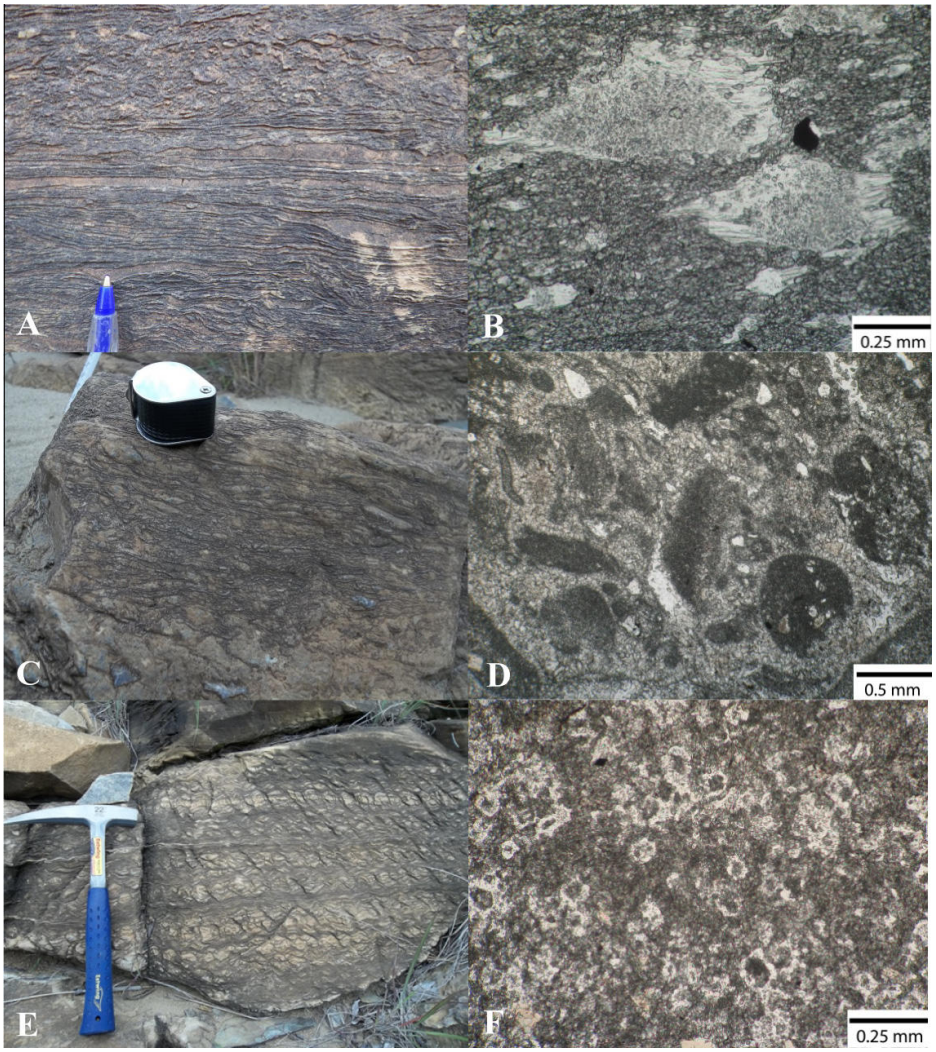

Fig. 3. Field photos (left) and thin section photomicrographs (plane-polarized light, right) of some Nsuze carbonate facies investigated in this study. (A) Stratiform stromatolite facies. (B) Stratiform stromatolite containing silicified particles and peloids with fibrous quartz forming pressure fringes (sample PO5-2). (C) Alternation of stratiform stromatolite with intrapeldolorudite. (D) Photomicrograph of partially silicified micritic compound intraclasts in microsparitic dolomite matrix that contains micritic peloids (sample PO5-3). (E) Wave-ripple laminated dololutite–dolarenite. (F) Peloids with silicified rims and micritic cores in micritic dolomite matrix (sample PO5-4).

weathering, except for two samples that contain minor secondary iron oxides (Table 1).

Banded iron formation consists of light red Si-rich jasper layers alternating with dark red Fe-rich layers along sharp to diffuse boundaries. Jasper layers consist predominantly of microquartz containing euhedral and droplet-like inclusions of Fe-oxide at the submicrometer scale. The dark layers are composed predominantly of euhedral to subhedral Fe-oxides (20–100 μm in diameter) in a microquartz matrix. Bedding-parallel and cross-cutting veins, as well as diffuse domains characterised by the development of quartz and Fe–Mn-oxides, attest to secondary alteration processes.

Shale below BIF consists of silt-sized detrital quartz and phyllosilicates, predominantly chlorite, and shows lamination due to grain size variation. Green shale above the BIF contains less detrital quartz, is rich in Fe-chlorite, and contains silt-sized euhedral carbonate crystals.

4.2. Major elements: carbonates and ironstones

Major element data are reported in Table 2 and graphically displayed in Fig. 4. Calculated averages for published ironstones from the Mozaan Formation (top/bottom and middle of stratigraphic column: Alexander et al., 2008; details of calculating averages in caption to Fig. 5) are shown for comparison. Regarding the XRF analyses neither correction nor subtraction of detrital or secondary, non-carbonate components was carried out. Besides a clastic quartz component, the carbonates are variably silicified as indicated by SiO_2 contents of 20–50 wt%. Al_2O_3 contents of 1.8–3.5 wt% document the presence of some (detrital?) aluminosilicates. SiO_2 contents of BIFs (including averages for BIFs representing top/bottom and middle portions of the stratigraphic column) are consistently higher at 50–80 wt%, with $Al_2O_3 < 0.5$ wt%. Fe_2O_3 in carbonates is <4 wt%, with sample PO5-8 having a Fe_2O_3 content of

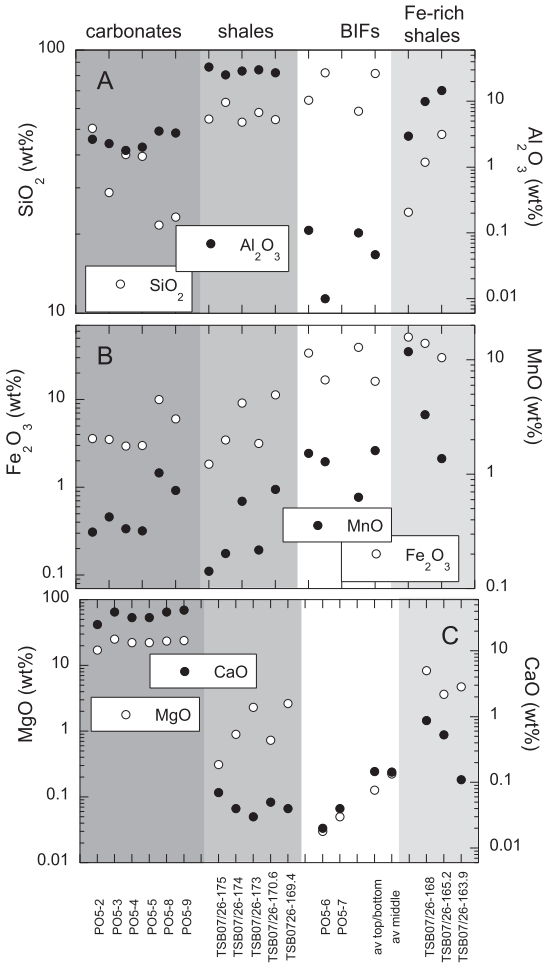

Fig. 4. Major element compositions of carbonates, shales, Fe-rich shales and ironstones (including average ironstone compositions: top/bottom and middle of the Mozaan Group BIF; from Alexander et al., 2008; details on calculating averages are given in caption to Fig. 5).

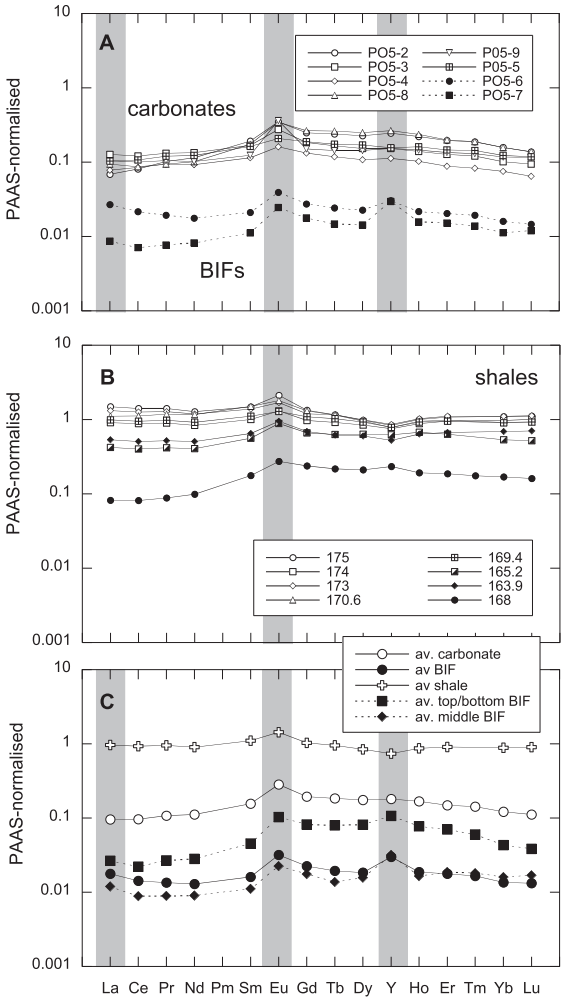

Fig. 5. Post Archaean Australian Shale-normalised (PAAS: Taylor and McLennan, 1985) REE+Y diagrams. (A) Comparison of dolomitic carbonates of the Nsuze Group and jaspilitic BIFs of the Mozaan Group. Note that ironstones have trace metal concentrations that are one order of magnitude lower than those in the carbonates, reflecting higher abundances of REE+Y-poor quartz. The carbonates are characterised by relative enrichments in Eu, whereas BIFs have anomalous La, Eu and Y concentrations. Carbonates and, to a lesser extent, ironstones show relative enrichment of MREE. (B) PAAS-normalised REE+Y compositions for shales. (C) Averaged compositions for the studied lithologies. Averages for ironstones from the top/bottom and middle part of the ironstone sequence from Alexander et al. (2008) are shown for comparison. These averages were calculated from samples with $Al_2O_3 \leqslant 0.13$ (top/bottom; $n = 3$) and $\leqslant 0.06$ wt% (middle; $n = 3$).

~10 wt%. Fe_2O_3 in BIFs is consistently higher at values of 16–45 wt%. CaO (<0.2 wt%) and MgO (<0.3 wt%) contents in BIFs are very low, and expectedly much higher in carbonates at values of 17–25 wt% (MgO) and 25–29 wt% (CaO).

4.3. Trace element data: carbonates and ironstones

REE+Y data for the stromatolitic carbonates and jaspilitic BIFs are reported in Table 2 and are graphically displayed in a PAAS (Post Archaean Australian shale)-normalised diagram (Fig. 5A). Carbonate rocks of the Nsuze Group are characterised by enrichment in the middle REE ($Pr/Tb_{shale} = 0.4–0.8$, $Tb/Yb_{shale} = 1.2–1.7$), and unfractionated light REE relative to the heavy REE ($Pr/Yb_{shale} = 0.6–1.3$). La and Gd abundances are not anomalous in relation to neighbouring REE ($La/La^* = 0.8–1.2$, $Gd/Gd^* = 1.0–1.1$), whilst Eu ($Eu/Eu^* = 1.3–2.8$) and, to a lesser extent, Y ($Y/Ho = 26–31$ versus $Y/Ho_{chondritic}$ ~26), are relatively enriched. Levels of ΣREE are 16–24 ppm, which is comparable to concentration levels in average microbialites from the Devonian Canning Basin (~20 ppm: Nothdurft et al., 2004), but significantly higher than in other Archaean stromatolites from southern African cratons (stromatolite carbonate average from the Campbellrand Formation: ~4 ppm, Kamber and Webb, 2001; stromatolite carbonate average from the Mushandike limestone: ~10 ppm, Kamber et al., 2004).

The two jaspilitic BIFs of the Mozaan Group have noticeably lower ΣREE concentrations (2–4 ppm), reflecting the higher abundance of REE-poor quartz. MREE are slightly enriched over the HREE ($Tb/Yb_{shale} = 1.3–1.5$) and LREE ($Pr/Tb_{shale} = 0.5–0.8$), whilst LREE are unfractionated relative to the HREE ($Pr/Yb_{shale} = 0.7–1.2$). La ($La/La^* = 1.2–1.3$) and Y ($Y/Ho = 38–51$) display distinct positive anomalies (Fig. 5A). Two types of Iron Formations (IFs) were previously identified by Alexander et al. (2008) on the basis of shale-normalised REE patterns, and were correlated with their relative stratigraphic position: BIFs with relative enrichment in MREE, generally higher levels of REE and smaller Y anomalies – obtained from the top and bottom of the sequence – and BIFs with little to no fractionation of the LREE and MREE relative to the HREE – sampled from the middle of the section (Alexander et al., 2008). The average composition of BIFs from this study resembles, but does not exactly match, ironstones from the middle of the sequence as described by Alexander et al. (2008) (Fig. 5C).

Average compositions for carbonates, ironstones and shales are shown in Fig. 5C.

4.4. Major and trace element data: shales

Shales (Mandeva Formation) display a wide range in SiO_2 (24–63 wt%), Al_2O_3 (3–33 wt%) and total Fe (as Fe_2O_3: 2–52 wt%) concentrations (Fig. 4A and B). Three shale samples (TSB07/26-168, 165.2, 163.9) are different in having very high Fe_2O_3 (>30 wt%), MnO (>5 wt%), MgO (>4 wt%) and correspondingly low SiO_2 (<50 wt%) and Al_2O_3 (<15 wt%), accompanied by high to very high LOI contents (9–28 wt%). These shales are classified as ferruginous shales intermediate to BIF. Cr and Ni contents are not correlated, and whilst concentrations are comparable to those of late Archaean shales (Taylor and McLennan, 1985), Pongola shales have higher Cr/Ni ratios, an observation also made by Wronkiewicz and Condie (1989). In terms of SiO_2/Al_2O_3 vs K_2O/Na_2O Pongola shales overlap the compositional field of Archaean shales (Wronkiewicz and Condie, 1987). As noted by Bolhar et al. (2005a) $K_2O/Na_2O > 2$ may point to K-metasomatism, as representative Archaean igneous source lithologies have values typically <2. In the case of some Pongola shales, elevated K_2O/Na_2O values are due to low Na_2O contents rather than high K_2O contents. In comparison to PAAS, Pongola shales have similar SiO_2, Al_2O_3, Na_2O and Zr contents, elevated Fe_2O_3 and Cr, and markedly depleted CaO and REE. Pairs of Zr–Hf and Nb–Ta define strongly correlated arrays translating into ratios of $Zr/Hf = 35.8$ ($R^2 = 0.999$) and $Nb/Ta = 12.1$ ($R^2 = 0.999$), similar to values for cratonic shale (Condie, 1993). Y and Ho are less well correlated ($Y/Ho = 22$; $R^2 = 0.8$), yielding ratios mostly below the chondritic range (~26: Pack et al., 2007). Strongly correlated arrays and ratios similar to chondritic values suggest that metasomatism and hydrothermal alteration were insignificant (Bau, 1996; Bolhar et al., 2005a). Shales are characterised by generally flat PAAS-normalised patterns ($Pr/Tb_{shale} = 1.0 \pm 0.2$, $Pr/Yb_{shale} = 1.0 \pm 0.2$) at ΣREE concentration levels of 80–255 ppm (Fig. 5B), with the exception of one shale showing LREE depleted patterns. Eu is variably enriched in all samples ($Eu/Eu^* = 1.4 \pm 0.1$). Chondrite-normalised REE patterns of the shales are relatively uniform showing enrichment of LREE relative to MREE but unfractionated HREE (Fig. 6A inset). Again, one Fe-rich shale is distinct in showing significantly lower overall concentrations. Geochemically, shale data from this study are compared to other documented shale occurrences in South Africa and representative source lithologies in Fig. 6A and B. Ti/Zr vs Ni and REE compositional characteristics are discussed in more detail under "shale provenance".

4.5. Pb isotope data: carbonates

Pb isotopic ratios for the Pongola whole rock carbonates are listed in Table 3 and graphically displayed in Fig. 7. In $^{207}Pb/^{204}Pb$ vs. $^{206}Pb/^{204}Pb$ space, the two ratios are moderately well correlated. Linear regression yields an errorchron date of 2412 ± 200 Ma (MSWD = 2.1). The large uncertainty of this date is due to the small spread of Pb isotope ratios, indicating relatively uniform U/Pb ratios in the carbonates.

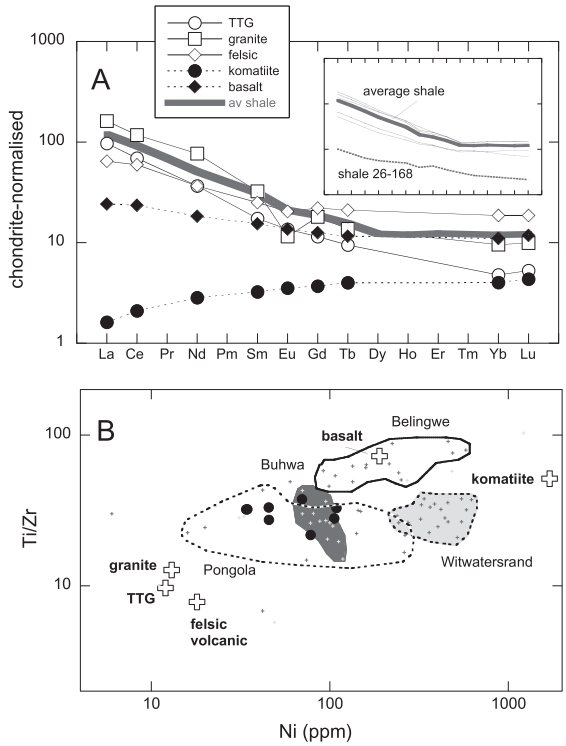

Fig. 6. (A) Chondrite-normalised (Boynton, 1984) REE patterns of average Pongola shale (this study) and representative igneous source lithologies (Condie, 1993); inset shows Pongola shale compositions and calculated average (excluding Fe-rich shale 26–168). (B) Diagram of Ti/Zr vs Ni showing representative igneous lithologies (same source as for A), and compositional fields for Archaean shales from southern Africa (Witwatersrand: Wronkiewicz and Condie, 1987; Belingwe: Hofmann et al., 2003; Buhwa: Fedo et al., 1996; Pongola: Wronkiewicz and Condie, 1989).

Table 3
Pb isotope data for stromatolitic carbonates from the Nsuze Group.

	$^{206}Pb/^{204}Pb$	2σ	$^{207}Pb/^{204}Pb$	2σ	$^{208}Pb/^{204}Pb$	2σ
P05-2	16.00	0.01	15.26	0.01	35.18	0.03
P05-3	16.40	0.03	15.32	0.03	35.76	0.08
P05-8	13.78	0.07	14.92	0.09	33.77	0.30
P05-9	14.28	0.16	14.98	0.17	34.06	0.43

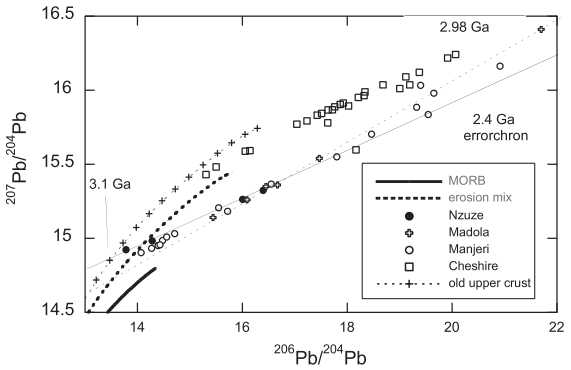

Fig. 7. Pb isotope diagram showing present-day isotope ratios of Nsuze carbonates (this study), Madola Formation (Mozaan Group) BIFs from Walraven and Pape (1994) and stromatolitic carbonates from the 2.7 Ga Manjeri and 2.6 Ga Cheshire formations of the Belingwe Greenstone Belt (Bolhar et al., 2002). Four Nsuze carbonates form a linear array corresponding to a regression date of 2.4 ± 0.2 Ga, whilst Mozaan BIFs form a regression line corresponding to an age of 2.89 Ga. Evolution curves for MORB source mantle, "old upper crust", and "erosion mix" of Kramers and Tolstikhin (1997) are shown for comparison. The latter two model compositions serve as approximations to the isotopic composition of Archaean continental crust. Isotopically, the Nsuze carbonates are similar to the Manjeri stromatolites, which were deposited in an ensialic basin with restricted access to the open ocean (Bolhar et al., 2002). The least radiogenic data point of the Nsuze carbonates plots close to the "old upper crust" at 3.1 Ga, suggesting that the lead was derived from continental crust that was ca. 100 myr old at the time of deposition of the Nsuze dolomites.

5. DISCUSSION

5.1. Crustal contamination and diagenesis of stromatolitic carbonates and ironstones

A range of processes may affect the primary distribution of rare earth elements in ancient carbonate rocks and BIFs, including syn-depositional clastic contamination, post-depositional diagenesis, metamorphism, hydrothermal alteration, and weathering. In the case of clastic contamination, (partial) dissolution of non-carbonate components during sample preparation may alter the primary aquatic signature of marine carbonates. Detrital material (including clay minerals, volcanic ash, oxides, sulphides) is variably enriched in REE+Y, by up to two orders of magnitude, when compared to REE+Y levels typically found in BIFs and carbonate rocks. This applies, in particular, to elements that are immobile in aqueous solutions (e.g., Th, Zr, Hf). Hence, high concentrations in marine sedimentary rocks may result from acid digestion of detritus during sample preparation rather than precipitation from solution at the time of formation. Possible detrital contamination is illustrated by the negatively correlated array in a diagram of Ce/Ce^* vs. Y/Ho for marine sedimentary rocks from various Precambrian and modern settings (see below, Fig. 8). Both ratios are sensitive to the presence of a primary seawater-derived component and terrigenous input. Ce/Ce^* ratios are calculated through extrapolation between neighbouring REE La and Pr (see Bolhar et al., 2004). Since Ce is not expected, and has not been reported, to be anomalous in Archaean chemical sediments due to low atmospheric oxygen levels (e.g., Kamber et al., 2014), an apparent Ce anomaly (i.e. $Ce/Ce^* < 1$) would, in fact, reflect anomalous concentrations of La in shale-normalised REE diagrams (Bau and Dulski, 1996). With increasing detrital contamination, both ratios are shifted towards terrestrial values and away from marine values (Y/Ho = 45–75, $Ce/Ce^* < 1$). Given the absence of diagnostic elemental anomalies in Nsuze carbonates, contamination by material not representing a primary aqueous precipitate and partial dissolution of silicates/oxides/sulphides during sample preparation requires critical assessment. Several approaches were taken to minimise such effects: (i) material was avoided that was associated with visible clastic detritus, (ii) only unweathered and pure carbonate was handpicked, and (iii) secondary cement (if visible) was avoided. However, the carbonates contain abundant carbonate-replaced particles, some of which may represent volcaniclastic material (ash and lapilli). In addition, very fine-grained siliciclastic detritus is likely present and silicification widespread, thus complicating matters further.

In view of this, a series of geochemical screening methods was applied to critically evaluate partial dissolution of, and contamination by, detrital material during acid treatment: (i) In diagrams of La/La^* vs REE (Fig. 9A) and Y/Ho vs. REE (not shown) both seawater-sensitive element ratios are expected to decrease as contamination increases (monitored by elevated REE). The lack of anti-correlation for carbonates, thus, suggests that dissolution of silicates and other non-carbonate phases was negligible. Hence, contamination by, and dissolution of, detritus appears unlikely. In contrast, shales have considerably higher REE contents and noticeably lower ratios of La/La^* (Fig. 5B), signifying their siliciclastic sedimentary nature. (ii) In addition to treatment by 2% HNO_3, three carbonates (PO5-2, PO5-3, PO5-4) were also subjected to selective digestion using 1 M acetic acid. Subparallel normalised REE patterns for both sets of carbonate analysis argue against contamination by detrital material

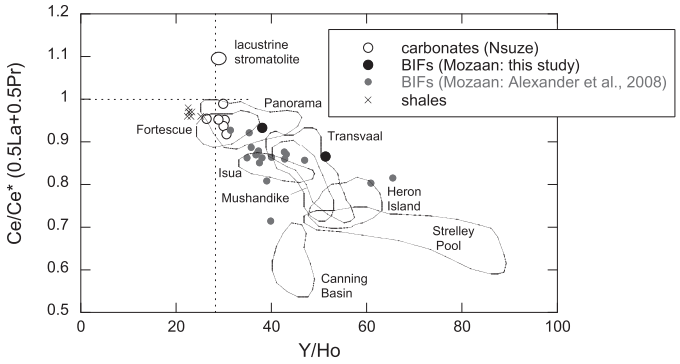

Fig. 8. Binary plot of Ce/Ce* vs. Y/Ho comparing Nsuze carbonates and Mozaan BIFs with other sedimentary rocks with an inferred marine origin (same data sources as for Fig. 10; additional data for Devonian microbialites from the Canning Basin: Nothdurft et al., 2004). The Nsuze dolomites plot within the compositional field defined by BIFs from the Panorama Formation (deposited in an inferred volcanic caldera setting) and stromatolites from the Fortescue Group (lacustrine or lagoonal). La anomalies are expressed as an apparent negative Ce anomaly (Bau and Dulski, 1996). The lack of overlap between Nsuze carbonates and other carbonates with an open-marine origin is consistent with the deposition of the former in a restricted, epicontinental basin. In contrast, Mozaan BIFs have compositions consistent with deposition in an outer-shelf environment. The lacustrine stromatolite represents the composition of a modern (Eocene) anoxic lake deposit from the Green River Formation (Bolhar and Van Kranendonk, 2007).

(Fig. 9B). Concentrations obtained by acetic acid digestion are generally lower reflecting lower degrees of partial dissolution. (v) Finally, mixing calculations were used in an attempt to reproduce REE patterns for Pongola carbonates by adding small amounts of a detrital material approximated by an average Pongola shale composition (Fig. 5C). The results are displayed in Fig 9C. Small amounts of shale (0.1–0.2%) admixed to ironstone PO5-7 (assumed to be a primary seawater precipitate with minimal detrital components) results in shale-normalised REE patterns with overall unfractionated LREE and HREE relative to MREE. Such patterns contrast with those for Pongola carbonates, which display distinct MREE enrichment, relative to LREE and HREE. Therefore, shale contamination cannot reproduce carbonate REE patterns. Considering all above observations, it is concluded that REE patterns of carbonates are not experimental artefacts.

Diagenetic modification of primary REE+Y also requires consideration, especially given that the carbonates are dolomites, SiO_2 content is as high as 50 wt% and recrystallization affected these rocks (Table 1). Dolomite and microquartz are most likely secondary phases that formed during interaction with diagenetic fluids. Banner et al. (1988) investigated the diagenetic effects on REE mobility in ancient limestones, with a focus on cathodoluminescence behaviour, isotopic ratios, and Fe, Ca and REE contents of Mississippian carbonates. Primary Nd isotope and REE compositions in these marine dolostones appear unchanged, despite extensive diagenetic dolomitization. Furthermore, the robustness of REE is supported by experimental studies demonstrating that REE substitute for Ca^{2+} in the carbonate lattice (e.g., Terakado and Masuda, 1988; Zhong and Mucci, 1995). Geochemically inert behaviour of REE during diagenesis was also observed by Parekh et al. (1977). In the present study, the dolomites of the Nsuze Group display coherent REE+Y patterns despite variable secondary overprints. Mozaan BIFs have parallel trace element patterns (albeit only two samples), consistent with preservation of primary compositions, despite evidence for alteration in the form of quartz and Mn-oxide veining. Diagenetic or other post-depositional effects would have had the strongest effect on the redox-sensitive elements Eu and Ce. Trivalent Eu can be reduced to Eu(II), whilst trivalent Ce can be oxidised to Ce(IV) (Brookins, 1988, 1989), both changes in valency being accompanied by changes in the ionic radii rendering Eu and Ce particularly susceptible to mobilisation in the presence of fluids. In diagrams of Ce and Eu versus neighbouring REE (Fig. 9D and E), any deviation from a linear trend would indicate anomalous behaviour of Eu and Ce. Both redox-sensitive elements define linear trends with a zero intercepts, corresponding to ratios of $La/Ce = 0.5–0.6$ and $Eu/Gd \sim 0.3$, indistinguishable from typical continental crustal values (shales: $La/Ce \sim 0.5$ and $Eu/Gd \sim 0.3$). Finally, the presence and potential dissolution of oxides and sulphides is tested by comparing elements that are preferably incorporated into these phases, namely Ni (a siderophile element enriched in oxides and sulphides) and Pb (a chalcophile element enriched in sulphides) against the seawater signal (Y/Ho). Neither Ni nor Pb are negatively correlated with Y/Ho as would be expected in the case of contamination by, and dissolution of, oxides and sulphides (Fig. 9F). Also, REE patterns are relatively uniform in all studied dolomites, despite variable Pb and Ni contents (~0 to 50 ppm).

In summary, Nsuze dolomitic carbonates and Mozaan BIFs appear to have preserved primary chemical signatures, displaying negligible effects from detrital contamination and associated leaching during sample preparation, diagenesis and metamorphism/weathering. Therefore, REE characteristics are considered reliable proxies for palaeoenvironmental chemistry.

5.2. Comparison of Nsuze carbonates with marine sedimentary rocks

REE+Y compositions of ancient marine carbonates provide a record of the ambient waters from which they

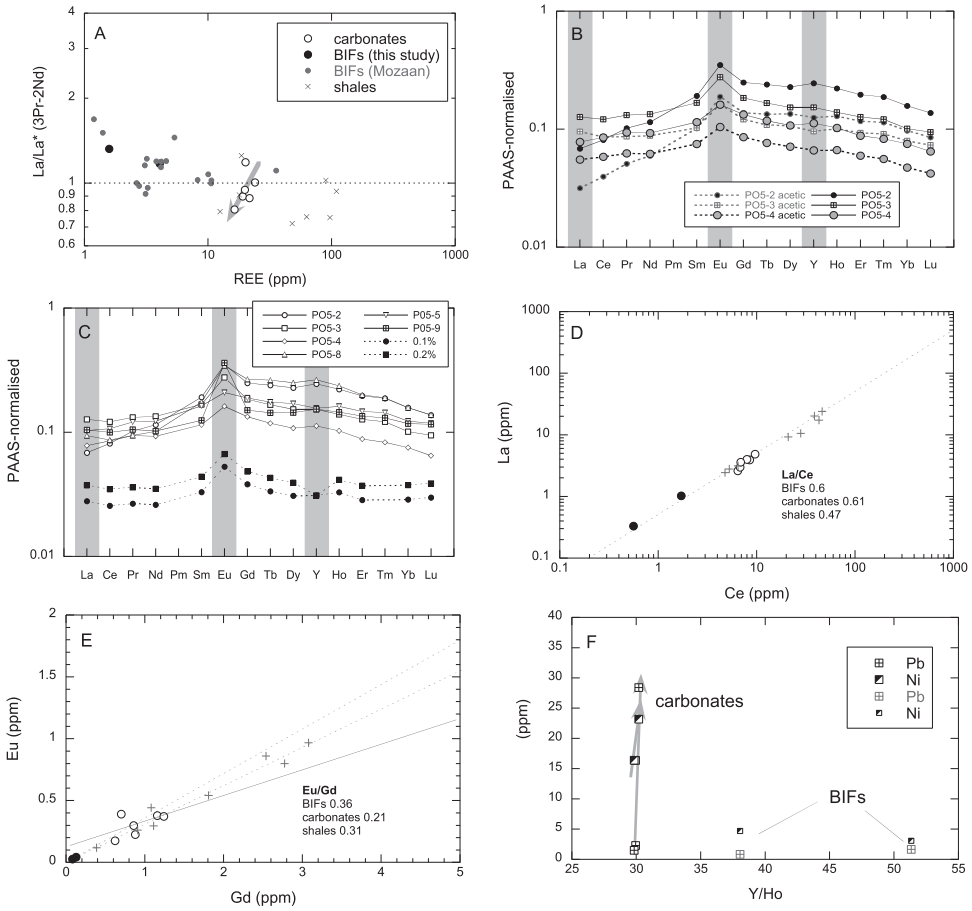

Fig. 9. Binary and normalised plots displaying Nsuze and Mozaan sedimentary rocks. (A) A positive correlation between La/La* and REE (in carbonates) is inconsistent with contamination by siliciclastic detritus. (B) Results from acid digestion using diluted nitric and acetic acid; REE patterns for carbonate samples PO5-2, PO5-3, PO5-4 are subparallel, but at different concentrations. The similarity in patterns argues against dissolution of detrital material. (C) Mixing calculations (PO5-7: uncontaminated end-member, average Pongola shale: contaminant, percentage numbers: detrital input) demonstrate that shale contamination cannot reproduce shale normalised REE patterns of Pongola carbonates. (D and E) Regression lines with near-zero intercepts document that the redox-sensitive elements Eu and Ce were not fractionated from neighbouring REE, suggesting that secondary effects (diagenesis, metamorphism, weathering) were minimal. (F) Ni and Pb data for carbonates and BIFs: effects arising from dissolution of oxides and sulphides appear unlikely because diagnostic elements are not systematically related to seawater sensitive elemental systematics.

precipitated (Webb and Kamber, 2000; Bolhar et al., 2002, 2005a,b; Kamber et al., 2004; Bolhar and Van Kranendonk, 2007). Precambrian carbonate rocks appear remarkably similar to modern seawater in displaying diagnostic geochemical features, such as positive La, Gd and Y anomalies and enrichment of the heavy REE when normalised to shale.

This characteristic signature appears to be developed in carbonates with depositional ages ranging from the early Archaean (Strelley Pool) to the Holocene (Heron Island), as illustrated in Fig. 10A. All average compositions for carbonate rocks are characterised by enriched La, Y, and Eu (in Precambrian rocks). The average composition of Mushandike stromatolites is unusual in having enriched LREE relative to the MREE and HREE when normalised to shale, a feature related to deposition in a confined basin, where water chemistry was strongly influenced by local tonalitic gneisses (Kamber et al., 2004). In contrast to other marine carbonates, e.g. the 2.5 Ga Campbellrand and 3.45 Ga Strelley Pool Formation carbonates, the average Pongola carbonate is characterised by weaker elemental anomalies, except for Eu which is noticeably enriched. Yttrium is also only weakly enriched and La enrichment is very subtle (when projected along the Ce, Pr, Nd join). Another difference in REE+Y patterns between Pongola and other bona-fide seawater-derived carbonates is the convex-upward, normalised REE+Y pattern, translating into MREE-enrichment in the former. MREE enrichment is observed in the colloidal fraction of modern rivers, such as the Hudson and Connecticut (e.g., Sholkovitz, 1994). Considering an epicontinental, fluvial to near-shore shallow-marine depositional environment inferred for many Nsuze and Mozaan sedimentary rocks (e.g., Beukes and Cairncross, 1991; Hicks and Hofmann, 2012), it appears likely that estuarine-type mixing and fractionation by Fe-oxyhydroxides was responsible for relative MREE

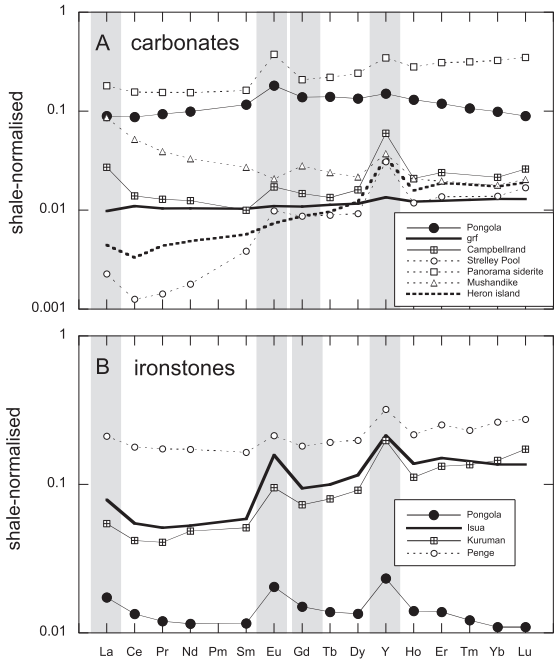

Fig. 10. PAAS-normalised REE+Y patterns: (A) Averaged compositions for the ~3.0 Ga Pongola carbonates (this study), 2.52 Ga Campbellrand Subgroup stromatolites (Kamber and Webb, 2001), 3.45 Ga Strelley Pool Chert stromatolites (Van Kranendonk et al., 2003), 3.45 Ga Panorama Formation siderites (Bolhar et al., 2005b), 2.82 Ga Mushandike Formation stromatolites (Kamber et al., 2004), Holocene reefal microbialites (Heron Island: Webb and Kamber, 2000), and one lacustrine stromatolite from the Green River Formation (grf: Bolhar and Van Kranendonk, 2007). (B) Averaged compositions for the Mozaan jaspilitic BIFs (this study), 3.7 Ga BIFs from the Isua Greenstone Belt (Bolhar et al., 2004) and BIFs from the 2.45 to 2.5 Ga Kuruman and Penge formations (Transvaal: Bau and Dulski, 1996). Note anomalous shale-normalised concentrations for La, Eu, Gd and Y.

enrichment in Pongola carbonates. Alternatively, due to microbial activity during carbonate precipitation, organic complexation may have controlled REE+Y speciation, leading to MREE enrichment as is observed in some modern freshwater and estuarine settings (Elderfield et al., 1990; Alexander et al., 2008). The Eocene lacustrine stromatolite from the Green River Formation is distinctly different when compared to marine precipitates in showing a complete lack of any elemental anomaly and almost flat REE+Y pattern (Fig. 10A, "grf"), suggesting that aquatic processes are distinctly different between lacustrine and marine environments.

Compositionally, Mozaan BIFs are different to Nsuze carbonates in having distinct positive La, Y anomalies, and concave upward patterns across the LREE (Fig. 5A and B). A similar REE+Y pattern is displayed by the average composition of Penge Formation BIFs (albeit at higher concentrations), whereas BIFs from Isua and the Kuruman Formation are more enriched in HREE and MREE relative to the LREE, with similar La and Y anomalies. Eu is enriched relative to neighbouring REE in all BIFs, signifying the input from hydrothermal sources into Precambrian oceans (Derry and Jacobsen, 1990; Danielson et al., 1992; Bau and Möller, 1993; Kamber and Webb, 2001; Bolhar et al., 2004; Klein, 2005). The contribution from high-temperature (>250 °C) hydrothermal sources, such as black smokers, to Mozaan BIFs was estimated by Alexander et al. (2008) at <0.1% and 1–5%, depending on trace element ratios used in mass balance calculations. Most compiled BIF and carbonate averages also show subtle relative enrichments in Gd (extrapolated from Tb and Dy) and Er (extrapolated from Tm and Ho). Nsuze carbonates are an exception, as they lack these anomalies.

In Fig. 8, Ce/Ce^* and Y/Ho ratios of Nsuze carbonates and Mozaan BIFs are compared to those of other documented marine precipitates. None of the carbonates plots within the fields defined by ancient and modern carbonates formed from open-marine seawater, such as those from the Devonian Canning Basin, the 3.45 Ga Strelley Pool, and the Holocene reefal microbialites from Heron Island. The latter are characterised by $Y/Ho > 40$ and $Ce/Ce^* < 0.8$, in contrast to carbonates from the Nsuze Group with $Y/Ho < 30$ and $Ce/Ce^* = 0.9–1.0$. Compositionally, the studied carbonate samples are similar to Archaean stromatolites from the Fortescue Group with a postulated lacustrine or shallow lagoonal origin (Bolhar and Van Kranendonk, 2007) and Fe-rich carbonates from the Panorama Formation, interpreted to have formed in a confined ocean basin (possibly a volcanic caldera setting) with intermittent connection to the open ocean (Bolhar et al., 2005b). Hence, geochemical evidence suggests deposition of the Nsuze carbonates in an environment with a restricted exchange with the open ocean. In contrast, Mozaan BIFs have Ce/Ce^* and Y/Ho ratios similar to those observed for BIFs from the Penge and Kuruman Formations of the Transvaal Supergroup (Bau and Dulski, 1996), suggesting similar conditions for their formation. According to Alexander et al. (2008), Mozaan BIFs were deposited in a sediment-starved continental shelf environment with some hydrothermal input and strong contribution from exposed weathered continental crust. On the basis of REE systematics, Delvigne et al. (2012) argued for the presence of a minor (ca. 10%) freshwater component in the depositional basin of the Mozaan BIF.

5.3. Geochemical variability of stromatolitic carbonates and ironstones

Temporal changes of ambient water chemistry across the Nsuze–Mozaan unconformity are reflected in diagnostic trace element ratios against relative stratigraphic position (Fig. 11). Nsuze carbonates are compositionally distinct from Mozaan BIFs in having lower La/La^* and Y/Ho ratios indicative of less influence from the open ocean. The carbonates seem to follow a trend from weaker towards stronger La/La^* anomalies and lower towards higher Y/Ho ratios. This trend projects towards the La/La^* values of Mozaan BIFs, although the transition appears more abrupt for Y/Ho. This change in REE composition between carbonates and BIFs is suggestive of

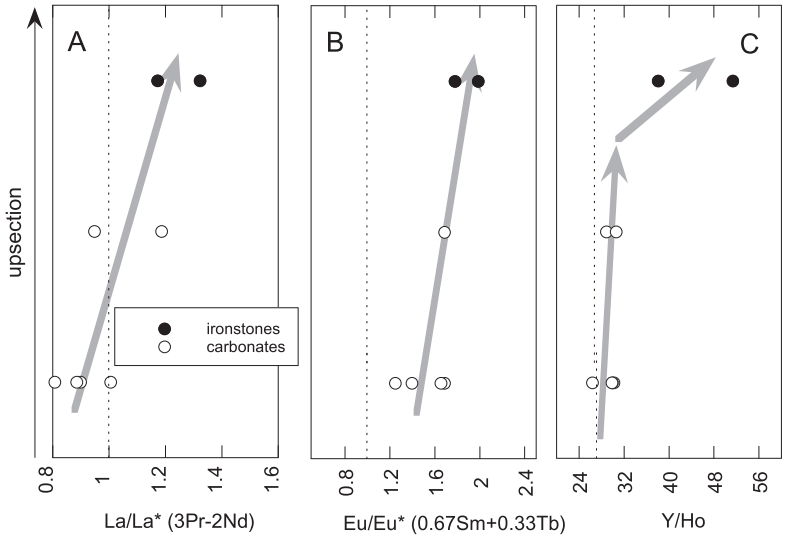

Fig. 11. Trace element ratios (La/La*: A; Eu/Eu*: B, Y/Ho: C) vs. relative stratigraphic height. Nsuze carbonates and Mozaan BIFs define a general trend from crustal to marine compositional signatures. All sedimentary rocks have elevated shale-normalised Eu abundances (A), suggesting the presence of a hydrothermal component. Broken line represents trace element ratios typically found in crustal rocks. Note that a major unconformity separates Nsuze and Mozaan groups.

a shift in water chemistry at the time of deposition, with implications for the regional geology. Most plausibly, an increase in the open marine signal may hint at a change in the extent of exchange between the depositional basin and an open ocean.

Like other documented Archaean microbialites and BIFs from southern Africa (e.g., 2.82 Ga Mushandike carbonates: Kamber et al., 2004), Pongola carbonates lack significant negative Ce anomalies ($[Ce/(2Pr - Nd)]shale = 0.89–1.00$). This is in contrast to modern seawater, where Ce is depleted relative to other REE due to particle scavenging by Fe–Mn-oxyhydroxides under oxidative conditions. The absence of anomalous Ce abundances in the studied samples is consistent with precipitation from water that was reducing with respect to the C^{4+}/Ce^{3+} couple. Inferred suboxic conditions are in line with positive shale-normalised Eu abundances in Nsuze carbonates and Mozaan BIFs: on the modern ocean floor, hydrothermal fluids with strongly enriched Eu abundances are emanated from vents, immediately followed by mixing with ambient seawater and co-precipitation of REE with Fe and Mn (e.g., Mitra et al., 1994). In the Archaean, on the other hand, dissolved Fe(II) was not precipitated as oxyhydroxide in deep waters, and therefore REE+Y, including Eu, would not have been removed from the water column as efficiently as in the modern oceans (e.g., Derry and Jacobsen, 1990; Kamber and Webb, 2001). This is evident in positive Eu anomalies for Archaean seawater precipitates (Fig. 10), in particular banded iron formations (Fryer, 1977). Hence, the presence of positive Eu anomalies in the studied dolomites and BIFs reflects contribution from hydrothermal activity in the open ocean. Kamber and Webb (2001) used covariations between Eu/Eu*, Ce/Ce* and Sm/Yb_{shale} to argue that Campbellrand stromatolites were precipitated in an environment with strongly variable aquatic REE+Y. More specifically, these authors observed that REE+Y signatures were correlated with bathymetry, with more pronounced Y/Ho and La/La* ratios reflecting water at greater depths.

In contrast, the carbonates in this study have Eu/Eu* ratios that are not correlated with La/La* or other geochemical indicators (Fig. 11). Enriched Eu was therefore not caused by continental run-off into the depositional basin or diagenesis/leaching of sediments (Holland, 1984), both scenarios likely to suppress marine signatures. We note that Nsuze carbonates show enrichment in Mn and Fe, either reflecting higher hydrothermal inputs (Veizer et al., 1990) or generally larger quantities of dissolved Fe and Mn in Archaean marine environments. In any case, elevated Mn concentrations require oxidation of Mn (II) to convert into insoluble Mn(IV), suggesting availability of some oxygen in the marine depositional environment. Planavsky et al. (2014) argued that oxygenic photosynthesis had already started accumulating significant levels of oxygen at the time of deposition of Mozaan BIF. An absence of negative Ce anomalies accompanied by fractionated Mo isotopes as a result of Mo sorption onto Mn-oxyhydroxides may, therefore, imply different levels of sensitivity of redox indicators to the presence of free dissolved O_2. In view of the missing co-variation between trace element ratios indicative of shallow vs deep water settings (i.e. Y/Ho, Ce/Ce* vs. Sm/Yb: Kamber and Webb, 2001) and enriched Mn and Fe, we argue that REE+Y variability was not controlled by bathymetry but rather reflects a temporal shift in the input from the open ocean into a more restricted Pongola Basin. Mozaan BIFs overlying Nsuze carbonates display a stronger open marine signature and, hence, signal a more pronounced exchange with the open ocean, consistent with an advanced opening of the Pongola basin. Alexander et al. (2008) have previously

argued that fluctuations in sea level were registered as systematic variations in REE for BIFs during deposition of the Mozaan Group. Stromatolites of the 2.52 Ga Campbellrand Formation were deposited in an estuarine environment (Kamber and Webb, 2001). In comparison, the Nsuze carbonates are depleted more strongly in LREE but less enriched in HREE. This contrast in REE+Y between both carbonate occurrences cannot be simply explained by variations in the degrees of particle scavenging (mainly via coagulation of colloids in response to salinity changes: e.g., Goldstein and Jacobsen, 1988; Elderfield et al., 1990). Specifically, if particle scavenging had a more profound effect on Nsuze carbonates than Campbellrand stromatolites, the former would be expected to have more strongly enriched HREE in comparison with the latter (Figs. 5 and 10). Hence, REE+Y in Nsuze carbonates reflect the interplay of hydrothermal venting in the deep ocean, exchange between open-ocean and restricted basin and particle scavenging, the latter probably a function of the salinity (estuarine mixing) and the degree of oxygenation (microbial activity). Given the restricted nature of the Pongola basin during deposition of Nsuze carbonates, it appears that local catchment played also a role. If local catchment was dominated by TTG-like continental crust (as in the case of the 2.82 Ga Mushandike stromatolites: Kamber et al., 2004), normalisation with a TTG-like composition (i.e. strongly depleted in HREE) would rotate the REE+Y pattern of Pongola hydrogenous sedimentary rocks, such that HREE would be more enriched and LREE more depleted. In view of the volumetric preponderance of TTG material in the Kaapvaal craton, this possibility deserves consideration, although remains largely speculative due to the lack of knowledge of the catchment that provided REE+Y via riverine transport. In any case, differences in REE+Y between studied samples and Campbellrand stromatolites suggest that depositional environments for both occurrences were different. If REE+Y systematics in Campbellrand stromatolites are indeed consistent with deposition in a setting transitional between open-marine and estuarine, i.e. shallow-water continental shelf, it follows that Nsuze carbonates were not formed in such an environment. We conclude that the latter were deposited in an epicontinental basin, with restricted but variable exchange with the open ocean.

5.4. Shales: mineral sorting, alteration and metamorphism

Secondary effects can obscure provenance signatures of clastic sediments and require assessment (e.g., Taylor and McLennan, 1985). Zircon accumulation would lead to elevated contents of Zr, Hf, Th, U, Y and HREE. A lack of correlation between Zr + Hf, Th + U and $Sm/Lu_{chond.}$ rules out fractionation of shale REE by zircon. A significant co-variation between K_2O and Al_2O_3 is indicative of detrital phyllosilicates and their metamorphic products, demonstrating that they control to a large degree REE systematics of shales. Dilution of REE by quartz appears minimal, as REE pattern and abundances do not vary systematically with SiO_2 content. Contribution from phosphate minerals (monazite, apatite) is likewise minimal, as no co-variation exists between P_2O_5 and Ce, total REE and Th. Ti-rich minerals (titanite, rutile) can affect shale compositions, and a correlation between diagnostic elements (TiO_2–Nb, $R^2 = 0.95$) is indeed observed. However, REE patterns for samples with the highest and lowest TiO_2 contents are sub-parallel and show no evidence of Ti-rich mineral fractionation. Finally, garnet accumulation can cause elevated HREE, which is not observed in PAAS-normalised REE patterns of Pongola shales.

Only alkali and alkaline earth elements and LILE are generally expected to experience mobilisation during diagenesis and metamorphism, whereas REE, HFSE, and some major oxides (TiO_2, Al_2O_3) are considered to be least susceptible to secondary redistribution. The generally low metamorphic grade of Pongola shales from the study area (lower greenschist facies) renders metamorphic effects on primary REE and other immobile trace elements unlikely. This notion is supported by uniform Zr/Hf and Nb/Ta ratios and coherent REE patterns, despite highly variable LOI contents (5–28 wt%), which corresponds to variable degrees of hydration and also the presence of carbonates.

5.5. Source weathering

In addition to diagenesis/alteration/metamorphism and sedimentary sorting, continental in-situ weathering or weathering during sedimentary transport can have a profound influence on the composition of detrital material. Cations with small ionic radii (Na, Ca, Sr) are particularly prone to leaching, whilst Al_2O_3 remains immobile due to incorporation into residual clays. Weathering is conventionally quantified by weathering indices (Chemical Index of Alteration, CIA: Nesbit and Young, 1989; Chemical Index of Weathering, CIW: Harnois, 1988). In this study, preference is given to CIW since only loss of Na and Ca relative to Al is considered, but not K which may be affected by processes other than weathering (Nesbitt and Young, 1989; Fedo et al., 1995). No correction of carbonate-hosted CaO was necessary due to very low values of CaO (<1 wt%). In any case, correction would have further increased already high CIW values. Pongola shales have a range in CIW values from 88 to 98 (average 94, $n = 7$; Table 2), comparable to that of shales from the Cheshire Formation of the Belingwe Greenstone Belt (CIW: 54–99, av. 88, $n = 12$; Hofmann et al., 2003), with the exception of the Fe/Mn/Mg-rich shale (TSB07/26-168; CIW = 64). Such values are considerably higher than those of unweathered igneous rocks commonly present in Archaean terrains (mafic volcanics: ~40, felsic volcanics: ~60, TTG: ~55, granites: ~65: Gao and Wedepohl, 1995), and indicative of high modal abundances of mica, chlorite and clays (CIW: 80–100). High degrees of weathering are consistent with the elevated Al_2O_3 (10–35 wt%) and low to very low Sr (2–44 ppm) contents of the shales when compared to shale averages (Al_2O_3: 15–19 wt%; Sr; 60–300 ppm; see Bolhar et al., 2005a for a compilation). Intense weathering is related to climate, extent and rate of sedimentary transport (including recycling), and erosion, the latter controlled by relief and vegetation. Long transport distances and several cycles of erosion and transport appear unlikely as the

major cause for high Al/(Na + Ca) ratios since no co-variation is observed with SiO_2 content (not shown). Likewise, elevated CIW due to a predominantly felsic provenance can be ruled out, as CIW do not vary as a function of $MgO + Fe_2O_3$ content, and input from mafic/ultramafic sources is indicated by elevated Cr and Ni contents (see below). It therefore appears that CIW values >88 record pronounced in-situ weathering during Pongola sedimentation, probably due to elevated atmospheric temperatures and CO_2 contents (e.g., Des Marais, 1994). K_2O contents in some shales are considerably higher than values observed for average shale compositions (PAAS: 3.7 wt%, cratonic shale: 3.1 wt%; Taylor and McLennan, 1985; Condie, 1993). This may indicate variable degrees of post-depositional K-metasomatism, an effect commonly observed in Archaean shales (e.g., Hofmann et al., 2003; Hofmann, 2005; Bolhar et al., 2005).

5.6. Shale provenance

In a chondrite-normalised diagram (Fig. 6A), average Mandeva Formation shale is compared to representative averaged compositions of igneous lithologies typically preserved in Archaean granite-greenstone terrains (Condie, 1993). The REE patterns for all but one specimen (shale 26–168) are subparallel, devoid of pronounced Eu anomalies, and characterised by relatively enriched LREE and unfractionated HREE. The REE pattern of average Mandeva Formation shale is remarkably similar to average Archaean granite, except for the missing Eu anomaly in the former (Fig. 6A). LREE enrichment requires input from evolved igneous sources, although the lack of depleted HREE in shales suggests no or only minor contribution from TTGs. Elevated concentrations of Fe, Mg, Cr and Ni in shales necessitate input from mafic and/or ultramafic sources. A diagram of Ti/Zr vs Ni (Fig. 6B) was employed by Bolhar et al. (2005a) to distinguish between a sedimentary and a metasomatic origin of high-grade garnet–biotite–plagioclase schists from the 3.8 to 3.7 Ga Isua Greenstone Belt. Ti/Zr–Ni also enables effective discrimination between highly evolved felsic and primitive mafic/ultramafic igneous protoliths. Shales from the Belingwe Greenstone Belt show affinity with basaltic sources (Hofmann et al., 2003) and shales of the Witwatersrand Basin are shifted noticeably towards a komatiitic source. Shales from the Buhwa Greenstone Belt show some overlap with Pongola shales from this study. The eight shale samples reported here plot within the compositional field defined by the larger dataset for Pongola shales of Wronkiewicz and Condie (1989), the latter data having a more comprehensive geographic and stratigraphic coverage. Based on Ti/Zr vs Ni relationships, quantification of input from felsic and mafic-to-ultramafic source is non-unique. Even when combined with REE constraints, the provenance of Pongola shales can be plausibly modelled by admixing any of the representative source lithologies. Wronkiewicz and Condie (1989) derived mixing relationships involving tonalitic, granitic, komatiitic and basaltic sources, with granite and basalt contributing approximately 70–95% in equal proportions, and tonalite and komatiite contributing 10–30 and <5%, respectively.

An interesting observation concerns the lack of negative Eu anomalies in chondrite-normalised REE patterns (Fig. 6A) for Pongola shales (positive Eu anomalies when PAAS-normalised: Fig 5B). This enrichment of Eu relative to average crust may reflect a secondary process involving either redox-related mobilisation of Eu or co-precipitation of REE and Fe–Mn-oxyhydroxides during deposition. In the later case, enriched Eu would reflect addition of a seawater-derived component. A genetic link between Fe-REE co-precipitation and relative Eu enrichment has been established for meta-shales from the Isua Greenstone Belt (Bolhar et al., 2005a), and a similar process has also been proposed by Watchorn (1980) and Wronkiewicz and Condie (1989) in their study of Mozaan and Nsuze shales.

5.7. Pb and Sr isotopic constraints on provenance

The timing of deposition of the Nsuze carbonates is bracketed by U–Pb crystallisation ages of 2980 ± 10 Ma and 2968 ± 6 Ma for lavas near the base and top of the Nsuze Group (Mukasa et al., 2013). An upper age limit for deposition of the Mozaan BIF is also provided by the intrusion of a quartz porphyry sill at 2837 ± 5 Ma (Gutzmer et al., 1999). Hence, the linear regression date of 2400 ± 200 Ma obtained in this study for Nsuze carbonates cannot represent the timing of deposition. Our preferred interpretation of the 2.4 ± 0.2 Ga errorchron is in terms of a widespread tectono-metamorphic or hydrothermal event that overprinted the Pongola Supergroup. Regional greenschist-grade metamorphism of Pongola Supergroup rocks in the White Umfolozi area took place at 2.61 ± 0.07 Ga (Rb–Sr on biotite; Elworthy et al., 2000). A whole rock Rb-Sr age of 2.35 ± 0.04 Ga from Nsuze volcanic rocks from the White Umfolozi area was interpreted as an event that caused isotopic resetting (Hegner et al., 1981). Both age estimates agree within errors with our 2.4 Ga whole rock Pb–Pb regression date. A possible tectono-thermal event in the eastern Kaapvaal Craton around 2.2–2.6 Ga is further indicated by Ar–Ar dates for cherts of the Barberton greenstone belt (Kramers et al., 2013). As the ages overlap with deposition of the Transvaal Supergroup, this event may be related to folding, faulting and basin inversion after carbonates and iron formations of the Malmani-Campbellrand subgroups were deposited, and before the onset of deposition of the Duitschland Formation and Pretoria Group (Bekker et al., 2001).

In Fig. 7, Pongola carbonates are compared to other marine carbonates from the Kaapvaal and Zimbabwe cratons, including the Manjeri and Cheshire Formations of the Belingwe Greenstone Belt. Isotopically, the Nsuze carbonates are similar to ironstones of the overlying Madola Member (stratigraphically equivalent to the Sinqeni/Mandeva Formation; Walraven and Pape, 1994), although linear regression yields slightly differing slopes, translating into a ca. 130 Ma age difference. In the range of $^{206}Pb/^{204}Pb = 15.5–17.5$, the Pongola carbonates are also indistinguishable from stromatolitic carbonates of the

2.7 Ga Manjeri Formation. The latter inherited a strong continental signature as evidenced by unradiogenic Nd isotopic compositions ($\varepsilon_{Nd} = -4$) and Nd model ages of ~3.3 Ga (Bolhar et al., 2002). Pb isotopic data for carbonates from the Manjeri and Cheshire Formations plot distinctly above the upper mantle evolution curve of Kramers and Tolstikhin (1997). Likewise, data for Pongola carbonates plot above the mantle curve, with the linear array intersecting the Pb evolution curve for "old upper crust" (Kramers and Tolstikhin, 1997) at ~3.1 Ga, suggesting derivation from an ancient, continental source. It therefore appears that Pb was not derived from open marine water with a MORB mantle signature. Instead, Pb isotopic data point to deposition in a restricted basin with strong continental influence. Pb isotope model calculations provide additional constraints: Fig. 12 summarises the results of two-stage modelling in a diagram of timing of melt extraction T (in Ma) from mantle versus μ_1 value ($^{238}U/^{204}Pb$ of a hypothetical igneous rock prior to formation of the sediment). In this model, the protolith forms via partial melting at time T from the upper mantle approximated by the MORB array. Upon extraction the melt starts to evolve isotopically with a Pb isotopic composition that was inherited from the mantle source. Finally, the source forms the sediment at 2.98 Ga, followed by subsequent metamorphism at ca. 2.6–2.4 Ga. Since reliable present-day μ-values for the carbonates cannot be obtained (U is known to be remobilised during diagenesis: Jahn and Cuvellier, 1994) the effects of metamorphism onto the Pb isotopic history cannot be fully considered. Calculations for both Nsuze carbonates and Mozaan ironstones yield values for T (4.2–3.0 Ga) that correspond to a large range in μ-values (10–40, 10–100, respectively). Assuming typical μ-values for upper continental crust in the Archaean (~14: Kramers and Tolstikhin, 1997), model extraction ages of >3.2 Ga (Nsuze) and >3.6 Ga (Madola) are estimated. Despite inherent limitations of this modelling approach, the Pb isotopic compositions clearly require a component from ancient material with elevated U/Pb (μ-value).

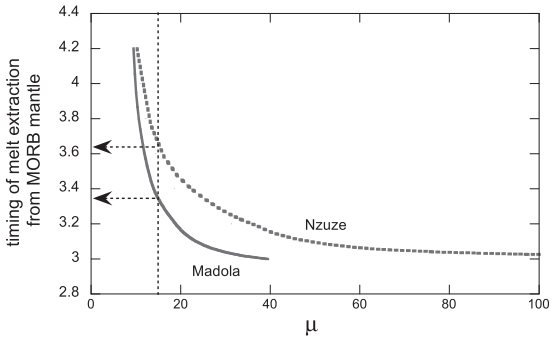

Fig. 12. Results of two-stage model calculations showing the relationship between μ ($^{238}U/^{204}Pb$ ratio in the crustal source) and timing of melt extraction from the mantle. Assuming that the precursor to the Nsuze carbonates had a $^{238}U/^{204}Pb$ ratio typical for Archaean continental crust ($\mu \sim 14$), the two-stage model returns melt extraction ages of 3.6–3.7 Ga (for Nsuze) and 3.3–3.4 Ga (for Mozaan).

A > 3.2 Ga old provenance is consistent with the geochronological framework of the Pongola Group and its basement (Hegner et al., 1994; Elworthy et al., 2000; Nhleko, 2003; Mukasa et al., 2013). Specifically, the source regions for Pongola sedimentary rocks exposed in the White Mfolozi Inlier were inferred to have existed to the west (Hicks and Hofmann, 2012), in the area currently occupied by the Nondweni granitoid-greenstone terrain, where ages up to 3.53 Ga have been reported (Xie et al., 2012).

Veizer et al. (1990) examined the effects of chemical alteration during diagenesis and metamorphism on trace element, stable (O, C) and radiogenic (Sr) isotope compositions of Pongola carbonates. Age-corrected Sr isotope ratios for the Nsuze Group from their study define two populations with values of ~0.715 and 0.730–0.750, which are considerably higher than the value for contemporaneous mantle (~0.701: using input parameters from Kamber and Webb, 2001). It appears therefore that both Pb and Sr isotope systematics consistently point to deposition in a restricted basin with sediments derived from mature crustal sources. The difference in (primary) Sr isotopic composition of the carbonates and coeval mantle allows estimation of the time since extraction from the mantle ("crustal residence time"). Selecting the least altered and most unradiogenic carbonates (Veizer et al., 1990; Eglington et al., 2003) and using a Rb/Sr ratio of 1.73 (average value for granitoids from the southeastern Kaapvaal Craton: Elworthy et al., 2000) calculated residence times range from 490 to 600 Ma. Considerably less radiogenic initial Sr isotope compositions for aragonitic Nsuze carbonates (Eglington et al., 2003) return source erosion ages of ~90–140 Ma. A model age of 3.4 Ga using shales from the Mozaan Group was also estimated by Alexander et al. (2008), lending additional support to our model calculation based on Sr and Pb isotope systematics. We concur with Alexander et al. (2008) that Pongola carbonates and BIFs derived REE, Sr and Pb from cratonic sources older than 3.1 Ga, and up to 3.6 Ga, implying that by 3.0 Ga a significant fraction of evolved continental crust was available for weathering and continental run-off via rivers into the intracratonic depositional basin.

6. CONCLUSIONS

REE+Y compositions of chemical sedimentary rocks provide a record of the ambient waters from which they precipitated. Ancient chemical sedimentary rocks are remarkably similar to modern seawater in displaying diagnostic geochemical features, such as positive La, Gd and Y anomalies and enrichment of the heavy REE, when normalised to shale. In addition, they typically show positive Eu anomalies that characterise Archaean seawater precipitates due to higher hydrothermal input and lower oceanic oxygen levels at the time of deposition.

Trace element systematics demonstrate that Pongola marine sedimentary rocks have preserved primary chemical signatures, displaying negligible effects from detrital contamination, diagenesis, and metamorphism. Unlike other Archaean marine carbonates, the average composition for

Pongola carbonates is characterised by weaker elemental anomalies, except for Eu, which is strongly enriched. In Nsuze carbonates, Y is only weakly enriched and La enrichment is also very subtle. Another difference in REE+Y patterns between Nsuze carbonates and other bona-fide seawater-derived carbonates is the general slope, which is convex-upward, translating into MREE-enrichment in the former. In contrast, the composition of Mozaan BIFs shows positive La, and Y anomalies, and slightly enriched MREE relative to LREE, similar to Palaeoproterozoic BIFs from the Transvaal Supergroup.

The geochemical evidence is suggestive of deposition of the Nsuze carbonates in an environment with a restricted exchange with the open ocean. In contrast, Mozaan BIFs formed in a more open setting, in line with general models of BIF formation, albeit with some evidence for freshwater addition. The increase in the "seawater signature" from the Nsuze to the Mozaan Group may hint at a change in the extent to which the Pongola depositional basin was connected to an open ocean.

The Pb–Pb whole-rock, linear regression date of 2.4 ± 0.2 Ga obtained for Nsuze carbonates is interpreted to reflect a widespread metamorphic or, less likely, fluid circulation event, in line with other documented geochronological evidence (Hegner et al., 1981; Elworthy et al., 2000; Kramers et al., 2013). The significance of this cryptic event is currently not known, but may point to tectonic processes along the eastern margin of the Kaapvaal Craton at that time.

ACKNOWLEDGEMENTS

RB acknowledges support through grants from the University of Queensland and the Australian Research Council. AH was supported by grants from the National Research Foundation of South Africa. The manuscript benefitted from discussions with Balz Kamber. Andrey Bekker and Michael Bau are thanked for detailed and constructive reviews, and Uwe Reimold is thanked for his editorial input.

REFERENCES

Alexander B. W., Bau M., Andersson P. and Dulski P. (2008) Continentally-derived solutes in shallow Archean seawater: rare earth element and Nd isotope evidence in iron formation from the 2.9 Ga Pongola Supergroup, South Africa. *Geochim. Cosmochim. Acta* **72**, 378–394.

Aries S., Valladon M., Polvé M. and Dupré B. (2000) A routine method for oxide and hydroxide interference corrections in ICP-MS chemical analysis of environmental and geological samples. *Geostand. Newslett.* **24**, 19–31.

Banner J. L., Hanson G. N. and Meyers W. J. (1988) Rare-earth element and Nd isotopic variations in regionally extensive dolomites from the Burlington-Keokuk Formation (Mississippian) – implications for the REE mobility during carbonate diagenesis. *J. Sediment. Petrol.* **58**, 415–432.

Bau M. (1996) Controls on the fractionation of isovalent trace elements in magmatic and aqueous systems: evidence from Y/Ho, Zr/Hf, and lanthanide tetrad effect. *Contrib. Miner. Petrol.* **123**, 323–333.

Bau M. and Möller P. (1993) Rare-earth element systematics of the chemically precipitated component in early Precambrian iron formations and the evolution of the terrestrial atmosphere-hydrosphere-lithosphere system. *Geochim. Cosmochim. Acta* **57**, 2239–2249.

Bau M. and Dulski P. (1996) Distribution of yttrium and rare-earth elements in the Penge and Kuruman iron formations, Transvaal Supergroup, South Africa. *Precambr. Res.* **79**, 37–55.

Bekker A., Kaufman A. J., Karhu J. A., Beukes N. J., Swart Q. D., Coetzee L. L. and Eriksson K. A. (2001) Chemostratigraphy of the Paleoproterozoic Duitschland Formation, South Africa: implications for coupled climate change and carbon cycling. *Am. J. Sci.* **301**, 261–285.

Bekker A., Holland H. D., Wang P. L., Rumble D., Stein H. J., Hannah J. L., Coetzee L. L. and Beukes N. J. (2004) Dating the rise of atmospheric oxygen. *Nature* **427**, 117–120.

Bekker A., Slack J. F., Planavsky N., Krapez B., Hofmann A., Konhauser K. O. and Rouxel O. J. (2010) Iron formation: the sedimentary product of a complex interplay among mantle, tectonic, oceanic, and biospheric processes. *Econ. Geol.* **105**, 467–508.

Beukes N. J. and Lowe D. R. (1989) Environmental control on diverse stromatolite morphologies in the 3000 Myr Pongola Supergroup, South Africa. *Sedimentology* **36**, 83–397.

Beukes N. J. and Cairncross B. (1991) A lithostratigraphic-sedimentological reference profile for the Late Archaean Mozaan Group, Pongola Sequence. application to sequence stratigraphy and correlation with the Witwatersrand Supergroup. *S. Afr. J. Geol.* **94**, 44–69.

Bolhar R., Hofmann A., Woodhead J. D., Hergt J. M. and Dirks P. (2002) Pb- and Nd isotope systematics of stromatolitic limestones from the 2.7 Ga Ngezi Group of the Belingwe Greenstone Belt: constraints on timing of deposition and provenance. *Precambr. Res.* **114**, 277–294.

Bolhar R., Kamber B. S., Moorbath S., Fedo C. M. and Whitehouse M. J. (2004) Characterisation of early Archaean chemical sediments by trace element signatures. *Earth Planet. Sci. Lett.* **222**, 43–60.

Bolhar R., Kamber B. S., Moorbath S., Whitehouse M. J. and Collerson K. D. (2005a) Chemical characterisation of Earth's most ancient clastic metasediments from the Isua Greenstone Belt, southern West Greenland. *Geochim. Cosmochim. Acta* **69**, 1555–1573.

Bolhar R., Van Kranendonk M. J. and Kamber B. S. (2005b) A trace element study of siderite-jasper banded iron formation in the 3.45 Ga Warrawoona Group, Pilbara Craton—formation from hydrothermal fluids and shallow seawater. *Precambr. Res.* **137**, 93–114.

Bolhar R. and Van Kranendonk M. J. (2007) A non-marine depositional setting for the northern Fortescue Group, Pilbara Craton, inferred from trace element geochemistry of stromatolitic carbonates. *Precambr. Res.* **155**, 229–250.

Bolhar R., Kamber B. S. and Collerson K. D. (2007) U–Th–Pb fractionation in Archaean lower continental crust: implications for terrestrial Pb isotope systematics. *Earth Planet. Sci. Lett.* **245**, 127–145.

Boynton W. V. (1984) Geochemistry of the rare earth elements: meteorite studies. In *Rare Earth Element Geochemistry* (ed. P. Henderson). Elsevier, pp. 63–114.

Brookins D. G. (1988) Seawater Sr-87/Sr-86 for the late Permian Delaware Basin Evaporites (New-Mexico, USA). *Chem. Geol.* **69**, 209–214.

Brookins D. G. (1989) Aqueous geochemistry of rare-earth elements *Rev. Mineral.* **21**, 201–225.

Burke K., Kidd W. S. F. and Kusky T. M. (1985) The Pongola structure of southern Africa: the world's oldest rift? *J. Geodyn.* **2**, 35–49.

Cole E. G. (1994) Lithostratigraphy and depositional environment of the Archaean Nsuze Group, Pongola Supergroup. M.Sc. thesis, Rand Afrikaans Univ. Johannesburg, p. 166.

Condie K. C. (1993) Chemical composition and evolution of the upper continental crust – contrasting results from surface samples and shales. *Chem. Geol.* **104**, 1–37.

Crowe S. A., Dossing L. N., Beukes N. J., Bau M., Kruger S. J., Frei R. and Canfield D. E. (2013) Atmospheric oxygenation three billion years ago. *Nature* **501**, 535–538.

Crow C., Condie K. C., Hunter D. R. and Wilson A. H. (1990) Geochemistry of volcanic rocks from the Nsuze Group, South Africa: arc-like volcanics in a 3.0 Ga-old intracratonic rift. *J. Afr. Earth Sc.* **9**, 589–597.

Danielson A., Möller P. and Dulski P. (1992) The europium anomalies in banded iron formations and the thermal history of the oceanic-crust. *Chem. Geol.* **97**, 89–100.

Derry L. A. and Jacobsen S. B. (1990) The chemical evolution of Precambrian seawater: evidence from REEs in banded iron formations. *Geochim. Cosmochim. Acta* **54**, 2965–2977.

Delvigne C. (2012) The Archaean silicon cycle – insights from silicon isotopes and Ge/Si ratios in banded iron formations, palaeosols and shales. Ph. D. thesis, Université Libre de Bruxelles, p. 181.

Delvigne C., Cardinal D., Hofmann A. and André L. (2012) Stratigraphic changes of Ge/Si, REE+Y and silicon isotopes as insights into the deposition of a Mesoarchaean banded iron formation. *Earth Planet. Sci. Lett.* **355–356**, 109–118.

Des Marais D. J. (1994) The Archaean atmosphere: its composition and fate. In *Developments in Precambrian geology* (ed. K. C. Condie), **11**, pp. 505–523.

Dix O. R. (1984) Early Proterozoic braided stream, shelf and tidal deposition in the Pongola Sequence. Zululand. *Trans. Geol. Soc. S. Afr.* **87**, 1–10.

Eggins S. M., Woodhead J. D., Kinsley L. P., Mortimer G. E., Sylvester P., McCulloch M. T., Hergt J. M. and Handler M. R. (1997) A simple method for the precise determination of ≥40 trace elements in geological samples by ICP-MS using enriched isotope internal standardization. *Chem. Geol.* **134**, 311–326.

Eglington B. M., Talma A. S., Marais S., Matthews P. E. and Dixon J. G. P. (2003) Isotopic composition of Pongola Supergroup limestones from the Buffalo River gorge, South Africa: constraints on their regional depositional setting. *S. Afr. J. Geol.* **106**, 1–10.

Elderfield H., Upstillgoddard R. and Sholkovitz E. R. (1990) The rare-earth elements in rivers, estuaries, and coastal seas and their significance to the composition of ocean waters. *Geochim. Cosmochim. Acta* **54**, 971–991.

Elworthy T., Eglington B. M., Armstrong R. A. and Moyes A. B. (2000) Rb–Sr isotope constraints on the timing of late to post-Archaean tectonometamorphism affecting the south-eastern Kaapvaal Craton. *J. Afr. Earth Sc.* **30**, 641–650.

Fedo C. M., Nesbitt H. W. and Young G. M. (1995) Unravelling the effects of potassium metasomatism in sedimentary rocks and paleosols, with implications for paleoweathering conditions and provenance. *Geology* **23**, 921–924.

Fedo C. M., Eriksson K. A. and Krogstad E. J. (1996) Geochemistry of shales from the Archaean (~3.0 Ga) Buhwa Greenstone Belt, Zimbabwe: implications for provenance and source-area weathering. *Geochim. Cosmochim. Acta* **60**, 1751–1763.

Fryer B. J. (1977) Rare-Earth evidence in iron-formations for changing Precambrian oxidation states. *Geochim. Cosmochim. Acta* **41**, 361–367.

Gao S. and Wedephol K. H. (1995) The negative Eu anomaly in Archaean sedimentary rocks: implications for decomposition, age and importance of their granitic sources. *Earth Planet. Sci. Lett.* **133**, 81–94.

Gold D. J. C. (2006) The Pongola Supergroup. In *The Geology of South Africa* (eds. M. R. Johnson, C. R. Anhaeusser and R. J. Thomas). Geological Society of South Africa, Johannesburg/ Council of Geoscience, Pretoria, pp. 135–148.

Gold D. J. C. and Von Veh M. W. (1995) Tectonic evolution of the Late Archaean Pongola-Mozaan Basin, South Africa. *J. Afr. Earth Sc.* **21**, 203–212.

Goldstein S. J. and Jacobsen S. B. (1988) Rare-earth elements in river waters. *Earth Planet. Sci. Lett.* **89**, 35–47.

Gross G. A. (1983) Tectonic systems and the deposition of iron-formation. *Precambr. Res.* **20**, 171–187.

Gutzmer J., Nhleko N., Beukes N. J., Pickard A. and Barley M. E. (1999) Geochemistry and ion microprobe (SHRIMP) age of a quartz porphyry sill in the Mozaan Group of the Pongola Supergroup: implications for the Pongola and Witwatersrand Supergroups. *S. Afr. J. Geol.* **102**, 139–146.

Harnois L. (1988) The CIW index: a new chemical index of weathering. *Sed. Geol.* **55**, 319–322.

Hegner E., Tegtmeyer A. and Kröner A. (1981) Geochemie und Petrogenese archaischer Vulkanite der Pongola-Gruppe in Natal, Suedafrika. *Chem. Erde* **40**, 23–57.

Hegner E., Kröner A. and Hofmann A. W. (1984) Age and isotope geochemistry of the Archaean Pongola and Usushwana suites in Swaziland, southern Africa: a case for crustal contamination of mantle-derived magma. *Earth Planet. Sci. Lett.* **70**, 267–279.

Hegner E., Kröner A. and Hunt P. (1994) A precise U–Pb zircon age for the Archaean Pongola Supergroup volcanics in Swaziland. *J. Afr. Earth Sc.* **18**, 339–341.

Hicks N. and Hofmann A. (2012) Stratigraphy, geochemistry and provenance of the auriferous-uraniferous, fluvial to shallow-marine Sinqeni Formation, Mozaan Group, northern KwaZulu-Natal, South Africa. *S. Afr. J. Geol.* **115**, 327–344.

Hofmann A. (2005) The geochemistry of sedimentary rocks from the Fig Tree Group, Barberton greenstone belt: implications for tectonic, hydrothermal and surface processes during mid-Archaean times. *Precambr. Res.* **143**, 23–49.

Hofmann A. and Bolhar R. (2007) Carbonaceous cherts in the Barberton greenstone belt and their significance for the study of early life in the Archean record. *Astrobiology* **7**, 355–388.

Hofmann A., Bolhar R., Dirks P. and Jelsma H. (2003) The geochemistry of Archaean shales derived from a mafic volcanic sequence, Belingwe Greenstone Belt, Zimbabwe: provenance, source area unroofing and submarine versus subaerial weathering. *Geochim. Cosmochim. Acta* **67**, 421–440.

Hofmann A., Bolhar R., Orberger B. and Foucher F. (2014) Cherts of the Barberton greenstone belt: petrology and trace element geochemistry of 3.5 to 3.3 Ga old silicified volcaniclastic sediments. *S. Afr. J. Geol.* **116**, 297–322.

Hofmann A., Kröner A., Xie H., Hegner E., Belyanin G., Kramers J., Bolhar R., Slabunov A., Reinhardt J. and Horváth P. (2015) The Nhlangano gneiss dome in south-west Swaziland – a record of crustal destabilization of the eastern Kaapvaal craton in the Neoarchaean. *Precambr. Res.* **258**, 109–132.

Horvath P., Reinhardt J. and Hofmann A. (2013) High-grade metamorphism of ironstones in the Mesoarchaean of southwest Swaziland. *Mineral. Petrol.* http://dx.doi.org/10.1007/s00710-013-0307-1.

Holland H. D. (1984) *The Chemical Evolution of the Atmosphere and Oceans*. Princeton University Press, Princeton, NJ, p. 582.

Jahn B. M. and Cuvellier H. (1994) Pb–Pb and U–Pb Geochronology of carbonate rocks – an assessment. *Chem. Geol.* **115**, 125–151.

Joubert P. and Johnson M. R. (1998) *Abridged Lexicon of South Africa Stratigraphy*. South African Committee for Stratigraphy, Council for Geoscience, p. 160.

Kamo S. L. and Davis D. W. (1994) Reassessment of Archean crustal development in the Barberton Mountain Land, South Africa, based on U–Pb dating. *Tectonics* **13**, 167–192.

Kamber B. S. and Webb G. E. (2001) The geochemistry of late Archaean microbial carbonate: implications for ocean chemistry and continental erosion history. *Geochim. Cosmochim. Acta* **65**, 2509–2525.

Kamber B. S., Bolhar R. and Webb G. E. (2004) Geochemistry of late Archaean stromatolites from Zimbabwe: evidence for microbial life in restricted epicontinental seas. *Precambr. Res.* **132**, 379–399.

Kamber B. S., Webb G. E. and Gallagher M. (2014) The rare earth element signal in Archaean microbial carbonate: information on ocean redox and biogenicity. *J. Geol. Soc. London* **171**, 745–763.

Klein C. (2005) Some Precambrian banded iron-formations (BIFs) from around the world: their age, geologic setting, mineralogy, metamorphism, geochemistry, and origin. *Am. Mineral.* **90**, 1473–1499.

Kramers J. D. and Tolstikhin I. N. (1997) Two terrestrial lead isotope paradoxes, forward transport modelling, core formation and the history of the continental crust. *Chem. Geol.* **139**, 75–110.

Kramers J. D., Belyanin, G. and Hofmann, A. (2013) *Extensive Palaeoproterozoic fluid percolation in cherts of the Onverwacht Group*. 6th Igneous and metamorphic studies group meeting, abstracts, University of Free State, p. 33.

Layer P. W., Linström A., McWilliams M. and Burghele A. (1988) Paleomagnetism and age of the Archean Usushwana Complex, southern Africa. *J. Geophys. Res.* **93**, 449–457.

Ludwig K. R. (2003) *User's manual for Isoplot 3: A Geochronological Toolkit for Microsoft Excel*. Berkeley Geochronology Centre, pp. 1–70.

Mason T. R. and von Brunn V. (1977) 3-Gyr-old stromatolites from South Africa. *Nature* **266**, 47–49.

Matthews P. E. (1967) The pre-Karroo formations of the White Umfolozi inlier, northern Natal. *Trans. Geol. Soc. S. Afr.* **70**, 39–63.

Matthews P. E. (1990) A plate tectonic model for the Late Archaean Pongola Supergroup in southeastern Africa. In *Crustal Evolution and Orogeny* (ed. S. P. H. Sychanthavong). New Delhi, pp. 41–73.

Mitra A., Elderfield H. and Greaves M. J. (1994) Rare earth elements in submarine hydrothermal fluids and plumes from the mid-Atlantic Ridge. *Mar. Chem.* **46**, 217–235.

Mukasa S. B., Wilson A. H. and Young K. R. (2013) Geochronological constraints on the magmatic and tectonic development of the Pongola Supergroup (Central Region), South Africa. *Precambrian Res.* **224**, 268–286.

Nesbitt H. W. and Young G. M. (1989) Formation and diagenesis of weathering profiles. *J. Geol.* **97**, 129–147.

Nhleko N. (2003) The Pongola Supergroup in Swaziland. Ph. D. thesis, Rand Afrikaans University, Johannesburg, p. 299.

Noffke N., Beukes N., Bower D., Hazen R. M. and Swift D. J. P. (2008) An actualistic perspective into Archean worlds – (cyano-)bacterially induced sedimentary structures in the siliciclastic Nhlazatse Section, 2.9 Ga Pongola Supergroup, South Africa. *Geobiology* **6**, 5–20.

Nothdurft L. D., Webb G. E. and Kamber B. S. (2004) Rare earth element geochemistry of Late Devonian reefal carbonates, Canning basin, Western Australia: confirmation of a seawater REE proxy in ancient limestones. *Geochim. Cosmochim. Acta* **68**, 263–283.

Olsson J. R., Hofmann A., Klausen M. B. and Söderlund, U. (2012) U–Pb baddeleyite ages constrain early Pongola, peripheral Ventersdorp and satellite Bushveld intrusion events in the south-eastern part of the Kaapvaal Craton. Litholund theses No 22, Lund Univ.

Pack A., Russell S. S., Shelley J. M. G. and van Zuilen M. (2007) Geo- and cosmochemistry of the twin elements yttrium and holmium. *Geochim. Cosmochim. Acta* **71**, 4592–4608.

Parekh P. P., Moller P., Dulski P. and Bausch W. M. (1977) Distribution of trace elements between carbonate and non-carbonate phases of limestone. *Earth Planet. Sci. Lett.* **34**, 39–50.

Planavsky N. J., Asael D., Hofmann A., Reinhard C. T., Lalonde S. V., Knudsen A., Wang X., Ossa Ossa F., Pecoits E., Smith A. J. B., Beukes N. J., Bekker A., Johnson T. M., Konhauser K. O., Lyons T. W. and Rouxel O. J. (2014) Evidence for oxygenic photosynthesis half a billion years before the Great Oxidation Event. *Nat. Geosci.* **7**, 283–286.

Robinson P., Townsend A. T., Yu Z. and Münker C. (1999) Determination of scandium, ytrium and rare earth elements in rocks by high resolution inductively coupled plasma-mass spectrometry. *Geostand. Newlett.* **23**, 31–46.

Saager R., Stupp H. D., Utter T. and Matthey H. O. (1986) Geological and mineralogical notes on placer occurrences in some conglomerates of the Pongola Sequence. In *Mineral Deposits of Southern Africa, I. Geol. Soc. S. Afr.* (eds. C. R. Anhaeusser and S. Maske), pp. 473–487.

SACS (South African Committee for Stratigraphy) (1980) Stratigraphy of South Africa. Part 1 (Comp. L. E. Kent). Lithostratigraphy of the Republic of South Africa, South West Africa/Namibia, and the Republics of Bophuthatswana, Transkei and Venda. *Handbk Geol. Surv. S. Afr.*, 8, pp. 690.

Sholkovitz E. R., Landing W. M. and Lewis B. L. (1994) Ocean particle chemistry: the fractionation of rare earth elements between suspended particles and seawater. *Geochim. Cosmochim. Acta* **58**, 1567–1579.

Tankard A. J., Jackson M. P. A., Eriksson K. A., Hobday O. K., Hunter D. R. and Minter W. E. L. (1982) *Crustal Evolution of Southern Africa*. Springer-Verlag, New York, p. 523.

Terakado Y. and Masuda A. (1988) The co-precipitation of rare earth elements with calcite and aragonite. *Chem. Geol.* **69**, 103–110.

Taylor S. R. and McLennan S. M. (1985) *The Continental Crust: Its Composition and Evolution*. Blackwell Scientific Publications, Palo Alto, p. 328.

Todt W., Cliff R. A., Hanser A. and Hofmann A. W. (1996) Evaluation of a $^{202}Pb + ^{205}Pb$ double spike for high precision lead isotopic analysis, In *Earth Processes: Reading the Isotopic Code, Geophysical Monograph* (eds. A. Basu and S. R. Hart), pp. 429–437.

Van Kranendonk M. J., Webb G. E. and Kamber B. S. (2003) Geological and trace element evidence for a marine sedimentary environment of deposition and biogenicity of 3.45 Ga stromatolitic carbonates in the Pilbara Craton, and support for a reducing Archaean ocean. *Geobiology* **1**, 91–108.

Veizer J., Clayton R. N., Hinton R. W., von Brunn V., Mason T. R., Buck S. G. and Hoefs J. (1990) Geochemistry of Precambrian carbonates – 3: shelf seas and non-marine environments of the Archean. *Geochim. Cosmochim. Acta* **54**, 2717–2729.

Von Brunn V. and Hobday D. K. (1976) Early Precambrian tidal sedimentation in the Pongola Supergroup of South Africa. *J. Sediment. Petrol.* **46**, 670–679.

Von Brunn V. and Mason T. R. (1977) Siliciclastic-carbonate tidal deposits from the 3000 Ma Pongola Supergroup, South Africa. *Sed. Geol.* **18**, 245–255.

Walraven F. and Pape J. (1994) Pb–Pb whole-rock ages for the Pongola Supergroup and the Ushushwana Complex, South Africa. *J. Afr. Earth Sc.* **18**, 297–308.

Watchorn M. B. (1980) Fluvial and tidal sedimentation in the 3000 Ma Mozaan basin, South Africa. *Precambr. Res.* **13**, 27–42.

Webb G. E. and Kamber B. S. (2000) Rare earth elements in Holocene reefal microbialites: a shallow seawater proxy. *Geochim. Cosmochim. Acta* **64**, 1557–1565.

Weilers B. F. (1990) *A review of the Pongola Supergroup and its setting on the Kaapvaal Craton*. Inform. Circ. Econ. Geol. Res. Unit, Univ. Witwatersrand, Johannesburg, **228**, p. 69.

Wilson A. H. (2003) A new class of silica enriched, highly depleted komatiites in the southern Kaapvaal Craton, South Africa. *Precambr. Res.* **127**, 125–141.

Wilson A. H. and Grant C. E. (2006) Physical volcanology and compositions of the basaltic lava flows in the Archean Nzuse Group, White Mfolozi Inlier, South Africa. In *Processes on the Early Earth* (eds. W. U. Reimold and R. Gibson). Geological Society of America Special Paper, **405**, pp. 255–289.

Wilson A. H., Groenewald B. and Grant C. E. (2013) Volcanic and volcaniclastic rocks of the Mesoarchaean Pongola Supergroup in South Africa and Swaziland: distribution, physical characteristics, stratigraphy and correlations. *S. Afr. J. Geol.* **116**, 119–168.

Wronkiewicz D. H. and Condie K. C. (1987) Geochemistry of Archaean shales from the Witwatersrand Supergroup, South Africa: source area weathering and provenance. *Geochim. Cosmochim. Acta* **51**, 2401–2416.

Wronkiewicz D. H. and Condie K. C. (1989) Geochemistry and provenance of sediments from the Pongola Supergroup, South Africa: evidence for a 3.0 Ga old continental craton. *Geochim. Cosmochim. Acta* **53**, 1537–1549.

Xie H., Hofmann A., Hegner E., Wilson A. H., Wan Y. and Liu D. (2012) Zircon SHRIMP dating confirms a Palaeo- to Mesoarchaean supracrustal terrain in the Kaapvaal craton, southern Africa. *Gondwana Res.* **21**, 818–828.

Zhong S. J. and Mucci A. (1995) Partitioning of rare-earth elements (REEs) between calcite and seawater solutions at 25 °C and 1 atm, and high dissolved REE concentrations. *Geochim. Cosmochim. Acta* **59**, 443–453.

Associate editor: Anders Meibom

Precambrian Research 278 (2016) 244–264

Contents lists available at ScienceDirect

Precambrian Research

journal homepage: www.elsevier.com/locate/precamres

Sedimentology and facies analysis of Mesoarchaean stromatolitic carbonate rocks of the Pongola Supergroup, South Africa

M. Siahi [a,c,*], A. Hofmann [b], E. Hegner [a], S. Master [c]

[a] Department of Earth and Environmental Sciences, Ludwig-Maximilians-Universität, München, Germany
[b] Department of Geology, University of Johannesburg, Johannesburg, South Africa
[c] Economic Geology Research Institute, School of Geosciences, University of Witwatersrand, Johannesburg, South Africa

ARTICLE INFO

Article history:
Received 18 May 2015
Revised 8 February 2016
Accepted 15 March 2016
Available online 22 March 2016

Keywords:
Stromatolite
Carbonate rocks
Archaean
Early life
Kaapvaal craton
Pongola Supergroup

ABSTRACT

The c. 3.0 Ga old Chobeni Formation (Nsuze Group, Pongola Supergroup) contains several carbonate successions interpreted to have been deposited in a tide-dominated, shallow-marine environment. Facies consist of mixed siliciclastic and carbonate rocks and include subtidal cross-bedded sandstone and oncolitic dolostone, intertidal wave-rippled oodolarenite, and supratidal wrinkly-laminated dolarenite–dololutite. Sedimentary facies are partially arranged in a shallowing-upward pattern reflecting cyclic variations of Mesoarchaean sea level. Microbialites occur in a variety of sedimentary sub-environments and include laminated as well as structureless, lenticular-domal types. Differences in microbialite morphology, macrofabric, and size suggest potentially distinct assemblages of microorganisms responding to different physicochemical and environmental conditions. Microbialite textures are consistent with *in situ* carbonate precipitation and to a lesser extent by trapping and binding of sediment. Despite their great age, the Pongola carbonates are compositionally and texturally very similar to much younger carbonate successions preserved in the geological record.

1. Introduction

Archaean sedimentary carbonate rocks are most commonly found in the Neoarchaean Era. The Wittenoom Formation and Carawine Dolomite of the Hamersley Group, Australia (Simonson et al., 1993) and the Campbellrand–Malmani subgroups of the Transvaal Supergroup, South Africa (Beukes, 1987; Sumner and Grotzinger, 2004) straddle the Archaean–Proterozoic boundary and represent the oldest large-scale carbonate platform deposits. These rocks are well known for their record of marine life (Beukes, 1987; Altermann and Schopf, 1995) and have provided important information on seawater composition (Sumner and Grotzinger, 2004). Similarly, carbonate rocks are widely developed in a number of greenstone belts, specifically in the Slave, Superior, Dharwar, and Zimbabwe cratons (Henderson, 1975; Srinivasan et al., 1989; Hofmann et al., 2004; Fralick and Riding, 2015). Carbonate rocks of inferred lacustrine setting have also been reported from intracontinental volcano-sedimentary basins of the Kaapvaal and Pilbara cratons (Ventersdorp and Fortescue Supergroups, respectively; Buck, 1980; Bolhar and Van Kranendonk, 2007; Altermann and Lenhardt, 2012).

Prior to the Neoarchaean Era carbonate rocks are relatively rare. This is specifically the case for Mesoarchaean carbonate rocks, exposures of which can be found in the c. 3.0 Ga Nsuze Group of the Pongola Supergroup, South Africa (Mason and Von Brunn, 1977; Beukes and Lowe, 1989; Dixon, 2004). Palaeoarchaean carbonate rocks are commonly silicified and include those from the 3.49 Ga Dresser Formation, the 3.42–3.35 Ga Strelley Pool Formation of the Pilbara Supergroup, Western Australia (Lowe, 1980; Van Kranendonk, 2006), and the 3.41 Ga Witkop Formation, Nondweni Group, South Africa (Wilson and Versfeld, 1994; Xie et al., 2012). Palaeoarchaean carbonate rocks typically form units less than 20 m thick and are believed to have been deposited in low-energy, shallow-marine environments between episodes of volcanism (Grotzinger, 1989; Van Kranendonk et al., 2003; Allwood et al., 2006).

Here we report on carbonate and associated siliciclastic facies from the Nsuze Group of the Pongola Supergroup in the White Mfolozi inlier of KwaZulu-Natal. Since the sedimentological study of Beukes and Lowe (1989) of a single outcrop, no detailed facies analysis has been undertaken on these rocks. This paper outlines and interprets the sedimentological characteristics and facies of three stratigraphically distinct sections in the White Mfolozi inlier

* Corresponding author at: Department of Earth and Environmental Sciences, Ludwig-Maximilians-Universität, München, Germany.
E-mail address: mehrnazsiahy56@yahoo.com (M. Siahi).

http://dx.doi.org/10.1016/j.precamres.2016.03.004
0301-9268/

with the goal to reconstruct depositional environments and to shed light on surface processes influencing the habitat of early life.

2. Geological setting

The Mesoarchaean Pongola Supergroup was deposited on the south-eastern Kaapvaal Craton and is one of the oldest well-preserved successions of epicratonic volcanic and sedimentary rocks (Fig. 1). It unconformably overlies granitoid-greenstone basement and crops out as inliers surrounded by younger Phanerozoic sedimentary rocks of the Karoo Supergroup. Following deposition between c. 3.0 and 2.9 Ga ago (Hegner et al., 1984, 1994; Mukasa et al., 2013), the Pongola Supergroup was intruded by mafic and ultramafic dykes and sheets of the c. 2.99–2.87 Ga Usushwana Complex, by granite plutons as young as 2.72 Ga, and by several distinct suites of dolerite dykes and sills (Schoene and Bowring, 2010; Olsson et al., 2010; Mukasa et al., 2013; Gumsley et al., 2015).

The Pongola Supergroup is composed of two stratigraphic units: the mainly volcanic Nsuze Group and overlying strata of the mainly sedimentary Mozaan Group (Fig. 2). Deposition occurred in a shallow-marine basin in which sediments were supplied from the northwest (Von Brunn and Hobday, 1976; Beukes and Cairncross, 1991; Gold, 2006).

The study area in the White Mfolozi inlier exposes the c. 1.4 km thick Nsuze Group and the c. 0.7 km thick Mozaan Group, the latter of which is overlain unconformably by Permian sedimentary rocks of the Karoo Supergroup (Matthews, 1967; Wilson and Grant, 2006; Hicks and Hofmann, 2012). The Nsuze Group comprises five formations in the White Mfolozi inlier (Fig. 2). The Bomvu

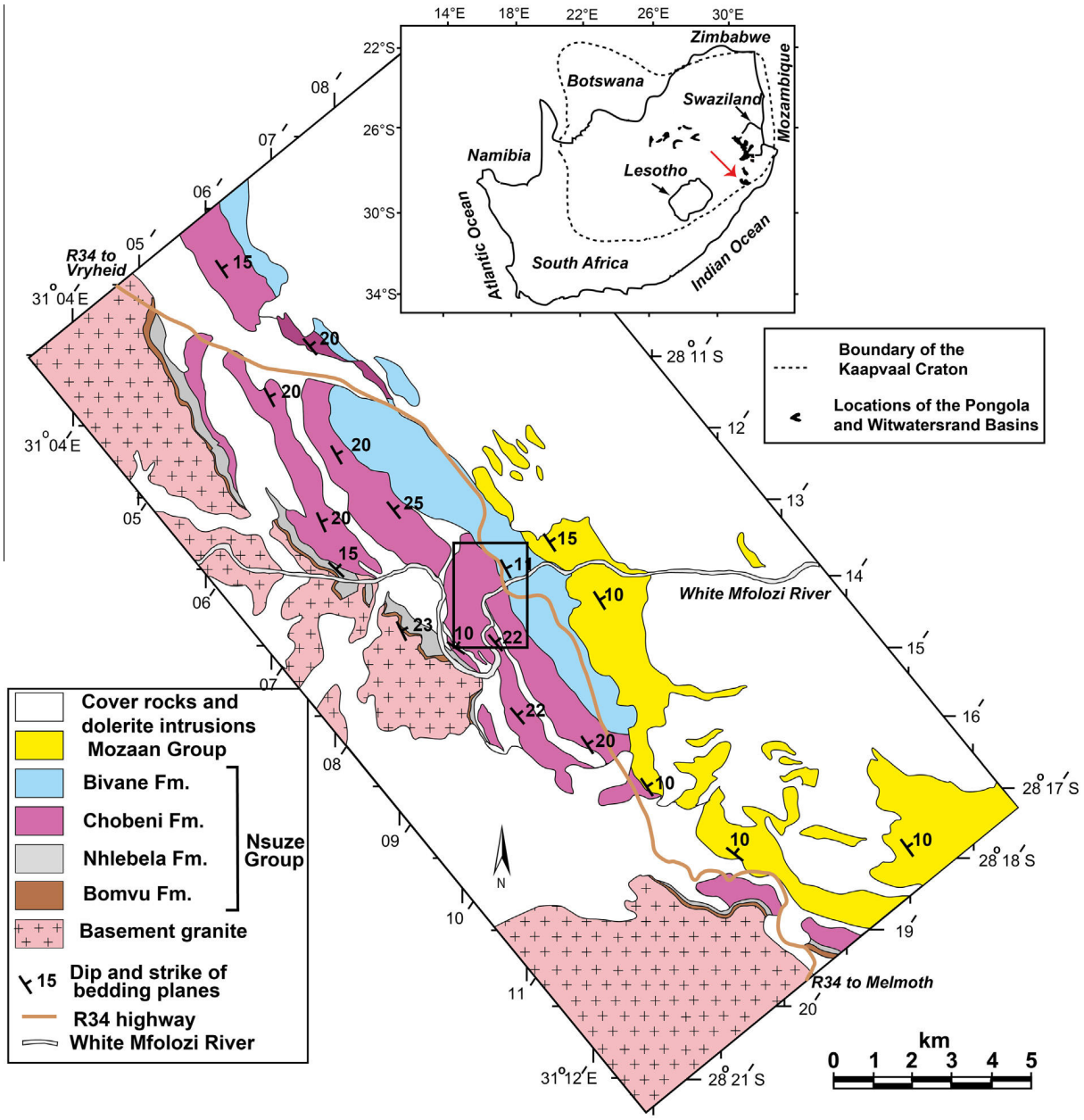

Fig. 1. Geological map of the White Mfolozi inlier (modified after Wilson et al., 2013). Rectangle shows outline of the study area (Fig. 3). Inset shows distribution of the Pongola and Witwatersrand supergroups in relation to the Kaapvaal Craton in South Africa; red arrow points to White Mfolozi inlier. (For interpretation of the references to color in this figure legend, the reader is referred to the web version of this article.)

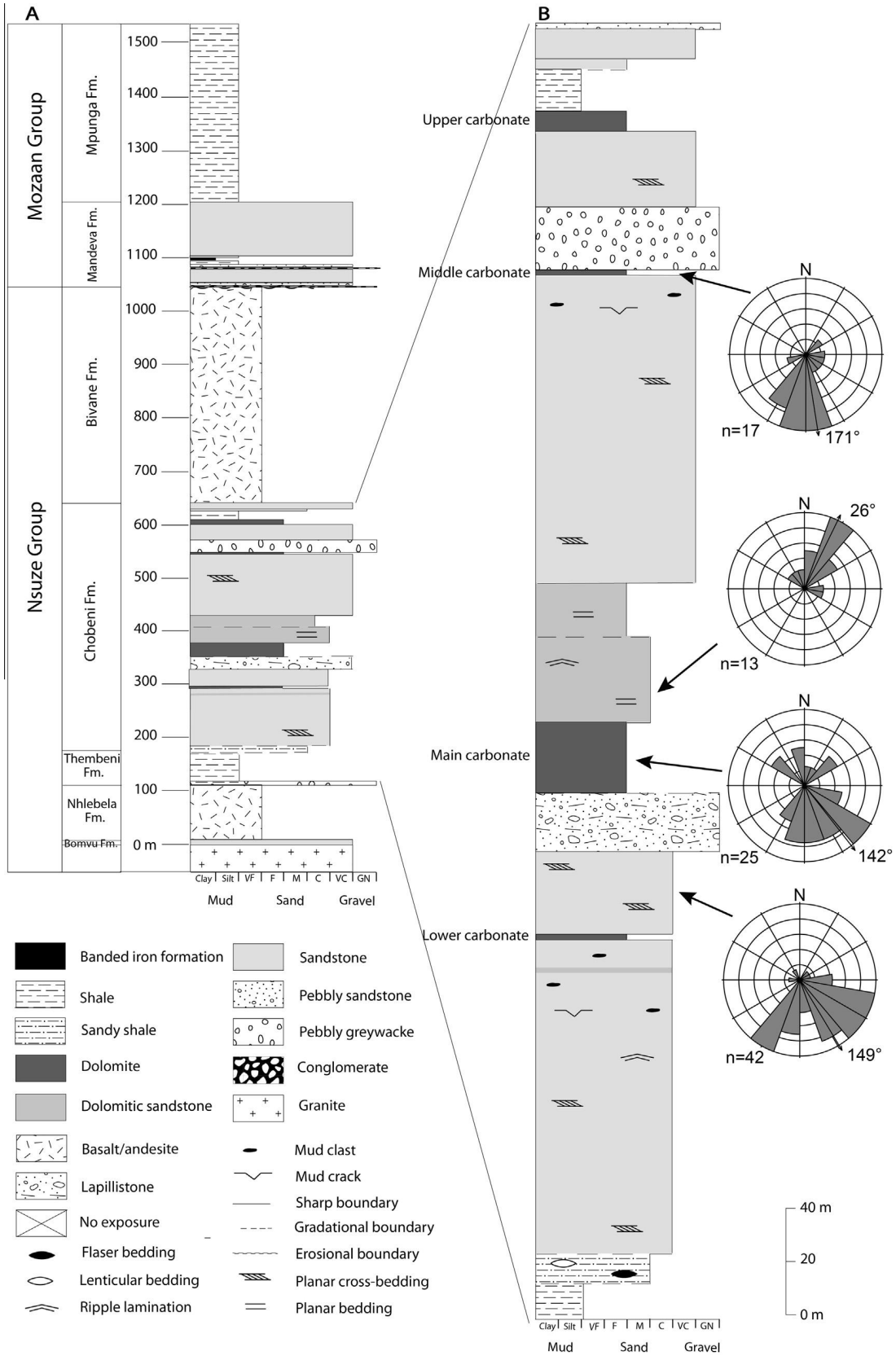

Fig. 2. Stratigraphic column of the Nsuze and Mozaan groups (column A) of the Pongola Supergroup in the White Mfolozi inlier. The Chobeni Formation, studied in detail, is shown in column B. Rose diagrams show results of palaeocurrent measurements of well exposed, predominantly tabular cross-bedding from four stratigraphic intervals of the Chobeni Formation.

Formation overlies granitoid basement along an irregular contact and consists of coarse-grained sandstones up to 10 m thick with local intercalations of pebble conglomerate. The Nhlebela Formation is up to 110 m thick, rests with a sharp contact on the basal sandstone or directly on granite and consists of basaltic to andesitic lava with pillow-structures near the base. The Thembeni Formation is c. 60 m thick and consists of shale with local intercalations of pebbly greywacke at the base. Shale grades into sandstones of the basal Chobeni Formation, which is c. 450 m thick and sharply overlain by up to 400 m of amygdaloidal basaltic lava of the Bivane Formation.

The Chobeni Formation is the focus of this study. Although dominantly siliciclastic, the Chobeni Formation contains several units of dolomite with locally well-developed stromatolites. Dolomite facies have been previously interpreted to have formed in a shallow, tide-dominated, marine setting (Mason and Von Brunn, 1977; Von Brunn and Mason, 1977; Beukes and Lowe, 1989). Four sedimentary units containing dolomite admixed with siliciclastic and volcaniclastic particles (cemented, and partly replaced, by dolomite) are referred to as the lower, main, middle, and upper carbonate sections (Figs. 2 and 3). The Chobeni Formation commences with thinly bedded sandstone and shale with lenticular to flaser bedding suggestive of a tide-influenced environment (Fig. 4A). This is overlain by cross-bedded quartz-arenite that consists of tabular co-sets of cross-bedded coarse-grained sandstone. This assemblage probably formed in a subtidal environment. Higher in the section, thinly bedded sandstone–shale units that show wave ripples and mud-cracks are intercalated with cross-bedded sandstones, suggesting broadly intertidal conditions with periodic emergence. In this unit, mud-clasts (Fig. 4B) are common, indicating regular reworking of the mud-cracked tidal flats. Near the top of the sandstone succession there are two thin units of quartz sand-rich dolomite, showing cross-bedding, in addition to massive domains of micritic dolomite and oodolorudite. The more prominent upper horizon is referred to here as the lower carbonate section (Figs. 2 and 3) and was not studied in detail. Palaeocurrent measurements in this part of the section show a predominantly southeast- and likely offshore-directed sediment transport (Fig. 2).

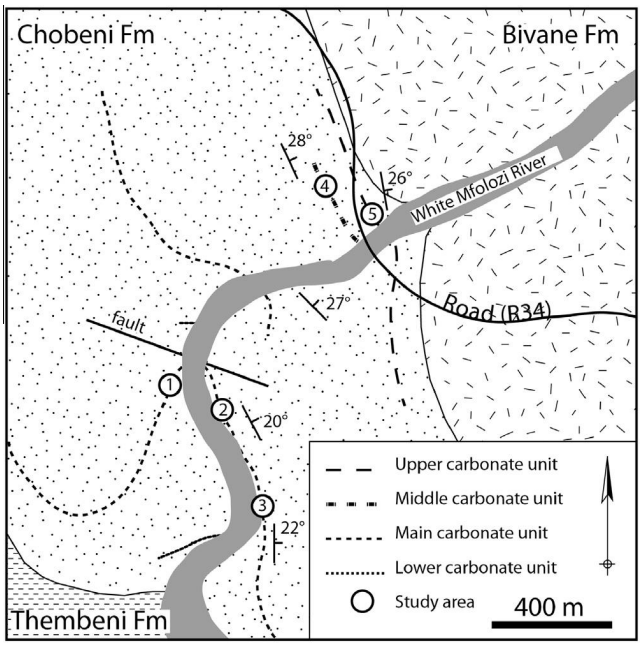

Fig. 3. Geological sketch map showing the localities of the five sections studied in the White Mfolozi inlier (see Fig. 1 for overview).

The sandstones are sharply overlain by a planar-bedded lapillistone (Fig. 2) containing accretionary lapilli that suggest an origin as a pyroclastic air fall deposit. The lapillistone is variably cemented or replaced by carbonate, especially near the top, and is gradationally overlain by the main carbonate section (Fig. 2). Small, non-laminated domal microbialites surrounded by lapillistone are present along the contact (Fig. 4C). The main carbonate section has a thickness of c. 28 m (Figs. 2 and 5) and is tectonically duplicated by faulting (Fig. 3). Cross-bedding in sandstone facies within the main carbonate section shows bimodal, but predominantly southeast-directed, sediment transport (Fig. 2). The carbonate rocks are overlain by co-sets of thin to medium beds of planar-bedded, tabular cross-bedded, and locally wave ripple-laminated sandstone. The sandstone shows irregular carbonate-cemented or carbonate-replaced domains (Fig. 4D) and contains intercalations of irregularly bedded carbonate rocks. Cross-bedding in the sandstone reflects sediment transport to the northeast, suggesting either local basin reorganization or longshore currents. The dolomitic sandstone is overlain by a thick succession of medium to thick beds of planar and cross-bedded, coarse-grained sandstone with minor mud clasts and thin intercalations of mud layers showing mud-cracks, interpreted as subtidal, and at times emerged, sand bars.

The middle carbonate section rests with a sharp contact on cross-bedded sandstone with wave ripple marks on bedding planes. It is c. 2 m thick, shows evidence for sediment transport to the south–southeast, and is overlain along a sharp, planar contact by pebbly greywacke (Figs. 2 and 6). The pebbly greywacke is more than 20 m thick, shows crude planar stratification, consists of poorly sorted matrix-rich sandstone with pebbles and cobbles of chert and quartz, and is interpreted as a mass flow deposit. Dolomite clasts occur in its lower portion. The middle carbonate section is absent in places along strike, suggesting erosion during deposition of the pebbly greywacke. The greywacke bed is overlain by cross-bedded sandstone and followed by the upper carbonate section, which is more than 9 m thick. Its upper contact is not exposed in the river section studied (Fig. 6). The upper carbonate is overlain by shale that coarsens upward into cross-bedded sandstones that form the top of the Chobeni Formation.

The rock assemblages in the White Mfolozi inlier have been subjected to greenschist facies metamorphism. Besides minor tilting, the cleavage in argillaceous dolomitic units indicates that this succession experienced open folding on a regional scale. Contact metamorphism occurs along the margin of some dolerite sills intrusive into the dolomite units, giving rise to talc–carbonate schists. Except for recrystallization of the carbonate rocks, their textures and sedimentary structures are very well preserved.

3. Materials and methods of study

The main, middle and upper carbonate sections were studied in detail in the field. The main carbonate section was measured at three localities (Fig. 3, localities 1–3) in order to evaluate lateral facies changes. Sedimentary textures are best preserved in the main and middle sections, whereas the upper carbonate section is more extensively recrystallized. Sixty-five representative samples were collected from these sections for additional studies on facies variation. Forty five polished slabs and 110 polished thin sections were studied for carbonate texture and microstructure using binocular and petrographic microscopes. The terminology of carbonate textures follows that of Folk (1959, 1962).

The mineralogical composition was determined by a combination of transmitted and reflected light microscopy, staining, scanning electron microscopy (SEM) and X-ray diffraction (XRD) analysis of bulk samples. Potassium ferricyanide and Alizarin

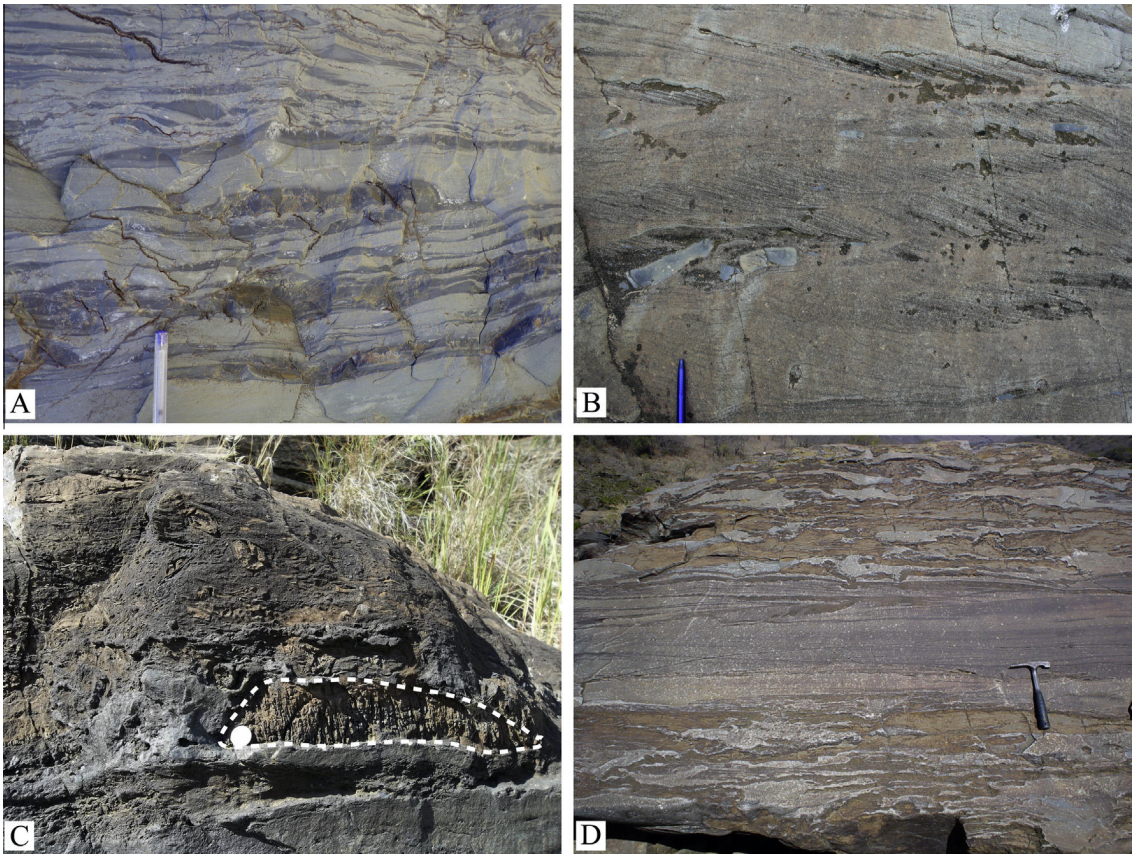

Fig. 4. Photographs of different stratigraphic units of the Chobeni Formation. (A) Alternating sandstone and shale with wavy-flaser bedding. (B) Cross-bedded sandstone with mudstone intraclasts (above pen). (C) Detail of gradational contact between lapillistone and carbonate. Non-laminated domal microbialites (outlined by dashed line) are surrounded by lapillistone. (D) Planar-bedded carbonate-cemented sandstone with irregular domains of primary and secondary dolomite.

red-S were used as staining agents to distinguish carbonate minerals in a few selected thin sections (Friedman, 1959; Dickson, 1966).

Raman spectroscopy was carried out on polished thin sections using an alpha300R (WITec) confocal laser Raman microscope configured with a frequency-doubled Nd-YAG laser (wavelength 532 nm) at the Department of Geology, University of Johannesburg. The system couples motorized sample positioning with a piezo-driven scan platform, allowing Raman mapping from micrometre- to centimetre-scale. The analyses were made using a 20× Nikon objective with a numerical aperture of 0.4 and with a maximum of 8 mW laser power to prevent thermal degradation.

Carbon-coated thin sections were examined and analyzed with the aid of an Oxford INCA Energy-Dispersive Spectrometer (EDS) attached to a Tescan SEM. X-ray diffraction of selected samples was performed with a Panalytical X-PertPro series X-ray diffractometer, also at the University of Johannesburg.

4. Constituents and composition of the carbonate units

The composition of the carbonates differs with stratigraphic position. The dominant composition of carbonates of the middle carbonate section is ankerite, whereas the main and upper carbonate sections consist of dolomite. The good state of preservation of these carbonates indicates that they had a stable primary mineralogical composition, i.e. calcite rather than aragonite, or that they originally precipitated as dolomite. Dolomitization of high-Mg calcite generally provides better fabric retention than if low-Mg calcite is the precursor mineral (Sibley, 1982). However, since low-Mg calcite is present as a diagenetic phase, filling early diagenetic fenestrae and replacing dolomitic allochems marginally, we suggest that the primary composition of the carbonates was either high-Mg calcite subjected to very early diagenetic dolomitization, or, less likely, dolomite. No significant differences in composition were detected among micrite matrix, allochems, and microbialites. The carbonate rocks are rarely monomineralic, however, as they contain a variety of allochems, siliciclastic detritus, pyroclastic particles as well as secondary diagenetic and metamorphic phases.

4.1. Allochems

A variety of allochems, including peloids, ooids, oncoids, and various intraclasts were identified in the carbonate facies. Peloids occur as partially silicified, structureless, sub-spherical micritic grains that range from 0.05 to 0.2 mm in diameter (Fig. 7A). When recrystallized, they are difficult to distinguish from the micrite matrix. Peloids are developed in several facies and are frequently associated with siliciclastic detritus and ooids. They are also common in microbialites and also constitute ripple bedforms.

Ooids occur as partially silicified, spherical to sub-spherical, single to compound grains 0.2–0.6 mm in diameter. The ooid nuclei consist of peloids, micritic and silicified rock fragments, and quartz grains. Their cortices are variable in thickness and show concentric, radial and radial–concentric laminae (Fig. 7B). In many cases, recrystallization results in partially to fully structureless, microcrystalline ooid types.

Oncoids occur as spherical to sub-spherical, discoidal and elongate forms of 2–10 mm in diameter, in which dominantly micritic nuclei are coated by micritic, microsparitic, and chert laminae.

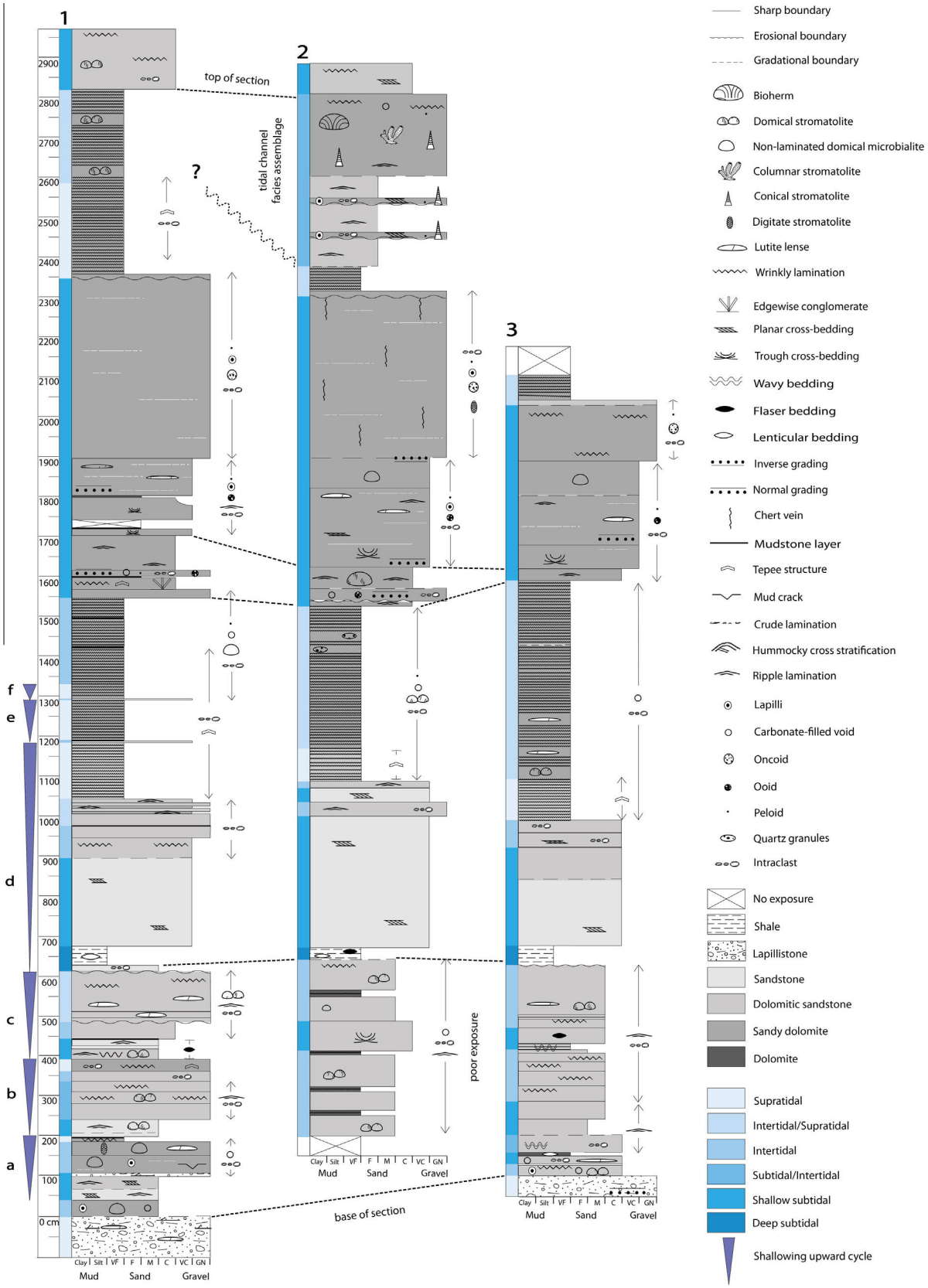

Fig. 5. Stratigraphic columns 1 to 3 of the main carbonate section of the Chobeni Formation. See Fig. 3 for locality.

Their cortices are often thicker on the presumed upper side (Fig. 7C and D), and smaller oncoids show more regular laminae than larger ones. Compound oncoid grains are also present. Primary textures are commonly preserved, but affected by recrystallization and silicification to various degrees. There is no petrographic evidence for a trapped clastic component in the

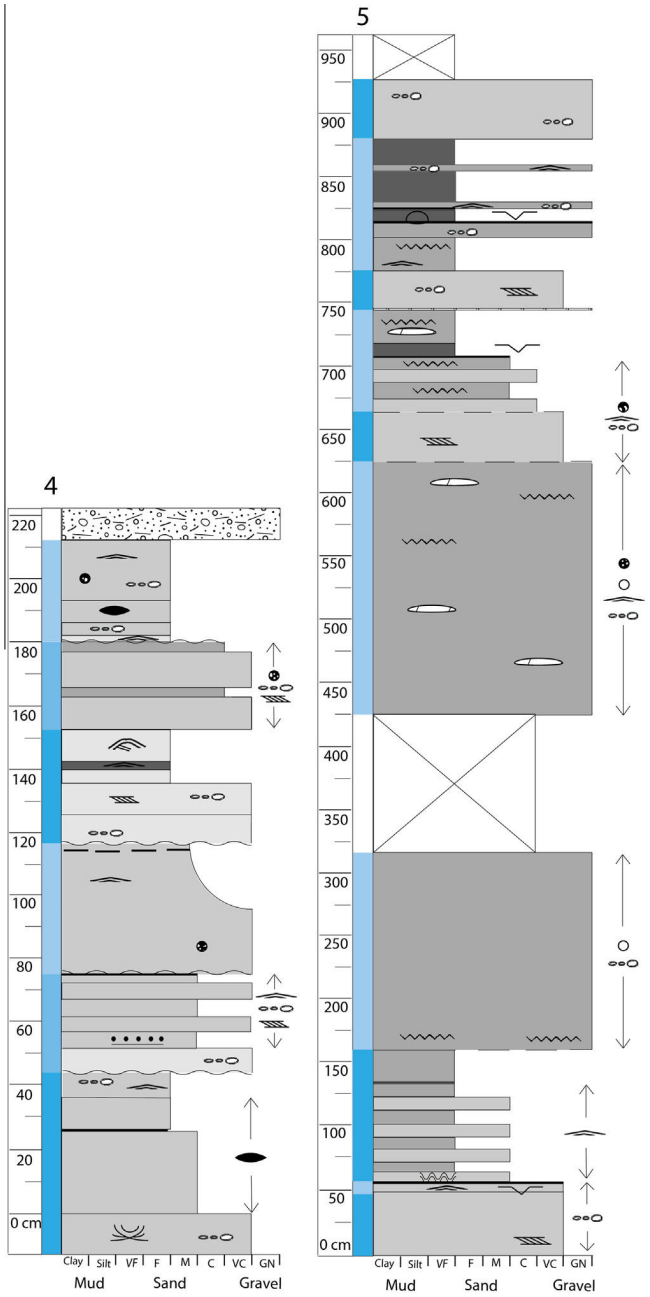

Fig. 6. Stratigraphic columns of the middle (4) and upper (5) carbonate sections of the Chobeni Formation. See Fig. 3 for locality and Fig. 5 for legend.

oncoids. Idiomorphic mica crystals 100–200 μm in length occur in some outer cortices, but they represent a secondary metamorphic phase. Nevertheless, they may point to the presence of a trapped, primary clay phase.

Finally, intraclasts and aggregate grains (Fig. 7E) are tabular to ellipsoidal and mm to cm in length. They consist primarily of partially silicified micrite and sand fragments, as well as dolomicrite-cemented allochems.

Taken together, the variety of allochems suggests deposition in relatively high-energy, shallow-marine settings. The origin of the peloids is uncertain, but they likely represent either inorganic and organically-induced precipitation (Macintyre, 1985; Gerdes et al., 1994; Reitner and Neuweiler, 1995; Kazmierczak et al., 1996), or reworking of micrite sediment (Fahraeus et al., 1974). Ooids and oncoids form in a variety of sedimentary environments, ranging from freshwater lakes to marine settings, where they are formed by microbial processes (Dahanayake et al., 1985; Davaud and Girardclos, 2001; Flügel, 2004). Variations in the ooid cortices may reflect differences in the degree of agitation during formation (Loreau and Purser, 1973; Halley et al., 1983). Variation in oncoid cortex may also reflect differences in agitation, with uniform laminae of smaller oncoids reflecting ease of movement. The presence of a variety of intraclasts and agglutinated grains further suggests the occurrence of high-energy events that resulted in erosion and reworking of early cemented or microbially agglutinated substrate materials (Hardie and Ginsburg, 1977; Shinn, 1983).

4.2. Siliciclastic–volcaniclastic detritus

Siliciclastic detritus is composed of sub-angular to rounded, sand-sized quartz and subordinate microcline and plagioclase grains. Accessory detrital heavy minerals include rutile, monazite, pyrite, apatite, and zircon up to 200 μm. Scattered flakes of muscovite may also be of detrital origin. Clastic grains are found as disseminated particles in the micritic matrix of different facies or concentrated in detritus-rich laminae including those of laminated microbialites.

Pyroclastic fragments include vesicular to non-vesicular lapilli that range from 0.2 to 20 mm in diameter and were observed in different facies (Fig. 7F). Lapilli frequently contain quartz sand particles entrained during lava/sediment interaction at the source of the ejecta. Vesicles are filled with chert or dolomite. The lapilli are extensively replaced by dolomite, chert, and chlorite and contain micron-sized, secondary crystallites of titanium oxide and apatite.

4.3. Diagenetic and metamorphic phases and textures

Early diagenetic features include calcite-filled voids/fenestrae and rare cm-sized pyrite nodules. Carbonate and chert partially replacing feldspar and other particles are probably also of early diagenetic origin. Stylolites formed during late diagenesis and contain high concentrations of accessory minerals (especially rutile), pyrite, and carbonaceous matter.

Metamorphic phases include quartz, sericite, muscovite, and chlorite. Quartz is present as fibrous crystals forming pressure fringes oriented parallel to bedding. Muscovite is concentrated in the margin and centre of micritized pyroclastic particles. Disseminated crystals of micron- to cm-sized euhedral pyrite, minor sphalerite and micron-sized apatite occur in specific facies and are likely metamorphic in origin.

4.4. Biogenic phases

Carbonaceous matter is rare, but locally present in ooids, peloids, intraclasts, and some microbialite laminae, where it is disseminated evenly or interwoven with authigenic dolomitic crystals. Recrystallization has, in some cases, led to the concentration of organic matter at crystal margins. Sub-micron sized apatite and pyrite crystals occur in close association with carbonaceous matter in coated grains. Their origin may be related to the activity and interaction of sulfate-reducing and sulfide-oxidizing bacteria (Donald and Southam, 1999; Crosby and Bailey, 2012).

5. Description of the characteristics of sedimentary facies

The carbonate-bearing sedimentary successions of the main, middle and upper carbonate sections have been subdivided into fourteen facies on the basis of field observations and sample petrography. These were grouped into three facies assemblages repre-

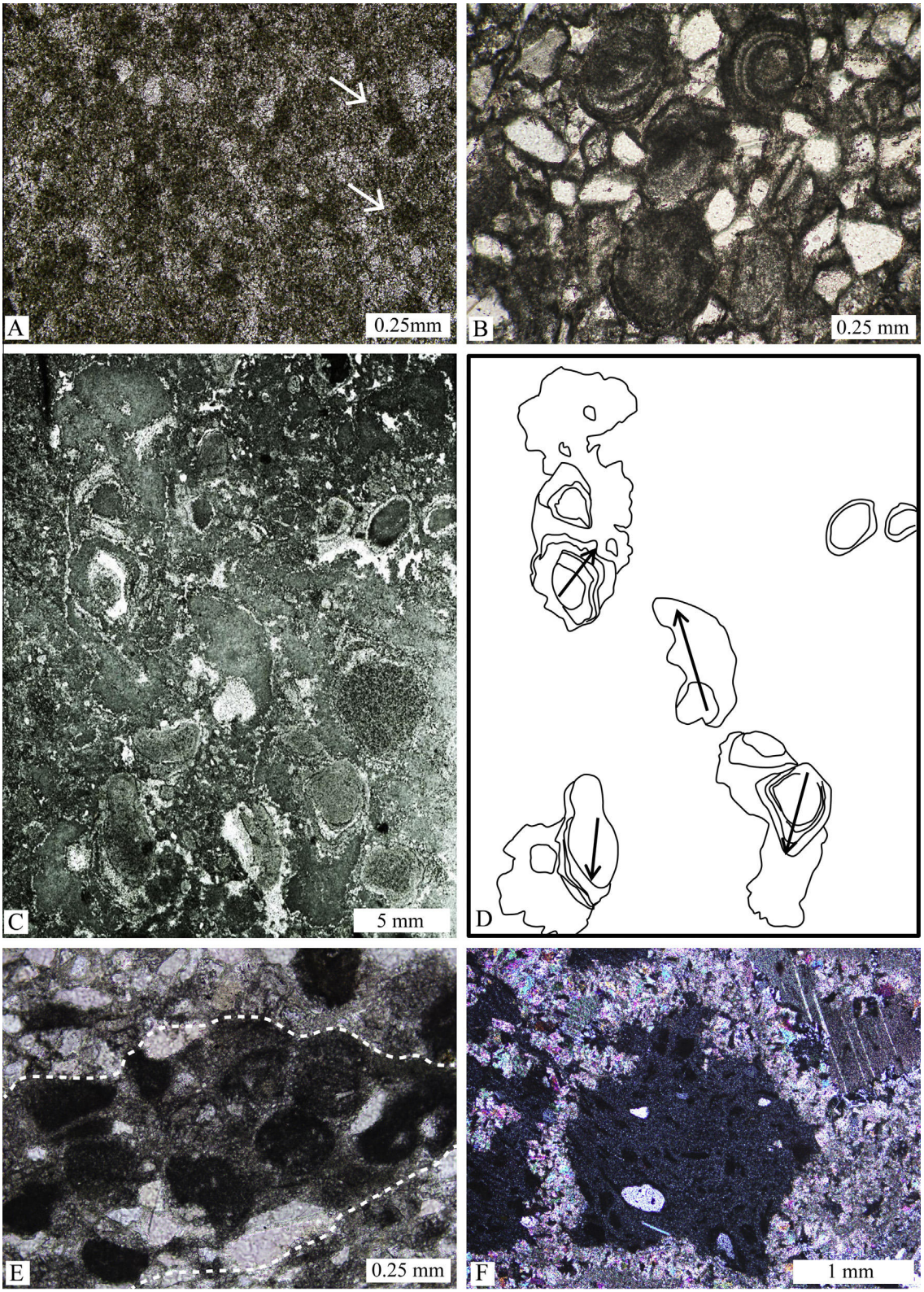

Fig. 7. Photomicrographs (A, B and E under plane-polarized light; F under crossed-polarized light) and thin section scan (C) showing different particles in the studied carbonate samples. (A) Peloids (arrows, dark spherical domains) and silicified particles (light spherical domains) in a partially recrystallized micritic matrix. (B) Concentric and micritic ooids surrounded by quartz sand. (C) Partially silicified oncoids; note thicker cortex on the one side of some oncoids reflecting the upper part of oncoid during cortex formation. (D) Sketch of C outlining some oncoids for better visualization; arrows show inferred growth directions of oncoids. (E) Composite grain of micritic ooids (dark subspherical particles) and siliciclastic particles (light grains) cemented by micrite and outlined by dashed line. (F) Pyroclastic fragments (dark) of chlorite with entrained quartz grains and surrounded by dolomitic cement.

senting deposition in (1) supratidal to upper intertidal, (2) middle intertidal to subtidal and (3) tidal channel environments. In the following sections the characteristics of the facies and their assemblages will be described. Additional information is presented in Table 1. The term sandy refers to the presence of sand-sized siliciclastic particles, i.e. mainly quartz.

5.1. Supratidal to upper intertidal facies assemblage

Supratidal to upper intertidal depositional environments of the main and upper carbonate sections are dominated by stratiform stromatolite facies. Intraclast dolomitic sandstone and sandy intradolorudite facies are present as minor facies in these zones. The middle carbonate section lacks supratidal deposits.

5.1.1. Stratiform stromatolite facies

The stratiform stromatolite facies (Fig. 8A and B; Table 1) is particularly well-developed in the centre of the main carbonate section (Fig. 5, at c. 12 m). It occasionally hosts discontinuous beds, up to several centimetres thick, of intraclastic and peloidal dolorudite–dolarenite. Abundant evidence for sediment disruption, including abundant tepee structures (Fig. 8C), which are indicative

Table 1
Description of facies.

Facies	Constituents	Bedding and sedimentary structures	Organo-sedimentary structures
Supratidal to upper intertidal facies assemblage			
Stratiform stromatolite	Dolomicritic/-microsparitic and detritus-rich laminae; intraclasts; partially silicified peloids; scattered detrital quartz particles	Wrinkly, continuous to discontinuous, partially silicified, sporadically disrupted laminae 0.1–4 mm in thickness; calcite-filled fenestrae up to 2 mm in diameter; mudcracks; tepees with up to 15 cm of vertical relief and a typical spacing of 50 cm	Stratiform stromatolites; isolated or laterally-linked, small-scale domal stromatolites with internal wrinkly lamination (up to 5 cm in diameter); massive microbialites
Intraclast dolomitic sandstone	Dolomite-cemented sandstone with rectangular, micritic and sandy intraclasts typically 1–3 cm but up to 20 cm in length	Disrupted thin bedding; calcite-filled fenestrae up to 1 cm in diameter	Stratiform and small-scale domal stromatolites (1–15 cm in width and 1–10 cm in height, synoptic relief up to 5 cm), massive microbialites
Sandy intradolorudite	Tabular micritic intraclasts up to 15 cm in length set in a matrix of fine to coarse sandy dolomite with scattered quartz particles; rare pyrite nodules	Massive; partially disrupted wrinkly laminae; calcite-filled fenestrae	Massive domal microbialites (c. 15 cm in width and height); stratiform stromatolites; single column digitate stromatolites (1 cm in width and up to 5 cm in height)
Middle–lower intertidal to subtidal facies assemblage			
Ripple-laminated dolomitic sandstone	Medium quartz sand; mud drapes	Wave-ripple lamination with mud drapes; flaser-wavy bedding	Domal stromatolites up to 20 cm in height and 10–15 cm in width
Planar cross-bedded sandstone	Well-sorted coarse to very coarse sand; local sandstone and micrite intraclasts concentrated along the foresets of cross-beds	Thin (<12 cm) tabular beds with planar cross-bedding; wave-ripple laminated intervals; hummocky cross stratification in the middle carbonate section	Microbially-induced sedimentary structures
Wave-rippled dolarenite-dololutite	Quartz-rich fine-grained dolarenite and silicified dololutite pairs; partly silicified peloids	Wave-ripple lamination; mud drapes	Isolated polylobate domal microbialites up to 150 cm in width and 60 cm in height
Edgewise conglomerate	Randomly oriented, steeply inclined, or vertically stacked micrite intraclasts up to several cm in length	Massive	–
Sandy oolitic intradolorudite	Flat-lying to randomly oriented micrite intraclasts up to 4 cm length; fine-medium sand-sized quartz sand up to 10 vol.% in a recrystallized micrite to microsparite matrix; partially silicified micritic peloids, concentric and composite ooids	Massive; normal coarse tail grading; fenestrae	Sporadic wrinkly laminae; massive dololutite lenses
Sandy oodolarenite	Quartz-rich and quartz-free dolarenite pairs; partially silicified/micritized superficial ooids and peloids; intraclasts; lapilli	Tabular bedding; planar to trough cross-bedding; normal graded bedding; wave ripples occasionally	Silicified wrinkly lamina; massive dololutite lenses up to 10 cm in length
Oncolite	Micritic, marginally silicified symmetric, asymmetric to irregularly concentric oncoids (2–10 mm in diameter). Minor micrite intraclasts up to 3 cm in size; volcaniclastic and quartz sand particles; heterogeneous groundmass of micrite and dolomite/quartz cement	Massive to crude thin planar bedding; fold-like structure	Small-scale digitate-like stromatolites
Dolomitized lapillistone	Partially dolomitized vesicular to massive lapilli up to several millimetres; micritic intraclast up to 2 cm; medium to coarse sand-sized quartz grains, set in a dolomicrosparitic to dolosparitic cement	Massive; calcite-filled voids up to 3 mm	Massive domal microbialites up to several cm in size
Shale	Silt- to fine sand-sized quartz	Planar lamination; lenticular bedding	–
Tidal channel facies assemblage			
Cross-bedded sandy intradolorudite	Intraclasts, very coarse quartz sand, rare lapilli up to 3 mm in diameter in a dolomite and chert cement; pebble to cobble-sized, tabular rip-up clasts of rippled dolarenite facies and silicified stromatolitic clasts	Planar and trough cross-bedding; erosional base; rip-up clasts form imbricated lag deposits and are aligned and concentrated within foresets	Conical stromatolites typically silicified
Conical/columnar stromatolite	Alternation of dolomicritic–dolomicrosparitic laminae; laminae enriched in detrital particles and silicified laminae	Parabolic to steeply convex lamination	Single and composite conical and columnar stromatolites

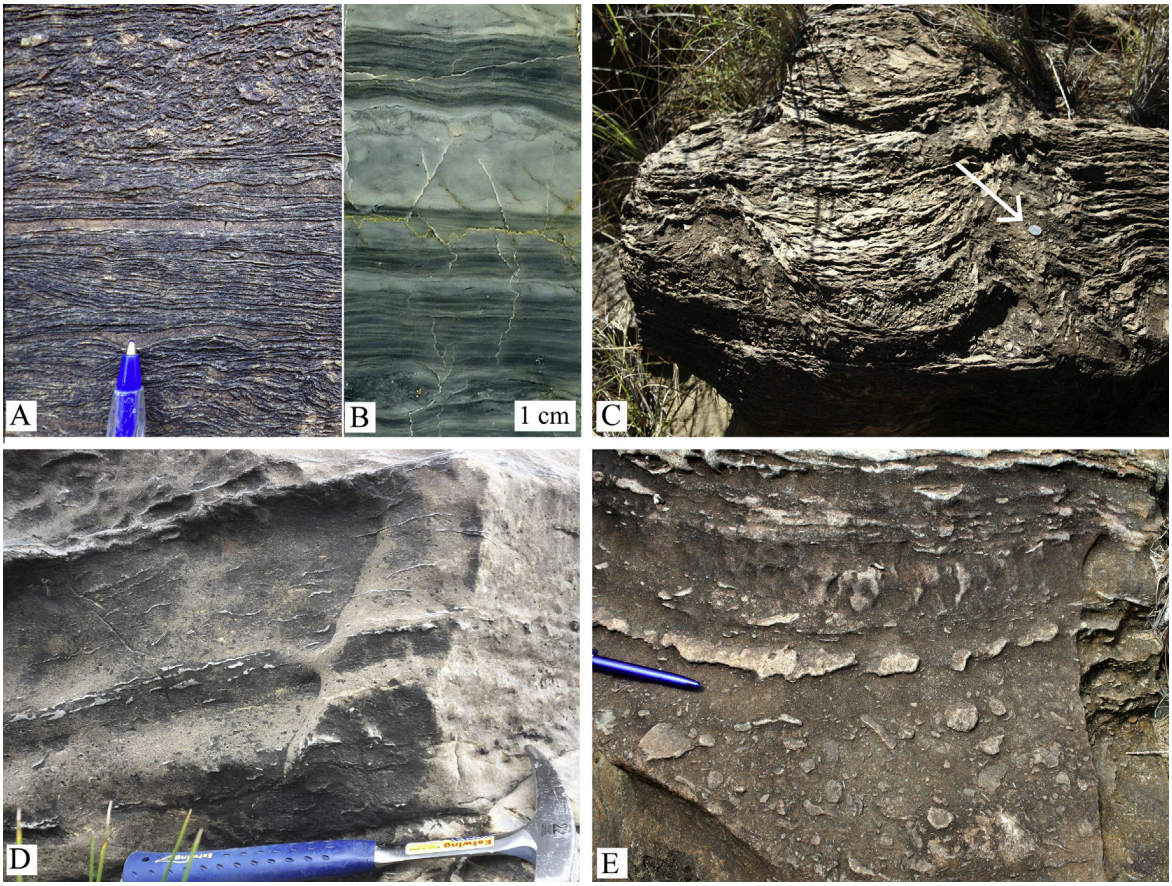

Fig. 8. Photographs showing features of the supratidal to upper intertidal facies assemblage. (A) Alternation of silicified stromatolitic (light bands) and dolomicritic laminae of the stratiform stromatolite facies. Note disrupted laminae and intraclasts at the top of photo. (B) Polished slab showing close-up image of stratiform stromatolite (laminated parts) and massive planar structureless microbialites. (C) Tepee structures in stratiform stromatolite facies; coin for scale (arrow). (D) Alternating intraclast dolomitic sandstone with ripple-laminated dolomitic sandstone. Note rip-up clasts of sandy rippled and wrinkled laminae. (E) Sandy intraclasts (positive relief) scattered in a micritic matrix of sandy dolomite.

of sediment convolution due to dewatering and/or gas escape, and small-scale domal stromatolites, suggest very shallow-water conditions and frequent subaerial exposure and desiccation (Shinn, 1986; Beukes and Lowe, 1989; Pratt et al., 1992; Chakrabarti et al., 2014).

5.1.2. Intraclast dolomitic sandstone facies

This facies (Fig. 8D; Table 1) alternates with stratiform stromatolite and the wave ripple-laminated dolomitic sandstone facies. It is well developed near the base of the main carbonate section (Fig. 5). The disruption and ripping up of micritic laminae and semi-cohesive, sandy laminae are indicative of periodic subaerial exposure. Reworking of disrupted sediment probably took place by storm surges inundating supratidal–intertidal environments (Hardie and Ginsburg, 1977; Shinn, 1983).

5.1.3. Sandy intradolorudite facies

Sandy intradolorudite (Fig. 8E; Table 1) is well developed near the base of the main and near the top of the upper carbonate sections (Figs. 5 and 6). The considerable amount of micritic intraclasts indicates that this facies was subjected to occasional high-energy events following desiccation on intertidal/supratidal flats.

5.2. Middle–lower intertidal to subtidal facies assemblage

Nine facies were defined to have formed in mid-intertidal to deep subtidal environments. The abundance of the different facies varies between the different sections studied in the field and not all facies are present in all sections.

5.2.1. Ripple-laminated dolomitic sandstone facies

This facies (Table 1; Fig. 9A) is sporadically developed near the base of the main carbonate section (Fig. 5) where it is associated with intraclast dolomitic sandstone and stratiform stromatolite. Sedimentary structures are characteristic for lower intertidal to shallow subtidal environments and record tidal current and slack water phases.

5.2.2. Planar cross-bedded sandstone facies

This facies (Table 1; Fig. 9B) can be found in all sections, but it is very prominent in the lower half of the main carbonate section (Fig. 5, at c. 8 m) where it was subjected to palaeocurrent analysis (Fig. 2). It accumulated in a shallow subtidal environment and represents sheet-like deposits of sand that was moved during continuous wave activity. Rare hummocky cross stratification indicates storm-induced currents. Cross-bedded intraclast dolomitic sandstone is a sub-facies and mostly alternates with wave ripple-laminated dolomitic sandstone. The latter shows a diverse assemblage of microbially-induced sedimentary structures (MISS, Noffke et al., 2001), including erosional pockets, microbial mat chips, sandy intraclasts, and gas escape holes that can be observed in plan view (Figs. 8E and 9C). Evidence for desiccation and rupturing of microbially-bound sand surfaces followed by reworking by currents and wind action indicates subaerial exposure at times.

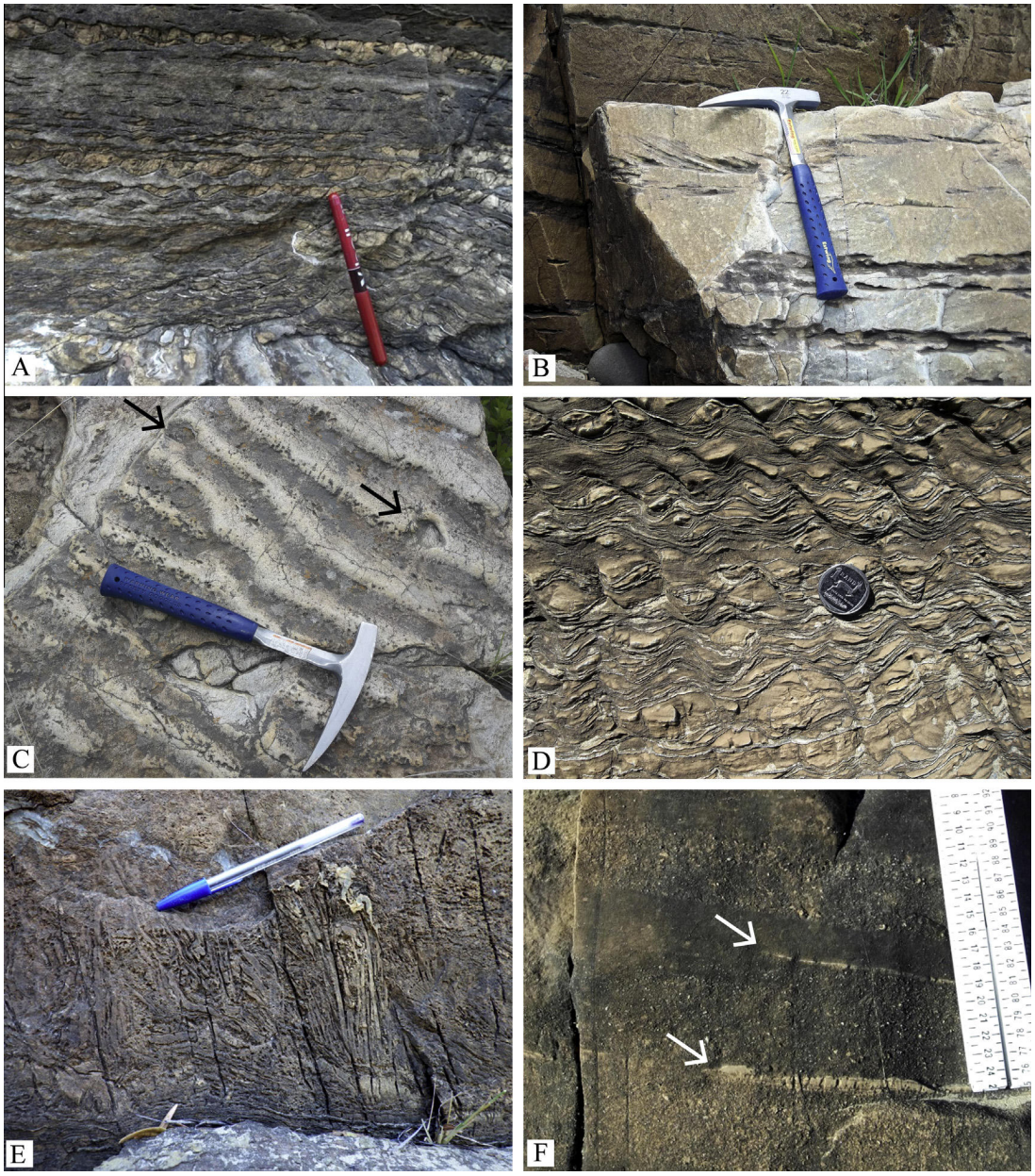

Fig. 9. Photographs showing features of the middle-intertidal to subtidal-facies assemblage. (A) Wavy bedding (centre of photo) grades upward into flaser bedding (top of photo) of the ripple-laminated dolomitic sandstone facies. (B) Thinly planar cross-bedded sandstone facies; note dolomitized ripple-laminated intervals in the lower part. (C) Fossilized "gas holes" (arrows) on top of intertidal sandstone with wave-ripple bedforms. (D) Wave ripple cross-lamination of rippled dolarenite-dololutite facies. Note silicified ripple drapes (light color). (E) Edgewise intraclast conglomerate. (F) Alternation of normally graded beds of sandy oodolarenite and sandy intradolorudite. Lenses of lutite are indicated by arrows.

5.2.3. Wave-rippled dolarenite–dololutite facies

This facies (Table 1; Fig. 9D) forms a distinct horizon in the main carbonate section (Fig. 5, at c. 16.5 m) that can be traced throughout the outcrop area. It is intercalated with sandy oolitic intradolorudite and sandy intradolorudite, but also occurs as part of the tidal channel facies assemblage. Wave ripple lamination indicates wave activity that, in association with mud drapes, point to periods of slack water in a tidal setting. The association with large domal stromatolite, the lack of evidence for exposure, and facies relationships indicate that this facies formed in a shallow subtidal setting.

5.2.4. Edgewise conglomerate facies

This facies (Table 1; Fig. 9E) was only observed at one locality (Fig. 5, at c. 16 m), where it formed a lenticular bed grading laterally into partially disrupted sandy dololutite. Edgewise conglomerates are characteristic deposits of high-magnitude storms in carbonate settings (Sepkoski, 1982; Mount and Kidder, 1993). The association of edgewise conglomerate with sandy dololutite indicate that this facies represents a storm deposit in a muddy subtidal setting.

5.2.5. Sandy oolitic intradolorudite facies

Sandy oolitic intradolorudite (Table 1) is a rare facies that is locally intercalated with rippled dolarenite–dololutite facies (Fig. 5, at c. 16 m). The presence of concentric ooids is indicative of formation in the agitated lower intertidal zone or subtidal sand shoal (Simone, 1981; Halley et al., 1983; Chow and James, 1987; Dill, 1991). The association with coarse-tail grading suggests deposition of this facies by storm events onto intertidal flats subsequently affected by reworking and disruption.

5.2.6. Sandy oodolarenite facies

This facies alternates with the sandy intradolorudite facies (Table 1; Fig. 9F) and is well developed below the prominent oncolite horizon in the main carbonate section (Fig. 5, at c. 18 m). Partially to completely silicified micritic ooids with indistinctive internal structures and superficial ooids are common (Fig. 10A). The association of ooids with current-induced sedimentary structures suggests that this facies formed in high-energy environments, likely in a lower intertidal to shallow subtidal environment that was agitated frequently. Normal graded bedding indicates rapid deposition and waning flow conditions during storm events.

5.2.7. Oncolite facies

The oncolite facies (Table 1; Fig. 10B) is particularly well developed in the main carbonate section. Here it forms a massive to crudely planar-bedded horizon capped by an erosional contact (Fig. 5, at c. 23.5 m). Remnants of silicified small-scale digitate-like stromatolites are rarely preserved and may have resulted from asymmetrical growth of oncoids. The process of deposition of this facies is unclear due to the near-absence of sedimentary structures. In general, oncoids are regarded as an indicator of a low sedimentation rate (Flügel, 2004). The co-occurrence of different oncoid types (large irregular and small spherical oncoids) with rare clastic detritus and crude planar bedding indicate that the oncoids formed in a relatively high-energy subtidal zone episodically influenced by storms.

5.2.8. Dolomitized lapillistone facies

This facies (Table 1; Fig. 4C) forms the immediate substrate of the main carbonate section (Fig. 5), occupying the gradational interval between lapillistone below and carbonate above. It also occurs as a thin single bed (Fig. 10C) intercalated with dolomitic rippled sandstone facies near the base of the main carbonate section (Fig. 5, at c. 1 m). The lapillistone represents a volcanic airfall deposit. Intercalation of lapillistone with carbonate rocks indicates synsedimentary volcanism during the deposition of at least the lower part of the main carbonate section.

5.2.9. Shale facies

Greenish-grey shale up to 45 cm in thickness is present in the lower part of the main carbonate section (Fig. 5). Some laminae consist of fine-grained sandstone and show lenticular bedding. This facies is interpreted to have been deposited in a subtidal environment below the fair-weather wave base. Lenticular bedding indicates the influence of storm waves at times.

5.3. Tidal channel facies assemblage

This assemblage occurs at the top of the main carbonate section (Fig. 5, Section 2). It is restricted to a lenticular unit of c. 5 m thickness and $\geqslant$50 m lateral extent, which is erosively incised into, but may also interfinger laterally with, stratiform stromatolite facies (Fig. 5). Conical/columnar stromatolite and cross-bedded sandy intradolorudite facies are specific characteristics of this assemblage. The rippled dolarenite–dololutite facies, introduced earlier, is common to this association (Fig. 5, Section 2). The tidal channel facies assemblage and the diverse types of stromatolites associated with it was the focus of the study by Beukes and Lowe (1989), who argued for the formation of different stromatolite morphologies under different hydrodynamic regimes in the channel.

5.3.1. Cross-bedded sandy intradolorudite facies

This facies (Table 1; Fig. 10D) forms erosive, lenticular beds up to 50 cm thick and several metres in width and alternates with silicified rippled dolarenite–dololutite. Conical stromatolites are

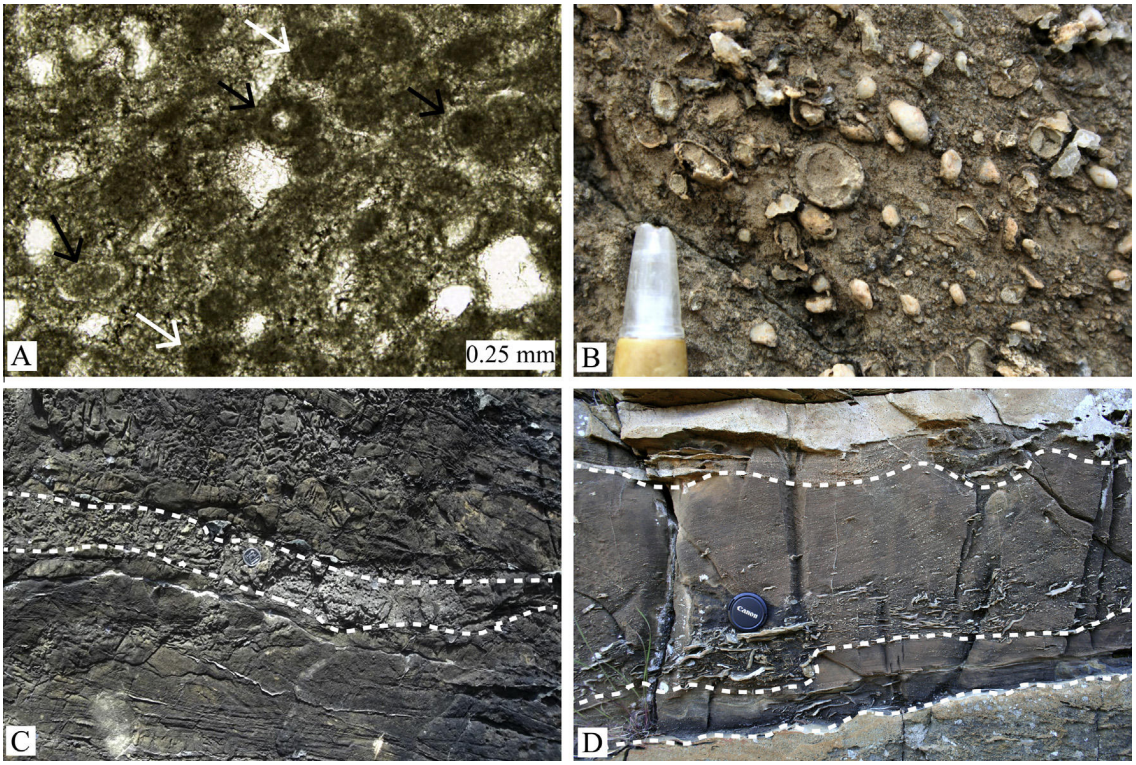

Fig. 10. Photographs showing features of the middle-intertidal to subtidal-facies assemblage. (A) Photomicrograph of micritic (white arrows) and superficial ooids (black arrows); some of the superficial ooids are partly silicified. (B) Silicified oncoids (light features) in a micritic matrix of the oncolite facies; pen tip for scale. (C) Thin bed of lapillistone (indicated by dashed-line) intercalated with dolomitic sandstone; coin for scale. (D) Three beds of the cross-bedded sandy intradolorudite facies of the tidal channel-facies assemblage showing basal lag and scour features; lense cap for scale; bedding planes indicated by dashed-lines.

present in this facies and show growth from the base of the beds upwards. Bi-directional cross-bedding was reported by Beukes and Lowe (1989) from this facies. Bedding characteristics suggest deposition of this facies in a high-energy tidal channel within the lower intertidal to subtidal zone (Fenies and Faugères, 1998; Dalrymple, 2010). It is unclear whether rare lapilli were derived from synsedimentary volcanism or erosion of previously deposited volcaniclastic sediment.

5.3.2. Conical/columnar stromatolite facies

This facies forms the uppermost horizon of the main carbonate section (Fig. 5, Section 2) and consists of morphologically different types of conical and columnar stromatolites that are partially silicified. The stromatolites alternate with, or are surrounded by, sandy dolarenite/intradolorudite and wave-rippled dolarenite–dololutite. A detailed description of stromatolite morphologies was presented by Beukes and Lowe (1989). The close association of stromatolites with coarse clastic carbonate sediment in a high-energy, tidal channel sub-environment suggests that columnar and conical stromatolites formed and remained submerged in a subtidal marine environment similar to some of their modern-day counterparts (Dravis, 1983; Dill et al., 1986; Reid et al., 2003; Jahnert and Collins, 2012).

6. Microbialite types, their microfabrics and carbonate precipitation

Microbialites with a variety of morphologies were observed in different sub-environments, in accordance with previous work (Mason and von Brunn, 1977; Beukes and Lowe, 1989). Minor changes in the physical conditions of the environment can influence microbial assemblage and as a result change microbialite morphology (Burns et al., 2004; Andres and Reid, 2006; Jahnert and Collins, 2012). While there is a clear environmental control on the different carbonate facies, the origin of carbonate precipitation needs to be evaluated. Carbonates can precipitate abiotically from supersaturated waters (Fouke et al., 2000), induced by oxygen-producing photosynthetic bacteria or mediated by

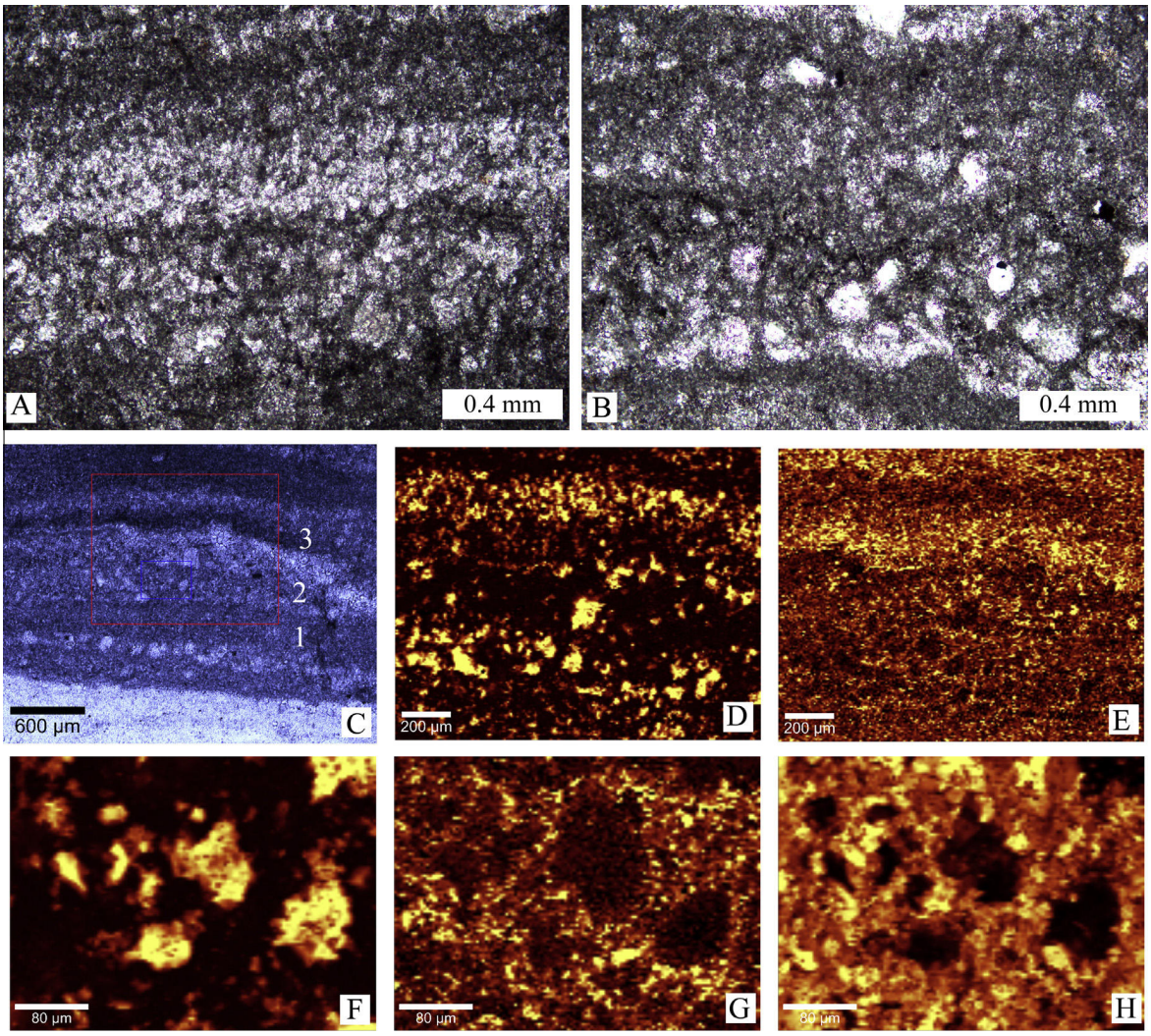

Fig. 11. Photomicrographs of stratiform stromatolite and results of Raman mapping of laminae of the stratiform stromatolite facies, showing relationship between dolomite, detrital quartz particles and carbonaceous matter. (A) Close-up image of the lower laminated part of stratiform stromatolite in image (8A), showing the alternation of dolomicrite and dolomicrosparite laminae, which are partially silicified. Dispersed dark material is carbonaceous matter. (B) Stratiform stromatolite showing dolomitic laminae with varying abundances of sand-sized detritus. Particles float in a micritic matrix with remnants of carbonaceous matter. (C) Photomicrograph showing areas subjected to Raman mapping which comprise of alternation of dolomicrosparite laminae free of quartz particles (1), dolomicrosparite laminae with quartz particles agglutinated with carbonaceous matter (2) and carbonaceous matter-rich laminae (3). Boxes show mapped areas. (D and F) Raman maps of the distribution of the quartz band at ~467 cm^{-1}, (H) dolomite band at ~1100 cm^{-1} and (E and G) carbonaceous matter G band at ~1589 cm^{-1} in stromatolitic laminae. Brighter areas within Raman maps reflect higher intensities of mineral-specific spectra. Note carbonaceous matter surrounding detrital quartz (F and G), indicating trapping of quartz by microbial mat.

degradation of organic matter by heterotrophic bacteria (Canfield and Raiswell, 1991; Chafetz and Buczynski, 1992; Andres and Reid, 2006). The carbonates reported here are mostly confined to facies with microbialites, which indicates that microbial processes played a major role in carbonate precipitation.

6.1. Stromatolites

Supratidal environments are characterized by stratiform stromatolites that formed by lateral growth as a result of limited accommodation space. They consist of alternation of dolomicrite and dolomicrosparite laminae (Fig. 11A). This may indicate that *in situ* precipitation of carbonate took place within microbial mats. This process has been recognized in Proterozoic stromatolites, considered comparable to some of their modern counterparts (Seong-Joo and Golubic, 1999; Seong-Joo et al., 2000; Préat et al., 2011). In places, quartz-free dolomitic laminae alternate with dolomitic laminae agglutinated with remnants of carbonaceous matter and floating quartz particles (Fig. 11B–H). This relationship is probably indicative of trapping and binding of carbonate mud and clastic detritus by bacteria-derived exopolymeric substances (Awramik, 1984; Golubic, 1991; Gerdes et al., 1993; Dupraz et al., 2004, 2009; Dupraz and Visscher, 2005), similar to processes that formed the same facies described in the rock record and in modern supratidal to intertidal environments (Golubic, 1992; Visscher et al., 1998; Reid et al., 2000).

In supra- to intertidal environments, laterally linked, small-scale domal stromatolites are developed sporadically (Fig. 12A). Domes are eccentrically laminated, isolated to contiguous ovoids on bedding planes. Small-scale, digitate stromatolites can be observed locally (Fig. 12B). Restricted environmental conditions, subject to periodic wetting by strong currents, has previously been suggested for the development of ancient digitate stromatolites (Howe, 1966; Grey and Thorne, 1985).

Facies that formed in middle–lower intertidal to shallow subtidal environments contain domal stromatolites with their size correlating positively with inferred water depth (Table 1; Fig. 12C). Similar morphological types are known from modern marine intertidal mudflats, protected lagoons, and shallow subtidal environments (Logan et al., 1964; Monty, 1967; Jahnert and Collins, 2012). Domal stromatolites consist of alternations of silicified sandy dolomitic laminae and dololutite laminae. Carbonate precipitation and minor trapping and binding is indicated.

In the tidal channel facies assemblage, conical and columnar stromatolites are present as single and composite forms and display variations in size and shape (Fig. 13A). Isolated single conical stromatolites are predominantly erect, slender and unbranched with asymmetrical, smooth, parabolic to steeply convex laminae. The majority of the conical stromatolites have smooth walls. Laminae are sharply pointed or rounded at their tops. Low-relief cones are 1–5 cm in width and 3–10 cm in height. Laterally-linked contiguously to closely-spaced conical stromatolites of 20–60 cm in width and up to 130 cm in height and positioned 4–25 cm apart are developed sporadically (Fig. 13B). In conical stromatolites, a slight inclination from one set of laminae to the other set can be observed (Fig. 13C), although the number of lamina in each set could not be determined. The thickness of laminae changes across cones and becomes thicker at the crest (Figs. 13D). Columnar stromatolites vary in terms of size, shape of laminae, and spacing from neighboring columns. Linkages between openly and closely spaced columns are common. Centimetre-sized branching columns, which are partly linked, form a compound mass of a colloform structure (Fig. 14A). Laminae are wrinkled, wavy and asymmetric and intersect uneven column margins at acute angles or are almost parallel thus forming thin-layered walls. Different types of laminae of columnar stromatolites were identified in polished slabs based on differences in color, composition and thickness (Fig. 14B). On the microscopic scale, they include dolomicritic to dolomicrosparitic laminae 0.2–0.8 mm in thickness, micritic laminae with detrital particles of quartz and micritic fragments up to 0.1 mm

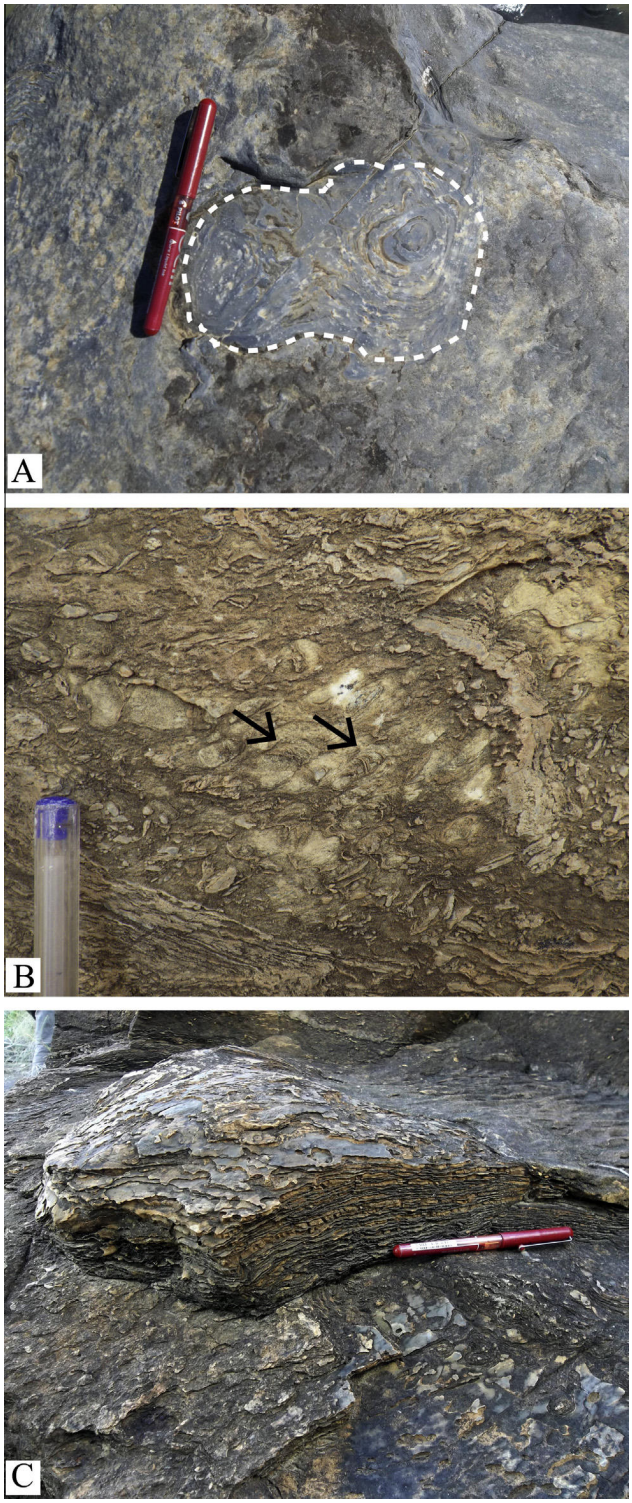

Fig. 12. Photographs showing different types of microbialites from supra- to shallow subtidal environments. (A) Plan view of laterally-linked domal stromatolites, outlined by dashed line, and surrounded by dolomitic sandstone of the intraclast dolomitic sandstone facies. (B) Digitate stromatolites (arrows) surrounded by intradolorudite. (C) Oblique view of partially silicified domal stromatolite in ripple-laminated dolomitic sandstone.

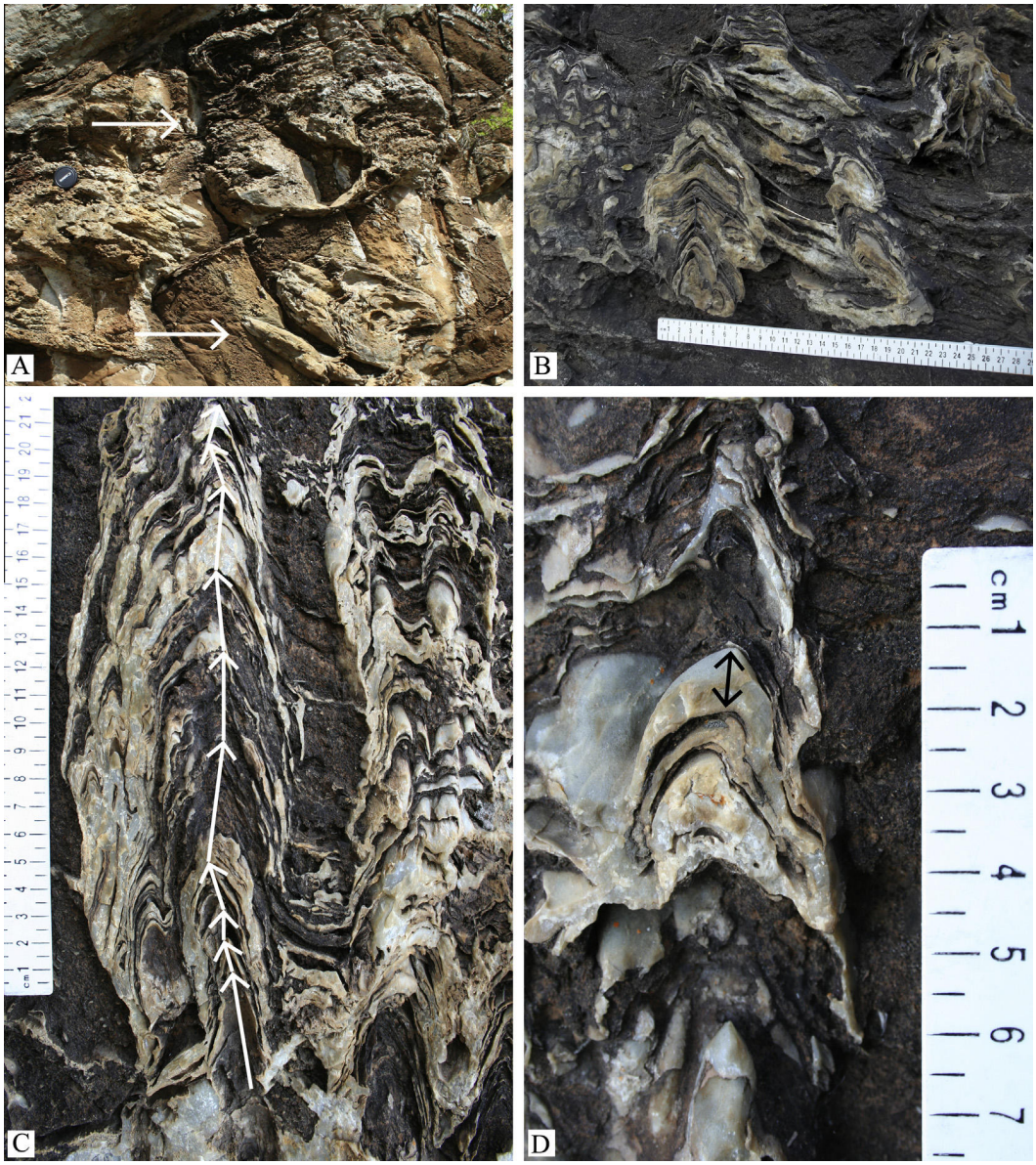

Fig. 13. Photographs showing different types of conical/columnar stromatolite facies; note the selective silicification of stromatolites in the light-colored domains. (A) Silicified composite conical stromatolite at the bottom and composite columnar stromatolites at the top of the image indicated by arrows. Note some rotation of the stromatolites into the plane of foliation. (B) Closely-spaced laterally-linked conical stromatolites. (C) Laterally linked conical stromatolite with centimetre-size silicified fragments within interspaces of cones; note inclination from one set of laminae to the other (arrows). (D) Crestal thickening (arrow) in a conical stromatolite.

thick, and silicified laminae with remnants of dolomite 0.2 mm in thickness.

The space between the columns of conical and columnar stromatolites is filled by sandy dolarenite/intradolorudite, while clastic particles within stromatolitic laminae consist of silt sized grains. The linkage and extension of stromatolitic laminae into the surrounding dolarenite/dolorudite indicates concomitant stromatolite growth and coarse detrital sediment deposition (Fig. 13C).

Abundant accommodation space along with strong tidal and (storm) wave-induced currents provided a suitable environment for the growth of conical, as well as large-scale stromatolites in the tidal channel at the top of the main carbonate section. This finding highlights once more the role of physical processes in sculpturing morphology of stromatolites. The conical stromatolites described here formed in shallower environments than their younger, especially Proterozoic counterparts, which seem to have predominantly formed in relatively deep subtidal settings below or close to the fair-weather wave base (Grotzinger, 1989; Kah et al., 2006).

The conical shape and crestal thickening of conical stromatolites (Fig. 13D) together with variations in the inclination from one set of laminae to the other set (Fig. 13C) can be explained with the presence of phototrophic microorganisms (Walter et al., 1976; Walter, 1983; Beukes and Lowe, 1989). Petroff et al. (2010) suggested that centimetre-scale spacing between conical stromatolites reflects competition for nutrients and corresponds to rhythmically fluctuating metabolism related to the length of day in support of an origin of conical stromatolites by photosynthetic bacteria. Sim et al. (2012) suggested that conical stromatolites from the 2.7 Ga Tumbiana Formation (Flannery and Walter, 2012) argue for O_2-dependent behavior of microbes in shallow-water environments. Therefore, we assume immediate

environmental conditions, such as availability and competition for nutrients, fluctuations in light intensities and microbial metabolic pathways, played an active role in shaping the conical morphology.

6.2. Oncoids

Microbialites in the form of coated grains are present as oncoids. Spherical oncoids with symmetric laminations are considered as products of continuous movement in high-energy conditions during growth from permanently submerged areas in lower intertidal and shallow subtidal environments (Logan et al., 1964; Leeder, 1975; Smith, 1986; Flügel, 2004). The larger, asymmetric oncoids with upright growth features (Fig. 7C and D) probably developed in static conditions below the wave base in which bacteria preferentially colonized the sides and top of nuclei, resulting in the asymmetric laminae in oncoids (Peryt, 1981; Ratcliffe, 1988). Variation in cortical thickness (thin cortex along the inferred undersides of oncoids in contrast to thicker laminae on opposite sides) is best explained by preferential growth along sides of a grain exposed to the sediment/water interface of well-illuminated areas by phototrophic microorganisms. The absence of trapped detrital particles within oncoid's laminae suggests microbially induced carbonate precipitation, but may also point to the dearth of clastic material associated with the oncolite facies.

6.3. Structureless microbialites

Non-laminated, i.e. structureless microbialites occur as two types, (1) massive domes and (2) dololutite lenses. They are developed in various, most commonly inter- to supratidal facies (Figs. 5 and 6). Massive domal microbialites are typically c. 30 cm in width and 15 cm in height (Fig. 14C and D). Some domes contain different carbonate particles including peloids and coated grains admixed with siliciclastic detritus and embedded in micrite and microsparite (Fig. 14E). Others are made of dololutite fragments with floating coarse quartz grains separated by a quartz sand-rich matrix. Some domes show concave-upward walls and *in situ* disruption of lamina remnants.

Dololutite lenses are a few centimetres in height and a few decimetres in width (Fig. 9F). The lenses are typically massive or have a faint lamination. Irregular to wavy tops indicate lense formation by microbial processes. Irregular to sub-spherical fenestrae up to 1.5 cm in diameter are common. The lenses contain generally less quartz sand than their host rocks.

The presence of allochems within some massive microbialite domes may suggest trapping of particles within microbial colonies brought to the site by high-energy currents. In contrast, the large variety of particles may also suggest possible disruption of previously deposited sediment during microbialite growth. *In situ* disruption is compatible with the notion that some domes have been initiated as tepees that experienced modification by microbial carbonate precipitation and possible sedimentation within tepee centres. On the basis of variation in composition and morphology, non-laminated microbial structures may have formed as a result of different processes, including differences in microorganism assemblage, variation in the nature of sediment supply (Braga et al., 1995), desiccation and disruption, and a combination thereof. Non-laminated microbialites were reported to form by *in situ* calcification of coccoid-dominated microbial communities (Awramik, 1984; Pratt, 1984; Chafetz and Buczynski, 1992).

7. Interpretation of depositional environments

The sedimentological features of the volcaniclastic–siliciclastic–carbonate succession of the Chobeni Formation support deposition in a tide-dominated shallow-marine environment (Mason and Von Brunn, 1977; Von Brunn and Mason, 1977; Beukes and Lowe, 1989; this study). The combination of symmetric and asymmetric ripple marks, abundant mud drapes, flaser, lenticular and wavy bedding, and evidence for bi-directional currents are consistent with tidal activity. The abundance of stratiform stromatolite facies with its characteristic assemblage of structures reflecting intermittent exposure and locally incised tidal channels reflects the presence of widespread intertidal flats at times. While lateral facies relationships could only be investigated for the main carbonate section, they nevertheless allow tracing of facies assemblages and even single beds over hundreds of metres (Figs. 3 and 5). The presence of coarse-grained clastic subtidal facies, ooids, evidence for storm deposits as well as the abundance of clastic detritus as part of the carbonate sections suggest deposition along a tide-influenced clastic–carbonate shoreline rather than a restricted lagoonal setting. A trace-element geochemical study of carbonates of the main and upper carbonate section supports deposition in a shallow-water epicontinental basin with restricted but variable exchange to the open-ocean (Bolhar et al., 2015).

7.1. Depositional environment of the main carbonate section

The lower part of the main carbonate section shows clearly defined sedimentary cycles that are best preserved in the western section (Fig. 5, Section 1). A total of 6 cycles were observed, ranging in thickness from 0.4 m to 5.7 m (Figs. 5 and 15). The facies are vertically arranged in a shallowing-upward succession that mostly commences with subtidal facies shallowing upward into intertidal and supratidal facies, the latter subjected to periods of subaerial exposure. Cycle boundaries are contacts along which there is an abrupt facies shift from intertidal–supratidal deposits to subtidal deposits. The contacts are sharp to erosional, and the immediately underlying strata show evidence of subaerial exposure.

The cycles begin with a subtidal facies including shale, cross-bedded to flaser-wavy bedded sandstone, rippled dolarenite–dololutite and intradolorudite at the cycle base. Thin intradolorudite beds at the base of some cycles probably represent a transgressive facies. The subtidal facies grade into those of the intertidal–supratidal assemblage such as sandy intradolorudite and stratiform stromatolite.

In one cycle (Fig. 5, cycle b), shale, the deepest sedimentary facies, is overlain by cross-bedded sandstone that grades upwards into intertidal rippled intraclast dolomitic sandstone. Several cycles start with cross-bedded to flaser-wavy bedded sandstone that is overlain by massive to wave-rippled, dolomitic sandstone and succeeded by stratiform stromatolite (Fig. 15B and C). The variation of cycle components may be related to non-deposition as a result of rapid transgression or removal due to subaerial exposure (Pratt and James, 1986).

In the field, cycles consisting of subtidal to inter-/supratidal facies are conspicuous, as they are characterized by clastic-dominated facies at the base, and carbonate-dominated facies at the top (e.g., Fig. 15B and C). In the stratigraphic column (Fig. 5) they are commonly shown with a coarsening-upward pattern, due to the abundance of granule to pebble-sized carbonate allochems such as intraclasts in the carbonate-dominated facies.

Shallowing-upward sedimentary cycles are common components of ancient carbonate platforms (e.g., Pratt et al., 1992), and of tidal flat carbonates in particular (Hardie and Shinn, 1986). Shallowing-upward cycles are a result of relative sea-level changes, and the underlying reasons for their presence have been a topic of long-lasting debate. Various autocyclic and allocyclic models have been proposed to explain the origin of cyclicity (Hinnov, 2013). Despite variations in the form of carbonate production through time, cyclicity in carbonates is not uncommon in Precambrian car-

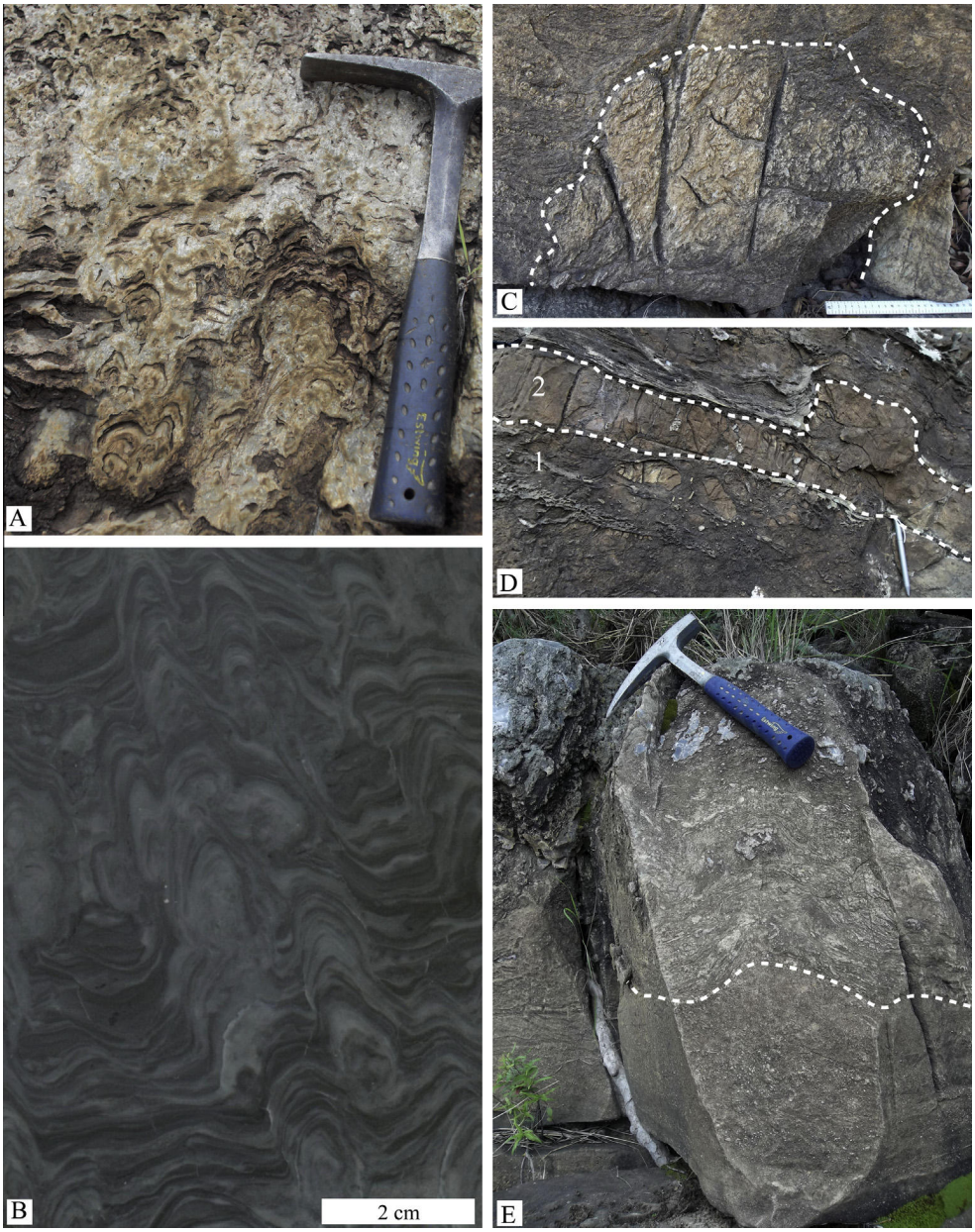

Fig. 14. Photographs showing different types of conical/columnar stromatolite facies and structureless microbialites. (A) Columnar stromatolites form a composite mass with colloform structure. (B) Polished slab of columnar stromatolite showing alternating silicified laminae (light grey), dolomicritic and detrital-rich laminae (dark grey). (C) Structureless domal microbialite outlined by white dashed line in the lower part overlain by crudely laminated stromatolite; pen for scale. (D) Sandy intradolorudite facies (1) overlain by a bed of massive micritic microbialite (2) forming a dome structure. (E) Structureless microbialites with a grain-dominated macrofabric below white dashed line.

bonate successions. The hitherto oldest cyclic carbonates have been described from the late Archaean, c. 2650 Ma Cheshire Formation, Belingwe greenstone belt, Zimbabwe where the controlling mechanism for the cyclicity was ascribed to high-frequency eustatic sea-level changes (Martin et al., 1980; Hofmann et al., 2004).

The cyclic interval is succeeded by a prominent stratiform stromatolite unit containing conspicuous tepee structures (Fig. 8C). There is a hint of cyclic facies development in a sense that wrinkly laminated carbonates are rhythmically interlayered with thin beds of mudstone representing flooding of the supratidal flats. It is not clear if the flooding represents relative sea-level changes or simply large storm events.

The stratiform stromatolite facies is succeeded by rippled dolarenite–dololutite, sandy oolitic intradolorudite, and sandy oodolarenite, suggesting marine transgression to an overall subtidal setting (Fig. 5, at c. 16 m). The presence of edgewise conglomerate together with sandy oolitic intradolorudite in this interval is indicative of episodic high-magnitude storm events. Microbialites are relatively rare in these facies, except for isolated domes.

The oolitic arenite facies grades into the more coarse-grained oncolite facies (Fig. 5, at c. 19 m), which probably formed in a moderately high-energy, permanently submerged subtidal setting. The reason for abundant oncoid formation at this level is unclear to us, but may be related to lack of input of siliciclastic material. This may be related to the formation of a barrier separating the offshore source of siliciclastic sediment from the carbonate tidal flat. The top of the oncolitic horizon is defined by an erosional surface overlain by intradolorudite containing reworked material (such as oncoids) from the underlying bed. Veins of translucent chert oriented perpendicular to bedding locally occur in the oncolite

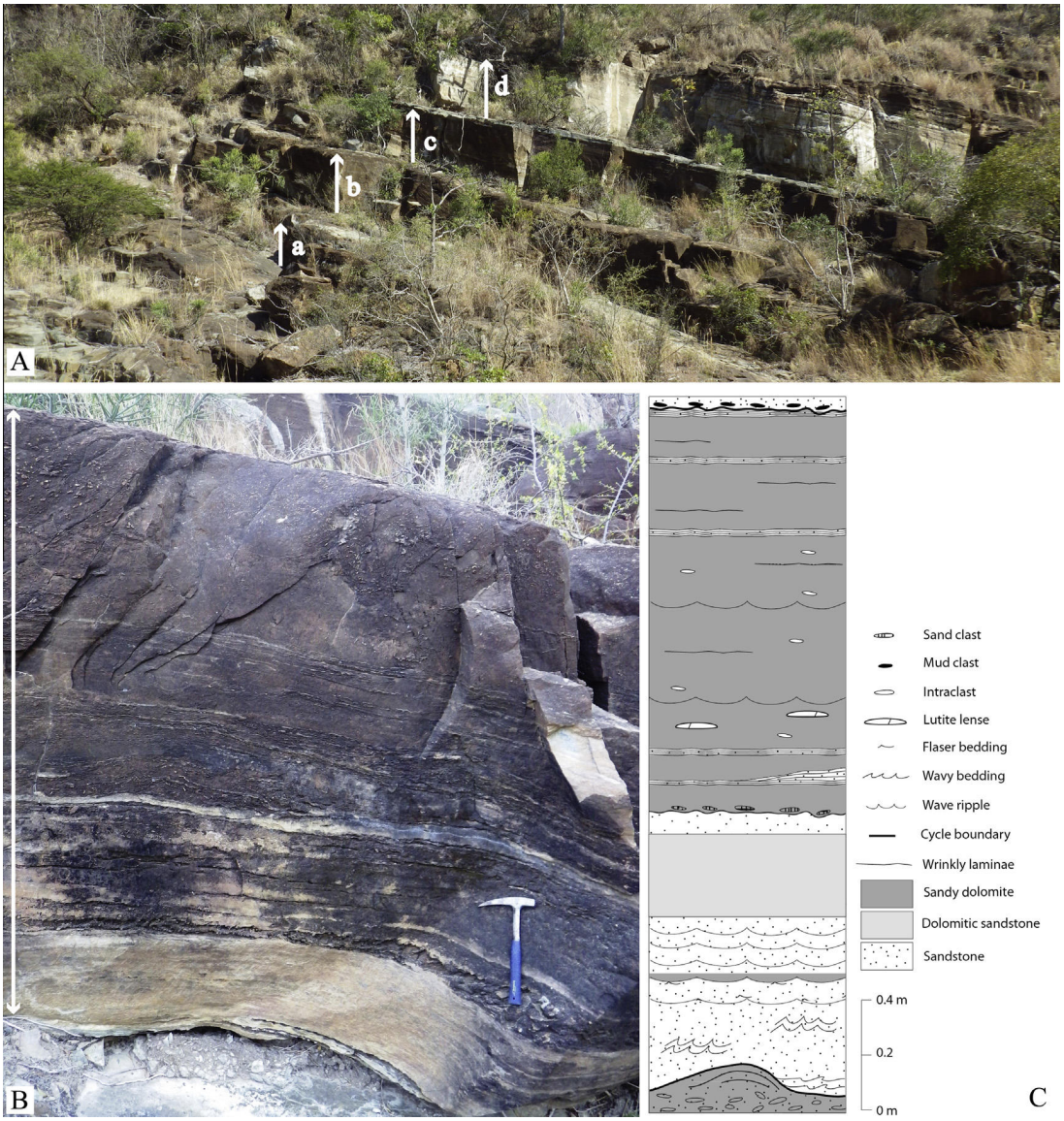

Fig. 15. Photographs showing four sedimentary cycles (a–d) of the lower part of the main carbonate section. See Fig. 5 for locality of cycles. (B) Close-up photograph of cycle c. Note decreasing amount of sand upwards as indicated by color change from light to dark. Arrow shows bottom and top of the cycle. (C) Stratigraphic column of shallowing-upward cycle c.

horizon, but seem not to transect the erosive surface (Fig. 5, Section 2). We thus interpret the erosive contact to have formed as a result of falling sea-level, giving rise to subaerial exposure and localized dissolution of the oncolitic carbonate horizon along narrow fissures. Exposure was followed by sea-level rise and deposition of transgressive intradolorudite overlain by stratiform stromatolite facies. The fissures were later filled with chert, although the timing of the silica precipitation needs to be clarified.

The tidal channel facies assemblage is erosively incised into stratiform stromatolite facies, contrary to the view of Beukes and Lowe (1989). However, discontinuous exposure does not exclude possible lateral interfingering of the two facies as proposed by these authors. Morphologically diverse stromatolites formed in the tidal channel. According to Beukes and Lowe (1989), it had a depth of c. 1.5 m. Single conical stromatolites with high synoptic relief near the base and coalesced domal stromatolites at the top formed as a result of filling of the channel over time.

Transgression led to the establishment of fully subtidal environmental conditions dominated by coarse-grained siliciclastic sediments. Minor carbonate beds and lenses in sandstone above the main carbonate section (Fig. 4D) suggest a return to conditions favorable for carbonate deposition at times.

In the main carbonate section, siliciclastic sediment is present throughout, but concentrated in deeper-water facies, specifically at the base of shallowing-upward cycles in the lower part of the section. Volcaniclastic lapillistone forms the base of the main carbonate section and also occurs as a thin bed interlayered with carbonate near the base. Upsection, the abundance of ash/lapilli diminishes, but it does not disappear completely. While volcanic activity was ongoing during deposition of the lower part, it is not clear if this was the case for the upper part, which may contain only reworked volcaniclastic particles. Hence, the question if the influence of volcanism provided a favorable local geochemical environment for biogenic processes and carbonate precipitation remains unresolved.

7.2. Depositional environment of the middle carbonate section

The middle carbonate section (Fig. 6) is dominated by poorly sorted sandstone. Carbonate is present as thin layers of dololutite,

allochems, and matrix and/or cement in sandstone facies. Common facies include (1) wavy-flaser bedded intraclast sandstone indicative of bimodal currents, (2) mud-cracked mud or lutite layers suggesting periodic subaerial emergence in a tidal flat setting, and (3) cross-bedded, hummocky cross-bedded or normally graded intraclast sandstone with erosive bases suggesting regularly occurring storm events. All of these facies indicate formation in a shallow subtidal to intertidal, predominantly high-energy environment. Palaeocurrent analysis (Fig. 2) indicates unimodal, offshore-directed sediment transport. In contrast to the main carbonate section, upper intertidal and supratidal facies are rare. The only direct evidence for microbial activity in this section includes carbonaceous matter-bearing ooids, peloids and ooid-bearing aggregates. Indirect evidence for microbial activity may be found in the poor sorting of some fine-grained dolomitic sandstone layers containing scattered and very coarse sand grains that may reflect wind- or water-transported material possibly trapped by microbial mats.

7.3. Depositional environment of the upper carbonate section

The upper carbonate section overlies a succession of predominantly cross-bedded and very coarse-grained subtidal sandstones (Fig. 2). It commences with cross-bedded intraclast dolomitic sandstone grading into rippled intraclast dolomitic sandstone with cracked mud drapes suggesting shallowing from a subtital to an intertidal environment (Fig. 6). Wavy bedded sandy dolomite and dolomitic sandstone facies follow and they indicate fluctuation in wave energy in a shallow subtidal environment.

A relatively massive, incompletely exposed unit of oolitic sandy intradolorudite facies forms the middle part of the section (Fig. 6). It shows layers of stratiform stromatolite, dololutite lenses, wave-ripple lamination and evidence for disruption. These features in combination with large intraclasts suggest deposition in a predominantly intertidal to supratidal setting.

Indistinct asymmetric cyclic stacking of facies is observed in the upper part of the succession (Fig. 6) where shallow subtidal facies are overlain by intertidal and supratidal carbonates that show frequent evidence for subaerial exposure. Typically, facies include (from base to top) cross-bedded intraclast dolomitic sandstone, rippled dolomitic sandstone or sandy oodolorudite and stratiform stromatolite with intercalations of intradolorudite that formed as a result of extensive sediment disruption. Lenses, continuous layers and domes of massive dololutite representing massive microbialites are present in supratidal facies of this part of the section. Wedge-shaped to irregular sand-filled fissures probably representing filled desiccation cracks are also common in this interval. Such cracks are frequently observed on the top of massive microbialite beds (Fig. 14D).

Siliciclastic material is present throughout the upper carbonate section, but is typically more concentrated in deeper water facies. Diagenetic pyrite nodules occur sporadically and have only been observed in this section. In contrast to the main carbonate section, microbialites are less diverse and include predominantly non-laminated microbialites and indistinct stratiform stromatolites. The absence of well-developed stromatolitic carbonates indicates unfavorable conditions for the flourishing of microbial communities that are responsible for the formation of laminated microbialites. This may be due to relatively high input of siliciclastic detritus.

8. Conclusions

1. Carbonate rocks of the c. 3.0 billion-years-old Nsuze Group in the White Mfolozi inlier are composed predominantly of dolomite and subordinate ankerite. Coarse-grained clastic subtidal facies, evidence for storm deposits, and the abundance of clastic detritus, as part of the carbonate sections, suggest deposition in a tide-influenced siliciclastic–carbonate shallow-marine environment.
2. Fluctuations of relative sea-level gave rise to cyclic stacking of lithofacies. There is insufficient preservation of sedimentary cycles to make any firm judgement on their origin. The cycles do however indicate that even as far back as 3 billion years ago, shallow-marine carbonates were subjected to cyclic variation in facies stacking much in the same way as in modern carbonate environments.
3. The carbonate rocks contain abundant microbially-induced sedimentary structures, stromatolites, massive microbialites, ooids, and oncoids. The morphology of the microbialites varies systematically with the depositional environment. In general, digitate, stratiform, and small-scale domal stromatolites are limited to supratidal and upper-intertidal settings. Larger domes, conical/columnar stromatolites and oncoids were formed in higher energy, lower intertidal and shallow subtidal settings. The variations in macrofabric, morphology, and size among various microbialites suggest that microbial communities were responding to differences in physical factors that operated in the shallow-marine environment during sea-level changes.
4. The upward growth of oncoids together with crestal thickening, inclination from one set of laminae to the other, and the coniform shape of conical stromatolites is consistent with a phototrophic behavior of microorganisms. Whether these microbes were oxygenic photosynthetic microorganisms remains to be resolved.

Acknowledgements

Field work was supported by funds from the National Research Foundation of South Africa to AH. We thank Lisborn Mangwane and Baldwin Tshivhiahuvhi for preparing the thin sections and polished slabs. MS is grateful to Roger Gibson, School of Geosciences, University of the Witwatersrand, for providing office space during research in South Africa. Two anonymous referees are acknowledged for their constructive criticism. We thank Linda Kah for her substantial editorial input.

References

Allwood, A.C., Walter, M.R., Kamber, B.S., Marshall, C.P., Burch, I.W., 2006. Stromatolite reef from the Early Archaean era of Australia. Nature 441, 714–718.

Altermann, W., Lenhardt, N., 2012. The volcano-sedimentary succession of the Archaean Sodium Group, Ventersdorp Supergroup, South Africa: Volcanology, sedimentology and geochemistry. Precambrian Res. 214–215, 60–81.

Altermann, W., Schopf, J.W., 1995. Microfossils from the Neoarchaean Campbell Group, Griqualand West Sequence of the Transvaal Supergroup, and their paleoenvironmental and evolutionary implications. Precambrian Res. 75, 65–90.

Andres, M.S., Reid, P.R., 2006. Growth morphologies of modern marine stromatolites: a case study from Highborne Cay, Bahamas. Sediment. Geol. 185, 319–328.

Awramik, S.M., 1984. Ancient stromatolites and microbial mats. In: Cohen, Y., Castenholz, R.W., Halvorson, H.O. (Eds.), Microbial Mats: Stromatolites, pp. 1–22, New York, Liss.

Beukes, N.J., 1987. Facies relations, depositional environments and diagenesis in a major early Proterozoic stromatolitic carbonate platform to basinal sequence, Campbellrand Subgroup, Transvaal Supergroup, South Africa. Sediment. Geol. 54, 1–46.

Beukes, N.J., Cairncross, B., 1991. A lithologic–sedimentological reference profile for the Late Archaean Mozaan Group, Pongola-Sequence: application to sequence stratigraphy and correlation with the Witwatersrand Supergroup. South Afr. J. Geol. 94, 44–69.

Beukes, N.J., Lowe, D.R., 1989. Environmental control on diverse stromatolite morphologies in the 3000 Ma Pongola Supergroup, South Africa. Sedimentology 36, 383–397.

Bolhar, R., Van Kranendonk, M.J., 2007. A non-marine depositional setting for the northern Fortescue Group, Pilbara Craton, inferred from trace element geochemistry of stromatolitic carbonates. Precambrian Res. 155 (3), 229–250.
Bolhar, R., Hofmann, A., Siahi, M., Feng, Y., Delvigne, C., 2015. A trace element and Pb isotopic investigation into the provenance and deposition of stromatolitic carbonates, iron stones and associated shales of the ~3.0 Ga Pongola Supergroup, Kaapvaal Craton. Geochim. Cosmochim. Acta 158, 57–78.
Braga, J.C., Martin, J.M., Riding, R., 1995. Controls on microbial dome fabric development along a carbonate–siliciclastic shelf-basin transect, Miocene, SE Spain. Palaios 10, 347–361.
Buck, S.G., 1980. Stromatolite and ooid deposits within the fluvial and lacustrine sediments of the Precambrian Ventersdorp Supergroup of South Africa. Precambrian Res. 12, 311–330.
Burns, B.P., Goh, F., Allen, M., Neilan, B.A., 2004. Microbial diversity of extant stromatolites in the hypersaline marine environment of Shark Bay, Australia. Environ. Microbiol. 6, 1096–1101.
Canfield, D.E., Raiswell, R., 1991. Carbonate precipitation and dissolution: its relevance to fossil preservation. In: Alison, P.A., Briggs, D.E. (Eds.), Taphonomy: Releasing the Data Locked in the Fossil Record. Plenum Press, New York, pp. 411–453.
Chafetz, H.S., Buczynski, C., 1992. Bacterially induced lithification of microbial mats. Palaios 7, 277–293.
Chakrabarti, G., Shome, D., Kumar, S., Stephens 111, G.M., Kah, L.C., 2014. Carbonate platform development in a Paleoproterozoic extensional basin, Vempalle Formation, Cuddapah Basin, India. J. Asian Earth Sci. 91, 263–279.
Chow, N., James, N., 1987. Facies-specific, calcite and bimineralic ooids from Middle and Upper Cambrian platform carbonates, Western Newfoundland, Canada. J. Sediment. Petrol. 57 (5), 907–921.
Crosby, C.H., Bailey, J.V., 2012. The role of microbes in the formation of modern and ancient phosphatic mineral deposits. Front. Microbiol. 3, 3–9.
Dahanayake, K., Gerdes, G., Krumbein, W.E., 1985. Stromatolites, oncolites and oolites biogenically formed *in situ*. Naturwissenschaften 72, 513–518.
Dalrymple, R.W., 2010. Tidal depositional systems. In: James, N.P., Dalrymple, R.W. (Eds.), Facies Models 4. Geological Association of Canada, St. John's, Newfoundland, pp. 201–231, 6.
Davaud, E., Girardclos, S., 2001. Recent freshwater ooids and oncoids from western lake Geneva (Switzerland): indications of a common organically mediated origin. J. Sediment. Res. 71 (3), 423–429.
Dickson, J.A.D., 1966. Carbonate identification and genesis as revealed by staining. J. Sediment. Petrol. 361 (2), 491–505.
Dill, R.F., 1991. Subtidal stromatolites, ooids and lime encrusted muds at the Great Bahama bank margin. In: Osborne, R.H. (Ed.), From Shoreline to Abyss. Contributions in Marine Geology in Honour of Farncis Parker Shephard, 46. SEPM Special Publication, pp. 147–171.
Dill, R.F., Shinn, E.A., Jones, A.T., Kelly, K., Steinen, R.P., 1986. Giant subtidal stromatolites forming in normal salinity water. Nature 324, 55–58.
Dixon, J.G.P., 2004. Archaean geology of the Buffalo River gorge (PhD thesis). University of KwaZulu-Natal, Durban, 263 p.
Donald, R., Southam, G., 1999. Low temperature anaerobic bacterial diagenesis of ferrous monosulfide to pyrite. Geochim. Cosmochim. Acta 63, 2019–2023.
Dravis, J.J., 1983. Hardened subtidal stromatolites, Bahamas. Science 219, 385–386.
Dupraz, C., Visscher, P.T., 2005. Microbial lithification in marine stromatolites and hypersaline mats. Trends Microbiol. 13, 429–438.
Dupraz, C., Visscher, P.T., Baumgartner, L.K., Reid, R.P., 2004. Microbe-mineral interactions: early carbonate precipitation in a hypersaline lake (Eleuthera Island, Bahamas). Sedimentology 51, 745–765.
Dupraz, C., Reid, R.P., Braissant, O., Decho, A.W., Sean Norman, R.S., Visscher, P.T., 2009. Processes of carbonate precipitation in modern microbial mats. Earth Sci. Rev. 96, 141–162.
Fahraeus, L.E., Slatt, R.M., Nowlan, G.S., 1974. Origin of carbonate pseudopellets. J. Sediment. Petrol. 44, 27–29.
Fenies, H., Faugères, J.C., 1998. Facies and geometry of tidal channel-fill deposits (Arcachon Lagoon, SW France). Mar. Geol. 150, 131–148.
Flannery, D.T., Walter, M.R., 2012. Archean tufted microbial mats and the Great Oxidation Event: New insights into an ancient problem. Aust. J. Earth Sci. 59, 1–11.
Flügel, E., 2004. Microfacies of Carbonate Rocks: Analysis, Interpretation and Application. Springer-Verlag, Germany, p. 976.
Folk, R.L., 1959. Practical petrographic classification of limestones. Am. Assoc. Pet. Geol. Bull. 43, 1–38.
Folk, R.L., 1962. Spectral subdivision of limestone types. In: Ham, W.E. (Ed.), Classification of Carbonate Rocks-A Symposium, vol. 1. American Association of Petroleum Geologists Memoir, pp. 62–84.
Fouke, B.W., Farmer, J.D., Des Marais, D.J., Pratt, L., Sturchio, N.C., Burns, P.C., Discipulo, M.K., 2000. Depositional facies and aqueous-solid geochemistry of travertine-depositing hot springs (Angel Terrace, Mammoth Hot Springs, Yellowstone National Park, USA). J. Sediment. Res. 70 (3), 565–585.
Fralick, P., Riding, R., 2015. Steep Rock Lake: Sedimentology and geochemistry of an Archean carbonate platform. Earth Sci. Rev. 151, 132–175.
Friedman, G.M., 1959. Identification of carbonate minerals by staining methods. J. Sediment. Petrol. 29, 87–97.
Gerdes, G., Claes, M., Dunajtschik-Piewak, K., Riege, H., Krumbein, W.E., Reineck, H. E., 1993. Contribution of microbial mats to sedimentary surface structures. Facies 29, 61–74.
Gerdes, G., Dunajtschik-Piewak, K., Riege, H., Taher, A.G., Krumbein, W.E., Reineck, H.E., 1994. Structural diversity of biogenic carbonate particles in microbial mats. Sedimentology 41, 1273–1294.
Gold, D.J.C., 2006. The Pongola Supergroup. In: Johnston, M.R., Anhaeusser, C.R., Thomas, R.J. (Eds.), The Geology of South Africa. Geological Society of South Africa/Council for Geoscience South Africa, pp. 135–147.
Golubic, S., 1991. Modern stromatolites-a review. In: Riding, R. (Ed.), Calcareous Algae and Stromatolites. Springer-Verlag, Heidelberg, pp. 541–561.
Golubic, S., 1992. Stromatolites of Shark Bay. In: Margulis, L., Olendzenski, L. (Eds.), Environmental Evolution: Effects of the Origin and Evolution of Life on Planet Earth. Cambridge University Press, Cambridge, pp. 131–147.
Grey, K., Thorne, A.M., 1985. Stratigraphic significance of stromatolites in shallowing sequences of the early Proterozoic Duck Creek dolomite, Western Australia. Precambrian Res. 29, 183–206.
Grotzinger, J.P., 1989. Facies and evolution of Precambrian carbonate depositional systems: emergence of the modern platform archetype. In: Crevello, P.D., Wilson, J.L., Sans, J.F., Read, J.F. (Eds.), Controls on Carbonate Platform and Basin Development, 44. SEPM Special Publication, Tulsa, pp. 79–106.
Gumsley, A.P., Olsson, J.R., Söderlund, U., De Kock, M.O., Hofmann, A., Klausen, M.B., 2015. Precise U–Pb baddeleyite age dating of the Usushwana Complex, southern Africa – implications for the Mesoarchaean magmatic and sedimentological evolution of the Pongola Supergroup, Kaapvaal Craton. Precambrian Res. 267, 174–185.
Halley, R.B., Harris, P.M., Hine, A.C., 1983. Bank margin environment. In: Scholle, P. A., Bebout, D.G., Moore, C.H. (Eds.), Carbonate Depositional Environments, vol. 33. American Association of Petroleum Geologists Memoir, pp. 463–506.
Hardie, L.A., Ginsburg, R.M., 1977. Layering: The origin and environmental significance of lamination and thin bedding. In: Hardie, L.A. (Ed.), Sedimentation on the Modern Carbonate Tidal Flats of Northwest Andros Island, Bahamas. Johns Hopkins University Press, Baltimore, pp. 50–123.
Hardie, L.A., Shinn, E.A., 1986. Carbonate depositional environments, modem and ancient. Part 3. Tidal flats. Colorado School Mines Q. 81, 1–74.
Hegner, E., Kröner, A., Hofmann, A.W., 1984. Age and isotopic geochemistry of the Archaean Pongola and Ushushwana suites in Swaziland, Southern Africa: A case for crustal contamination of mantle-derived magmas. Earth Planet. Sci. Lett. 70, 267–279.
Hegner, E., Kröner, A., Hunt, P., 1994. A precise U–Pb zircon age for the Archaean Pongola Supergroup volcanics in Swaziland. J. Afr. Earth Sci. 18 (4), 339–341.
Henderson, J.B., 1975. Archean stromatolites in the northern Slave province, Northwest Territories, Canada. Can. J. Earth Sci. 12, 1619–1630.
Hicks, N., Hofmann, A., 2012. Stratigraphy, geochemistry and provenance of the auriferous–uraniferous, fluvial to shallow-marine Sinqeni Formation, Mozaan Group, northern KwaZulu-Natal, South Africa. South Afr. J. Geol. 115 (3), 327–344.
Hinnov, L.A., 2013. Cyclostratigraphy and its revolutionizing applications in the earth and planetary sciences. Geol. Soc. Am. Bull. 125 (11–12), 1703–1734.
Hofmann, A., Dirks, P.H.G.M., Jelsma, H.A., 2004. Shallowing-upward carbonate cycles in the Belingwe Greenstone Belt, Zimbabwe: a record of Archaean sea-level oscillations. J. Sediment. Res. 74 (1), 64–81.
Howe, W.B., 1966. Digitate algal stromatolite structures from the Cambrian and Ordovician of Missouri. J. Paleontol. 40, 64–77.
Jahnert, R.J., Collins, L.B., 2012. Characteristics, distribution and morphogenesis of subtidal microbial systems in Shark Bay, Australia. Mar. Geol. 303–306, 115–136.
Kah, L.C., Bartley, J.K., Frank, T.D., Lyons, T., 2006. Reconstructing sea level change from the internal architecture of stromatolite reefs: an example from the Mesoproterozoic Sulky Formation, Dismal Lakes Group, arctic Canada. Can. J. Earth Sci. 43, 653–669.
Kazmierczak, J., Coleman, M.L., Gruszczynski, M., Kempe, S., 1996. Cyanobacterial key to the genesis of micritic and peloidal limestones in ancient seas. Acta Palaeont. Pol. 41, 319–338.
Leeder, M., 1975. Lower Border Group (Tournaisian) stromatolites from the Northumberland basin. Scot. J. Geol. 11, 207–226.
Logan, B.W., Rezak, R., Ginsburg, R.N., 1964. Classification and environmental significance of algal stromatolites. J. Geol. 72, 68–83.
Loreau, J.P., Purser, B.H., 1973. Distribution and ultrastructure of Holocene ooids in the Persian Gulf. In: Purser, B.H. (Ed.), The Persian Gulf. Springer, Berlin, pp. 279–328.
Lowe, D.R., 1980. Stromatolites 3400-Myr old from the Archaean of Western Australia. Nature 284, 441–443.
Macintyre, I.G., 1985. Submarine cements-the peloidal question. In: Schneidermann, N., Harris, P.M. (Eds.), Carbonate Cements, 36. SEPM Special Publication, Tulsa, USA, pp. 109–116.
Martin, A., Nisbet, E.G., Bickle, M.J., 1980. Archaean stromatolites of the Belingwe Greenstone Belt, Zimbabwe (Rhodesia). Precambrian Res. 13, 337–362.
Mason, T.R., Von Brunn, V., 1977. 3-Gyr-old stromatolites from South Africa. Nature 266, 47–49.
Matthews, P.E., 1967. The pre-Karoo formations of the White Umfolozi inlier, northern Natal. Trans. Geol. Soc. South Afr. 70, 39–63.
Monty, C.L.V., 1967. Distribution and structure of recent stromatolitic algal mats, eastern Andros Island, Bahamas. Ann. Soc. Geol. Belgique 90, 55–100.
Mount, J.F., Kidder, D., 1993. Combined flow origin of edgewise intraclast conglomerates: Sellick Hill Formation (Lower Cambrian), South Australia. Sedimentology 40, 315–329.

Mukasa, S.B., Wilson, A.H., Young, K.R., 2013. Geochronological constraints on the magmatic and tectonic development of the Pongola Supergroup (Central Region), South Africa. Precambrian Res. 224, 268–286.
Noffke, N., Gerdes, G., Klenke, Th., Krumbein, W.E., 2001. Microbially induced sedimentary structures-a new category within the classification of primary sedimentary structures. J. Sediment. Res. 71, 649–656.
Olsson, J.R., Söderlund, U., Klausen, M.B., Ernst, R.E., 2010. U–Pb baddeleyite ages linking major Archean dyke swarms to volcanic-rift forming events in the Kaapvaal Craton (South Africa), and a precise age for the Bushveld Complex. Precambrian Res. 183, 490–500.
Peryt, T.M., 1981. Phanerozoic oncoids – an overview. Facies 4, 197–214.
Petroff, A.P., Sim, M.S., Maslov, A., Krupenin, M., Rothman, D.H., Bosak, T., 2010. Biophysical basis for the geometry of conical stromatolites. Proc. Acad. Nat. Sci. 107, 9956–9961.
Pratt, B.R., 1984. *Epophyton* and *Renalcis*-diagenetic microfossils from calcification of coccoid blue-green algae. J. Sediment. Petrol. 54, 948–971.
Pratt, B.R., James, N.P., 1986. The St George group (Lower Ordovician) of western Newfoundland: tidal flat island model for carbonate sedimentation in shallow epeiric seas. Sedimentology 33, 313–343.
Pratt, B.R., James, N.P., Cowan, C.A., 1992. Peritidal carbonates. In: Walker, R.G., James, N.P. (Eds.), Facies Models: Response to Sea Level Change. Geological Association Canada, pp. 303–322.
Préat, A.L., Delpomdor, F., Kolo, K., Gillan, D.C., Prian, J.P., 2011. Stromatolites and cyanobacterial mats in peritidal evaporative environments in the Neoproterozoic of Bas-Congo (Democratic Republic of Congo) and South Gabon. In: Tewari, V.C., Seckbach, J. (Eds.), Stromatolites: Interaction of Microbes with Sediments, Cellular Origin, Life in Extreme Habitats and Astrobiology, 18. Springer, pp. 43–63.
Ratcliffe, K.T., 1988. Oncoids as environmental indicators in the Much Wenlock Limestone Formation of the English Midlands. J. Geol. Soc. London 145, 117–124.
Reid, R.P., Visscher, P.T., Decho, A.W., Stolz, J.F., Bebout, B.M., Dupraz, C., Macintyre, I.G., Paerl, H.W., Pinckney, J.L., Prufert-Bebout, L., Steppe, T.F., DesMarais, D.J., 2000. The role of microbes in accretion, lamination and early lithification of modem marine stromatolites. Nature 406, 989–992.
Reid, R.P., James, N.P., Macintyre, I.G., Dupraz, C.P., Burne, R.V., 2003. Shark Bay stromatolites: microfabrics and reinterpretation of origins. Facies 49, 45–53.
Reitner, J., Neuweiler, F., 1995. Mud mounds: A polygenetic spectrum of fine-grained carbonate buildups. Facies 32, 1–70.
Schoene, B., Bowring, S.A., 2010. Rates and mechanisms of Mesoarchaean magmatic arc construction, eatern Kaapvaal craton, Swaziland. Geol. Soc. Am. Bull. 122, 408–429.
Seong-Joo, L., Golubic, S., 1999. Microfossil populations in the context of synsedimentary micrite deposition and acicular carbonate precipitation: Mesoproterozoic Gaoyuzhuang Formation, China. Precambrian Res. 96, 183–208.
Seong-Joo, L., Browne, K.M., Golubic, S., 2000. On stromatolite lamination. In: Riding, R.E., Awramik, S.M. (Eds.), Microbial Sediments. Springer-Verlag, Heidelberg, pp. 16–24.
Sepkoski, J.J., 1982. Flat-pebble conglomerates, storm deposits, and the Cambrian bottom fauna. In: Einsele, G., Seilacher, A. (Eds.), Cyclic and Event Stratification. Springer-Verlag, New York, pp. 371–385.
Shinn, E.A., 1983. Tidal flat environment. In: Scholle, P.A., Bebout, D.G., Moore, C.H. (Eds.), Carbonate Depositional Environments, vol. 33. American Association of Petroleum Geologists Memoir, pp. 171–210.
Shinn, E.A., 1986. Modern carbonate tidal flats: their diagnostic features. In: Hardie, L.A., Shinn, E.A. (Eds.), Carbonate Depositional Environments; Part 3: Tidal Flats, vol. 81. Colorado School of Mines Quarterly, pp. 7–35.
Sibley, D.F., 1982. The origin of common dolomite fabrics: clues from the Pliocene. J. Sediment. Res. 52 (4), 1087–1100.
Sim, M., Liang, B., Petroff, A.P., Evans, A., Klepac-Ceraj, V., Flannery, D.T., Walter, M. R., Bosak, T., 2012. Oxygen-dependent morphogenesis of modern clumped photosynthetic mats and implications for the Archean stromatolite record. Geosciences 2, 235–259.
Simone, L., 1981. Ooids: A review. Earth Sci. Rev. 16, 319–355.
Simonson, B.M., Schubel, K.A., Hassler, S.W., 1993. Carbonate sedimentology of the early Precambrian Hamersley Group of Western Australia. Precambrian Res. 60, 287–335.
Smith, D.B., 1986. The Trow Point Bed-a deposit of Upper Permian marine oncoids, peloids and columnar stromatolites in the Zechstein of NE England. Geol. Soc. Lond. Spec. Publ. 22, 113–125.
Srinivasan, R., Shukla, M., Naqvi, S.M., Yadav, V.K., Venkatachala, B.S., Raj, B.U., Rao, D.V.S., 1989. Archaean stromatolites from the Chitradurga schist belt, Dharwar Craton, South India. Precambrian Res. 43, 239–250.
Sumner, D.W., Grotzinger, J.P., 2004. Implication for Neoarchaean ocean chemistry from primary carbonate mineralogy of the Campbellrand-Malmani Platform, South Africa. Sedimentology 51, 1273–1299.
Van Kranendonk, M.J., 2006. Volcanic degassing, hydrothermal circulation and the flourishing of early life on Earth: A review of the evidence from c. 3490–3240 Ma rocks of the Pilbara Supergroup, Pilbara Craton, Western Australia. Earth Sci. Rev. 74, 197–240.
Van Kranendonk, M.J., Webb, G.E., Kamber, B.S., 2003. Geological and trace element evidence for a marine sedimentary environment of deposition and biogenicity of 3.45 Ga stromatolitic carbonates in the Pilbara Craton, and support for a reducing Archaean ocean. Geobiology 1 (2), 91–108.
Visscher, P.T., Reid, R.P., Bebout, B.M., Hoeft, S.E., Macintyre, I.G., Thompson Jr., J., 1998. Formation of lithified micritic laminae in modem marine stromatolites (Bahamas): the role of sulfur cycling. Am. Mineral. 83, 1482–1491.
Von Brunn, V., Hobday, D.K., 1976. Early Precambrian tidal sedimentation in the Pongola Supergroup of South Africa. J. Sediment. Res. 46, 670–679.
Von Brunn, V., Mason, T.R., 1977. Siliciclastic–carbonate tidal deposits from the 3000 m.y. Pongola Supergroup, South Africa. Sediment. Geol. 18, 245–255.
Walter, M.R., 1983. Archaean stromatolites: Evidence of the earth's earliest benthos. In: Schopf, W. (Ed.), Earth's Earliest Biosphere: Its Origin and Evolution. Princeton University Press, Princeton, NJ, pp. 187–213.
Walter, M.R., Bauld, J., Brock, T.D., 1976. Microbiology and morphogenesis of columnar stromatolites (Conophyton, Vacerilla) from hot springs in Yellowstone National Park. In: Walter, M.R. (Ed.), Stromatolites: Developments in Sedimentology 20. Elsevier, Amsterdam, pp. 273–310.
Wilson, A.H., Grant, C.E., 2006. Physical volcanology and compositions of the basaltic lavas in the Archean Nsuze Group, White Mfolozi inlier, South Africa. In: Reimold, W.U., Gibson, R.L. (Eds.), Processes on the Early Earth, vol. 405. Geological Society of American Special Papers, pp. 225–289.
Wilson, A.H., Versfeld, J.A., 1994. The early Archaean Nondweni greenstone belt, southern Kaapvaal Craton, South Africa; Part 2. Characteristics of the volcanic rocks and constraints on magma genesis. Precambrian Res. 67 (3–4), 277–320.
Wilson, A.H., Groenewald, B., Palmer, C., 2013. Volcanic and volcaniclastic rocks of the Mesoarchaean Pongola Supergroup in South Africa and Swaziland: distribution, physical characteristics, stratigraphy and correlations. South Afr. J. Geol. 116 (1), 119–168.
Xie, H., Hofmann, A., Hegner, E., Wilson, A.H., Wan, Y., Liu, D., 2012. Zircon SHRIMP dating confirms a Palaeoarchaean supracrustal terrain in the southeastern Kaapvaal Craton, Southern Africa. Gondwana Res. 21 (4), 818–828.

perhaps a later period of erosion – in this part of the Basin, which lends support to the reciprocal stratigraphic depositional model for the Karoo Basin.

Funding acknowledgement: National Research Foundation/Department of Science and Technology Centre of Excellence for Palaeosciences; University of the Witwatersrand; Palaeontological Scientific Trust and its Scatterlings of Africa programmes.

Palaeomagnetic analysis of the Lower Elliot – Upper Elliot Formation transition (Triassic–Jurassic boundary) in South Africa and Lesotho: an overview

Sciscio, L.[1]; Bordy, E.M.[1]; de Kock, M.[2]

[1]*Department of Geological Sciences, University of Cape Town, Cape Town, South Africa; l.sciscio@gmail.com*

[2]*Department of Geology, University of Johannesburg, Johannesburg, South Africa*

The Elliot Formation, encompassing the Triassic-Jurassic boundary (TJB) within the Karoo Basin, can provide insight into one of the five main Phanerozoic mass extinction events. Dating of the formation and the exact position of the TJB is still tentative. Dinosaur-based biostratigraphic framework suggests a Norian lower Elliot (LEF) and Toarcian upper Elliot Formation (UEF). The first formal magnetostratigraphic column for the Elliot Formation was generated by De Kock in 2003, and produced a composite magnetic zonation pattern splitting the Elliot Formation into four polarity pairs (EF1, EF2, EF3 and EF4), with the TJB falling into a period of normal polarity at the junction of *Euskelosaurus* Range Zone (LEF) and the *Massospondylus* Range Zone (UEF).

The null hypothesis of the current study is that the TJB is marked by geomorphological feature, which based on previous studies, coincides with the biostratigraphic and sedimentological change between the mainly perennial meandering fluvial system deposits of the lower Elliot, and the semi-arid ephemeral stream and floodplain deposits of the upper Elliot formations. Several sites in South Africa and Lesotho (Barkly Pass, Damplaats, Golden Gate National Park, Maseru, Quthing, Likhoele) were drilled at ≤1 m scale over this divide between the LEF and UEF. Two northern sites (Damplaats and Golden Gate National Park) encompass the entirety of the Elliot Formation, with the type section of the formation, in the Barkly Pass, making up almost a complete magnetostratigraphic section of the formation in the southern part of the basin. An additional outcome of the magnetostratigraphic investigations is the attempt to constrain the age of the *Trityldon* Acme Zone in the upper Elliot Formation. To date, the preliminary results demonstrate the stability of the palaeomagnetic samples in the consistency and similarity of polarity patterns between geographically widely separated study sites.

Funding acknowledgement: National Research Foundation; DAAD.

Diverse stromatolite morphologies in the 3 Ga Nsuze Group, Pongola Supergroup, South Africa

Siahi, M.[1]; Hofmann, A.[2]; Hegner, E.[1]; Master, S.[3]

[1]*Department of Earth and Environmental Sciences, Ludwig Maximilian University, Munich, Germany; mehrnazsiahy56@yahoo.com*

[2]*Department of Geology, University of Johannesburg, Johannesburg, South Africa*

[3]*School of Geosciences, University of Witwatersrand, Johannesburg, South Africa*

Sedimentary carbonates are extremely rare in the Palaeo- to Mesoarchaean geological record. They were typically deposited in shallow-water settings as relatively thin sedimentary successions in between episodes of volcanism. Replacement by chert frequently took place. Mesoarchaean stromatolitic carbonates from the *c.* 3.0 Ga Nsuze Group of the Pongola Supergroup in South Africa are amongst the oldest known marine carbonates, and have the potential to record important information on ocean chemistry and the habitat of life on the early Earth. Detailed sedimentological and microfacies analyses of three different stratigraphic sections of carbonates 2–25 m thick exposed in the White-Umfolozi Inlier of KwaZulu-Natal was undertaken to delineate depositional environments of carbonates. The carbonates are intercalated with shallow-marine siliciclastic and volcaniclastic deposits. They consist essentially of dolomite, with minor calcite and ankerite. Siliciclastic detritus is common and suggests trapping and binding by microbial mats. Carbonaceous matter is preserved locally, but does not delineate microbial structures due to dolomitization and recrystallization, the latter associated with greenschist facies metamorphism. Sedimentological investigations revealed different, in part cyclically-stacked sedimentary facies that were deposited in tide-dominated, deep subtidal to supratidal shallow marine environments. Different types of organo-sedimentary structures with a variety of morphologies and sizes are present. Stratiform, small-scale domical and digitate stromatolites formed in supratidal to upper-intertidal settings. Columnar and domical stromatolites, oncoids and domical thrombolite-like fea-

tures formed in lower intertidal to upper subtidal environments and finally, conical stromatolites and composite bioherms with colloform texture formed in the permanently submerged part of a deeper subtidal environment. Distinctive stromatolite/thrombolite morphology suggests the presence of a distinctive assemblage of microorganisms and their response to the different physicochemical conditions of the environment.

Anatomy of a mass extinction: sedimentological and taphonomic evidence for drought-induced die-offs at the Permo-Triassic boundary in the main Karoo Basin, South Africa

Smith, R.M.H.[1]; Botha-Brink, J.[2]

[1]*Iziko South African Museum, Cape Town; rsmith@iziko.org.za*

[2]*National Museum, Bloemfontein*

The southern part of the Karoo Basin of South Africa contains a near complete stratigraphic record of the Permo-Triassic boundary (PTB). Isotope- and magneto-stratigraphy confirm that these predominantly fluvial strata are approximately the same age as zircon-dated marine PTB sections (252 Mya). By August 2013, our team had found 580 *in situ* vertebrate fossils, mostly of the clade Therapsida, in PTB exposures at three widely separated locations in the southern Karoo Basin. Biostratigraphic ranges of the various taxa found in each of the sections reveal three separate phases of die-off within the same roughly 75 metre-thick stratigraphic interval displaying the same sequence of sedimentary facies interpreted as indicative of climatic drying, increased seasonality and the onset of an unpredictable monsoon-type rainfall regime. The three phases of an inferred ecologically-stepped mass extinction are: Phase 1 (45 mB30 m below PTB datum) brought on by lowered watertables, which led to loss of shallow rooting groundcover in the more elevated proximal floodplain areas and the disappearance of the smaller groundcover-grazing herbivorous dicynodonts and their attendant small carnivores. Phase 2 (20B0 m below PTB datum), is the main extinction that occurs in massive maroon/grey mudrock culminating in an event bed of laminated reddish-brown siltstone/mudstone couplets. This facies reflects progressively unreliable rainfall leading to vegetation loss in proximal and distal floodplain areas. The larger tree-browsing herbivores and their attendant carnivores are confined to watercourses before finally disappearing. Phase 3 (25–30 m above PTB datum) occurs in massive maroon siltstone facies with evidence of climatic aridity including the accumulation of mummified carcasses buried by windblown dust. All of the surviving Permian taxa disappear within 30 m of the PTB. Temporal resolution based on accretion rates and pedogenic maturity of each stratigraphic section reveals that Phase 1 and Phase 2 die-offs lasted 21 000 and 33 000 years separated by a short period of 7000 years where no disappearances are recorded and this was followed by 50 000 years of stasis for the final extinction phase, lasting only 8000 years, that removed all the Permian survivor taxa. We propose that the recorded disappearances are real (rather than preferential preservation failure) and that they represent drought-induced die-offs moving progressively up the food chain as the terrestrial ecosystem collapsed; the latter mostly likely caused by volcanogenic greenhouse gas emissions and rapid global warming.

Funding acknowledgement: Department of Science and Technology/National Research Foundation Centre of Excellence for Palaeosciences; National Research Foundation: African Origins Platform.

Breeding behaviour of Early Jurassic sub-polar sauropodomorphs in Patagonia

Smith, R.M.H.[1]; Marsicano, C.A.[2]; Mancuso, A.C.[3]; Pol, D.[4]

[1]*Iziko South African Museum, Cape Town; rsmith@iziko.org.za*

[2]*University Buenos Aries, Argentina*

[3]*CCT-CONICET, Mendoza, Argentina*

[4]*Museo Paleontológico Egidio Feruglio, Trelew, Argentina*

The Late Triassic/Early Jurassic Laguna Colorada Formation of Patagonia contains a unique sub-polar fossil assemblage dominated by the basal sauropodomorph *Mussaurus patagonicus*. This taxon was originally described from several well-preserved post-hatchling specimens associated with egg remains found at the Laguna Colorada type section. Our recent expeditions to this locality have yielded 25 new specimens of this taxon, comprising skeletons of six different ontogenetic stages along with several complete 'nests' of unhatched eggs. We have obtained good zircon dates for the egg-bearing interval at ±192.57 Ma which makes them contemporaneous with the recently described *Massospondylus* egg sites in South Africa. Detailed sedimentological investigation shows the skeletal remains and eggs occur in three distinct horizons within a 3 m-thick bed of mottled light reddish-brown/olive-grey massive siltstone. The bones

Stromatolitic carbonates of the Pongola Supergroup, South Africa: a unique record of surface conditions 3 billion years ago

Siahi M[1*], Hofmann A[2], Hegner E[1], Master S[3], Mayr C[1]

1 – Earth Sciences, LMU, Munich, Germany, *mehrnazsiahy56@yahoo.com 2 - University of Johannesburg, Johannesburg, South Africa 3 - Geosciences, University of the Witwatersrand, Johannesburg, South Africa

Sedimentary carbonates are extremely rare in the geological record older than 2.9 billion years, probably reflecting specific environmental and/or physico-chemical conditions of the oceans not conducive for carbonate precipitation. Rare occurrences of stromatolite-bearing dolomite are present in the c. 3.0 Ga Nsuze Group, Pongola Supergroup, the oldest well preserved successions of epicratonic volcanic and sedimentary rocks on Earth [1].

Three different stratigraphic sections of carbonates 2 - 25 m thick were observed in the Nsuze Group exposed in the White-Umfolozi Inlier of KwaZulu-Natal and investigated sedimentologically, petrographically and geochemically. The carbonates are intercalated with shallow-marine siliciclastic deposits locally containing mafic-ultramafic ash-fall deposits. They consist essentially of dolomite, with minor calcite and ankerite. Secondary silicification and a detrital component are common. Detritus includes abundant carbonate-replaced pyroclastic material and terrigeneous material.

Sedimentological investigations revealed different, in part cyclically-stacked sedimentary facies that were deposited in a tide-dominated, deep subtidal to supratidal shallow marine environment. Different types of organo-sedimentary structures are present, including stratiform stromatolite, domical thrombolite and oncolite. Conical and columnar stromatolites were observed in one section. The presence of a variety of these structures suggests formation by different types of bacteria under different physico/chemical conditions. Carbonaceous matter is preserved, but does not delineate microbial structures due to dolomitisation and recrystallization, the latter associated with greenschist facies metamorphism.

C, O, and Sr isotope analyses are in agreement with previous studies [2]. $\delta^{18}O_{PDB}$ values range from -19.7 to -12.0 ‰, reflecting alteration during metamorphism and/or hydrothermal activity. $\delta^{13}C_{PDB}$ values range from 0.1 to 2.3 ‰ similar to, but slightly more positive, than Phanerozoic marine carbonates. $^{87}Sr/^{86}Sr$ ratios ranges from 0.710 to 0.752, which can be explained, in part, by isotopic exchange with non-carbonate fraction during alteration and, possibly, by high continental influx into the epicontinental setting in which the carbonates were deposited.

[1] Mason T.R. and von Brunn V. (1977). *Nature*, 266, 47-49.

[2] Veizer J., Clayton R.N., Hinton R.W., von Brunn V., Mason T.R., Buck S.G. and Hoefs J. (1990). *Geochim. Cosmochim. Acta*, 54, 2717-2729.

Carbonaceous material characterization of the 3.2 Ga Mapepe Fm, Fig Tree Group, Barberton Greenstone Belt, South Africa (BARB5 drill core, ICDP project, Cradle of Life): new insights from micro Raman spectroscopy analysis

Storme J-Y*, Javaux E J

University of Liège, Belgium, *jystorme@ulg.ac.be

Raman spectra of carbonaceous material (CM) from 30 samples of the BARB 5 drill core (ICDP project, Cradle of Life) were used to characterize thermal maturity, metamorphic grade and metamorphic temperature that have affected rocks of the middle Mapepe Formation (Fig Tree Group, BGB, South Africa). Raman analyses were performed with a Renishaw In via Raman spectrometer coupled to a Leica DM 2500 confocal microscope and with an Ar-ion-50 mW monochromatic 514.5 nm laser source. Laser excitation was adjusted to an on-sample intensity of ca. 2mW (measured with a Coherent Lasercheck Analyser) and focused through a 50x objective to obtain a 1-2 µm spot size. Acquisitions were obtained with an 1800/mm grating with an air cooled (-70°C) 1024x256 pixel CCD array detector. This method enabled a 2000 cm^{-1} spectral detection range. Beam centering and Raman spectra calibration were performed daily on a Si-Al microprocessor chip with a characteristic Si Raman band at 520.5 cm^{-1}. Spectra were manipulated with Wire 3.4™ software. Point analysis measurements were made in static mode (fixed at 1150 cm^{-1}), spectra were collected from 10 different points in each sample, and each spectrum was acquired at 1x10 s running time. Peak parameters (G, D_1, D_2, D_3, D_4-bands; FWHM-D_1, FWHM-D_2; I_G, I_{D1}, I_{D2}, I_{D3}, I_{D4}; A_G, A_{D1}, A_{D2}, A_{D3}, A_{D4}) were obtained by fitting spectra (2-10 spectra by sample) with mixed Lorentzian-Gaussian curves.

Two peaks characteristic of disordered CM were observed in the samples. The G bandsis located at ~1597± 5 cm^{-1} (n=300; ±2σ) and results from in plane vibrations in ordered graphite. The D band (D for disordered) is located at ~1351± 2 cm^{-1} (n=300; ±2σ). The presence of well-developed D_3 and D_4 bands with D_1 band that is more intense than G band (FWHM-D_1 ~60 cm^{-1}) are indicative of rather poorly ordered CM that is typically encountered in lower greenschist-facies. Thermal maturity of CM was evaluated by comparing FWHM-G with G-position. The values fall in the range of those of the ~1.9 Ga Gunflint chert, ~2.7 Ga Tumbiana Fm or ~3.5 Ga Strelley Pool and Apex cherts which indicate that samples have experienced sub-greenschist to lower greenschist facies metamorphism. Another Raman thermal maturity "proxy" consisting in the relation between A_{D1}/A_G and I_{D1}/I_G ratios, which vary systematically with increasing metamorphic grade in metapelites, shows that the CM studied has a crystallinity equivalent to that of the chlorite-zone shales corresponding to lower greenschist facies or less. A tentative geothermometry based on 65 analyses is also proposed for the Mapepe Formation. Four different geothermometers involving R_1, R_2, R_{A1}, R_{A2} parameters were investigated giving a range of mean temperatures evolving from 210°C to 355°C. This range of temperature is in line with the temperature expected for a lower greenschist-facies metamorphism.

Even if all these Raman characterization parameters described above do not allow to elucidate the origins of CM, the parameter FWHM-D_1 plotted against I_{D1}/I_G ratio could, however, give some information about the precursor carbonaceous material of the sample. The values obtained for the Mapepe Formation could be compared to those of the Tumbiana Fm, Strelley Pool Fm and Apex chert but are different from those of the Gunflint chert.

Acknowledgement: This work was supported by EU FP7-ERC StG ELiTE.

Mesoarchaean oxidative shallow marine environment in the Pongola Supergroup, South Africa

M. SIAHI1-2', S. MASTER2, AND A. HOFMANN3

'Department of Earth and Environmental Sciences, Ludwig-Maximilians-Universität, München, Germany (M. SIAHI": mehrnazsiahy56@yahoo.com)
2School of Geosciences, University of Witwatersrand, Johannesburg, South Africa (sharad.master®wits.ac,za)
'Department of Geology, University of Johannesburg, Johannesburg, South Africa (ahofmann@uj.ac.za)

The c. 3.0 Pongola Supergroup is the oldest continental volcano-sedimentary succession deposited on the southeastern Kaapvaal Craton in South Africa and Swaziland, and hosts some of the oldest carbonate rocks on Earth. Sedimentary carbonates older than 2.9 Ga are extremely rare in the geological record due to the absence of physico¬chemical conditions in the oceans favouring biogenic and/or abiogenic carbonate precipitation.

The stromatolite-bearing carbonate rocks of the Nsuze Group, Pongola Supergroup, are intercalated with shallow-marine siliciclastic deposits, and locally contain mafic-ultramafic ash-fall deposits. Microbialites occur in deep subtidal to supratidal shallow marine environments. They are locally closely associated with ash-fall lapillistones, which suggests that volcanic activity may have provided local geochemical environments ideal for microbial colonization and development.

The negative $\delta^{18}O$ (-11.9 to -19.7 ‰ VPDB) and radiogenic Sr isotope (Sr_i = 0.708 to 0.770) values of the carbonates are explained, in part, by isotopic exchange with a non-carbonate fraction during alteration and, possibly, by high continental influx into the epicontinental setting in which the carbonates were deposited. Petrographic and geochemical evidence which suggests the presence of oxygenic photosynthetic bacteria includes 1) the presence of conical stromatolites with features such as erestal thickening and inclination in different sets of laminae, similar to those that have oxygenic photosynthetic metabolism; and 2) a negative Ce anomaly (Ce/Ce^* = 1.05 to 1.12) in carbonate rocks, indicating that seawater from which carbonates precipitated was oxidative. The localized oxidative removal of dissolved Fe^{2+} by photosynthetic microorganisms may have led to the carbonate precipitation within a restricted shallow marine setting. This does not preclude abiogenic carbonate precipitation.

Paper Number: 4843

Textural and geochemical characteristics, and process of formation, of ooids in the Mesoarchaean Pongola Supergroup, South Africa

Siahi, M.[1, 3], Hofmann, A.[2], Hegner, E.[1], Master, S.[3] and Müller, C.W.[4]

[1]Department of Earth and Environmental Sciences, Ludwig-Maximilians-Universität, München, Germany, mehrnazsiahy56@yahoo.com
[2]Department of Geology, University of Johannesburg, Johannesburg, South Africa
[3]School of Geosciences, University of Witwatersrand, Johannesburg, South Africa
[4]Department of Ecology and Ecosystem Management, Soil Science, Technische Universität, München, Germany

Ooids from the Mesoarchaean c. 3.0 Ga Nsuze Group, Pongola Supergroup, South Africa, are the oldest well-preserved microbial coated grains that are known today. They are mostly made of dolomite and, to a lesser extent, ankerite and show a concentric, radial-concentric, micritic and radial fabrics. The Sr content is variable among ooids with different fabrics, with the least amount in the radial ooids (ca.100-140ppm) and the highest amount in the concentric ooids (140-350 ppm). It is very likely that the primary chemical composition of radial ooids was different from that of radial-concentric and concentric ooids. It is possible that concentric ooids with a higher Sr content and better degree of fabric preservation had an aragonite precursor, while radial ooids with the least Sr content and poorer fabric preservation had a calcite precursor.

The mechanisms of ooid formation have long been debated. A number of formation processes have been suggested, including inorganic physico-chemical mechanisms in which carbonate ooids precipitated from agitated shallow-sea water supersaturated with calcium bicarbonate [1], and biologically-mediated mechanisms in which carbonate ooids were synthesized in the presence of humic acids [2].

Evidence from a combination of NanoSIMS ion mapping and scanning electron microscope (SEM) imaging, and Raman spectroscopic imaging of carbonaceous matter interwoven with the internal structure of ooids suggests that bacteria probably played an active role in the formation of the ooids. On the other hand, the mineralogical differences in the cortices of the ooids are suggested to have been a result of the degree of water agitation and the presence and concentration of specific organic acids in the environment at the time of carbonate precipitation. For example, it has been shown that the presence of certain organic acids cause Mg-calcite to crystallize from solutions which, in their absence, would crystallize aragonite [3].

In the Nsuze Group, the distribution of oolitic facies in the high-energy depositional settings of intertidal to shallow-subtidal and, to a lesser extent, to microbialite facies indicates that turbulent hydrodynamic conditions probably were controlling microbial communities that were responsible for determining ooids with different fabrics and mineralogy. It is likely that combinations of both biogenic and non-biogenic processes (hydrodynamic conditions) were responsible for ooid formation in the Nsuze Group.

References:

[1] Duguid SMA et al. (2010) J Sediment Res 80:236-251

[2] Brehm U et al. (2006) Geomicrobiol J 23:500-545

[3] Land LS et al. (1979) J Sediment Petrol 49(4):1269-1278

Paper Number: 866

The Mid-Archaean Pongola Supergroup: volcanism, sedimentation and early life development on Earth's oldest stable continental margin

Wilson, A.H.[1], Hofmann, A.[2] and Siahi, M.[1]

[1]School of Geosciences, University of the Witwatersrand, Johannesburg: allan.wilson@wits.ac.za
[2]Department of Geology, University of Johannesburg, Johannesburg

---

The Pongola Supergroup is the best preserved, lithologically continuous (270 km in length) and varied mid-Archaean volcano-sedimentary succession deposited c. 2.98 – 2.86 Ga ago on the SE side of the Kaapvaal Craton in South Africa and Swaziland. It consists of the lower Nsuze Group and the upper Mozaan Group. The Nsuze Group attains a maximum thickness in the north of 4500 m and is dominantly volcanic with increasing sedimentary components further south. The Mozaan Group has a thickness of 5000 m in the south and central areas and contains important volcanic and volcaniclastic units towards the top of the succession. Most of the volcanic rocks of the Nsuze group were deposited subaerially and although pillow lavas occur in some areas in the south they are highly vesicular and fragmented attesting to shallow water conditions. The sedimentary succession is dominated by shallow-marine sandstones and offshore shelf deposits of ferruginous shales and banded iron formations. Fluvial deposits are rare, but locally include conglomerate containing sub-economic gold and uranium mineralization.

The striking feature of the Pongola volcano-sedimentary belt is the high degree of preservation. In the northern area the stratigraphy is essentially flat lying and contrasts with the strongly deformed, pre-3.3 Ga granitoid-greenstone basement. The Pongola Supergroup, overall, represents volcanic and sedimentary deposits on a stable continental margin setting that has undergone extension producing strike-slip fault controlled basins in the upper part. Marked cyclicity both for the sedimentary units and the volcanic sequences is indicated, the latter encompassing the range from explosive to effusive lavas, and compositions from rhyolite through basalt to ultramafic remnants. Incompatible trace element ratios show differences between each volcanic segment indicating derivation from multiple sources with varying degrees of crustal contamination. An important feature throughout the entire belt is the substrate of granitoid basement (age c.3.32-3.25 Ga) which in many areas shows a well-developed palaeosol horizon, indicating denudation of the young craton prior to initiation of the Pongola Basin.

Rocks of the Pongola Supergroup therefore allow a detailed and comprehensive insight into the surface processes at that time and the interaction of sedimentation and volcanism. The interplay of shallow water, intertidal processes and volcanic activity would have provided an ideal habitat for the development of primitive life forms and these are indeed in evidence locally in the Nsuze Group. Laminated (stromatolite) and non-laminated microbialite types occur in a variety of tide-dominated shallow marine environments. An association with volcaniclastic sediments is frequently, but not always observed. Minor changes in the physical conditions of the environment may have influenced microbial assemblages and as a result changed microbialite morphologies. Therefore, differences in microbialite morphology, macrofabrics, and size within different sub-environments suggest that potentially distinct assemblages of microorganisms were present and responded differently to physical and environmental conditions.

There remain many outstanding geological issues to be resolved. Apart from further advancing the understanding of early life forms, these include the lithological correlations of the south region with the north. The high-Cr (of komatiite derivation) volcaniclastic rocks in the Mozaan Group appear to be geochemically identical to similar units in the supposed thrust sequence of the Ndikwe Formation in the south which is at variance with suggestions that the latter is the basal sequence of the entire Pongola Supergroup.